

Cyclic Inelastic Behavior of Concrete Filled Sandwich Panel Walls Subjected to In-Plane Flexure

by
Yasser Alzeni and Michel Bruneau



Technical Report MCEER-14-0009

December 19, 2014

NOTICE

This report was prepared by the University at Buffalo, State University of New York, as a result of research sponsored by the American Institute of Steel Construction. Neither MCEER, associates of MCEER, its sponsors, the University at Buffalo, State University of New York, nor any person acting on their behalf:

- a. makes any warranty, express or implied, with respect to the use of any information, apparatus, method, or process disclosed in this report or that such use may not infringe upon privately owned rights; or
- b. assumes any liabilities of whatsoever kind with respect to the use of, or the damage resulting from the use of, any information, apparatus, method, or process disclosed in this report.

Any opinions, findings, and conclusions or recommendations expressed in this publication are those of the author(s) and do not necessarily reflect the views of MCEER or other sponsors.

Cyclic Inelastic Behavior of Concrete Filled Sandwich Panel Walls Subjected to In-Plane Flexure

by

Yasser Alzeni¹ and Michel Bruneau²

Publication Date: December 12, 2014

Submittal Date: August 27, 2014

Technical Report MCEER-14-0009

This research was sponsored by the American Institute of Steel Construction.

- 1 Graduate Student, Department of Civil, Structural and Environmental Engineering, University at Buffalo, State University of New York
- 2 Professor, Department of Civil, Structural and Environmental Engineering, University at Buffalo, State University of New York

MCEER

University at Buffalo, State University of New York

212 Ketter Hall, Buffalo, NY 14260

E-mail: mceer@buffalo.edu; Website: <http://mceer.buffalo.edu>

Preface

MCEER is a national center of excellence dedicated to the discovery and development of new knowledge, tools and technologies that equip communities to become more disaster resilient in the face of earthquakes and other extreme events. MCEER accomplishes this through a system of multidisciplinary, multi-hazard research, in tandem with complimentary education and outreach initiatives.

Headquartered at the University at Buffalo, The State University of New York, MCEER was originally established by the National Science Foundation in 1986, as the first National Center for Earthquake Engineering Research (NCEER). In 1998, it became known as the Multidisciplinary Center for Earthquake Engineering Research (MCEER), from which the current name, MCEER, evolved.

Comprising a consortium of researchers and industry partners from numerous disciplines and institutions throughout the United States, MCEER's mission has expanded from its original focus on earthquake engineering to one which addresses the technical and socio-economic impacts of a variety of hazards, both natural and man-made, on critical infrastructure, facilities, and society.

The Center derives support from several Federal agencies, including the National Science Foundation, Federal Highway Administration, National Institute of Standards and Technology, Department of Homeland Security/Federal Emergency Management Agency, and the State of New York, other state governments, academic institutions, foreign governments and private industry.

This report presents the results of an experimental and analytical study on the in-plane flexural inelastic behavior of concrete filled sandwich steel panel walls. Four large scale walls were tested under cyclic loading; the tested walls included specimens with and without boundary elements, two different spacing of the tie bars, and effectiveness of tie bar connection details. The tested walls had an aspect ratio larger than two. Ductile performance was achieved by development of the plastic moment capacity of the cross section. All tested specimens showed stable ductile performance. Finite element analysis was used to establish models simulating the behavior of the tested specimens and to conduct limited parametric studies. Based on the experimental and analytical findings, seismic design recommendations were formulated.

ABSTRACT

Research was conducted on concrete filled steel sandwich panel walls (CFSSP-Walls) in order to investigate the ductility and seismic performance of this structural system under in-plane flexure. The research focused on walls which have an aspect ratio (height to cross section depth), h/W , over 2, such that the ductile behavior of the wall is induced by developing the plastic moment capacity of the cross section, M_p . Accordingly, an experimental program was executed at the Structural Engineering and Earthquake Simulation Laboratory (SEESL) at the University at Buffalo, followed by analytical investigation that involved plastic analysis, fiber analysis, and finite element analysis. The experimental and analytical results were used to develop seismic design recommendations for the CFSSP-Walls.

Previous studies on composite shear walls focused on walls that developed ductile behavior through shear yielding, with relatively little work available on walls that developed flexural yielding, as reflected in existing design recommendations in AISC 341-10.

In the experimental program, four CFSSP-Wall specimens were tested under quasi-static cyclic loading (following the ATC-24 protocols) and had a height to width ratio of 2.5 and 2.72, respectively. These walls were divided into two groups, namely: Group NB and B. Group NB consisted of walls with no boundary elements, where the end flanges of the specimens consisted of half round Hollow Steel Sections (HSS) in order to avoid stress concentration at the corner welds.

Group B specimens had full round HSS at their ends, which served as boundary elements, and again the two tested walls were different in their S/t ratio, which was taken to be equal to 25.6 in specimen CFSSP-B1 and 38.4 in specimen CFSSP-B2. Other differences from group B include the fact that specimen CFSSP-B2 tie bars were fillet welded to the web skin plates (instead of plug welded), and that fiber concrete was used in that specimen in an attempt to reduce the tension cracks in the concrete at ultimate behavior.

The four tested specimens were able to attain/exceed the expected plastic moment capacity and were able to sustain their load capacity up to a drift exceeding 3%, which emphasized the ductile behavior of these CFSSP-Walls.

The finite element method using ABAQUS 6.10EF2 explicit solver was then used to establish models to simulate the behavior of the tested walls, and the calibrated models were further used to conduct a limited

parametric study to investigate design parameters that were not covered in the experimental program. This included cases with S/t ratios of 50, D/t equal to 0.076 (E/F_y), and finally the use of thicker concrete (taken to be equal to $0.35b$ instead of $0.2b$, where b is the length of the steel web of the CFSSP-Wall).

Finally, the experimental and analytical results were used to develop design recommendations for CFSSP-B and CFSSP-NB walls, including expressions to limit the S/t and D/t ratios, and an expression to calculate the required diameter of the tie bars (based on the plastic deformation of the steel skin plate during local buckling). Simple plastic theory was used to derive expressions to calculate the plastic moment capacity of CFSSP-NB and CFSSP-B walls.

ACKNOWLEDGEMENT

The authors thank the staff of the Structural Engineering and Earthquake Simulation Laboratory (SEESL) at the University at Buffalo, and more specifically Mark Pitman, the late Duane Kozlowski, Robert Staniszewski, and Scott Weinreber, for their valuable contribution to execution of this project.

Sincere thanks also to Mr. Rafael Sabelli (Walter P. Moore Inc.) and Bob Hazelton (Herricks Co.) for their feedback and technical advice as part of a project advisory panel, as well as to Mr. Tom Schlafly, AISC Director of Research.

This research project was funded, in part, by the American Institute for Steel Construction (AISC) and by Egyptian Ministry of Higher Education. This support is sincerely appreciated. However, the opinions expressed in this report are those of the writers and do not reflect the views of the aforementioned sponsors.

TABLE OF CONTENTS

CHAPTER 1.....	1
INTRODUCTION	1
1.1. GENERAL.....	1
1.2. SCOPE AND OBJECTIVE	3
1.3. REPORT ORGANIZATION	4
CHAPTER 2.....	7
LITERATURE REVIEW	7
2.1 INTRODUCTION	7
2.2 COMPOSITE ORDINARY/SPECIAL SHEAR WALLS (C-OSW AND C-SSW)	8
2.2.1 General.....	8
2.2.2 Differences between C-OSW and C-SSW	8
2.2.3 Examples of Past Research on Ductility and Performance of Reinforced Concrete Shear Walls with Structural Steel.....	9
2.2.4 AISC and ASCE Requirements for the Seismic Design of C-OSW/C-SSW.....	15
2.3 COMPOSITE PLATE SHEAR WALLS (C-PSW)	17
2.3.1 General.....	17
2.3.2 C-PSW with VBE and HBE	18
2.3.3 C-PSW Composed of Steel Sandwich Panel Filled with Concrete.....	26
2.4 SUMMARY.....	50
CHAPTER 3.....	53
PRELIMINARY INVESTIGATION OF CFSSP-WALL CONCEPT	53
3.1 INTRODUCTION	53
3.2 PRELIMINARY ANALYTICAL INVESTIGATION AND BEHAVIOR OF CFSSP-WALLS	54
3.3 EXAMPLE OF CFSSP-WALL INVESTIGATED	55
3.4 ANALYSIS OF CFSSP-WALL CROSS-SECTION USING PLASTIC STRESS DISTRIBUTION.	56
3.5 ANALYSIS OF THE RECTANGULAR CFSSP-WALL USING XTRACT	59
3.6 ANALYSIS OF CFSSP-WALLS USING FINITE ELEMENT.....	60
3.6.1 General.....	61
3.6.2 Finite Elements Selection	61
3.6.3 Steel Material Model	65
3.6.4 Concrete Material Model.....	65
3.6.5 Boundary Conditions and Loading	73
3.6.6 Pushover Analysis	74
3.6.7 Evaluation of the Pushover Loading Results	76
3.6.8 Cyclic Loading of the Rectangular CFSSP-Wall Finite Element Model.....	94
3.7 ANALYSIS FOR RECTANGULAR CFSSP-WALLS AVAILABLE IN LITERATURE	95
3.7.1 General.....	95
3.7.2 Plastic Analysis of the Cross-Section	96
3.7.3 XTRACT Fiber Analysis	97
3.7.4 Finite Element Analysis Using Abaqus	98
3.7.5 Summary of Analysis.....	103

CHAPTER 4.....	105
EXPERIMENTAL PROGRAM.....	105
4.1 INTRODUCTION	105
4.2 CROSS SECTIONS OF THE TESTED CFSSP-WALLS SPECIMENS.....	105
4.3 MATERIALS.....	108
4.3.1 Concrete.....	108
4.3.2 Steel.....	109
4.4 TEST SETUP COMPONENTS.....	112
4.4.1 General.....	112
4.4.2 Actuator Type.....	114
4.4.3 Head Plate and Threaded Bars.....	114
4.4.4 Foundation and Strong Floor Connection.....	115
4.4.5 Load Transfer to Reinforced Concrete Foundation.....	117
4.4.6 Side Restraint System.....	123
4.5 SPECIMEN ASSEMBLY.....	126
4.6 INSTRUMENTATION.....	134
4.6.1 Strain Gauges.....	134
4.6.2 Displacement Potentiometers.....	135
4.6.3 Krypton Dynamic Measurement System.....	144
4.6.4 Video Recording.....	146
CHAPTER 5.....	147
EXPERIMENTAL RESULTS AND OBSERVATIONS	147
5.1 GENERAL.....	147
5.2 LOADING PROTOCOL.....	147
5.3 TEST OBSERVATIONS.....	149
CHAPTER 6.....	191
TEST DATA ANALYSIS.....	191
6.1 INTRODUCTION	191
6.2 DATA ANALYSIS.....	191
6.2.1 General.....	191
6.2.1 Strain Distribution for Specimen CFSSP-NB1.....	191
6.2.2 Displacement Ductility Assessment for Specimen CFSSP-NB1.....	193
6.2.4 Curvature Ductility for Specimen CFSSP-NB1.....	196
6.2.5 Shape Factor for Specimen CFSSP-NB1.....	205
6.2.6 Shear Analysis for Specimen CFSSP-NB1.....	205
6.2.7 Strain Distribution for Specimen CFSSP-NB2.....	208
6.2.8 Displacement Ductility of Specimen CFSSP-NB2.....	210
6.2.9 Curvature Ductility of Specimen CFSSP-NB2.....	210
6.2.10 Strain Distribution for Specimen CFSSP-B1.....	214
6.2.11 Displacement Ductility for Specimen CFSSP-B1.....	216
6.2.12 Curvature Ductility for Specimen CFSSP-B1.....	217
6.2.13 Shape Factor for Specimen CFSSP-B1.....	218
6.2.14 Strain Distribution for Specimen CFSSP-B2.....	221
6.2.15 Displacement Ductility for Specimen CFSSP-B2.....	223
6.2.16 Curvature Ductility for Specimen CFSSP-B2.....	224

6.3	SUMMARY OF TEST RESULTS	227
CHAPTER 7.....	229
ANALYSIS OF THE CFSSP-WALLS	229
7.1	INTRODUCTION	229
7.2	ANALYSIS USING XTRACT	230
7.2.1	General.....	230
7.2.2	Specimen CFSSP-NB	230
7.2.3	Specimen CFSSP-B	232
7.3	FINITE ELEMENT ANALYSIS.....	233
7.3.1	General.....	233
7.3.2	Type of Finite Elements Used.....	234
7.3.3	Modeled Material Properties.....	234
7.3.4	Interaction between Different Components of the Model.....	241
7.3.5	Criteria for Analysis Acceptance and Parameters.....	241
7.3.6	Specimen CFSSP-NB1 Simulation.....	241
7.3.7	Specimen CFSSP-NB2 Simulation.....	247
7.3.8	Specimen CFSSP-B Simulation.....	250
7.3.9	Parametric Study on the CFSSP-Walls.....	254
7.4	SUMMARY.....	260
CHAPTER 8.....	263
CFSSP-WALLS DESIGN PROCEDURE.....	263
8.1	INTRODUCTION	263
8.2	SEISMIC DESIGN RECOMMENDATIONS FOR CFSSP-WALL DESIGN	264
8.2.1	Introduction.....	264
8.2.2	ASCE Seismic Design Recommendations for CFSSP-Walls	264
8.2.3	AISC Seismic Design Recommendations.....	265
8.3	PLASTIC MOMENT CAPACITY OF THE CFSSP-WALL	266
8.4	LOCAL BUCKLING OF THE CFSSP-WALL	272
8.4.1	Theoretical Plate Buckling Equation	272
8.4.2	Elastic Buckling of Skin Plate	273
8.5	DESIGN OF THE TIE BARS.....	274
8.6	EQUIVALENT ELASTIC STIFFNESS	276
8.7	PROPOSED DEFORMATION LIMIT FOR THE CFSSP-WALLS	277
8.8	PROPOSED DESIGN PROCEDURE FOR CFFSP-WALLS	279
8.8.1	Preliminary Dimensions of the CFSSP-Wall Cross-section	279
8.9	DESIGN EXAMPLE	290
8.9.1	Building Description and Proposed Lateral Load Resisting System	290
8.9.2	Construction Materials used for the CFSSP-Walls	290
8.9.3	Seismic Loads.....	290
8.9.4	Design of the CFSSP-Walls.....	294
8.9.5	Design Procedure of CFSSP-Wall.....	294
CHAPTER 9.....	303
SUMMARY, CONCLUSIONS, AND RECOMMENDATIONS FOR FUTURE WORK.....	303
9.1	SUMMARY.....	303
9.2	CONCLUSIONS.....	304

9.3	RECOMMENDATIONS FOR FUTURE WORK.....	305
CHAPTER 10.....	307
REFERENCES	307
APPENDIX A.....	311
EXCERPT OF TEST SETUP CONSTRUCTION DRAWING	311
APPENDIX B.....	317
SPECIMEN DESIGN.....	317
B.1	INTRODUCTION	317
B.2	PLASTIC MOMENT CAPACITY OF THE CFSSP-NB SANDWICH WALL SPECIMEN	317
B.3	MOMENT CAPACITY OF CFSSP-NB SANDWICH WALLS USING PLASTIC ANALYSIS	318
B.4	MOMENT CAPACITY OF CFSSP-NB SANDWICH WALLS USING FIBER ANALYSIS	324
B.5	PLASTIC MOMENT CAPACITY OF THE CFSSP-B WALLS	326
B.6	DESIGN OF THE TEST RIG COMPONENTS	331
B.6.1	Actuator Type	332
B.6.2	Head Plate Design.....	333
B.6.3	Threaded Bars at the Head Plate	336
B.7	LOAD TRANSFER TO THE FOUNDATION.....	336
B.8	LOAD TRANSFER AT THE WEB USING REINFORCEMENT BARS	337
B.9	LOAD TRANSFER AT THE FLANGES USING ANNULAR RINGS	341
B.10	FOUNDATION DESIGN	351
B.11	CHECK FOR FOUNDATION SLIDING	361
B.12	DESIGN OF LIFTING POINTS	361
B.13	DESIGN OF THE LATERAL SUPPORT SYSTEM.....	362
B.14	STABILITY OF THE SPECIMEN DURING CONSTRUCTION	372
APPENDIX C.....	373
EXCERPTS FROM XTRACT ANALYSIS.....	373

LIST OF FIGURES

Figure 2-1 Typical Cross Section for the C-OSW/CSSW, AISC-341 (2010)	9
Figure 2-2 Tested Composite Reinforced Concrete Wall Specimens, Cho et al (2004).....	10
Figure 2-3 Tested Composite Reinforced Concrete Wall Specimens, Dan et al. (2011).....	11
Figure 2-4 Material Model Used for Finite Element, Dan et al. (2011)	12
Figure 2-5 Force -Displacement Relationship a) Experimental-b) Analysis, Dan et al. (2011)	12
Figure 2-6 Tested Specimen with Steel Boundary Elements, Liao et al. (2012)	13
Figure 2-7 Specimens Simulated with ABAQUS, Liao et al. (2012)	13
Figure 2-8 Finite Elements Analysis against Test Results, Liao et al. (2012)	14
Figure 2-9 Different Configuration for C-PSW, AISC-341 (2010).....	18
Figure 2-10 Configuration of Composite Shear Walls tested by Astaneh-Asl and Zhao (2001).....	19
Figure 2-11 Gap between Reinforced Concrete Infill and Steel Frame, Zhao and Astaneh-Asl (2004) ...	20
Figure 2-12 Tested Specimen and Test Rig, Zhao and Astaneh-Asl (2004).....	21
Figure 2-13 Test Results for the First Story, Zhao and Astaneh-Asl (2004)	21
Figure 2-14 Finite Elements Model of C-PSW, Zhao and Astaneh-Asl (2007)	22
Figure 2-15 Comparison of Experimental and Analytical Push-over Curves for C-PSW, Zhao and Astaneh-Asl (2007).....	23
Figure 2-16 Calibration of Finite Elements Models, Rahai and Hatami (2009)	24
Figure 2-17 Results for the Numerical Analysis, Rahai and Hatami (2009)	24
Figure 2-18 Test Set-up Arabzadeh et al. (2011).....	25
Figure 2-19 Comparative Study, Arabzadeh et al. (2011)	26
Figure 2-20 Schematic Diagram for the Composite Wall, Wright (1998).....	28
Figure 2-21 Different Loading Methods in the Experimental Program, Wright (1998).....	28
Figure 2-22 General Details of Shear Rig, Hossain and Wright (1998)	29
Figure 2-23 Cross section of SC Walls, Ozaki et al. (2004)	31
Figure 2-24 Test Specimen and Test Set-up, Ozaki et al. (2004)	32
Figure 2-25 Membrane Forces Calculated by the MBM, Varma et al. (2011)	33
Figure 2-26 Free Body Diagram and Force Equilibrium SC Cross-section, Varma et al. (2011)	34
Figure 2-27 Interaction Surface for Composite SC Wall Panels in Principle Force Space, Ozaki et al (2004).....	35
Figure 2-28 Interaction Surface in Principle Force Space for Each Notional Half, Ozaki et al (2004).....	35
Figure 2-29 Tested Specimen with and without Shear Reinforcement, Varma et al. (2011)	37
Figure 2-30 Force- Displacement for Typical Specimen, Varma et al. (2011).....	37
Figure 2-31 Flexural Stiffness of SC Cracked Transformed Section, Sener et al. (2012)	38
Figure 2-32 In-plane Shear Behavior of SC Walls, Sener et al. (2012).....	39
Figure 2-33 Bi-Steel Product COREFAST a) Single Units, b) Assembled Core, Bi-steel Corus (2007)...	41
Figure 2-34 Forty Spring Garden Manchester's Financial District, Corus (2006)	42
Figure 2-35 Dunderum Cinema Lift Core, Corus (2004)	42
Figure 2-36 Birmingham 1, Tallest Core Fast (16--story), Corus (2006).....	42
Figure 2-37 Finite Element Model and Simulated Bi-steel Beam, Foundoukos and Chapman (2008)....	44
Figure 2-38 Results of Parametric Study, Foundoukos and Chapman (2008).....	45
Figure 2-39 Secant Stiffness for SC Walls, Sener et al. (2012)	46

Figure 2-40 Tested Specimens, Eom et al (2009).....	47
Figure 2-41 Force Displacement Relationship for the Tested Specimens, Eom et al. (2009)	48
Figure 3-1 Proposed Rectangular CFSSP-Wall Cross-section Configuration	53
Figure 3-2 Dimensions of the CFSSP-Wall Example.....	56
Figure 3-3 Plastic Stress Distribution on the Proposed CFSSP-Wall	57
Figure 3-4 Unconfined Bilinear Concrete Model Used in the Analysis	59
Figure 3-5 Moment Curvature Relationship for the Rectangular Section, XTRACT.....	60
Figure 3-6 CFSSP-Wall Steel Skin Modeled Using C3D8R ABAQUS Element	62
Figure 3-7 CFSSP-Wall Concrete Core Modeled Using C3D8R Abaqus Element.....	63
Figure 3-8 Tie Bars were Modeled Using Beam Element B31 in ABAQUS	63
Figure 3-9 Concrete Damage Plasticity Model, ABAQUS 6.10EF2 User's Manual.....	67
Figure 3-10 Cyclic Behavior of CDP Model, ABAQUS 6.10EF2 User's Manual	68
Figure 3-11 Yield Surface in the Deviatoric Plane Corresponding to Different Values of K_c , ABAQUS 6.10 EF2.....	70
Figure 3-12 Stress Strain Curve for Confined Concrete in CFST Beam-Column, Liang (2008).....	71
Figure 3-13 Uni-axial Compression Stress/Strain Relationship Used for the CDP Model.....	72
Figure 3-14 Model Boundaries, Loaded End, and Fixed Base	74
Figure 3-15 Base Shear vs Lateral Drift% for the Rectangular CFSSP-Wall.....	76
Figure 3-16 Longitudinal Stress Distribution, S33, at 0.5% Drift	77
Figure 3-17 Longitudinal Stress Distribution in CFSSP-Wall at Lower 5 Feet: (a) 0.5% Drift;(b) 1% Drift	79
Figure 3-18 Longitudinal Stress Distribution in Steel Skin Plate at Lower 5 Feet: (a) 1.5% Drift;(b) 2.0% Drift.....	80
Figure 3-19 Longitudinal Stress Distribution in the Steel Skin Plate at Lower 5% Feet: (a) 3% Drift; (b) 4% Drift	81
Figure 3-20 Behavior of Skin Plate Post Local Buckling	82
Figure 3-21 Longitudinal Stress Distribution at 8 inches from base for Different Drift Values	84
Figure 3-22 Longitudinal Stress Distribution at 16 inches from Base for Different Drift Values.....	84
Figure 3-23 Longitudinal Stress Distribution in Concrete at 8 inches from Fixed Base: (a) 0.5% Drift; (b) 1% Drift	87
Figure 3-24 Longitudinal Stresses in Concrete at 8 inches from Fixed Base: (a) 1.5% Drift; (b) 2.0% Drift	88
Figure 3-25 Longitudinal Stress Distribution in Concrete at 8 inches from Base: (a) 3.0 % Drift: (b) 4.0% Drift.....	89
Figure 3-26 Average Stress Distribution across the CFSSP-Wall Cross-section	90
Figure 3-27 Longitudinal Plastic Strain Distribution in Concrete at 8" from base:(a) 0.5% Drift;(b) 1.0% Drift.....	91
Figure 3-28 Longitudinal Strain Distribution in Concrete at 8" from Base:(a) 1.5% Drift;(b)2.0% Drift .	92
Figure 3-29 Longitudinal Strain Distribution in Concrete at 8" From Base:(a) 3.0% Drift;(b) 4.0% Drift	93
Figure 3-30 Cyclic Response of Rectangular CFSSP-Wall.....	94
Figure 3-31 Test Results for Rectangular "Isolated" Composite Walls, Eom et al (2009)	95
Figure 3-32 Proposed Stress Distribution on the Tested Walls	96
Figure 3-33 Unconfined Concrete Material Model used in XTRACT Analysis	98
Figure 3-34 Moment Curvature Relationship for the Tested Walls by XTRACT.....	98

Figure 3-35 Stress Distribution in the Tested Walls at 1% Drift	99
Figure 3-36 Onset of Local Buckling at a lateral Drift of 1%	100
Figure 3-37 Visual Local Buckling of the Skin Plate at 1.5% Drift	100
Figure 3-38 Moment vs Lateral Drift, Abaqus Analysis.....	101
Figure 3-39 Cyclic Response of the Abaqus Model for Isolated Specimens Tested by Eom et al (2009)	102
Figure 3-40 Local Buckling of the Skin Plate at 1% Drift for Walls Tested by Eom et al (2009)	102
Figure 4-1 Cross Sections of Group NB Specimens.....	106
Figure 4-2 Cross Sections of Group B Specimens.....	107
Figure 4-3 NOVOCON Steel Fibers used in Specimen CFSSP-B2, http://www.novocon.co.nz	108
Figure 4-4 Tension Coupon Result for HSS from Flange/Boundary Element of CFSSP-Wall.....	110
Figure 4-5 Tension Coupon Result for Plate from CFSSP-Wall Web.....	112
Figure 4-6 Elevation of Specimen CFSSP-NB1 Setup	114
Figure 4-7 Head Plate Dimensions	115
Figure 4-8 Footing Footprint and DYWIDAG Location	116
Figure 4-9 CFSSP-NB1 and Web Re-bar Connectors	120
Figure 4-10 CFSSP-NB2 and Web Re-bar Connectors	120
Figure 4-11 CFSSP-B1 and Web Re-bar Connectors	121
Figure 4-12 CFSSP-B2 and Web Re-bar Connectors	121
Figure 4-13 Stiffened Annular ring for Group NB Specimens	122
Figure 4-14 Stiffened Annular Ring used for Group B Specimens	122
Figure 4-15 Re-bars Used to Transfer the Web Forces and Foundation Reinforcement	123
Figure 4-16 Side Restraint System.....	125
Figure 4-17 Parts of Lateral Restraint System	126
Figure 4-18 Water Jet Cutting of HSS	127
Figure 4-19 Welding between Half HSS and Steel Web Plate	127
Figure 4-20 Assembly of CFFSP-NB1 Specimen	128
Figure 4-21 Base of Specimen CFSSP-B1	128
Figure 4-22 Welding Pipe Sleeves for the Steel Cage	129
Figure 4-23 Setting CFSSP-Wall in Position.....	131
Figure 4-24 Stiffened Annular Ring and CFSSP-Wall Positioning.....	131
Figure 4-25 Web Re-bars and Stirrups	132
Figure 4-26 Final Assembly for the Foundation Re-bars.....	132
Figure 4-27 Shoring of Specimen Preparing for Concrete Pouring	133
Figure 4-28 Specimen CFSSP-NB1 After Concrete Pouring	133
Figure 4-29 Tested CFSSP-Wall Specimen after Erection of Lateral Restraint System	134
Figure 4-30 North South View of Strain Gauges Arrangement of Specimen CFSSP-NB1	136
Figure 4-31 North South View of Strain Gauges Arrangement of Specimen CFSSP-NB2	137
Figure 4-32 North South View of Strain Gauges Arrangement of Specimen CFSSP-B1	138
Figure 4-33 North South View of Strain Gauges Arrangement of Specimen CFSSP-B2	139
Figure 4-34 Liner Potentiometers Arrangement	140
Figure 4-35 Schematic Diagram for a Typical West Side View of Tested CFSSP-Wall Specimen	141
Figure 4-36 Schematic Diagram for a Typical West Side View of Tested CFSSP-Wall Specimen	142
Figure 4-37 String Potentiometers Arrangement East Side	143
Figure 4-38 Typical Layout of String Potentiometers	144

Figure 4-39 Krypton Camera LEDs Distribution for Specimen CFSSP-B2.....	145
Figure 5-1 North West View for Specimen CFSSP-NB1 at 0.2% Drift.....	150
Figure 5-2 North West View for Specimen CFSSP-NB1 at 0.4% Drift.....	151
Figure 5-3 North West View for Specimen CFSSP-NB1 at 0.6% Drift.....	154
Figure 5-4 North West View for Specimen CFSSP-NB1 at 0.9% Drift.....	154
Figure 5-5 North West View for Specimen CFSSP-NB1 at 1.2% Drift.....	154
Figure 5-6 North West View for Specimen CFSSP-NB1 at 1.8% Drift.....	155
Figure 5-7 South West View for Specimen CFSSP-NB1 at 1.8% Drift.....	155
Figure 5-8 Buckling Wave Between First and Second Row of Tie Bars at 1.8%	156
Figure 5-9 Local Buckling of the HSS Part at 2.4% Drift	156
Figure 5-10 Specimen CFSSP-NB1 Tie Bars Plug Welding Cracks at 2.4% Drift.....	156
Figure 5-11 Specimen CFSSP-NB1 Tie Bars Plug Welding Cracks Near Mid Cross-section at 2.4% Drift	157
Figure 5-12 Plug Welding Fracture on the Full Diameter of the Tie Bar at 3% Drift	157
Figure 5-13 Propagation of Cracks from Tie Bar Circumference on East Side to CFSSP-NB1 Skin Plates at 3% Drift.....	158
Figure 5-14 Propagation of Cracks on the West Side Tie Bar Circumference to CFSSP-NB1 Skin Plates at 3% Drift	158
Figure 5-15 First Crack in the HSS Part of the CFSSP-NB1 at West side at 3.6% Drift	158
Figure 5-16 Fracture of the CFSSP-NB1 Specimen West Side at 3.6% Drift.....	159
Figure 5-17 Fracture of the CFSSP-NB1 Specimen East Side at 3.6% Drift	159
Figure 5-18 Propagation of Fracture of the CFSSP-NB1 for Specimen East Side at 3.6% Drift	160
Figure 5-19 The Cut Cross-section Part of Specimen CFSSP-NB1 attached to Foundation.....	160
Figure 5-20 North West View for Specimen CFSSP-NB2 at 0.4% Drift.....	162
Figure 5-21 North west View for Specimen CFSSP-NB2 at 0.6% Drift.....	163
Figure 5-22 South West View for Specimen CFSSP-NB2 at 1.2% Drift.....	163
Figure 5-23 Flaking of Paint on Tie Bar Perimeter of Specimen CFSSP-NB2 at 1.2% Drift	164
Figure 5-24 First Wave of Local Buckling Specimen, North West Side, CFSSP-NB2 at 1.8% Drift.....	164
Figure 5-25 First Wave of Local Buckling Specimen, South East Side, CFSSP-NB2 at 1.8% Drift.....	165
Figure 5-26 Fracture of Plug Weld at Half Diameter of Tie Bar of CFSSP-NB2 at 1.8% Drift	165
Figure 5-27 Local Buckling of the HSS Part in Specimen CFSSP-NB2 at 2.4% Drift.....	166
Figure 5-28 Propagation of Cracks in the Steel Web Specimen CFSSP-NB2 at 2.4% Drift.....	166
Figure 5-29 Propagation of Local Buckling in Specimen CFSSP-NB2 at 3% Drift	167
Figure 5-30 Fracture Propagation from Tie Bars Circumference in CFSSP-NB2 at 3.0% Drift.....	167
Figure 5-31 Fracture Propagated in the HSS part of Specimen CFSSP-NB2 at 3.0% Drift.....	168
Figure 5-32 Failure of Plug Weld for Inner Tie Bars of Specimen CFSSP-NB2 at 3.0% Drift	168
Figure 5-33 Propagation of Cracks in Specimen CFSSP-NB2 at 3.6% Drift.....	169
Figure 5-34 Crushed Concrete Debris Spalling from Cracked Skin of CFSSP-NB2 at 3.6% Drift	169
Figure 5-35 Fracture of Specimen CFSSP-NB2 at 4.2% Drift	170
Figure 50-36 South West View of the Specimen CFSSP-B1 at 0.67% Drift	172
Figure 5-37 South East View of Specimen CFSSP-B1 at 1% Drift.....	173
Figure 5-38 South West View Specimen CFSSP-B1 at 1.33% Drift	173
Figure 5-39 Full Diameter Cracks in the Tie Bars Plug Welding of Specimen CFSSP-B1 at 2% Drift ..	174
Figure 5-40 Half Diameter Crack of Inner Tie Bar Plug Welding of Specimen CFSSP-B1 at 2% Drift .	174

Figure 5-41 Local Buckling of Web Plate for Specimen CFSSP-B1 at 2% Drift	175
Figure 5-42 Half Diameter Fracture of Tie Bars Plug Welding of CFSSP-B1 at 2% Drift.....	175
Figure 5-43 Local Buckling of the HSS in Specimen CFSSP-B1 at 2.67% Drift	176
Figure 5-44 Crack in Foundation Top Cover of Specimen CFSSP-B1 at 2.67% Drift	176
Figure 5-45 Fracture of Plug Welding of an Inner Tie Bar of Specimen CFSSP-B1 at 3.33% Drift	177
Figure 5-46 Fracture Propagation at Specimen CFSSP-B1 at 3.33% Drift	177
Figure 5-47 Fracture Propagation Pattern in Specimen CFSSP-B1 at 4% Drift.....	178
Figure 5-48 Fracture of the HSS Portion of Specimen CFSSP-B1 at 4% Drift.....	178
Figure 5-49 Cut Base of Specimen CFSSP-B1 After Testing	179
Figure 5-50 Condition of Concrete in the Buckled Zone of Specimen CFSSP-B1	179
Figure 5-51 South West View Specimen CFSSP-B2 at 0.56% Drift	182
Figure 5-52 South West View Specimen CFSSP-B2 at 1% Drift	182
Figure 5-53 South West View Specimen CFSSP-B2 at 1.33% Drift	183
Figure 5-54 Onset of Local Buckling for Specimen CFSSP-B2 at 2% Drift.....	183
Figure 5-55 Local Buckling of Specimen CFSSP-B2 at 2.67% Drift.....	184
Figure 5-56 HSS Local Buckling in Specimen CFSSP-B2 at 2.67% Drift.....	184
Figure 5-57 Local Buckling of HSS in Specimen CFSSP-B2 at 2.67% Drift	185
Figure 5-58 South West View Specimen CFSSP-B2 at 3.33% Drift	185
Figure 5-59 Cracks in the Tie Bar Fillet Welds of CFSSP-B2 at 3.33% Drift	186
Figure 5-60 Intact Welding for Intermediate Tie Bar of Specimen CFSSP-B2 at 4% Drift.....	186
Figure 5-61 Propagation of Cracks at Outer Tie Bars in Specimen CFSSP-B2 at 4% Drift	187
Figure 5-62 Spalling of Crushed Concrete in Specimen CFSSP-B2 at 4% Drift	187
Figure 5-63 Fracture of the HSS Part of CFSSP-B2 at 4.67% Drift.....	188
Figure 5-64 Propagation of Crack from Web to HSS of Specimen CFSSP-B2 at 4.67% Drift.....	188
Figure 5-65 Base Fracture of Specimen CFSSP-B2 at 4.67% Drift	189
Figure 5-66 Cut Base of Specimen CFSSP-B2 After Testing	189
Figure 5-67 The Intact Steel Fiber Used in the Filled-in Concrete Mix	190
Figure 6-1 Vertical Axial Strain Distribution across CFSSP-NB1 Steel Skin at 10 inch from Base	194
Figure 6-2 Vertical Axial Strain Distribution Across CFSSP-NB1 Steel Skin at 16 inch from Base	194
Figure 6-3 Force vs Displacement Relationship for Specimen CFSSP-NB1	195
Figure 6-4 Force Displacement Envelope and Ductility Evaluation for CFSSP-NB1	195
Figure 6-5 Moment vs Curvature for Specimen CFSSP-NB1 at 2 inch from Base.....	200
Figure 6-6 Moment vs Curvature for Specimen CFSSP-NB1 at 6 inch from Base.....	200
Figure 6-7 Moment vs Curvature for Specimen CFSSP-NB1 at 10 inch from Base.....	200
Figure 6-8 Moment vs Curvature for Specimen CFSSP-NB1 at 14 inch from Base.....	201
Figure 6-9 Moment vs Curvature for Specimen CFSSP-NB1 at 18 inch from Base.....	201
Figure 6-10 Moment vs Curvature for Specimen CFSSP-NB1 at 22 inch from Base.....	201
Figure 6-11 Moment vs Curvature for Specimen CFSSP-NB1 at 15 inch from Base.....	202
Figure 6-12 Curvature Distribution along CFSSP-NB1 at 0.6% and 1.8% Drift	204
Figure 6-13 Typical 45° Rectangular Rosette gage, http://www.ecourses.ou.edu/cgi-bin	207
Figure 6-14 Shear Strain Distribution Across the Steel Web of Specimen CFSSP-NB1	208
Figure 6-15 Vertical Axial Strain Distribution Across CFSSP-NB2 Steel Skin at 12 inch from Base	209
Figure 6-16 Vertical Axial Strain Distribution Across CFSSP-NB2 Steel Skin at 22 inch from Base	209
Figure 6-17 Actuator Force vs Lateral Displacement, Specimen CFSSP-NB2.....	210

Figure 6-18 Moment vs Curvature using Linear Potentiometers at 2 inch from Base , CFSSP-NB2	212
Figure 6-19 Moment vs Curvature using Linear Potentiometers at 6 inch from Base, CFSSP-NB2	212
Figure 6-20 Moment Vs Curvature using Linear Potentiometer at 10 inch from Base, CFSSP-NB2	213
Figure 6-21 Moment vs Curvature using Linear Potentiometer at 18 inch from Base, CFSSP-NB2	213
Figure 6-22 Moment vs Curvature using Linear Potentiometer at 22 inch from Base, CFSSP-NB2	213
Figure 6-23 Moment vs Curvature using String Potentiometers at 15 inch from Base, CFSSP-NB2	214
Figure 6-24 Curvature Distribution along the Length of Specimen CFSSP-NB2	214
Figure 6-25 Vertical Axial Strain Distribution Across CFSSP-B1 Steel Skin at 10 inch from Base	215
Figure 6-26 Vertical Axial Strain Distribution Across CFSSP-B1 Steel Skin at 16 inch from Base	215
Figure 6-27 Actuator Force vs Lateral Drift for Specimen CFSSP-B1	216
Figure 6-28 Moment Vs Curvature using Linear Potentiometer at 2 inch from Base, CFSSP-B1	218
Figure 6-29 Moment Vs Curvature using Linear Potentiometer at 6 inch from Base, CFSSP-B1	218
Figure 6-30 Moment Vs Curvature Linear Potentiometer at 10 inch from Base, CFSSP-B1	219
Figure 6-31 Moment vs Curvature using Linear Potentiometer at 2 inch from Base, CFSSP-B1	219
Figure 6-32 Moment vs Curvature using Linear Potentiometer at 6 inch from Base, CFSSP-B1	219
Figure 6-33 Moment vs Curvature using Linear Potentiometer at 10 inch from Base, CFSSP-B1	220
Figure 6-34 Moment vs Curvature using Linear Potentiometer at 15 inch from Base, CFSSP-B1	220
Figure 6-35 Curvature Distribution along the Length of Specimen CFSSP-B1	221
Figure 6-36 Vertical Axial Strain Distribution across CFSSP-B2 Steel Skin at 12 inch from Base	222
Figure 6-37 Vertical Axial Strain Distribution Across CFSS-B2 Steel Skin at 22 inch from Base	222
Figure 6-38 Actuator Force Vs Lateral Drift for Specimen CFSSP-B2	223
Figure 6-39 Moment Vs Curvature using Linear Potentiometer at 2 inch from Base, CFSSP-B2	225
Figure 6-40 Moment vs Curvature using Linear Potentiometer at 6 inch from Base, CFSSP-B2	225
Figure 6-41 Moment vs Curvature using Linear Potentiometer at 10 from Base, CFSSP-B2	225
Figure 6-42 Moment vs Curvature using Linear Potentiometer at 14 inch from Base, CFSSP-B2	226
Figure 6-43 Moment vs Curvature using Linear Potentiometer at 18 inch from Base, CFSSP-B2	226
Figure 6-44 Moment vs Curvature using Linear Potentiometer at 22 inch from Base, CFSSP-B2	226
Figure 6-45 Moment vs Curvature using String Potentiometer at 15 inch from Base, CFSSP-B2	227
Figure 7-1 Confined Concrete Model Used in XTRACT Analysis	230
Figure 7-2 Moment Curvature Relation for Specimen CFSSP-NB in Xtract Analysis	231
Figure 7-3 Moment Curvature Relationship for Specimen CFSSP-B in XTRACT	233
Figure 7-4 Concrete Backbone Curve Constructed for CFSSP-NB1Abaqus Model	235
Figure 7-5 Average True Stress-True Strain for HSS	237
Figure 7-6 Average True Stress-Strain for the Steel Web	237
Figure 7-7 Typical uniaxial Stress-Strain Response of a metal Specimen, Abaqus User's Manual	238
Figure 7-8 Calculation of the Damage Factor, Abaqus user's Manual	239
Figure 7-9 Damage factor vs Plastic Displacement (Abaqus User's Manual)	240
Figure 7-10 Analysis of Specimen CFSSP-NB1 using Abaqus, Stress distribution shown at 0.6% Drift	244
Figure 7-11 Local Buckling of the Web Plate at 1.8% Drift	244
Figure 7-12 Buckling of the HSS Part of CFSSP-NB1 at 2.4% Drift	245
Figure 7-13 Force Displacement Relationship for Specimen CFSSP-NB1, Abaqus vs Test Values	245
Figure 7-14 Elastic Stiffness of the Modeled CFSSP-NB1, Fixed Base Model	246
Figure 7-15 Full Model of Tested Specimen CFSSP-NB1	246
Figure 7-16 Deflected Shape for the Tested Specimen, Full Model	247

Figure 7-17 Comparison Test results to Analysis Results for Specimen CFSSP-NB2	248
Figure 7-18 Fixed Base Abaqus Model for Specimen CFSSP-NB2, 0.6% Drift.....	248
Figure 7-19 Local Buckling of the Web Plate at 1.2% Drift, CFSSP-NB2 Abaqus Model.....	249
Figure 7-20 Buckling of the HSS part for the CFSSP-NB2 Model	249
Figure 7-21 Local Buckling of the Skin Plate for Specimen CFSSP-NB2 at 2.8% Drift	250
Figure 7-22 Force Displacement Relationship for Specimen CFSSP-B1	251
Figure 7-23 Model for Specimen CFSSP-B1	251
Figure 7-24 Skin Plate and Tie Bars for Specimen CFSSP-B1	252
Figure 7-25 Buckled Web at 1.67% Drift, Abaqus Model CFSSP-B1	252
Figure 7-26 Buckling of the Round HSS of Specimen CFSSP-B1	253
Figure 7-27 Force Displacement Relationship for Specimen CFSSP-B2.....	253
Figure 7-28 Model for CFSSP-NB-M1	256
Figure 7-29 Base Shear vs Lateral Drift for CFSSP-NB-M1 Wall.....	257
Figure 7-30 Model CFSSP-NB-M2 Stress Contours	258
Figure 7-31 Longitudinal Stresses in CFSSP-NB-M3 Wall Skin Plate.....	259
Figure 7-32 Force Displacement relationship for CFSSP-NB-M3	259
Figure 8-1 Schematic Diagram for Stress Distribution on CFSSP-NB cross-section.....	268
Figure 8-2 Schematic Diagram for Stress Distribution on CFSSP-B Cross-section.....	270
Figure 8-3 Buckling of the Skin Plates and Formation of Plastic Hinges.....	275
Figure 8-4 Design Curves for CFSSP-NB, $D = 0.10b$	283
Figure 8-5 Design Curves for CFSSP-NB, $D = 0.15b$	284
Figure 8-6 Design Curves for CFSSP-NB, $D = 0.20b$	285
Figure 8-7 Design Curves for CFSSP-B, $D = 0.10b$	286
Figure 8-8 Design Curves for CFSSP-B, $D = 0.15b$	287
Figure 8-9 Design Curves for CFSSP-B, $D = 0.2b$	288
Figure 8-10 CFSSP-NB Wall Capacity for $f_c' = 4\text{ksi}$, and Different D Values.....	289
Figure 8-11 CFSSP-B Wall Capacity at $f_c' = 4\text{ksi}$, and Different D Values	289
Figure 8-12 Schematic Plan of the Building and Location of CFSSP-Walls.....	291
Figure 8-13 Preliminary Design of CFSSP-NB Walls using Aid of Curves	296
Figure 8-14 Preliminary Design of CFSSP-B Walls using Aid of Curves	300
Figure B-1 Specimen CFSSP-NB	318
Figure B-2 Free Body Diagram for Specimen CFSSP-NB.....	319
Figure B-3 Outer Dimensions for Specimen of Group CFSSP-NB.....	323
Figure B-4 Cross-section of the CFSSP-B Specimens	326
Figure B-5 Free Body Diagram for Specimen CFSSP-B.....	327
Figure B-6 Different Components of Test Setup	332
Figure B-7 Failure Mechanism of the Head Plate.....	333
Figure B-8 Failure of Head Plate In Case of Stiffeners	334
Figure B-9 Stirrups used to Transfer Load to shear Connectors Group.....	339
Figure B-10 Formed Cone for Top Bar Pulling.....	340
Figure B-11 Proposed Concrete Fracture Surface in Foundation	342
Figure B-12 Plan of the Failure Surface	343
Figure B-13 Failure Wedge in the Annular Ring, Roeder et al 2003	343
Figure B-14 Free Body Diagram Showing Force Transferred to Annular Ring.....	345

Figure B-15 Free Body Diagram for the Loads on the Annular Ring.....	346
Figure B-16 Stiffened Annular Ring.....	347
Figure B-17 Proposed Failure Mechanisms of Annular Ring Plate.....	347
Figure B-18 Forces Acting on Stiffeners of Annular Ring	349
Figure B-19 Dimensions of the Annular Ring Stiffeners.....	350
Figure B-20 Annular Ring and the Stiffeners	351
Figure B-21 Technical Data for DYWIDAG Bars, Dywidag System International.....	352
Figure B-22 3-D STAAD Pro Model.....	354
Figure B-23 Foundation Deformation.....	354
Figure B-24 Stress Distribution Under Foundation	355
Figure B-25 Forces Acting on the Foundation Critical Section.....	356
Figure B-26 Foundation Critical Section	357
Figure B-27 Reinforced Bars and Stirrups Transferring Load from Wall Web.....	360
Figure B-28 Foundation Reinforced Arrangement	361
Figure B-29 Schematic Diagram for Lateral Bracing System	362
Figure B-30 Loading of Lateral Bracing System.....	363
Figure B-31 Bracing System Displacements in Horizontal Direction	364
Figure B-32 Out of Plan Force acting on the Bracing System.....	366
Figure B-33 Cross Section of Member M1	367
Figure B-34 Schematic Side View of Lateral Bracing.....	368
Figure B-35 Failure Mechanism for Gusset Plate.....	369
Figure B-36 Elevation of the Bracing System	370
Figure B-37 Plan of Lateral Support System in Case of Group B Specimen	371
Figure B-38 Plan of Lateral Support System in Case of Group NB Specimen	371

LIST OF TABLES

Table 2-1 Seismic Design Factors for C-OSW and C-SSW Walls per ASCE 7-10	16
Table 2-2 Seismic Design Parameters for C-PSW, AISC-341 (2010).....	50
Table 3-1 Material Parameters of CDP Model for 4 ksi Concrete.....	73
Table 3-2 Loading Cycles Used In the Analysis.....	94
Table 4-1 Strength of Concrete in the Tested Specimens	109
Table 4-2 HSS Tested Coupons	110
Table 4-3 Web Plate Tested Coupons.....	111
Table 4-4 Geometric and material properties of the Tested Specimens	112
Table 5-1 Loading Protocol for Group NB Specimens.....	148
Table 5-2 Loading Protocol for Group B Specimens.....	149
Table 6-1 Parameters Used in Moment Curvature Calculation	199
Table 6-2 Curvature Values of Specimen CFSSP-NB1.....	205
Table 6-3 Contribution of the Steel Web to the CFSSP-NB1 Shear Strength	207
Table 6-4 Summary of the Test Results.....	228
Table 7-1 Summary of Xtract Analysis for Specimen CFSSP-NB.....	232
Table 7-2 XTRACT Analysis Results for Specimen CFSSP-B.....	232
Table 7-3 Stress-Strain Values used for Concrete Backbone Curve, Abaqus Model for CFSSP-NB1.	236
Table 7-4 Damage Initiation Parameters	239
Table 7-5 Geometric Properties for Models Used in the Parametric Study.....	255
Table 7-6 Loading Protocol for the Different Models	255
Table 7-7 Finite Element Analysis Data Compared to Experimental Data	261
Table 8-1 Seismic Design Factors used for CFSSP-Wall Design as per ASCE 7	265
Table 8-2 Plastic Moment Capacity Expressions Compared to Tests Peak Values.....	272
Table 8-3 Calculated C_3 Factor Based on Test Results.....	277
Table 8-4 Vertical Distribution Factors and Floor Forces	293
Table 8-5 Forces and Shear on CFSSP-Wall	293
Table B-1 Dimensions of the Proposed CFSSP-NB	321
Table B-2 Capacity of the CFSSP-NB Wall.....	323
Table B-3 Specimens of Group NB	330
Table B-4 Specimen CFSSP-B M_p	331
Table B-5 Member Forces	365
Table B-6 Member M1 Straining Actions and Properties	366

ACRONYMS

AISC	American Institute of Steel Construction
ASTM	American Society for Testing and Materials
ASCE	American Society of Civil Engineers
CFSSP-Wall	Concrete Filled Steel Sandwich Panel Wall.
CFSSP-NB	Concrete Filled Steel Sandwich Panel Wall with no Boundary Elements
CFSSP-B	Concrete Filled Steel Sandwich Panel Wall with Boundary Elements
C-OSW	Composite Ordinary Shear Wall
C-PSW	Composite Plate Shear Wall
C-SSW	Composite Special Shear Wall
HBE	Horizontal Boundary Element
SEESL	Structural Engineering and Earthquake Simulation Laboratory
SC	Steel Plate Reinforced Concrete Structures
SPSW	Steel Plate Shear Wall
VBE	Vertical Boundary Element

NOTATIONS

A_g = Gross section area

A_{net} = Net section area

C = Length of the web plate under compression, inch.

C_n = Compression force acting on the CFSSP-Wall cross-section, kips (n=1,2,3,.....)

C_d = Deflection Amplification Factor

D = Diameter of the HSS part of the CFSSP-Wall cross-section

E_c = Concrete Elastic Modulus, ksi.

E_s = Steel Elastic Modulus, ksi

F_y = Yield strength of steel, ksi

G = Shear Modulus

H = Height of the Cantilever Wall, (Ft, inch)

I_c = Moment of Inertia of concrete part of the CFSSP-Wall cross-section (in⁴)

I_s = Moment of Inertia of Steel part of the CFSSP-Wall cross-section (in⁴)

K = Shape factor for CFSSP-Wall cross-section

L_p = Length of the plastic hinge (inch, feet)

M_C = Plastic Moment Capacity of the Concrete part of a composite section (kip-in)

M_p = Plastic Moment Capacity of a cross-section (kip-in)

M_s = Plastic Moment Capacity of the Steel part of a composite section (kip-in)

M_C = Plastic Moment Capacity of the Concrete part of a composite section (kip-in)

M_D = Flexural demand on the CFSSP-Wall

N = Number of Dywidag Bars

$P_{Actuator}$ = Actuator Load (kips)

R = Response Modification Factor

S = spacing of the tie bars., Inch

NOTATIONS (Cont'd)

T_i = Tension force acting on the wall cross-section

V_b = Base shear

V_{bar} = Shearing force transferred to the tie bars

V_{steel} = Shear Force acting on the steel web of the CFSSP-Wall

W = Total width of the cross-section (feet, inch)

X = Part of the wall cross-section

d = Diameter of the seamless tie bar, inch

d_c = Elastic modulus degradation variable for the concrete material model under compression.

d_{min} = Minimum diameter of tie bars

d_t = Elastic modulus degradation variable for the concrete material model under tension.

c = Length of the steel web subjected to compression stresses.

f_{bo} = Strength of Concrete under biaxial state of stress

f_{co} = Strength of Concrete under uniaxial state of stress

f'_c = Strength of concrete, ksi

h = Total length of the steel web

k = Buckling coefficient of the web skin plate.

t_n = Tension force acting on the CFSSP-Wall cross-section, kips (n=1,2,3,.....)

t_s = thickness of the steel web of the CFSSP-Wall, inch

t_{HSS} = thickness of the HSS part of the CFSSP-Wall, inch

Δ_y = Yield displacement

Δ_{max} = Maximum displacement that corresponds to 80% of the peak load

ϵ_c^{in} = the in elastic compression strain

NOTATIONS (Cont'd)

ε_c^t = the total strain given by the axial compression backbone curve

ε_c^{el} = the elastic strain

ε_y = Yield strain (in/in)

θ = Rotation angle

ν = Poisson's Ratio

μ_Δ = Displacement ductility ratio

μ_ϕ = Curvature ductility ratio

σ_{cr} = Critical buckling stress

ϕ = Curvature values

CHAPTER 1

INTRODUCTION

1.1. General

Reinforced concrete shear walls have been used as an effective lateral load resisting system in high-rise and mid-rise buildings for decades. In particular, such walls have been commonly used as the lateral-load resistance system in high-rise buildings in seismic regions. In such applications, reinforced concrete walls can become quite thick, which adds weight (and, thus, inertia forces) to buildings. High seismic demands on the wall, especially in regions of high seismicity, also lead to congested reinforcement details to meet the ductility and strength demands on the wall. Most importantly, the relatively large foot-print of reinforced concrete shear walls decrease the leasable area in high-rise buildings. During an earthquake, a typical reinforced concrete shear wall will develop cracks in tension, and experience crushing and spalling of the concrete in compression, leading to reduction of stiffness (and eventually strength) during large inelastic displacement cycles.

Steel plate shear walls (SPSWs) are a good alternative to reinforced concrete shear walls. In terms of constructability, they are fast to build, “compatible” with steel floor systems, relatively light, and have a smaller footprint than corresponding concrete walls (thus providing more leasable area). The reduced wall weight also advantageously reflects on seismic demand due to mass reduction. SPSWs have good ductility; research performed on SPSW showed that they sustain drifts of 3 to 4% without significant damage. However, tall SPSWs can have greater flexural flexibility than comparable reinforced concrete shear walls, which can lead to greater drifts. Furthermore, overall buckling of the steel plate in such walls leads to an overall reduction in the shear strength, lateral stiffness and energy dissipation capacity of the system upon repeated cycles of inelastic deformations. SPSWs have been used in high rise buildings as the main lateral load resisting system, but capacity design requirements typically results in relatively large sized horizontal and vertical boundary elements.

Different approaches have been taken in recent years to develop composite shear walls (made of structural steel and reinforced/plain concrete) to improve the performance of the aforementioned types of walls. Some of these approaches are intended to enhance the behavior of concrete walls, others to improve behavior of SPSWs.

In one approach, reinforced concrete shear walls are reinforced with embedded structural steel shapes (in addition to conventional longitudinal reinforcement) located such as to act as boundary elements for the walls, or with an encased steel plate “web” to increase the shear strength of the wall. Another approach has been to use structural steel or composite coupling beams spanning between adjacent closely spaced reinforced concrete walls (i.e., a dual wall system in which the walls are connected by ductile link beams). In all of these cases, the structural steel and/or composite beams are used to provide inelastic deformations at the design story drift through flexural or shear yielding.

Among approaches proposed to enhance the behavior of SPSWs, concrete panels added to one or both sides of the SPSW’s web plate are intended to prevent its local buckling. The web plate in this case resists the seismic loads through shear yielding rather than axial tension field action, allowing the wall to sustain relatively higher seismic demand and provide (by delaying buckling of the steel plate infill) repeatable hysteretic behavior.

Another approach is to use composite shear walls that consist of steel sandwich panels filled with concrete (note that different techniques have been used to fabricate the panels and tie the panels together). This type of wall has many benefits. First, construction is accelerated by making it possible to use the steel skin of the system as formwork for erection purposes, particularly when the skin is designed to be self-bracing (i.e., not requiring lateral bracing prior to casting of concrete) and able to sustain the corresponding construction axial loads and self weight of the wet-concrete. After curing of the concrete, the resulting composite system can provide relatively high lateral stiffness and can sustain large seismic demands for a relatively smaller cross section (compared to reinforced concrete walls), which translates in more rentable space in buildings. Note that this system can also sustain gravity loads and have good blast resistance. This type of sandwich construction has been implemented in some buildings in non-seismic regions.

It is that last type of composite wall, called a Concrete-filled Steel Sandwich Panel Wall (CFSSP- Wall), which is of interest here. CFSSP-Walls are being considered by practicing engineers as potentially ductile flexural walls for high-rise construction in seismic regions. However, while they are envisioned to be highly ductile, redundant, of high strength, and easy and rapid to construct, there is a critical lack of knowledge on their in-plane seismic behavior. There is consequently no verified and validated procedure for their design. The lack of quantitative knowledge on their expected seismic performance, in spite of all the foreseen excellent attributes of the structural system, is an absolute impediment to their implementation.

The work presented here is intended to provide some of this missing knowledge. Specific walls cross-sections and methods to tie the steel plates are proposed for this purpose. Scope of the research and specific objectives are presented in the following section, followed by a description of the organization of this report.

1.2. Scope and Objective

In this research, the in-plane flexural strength of a concrete filled sandwich panel wall system (CFSSP-Wall) is investigated. The type of CFSSP-Wall considered here is built by connecting the two steel skin plates using tie bars either plug welded or fillet welded to the plates. The research focuses on walls whose ultimate behavior is flexural yielding, as this is typically the case for walls that have height to depth ratio larger than 2. Furthermore, focus here is on flexural walls having cross-sections able to develop their full plastic strength.

The wall cross sections considered here are rectangular, with and without boundary elements. For the rectangular CFSSP-Wall without boundary elements, each end of the wall consists of a half HSS section used to avoid the premature failure of the weld between the flange and the web often observed in composite columns of a rectangular cross-section. For the CFSSP-Wall with boundary elements, concrete filled HSS sections were used as boundary elements. In the current study, spacing of the tie bars is taken to be equal in both the vertical and horizontal directions, and diameter of the tie bars was selected to ensure that they behave elastically.

The objectives of this research are to understand the in-plane flexural behavior of CFSSP-Walls, to evaluate their cyclic inelastic performance for possible use as a seismic lateral-loads resisting system, and to formulate a proposed design procedure for seismic applications.

To achieve these objectives, the in-plane inelastic flexural behavior of CFSSP-Wall was first investigated analytically using plastic analysis, fiber analysis, and finite element analysis, to determine how these different analysis methods can be used to predict the plastic moment capacity of the walls. In these first analyses, the finite element model was calibrated using data from the literature and used to investigate the mechanics of the proposed system.

Second, experiments were conducted at the University at Buffalo's Structural Engineering and Earthquake Simulation Laboratory (SEESL), on four large scale cantilever walls. Two of the tested specimens were walls without boundary elements, and two had boundary elements. The walls length-to-depth ratios were 2.45 and 2.67, respectively. The tested specimen had ratios of tie bars spacing to skin

plate thickness, S/t , of 25.6 and 38.4. Tie bars of 1 inch diameter were used. The specimens were tested under cyclic quasi static loads.

After the experiments, finite element models initially used to predict response of the tested specimen were revised by calibrating against the known experimental responses. Using these calibrated models, finite element analyses were used to conduct a limited parametric study, considering different S/t ratios, different percentages of steel area to total cross section area, and different aspect ratios of the wall.

Finally, the experimental and analytical results were used to develop a design procedure for CFSSP-Walls. This procedure is illustrated through design examples of CFSSP-Walls as the lateral load resisting system for a 9 story building.

1.3. Report Organization

Chapter 2 contains a brief overview of past experimental and analytical research related to composite shear walls. It includes a brief overview of different types of composite shear walls, their respective inelastic behavior, a summary of some of their respective advantages and disadvantages, and their design recommendations as found in some international codes. This overview includes information on concrete filled sandwich panels used in different structural applications, including a significant number of cases that investigated the walls out-of-plane behavior.

Chapter 3 contains the results from a preliminary investigation of the in-plane flexural behavior of concrete filled sandwich panel walls (CFSSP-Walls), where a rectangular CFSSP-Wall is analyzed using different methods, such as simple plastic analysis, cross-section fiber analysis, and finite element analysis. The flexural strength of the cross section is estimated using the aforementioned types of analyses. The fiber analysis method is used to generate moment/axial load interaction diagram for rectangular CFSSP-Walls. The finite element analysis method is then used to further investigate the behavior of the CFSSP-Wall, using pushover analysis and quasi-static cyclic analysis. The finite element analysis model used at that stage is calibrated against experimental results obtained for rectangular CFSSP-Walls from the literature.

Chapter 4 describes the experimental program. Specimens' geometry, material properties (determined through coupon tests for steel and cylinder tests for concrete), and the design and detailing of the four large-scale CFSSP-Walls with and without boundary elements, are summarized. Design of the head plates, reinforced concrete foundation, and wall lateral-bracing system, are also presented, together with the instrumentation layout used (showing the different devices used to measure response).

Chapter 5 describes the loading protocols used in the testing program, and the observations made during testing of each of the four specimens. Photos of the specimens' condition during and after testing are presented to document descriptions of observed behavior.

In Chapter 6 analysis of the testing data is presented; results include axial strain distribution, force-displacement relationships, moment-curvature relationships, shear strain distribution, and evaluation of the different types of displacement ductility.

Chapter 7 presents finite element models simulating the tested specimens, taking into account the foundation and strong floor in attempts to closely replicate the experimentally obtained response, in terms of (but not limited to) flexural plastic capacity, elastic stiffness, location of local buckling, and maximum drift. Models varied from cantilever like model with fixed base, to models including the foundations, with observations on how the degree of model complexity affects the results extracted from the finite element model. This chapter also presents the results of a parametric study conducted using the finite element models calibrated against test results. The parametric study investigates the effect of increased spacing of the tie bars in both the vertical and horizontal directions, the effect of greater wall length-to-depth (aspect) ratio, h/w using ratios of 3 and 3.5, and the, and finally the effect of changing the ratio of steel to concrete in a CFSSP-Wall cross section.

Chapter 8 presents some design recommendations for CFSSP-Walls with and without boundary elements, a preliminary design approach to select the outer dimensions and elastic stiffness of CFSSP-Walls, tie bars spacing, tie bar diameter. Expressions for the plastic moment of CFSSP-Wall with and without boundary elements are also proposed. This chapter also presents two examples for the seismic design of CFSSP-Walls for a 9 story building. In these examples, the design process from selection of dimension to detailing of the CFSSP-Wall is presented.

Chapter 9 summarizes the research results and presents conclusions from the research project and recommendations for the future work. Chapter 10 lists the references cited in this report.

Appendix A includes selected details drawing for the tested specimens. Appendix B presents detailed design calculations for the tested specimens and its foundation, as well as for the test set-up components (i.e., head plate, lateral support system, etc.), and finally Appendix C includes XTRACT analysis reports for the different cross sections.

CHAPTER 2

LITERATURE REVIEW

2.1 Introduction

There exist many different types of structural composite shear walls with different cross section configuration, that have been used in different structural applications, either as gravity load supporting system or lateral load resisting system in non-seismic applications, nuclear industry applications, and seismic applications. The different types of composite walls and their applications (as reported in the available literature) are described in this chapter. Note that there is different nomenclature used in describing the walls, depending on applications or research origin (i.e., the same structural configuration is given different names/acronyms in different country or by different researchers). However, here, the nomenclature of AISC-341 (2010) will be followed as much as possible to minimize confusion.

There are two types of composite shear walls that are addressed in the literature. A first type, which includes composite ordinary shear walls (C-OSW) and composite special shear walls (C-SSW), consists of reinforced concrete shear walls that are made composite with structural steel elements by having structural steel or composite sections acting as boundary elements for the reinforced concrete walls. This category of walls also encompasses coupled reinforced concrete walls that have steel or composite coupling beams. The differences between C-OSW and C-SSW are addressed in Section 2.2. However, for the most part, the main difference between the two types of walls mainly lies in the structural detailing of the systems.

A second type is the composite plate shear walls (C-PSW), which consists of steel plates with reinforced concrete encasement on one or both sides of the steel plate, or steel plates on both sides of a concrete infill, and which might have structural steel or composite boundary elements.

Although all of these wall types share the characteristic that structural steel plates or shapes are acting compositely with reinforced or plain concrete (with connectors to engage the composite action), the principles of their ductile energy-dissipation mechanisms are fundamentally different. This chapter summarizes the available literature on these different types of structural composite walls

The literature is organized based on the configuration of the composite structural wall (arrangement of the structural steel and concrete); the available research for each configuration is summarized and divided into the non-seismic applications (in-plane and out-of-plane loading, non-seismic lateral load resisting

systems, and nuclear applications) and the seismic application of composite walls. Seismic application of composite walls is the subject of this research; accordingly, whenever feasible, emphasis will be placed on the ductility and seismic performance of the different structural composite wall systems. Where applicable seismic design recommendation by the AISC-341 (2010) will be summarized.

2.2 Composite Ordinary/Special Shear Walls (C-OSW and C-SSW)

2.2.1 General

Composite Ordinary/Special Shear Walls are reinforced concrete shear wall that have structural steel profiles or composite elements as boundary elements, and/or coupling beams in case of coupled walls. C-OSW and C-SSW are of similar configuration, the main difference being in the structural detailing used to achieve the required performance under seismic loads. In Section 2.2, the difference between C-OSW and C-SSW is explained in more details. Section 2.3 presents examples of research on C-OSW and C-SSW, focusing on ductility and the seismic performance of the walls. Section 2.4 presents a summary of the AISC-341 (2010) recommendations for seismic design of those walls.

2.2.2 Differences between C-OSW and C-SSW

A C-OSW is composed of reinforced concrete wall acting compositely with structural steel elements, including composite sections, acting as boundary elements for the reinforced concrete wall and/or structural steel or composite coupling beams connecting adjacent reinforced concrete walls. These walls offer limited inelastic flexural deformation capacity through yielding of the reinforced concrete wall and the steel or composite elements. In coupled C-OSW, coupling beams are expected to remain elastic; however, they must be detailed to be ductile if yielding in shear or flexure.

A C-SSW is a coupled reinforced concrete wall with or without structural steel or composite boundary elements but having structural steel or composite coupling beams. These walls are expected to deliver significant inelastic deformation by yielding of the coupling beams over the entire height of the structure prior to yielding of the coupled walls at their bases, which dictates the detailing of the coupling beams' connections and calculation of the beams' embedment lengths. Figure 2-1 shows a typical cross section for the wall with steel or composite boundary elements, as in the case of C-OSW/C-SSW.

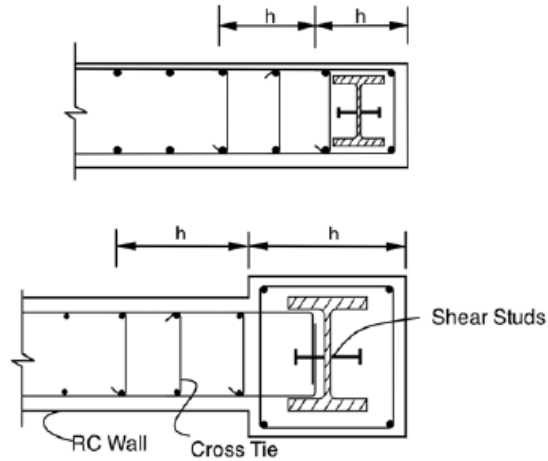
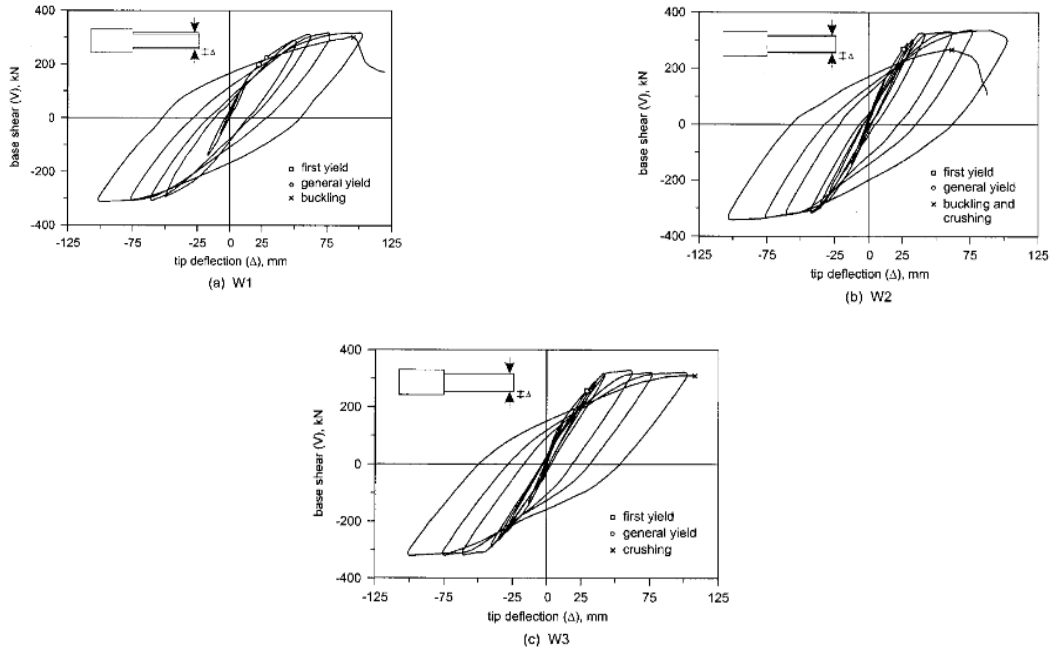


Figure 2-1 Typical Cross Section for the C-OSW/CSSW, AISC-341 (2010)

2.2.3 Examples of Past Research on Ductility and Performance of Reinforced Concrete Shear Walls with Structural Steel

To overcome reinforcement congestion in structural reinforced concrete walls and to reduce the on-site labor related to bar placement, researchers investigated the behavior of reinforced concrete shear walls in which structural steel sections are used as boundary elements replacing both vertical reinforcing bars, and with confining ties in the boundary regions of the wall. Three specimens were tested under reversed cyclic loading and a constant axial load causing an equivalent stress of 4 MPa on the gross section. Specimen one had an HSS section (yield strength of 377 MPa) as boundary element, the second specimen had a channel section (yield strength of 402 MPa), and the third specimen had conventional vertical reinforcement bars (yield strength between 450 to 488 MPa) and ties (yield strength of 381 MPa); in all cases, concrete strength varied between 26 MPa and 39 MPa. The tested walls, shown in Figure 2.2, had an aspect ratio of 3.9, and were designed to have the same flexural capacity. The steel boundary elements were designed to be capable of developing significant compressive strains before local buckling; consequentially, the composite walls were able to exhibit ductile flexural yielding. The development of composite action in the walls was achieved by using stud connectors in the case of the steel channel, and by welding transverse reinforcement to the wall of the HSS. The test results showed that hysteretic response of composite walls with steel boundary elements is similar to that of typical reinforced concrete ductile wall, and that use of the plane section theory for flexure, together with the ACI stress block factors and maximum concrete compressive strain of 0.003, provides a reliable and simple method to estimate the nominal flexural resistance of the walls. Specimen's details and results are summarized in Figure 2-2



Load versus deflection responses: (a) W1, (b) W2, and (c)

W3

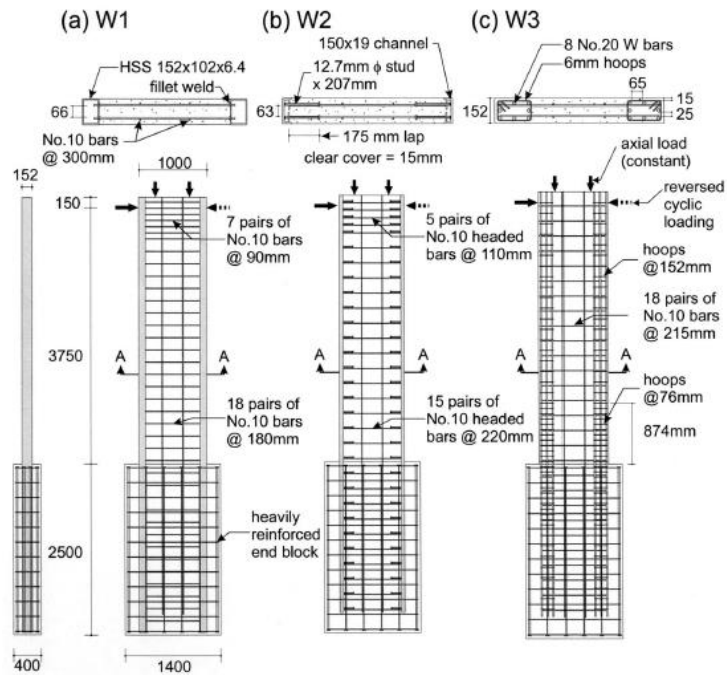


Figure 2-2 Tested Composite Reinforced Concrete Wall Specimens, Cho et al (2004)

Dan, Fabian et al. (2011) investigated the behavior of concrete walls reinforced by vertical steel sections, using experimental tests and theoretical study. Of the six specimens tested (shown in Figure 2-3), five had vertical steel shapes used as boundary elements, varying between hollow square section and rolled I sections with headed studs to ensure composite action, while the sixth specimen had conventional vertical reinforcement and tie bars (stirrups). The walls were designed in accordance to Eurocode 8, Eurocode 4, and Eurocode 2 to assure ductility of the tested specimens, and all specimens had the same reinforcement ratio. The parameters addressed in the experimental program were type of vertical reinforcement, section of the structural steel used as boundary element, and positioning of the structural steel in the reinforced concrete section. The yield strength of the structural steel used in testing varied between 331 and 559 MPa and the concrete strength varied between 46 and 66 MPa. The specimens were loaded by constant axial load of 100 kN and increasing cycling lateral load.

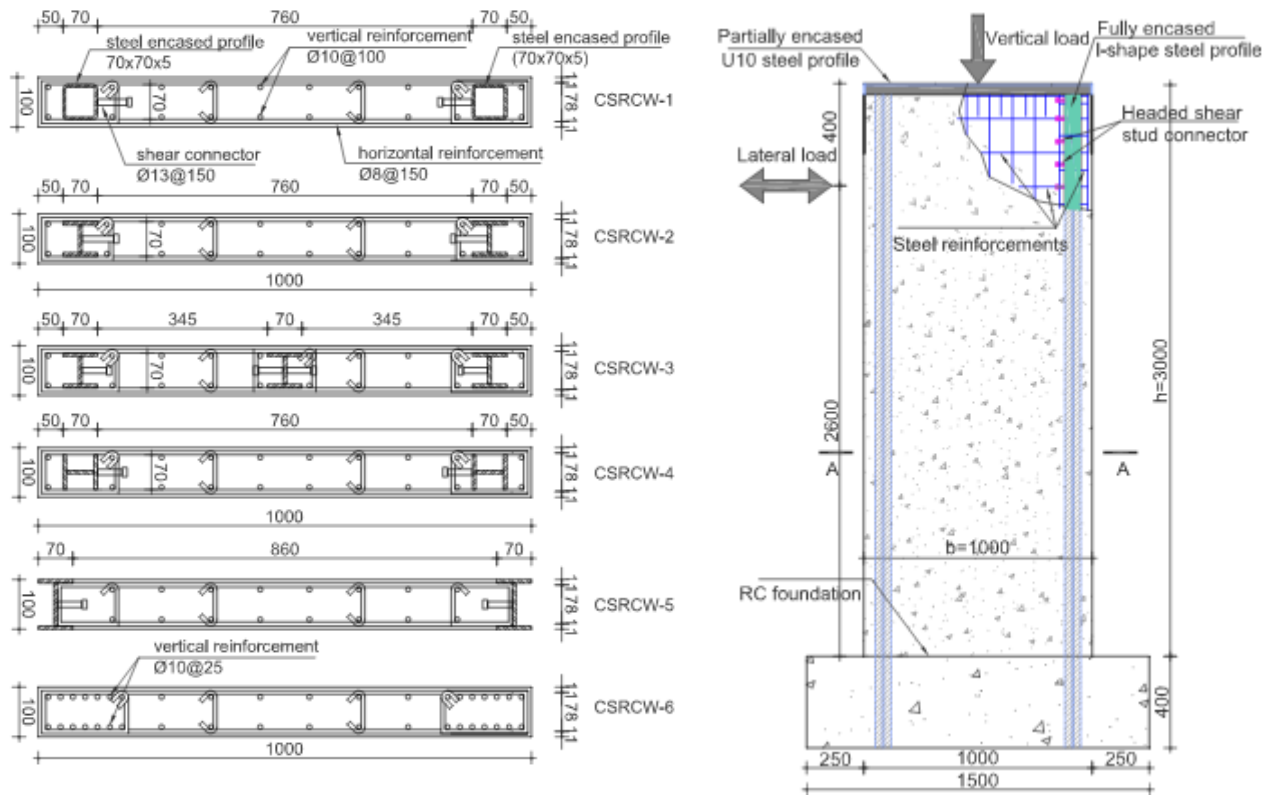


Figure 2-3 Tested Composite Reinforced Concrete Wall Specimens, Dan et al. (2011)

The finite element software ATENA 2D was used to analyze the tested specimens; the non-linear material models used for steel and concrete are shown in Figure 2-4. Triangular shell elements were used. This study reported that reinforced concrete walls with structural steel boundary elements have more displacement ductility than conventional reinforced concrete walls with the same steel area, and that the

proposed finite element model can be used to predict the behavior of composite reinforced concrete walls. Figure 2-5 presents the backbone of the cyclic force displacement relationship obtained for the tested specimens, compared with results from finite elements pushover analysis used to estimate performance.

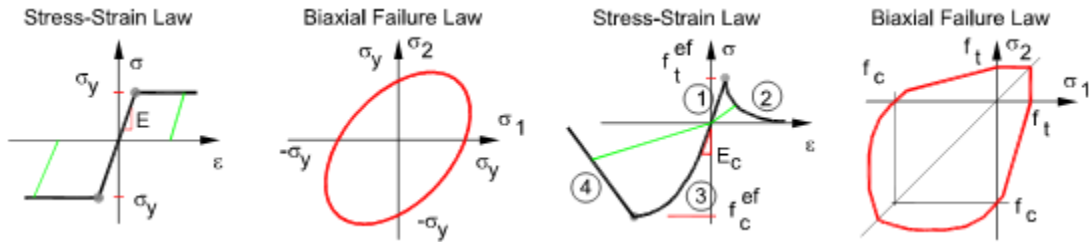


Figure 2-4 Material Model Used for Finite Element, Dan et al. (2011)

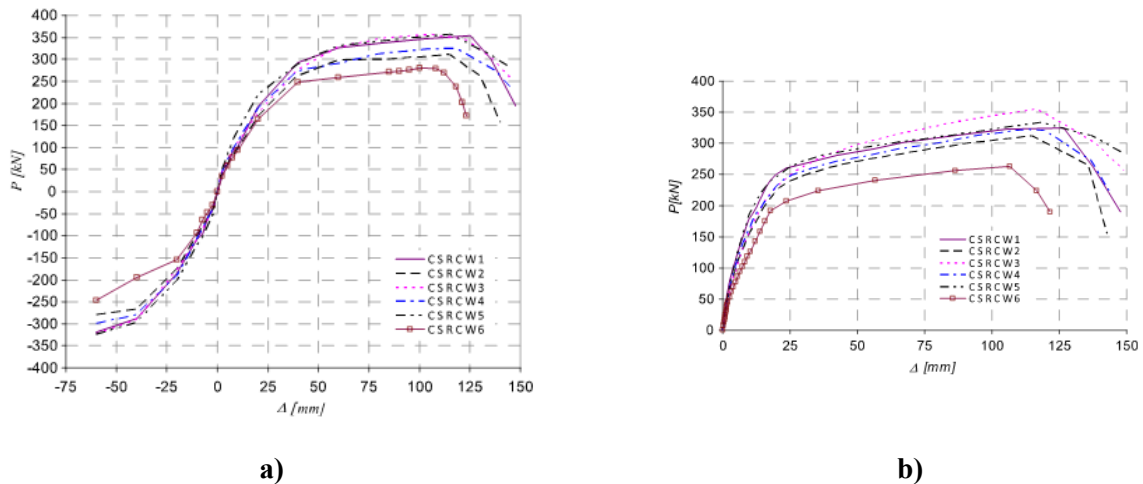


Figure 2-5 Force -Displacement Relationship a) Experimental-b) Analysis, Dan et al. (2011)

Liao et al. (2012) investigated the behavior of reinforced concrete shear walls with structural steel boundary elements, through a series of test on six reinforced concrete walls: three having structural steel as boundary elements, and three having reinforced concrete boundary elements. All specimens were loaded with a constant axial loading, and subjected to increasingly cyclic loads. The testing parameters were the aspect ratio of the walls (specifically 0.62 and 0.95) and the ratio between the applied axial load and the ultimate axial capacity of the boundary element as a column (specifically ratios of 0.26 and 0.52). The yield strength of the structural steel ranged between 263 MPa and 397 MPa and the ultimate strength of concrete between 31 MPa and 49 MPa. Figure 2-6 shows a reinforced concrete wall with structural steel boundary element specimen.

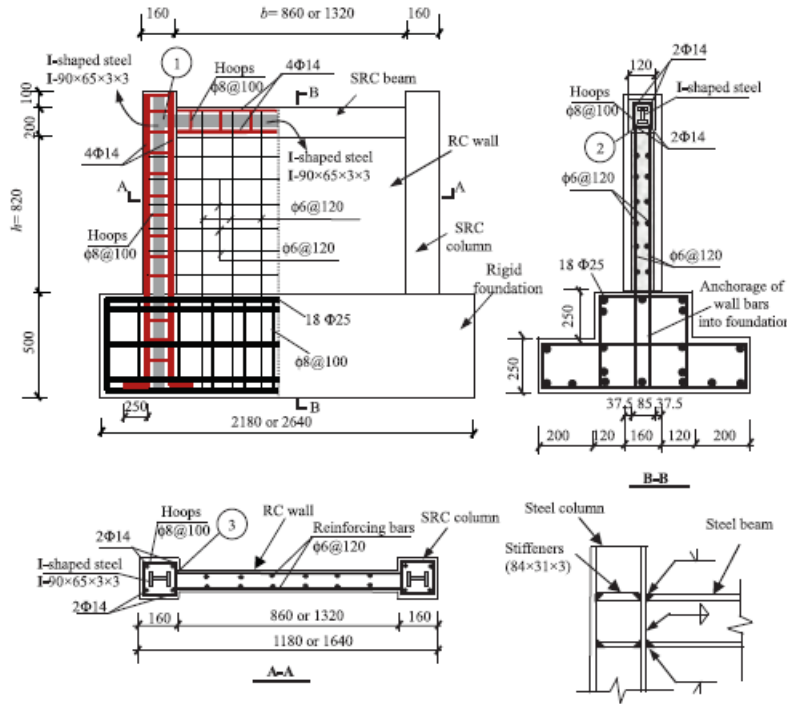


Figure 2-6 Tested Specimen with Steel Boundary Elements, Liao et al. (2012)

Finite element models using the ABAQUS software were developed and used to simulate the behavior of the tested composite shear walls; 4 node shell elements were used to model the steel I shapes, 8 node brick elements were used to model the concrete, and re-bars were modeled using 2 node truss elements. Steel was modeled as a bi-linear material while concrete was modeled using the concrete damage plasticity model available in ABAQUS. Fixed base was chosen as a boundary condition for the simulated wall, as shown in Figure 2-7. The finite element analyses were able to predict the tested results with reasonable precision, as shown in Figure 2-8.

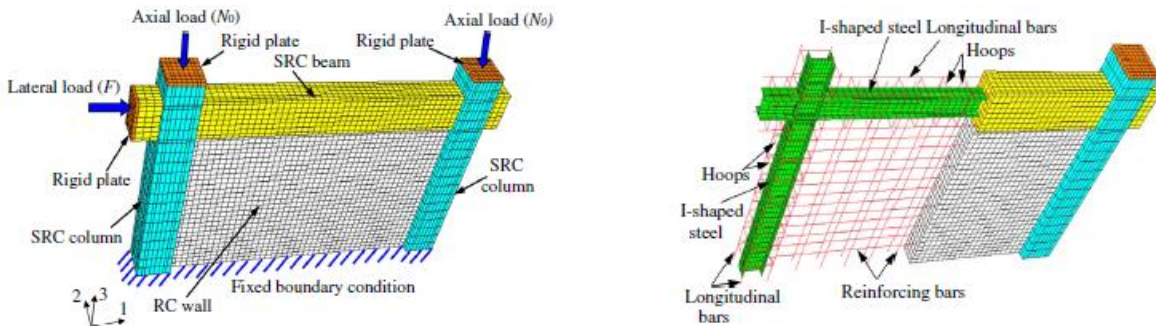
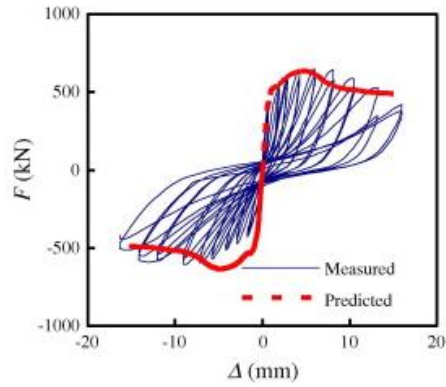
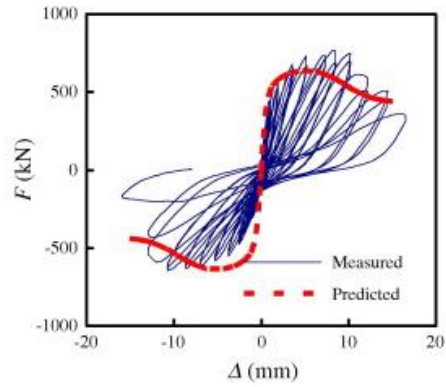


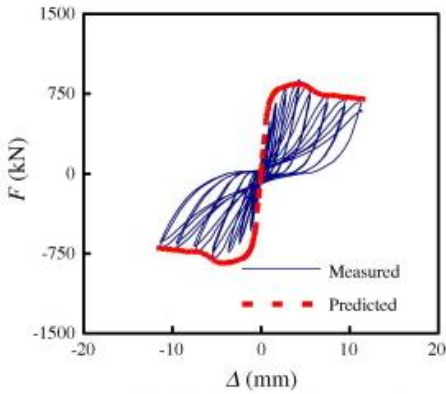
Figure 2-7 Specimens Simulated with ABAQUS, Liao et al. (2012)



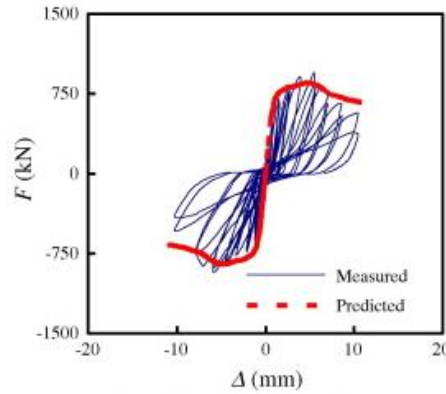
(a) SRC-S-1 ($n=0.26$, $h/b=0.95$)



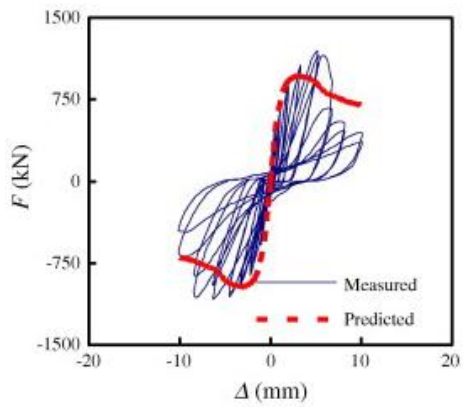
(b) RC-S-1 ($n=0.26$, $h/b=0.95$)



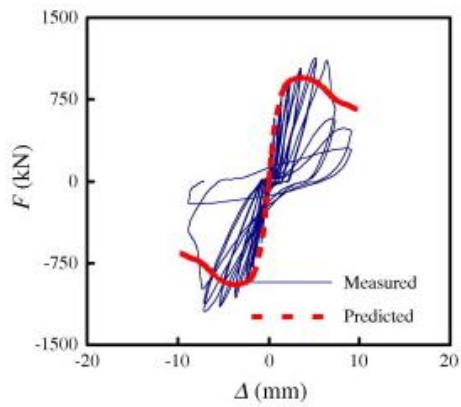
(c) SRC-L-1 ($n=0.26$, $h/b=0.62$)



(d) RC-L-1 ($n=0.26$, $h/b=0.62$)



(e) SRC-L-2 ($n=0.52$, $h/b=0.62$)



(f) RC-L-2 ($n=0.52$, $h/b=0.62$)

Figure 2-8 Finite Elements Analysis against Test Results, Liao et al. (2012)

Liao et al. (2012) reported that the lateral load resistance of reinforced concrete walls with steel boundary elements increased with increasing axial load level, and that using steel sections as boundary elements improved the wall ductility over reinforced concrete boundary elements. At the peak load, the boundary elements resisted most of the overturning moment while the reinforced concrete wall panel carried the majority of the shear load. The shearing force was mainly resisted by the diagonal compressive strut formed in the concrete wall panel, while the reinforcing bars in the wall served as horizontal ties and vertical ties simultaneously to restrain the shear deformation of concrete. Meanwhile, the I-shaped steel in the column also resisted a part of shear force. It was also reported that the failure mode of reinforced concrete walls with boundary elements changes from shear-dominant to flexure-shear mixed mode when the height-to-width ratio increased from 0.62 to 3.

2.2.4 AISC and ASCE Requirements for the Seismic Design of C-OSW/C-SSW

As mentioned previously, AISC-341 refers to reinforced concrete with boundary elements as either C-OSW or C-SSW. The C-OSW design requirements are provided in section H-4 of AISC 341. C-OSW are expected to undergo limited inelastic deformation through yielding in the reinforced concrete walls and the steel or composite boundary elements. The reinforced concrete shall satisfy requirements of ACI 318, except for the seismic detailing requirements of Chapter 21 (requirements for earthquake-resistant structures), since C-OSW are expected to only undergo limited inelastic displacements.

For C-OSW, un-cracked effective stiffness is used for coupling beams for elastic analysis in conformance with ACI-318 Chapter 10. Flexibility of the connection between coupling beams and walls, and shear deformations of the coupling beam and wall, shall be taken in account.

The boundary elements, together with the reinforced concrete wall, shall be designed to sustain gravity loads and axial loads resulting from the overturning moment, while the shear is resisted by the reinforced concrete wall. Boundary element with steel shapes encased in concrete shall be designed according to Chapter I of AISC 341. Use of headed studs or welded reinforcement is specified to transfer load between the boundary elements and reinforced concrete wall. C-SSW are designed accordance to Section H-5 of AISC 341. C-SSW are expected to undergo significant inelastic deformations; detailing of the reinforced concrete part of those wall shall conform to Chapter 21 of ACI 318. The steel or composite coupling beams are expected to undergo yielding in shear or flexure while the boundary elements are expected to yield due to axial force. The cracked effective stiffness is considered for design of wall piers and coupling beams.

The axial design strength of the wall at balanced condition, P_b , is:

$$P_b \geq 1.1R_y V_n \quad (2.1)$$

Equation Section (Next)

where V_n is the sum of the gravity load acting on the wall and the expected link beam end-shear multiplied by 1.1 to account for strain hardening, and by R_y to account for expected strengths of the link beam elements.

Section H-5 of AISC 341 provides requirements for the design of members, ductile elements and boundary elements in C-SSW. The design seismic design factors per ASCE-7 (2010) for C-OSW and C-SSW are given in Table 2-1

Table 2-1 Seismic Design Factors for C-OSW and C-SSW Walls per ASCE 7-10

Type of Wall	Response Modification Factor, R	Over-strength Factor, Ω_o	Deflection Amplification Factor, C_d
C-OSW	6	2.5	6
C-SSW	7	2.5	5

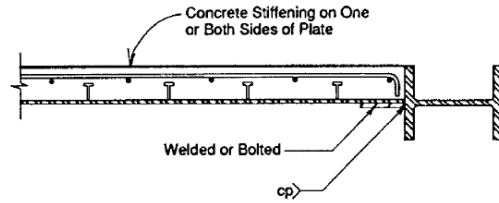
2.3 Composite Plate Shear Walls (C-PSW)

2.3.1 General

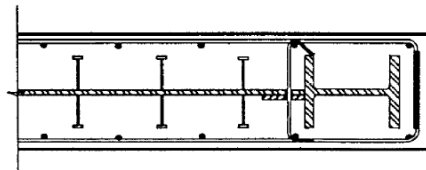
The C-PSW category of composite walls, per AISC 314, encompasses two main wall configurations:

First, as an enhancement to conventional Steel Plate Shear Walls (SPSW), when the steel plate infills of such walls are tied to reinforced concrete panels on one or both sides; second, as different configuration, with steel plates added on both sides of a reinforced concrete infill. For both configurations, shear connectors (mostly studs) are required by AISC to transfer shear between the steel and concrete. In both configurations, the main function of the concrete is to delay local buckling of the steel plates and change the ductile performance mechanism. Concrete panels attached to SPSW are used to change the ductile mechanism of the steel infill, from diagonal tension axial yielding to shear yielding in the steel plates, resulting in a relatively larger seismic resistance and enhanced inelastic deformation capacity. As for conventional SPSWs, horizontal and vertical boundary elements (HBEs and VBEs), which could be structural steel or composite sections, shall remain essentially elastic under the forces resulting from steel plate yielding and HBE plastic hinging (recognizing that plastic hinging is only acceptable at the ends of HBEs). The second form of the C-PSW consists of steel sandwich panels filled with concrete, without horizontal or vertical boundary elements, for which the ductile mechanism is developed by flexural yielding or a combination of flexure and shear yielding, depending on the aspect ratio (height to depth) of the wall.

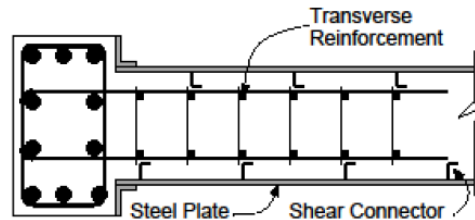
The following sections summarize the research done on different configurations of C-PSWs with respect to their configuration and structural applications. Section 2.3.2 summarizes selected research on C-PSW of the first time (with horizontal and vertical boundary elements), focusing on ductility performance and seismic applications. Section 2.3.3 presents C-PSW walls composed of steel sandwich panels filled with concrete. More specifically: Section 2.3.3.1 provides a general introduction on C-PSW composed from sandwich panels; Section 2.3.3.2 presents non-seismic applications for that type of walls subjected to in-plane and out-of-plane loading (typically used in building and nuclear applications); Section 2.3.3.3 summarizes research performed on C-PSW in seismic applications, and; Finally, Section 2.3.4 presents a summary of the AISC-341 (2010) design provisions for C-PSW. Figure 2-9 shows the different types of C-PSW walls.



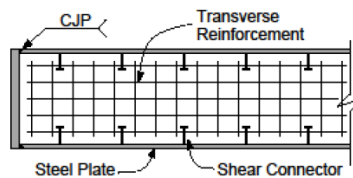
a) Concrete Stiffened Steel Shear Wall with Steel Boundary Member



b) Concrete Stiffened Steel Shear Wall with Composite (encased) Boundary Member



c) Concrete Filled C-PSW with a Boundary Element and Transverse Reinforcement.



d) Concrete Filled C-PSW with Transverse Reinforcement to Provide Integrity of the Concrete Infill

Figure 2-9 Different Configuration for C-PSW, AISC-341 (2010)

2.3.2 C-PSW with VBE and HBE

This section presents C-SPW walls with VBE and HBE, where the concrete panels are mainly used to minimize local buckling of the steel plate infill, and accordingly change the yielding mechanism of the wall from tension field action to shear yielding of the infill plate. This section presents some of the research done on the seismic performance of such C-PSW with VBE and HBE.

Zhao and Astaneh-Asl (2004) investigated the cyclic behavior of composite shear walls by testing two specimens. Both were conventional SPSW made composite by adding precast reinforced concrete panels

bolted to the web plate of the SPSW. The gap between the precast reinforced concrete panel and the steel of the boundary elements was proposed to be left empty, or filled with soft material such as Styrofoam, to prevent the panel from engaging with the boundary frame during wall deformation. Figure 2-10 shows the schematics of the tested walls configurations; one specimen was tested with a gap, and one without gap.

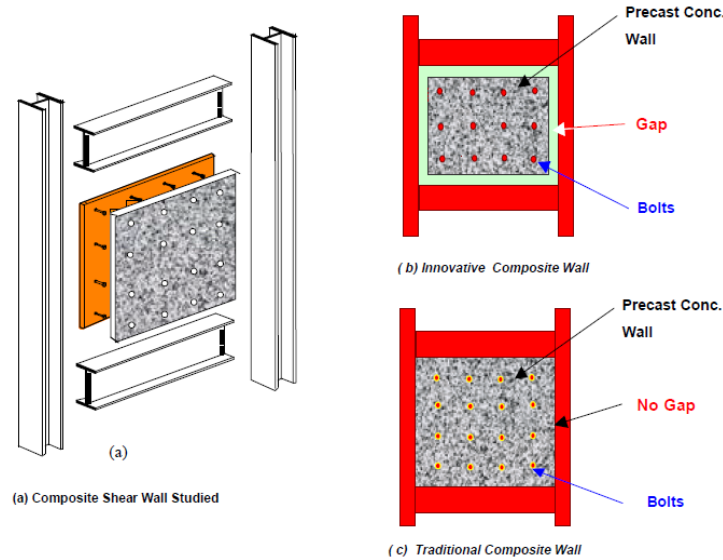


Figure 2-10 Configuration of Composite Shear Walls tested by Astaneh-Asl and Zhao (2001)

In composite shear walls without gap, from start of loading, concrete contributed to the stiffness and strength of the system, which attracted higher forces and damaged concrete at relatively small lateral displacements. In the system with gap, at small lateral displacements, the concrete was not engaged until the gap closed, as shown in Figure 2-11, such that, at small displacements, the concrete just served to prevent local buckling of the infill plate, allowing it to reach shear yielding. However, when the gap closed, concrete started to add to stiffness and strength to the wall.

The two specimens tested were 1/2-scale three stories, one bay structures with steel frame as the boundary elements. Figure 2-12 shows the tested specimen. The two specimens were identical, except that one specimen had a gap of 1.25" the between reinforced concrete and surrounding frame, and the other did not. The material used for the steel infill plate was ASTM-A36 grade, and steel for the rest of the frame was ASTM A572 grade. The concrete had a specified compressive strength of 4ksi. The tested specimens were subjected to quasi-static cyclic lateral load.

The tested specimens performed in a ductile manner reaching a 5% inter story drift before strength dropped to below 80% of peak strength. The system with gap exhibited better ductility than the one without, as shown in Figure 2-13 for the first floor force-displacement relationship, because the gap prevented damage to the concrete wall until large deformation cycles, contrary to the wall without gap.

For design, Zhao and Astanceh recommended that:

1. Ductile failure modes (i.e., shear yielding of the steel infill) of the wall occur first, and the infill steel plates be designed accordingly.
2. Fracture in tension or buckling in compression of the boundary columns be avoided.
3. Shear capacity of the concrete be ignored as a conservative approach for strength, but that stiffness of the concrete wall be considered in calculating the period of vibration of the whole system.
4. Shear connectors be able to resist the tension force resulting from inelastic local buckling of the steel plate.
5. Shear connectors be able to transfer the shear capacity of the steel plate or reinforced concrete panel, whichever is smaller.
6. Beams and columns of the boundary frames be designed according to provisions for special moment frames.

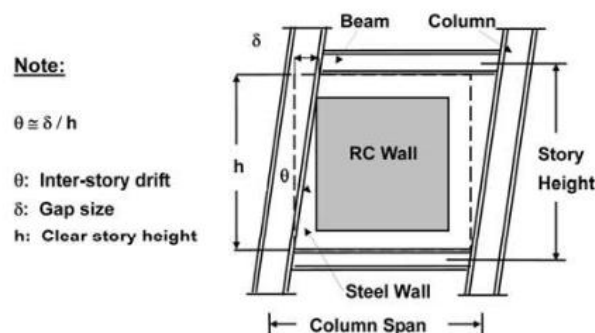


Figure 2-11 Gap between Reinforced Concrete Infill and Steel Frame, Zhao and Astanceh-Asl (2004)

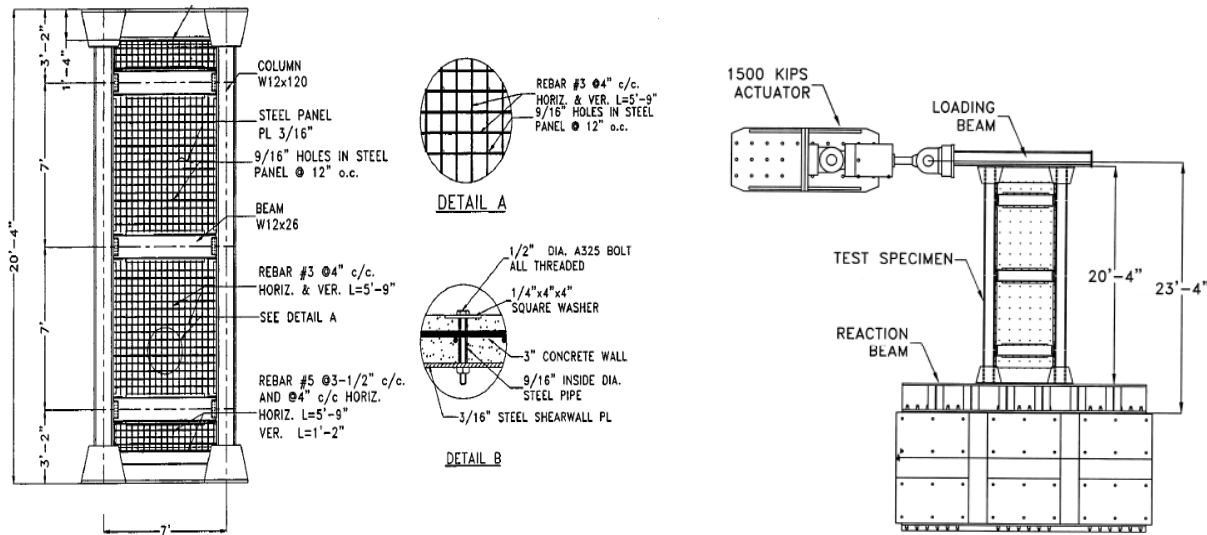


Figure 2-12 Tested Specimen and Test Rig, Zhao and Astaneh-Asl (2004)

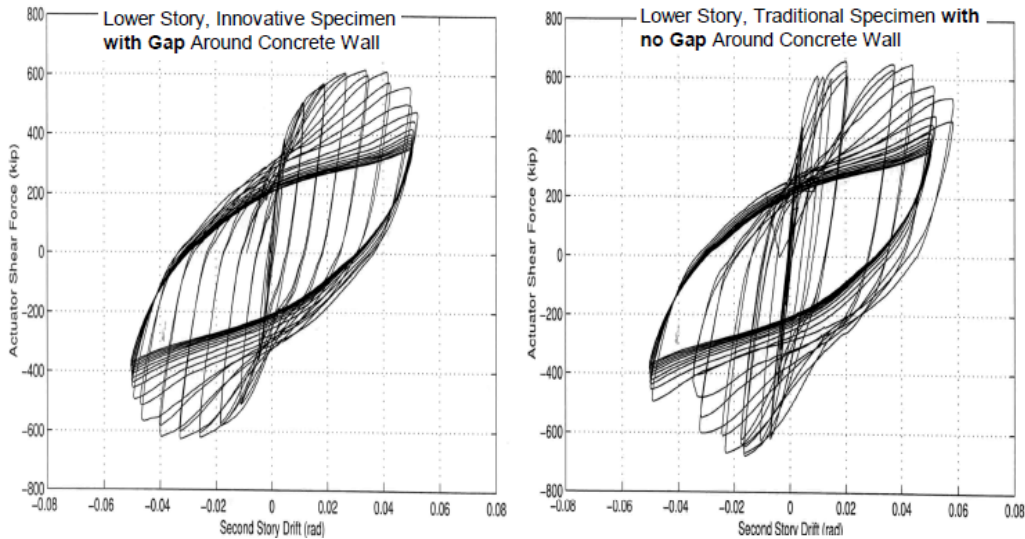


Figure 2-13 Test Results for the First Story, Zhao and Astaneh-Asl (2004)

Zhao and Astaneh-Asl (2007) conducted finite element analyses to replicate the behavior of the above composite shear wall specimens, and to perform some parametric studies. The finite element models, shown in Figure 2-14, were analyzed using MSC Nastran, with structural components modeled as non-linear shell elements, except for studs which were modeled as 1-D beam elements. The structural steel material model was a bilinear model with strain hardening, and the concrete material was taken as an

elasto-plastic material model. In addition, the elastic modulus of the steel material for plates was reduced by 30% to take into account initial warping, geometric imperfections, and residual stresses. Non-linear push over analysis was performed. The lateral force versus overall displacement curve from the push-over analysis matched with the test results to a reasonable extent, for both specimens, as shown in Figure 2-15.

A limited parametric study investigated the effect of thickness of the steel web, strength of steel, concrete thickness, and concrete strength, on the performance of the C-PSW. It showed that for that type of composite shear wall system, the steel wall was the major contributor to the overall system stiffness and strength (even though it was recommended to consider the contribution of concrete in stiffness calculations).

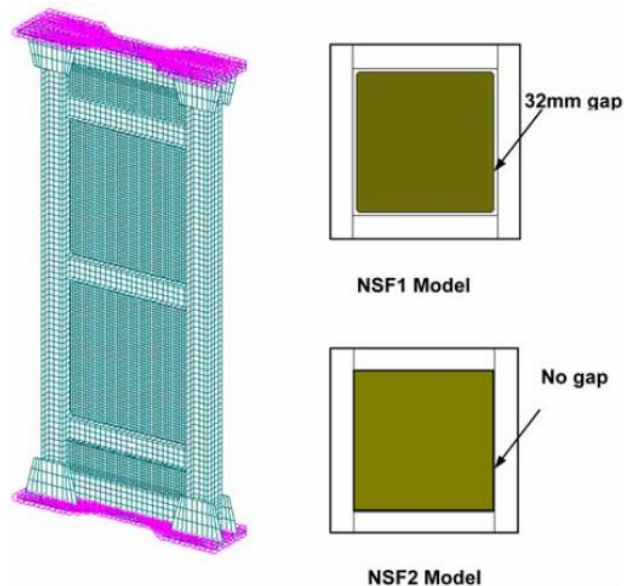


Figure 2-14 Finite Elements Model of C-PSW, Zhao and Astaneh-Asl (2007)

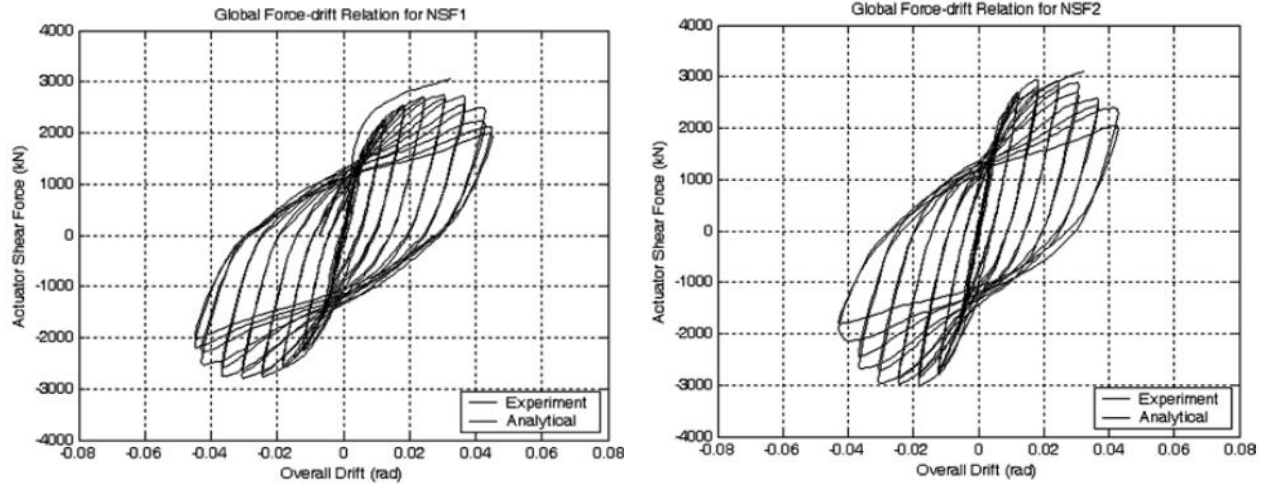
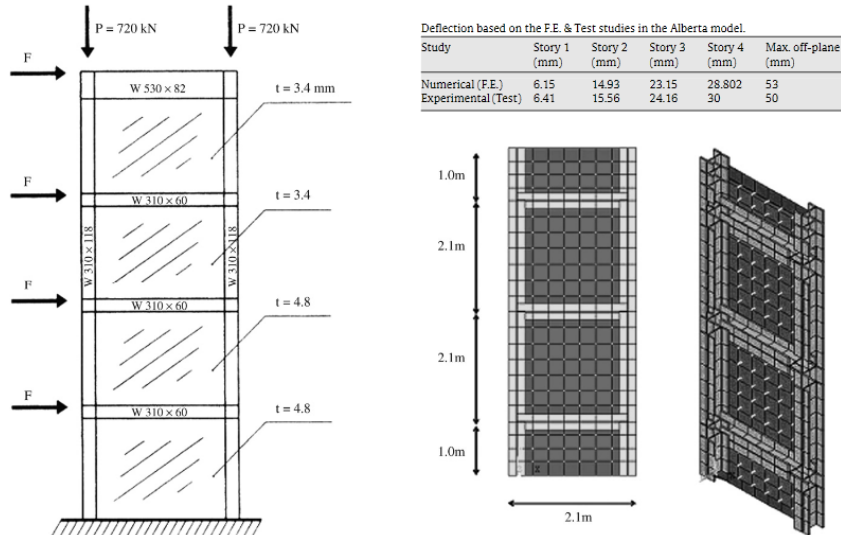


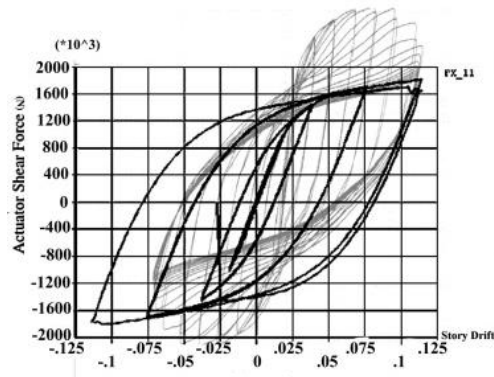
Figure 2-15 Comparison of Experimental and Analytical Push-over Curves for C-PSW, Zhao and Astaneh-Asl (2007)

Rahai and Hatami (2009) conducted an analytical study to evaluate the effect of variation of shear studs spacing. Using ANSYS version 11 for analysis, the model used 3-D beam elements to simulate the headed studs, and 3-D shell elements to model the steel components (beams, columns, and web plates). The model was calibrated using the wall tested by Driver et al. (2002). The finite element model was further calibrated using the data from the 4 story frame tested by Astaneh-Asl and Structural Steel Educational Council (2002). The resulting force-displacement relationship and the models used for calibration are shown Figure 2-16.

Numerous models with panels (i.e., infills surrounded by HBE and VBE) having 6.5 m width and 3 m height were studied to investigate the effect of the distance between the shear studs on the behavior of the composite shear wall. Results are shown in Figure 2-17. Note that these analyses assumed fixed wall base, no friction between steel and concrete, bi-linear material for steel and concrete, f'_c of 45 MPa, F_y of 235 MPa, and no contact between the steel and concrete due to presence of a 0.3 mm gap. Thickness of the concrete panels varied from 20 to 100 mm, and all specimens were subjected to cyclic loading.



a) Finite Elements Simulation Model, Driver et al. (2002)



b) Finite Elements Simulation Results for Berkley Model, Rahai and Hatami (2009)

Figure 2-16 Calibration of Finite Elements Models, Rahai and Hatami (2009)

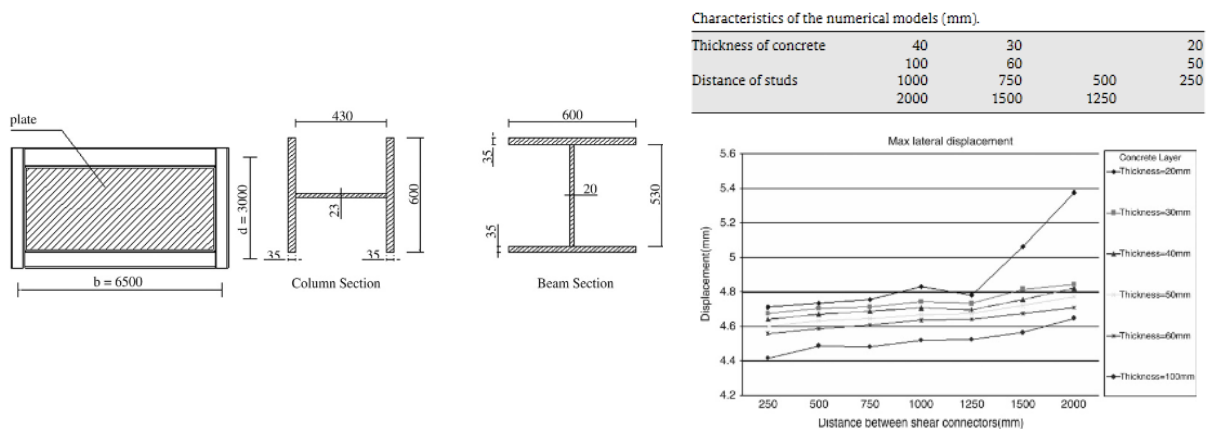


Figure 2-17 Results for the Numerical Analysis, Rahai and Hatami (2009)

Arabzadeh et al. (2011) investigated the effect of some parameters affecting C-PSW seismic performance by testing 4 specimens. A single one-bay wide, three-story, C-PSW specimen at scale 1:3, and 3 specimens one-bay and one-story at scale 1:4, were tested using the test set-up shown in Figure 2-18. The parameters under investigation were spacing of bolts (stud connectors), strength of concrete in the reinforced concrete infill panel, presence of gap between the reinforced concrete infill and the boundary elements, and whether concrete panels were used on one or both sides of the infill web plate. ASTM A572 Grade 50 was used for the frame steel and ASTM A36 steel was used for the plate infill. Steel studs were ASTM A490, and concrete strength varied between 45 to 75 MPa. The specimens were tested under cyclic loading following the ATC 24 protocol.

The research showed that connectors should be designed for shear and tension forces. It also demonstrated that using RC panels on both sides of the steel infill plate improves strength and energy dissipation of the C-PSW system, but decreases its ductility, and that using high strength concrete reduces damage to the reinforced concrete panel but does not affect the strength of the system. Figure 2-19 shows comparison of the force-displacement relationship for the different specimens.

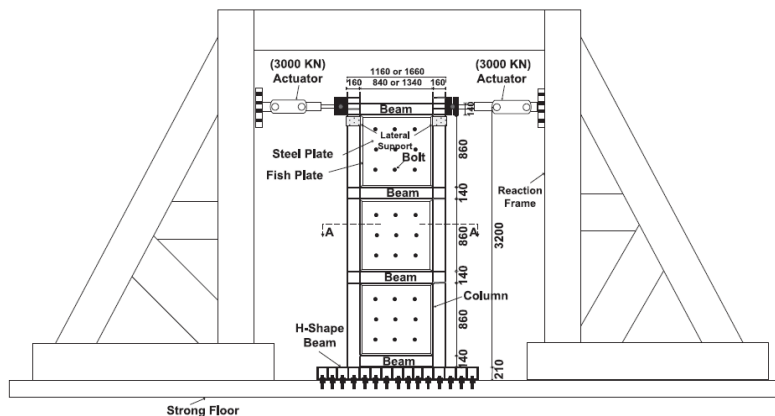
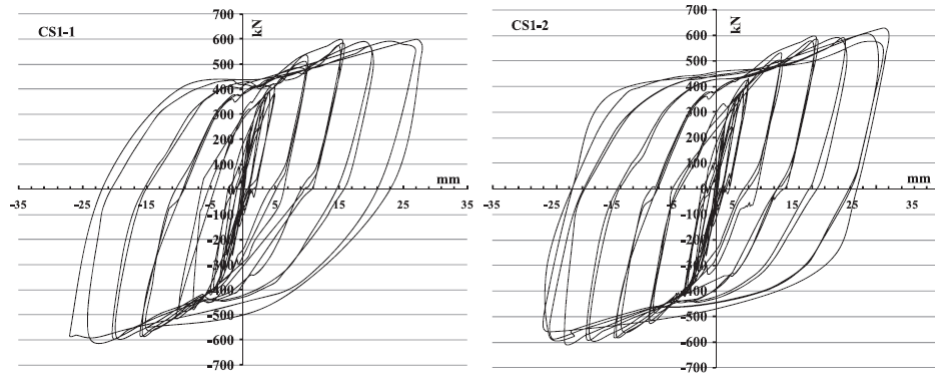
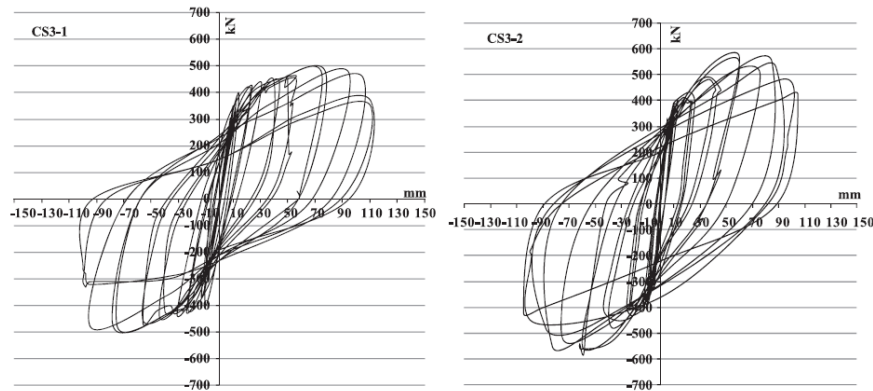


Figure 2-18 Test Set-up Arabzadeh et al. (2011)



a) RC on One Side of infill Plate

b) RC on Both Sides of Infill Plate



a) 30 mm Gap between RC panel and Boundary Elements

b) No Gap between RC Panel & Boundary Elements

Figure 2-19 Comparative Study, Arabzadeh et al. (2011)

2.3.3 C-PSW Composed of Steel Sandwich Panel Filled with Concrete

2.3.3.1 General

Sandwich steel panels filled with concrete have been used in many applications, including as gravity load supporting systems and lateral load resisting system. Much research has been done on such walls subjected to out-of-plane loading, and on their elastic response for use in nuclear applications. Significantly less research has been conducted on their inelastic seismic response.

The following sections summarizes some of the research on the use of sandwich steel panel filled with concrete, starting with selected non-seismic applications with a focus on their axial strength and out-of-plane (flexural) strength, often for nuclear applications, in Section 2.3.3.2, followed by seismic applications in Section 2.3.3.3. Finally, Section 2.3.4 summarizes the AISC-341 (2010) design provisions for C-PSW composed of sandwich steel panels filled with concrete.

2.3.3.2 Gravity In-plane (Axial) and Out-of-plane (Flexural) Loading for C-PSW with Sandwich Steel Panels Filled with Concrete

Wright (1998) investigated the behavior of a composite wall system composed of two skins of profiled steel and concrete-infill (schematically shown in Figure 2-20) subjected to axial loads and out-of-plane bending moment. The proposed system's concept, using fluted steel deck for the skins, was largely inspired from the composite floor systems commonly used in steel frame structures. The system gains its axial, lateral and out-of-plane strength after hardening of the filled-in concrete. Wright tested twenty full-scale walls; 15 of them were subjected to pre-dominant axial load and 5 were tested under a combination of axial, eccentric axial, and lateral loads. The tested parameters were profiled steel from different manufacturers (difference in width of the corrugated part and thickness), placement of construction ties, axial loading distribution (concrete core loading or simultaneous loading of steel profile and concrete core), grade of concrete, axial load as a percentage wall ultimate load (ranging between 33% to 75%), axial load eccentricity (eccentricity ratio ranging between 0.05 to 0.8), and finally grade of steel used in the profiled sheets ($F_y = 280$ to 361Mpa). The different test rigs used for walls testing under different loading conditions are shown in Figure 2-21.

The test results showed that using equation 2.2 (shown with no safety factors) from the British "Structural Concrete Code of practice for design and construction" BS8110 (1985) overestimated the axial capacity of the walls. Axial load capacity was influenced by local buckling of the profiled steel plates and the shape of the profile due to "difficulty in maintaining the bond between steel and concrete," which indicates that the presence of inner concrete was not sufficient to prevent local buckling of the steel profile as the thicknesses of the profiled sections were not enough to prevent local buckling. Reduction factors were proposed to account for local buckling of the component plates in the steel sheeting and the profiled shape of the concrete cross section.

$$N = 0.6f_{cu}A_c + 0.87A_sP_y \quad (2.1)$$

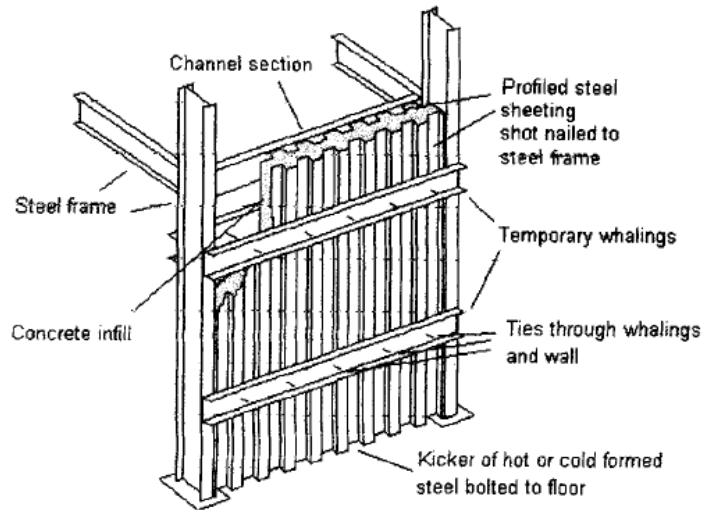
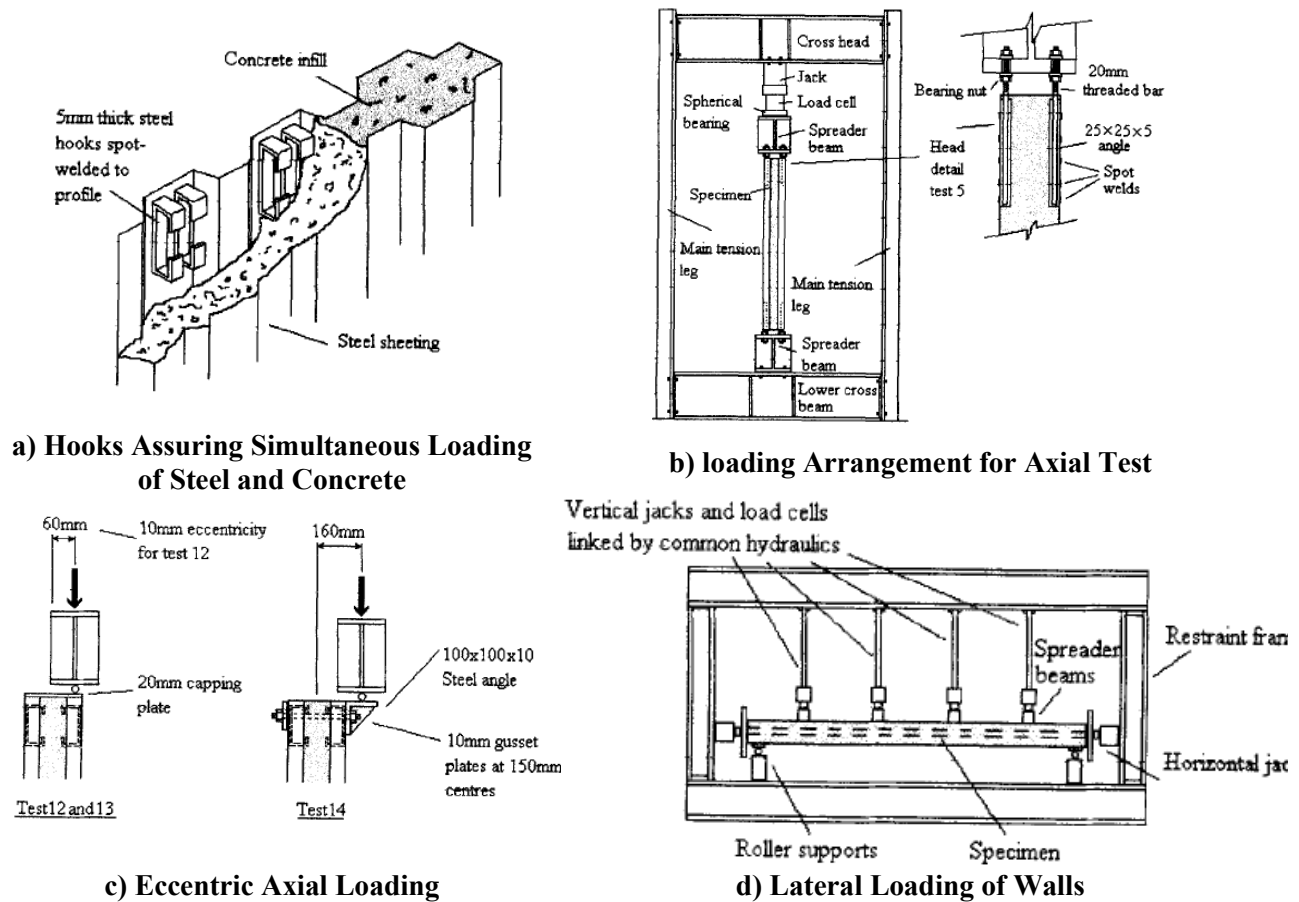


Figure 2-20 Schematic Diagram for the Composite Wall, Wright (1998)



a) Hooks Assuring Simultaneous Loading of Steel and Concrete

b) loading Arrangement for Axial Test

c) Eccentric Axial Loading

d) Lateral Loading of Walls

Figure 2-21 Different Loading Methods in the Experimental Program, Wright (1998)

Hossain and Wright (1998) tested five profiled concrete shear panels specimens (similar in construction to specimen in Figure 2-21) having a scale of 1:6 under in-plane shear load. Figure 2-22 shows the general details of the test set-up. The 560 × 560 mm square shear panels were tested by applying tension or compression forces across the diagonal of the test frame. Three profiled concrete panel specimens and a plain concrete one were subjected to incremental shear forces (applied as tension or compression force along a diagonal, as shown in the test set-up, by virtue of geometry and principal stress relationships) up to failure. A profiled concrete panel was subjected to hysteretic behavior by alternatively subjecting the specimen to tension and compression forces up to failure. The experimental results were used to verify finite element models of the tested walls. Equations for estimating the strength and the stiffness of profiled concrete panels were derived and verified by tests and finite elements analyses.

An expression for the shear stiffness (k) of the plain concrete and profiled concrete panel was derived considering concrete as a linear elastic material, such that:

$$k = \frac{E'_c at}{2b(1+\nu)} \quad (2.2)$$

$$V = \beta \frac{f'_c f'_t \cdot at_{eq}}{f'_c + f'_t} \quad (2.3)$$

where the reduction factor β ranged between 0.73-0.80

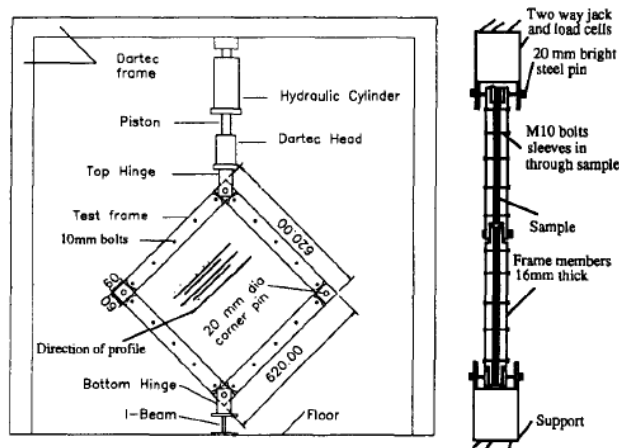


Figure 2-22 General Details of Shear Rig, Hossain and Wright (1998)

Hossain and Wright (2004) also developed guidelines for the design of double skin profiled composite shear walls. A formula was developed to predict the flexibility, C_w , and the ultimate shear resistance of the panel, V_w :

$$C_w = \frac{1}{K_w} = \frac{2ab(1+\nu_c)(1+\nu_s)}{a[2E_s t_s(1+\nu_c) + \alpha E_c t_{eq}(1+\nu_s)]} \quad (2.4)$$

$$V_w = 72\beta \frac{D_x^{1/4} D_y^{3/4}}{b^2} + 0.074bt_{eq}f'_{cu} \quad (2.5)$$

where,

K_w is Wall stiffness, kN/mm

a, b are Panel dimensions, mm

E_s is Elastic modulus of steel, MPa

E_c is Elastic modulus of concrete, MPa.

t_s is Thickness of the skin plate, mm

t_{eq} is Equivalent thickness , average thickness of the panel, mm

ν_c is Poisson's ratio for concrete

ν_s is Poisson's ratio for steel

α is Ratio between profile projected length and its height

D_x, D_y are Shear resistance of the concrete core based on biaxial state of stress, kN.

More commonly, flat plates have been used in C-PSW sandwich steel panels. In research performed for the nuclear industry (focused on out-of-plane and in-plane behavior in the elastic range), this system has been often called SC walls (or steel plate reinforced concrete structures). The flat composite panels are built by connecting a pair of steel plates with tie bars, and possibly partitioning webs, and made composite by using headed studs. The resulting boxes are filled with concrete, as shown in Figure 2-23. The stud bolts serve as shear connectors between the steel plates and concrete. This section summarizes some of the work conducted on this structural system. Note that the structural system was designed to remain elastic for this particular application.

Ozaki et al. (2004) derived expressions for evaluating the strength of steel plate reinforced concrete structures (SC), and conducted two experimental research programs investigating the influence of openings on the SC strength. The parameters under investigation were thickness of the surface steel plate, the effects of the partitioning web, and the axial force.

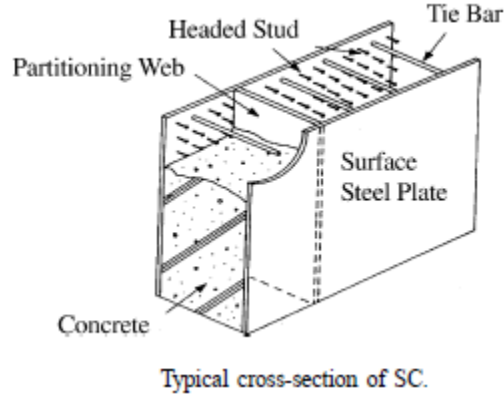


Figure 2-23 Cross section of SC Walls, Ozaki et al. (2004)

Expressions were derived by Ozaki et al (2004) to estimate shear stress of the SC structures in the presence of axial load at different stages are:

1) In-plane cracking shear stress, Q_c

$$Q_c = \left(A_c + \frac{G_s}{G_c} A_w \right) \sqrt{0.33\sqrt{F_c} (0.33\sqrt{F_c}) + \sigma_v}$$

2) In plane shear stress corresponding to surface plate yielding, Q_y

$$Q_y = \frac{k(G_c + G_s)}{\sqrt{G_c^2 + 3k^2 G_s^2}} \sigma_y^* \cdot \frac{A_w}{2} \quad (2.6)$$

$$k = 1 + (1 - \nu_s) Pdx \quad (2.7)$$

3) Ultimate transverse shear stress, Q_u

$$Q_u = (A_w + A_p) \sigma_y^* \quad (2.8)$$

where,

A_w , The cross-sectional area of total surface steel plate

A_p , Cross sectional area of total surface steel plate

G_c , shear modulus of concrete

G_s , shear modulus of steel

F_c , Concrete strength

σ_y^* , Yield stress of steel

The experimental program involved testing 9 SC walls under in-plane cyclic shear. The tested panels external dimensions were 1200×1200 mm and thickness of the panels was 200 mm. The thickness of the surface plates, t , were 2.3, 3.2, and 4.5 mm, with spacing of the stud connectors, b , altered such as to keep $b/t=30$. Another parameter considered was partitioning of the web instead of using studs, comparing results with SC walls having welded studs. The yield stress of steel was 351 MPa while the concrete strength was 40 MPa. The test set-up is shown in Figure 2-24. The test showed that yield strength of the walls increased linearly as the thickness of the surface steel plate increased. The shear cracking strength of the SC wall was influenced by axial force acting on the wall. The partitioning web increased the stiffness of the SC wall. Predictions from the derived equations were in good agreement with the experimental results.

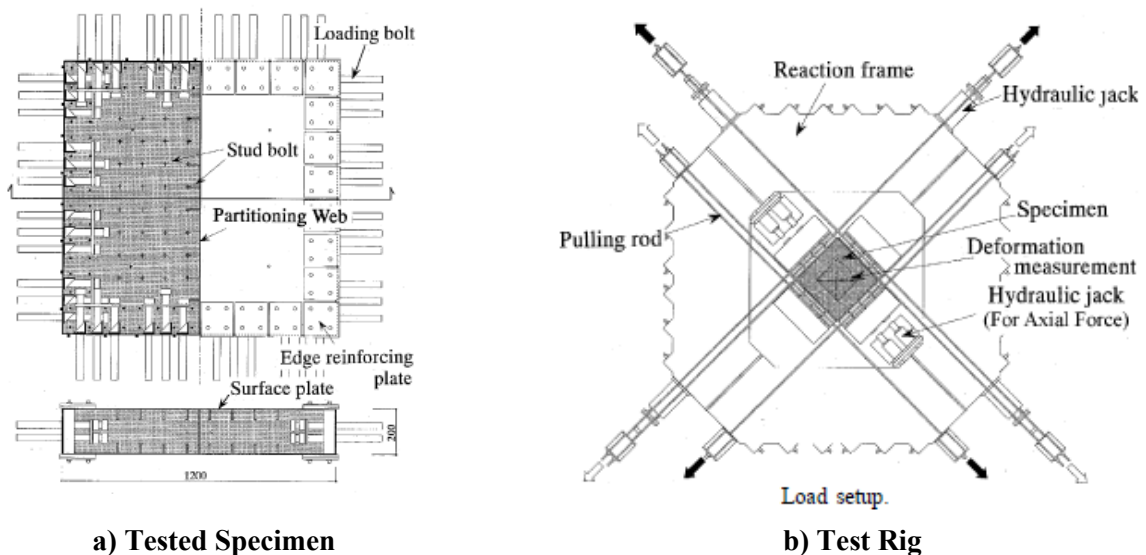


Figure 2-24 Test Specimen and Test Set-up, Ozaki et al. (2004)

Varma et al. (2011) developed a mechanics based model (MBM) to predict the behavior of SC walls panels subjected to in-plane membrane forces. The Model was verified using the experimental data from Ozaki et al (2004) and Varma et al (2006), and using detailed non-linear finite element analysis. The model was used to calculate the stresses in the face steel plates and the concrete of the SC walls and accordingly predict elastic behavior under in-plane forces. That model assumed that stud shear connectors were provided in sufficient number, size, and length to ensure strain compatibility between the steel plates and concrete, in terms of the principal forces S_{p1} and S_{p2} . Through strain compatibility, stresses in both steel and concrete were calculated. The concrete was considered cracked when either of the principle forces exceeded the value of the concrete cracking force, S_{cr} . Figure 2-25 shows the membrane forces and the proposed corresponding equations by which, knowing the section average strains, the principal stresses can be calculated and used to determine conditions on the von-Mises yield surface.

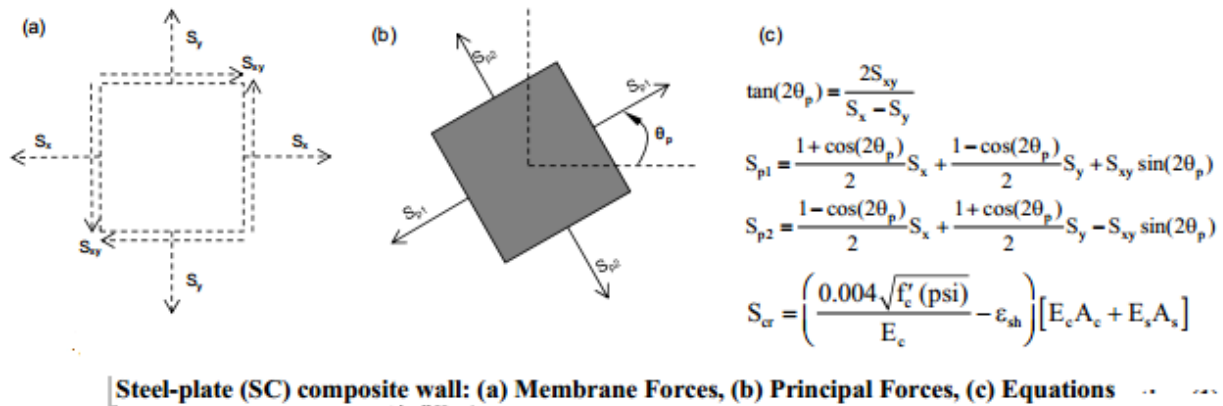


Figure 2-25 Membrane Forces Calculated by the MBM, Varma et al. (2011)

Per the free body diagram shown in Figure 2-26, the averaged strain can be used to calculate the stresses on the individual cross section components (steel face plate and concrete infill), using the stiffness matrix, $[K]$, and the stress transformation matrix, $[T]$. The principal stresses in the face plate of the SC can be calculated and limited to the yield stresses (per the Von Misses criteria), and the minimum principal stresses in the concrete infill should not exceed $0.7 f'_c$ to ensure that concrete remains in the elastic range.

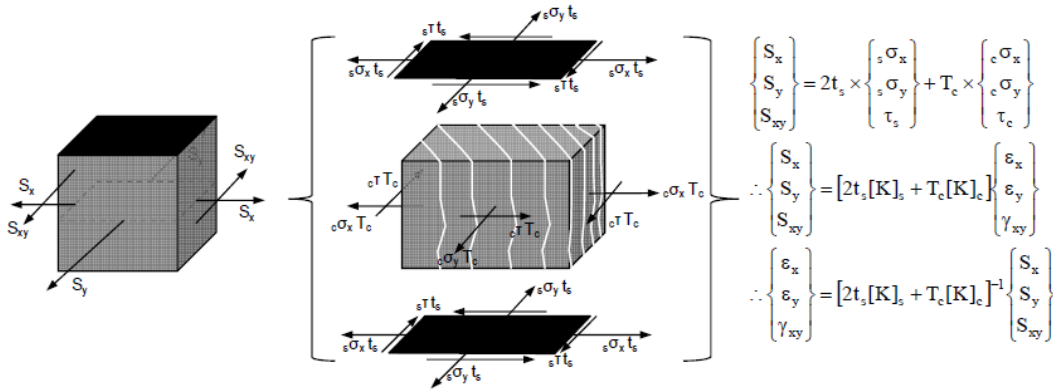


Figure 2-26 Free Body Diagram and Force Equilibrium SC Cross-section, Varma et al. (2011)

A finite element model developed using layered composite shell (LCS) finite elements was also established and verified using the experimental results of Ozaki et al (2004). Used to predict the in-plane behavior of SC walls, the model considered steel material non-linearity and inelastic behavior of concrete (in compression) and its brittle post cracking in tension. The interaction diagram, shown in Figure 2-27, and developed through those studies, shows four regions of behavior. Region I corresponds to the state of biaxial tension, region II corresponds to the state of axial tension + in-plane shear, region III corresponds to the state of axial compression + in-plane shear, and region IV corresponds to the state of biaxial compression.

The results from the finite elements analysis and mechanics based model were used to develop simple design approach for the SC walls subjected to in-plane forces and out-of-plane moments. The approach considers SC walls as two halves (top and bottom) subjected to in-plane forces by dividing the out-of-plane forces by a moment arm equals to $0.9T$, where T is the total thickness of the wall. The membrane principle forces S_{p1} and S_{p2} must lie within the interaction diagram shown in Figure 2-28.

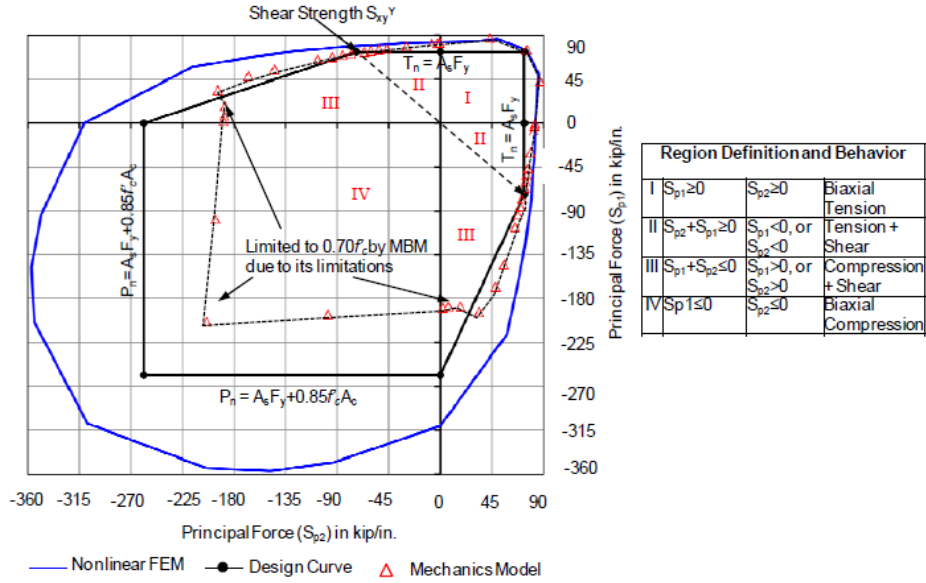


Figure 2-27 Interaction Surface for Composite SC Wall Panels in Principle Force Space, Ozaki et al (2004).

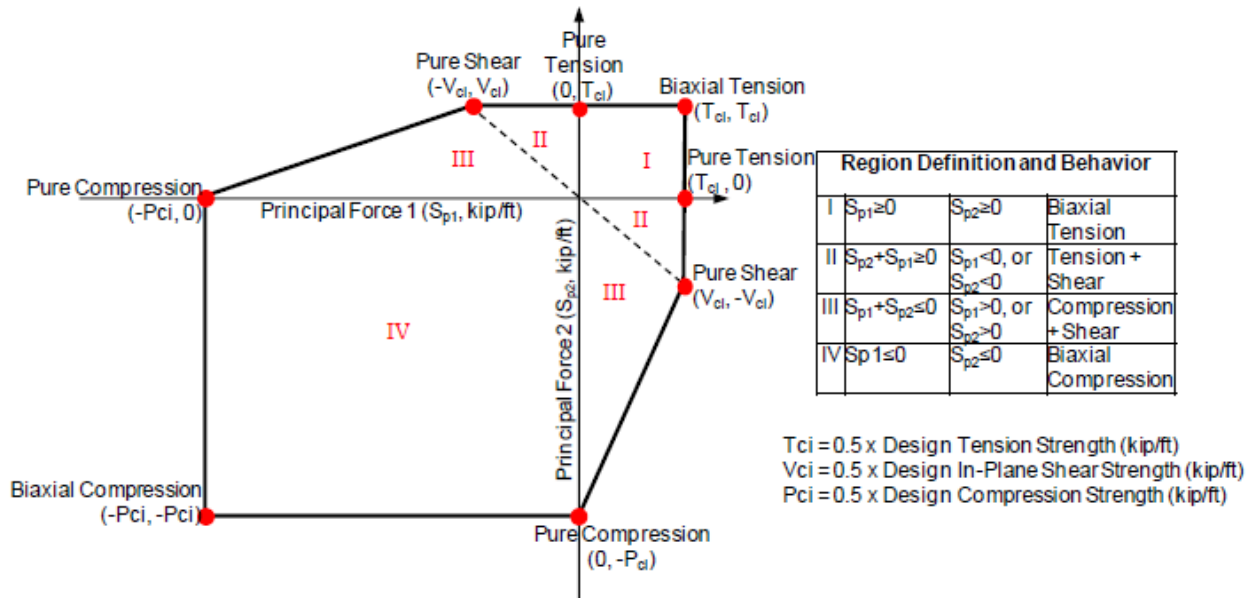


Figure 2-28 Interaction Surface in Principle Force Space for Each Notional Half, Ozaki et al (2004)

Sener et al (2011b) tested eight large-scale SC beam specimens to determine their out-of-plane shear strength. A 3D finite element model was developed and verified through an experimental program; the experimental and analytical results were also compared to the shear strength equations for reinforced concrete beams given by the ACI 318 as follows:

$$V_n = V_c + V_s \quad (2.9)$$

$$V_c = 2\sqrt{f'_c} \cdot A_c \quad (2.10)$$

$$V_s = A_v f_{vt} \frac{d}{s} \quad (2.11)$$

where,

A_c =Cross-sectional area of concrete

A_v = Cross sectional area of shear reinforcement

d =Section Depth

s = Shear reinforcement spacing

The tested specimens by Sener et al (2011b) had depth to shear span ratio that ranged between 2.5 to 5.5. Five of the tested specimens had no special shear reinforcement and three specimens had shear reinforcement in the form of tie bars. The parameters under investigation were section depth, T , steel plate thickness, t_s , and reinforcement ratio, $2 t_s/T$. Typical tested specimens are shown in Figure 2-29 the yield stress for the specimens steel plates was 65 ksi, and the concrete strength varied between 6.1 ksi and 7.5 ksi.

The tested specimens were simulated using 3D non-linear finite element models using ABAQUS, which showed good agreement with experimental results, as shown in Figure Figure 2-30. The analytical and experimental data showed that the out-of-plane shear strength of the SC walls can be predicted using the ACI 318 equations, irrespective of whether special shear reinforcement is provided or not.

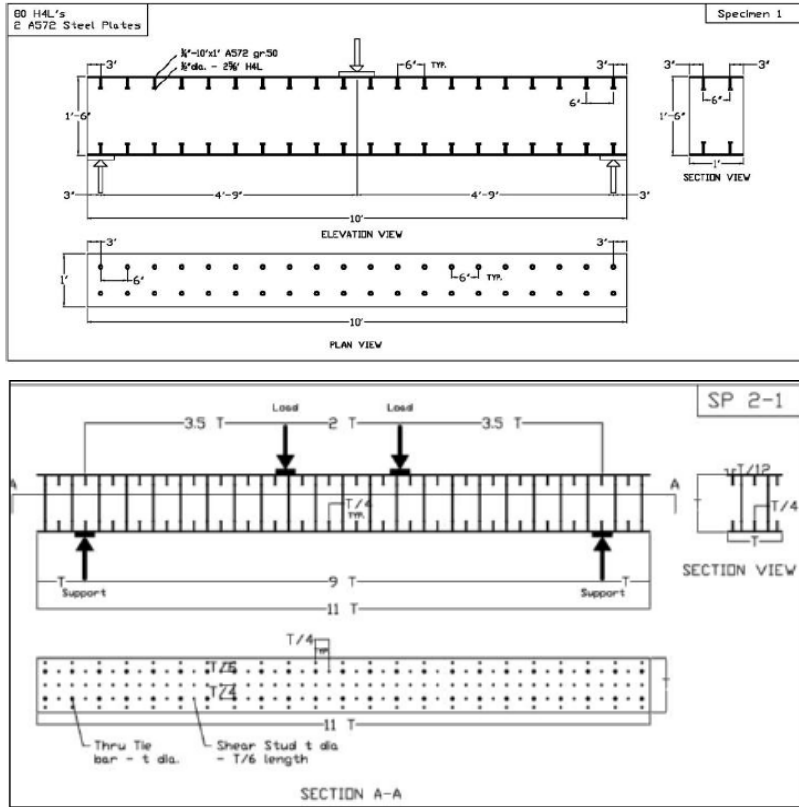


Figure 2-29 Tested Specimen with and without Shear Reinforcement, Varma et al. (2011)

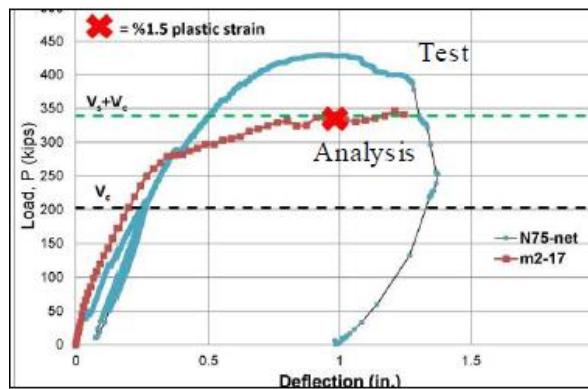


Figure 2-30 Force- Displacement for Typical Specimen, Varma et al. (2011)

Sener et al. (2012) provided recommendations for estimating the structural stiffness of SC walls subjected to accidental thermal loading (an important load case when using this system in nuclear reactors containment buildings), estimating the maximum moments induced due to thermal gradients, and

developed linear elastic finite element model of SC walls that can be used for elastic dynamic seismic analysis.

The flexural out-of-plane stiffness of SC walls was predicted using cracked transformed section properties using the stress, strain, and force block shown in Figure 2-31.

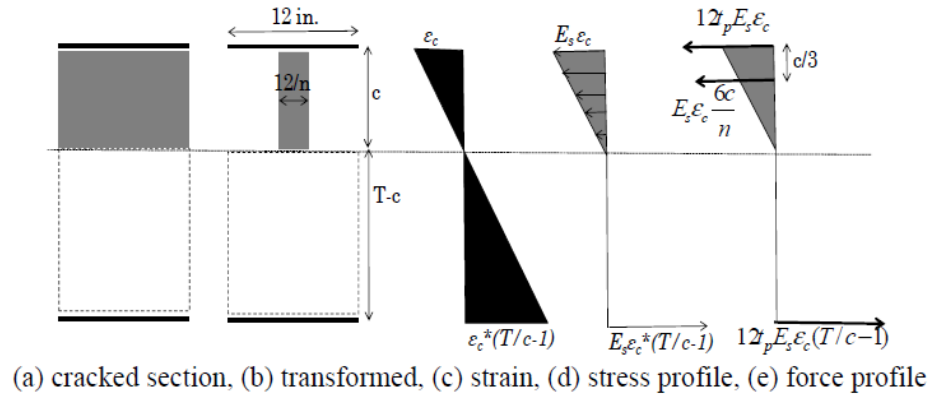


Figure 2-31 Flexural Stiffness of SC Cracked Transformed Section, Sener et al. (2012)

The cracked-transformed flexural section stiffness (EI_{cr-tr}) is given by:

$$EI_{cr-tr} = E_s \left[12t_p T^2 \left[1 + 2 \left(\frac{c}{T} \right)^2 - 2 \frac{c}{T} - \frac{t_p}{T} \right] + \frac{4T^3}{n} \left(\frac{c-t_p}{T} \right)^3 \right] \quad (2.12)$$

where,

$$\rho' = \frac{2t_p}{T} \cdot \frac{E_s}{E_c} \quad (2.13)$$

$$\frac{C}{T} = \sqrt{\rho'^2 + \rho'} - \rho' \quad (2.14)$$

Equation 2.12 was calibrated to a simpler form given by:

$$EI_{cr-tr} = EI_s + \alpha EI_{cr-tr} \quad (2.14)$$

where,

$$\alpha = 0.48\rho' + 0.10$$

The flexural stiffness for use in calculation of thermal effects was given by:

$$EI_{eff} = (E_s I_s + \alpha E_c I_c) \left[1 - \frac{\Delta T_s}{150F} \right] \geq E_s I_s \quad (2.15)$$

where,

ΔT_s , Temperature change from 0 to 150⁰ F

When the change in Temperature is larger than 150⁰F, the stiffness was limited to that of the steel only.

The equations needed to construct a tri-linear model for the shear stiffness of SC walls (K_{xy}), developed for analyses conducted to replicate the experimental results, are shown in Figure Figure 2-32. The model requires that the following parameters are known: steel elastic modulus, E_s , concrete elastic modulus, E_c , steel poison's ratio, ν_s , concrete poison's ratio, ν_c , steel area, A_s , concrete area, A_c , steel shear modulus, G_s , concrete shear modulus, G_c , steel yield strength, F_y , and concrete strength, f'_c .

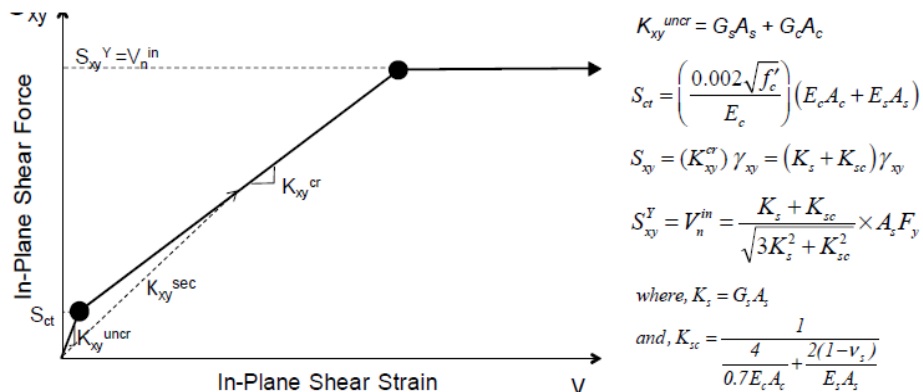


Figure 2-32 In-plane Shear Behavior of SC Walls, Sener et al. (2012)

Much of the research conducted on the out-of-plane flexural strength of sandwich panel walls was conducted in support of the development of the Bi-Steel product, originally developed by British Steel (which became part Corus steel in the late 1990s, itself acquired by Tata Steel around 2011). In this sandwich composite system, the two steel plates are interconnected by bar connectors friction welded to the skin plates at both ends. Multiple steel panels are welded together on site and filled with concrete. The Bi-Steel sandwich system has been used as flooring system, beam, column, fire resisting system, and as a building core systems for multi-story buildings marketed as the Core-fast system by Bi-steel Corus (2007). A design guide was published by Corus (2003) based on testing and existing codes for concrete and steel design. Although the Bi-Steel system has not been investigated as a seismic resistance system, and the available design guides and research conducted in support of the product revolved around out-of-plane loading and behavior, a summary of relevant research is summarized in this section.

Figure 2-33 shows Bi-Steel units and its assembly as a core for a multistory structure. Some applications for the Corefast system in Europe include a nine story office building in Manchester, UK, shown in Figure 2-34, a six story elevator core in Dundrum, UK, shown in Figure 2-35, and a 16-story commercial building in Birmingham, UK shown in Figure 2-36 (Corus 2006).



a) The Steel Panel Forming the Bi-Steel Product



b) Corefast Walls used in Multi-story Buildings and Made of Bi-steel Panels

Figure 2-33 Bi-Steel Product COREFAST a) Single Units, b) Assembled Core, Bi-steel Corus (2007)



Figure 2-34 Forty Spring Garden Manchester's Financial District, Corus (2006)

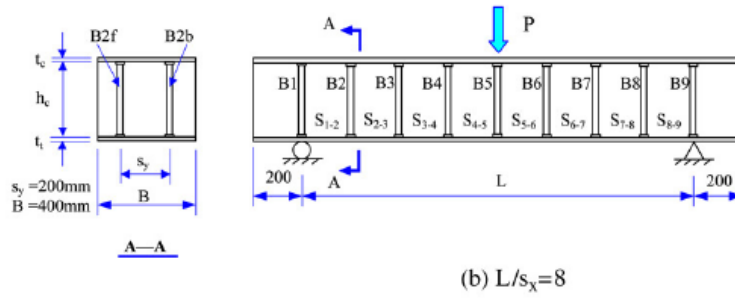


Figure 2-35 Dundrum Cinema Lift Core, Corus (2004)

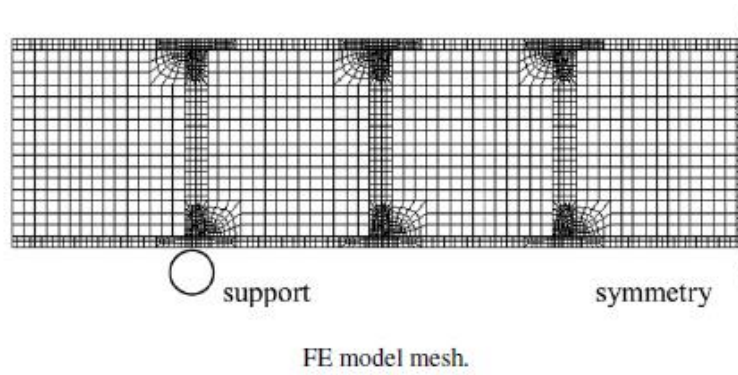


Figure 2-36 Birmingham 1, Tallest Core Fast (16--story), Corus (2006)

Foundoukos and Chapman (2008) simulated the static out-of-plane flexural behavior of Bi-Steel beams using the finite element analysis software ABAQUS. A 2-D model was used to reduce analysis time. The original choice of analysis was the ABAQUS/Standard package, which is more suited for static analyses, including reinforced concrete applications, but it was found that the concrete material model used was causing the analysis to diverge at a small proportion of the specified maximum applied load. It was observed that convergence problems occurred for the post tension-cracking part of the concrete material curve (the tension stiffening curve). When the concrete tension resistance was reduced to zero, the element stiffness was correspondingly reduced to zero in the direction normal to the crack, since no bonded reinforcement was defined to resist tensile stresses and the solution diverged. Foundoukos and Chapman therefore use the solver in the ABAQUS/Explicit package to analyze the Bi-Steel beams, which is a dynamic analysis package, and therefore a quasi-static analysis was defined. The model used, shown in Figure Figure 2-37, was calibrated using relevant test data, and then used to study how different parameters affected the transversal shear capacity of the Bi-Steel panel under uniformly distributed load. The parameters considered to affect the transversal shear capacity of Bi-Steel panels are, the ratio of longitudinal spacing of tie bars, S_x , to thickness of concrete, h_c , ratio of thickness of the skin plate under tension, t_t , to h_c , variation of concrete thickness, and the ratio between beam span, L , and h_c . Selected parametric study results are shown in Figure 2-38.



Details of the Simulated Beam



The 2-D Finite Element Model

Figure 2-37 Finite Element Model and Simulated Bi-steel Beam, Foundoukos and Chapman (2008)

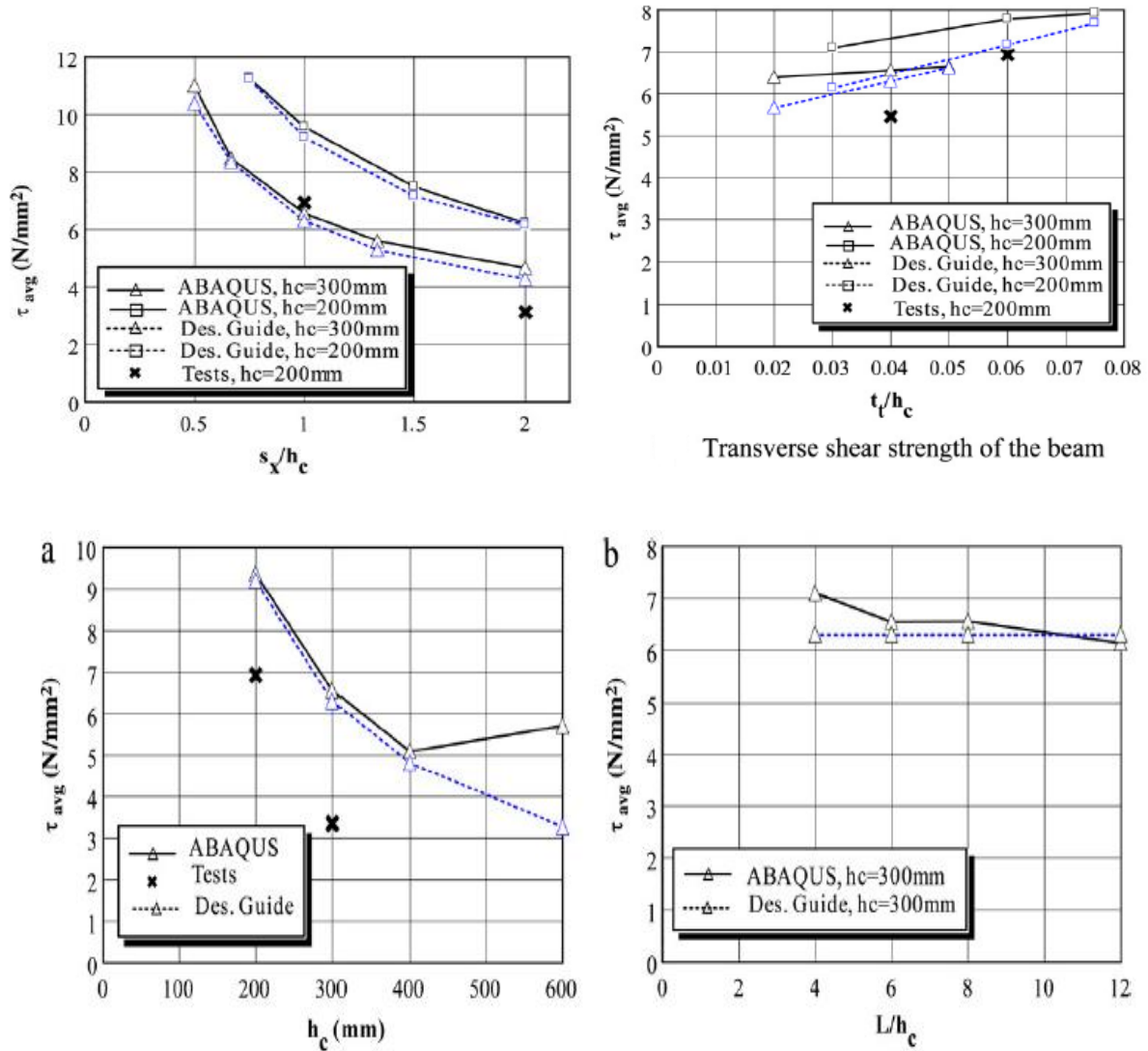


Figure 2-38 Results of Parametric Study, Foundoukos and Chapman (2008)

2.3.3.3 Seismic Application of C-PSW Consisting of Sandwich Steel Panel Filled with Concrete.

For seismic applications, Varma et al. (2011) proposed using a secant stiffness approach to capture the cyclic behavior of the SC walls. This stiffness, k_{xy}^{sec} , is given by the simple three-step model shown in Figure 2-39 given by:

$$K_{xy}^{sec} = 0.5(\rho)^{-0.42G_s A_s} \quad (2.16)$$

where,

$$\rho = \frac{A_s F_y}{A_c \sqrt{f_c X_c}}$$

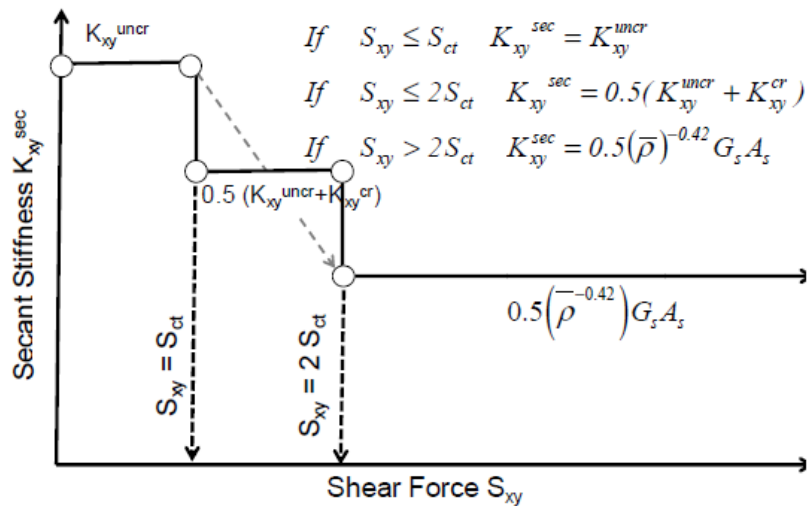


Figure 2-39 Secant Stiffness for SC Walls, Sener et al. (2012)

Eom et al. (2009) investigated the seismic behavior of C-PSW with steel sandwich panels composed of two steel skin plates connected using tie bars, with the space between them filled with concrete. In this investigation, individual and coupled walls, with rectangular and T-shaped section, were tested under cyclic loads. Three isolated walls and two coupled walls representing 1/3 and 1/4 scale models for a 30 story prototype were tested. Figure 2-40 shows the tested specimens. The tested walls had a ratio of tie bar spacing to steel plate thickness of 30 for the isolated walls, and of 50 for the coupled walls. The aspect ratio of the isolated wall was 3.7, intended to ensure a dominant in-plane flexural behavior.

The isolated walls were made of steel plates having yield and ultimate strength, F_y and F_u , of 383 and 544 MPa, respectively. The coupled walls specimens had a yield and ultimate strength, F_y and F_u , of 372 and 453 MPa, respectively. The compressive strength, f_c' , of the filled concrete was 39.7 and 58.7 MPa for the isolated and the coupled wall specimens, respectively. Figure 4.30 shows the tested specimens.

Under reversed cyclic loading, the double skin composite walls with large depths experienced early fracture of the welded connections at the wall base and coupling beams. This was due to a high concentration of stress at the welded joints, as well as a large plastic strain demand arising from the large depth of the walls. After the premature failure of the welds, different methods were used to strengthen the wall, and ductility of the walls was somewhat dependent on the strengthening method.

When premature weld failure was avoided, the main mode of failure was local buckling of the steel skin and crushing of the concrete. Despite the development of this local buckling in the steel plates, it was reported that the plastic stress distribution in both steel and concrete could be used to calculate the load carrying capacity of the walls; in this process, the equivalent strength of concrete was considered to be $f_{ce} = 0.85f'_c$ while a β factor of 0.85 was considered to define the depth of the concrete block under compression. Figure 2-41 shows the force displacement relationship for the tested specimens.

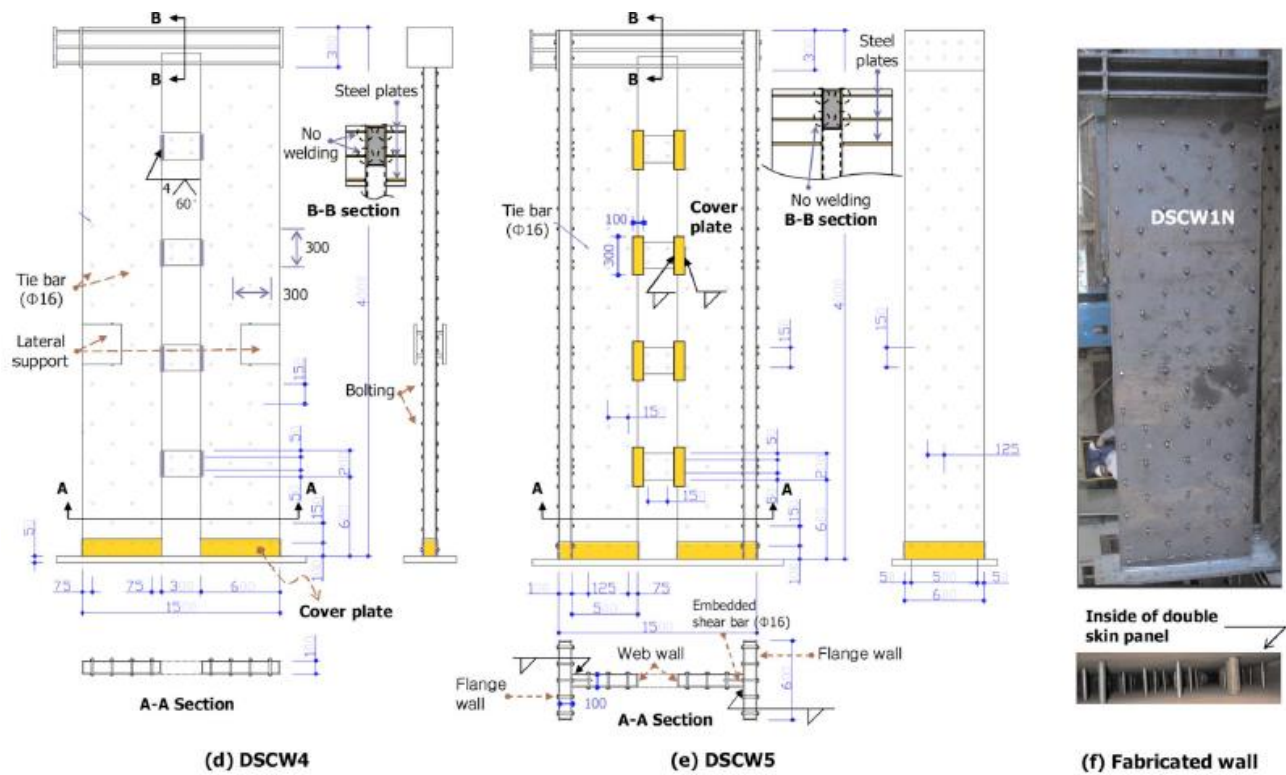


Figure 2-40 Tested Specimens, Eom et al (2009)

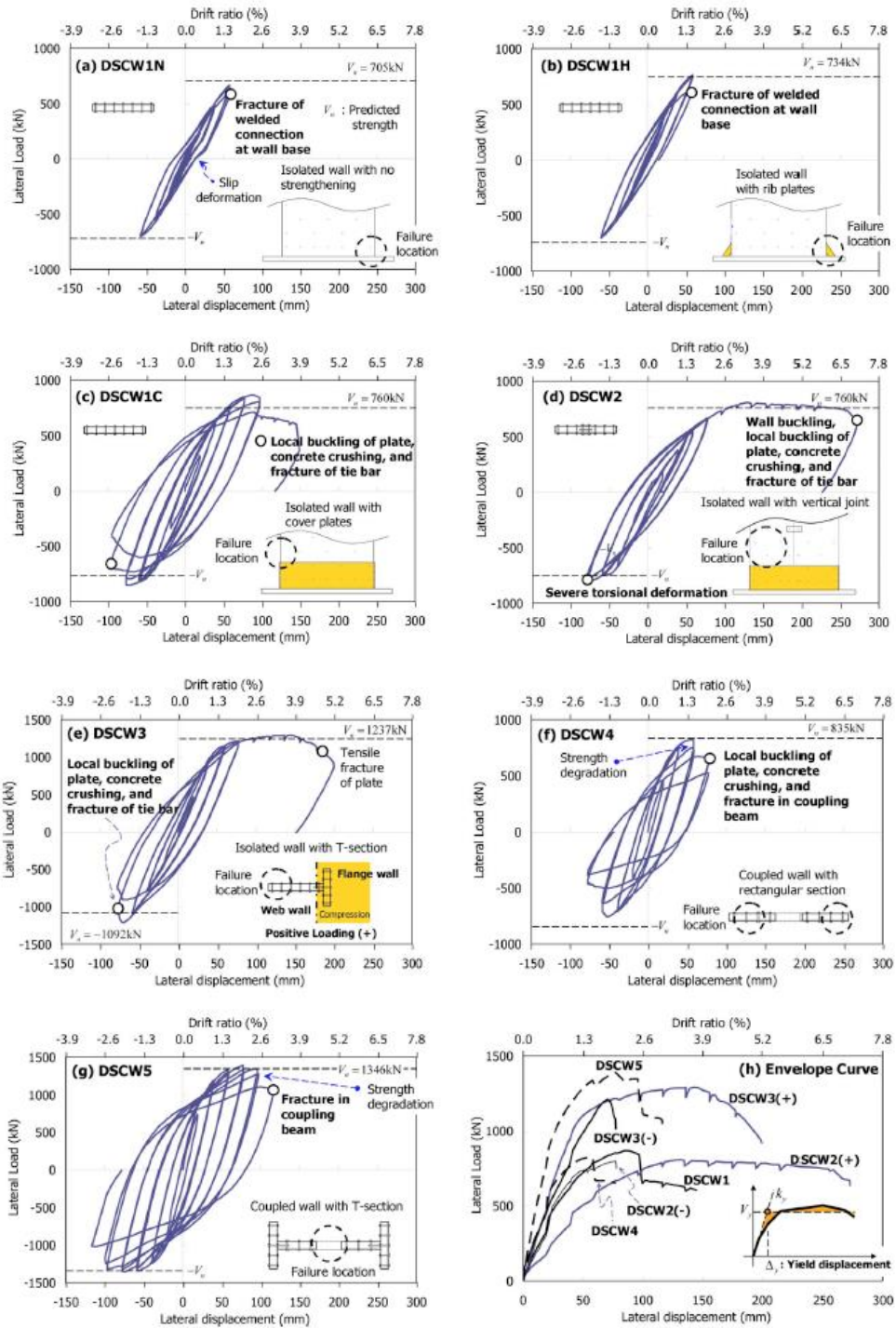


Figure 2-41 Force Displacement Relationship for the Tested Specimens, Eom et al. (2009)

The testing program executed by Eom et al. (2009) showed that:

- 1- Concrete filled steel sandwich panels filled with concrete having aspect ratio of 3.7 were able to attain their plastic moment capacity, M_p , where plastic moment capacity was calculated assuming full yielding of the steel cross section and that the concrete in compression attained a strength of f'_c , including factors accounting for rectangular distribution.
- 2- Rectangular cross-section walls developed premature failure at their *corners* due to the large strains generated at the ends of the deep cross-section.
- 3- Local buckling of the wall occurred between the lowest two rows of the tie bars
- 4- The displacement ductility of the wall is almost equals to 2.86

2.3.3.4 Design Recommendation for C-PSW Walls

Section H6 of AISC-341 (2010) is dedicated to Composite Plate Shear Walls (C-PSW). Yet the section focuses on C-PSW system that achieves the required ductility through shear yielding of the steel web. Section H-6 emphasizes C-PSW walls with HBEs and VBEs where “significant inelastic deformation capacity through yielding in the plate webs” and HBEs and VBEs are expected to remain inelastic. On that basis, the C-PSW steel web is required to be designed to resist the seismic load defined by the applicable building codes, using the nominal shear strength of the steel web, V_n , given by:

$$V_n = 0.6R_y F_y A_{sp} \quad (2.17)$$

$$\phi = 0.9(LRFD) \quad \Omega = 1.67(ASD)$$

where,

A_{sp} =Horizontal area of stiffened steel plate, in² (mm²)

F_y =Specified minimum yield stress of the web plate, ksi (MPa)

V_n =Nominal shear strength of the steel plate, kips (N)

Section H-6-4a specifies a minimum thickness of the web plate of $3/8$ " (9.5 mm). It is also specified that the concrete thickness shall be a minimum of 4 in (100 mm) on each side when concrete is provided on both sides of the steel plate and 8 in (200 mm) when concrete is provided on one side of the steel plate, and that steel headed stud anchors or other mechanical connectors be provided to prevent local buckling and separation of the plate and reinforced concrete. Section H-6 does not provide design

recommendations for C-PSW composed of steel sandwich panels filled with concrete, even though these are claimed to fall within the scope of H-6. The seismic design parameters for C-PSW per ASCE-7 (2010) are shown in Table 2-2.

Table 2-2 Seismic Design Parameters for C-PSW, AISC-341 (2010)

Type of Wall	Response Modification Factor, R	Over-strength Factor, Ω_o	Deflection Amplification Factor, C_d
C-PSW	6.5	2.5	5.50

2.4 Summary

Research on composite shear walls made of steel and concrete has been reviewed for composite shear walls having different structural configurations and accordingly different mechanisms for ductile performance. Referring to AISC-341 (2010) terminology, selected research on C-OSW/CSSW was summarized along with AISC-341(2010) recommendations for the seismic design of such walls. Then, research and design provisions for the two types of C-PSW covered by AISC-341(2010) were reviewed: first, steel plate shear wall with concrete panel attached to the steel infill with connectors; second (and of greater interest), steel sandwich panels filled with concrete. In the latter case, general elastic axial and flexural behavior was first described, followed by a description of the limited research findings to date on ductile performance and seismic applications.

The presented literature showed that different types of composite shear walls are ductile and can be used in seismic applications, but also that there exists only limited knowledge on the in-plane ductile flexural behavior of C-PSW consisting of steel sandwich panel filled with concrete. There does not exist sufficient experimental data in support of whether concrete filled steel sandwich panel walls can provide satisfactory ductile response when undergoing in-plane flexure and consistently reach the plastic moment capacity of the cross-section, for different geometric configurations. There is also insufficient data on how to design the connection between the concrete filled sandwich panel wall for that application, to allow the cross-section to attain its plastic moment capacity, and on how to design the foundation of such wall to develop its full composite strength. Finally, detailing for this type of walls must be developed to prevent premature failures due to stress concentration in the corners of built-up (welded) rectangular cross-sections.

In parallel to the need to develop enhanced knowledge about the inelastic in-plane flexural behavior of concrete filled sandwich panel walls, is a need to provide seismic design recommendations for consideration by current design codes and specifications. This is particularly important given that the system is appealing to engineers on the basis of its fast constructability and economic advantages. Note that the concrete filled sandwich panel walls considered here are foreseen to be a possible alternative to conventional reinforced concrete walls (for walls with and without boundary elements).

The following chapters presents the results of experimental and analytical studies focusing on concrete filled steel sandwich panel walls (CFSSP-Walls) subjected to in-plane flexure, in an attempt to answer the above questions, particularly to provide insight on the ductility of the system and its potential value in providing seismic resistance.

CHAPTER 3

PRELIMINARY INVESTIGATION OF CFSSP-WALL CONCEPT

3.1 Introduction

This report investigates the seismic behavior of concrete filled steel sandwich panel walls (CFSSP-Walls) with a dominant flexural behavior such that the wall cross section can attain its full plastic moment capacity in the direction normal to its strong axis. It is assumed here that flexural behavior will dominate over shear behavior when the structural wall height-to-width aspect ratio is larger than two, which would be the case for of high rise buildings having wall core of the type considered here as a lateral load resisting system.

A CFSSP-Wall, of depth, h , and thickness, b , as shown in Figure 3-1, is composed of two skin plates connected together through tie bars spaced at a distance, S , with the space between the two plates filled with concrete. The result is sometimes called a double-skin composite panel. For the case considered here, the ties are assumed to be continuously welded to the skin plates (various ways to achieve this are presented elsewhere in this report).

An important parameter believed to impact the seismic behavior of such composite walls is the ratio between tie bars spacing and thickness of the web skin plate, S/t , which is defined as the ratio of the maximum of the horizontal or the vertical spacing of the tie bars to the thickness of the skin steel plate of the panel. Figure 3-1 shows the rectangular cross section for a general CFSSP-Wall.

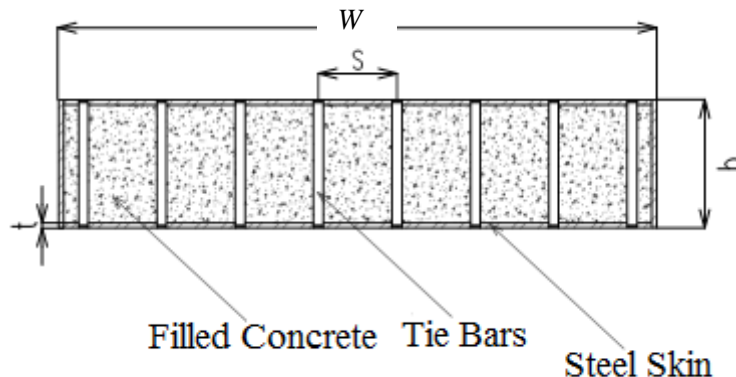


Figure 3-1 Proposed Rectangular CFSSP-Wall Cross-section Configuration

Ideally, a ductile CFSSP-wall section should develop its plastic moment, achieved through yielding of the steel plate in both tension and compression, with concrete attaining its maximum strength. The filled-in concrete not only contributes to the CFSSP-wall section capacity, but also helps restrain the local buckling of the sandwich panel steel plates by preventing their inward buckling and only allowing outward buckling. The tie bars serve to minimize outward local buckling of the steel plate of the sandwich panel and provide the load transfer between steel and concrete needed to the required composite action in the CFSSP-Wall cross section.

This chapter investigates the behavior of the proposed CFSSP-Walls using different analytical techniques to shed light on the mechanics of the proposed system. Towards that purpose, an example of the proposed CFSSP-Wall is analyzed using different models and analytical methods. To further investigate rectangular CFSSP-Walls, the walls tested by Eom et al (2009) were modeled using finite element analysis through Abaqus 6.10EF2. The resulting numerical models, developed here based on the available limited information, will eventually be verified experimentally in subsequent chapters.

Section 3.2 lists the different analysis methods that will be used in this Chapter to evaluate the strength and non-linear behavior of CFSSP-Walls. Section 3.3 presents an example rectangular wall first used for this purpose. Section 3.4 presents calculation of the theoretical plastic moment using simple plastic cross-section analysis (i.e., for plastic stress distribution). Section 3.5 presents the results of a fiber analysis of the same rectangular section. Analysis of this rectangular section using finite elements analysis is presented in Section 3.6. Finally, in Section 3.7, analysis of the isolated CFSSP-Walls tested by Eom et al (2009) using the same three methods is presented.

3.2 Preliminary Analytical Investigation and Behavior of CFSSP-Walls

To get an understanding for the behavior of CFSSP-Walls having a dominant flexural behavior, an example rectangular CFSSP wall was investigated using different analysis methods. From simple to complex, they can be outlined as follows:

1. The first method is a simple cross section analysis considering a fully plastic stress distribution across the CFSSP wall cross section, used to calculate the plastic moment of the proposed wall section.
2. The second method of analysis is a fiber analysis of the wall cross section level, conducted using the XTRACT software, which is used to calculate the moment-curvature relationship of the cross-section assuming idealized material properties, and strains in materials at large curvatures. The plastic analysis and XTRACT software were used to calculate the plastic moment capacity of the CFSSP-Wall section and to estimate the contribution of the different components of the CFSSP wall section, steel and concrete, to the plastic moment capacity, M_p , of the section.

3. Finally, the finite element analysis method (using the ABAQUS 6.10 EF2 software) was used to get a more profound understanding of stresses and strains in CFSSP-Walls, and to explain the mechanics of CFSSP walls' ultimate behavior, focusing on how the different components of the wall interact and how that affects the walls capacity, deformation and both the local and the global behavior of the wall.. Finite elements analysis was also used to evaluate the ductility of CFSSP-Walls and their seismic performance for assumed material models.

3.3 Example of CFSSP-Wall Investigated

The CFSSP-wall example under investigation is an arbitrarily selected cantilever wall having a length of 22' feet and outside cross section dimensions of 1'×5', resulting in a wall aspect ratio (wall height to depth) of 4.4. The cross section with 12"×60" outer dimensions and a steel skin plate of 1/2" thickness leads to corresponding inner dimensions of 11"×59" for the steel "box". The tie bars have a 1 inch diameter and are spaced at 8" in both vertical and horizontal direction leading, corresponding to S/t ratio, of 16.

For the CFSSP-Wall example, all steel was chosen to have yield strength of 50 ksi, and specified concrete strength of 4 ksi. The tie bars were expected to behave elastically, and also assumed to have yield strength of 50 ksi.

Figure 3-2 shows dimensions of the proposed rectangular cross-section. In subsequent sections of this chapter, different analysis methods are presented and the results of the analysis are discussed to clarify the concept beyond the proposed CFSSP-Walls.

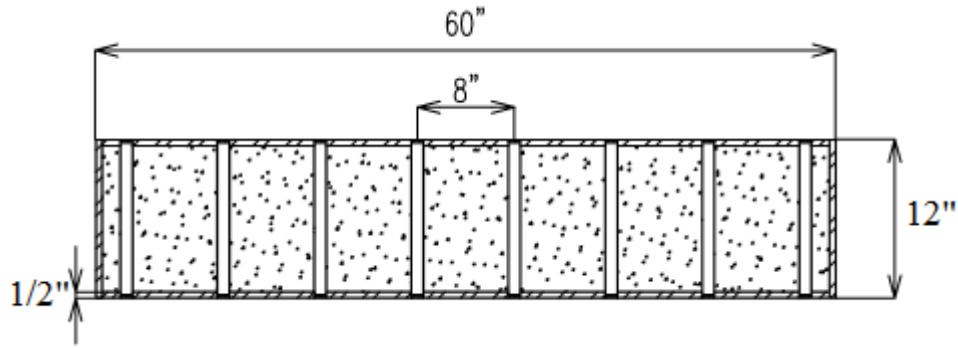


Figure 3-2 Dimensions of the CFSSP-Wall Example

3.4 Analysis of CFSSP-Wall Cross-section Using Plastic Stress Distribution.

To understand the behavior of CFSSP walls that have a dominant flexural behavior, the example rectangular CFSSP-Wall cross section was analyzed considering a fully plastic stress distribution on the entire cross section. The aim of this analysis is to calculate the plastic moment of the cross section under investigation and to use this value as a reference for comparison when evaluating the results of more complicated analyses. This analysis is also useful to evaluate the respective contributions of steel and concrete to the plastic moment of the cross section. This plastic moment is calculated about the strong axis of the cross section. In this case the steel is considered to have reached the yield stress of 50 ksi in both the tension and compression, and the concrete in compression is considered to have reached the strength, f'_c , of 4 ksi. The tensile strength of concrete is neglected. A uniform distribution of the concrete stress over the entire compression part of the cross-section is considered, without any reduction coefficient.

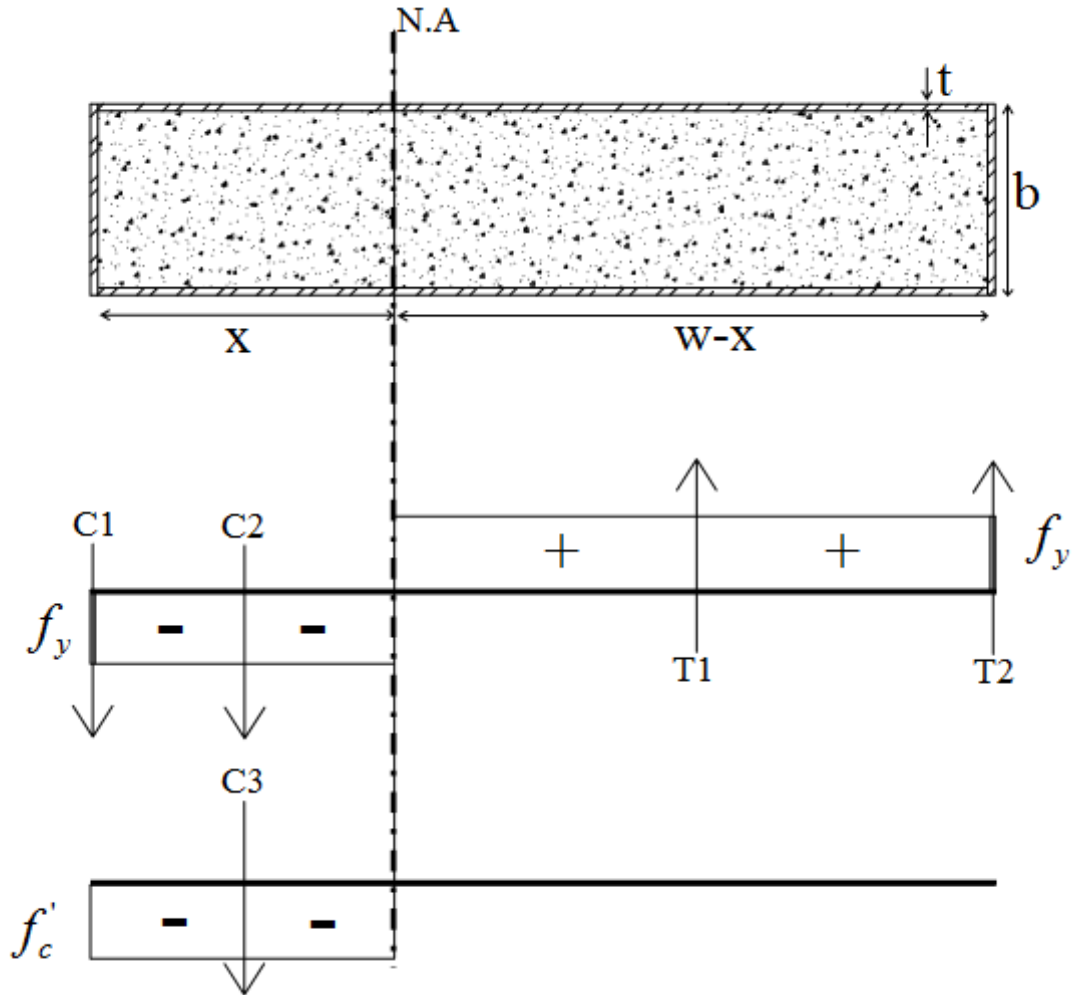


Figure 3-3 Plastic Stress Distribution on the Proposed CFSSP-Wall

Figure 3-3 shows the resulting plastic stress distribution on the CFSSP wall cross section, where the individual forces on parts of the cross section can be summarized as follows:

Forces on the tension side T_1 and T_2

$$T_1 = 2t(w-x) \cdot f_y$$

Equation Chapter 3 Section 1(3.1)

$$T_2 = tb \cdot f_y \tag{3.2}$$

Forces on the compression side C_1 , C_2 and C_3

$$C_1 = tb.f_y \quad (3.3)$$

$$C_2 = 2tx.f_y \quad (3.4)$$

$$C_3 = (b-2t)x.f'_c \quad (3.5)$$

where,

w, is the length of the steel web

By imposing equilibrium, for the cross-section dimensions presented earlier, the distance x locating the plastic neutral axis, can be calculated as:

$$x = \frac{2twf_y}{4t'_y + (b-2t)f'_c} = \frac{2(\frac{1}{2})(59)(50)}{4(\frac{1}{2})(50) + (12-2 \times \frac{1}{2})(4)} = 20.49" \quad (3.6)$$

Calculating the moment around the plastic neutral axis of the section, the plastic moments can be divided in two main components, namely the part due to contribution of the steel skin, and that due to the contribution of the concrete.

The moment due to contribution of the steel skin, M_s is:

$$\begin{aligned} M_s &= tb.f_y \times \left(x + \frac{t}{2}\right) + 2tx.f_y \left(\frac{x}{2}\right) + 2(w-x).f_y \left(\frac{w-x}{2}\right) + tb.f_y \left(w-x + \frac{t}{2}\right) = \\ &0.5 \times 12 \times 50 \times (20.49 + 0.5 \times 0.5) + 2 \times 0.5 \times 20.49 \times 50 \times 0.5 \times 20.49 \\ &+ 2 \times 0.5 \times (59 - 20.49) \times 50 \times \left(\frac{59 - 20.49}{2}\right) + 0.5 \times 12 \times 50 \times (59 - 20.49 + 0.25) = 65421 \text{kip} \cdot \text{in} \end{aligned} \quad (3.7)$$

The moment due to contribution of the concrete, M_c is:

$$M_c = (b-2t)x.f'_c \left(\frac{x}{2}\right) = (12-2 \times 0.5)(20.49)(4)(0.5 \times 20.49) = 9236 \text{kip} \cdot \text{in} \quad (3.8)$$

The total plastic moment, $M_p = M_s + M_c = 74,657 \text{kip} \cdot \text{in}$

For a lateral force applied at the top of this 22' cantilever wall, the corresponding base shear when

$$\text{reaching the plastic moment of the section} = \frac{74657}{264} = 282.8 \text{kip}$$

For this specific example, concrete contributes only 12.3% of the plastic moment of the section. It would be slightly less for any reduction for the concrete strength and if the uniform stress distribution was not

considered over the entire length of concrete under compression. This value would also change somewhat if the part of concrete under tension hadn't been considered cracked and of negligible strength. These assumptions could be modified in accordance to the outcomes of the different types of analysis presented later in this chapter.

3.5 Analysis of the Rectangular CFSSP-Wall using XTRACT.

The XTRACT software for fiber analysis was used to analyze the rectangular CFSSP-Wall cross-section under investigation, taking into consideration a bilinear steel material model with F_y of 50 ksi, and an unconfined bilinear concrete model that has both a 28 day compressive strength and a crushing strength of 4 ksi. The used concrete model is shown in Figure 3-4. This was done to achieve bi-linear properties and allow comparison with the theoretical values of M_p calculated above.

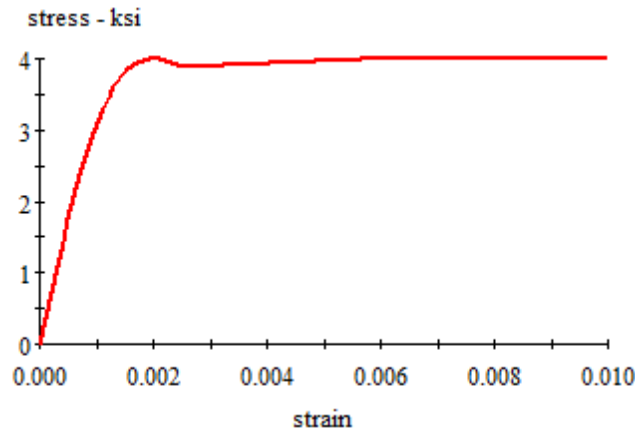


Figure 3-4 Unconfined Bilinear Concrete Model Used in the Analysis

The maximum moment obtained per XTRACT is 73,840 kip-in which represents 99% of the M_p value calculated above. The value of M_y per XTRACT is 50,590 kip-in, for M_y defined as the moment corresponding to first occurrence of yield in the steel case. Considering a linear moment distribution (for the cantilever wall), based on the ratio of M_y to M_p , the length of the plastic hinge would be equal to 32% of the wall height, and 1.4 times the total depth of the cross-section, W . The moment curvature relationship obtained from XTRACT is shown in Figure 3-4. The summary of the XTRACT analysis report is in Appendix C of this report.

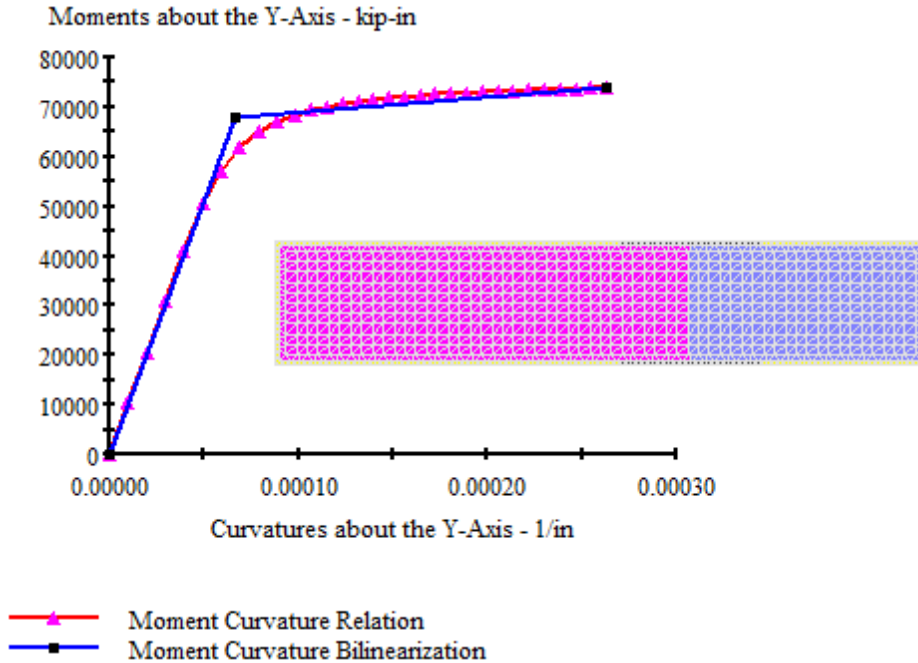


Figure 3-5 Moment Curvature Relationship for the Rectangular Section, XTRACT

3.6 Analysis of CFSSP-Walls Using Finite Element

The rectangular CFSSP-Wall section introduced in the previous sections of this chapter was modeled using the finite element analysis software ABAQUS 6.10 EF2. The objectives of these analyses were to investigate various factors that impact results, assess the best techniques to simulate the real behavior of the CFSSP-Wall walls using the finite elements method, and replicate the experimentally observed composite action in the CFSSP-Walls reported in the literature (presented in Chapter 2 of this document). Finite element simulation of CFSSP-walls is intended to make it possible to better understand the behavior of such walls and to extrapolate this understanding to the different geometric configurations of CFSSP-Walls presented in subsequent chapters, different S/t of the wall's skin plate, and different material properties (e.g., high strength concrete).

The finite element analysis results are also compared to those obtained from the simplified analysis using plastic stress distribution and the XTRACT software, in terms of plastic neutral axis location and plastic moment of the CFSSP-Wall section. Free body diagrams, spatial distribution of stresses and strains, and static pushover and quasi-static cyclic curves are used to illustrate the CFSSP-Wall behavior. The finite element models developed to simulate cyclic response of the CFSSP walls are verified by comparing with the limited test results for CFSSP walls available in the literature (Qian, Jiang et al. 2012)

3.6.1 General

The modeling of CFSSP-walls using the finite element method requires the consideration of many details that can affect the analysis results drastically. Such important details include:

1. Choosing the appropriate types of elements to simulate the behavior of different components of the CFSSP-WALL walls.
2. Meshing the different elements of the model in way that capture the structural behavior as precisely as possible, while avoiding analysis anomalies that result from poor mesh choices.
3. Simulating the contacts between the different components of the CFSSP walls, including the contact between the concrete core and the steel skin, the contact between the tie bars and the steel skin, and the contact between the tie bars and the concrete core.
4. Selecting material constitutive models able to replicate the key aspects of the observed non-linear behaviors and, more-specifically, prescribing backbone curves that describes uni-axial behavior and from which tri-axial behavior is inferred.

3.6.2 Finite Elements Selection

Both the steel skin of the sandwich panel and the concrete were modeled using the ABAQUS general purpose solid element C3D8R, which is an 8-node linear brick with reduced integration element having hourglass control and three displacement degrees of freedom per node, Reduced integration uses a lower-order integration scheme to form the element stiffness. The mass matrix and distributed loadings use full integration schemes. The reduced integration scheme reduces running time, which can be considerable for three dimensions (ABAQUS Analysis User's Manual 6.10 EF2). Figure 3-6 shows the steel skin of the rectangular CFSSP-Wall modeled using the C3D8R solid element. In order ensure the integrity of the analysis, mesh sensitivity was investigated by performing analyses using different mesh densities (number of elements per unit length), where smaller sized elements were used in those parts of the CFSSP-Wall subjected to high plasticity (which in this case, is taken as the lower third of the wall). The different analyses (with different mesh sizes) were performed until convergence of the solution was reached (i.e. when a finer mesh gave the same results as the previous coarser one). In Section 3.6, the results reported are those for the analyses in which the lower half of the wall had a mesh of $1'' \times 1'' \times 1/2$ elements for the steel skin plate, while the upper half had a mesh size of $3'' \times 1'' \times 1/2$.

The concrete core was meshed following the same above principles. As a result, regions subjected to high deformations had a denser mesh: the lower half of the wall had a mesh size of

1"×1"×1" and the upper half had a mesh size of 3"×1"×1". Figure 3-7 shows the element C3D8R used for simulating the concrete core and the mesh used in the CFSSP wall example analysis.

The tie bars connecting the two opposite skin plates of the CFSSP wall were modeled using ABAQUS's 3D beam element B31, which is a 3D element and first order interpolation. The layout of those tie bars is shown in Figure 3-8. The beam element B31 follows Timoshenko's beam theory, where transverse shear remains linear elastic with a fixed modulus.

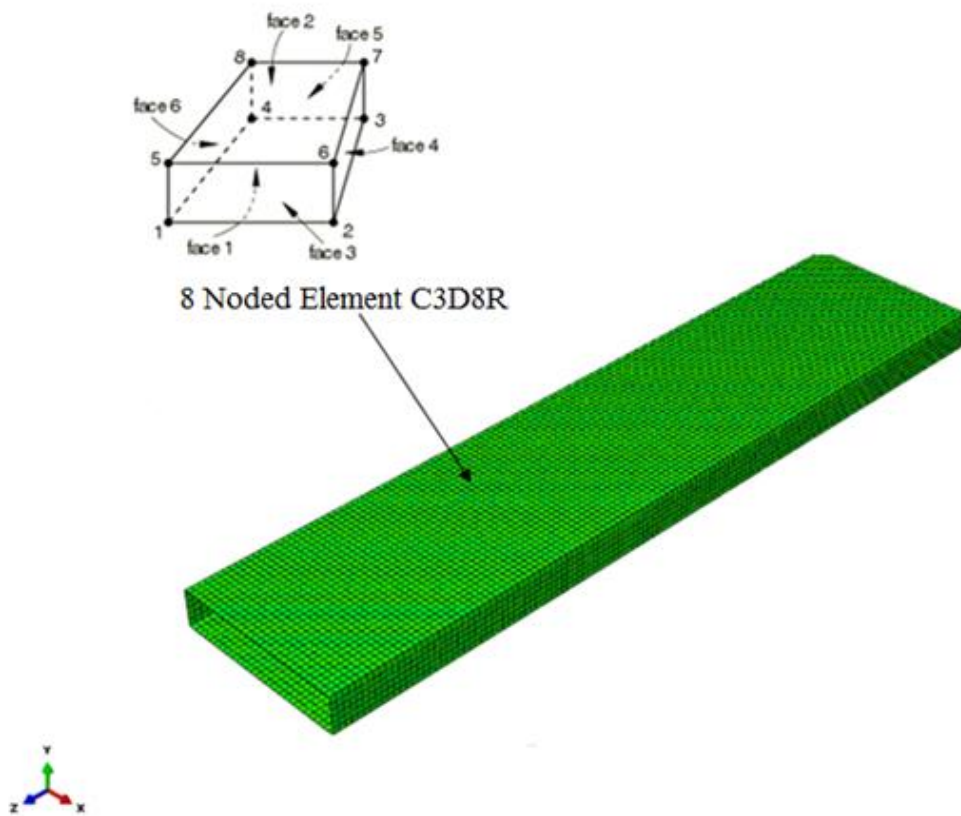


Figure 3-6 CFSSP-Wall Steel Skin Modeled Using C3D8R ABAQUS Element

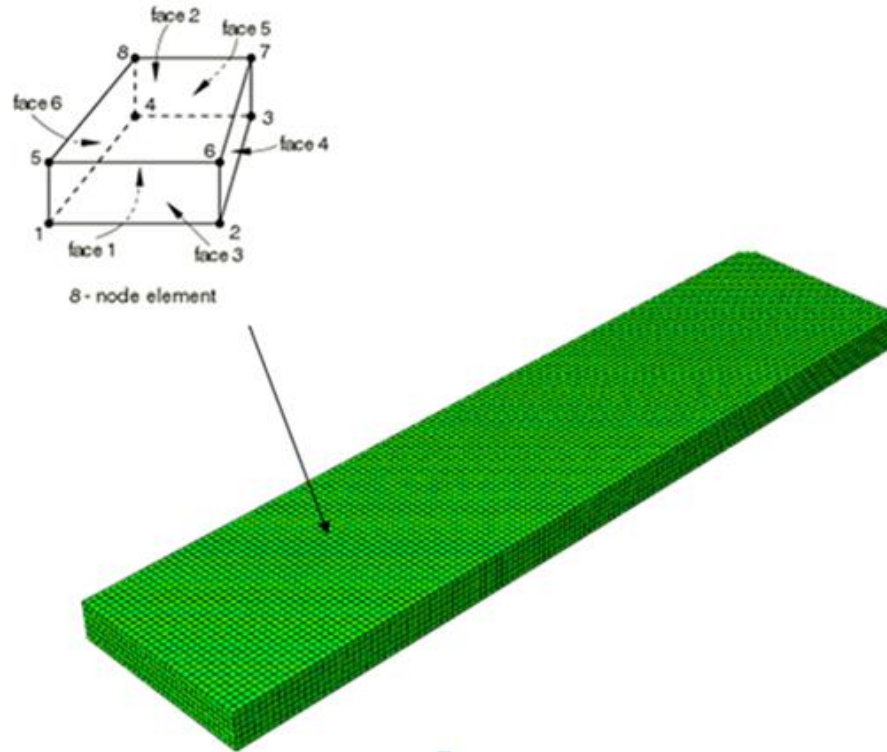


Figure 3-7 CFSSP-Wall Concrete Core Modeled Using C3D8R Abaqus Element

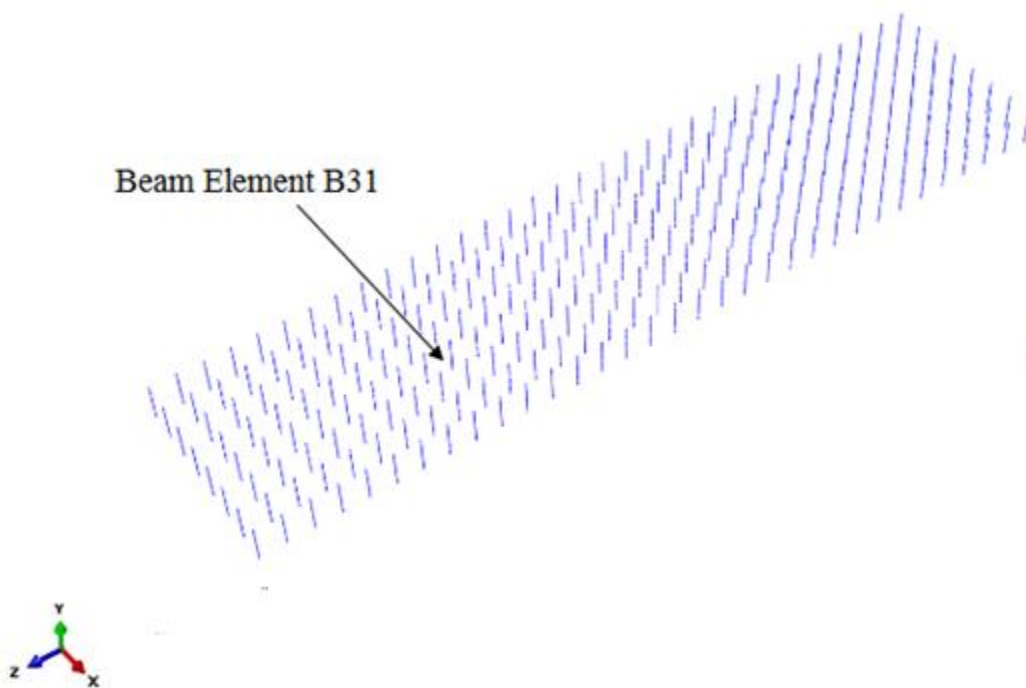


Figure 3-8 Tie Bars were Modeled Using Beam Element B31 in ABAQUS

The modeling of interaction between the different components of the CFSSP wall is important in simulating the actual behavior of the wall. The tie bars are welded to the skin plates and are embedded in the concrete; as such, they serve to transfer the load between the steel skin and the concrete core.

The contact between the steel skin and the concrete core is modeled using a contact pair algorithm in ABAQUS Explicit (ABAQUS Explicit 6.10 EF2), where a surface to surface interaction between the solid elements representing the steel skin and those representing the concrete is considered. The method used to apply contact implements tracking algorithms to ensure that proper contact conditions are enforced. The contact properties that define the mechanical surface interaction models that govern the behavior of surfaces when they are in contact are defined by the user. When surfaces are in contact, they can transmit shear as well as normal forces across their interface. The maximum shear stresses that can be transferred by the contact element are equal to the normal stresses times a friction coefficient. The friction models used in this analysis assumes that the friction coefficient, μ , is the same in all directions, i.e., *isotropic friction*. A value of 0.3 was specified in the model. In the normal direction, perpendicular to the contact surfaces, the default Contact Pressure over-closure relationship specified in ABAQUS (referred to as the “Hard” contact model) was used. Hard contact implies that the surfaces transmit no contact pressure unless the nodes of the slave surface contact the master surface. No penetration of one surface into the other is allowed at each constraint location and there is no limit to the magnitude of contact pressure that can be transmitted when the surfaces are in contact. In addition, that contact element does not allow the transfer of tensile stress across the interface (ABAQUS Analysis User's Manual 6.10 EF2).

To simulate the welding between the tie bar and the steel skin of the CFSSP wall, the end nodes of the beam element used to model the tie bar were tied as slave to the inner surface of the solid elements representing the steel shell. The interaction between the tie bars and the concrete core was modeled using the embedded element technique available in ABAQUS 6.10 EF2 in which the beam elements representing the tie bars lie embedded in a group of host element representing the concrete core. The embedded element technique is used to specify an element or a group of elements that lie embedded in a group of host elements whose response will be used to constrain the translational degrees of freedom of the embedded nodes (i.e., nodes of embedded elements which are that of the tie bars beam elements); this modeling option can be used in geometrically linear or nonlinear analysis and is not available for host elements with rotational degrees of freedom. This technique is recommended (per ABAQUS Analysis User's Manual 6.10 EF2) to model either rebar-reinforced membrane, shells, or surface elements embedded in three-dimensional solid (continuum) elements, truss or beam elements embedded in solid

elements; solid elements embedded in other solid elements (with the caveat that this approach will not constrain rotational degrees of freedom of the embedded nodes)

3.6.3 Steel Material Model

In these preliminary finite element analyses, the type of steel material model used for the CFSSP-wall skin plates is an elasto-perfectly plastic material of yield strength equal to 50 ksi. For the elastic part of the material model, the elastic modulus was taken equal to 29000 ksi and Poisson's ratio, ν , to 0.3. The Von Mises yield surface was associated with the plastic flow, which allow for isotropic yielding in this case. For simplicity, the steel material used for the tie bars was considered as elastic, with an elastic modulus of 29000 ksi

3.6.4 Concrete Material Model

The concrete damage plasticity (CDP) material model in ABAQUS was used to model the concrete core of the rectangular CFSSP wall. This model was used for monotonic, cyclic, and dynamic loading. The model assumes two main failure mechanisms, namely: tensile cracking and compression crushing of concrete material. The model uses a "multi-axial plasticity model with non-associated flow and isotropic scalar hardening", where the hardening variable controls the evolution of the yield surface. Figure 3-9 shows the behavior of the ABAQUS model in uni-axial tension and uni-axial compression.

The elastic part of the model is described through the values initial elastic modulus, E_0 , and the poisson's ratio, ν . The plastic part is described through the relation between the stress and the inelastic strain, such that the values of the stress against the inelastic strains for the compression part of the backbone curve are given by

$$\varepsilon_c^{in} = \varepsilon_c^t - \varepsilon_c^{el} \quad (3.9)$$

where;

ε_c^{in} is the in elastic compression strain

ε_c^t is the total strain given by the axial compression backbone curve

ε_c^{el} is the elastic strain

In the case of cyclic loading, there is degrading in the initial elastic modulus (stiffness degrading) with each cycle. The elastic modulus changes in terms of a scalar degradation variable d_c such that:

$$E = (1 - d_c)E_o \quad (3.10)$$

$$d_c = \frac{\sigma_{c\max} - \sigma}{\sigma_{c\max}} \quad (3.11)$$

where $\sigma_{c\max}$ is the ultimate compressive strength of the concrete

σ is the compression stress at any point on the degrading part of the curve

The cyclic behavior of the CDP model is shown in Figure 3-10. The value of the stress and inelastic strains for the tension part of the backbone curve is given by:

$$\varepsilon_t^{in} = \varepsilon_t^t - \varepsilon_t^{el} \quad (3.12)$$

where;

ε_t^{in} is the inelastic tension strain

ε_t^t is the total strain given by the axial tension backbone curve

ε_t^{el} is the elastic strain

For the tension part the stiffness or the value of the initial elastic modulus degrades in case of cyclic loading where the elastic modulus changes in terms of a scalar degradation variable is given by

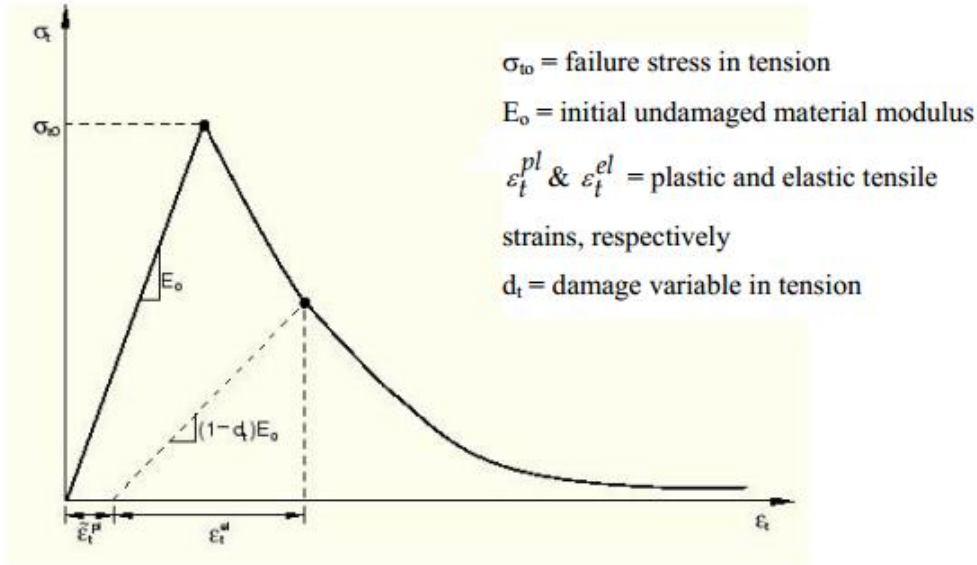
$$E = (1 - d_t)E_o \quad (3.13)$$

$$d_t = \frac{\sigma_{t\max} - \sigma}{\sigma_{t\max}} \quad (3.14)$$

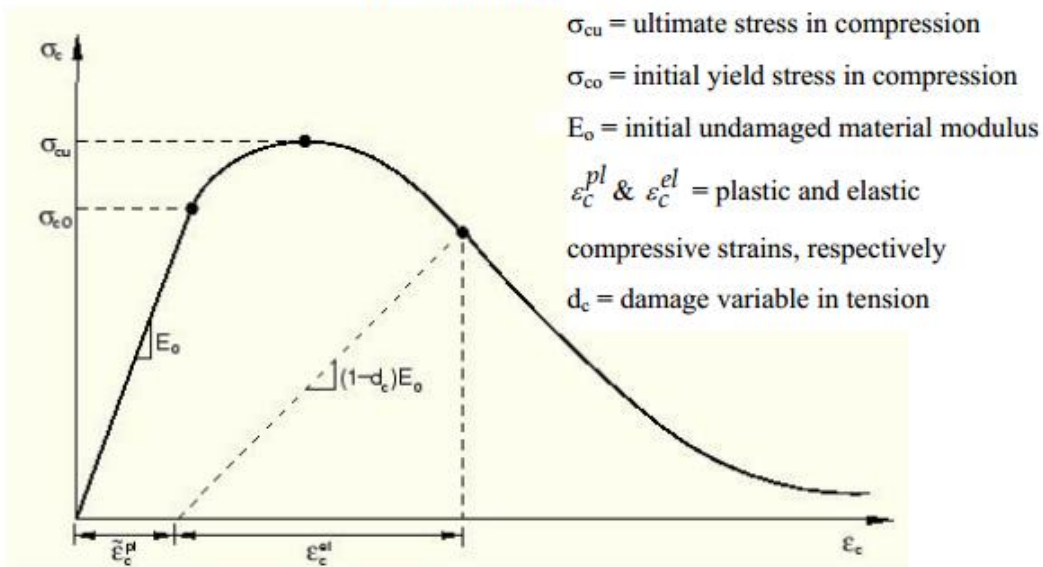
where

$\sigma_{t\max}$ is the ultimate tensile strength of the concrete

σ is the tension stress at any point on the degrading part of the curve.



(a) Uniaxial Tensile Loading



(b) Uniaxial compressive loading

Figure 3-9 Concrete Damage Plasticity Model, ABAQUS 6.10EF2 User's Manual

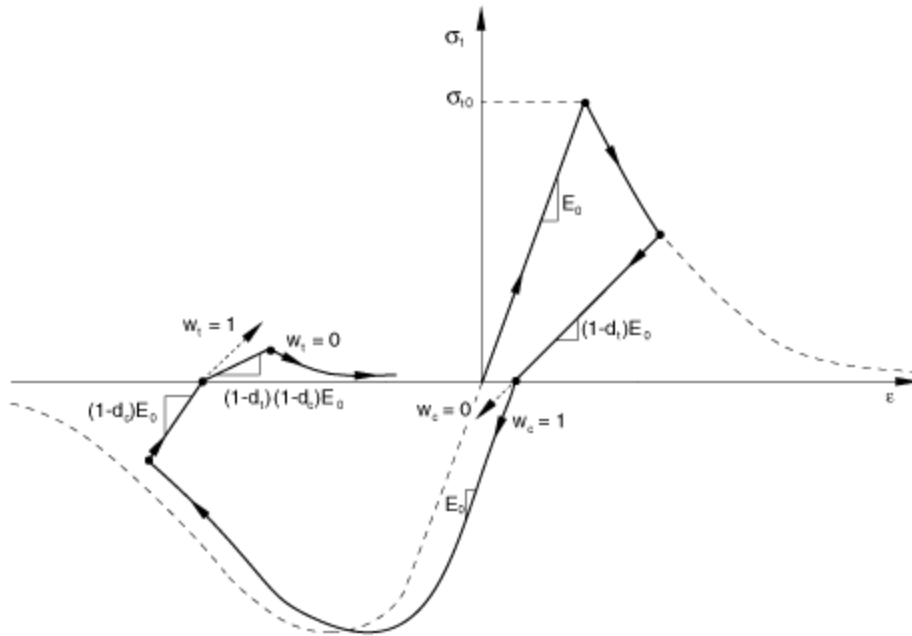


Figure 3-10 Cyclic Behavior of CDP Model, ABAQUS 6.10EF2 User's Manual

There are other parameters in the CDP model that are related to the concrete plasticity, such that the model can represent the stress-strain behavior of the concrete successfully. According to Chen and Han (1995) the three basic assumptions in a material plasticity model are:

- I. An initial yield surface in the stress space that defines the stress levels at which plastic deformation begins.
- II. A flow rule which is related to a plastic potential function and gives an incremental plastic stress-strain relation.
- III. A hardening rule that defines the change of loading surface as well as the change of the hardening properties of the material during the course of plastic flow.
- IV. The CDP model used in the ABAQUS is a modification of the Drucker Prager yield criteria with augmented modification from Lubliner et al. (1989) and Lee and Fenves (1998). According to these modifications, the failure surface in the deviatoric cross-section needs not to be a circle and tends to be an hyperbola, and is governed in this case by a parameter K_c , described below. The resulting yield surface in the deviatoric plane is shown in Figure 3-11. In general, the parameters that can affect the shape of the yield surface in the CDP model can be summarized as follows:

- The parameter K_c is the ratio of the distances between the hydrostatic axis and respectively the compression meridian and tension meridian in the deviatoric cross section. Typically, the value of this coefficient ranges from 0.5 to 1, and is recommended by ABAQUS 6.10EF2 to be taken equal to 0.67.
- The shape of the yield surface is adjusted by an eccentricity factor (known as the plastic potential eccentricity), which represents the length of the segment between the vertex of the hyperbola and its center; it is recommended by ABAQUS 6.10 EF2 to take this value equal to 0.1
- The point at which the concrete undergoes failure under biaxial compression is represented by the ratio between the strength of the concrete in the biaxial state of stress, f_{bo} , and the uniaxial state of stress, f_{co} ; the recommended value for f_{bo}/f_{co} is 1.16.
- The dilation angle ψ which is physically interpreted as a concrete internal friction angle, which for concrete ranges between 36° and 40° .

From the aforementioned information, the input parameters required to define concrete material model are:

- (i) the uniaxial compression stress- strain curve;
- (ii) the uniaxial tension stiffening stress–strain curve;
- (iii) the volumetric dilation angle ψ ;
- (iv) the biaxial compression strength ratio, and;
- (v) the ratio of tensile-to-compressive meridian K_c .

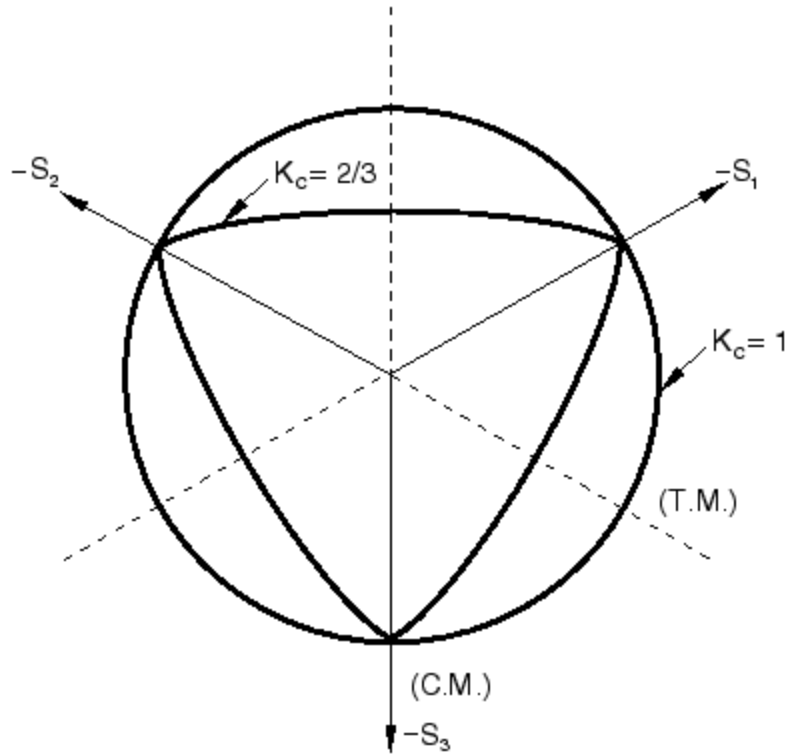


Figure 3-11 Yield Surface in the Deviatoric Plane Corresponding to Different Values of K_c , ABAQUS 6.10 EF2

The concrete inside the CFSSP-Wall was considered to be confined concrete, with a degree of confinement that depends on the horizontal spacing of the tie bars and the thickness of the CFSSP wall steel skin plates, namely the S/t value and, to an extent, the aspect ratio of the wall. Generally, confinement of concrete could lead to an increase of both the concrete strength and ductility, or only an increase in ductility. Here, to define the properties of the confined concrete for the ABAQUS 6.10EF2 CDP material modeling presented in this Chapter, it was decided to use the concrete backbone curve proposed by Liang (2008). Figure 3-12 shows the resulting general stress-strain curve for confined concrete. Note that Liang's model was developed for CFST (concrete filled steel tubes) beam-columns, but was assumed to be applicable here (failing availability of an alternative model).

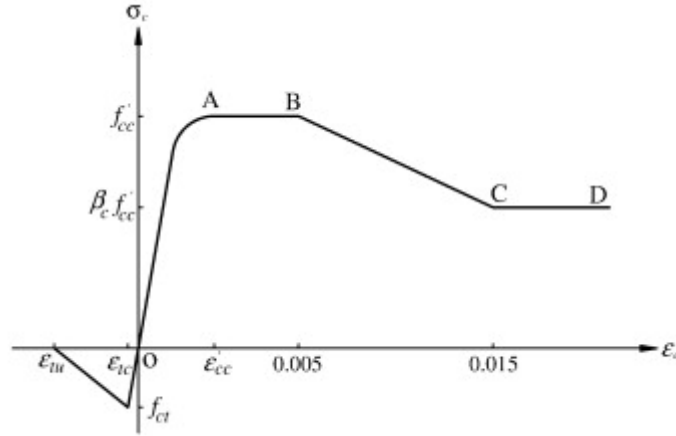


Figure 3-12 Stress Strain Curve for Confined Concrete in CFST Beam-Column, Liang (2008)

For the current CFSSP-Wall example, the strength of concrete is 4 ksi (27.6 Mpa) and the horizontal spacing of the tie bars in both horizontal direction is 8 inches, giving an S/t value of 16. Accordingly, the different parameters for the compression part of the CDP backbone curve according to Liang (2008) can be calculated as follows:

The elastic modulus is calculated according to ACI 318-08

$$E = 57,000 \sqrt{4000} = 3,604,996 = 3605 \text{ ksi} \quad (3.15)$$

According to Liang (2008) and Mander (1988), the longitudinal compressive strain is calculated such that

$$\because f'_c \leq 28 \text{ (MPa)} \text{ then } \epsilon'_c = 0.002 \quad (3.16)$$

The value of β_c , shown in Figure 3-12, is used to reflect the effect of confinement on the concrete ductility, and depends on b/t , where the ratio b/t in Liang's equation, which is the ratio between the largest width-to-thickness ratio in a rectangular CFST cross-section, is replaced here by S/t in case of CFSSP-Walls. Although Liang calibrated the β_c values based on results obtained for concrete filled columns by Tomii and Sakino (1979), by analogy, for the case of the CFSSP-wall steel skin plate, the applicable results from Liang applicable to the case at hand indicate:

$$\because \frac{b}{t} \leq 24, \beta_c = 1$$

The uni-axial compressive stress-strain curve obtained based on the above parameters, and used in the finite element analyses, is shown in Figure 3-13. However, there are some differences between the

concrete backbone curve as proposed by Liang (2008) and the one used in the finite element model. First, at a strain value of 0.015, a strength of 0.4 ksi was used (instead of the 4 ksi value shown in Figure 3-12), and; Second, for the rest of the curve at strains higher than 0.015, stresses vary linearly down to a zero stress value at a total strain of 0.02. Also, here the tension part of the backbone was chosen to follow a quadratic path instead of the linear degrading path originally proposed by Liang (2008). Note that this choice of tension degradation model was arbitrary and reached after making several analysis which confirmed that the concrete tension model does not have significant impact on the analysis results, given that concrete contributes only about 15% of the total wall strength, and, therefore, concrete in tension even less. For that matter, the contribution of the tensile strength of concrete could have been totally neglected.

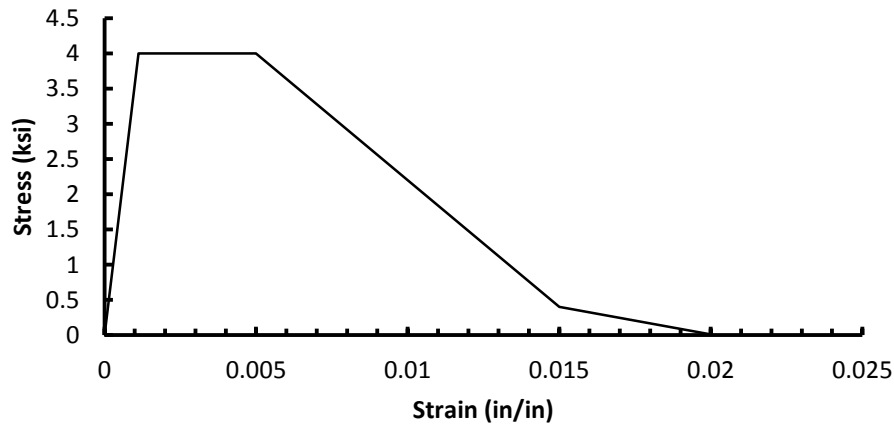


Figure 3-13 Uni-axial Compression Stress/Strain Relationship Used for the CDP Model

. The tensile strength was calculated (for a 4 ksi strength concrete) by the AC1-318-08 equation

$$f_{ct} = 6.5\sqrt{f'_c} = 411 \text{ psi} = 0.41 \text{ ksi}$$

The cracking strain is equal to 0.00013 while the ultimate tensile strain is taken as 10 times of the strain at cracking. Beyond that point, tensile strength rapidly drops to zero per the model described above.

The above backbone concrete curves for tension and compression were used with the concrete damaged plasticity model available in Abaqus Explicit 6.10 EF2. The details of the concrete damage plasticity model and its different parameters are illustrated earlier in the section. The values of the different parameters used here to define the CDP model are summarized in Table 3-1.

In Table 3-1, the elastic modulus and poisson's ratio are shown in section (1) of the table, which are needed for elastic analysis. Section (2) in the table lists the parameters for the concrete damage plasticity

that describe the flow potential function, namely the dilation angle ψ . The flow potential eccentricity, ϵ , is taken equal to the default value of 0.1. As for the parameters responsible for the shape of the yield function, namely the ratio of initial equibiaxial compressive yield stress to initial uni-axial compressive yield stress, f_{bo}/f_c , it is taken equal to the default value of 1.16. The ratio of the second stress invariant on the tensile meridian to that of the compressive meridian at initial yield, K_c , is taken equal to default value of 0.67. Parts (3) and (4) of Table 3-1 summarize the values of the stresses and strains that define the compression and tension parts of the backbone response curve, while parts (4) and (6) of Table 3-1 list the degrading coefficients for the compression and tension parts of the curve respectively. The degrading coefficient is calculated at the stresses after reaching the peak (maximum) values.

Table 3-1 Material Parameters of CDP Model for 4 ksi Concrete

Material's Parameters, $f'_c = 4$ ksi		Parameters of CDP Model (2)	
<i>Concrete Elasticity (1)</i>		ψ	38°
E (ksi)	3605	K	0.67
ν	0.2	f_{bo}/f_c	1.16
Concrete Compression Hardening (3)		Concrete Compression Damage (4)	
<i>Stress (ksi)</i>	<i>Inelastic Strain</i>	Damage, d_c [-]	Crushing Strain
4	0	0	0
4	0.00388	0	0.00388
0.4	0.0149	0.005	0.00388
0.01	0.016	0.9	0.0149
Concrete Tension Stiffening (5)		Concrete Tension Damage (6)	
<i>Stress (ksi)</i>	<i>Cracking Strain [+]</i>	Damage, d_t [+]	Cracking Strain
0.289	0	0	0
0.4121	3.333E-005	0	3.33E-005
0.271	0.000160427	0.342	0.000160427
0.125	0.0002797	0.697	0.0002797
0.0328	0.000684593	0.92	0.000684
0.0082	0.00108673	0.98	0.0010861

3.6.5 Boundary Conditions and Loading

The boundary conditions were specified by restraining the six degrees of freedom for all the nodes located at the base of the wall, including both those for the solid element representing the steel case and those for the concrete core.

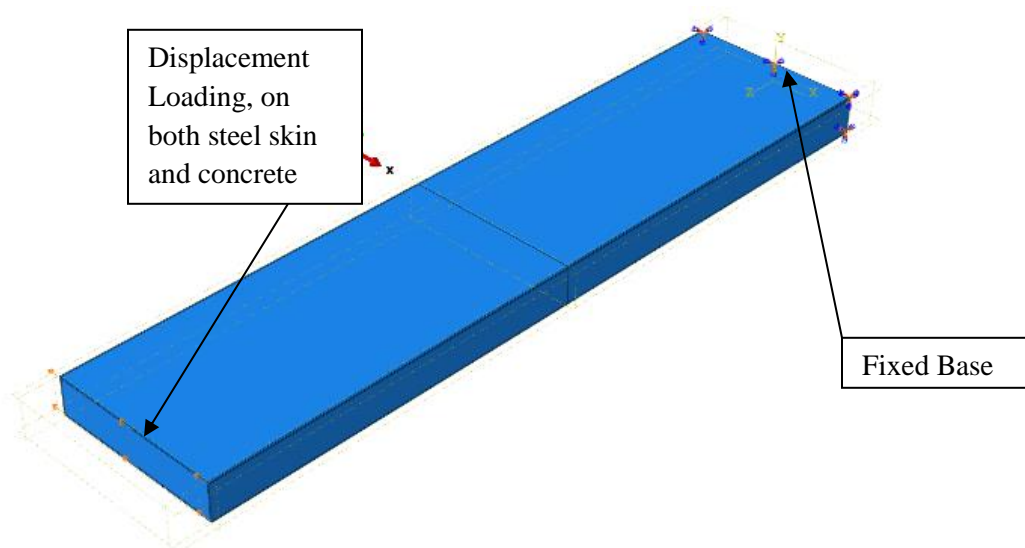


Figure 3-14 Model Boundaries, Loaded End, and Fixed Base

The loading was applied as horizontal monotonic displacement on the top surface of the model. To prevent undesirable local buckling at the top of the model where the load was applied, the nodes of the CFSSP wall top surface in both steel and concrete were tied together such that all those nodes moved horizontally together (this eliminated the local effects, such as high stress concentration, that were observed with other schemes considered). Figure 3-14 shows the distribution of loading and fixed boundaries of the model.

3.6.6 Pushover Analysis

The model of the CFSSP-Wall was pushed laterally with monotonic displacement in a direction normal to the strong axis of the CFSSP-Wall, up to a lateral displacement of 13.2" which is equivalent to 5% drift. The purpose of this analysis was to compare the strength of the wall obtained from the finite element analysis results with those obtained from simple calculations using plastic stress block distribution and fiber analysis results from the XTRACT software, as well as to obtain additional information with respect to other aspects of the wall's structural behavior. Results are also evaluated through the use of free body diagrams and by verifying equilibrium and strain compatibility conditions. The resulting base shear versus lateral drift is shown in Figure 3-15, where a horizontal thick line represents the value of the estimated base shear that is equivalent to M_p value (calculated per the procedure described in Section 3.4). The base shear peak value obtained from the finite element analysis is 324.7 kips, which exceeds the estimated base shear by 13.5%. That is attributed to the 3D nature of the model. In other words, this is because the values of F_y and f'_c specified in the model represents respectively the cap strengths for either

the Von Misses criteria used in the steel model or the Modified Drucker-Prager model used in concrete. Accordingly, in the vertical direction (direction of stresses used to calculate M_p), the stresses in the steel in this direction could be greater or less than 50 ksi at yield, depending on the magnitude of the stresses acting in the orthogonal direction at the time the stress conditions combine to correspond to a point on the yield surface for the reference yield strength F_y . Similarly, confinement of the concrete due to triaxial stress conditions for the given concrete yield surface model can result in some of the compressed concrete elements developing stresses in excess of 4 ksi in the vertical direction. Overall, the greater flexural capacity translates into a value a maximum of base shear obtained from the finite elements greater than that estimated by plastic stress distribution. However, this increase beyond the specified uniaxial yield value for the stresses in the direction used to calculate M_p is further illustrated later in this chapter.

Finite element analysis results also show that, at a drift value of approximately 1.5%, local buckling developed in the CFSSP-Wall. Local buckling of the skin plate took place in the lower part of the wall between the first and second row of tie bars, occurring simultaneously in the web and flange of the steel skin.

The following section further investigates how the CFSSP-Wall performed at different load/drift levels. More specifically, the stress distribution in the steel skin plates, concrete core and tie bars is examined at different stages of drift, and the interaction between the different CFSSP-Wall components is addressed taking into account the state of tri-axial stresses on the CFSSP-Wall components.

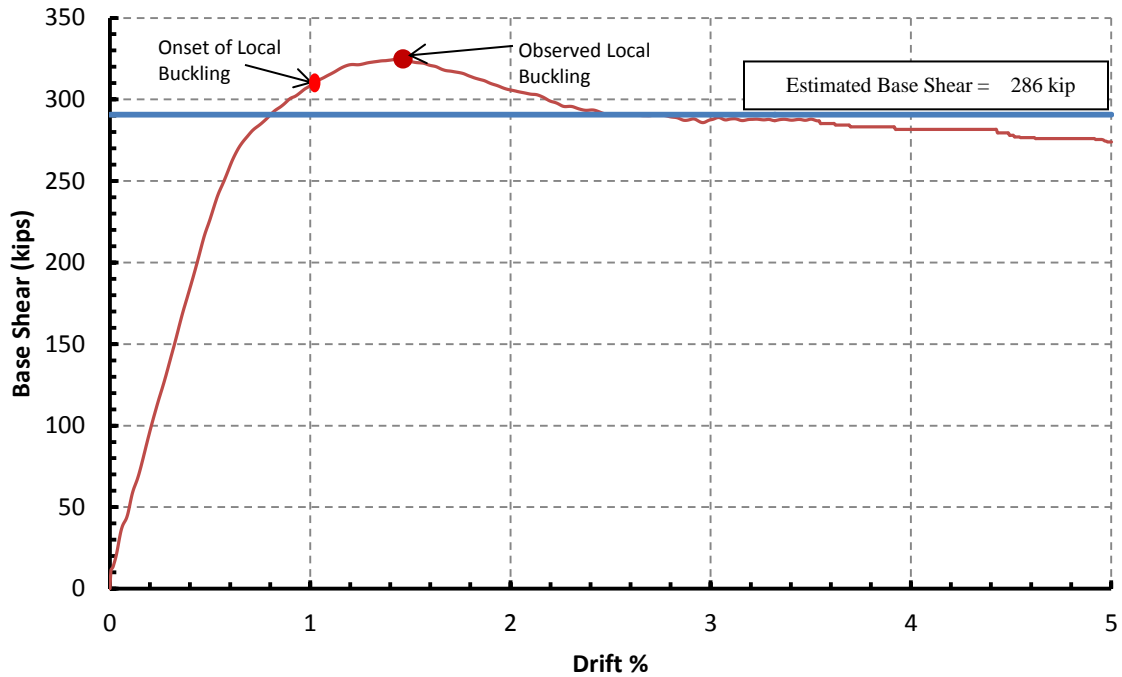


Figure 3-15 Base Shear vs Lateral Drift% for the Rectangular CFSSP-Wall

3.6.7 Evaluation of the Pushover Loading Results

A further evaluation of the CFSSP-Wall performance was done by reviewing the stress distributions in the different components of the model, and by using those stress distribution to establish free body diagrams in an attempt to develop an understanding of the wall's three dimensional internal behavior.

For the steel skin plate of the wall and for the concrete (both modeled using 3D solid elements), the stresses normal to the CFSSP-Wall cross-section are referred to as longitudinal stress (acting in longitudinal direction of the wall). Per orientation of the model in ABAQUS, these are referred to as the stresses in the Z direction, or alternatively, S33 stresses. As for the stress components that are considered to lay in the plane of the CFSSP-Wall cross-section, in the global X and Y direction per the ABAQUS model orientation, they are referred to as transversal stresses. The stresses in the X direction are referred to as S11 stresses, and those in the Y direction are referred to as S22 stresses. Accordingly, the normal stresses due to flexure correspond to the S33 stresses, while stresses at the interface between steel and concrete is investigated through the S22 stresses (on the long sides of the wall). Figure 3-16 shows the longitudinal stress distribution (stresses in Z direction, along the wall height) in the CFSSP-Wall skin plate at 0.5% drift (elastic range). The stress distribution is almost symmetric, which indicates that the

wall is slightly beyond the elastic response, the flanges on both the tension and the compression ends of wall's cross-section have started to yield (stresses have reached or exceeded 50ksi). The figure also indicates that, at 0.5% drift, yielding has started to propagate along the height of the wall, as well as in the web. The high stress at the wall flanges at low drifts is because of the relatively deep wall cross section, which induces high strains at the extreme tension or compression fibers.

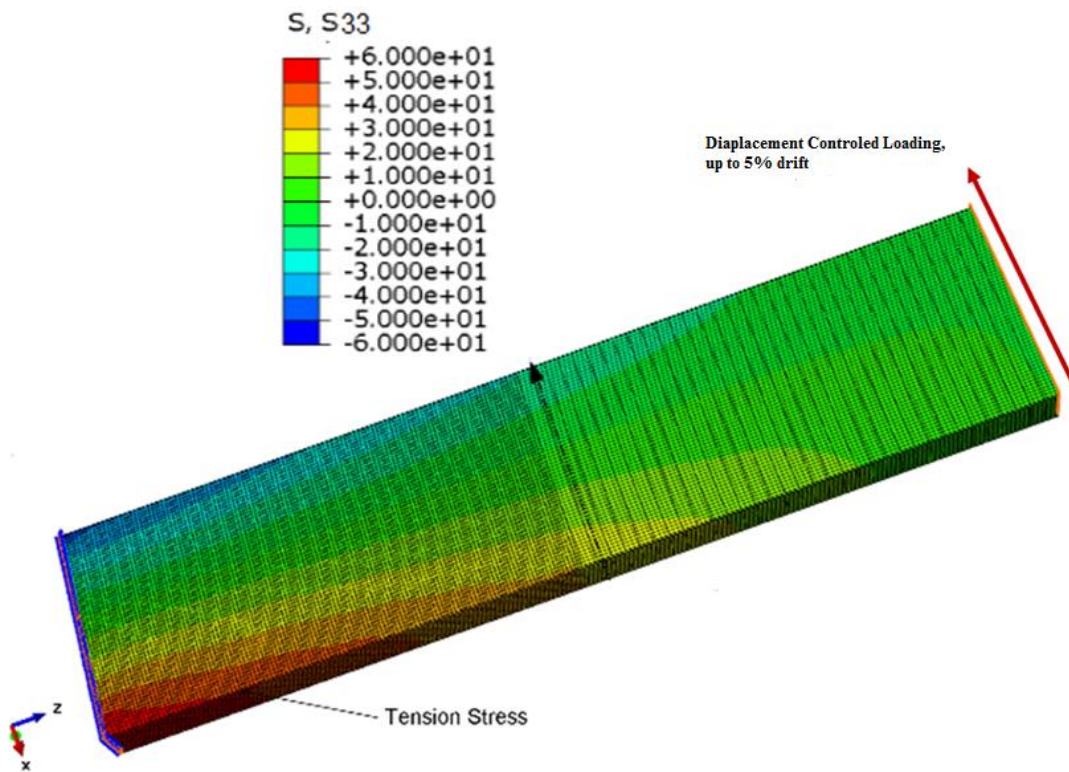


Figure 3-16 Longitudinal Stress Distribution, S33, at 0.5% Drift

For the rest of this section, focus in on behavior of the wall near its base, namely along the first 5 feet above the fixed base, as this is the region of the wall where M_p is expected to develop, along with (at larger drifts) local buckling of the skin plates and crushing of the concrete. Figure 3-17, 3-19, and 3-20, shows the longitudinal stress distributions over the lower 5 feet of the rectangular CFSSP wall, at different drift values. In Figure 3-18, the steel skin plate longitudinal stress distribution is shown at 0.5% and 1% drift. At 0.5% drift, the wall section at the base has started developing M_y ; since the CFSSP-Wall has a relatively deep cross section, large strains are generated at the extreme fibers of the cross section at

relatively low drifts. At 1% drift, the highlighted localized stresses shown in the figure were found to correspond to the onset of local buckling in the compressed web in the region located between the first and the second row of tie bars. There are also stress concentrations in the skin plate where the skin plate elements are in contact with the tie bars, with smaller values of compression stresses at that location than in the rest of the skin plate. This phenomena localized in the vicinity of the tie bars encompasses the region of the skin plate at the onset of local buckling and after formation of the local buckling, which underscores the role of the tie bars in CFSSP-Walls, which mainly consist in providing support at the edge of the buckled plate. Note that the fixity corresponding with this support could vary between a fixed end to hinged support, depending on the diameter of the tie bar and how it is connected to the skin plate.

Analysis of cross-section S33 stresses at the base of the wall also allow to observe the shifting of the neutral axis (as a function of drift), from its elastic location to the plastic location. These results are presented later in this section.

Figure 3-18 shows the longitudinal stress at 1.5% and 2.0% drift, respectively. At those drifts, most of the web skin plate in tension has reached F_y and yielding has migrated vertically in the web. For the parts of the skin plate under compression, local buckling further developed in the web between the first and second rows of tie bars, and in the flanges of the skin plate at the corresponding locations.

The value of the longitudinal stresses in the buckled region of the web started to drop to values below half of the yield stress; yet, there was no corresponding sharp drop in the moment capacity. This phenomena is explained later in this chapter, when investigating the state of stresses in both the steel skin plate and concrete core of the CFSSP wall.

In Figure 3-20, the longitudinal stresses in the CFSSP wall skin plates are presented for drift values of 3% and 4%, respectively. There is little difference in behavior at this drift level compared to what was observed at the 2% drift level, except that the local buckling waves on the compression parts of the wall increased in severity, and the compression longitudinal stresses in the skin plate laying between the first and the second row of ties further decreased. As the same time, the steel skin plate elements in contact with the tie bars started to exhibit tension longitudinal stress instead of compression stresses.

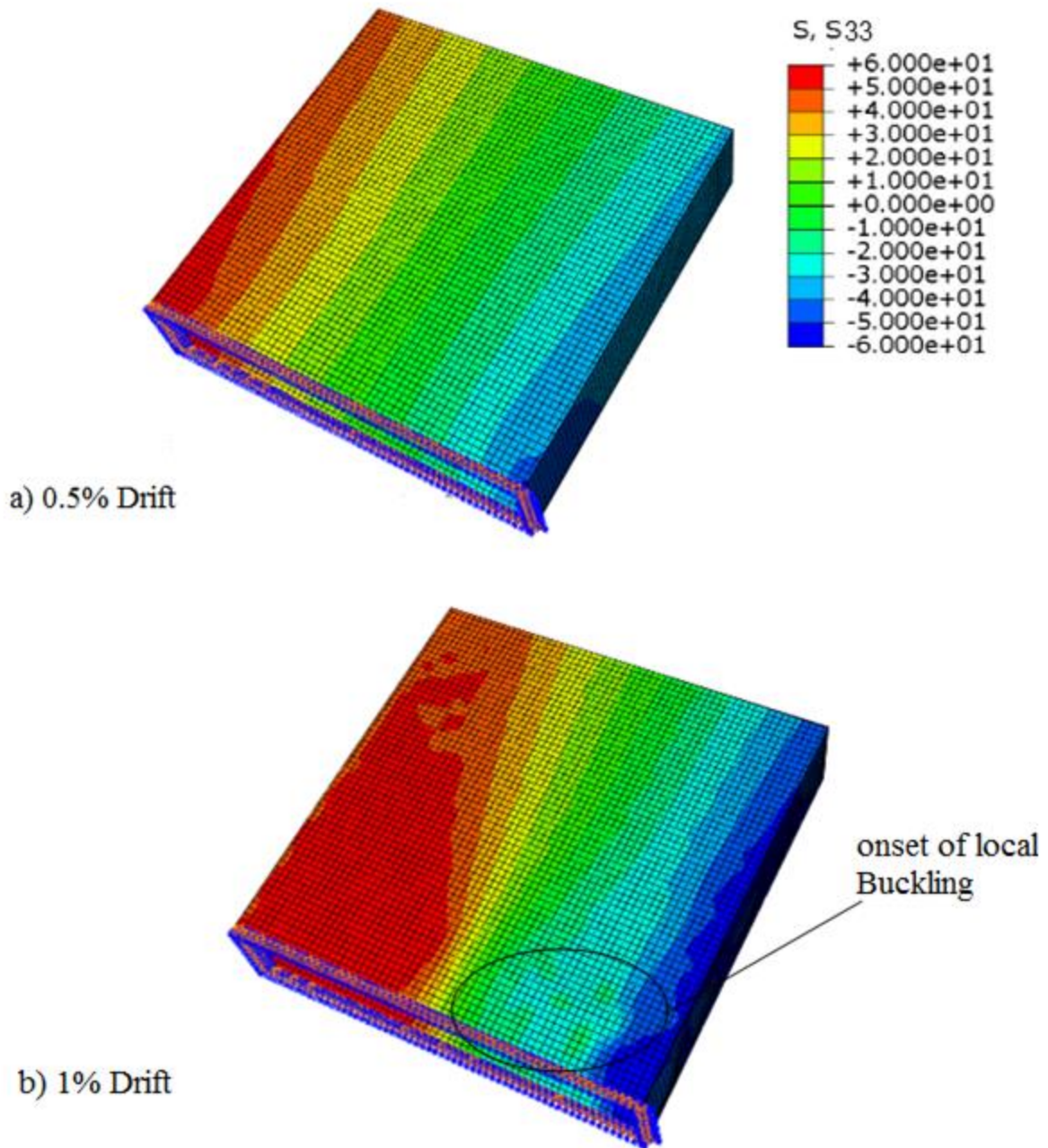


Figure 3-17 Longitudinal Stress Distribution in CFSSP-Wall at Lower 5 feet: (a) 0.5% Drift;(b) 1% Drift

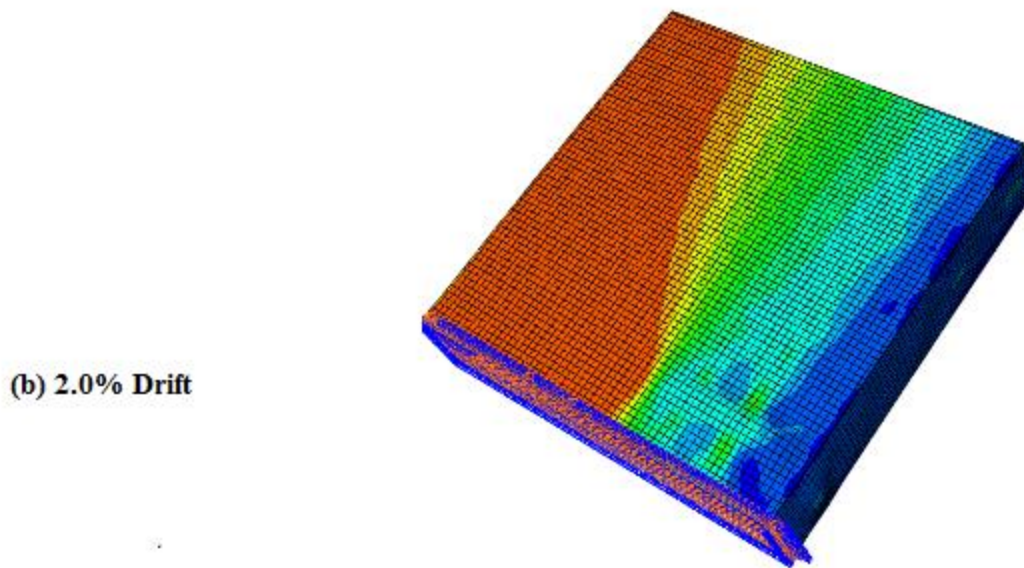
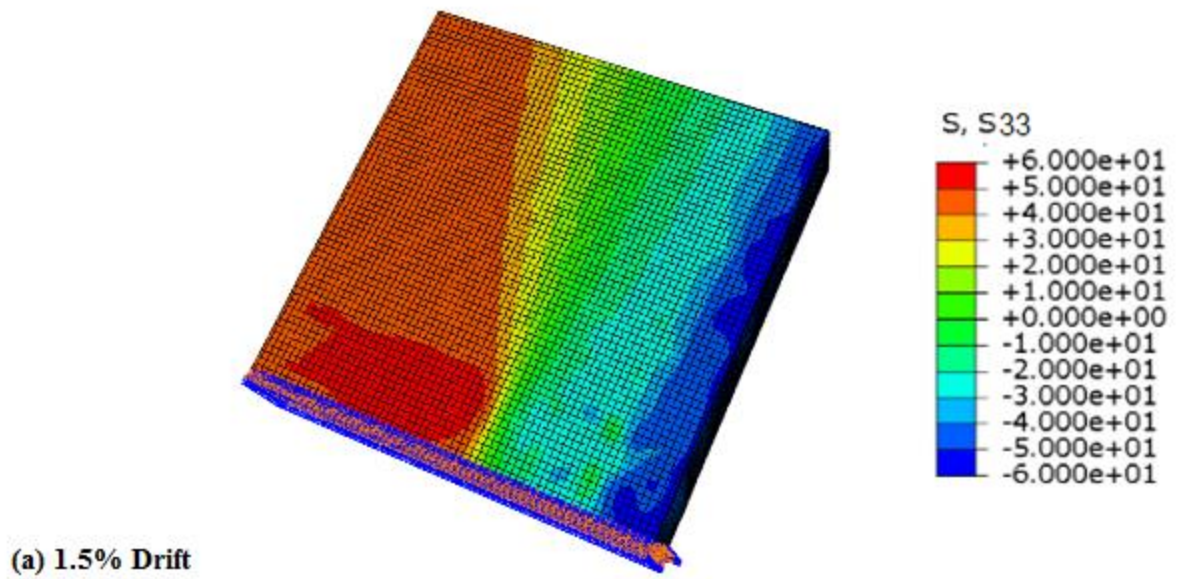


Figure 3-18 Longitudinal Stress Distribution in Steel Skin Plate at Lower 5 feet: (a) 1.5% Drift;(b) 2.0% Drift

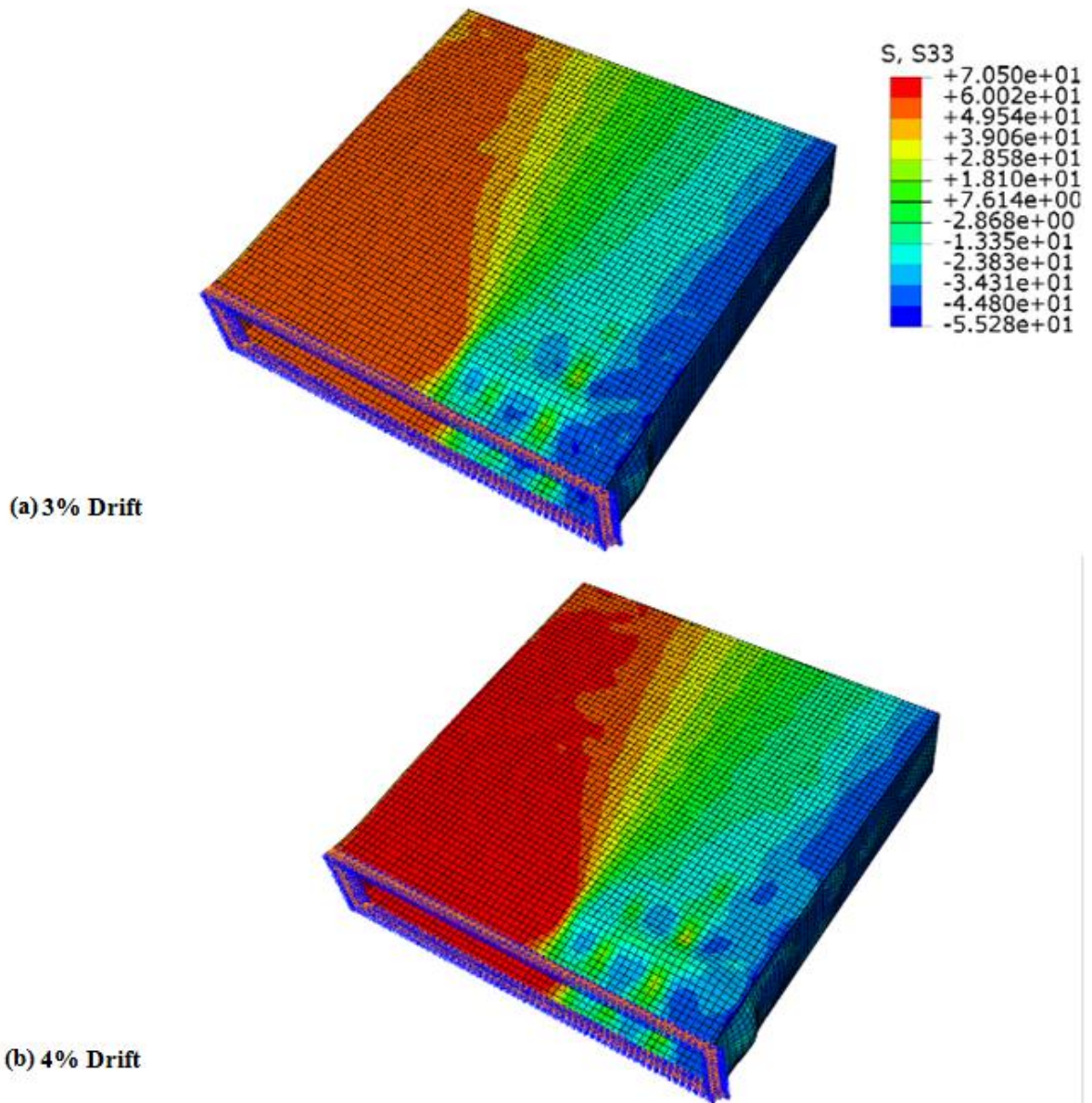


Figure 3-19 Longitudinal Stress Distribution in the Steel Skin Plate at Lower 5% Feet: (a) 3% Drift; (b) 4% Drift

Note that the shape of the local buckling wave that occurred between the two lower tie bar rows (under stresses in the longitudinal direction) was such that its apex occurred almost midway between the tie bar rows, comparing Figure 3-19 parts a and b with Figure 3-18. Also note that when the longitudinal compression stresses in the buckled region started to drop in magnitude, the transversal stresses S_{22} started to increase. Finally, note that, in the vicinity of the tie bars, in the steel skin plate elements tied to tie bars, the fact the stresses locally changed from compression to tension stresses suggests that the tie bars acted as anchors at the edges of the buckled zone. The deflected shape of the skin plate at those locations also indicates that fixity at the end of the buckled plate was closer to fixed ends rather than hinged ends. This also highlights the role of the tie bars in resisting local buckling of the skin plates.

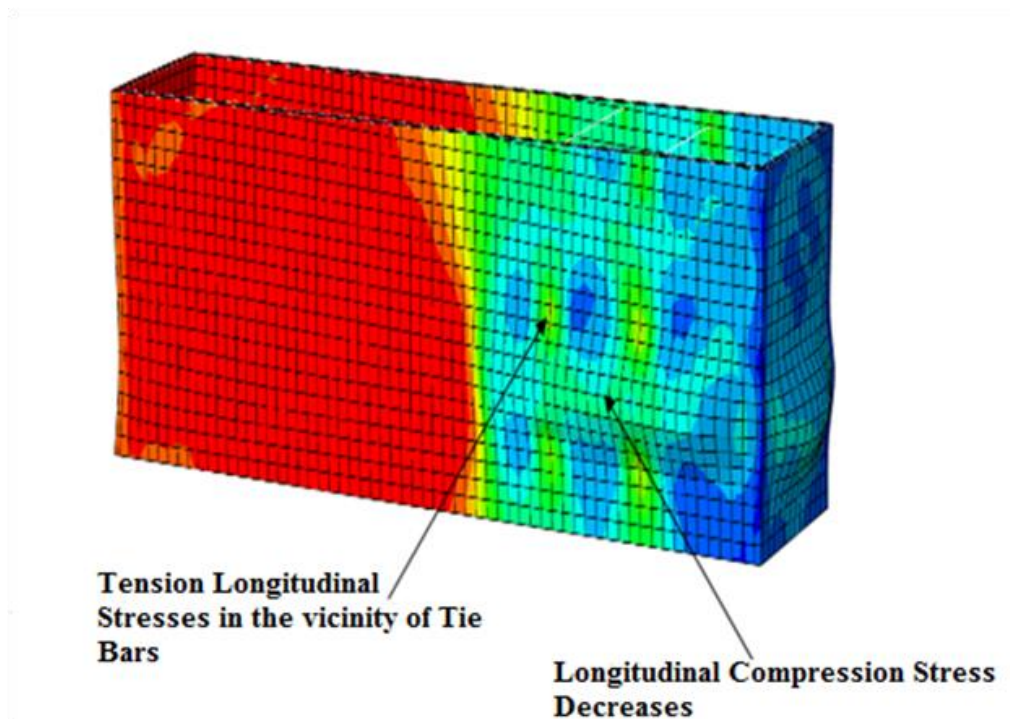


Figure 3-20 Behavior of Skin Plate Post Local Buckling

To further investigate the behavior of the skin plate of the CFSSP-Wall, the longitudinal stress distribution across the steel skin plate is plotted for a cross-section located 8 inches above the fixed base of the wall (Figure 3-21). It is found that the position of the plastic neutral axis lies at 23 inches from the compression flange. For comparison, the calculations using the assumption of uniform plastic stress distribution gives a position of the plastic neutral axis at 20.67 inches from the compression flange.

In the part of the web subjected to tensile longitudinal stresses, most of the web plate have yielded at drift value of 1.5%. In the part of the web subjected to compression stresses, the longitudinal compression stresses values do not reach F_y except for the part of the web that is close to the compression flange of the CFSSP wall. Yet, it was verified that the plates in compression above the neutral axis yields on the basis of the Von Mises criteria. This is because significant S11 stresses are simultaneously occurring at those locations. However, taking all obtained stress values into account, it was verified that the combined stresses acting on the steel never violated the Von Mises criteria prescribed for a yield value of 50 ksi.

The stresses shown in Figure 3-21 are for the section at 8 inch from the fixed base, which corresponds to a location exactly at the mid distance between the first and the second row of tie bars, which is where the peak of the local buckling wave occurs. The zone subjected to local buckling starts to exhibit a decrease in the value of the longitudinal compression stresses when away from the compression flange, and, as shown in the longitudinal compression stresses in the CFSSP wall web at about a 9" horizontally from the compression flange.

Also, in the compression zone of the skin plate, localized longitudinal compression stresses decrease at the locations of the tie bars, with values dropping almost to zero at some tie bars. Figure 3-22 shows the longitudinal stress distribution across the CFSSP wall rectangular section at 16" from the base. The figure indicates that longitudinal stresses propagate vertically in the wall with less stress discrepancies at the locations of the tie bars. This lesser tie-bar and skin plate interaction is attributed to the fact that there is no local buckling at the location of the selected cross-section.

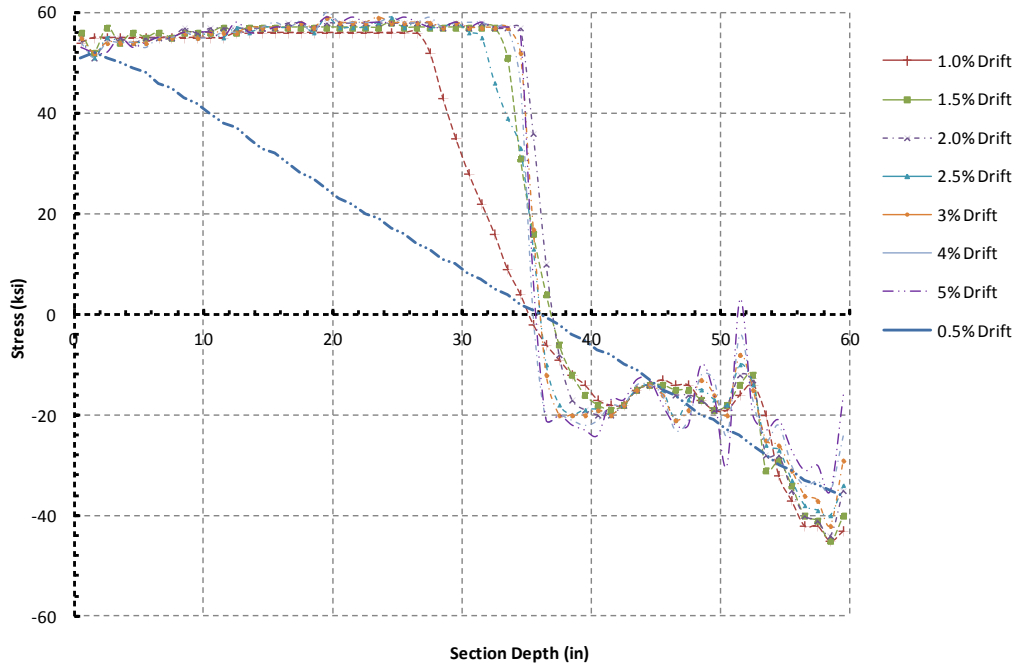


Figure 3-21 Longitudinal Stress Distribution at 8 inches from base for Different Drift Values

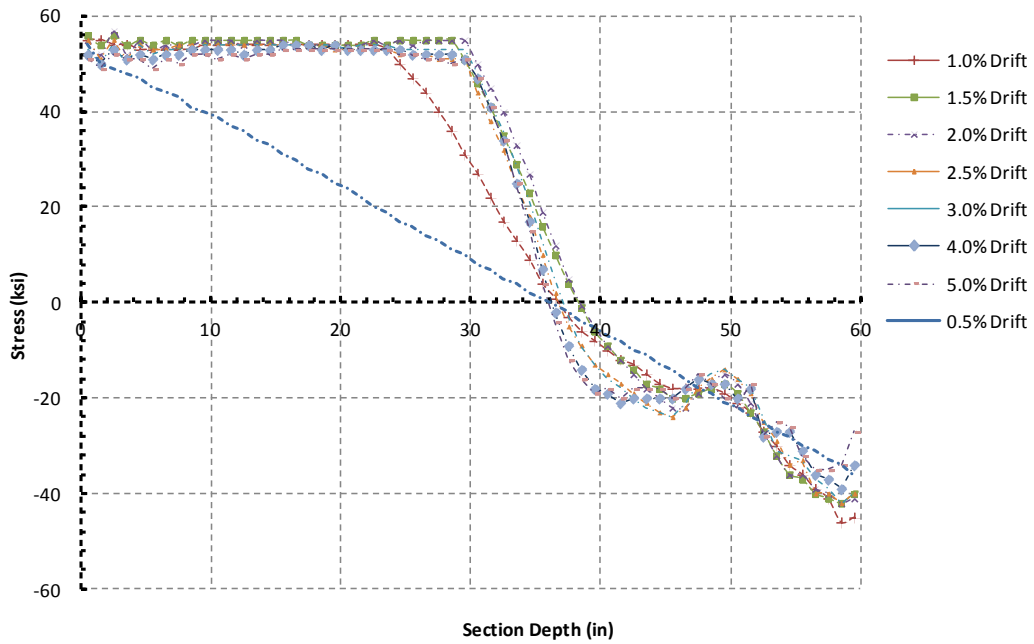


Figure 3-22 Longitudinal Stress Distribution at 16 inches from Base for Different Drift Values

To further understand how the plastic moment capacity of the rectangular CFSSP wall section develops despite the fact that the longitudinal stresses in the compressed part of the web skin plate web do not reach the yield value F_y along the full length of the compressed web, the longitudinal stresses in the concrete was also examined at 8" from the fixed base of the rectangular CFSSP wall.

In Figure 3-23 the longitudinal stresses in the concrete of the CFSSP wall is shown, at drift values of 0.5% and 1.0 % in parts a and b of the figure, respectively. At drift value of 0.5%, the stresses in the compression region reach the value of f'_c in the part of the section measured from the compression extreme fiber to about 6" horizontally in the cross section. Correspondingly, the part of the cross section subjected to longitudinal tension stresses does not reach f'_{ct} . When the drift reaches a value of 1%, the longitudinal compression stresses of values greater or equal f'_c start to propagate horizontally up to a depth of 13" in the cross section (the part of the concrete under tensile stresses still does not reach the f'_{ct} value).

Figure 3-23, the longitudinal stress distribution across the rectangular CFSSP wall section taken at 8" from the fixed base is presented, for lateral drift values of 1.5% and 2.0%. At drift value of 1.5%, the longitudinal compression stresses start to have an increased magnitude in the elements laying at the middle core of the compression zone and a decreased magnitude in the elements in the outer skirt of the filled in concrete. At 2% drift, the concentration of longitudinal compression stresses further increase in the core of the concrete compressed zone and further decrease on the outer perimeter of the compressed zone. This decrease is also observed to progressively spread more toward the inner core of the compressed zone. Longitudinal stresses typically decrease in the elements of the concrete that lie in the vicinity of the locally buckled steel skin plate.

In Figure 3-25, the longitudinal stress distribution across the section of concrete taken at 8" from the fixed base at 3% and 4% drift is shown. At 3% drift, the part forming the core of the compressed elements with high magnitude of stresses starts to shift toward the plastic neutral axis, while the longitudinal stresses in the concrete elements at the perimeter of the compressed zone and in those elements next to it starts to drop sharply. At 4% drift, the value of stresses at the edge elements (outer skirt elements) in the compressed zone undergo high longitudinal strains and the stress there continue declining, the magnitude of the stresses in the compressed core keeps dropping.

To integrate this information in a format that makes it possible to compare with the stress distributions along the depth of the wall, as considered in the simple plastic moment calculations, the concrete longitudinal stresses across the wall thickness have been averaged. The resulting averaged longitudinal stress distribution across the CFSSP-Wall cross-section is presented in Figure 3-26, in which the increase in values of concrete strength due to triaxial stresses in the concrete elements can be observed (as a consequence of the concrete damage plasticity model used). The values significantly exceed the specified concrete strength of 4ksi, which explains why the full plastic moment of the wall could be attained in spite of the loss in longitudinal steel stresses.

In order to further verify contribution of the filled-in concrete to the plastic moment capacity of the rectangular CFSSP wall section, an overview of the longitudinal plastic strain distribution is presented in Figure 3-27, Figure 3-28, and Figure 3-29 for a cross section taken in the concrete of the rectangular CFSSP wall at 8" from the wall fixed base and that for different lateral drift values. Figure 3-24 shows the longitudinal strain distribution across the filled in concrete of the rectangular CFSSP wall at 8" from the fixed base and at lateral drift values of 3% and 4%. The elements at the edge of the compression zone exhibits large longitudinal strain and this large strain progressively propagates from the edges to the inner core of the compressed zone.

Correlating the longitudinal strain values resulting from the analysis to the stress values provided through the uniaxial stress-strain curve model is not rigorously possible. This is because the prescribed uniaxial backbone stress-strain curve, if used as a criteria to determine the degree of damage in the concrete, is not directly applicable to the concrete elements subjected to bi-axial or tri-axial stresses (the backbone curve is only true for a uni-axial state of stress). However, in the absence of a simple constitutive equation to capture by hand-calculations the progressive damage of the concrete elements, the uniaxial stress-strain relationship can be used to provide an approximation. Note that this approximation would be further in error if used to verify results from cyclic analysis (described in the next section), because, as mentioned earlier in this chapter, the constitutive model of concrete damage plasticity accounts for stiffness degradation in the case of cyclic loading by using degradation coefficients for both uni-axial tension and uni-axial compression backbone curves for concrete.

According to the uni-axial stress-strain model used, elements for which the longitudinal strain exceeds the value of 0.005 would suffer damage and starts to lose their ability to sustain load. However it is found that most of the elements that lay on the edges of the compressed part in the vicinity of the locally buckled steel skin plate reaches high strain values at relatively low drifts, accordingly they started to lose strength

at a drift value of 1%, and this loss of strength propagated from the edges of the compressed region to the inside core of the compressed zone.

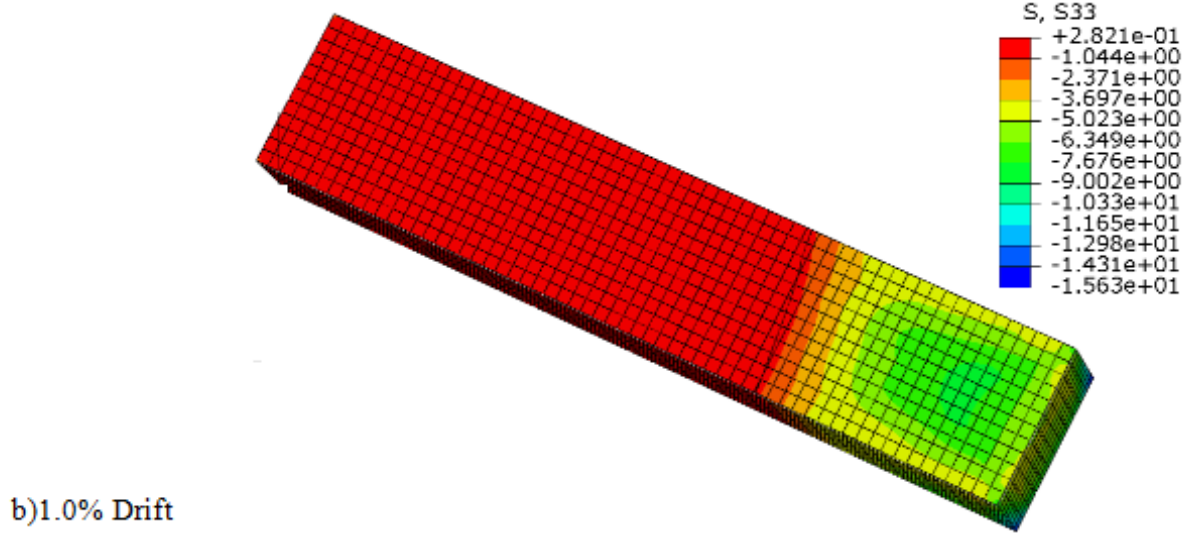
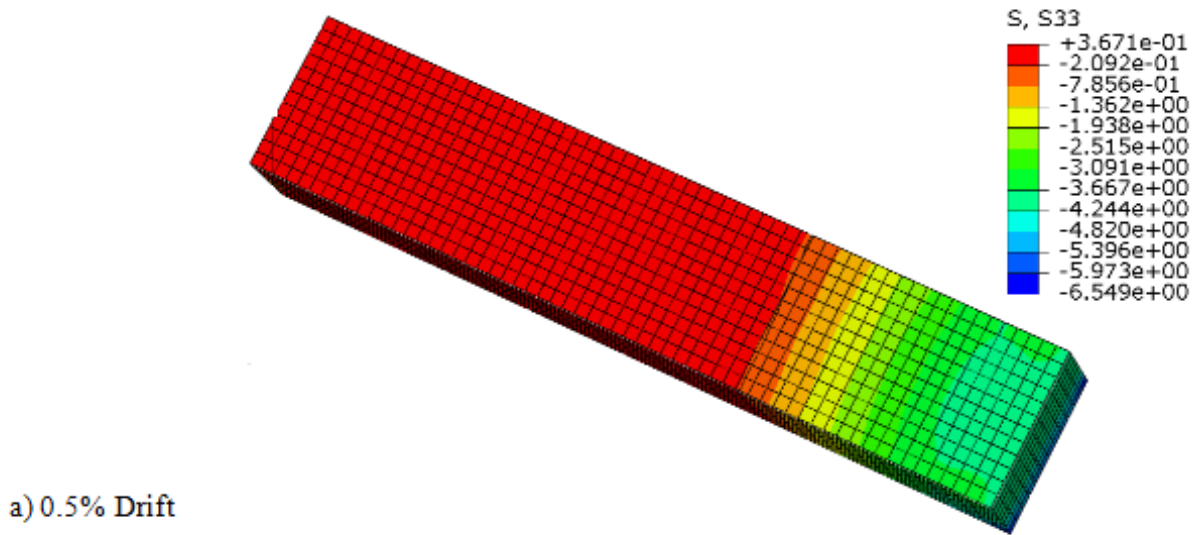


Figure 3-23 Longitudinal Stress Distribution in Concrete at 8 inches from Fixed Base: (a) 0.5% Drift; (b) 1% Drift

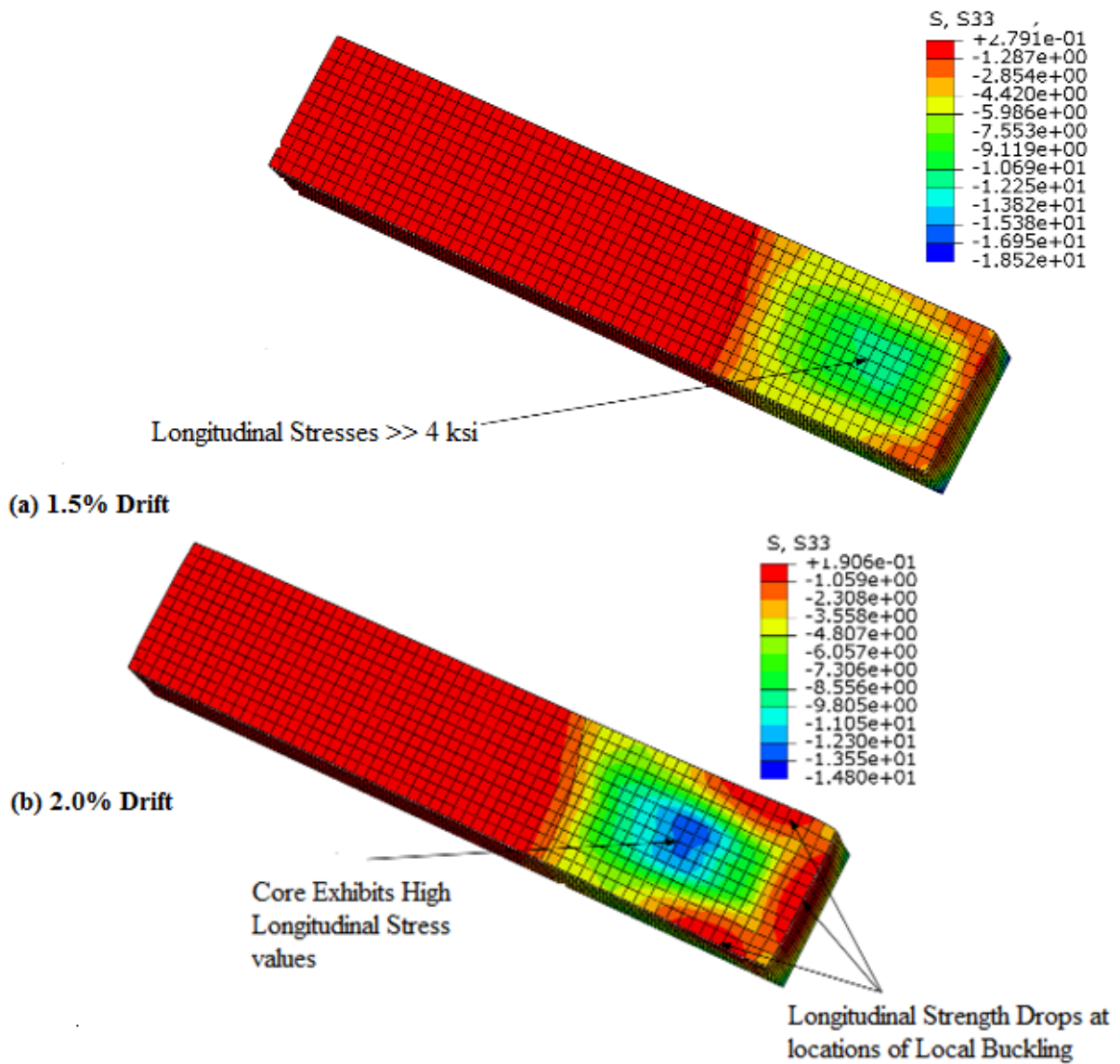


Figure 3-24 Longitudinal Stresses in Concrete at 8 inches from Fixed Base: (a) 1.5% Drift; (b) 2.0% Drift

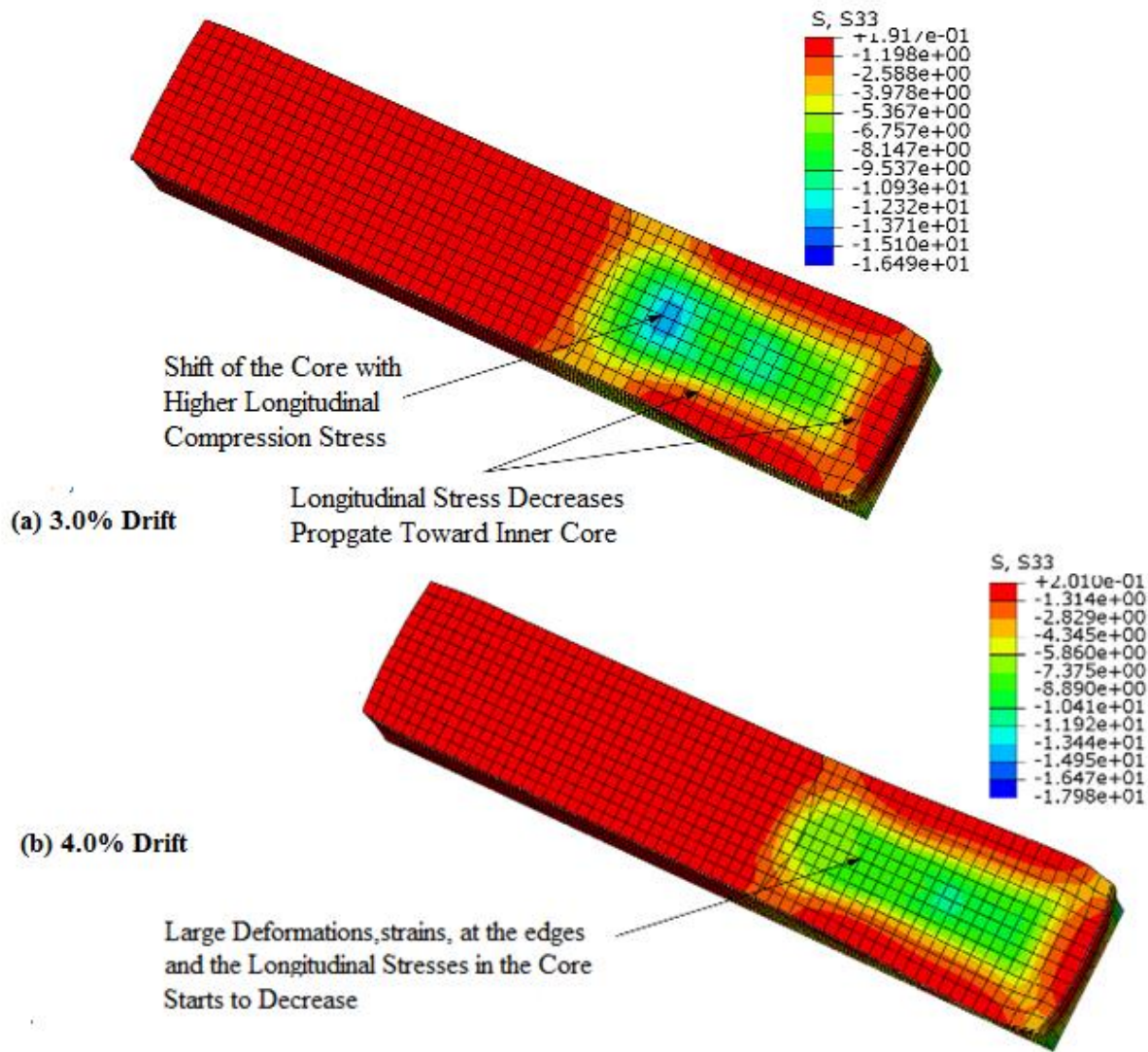


Figure 3-25 Longitudinal Stress Distribution in Concrete at 8 inches from Base: (a) 3.0 % Drift: (b) 4.0% Drift

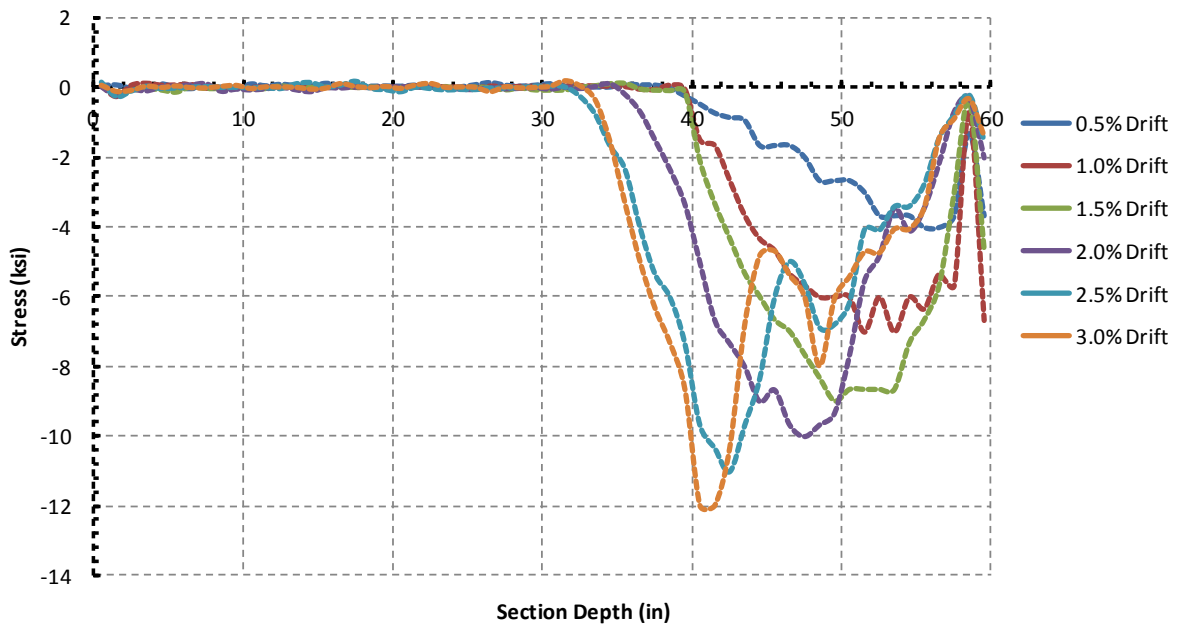
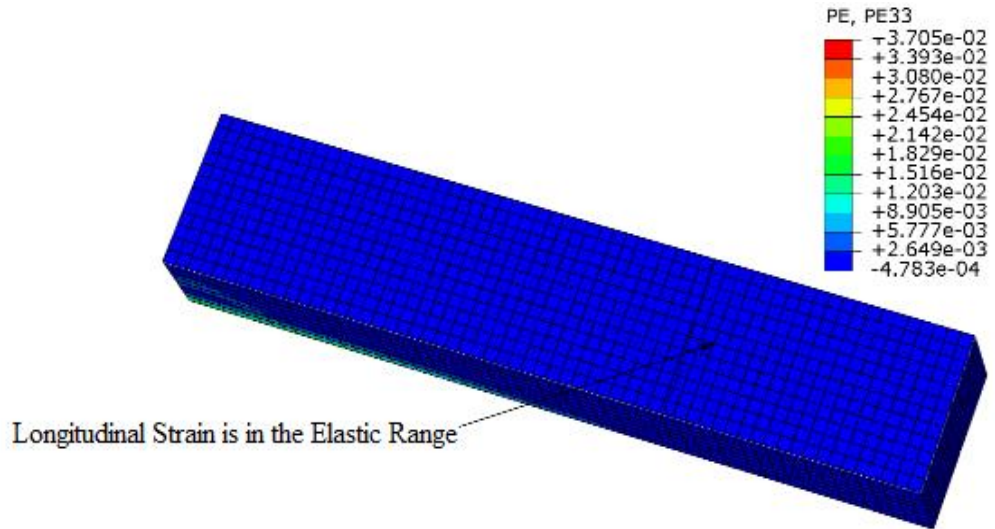
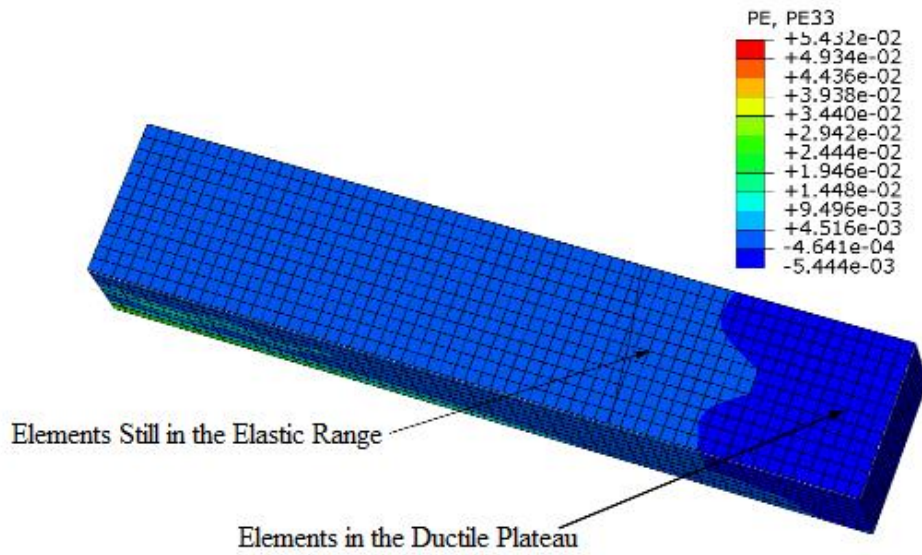


Figure 3-26 Average Stress Distribution across the CFSSP-Wall Cross-section



(a) 0.5% Drift



(b) 1% Drift

Figure 3-27 Longitudinal Plastic Strain Distribution in Concrete at 8" from base:(a) 0.5% Drift;(b) 1.0% Drift

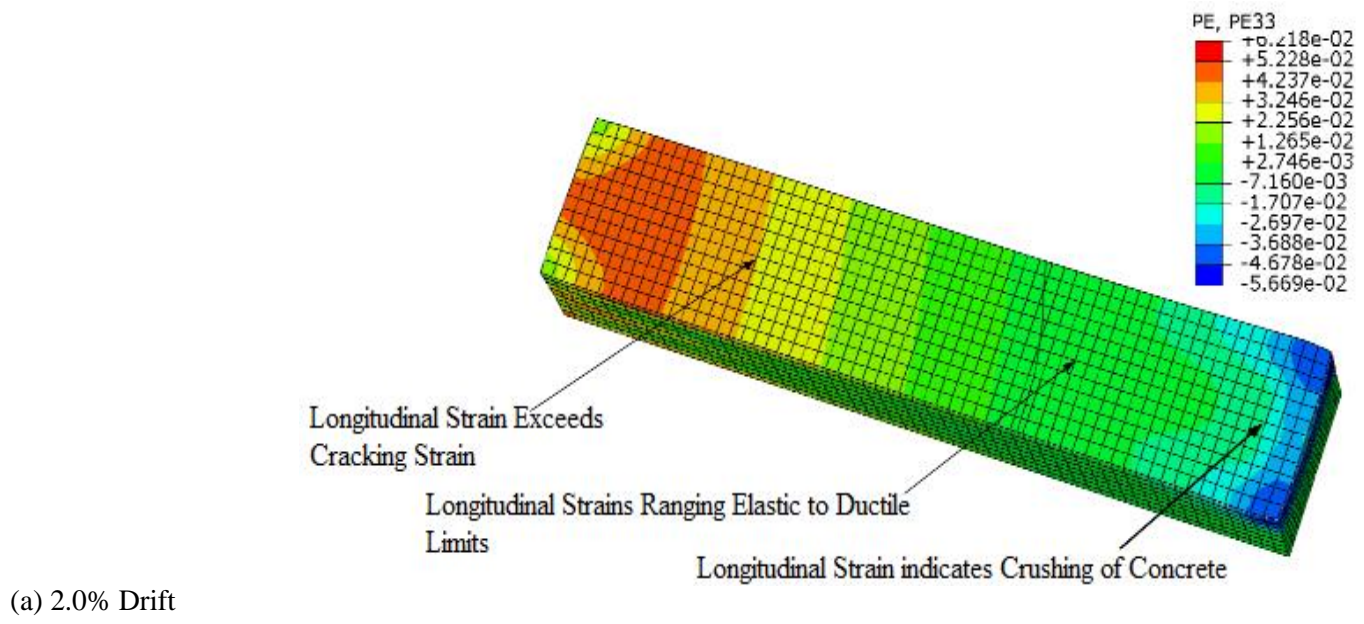
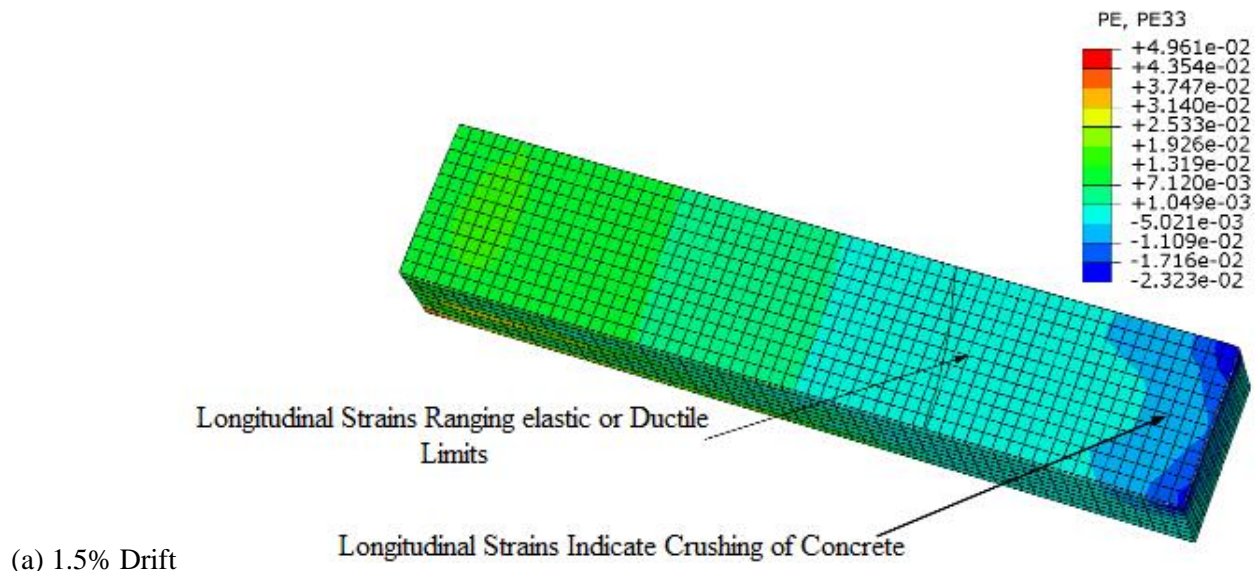
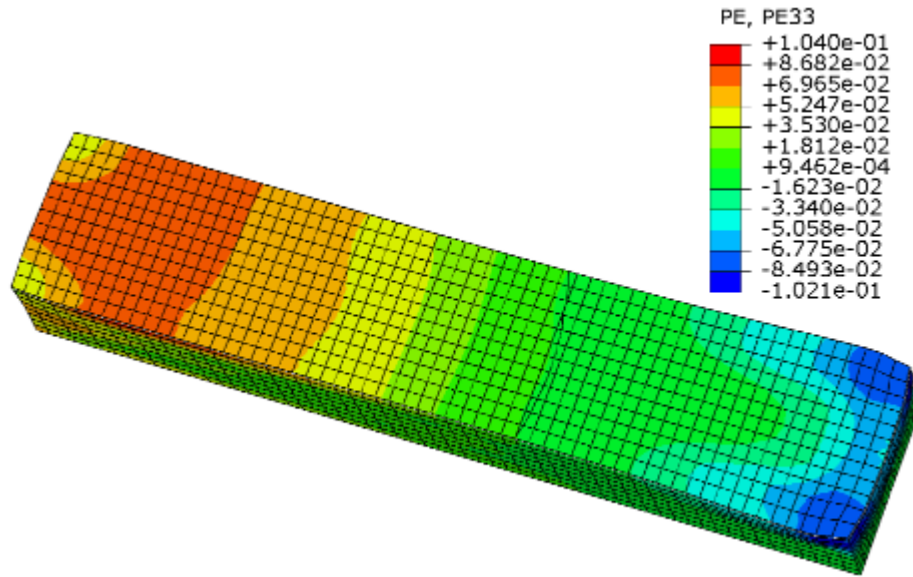
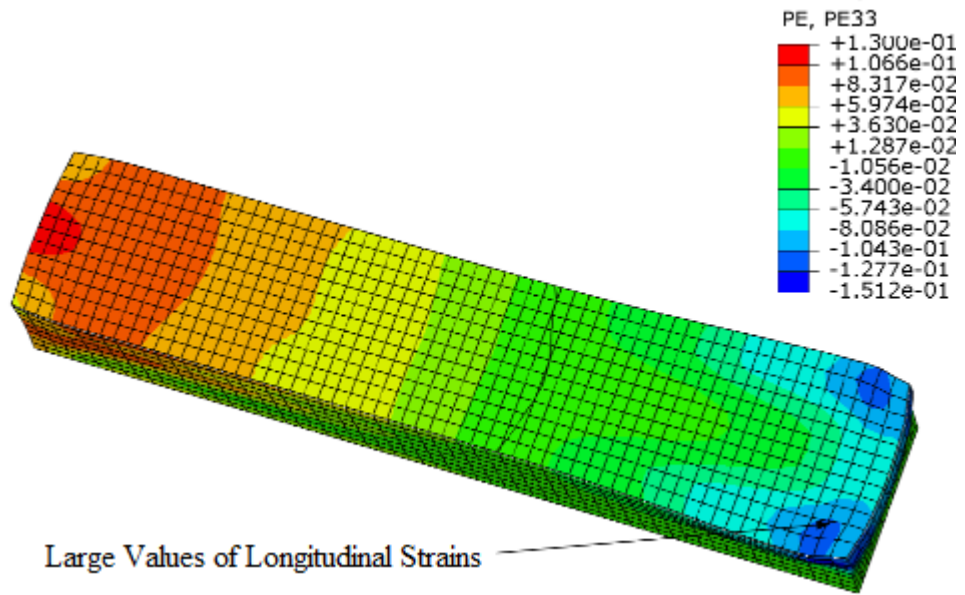


Figure 3-28 Longitudinal Strain Distribution in Concrete at 8" from Base:(a) 1.5% Drift;(b)2.0% Drift



(a) 3% Drift



(b) 4.0% Drift

Figure 3-29 Longitudinal Strain Distribution in Concrete at 8" From Base:(a) 3.0% Drift;(b) 4.0% Drift

3.6.8 Cyclic Loading of the Rectangular CFSSP-Wall Finite Element Model

The aforementioned rectangular CFSSP-Wall finite element model was also loaded cyclically loading. The displacement loading starts with cycles of lateral displacement at 0.5% drift and ended with cycles at 3% drift, with increments of 0.5% drift in each step. The loading cycles are presented in Table 3-2.

The resulting force-displacement hysteretic loops are presented in Figure 3-30. The model showed stable hysteretic behavior up to a lateral drift of 3%. Local buckling started to develop at 1% drift. The section reached its maximum strength of $1.15 M_p$ at that drift of 1%. The section sustained a strength of at least M_p up to 3% drift.

Table 3-2 Loading Cycles Used In the Analysis

Loading Step	No of Cycles	Displacement (in)	Drift%
1	1	1.32	0.5
2	1	2.64	1.0
3	1	3.96	1.50
4	1	5.20	2.0
5	1	6.6	2.5
6	1	7.92	3.0
7	1	10.56	4.0

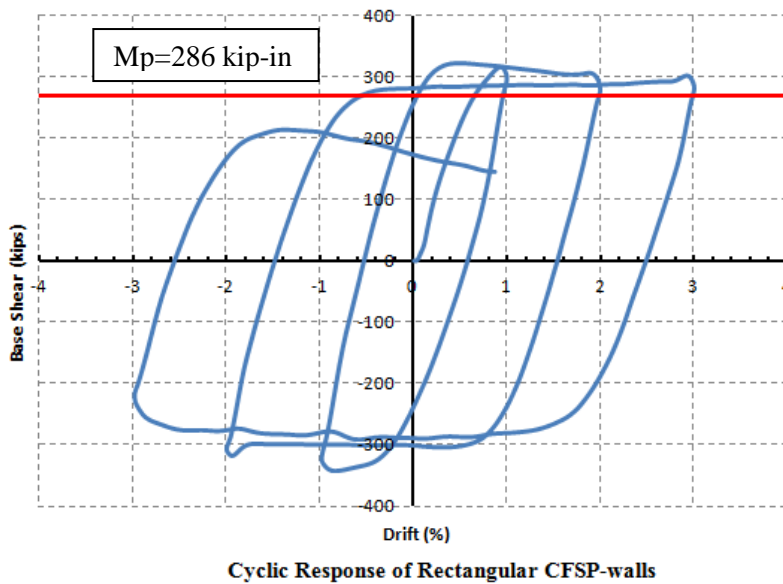


Figure 3-30 Cyclic Response of Rectangular CFSSP-Wall

3.7 Analysis for Rectangular CFSSP-Walls Available in Literature

3.7.1 General

Eom, Park et al. (2009) have tested double skin composite walls under in-plane cyclic loadings, as reported in Chapter 2. Different geometric configurations of CFSSP-Walls were tested, including rectangular cross section, T-shaped walls, and coupled rectangular walls. In an attempt to replicate some of these experimental results, the analysis methods presented earlier in this chapter were applied to the rectangular non-coupled tested walls. The analysis methods considered were plastic analysis using the aforementioned assumptions concerning stress distribution, fiber analysis using the XTRACT software, and finally finite element pushover and cyclic analysis. The results obtained by each method of analysis were compared to the Eom, Park et al. test results for the specimen DSCW1 shown in Figure 3-31.

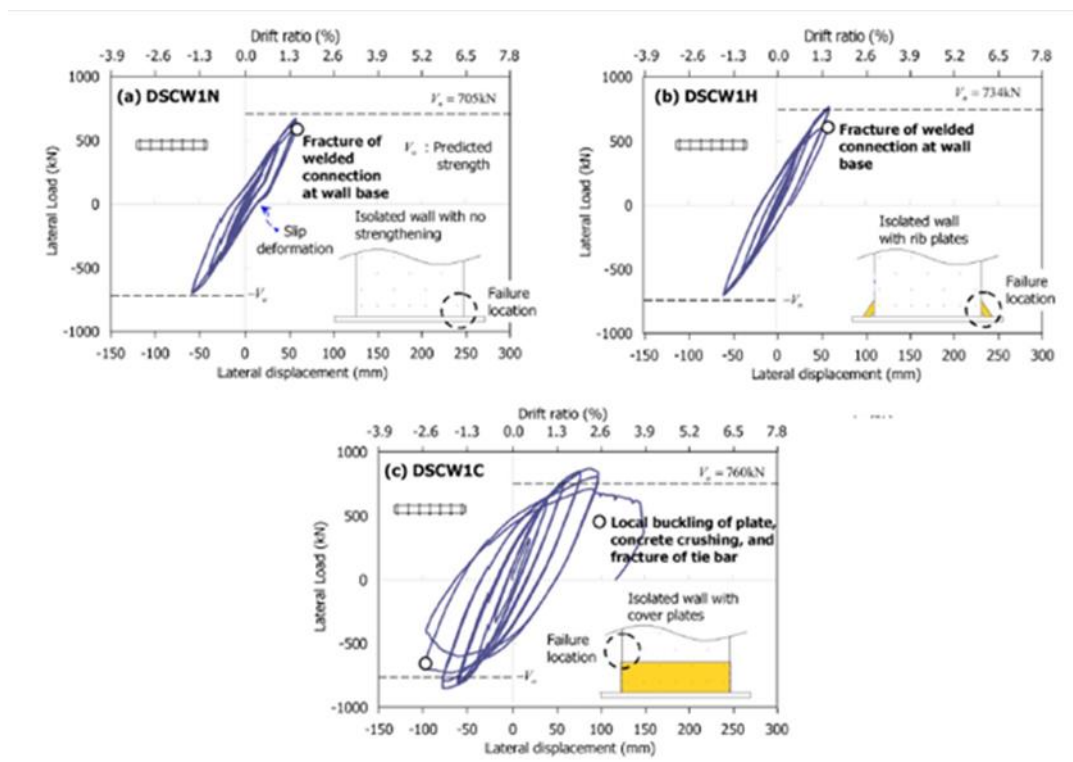


Figure 3-31 Test Results for Rectangular "Isolated" Composite Walls, Eom et al (2009)

Note that Eom, Park et al.'s specimen DSCW1 interest here suffered from premature weld failure at its base when first tested (labeled specimen DSCW1N in Figure 3-31a). Accordingly, it was strengthened first using stiffeners at its base and retested to failure (DSCW1H in Figure 3-31b) and then using cover plates for completion of the test (DSCW1C in Figure 3-31c). The rectangular section without any form of

strengthening achieved maximum moment of of 2,567,950 kN-mm at lateral drift of 1.5% before the tested specimen exhibited failure at welding location. Then the wall was strengthened by welding trianglaur ribs at the base of the wall and achieved an ultimate moment of 2,945,250 kN-mm at a lateral drift of 1.5%. Finally, the wall was strengthened by using cover plates to achieve a maximum moment of 3,088,050 kN-mm (just above the strengthened region) at a lateral drift of 2.25%. Note that both the ribs and the cover plates used in the above modifications elevate the value of ultimate strength at the base, which was accomplished to move up the point of plastic hinging; particularly, the latter case is directly equivalent to an increase of 200% of the steel in the cross-section. Accordingly the comparison in this section is focused on the moment capacity of the unstrengthened cross-section, for example the wall strengthened with cover plates the moment is calculated at section where cover plate stops (moment on original cross-section).In this Chapter, the analysis methods considered focus only on the moement capacity of the original cross-section.

3.7.2 Plastic Analysis of the Cross-Section

The cross section under consideration is a rectangular section having outer dimensions of 1000 x 12 mm and steel plate thickness of 10 mm. The steel used have yield strength of 55.55 ksi (383 MPa) and ultimate strength of 78.9 ksi (544 MPa). The concrete strength is 5.76 ksi (39.7 MPa). The stress distribution on the cross section is shown in Figure 3-32.

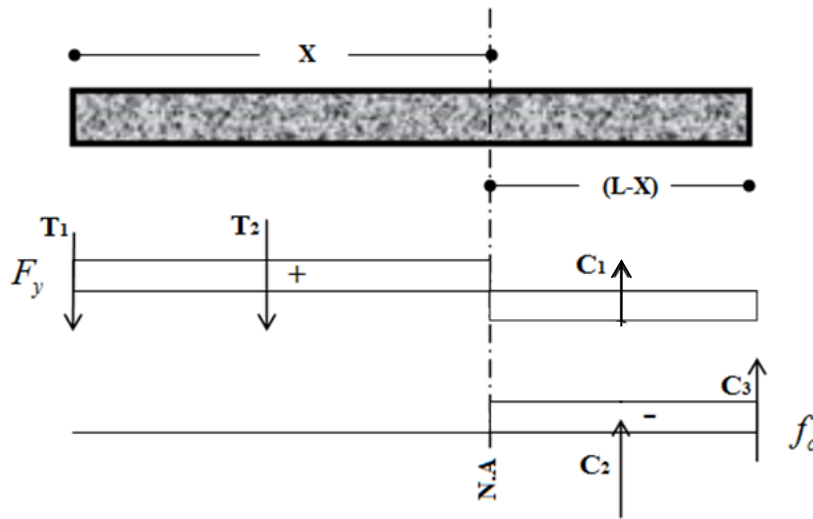


Figure 3-32 Proposed Stress Distribution on the Tested Walls

Considering the presumed stress distribution on the wall cross section, the forces acting on the cross section are:

$$T_1 = C_3 = (b_f t_f) F_y \quad (3.17)$$

$$T_2 = 2xt.F_y \quad (3.18)$$

$$C_1 = 2(L-x)t.F_y \quad (3.19)$$

$$C_2 = (L-x)t_c.f'_c \quad (3.20)$$

The part of the web under tension, x, is given by:

$$x = \frac{2t_w.L.F_y + t_c.L.f'_c}{4t_w.F_y + t_c.f'_c} \quad (3.21)$$

where,

L = is the web length

t_w = steel web thickness

t_c = concrete web thickness

The plastic moment capacity calculated is given by:

$$M_p = b_f t_f (L+t) F_y + 2xtF_y \left[\frac{x}{2} \right] + 2(L-x)tF_y \left(\frac{L-x}{2} \right) + t_c (L-x) f'_c \left(\frac{L-x}{2} \right) \quad (3.22)$$

The distance x calculated =590.84 mm

M_p =2,672,681,614 N-mm = 2,672,682 Kn-mm

The corresponding base shear, given the cantilever length of 3850 mm

3.7.3 XTRACT Fiber Analysis

The fiber analysis in XTRACT was used to calculate the capacity of the tested rectangular walls cross-section, the steel material used was bilinear steel with F_y of 383 MPa (55.6 ksi), and the unconfined bilinear concrete model with strength 39.7 MPa (5.75 ksi) shown in Figure 3-33 Note that the default confined concrete model was altered to become more of a bilinear model, as a way to benchmark the hand calculations against the XTRACT results. From the XTRACT analysis, the resulting ultimate moment is 2,623,950 kN-mm as shown in Figure 3-34.

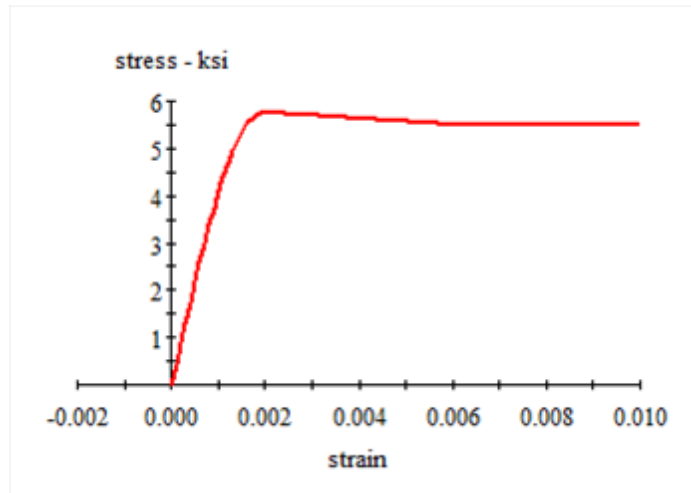


Figure 3-33 Unconfined Concrete Material Model used in XTRACT Analysis

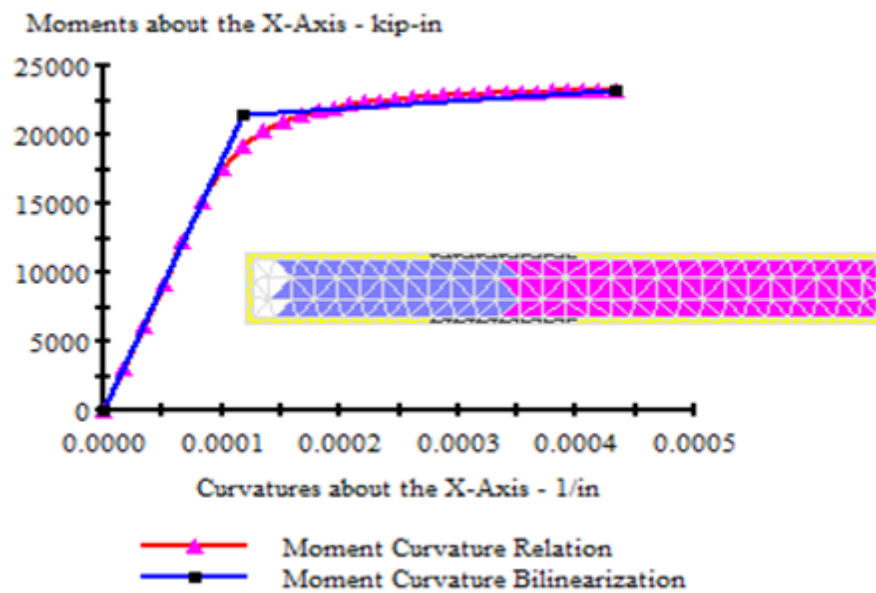


Figure 3-34 Moment Curvature Relationship for the Tested Walls by XTRACT

3.7.4 Finite Element Analysis Using Abaqus

Eom, Park et al. (2009)'s rectangular wall "DSCW1N" was modeled using Abaqus 6.10 EF2. The model was built using the same elements used earlier in section 3.6, using a bilinear steel material model, and the concrete model described in section 3.6.4. The model was subjected to lateral monotonic displacement up to a lateral drift of 5%. Boundary conditions were applied to model the fixed base cantilever wall and

displacements were imposed at the top of the cantilever wall. Then, in another analysis, the same model was subjected to monotonic cyclic loading following the same cyclic displacements magnitude as that applied during the test by Eom, Park et al. In the following sections, results from these pushover and monotonic cyclic finite element analyses are presented.

For the pushover analysis of the DSW1N, the stress distribution S33 in the steel case at a lateral displacement of 0.5% is shown in Figure 3-35, where the wall had just crossed the elastic range.

Note that local buckling in the skin plate of the model DSCW1N wall started at a lateral drift of 1.0%, as revealed by the stress contours in Figure 3-36, and became visually noticeable at 1.5% as shown in Figure 3-37.

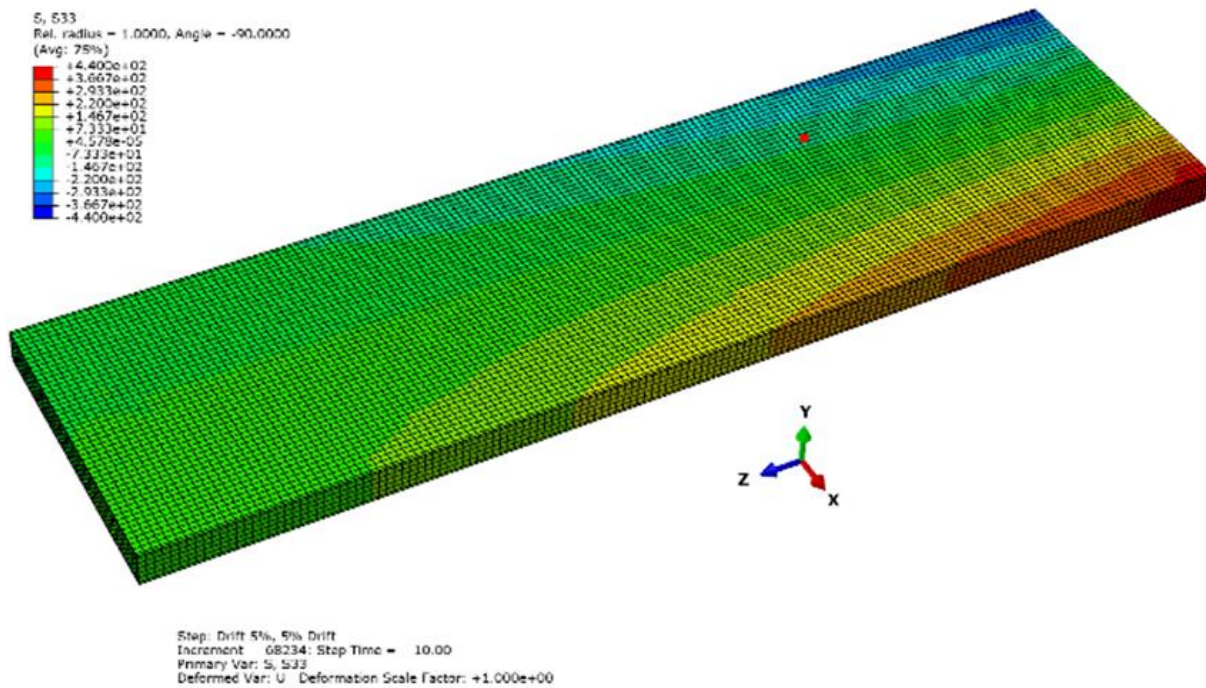


Figure 3-35 Stress Distribution in the Tested Walls at 1% Drift

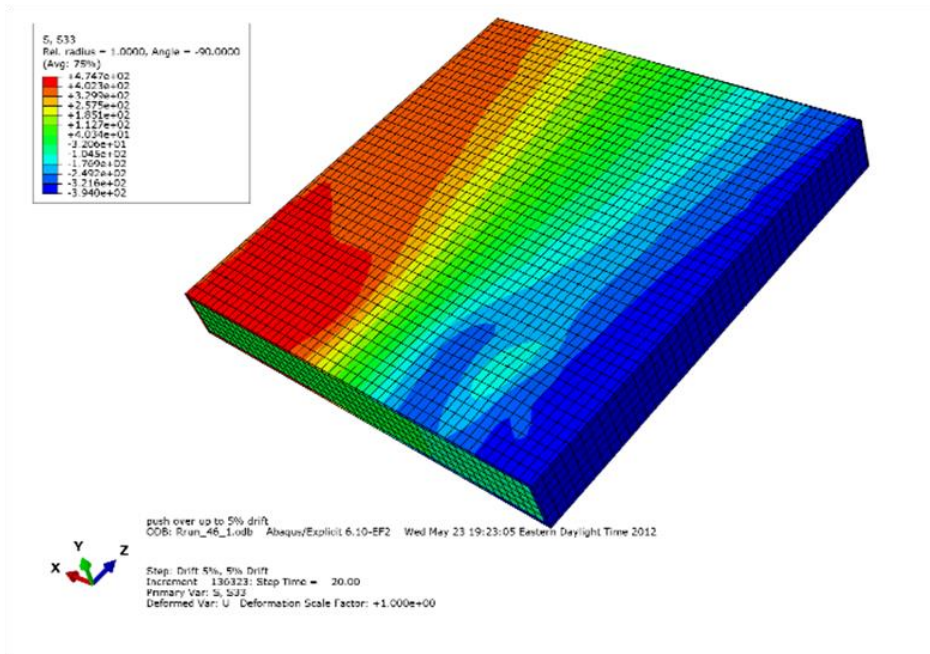


Figure 3-36 Onset of Local Buckling at a lateral Drift of 1%

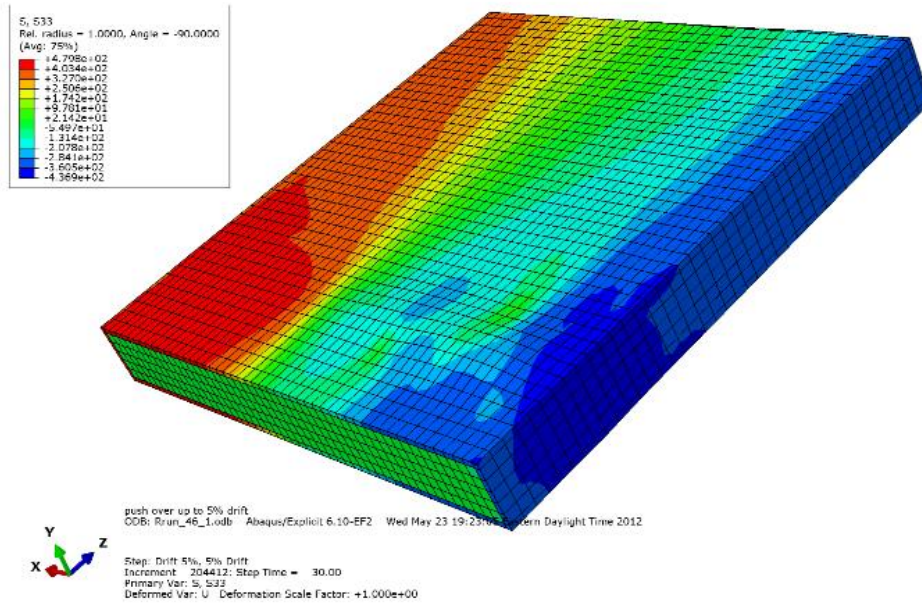


Figure 3-37 Visual Local Buckling of the Skin Plate at 1.5% Drift

Figure 3-38 shows the base shear versus the lateral drift obtained from the push-over finite element analysis. The resulting maximum moment was 2,707,143 kN-mm, which is actually 87.6% of the ultimate moment capacity achieved in the test (represented by the heavy red line).

Finite element results presented in Figure 3-38 shows that the strength of the wall starts to decrease at drifts when the wall suffers from local buckling. Note that this is also the same drift at which wall DSCW1N started to develop its premature failure in the welds.

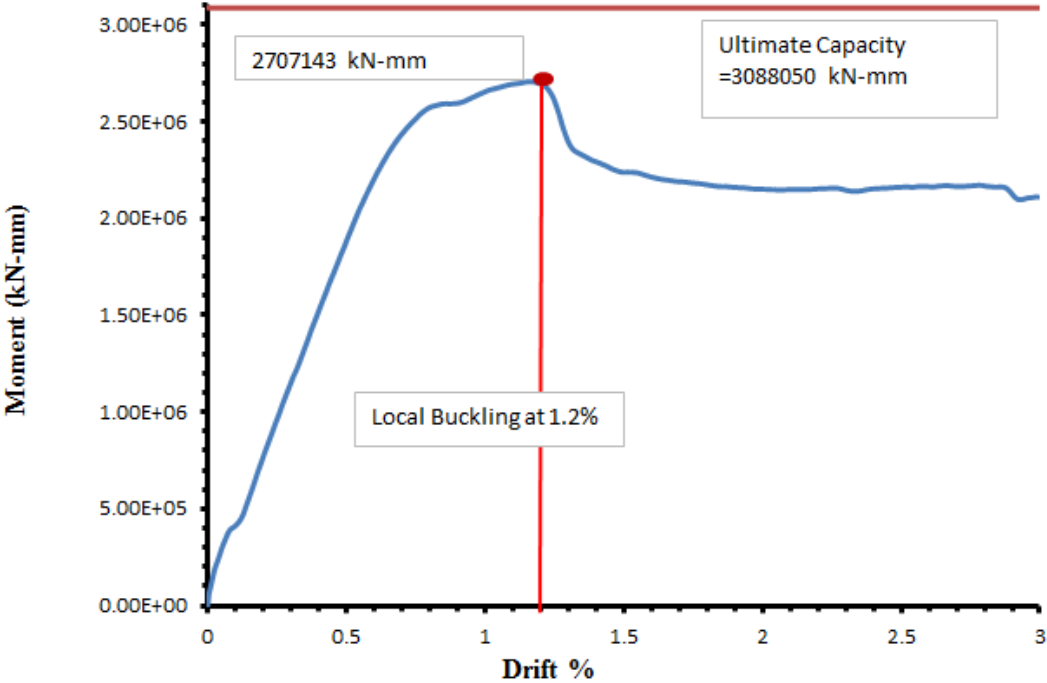


Figure 3-38 Moment vs Lateral Drift, Abaqus Analysis

Cyclic finite element analysis results for wall DSCW1N (subjected to cyclic displacement excursions) are shown in Figure 3-39, where the relation between the lateral drift and base shear is presented. As seen in Figure 3-40, the skin web plate started to develop local buckling at 1% drift, with corresponding drop in the load carrying capacity of the wall.

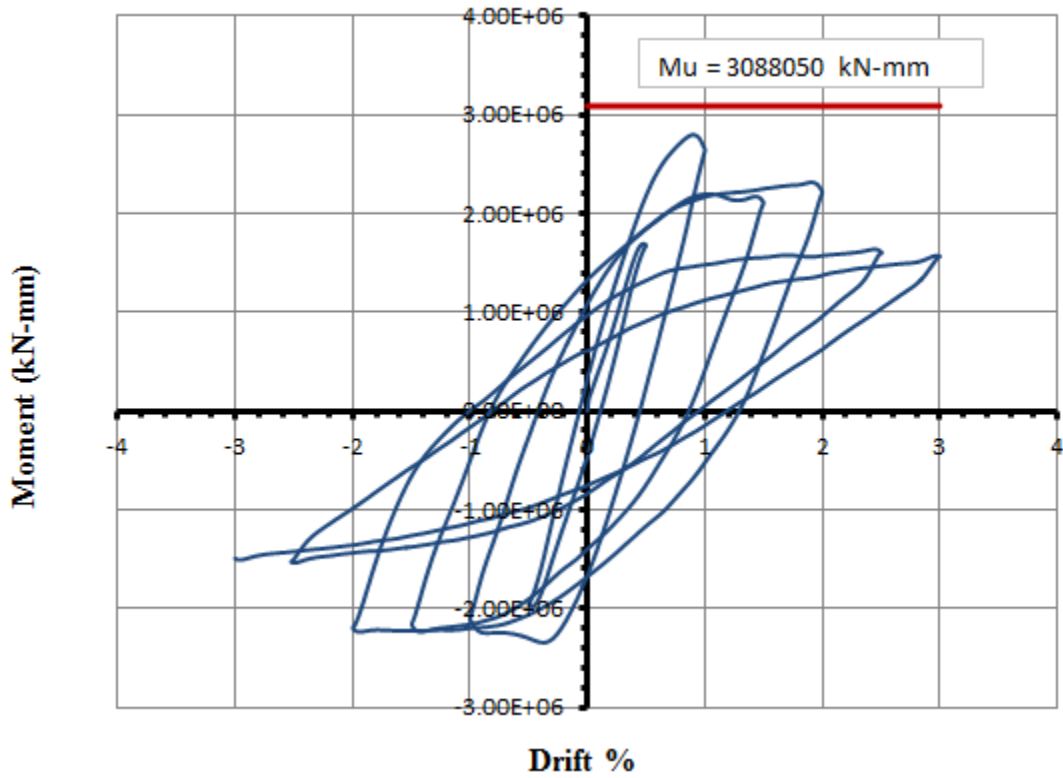


Figure 3-39 Cyclic Response of the Abaqus Model for Isolated Specimens Tested by Eom et al (2009)

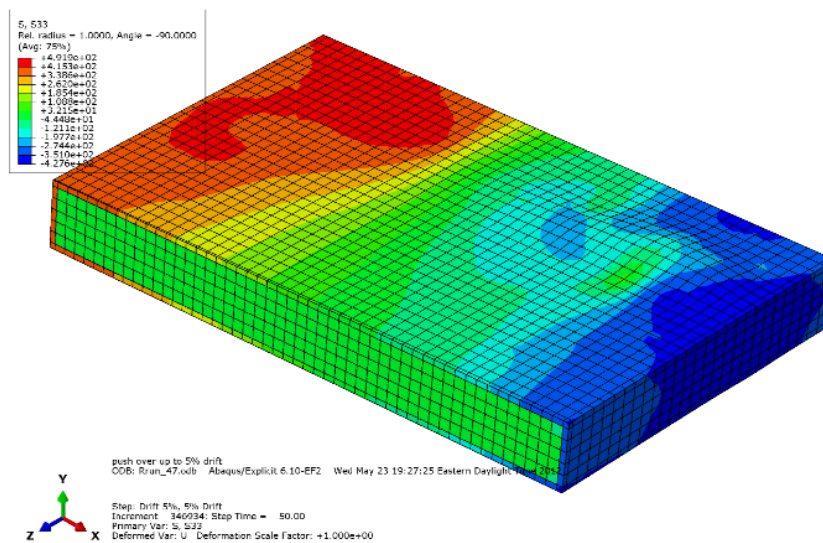


Figure 3-40 Local Buckling of the Skin Plate at 1% Drift for Walls Tested by Eom et al (2009)

3.7.5 Summary of Analysis

The different methods of analysis considered in predicting the capacity of the tested wall were compared to the ultimate capacity of the wall strengthened using cover plates as this was the only one of the three specimens tested by Eom et al. that achieved ductile behavior. Note that, in this comparison, the ultimate moment achieved in the test is taken as the maximum base shear multiplied by the lever arm (3570 mm) calculated from point where the load is applied (at the top of the wall) to the top of the reinforced section, as plastic hinging developed above that reinforced segment. The results for all analysis methods considered are summarized in Table 3-3. Note that the different methods of analysis underestimated the ultimate strength of the wall by 15% to 10%.

Table 3-3 Ratio between Analysis Results and Test Results

Method of Analysis (1)	Analysis Base Shear/Test Base Shear		
	Analysis Moment Value (kN-mm) (2)	Ultimate Moment(Kn-mm) (3)	Ratio (2)/(3) (4)
Plastic Analysis	2,672,682	3,088,050	0.87
XTRACT	2,623,950	3,088,050	0.85
Abaqus Pushover	2,707,143	3,088,050	0.88
Abaqus Cyclic	2,788,663	3,088,050	0.90

CHAPTER 4

EXPERIMENTAL PROGRAM

4.1 Introduction

This chapter describes the experimental program for testing four large scale CFSSP-Wall specimens in the Structural Engineering and Seismic Simulation Laboratory (SEESL) at the University at Buffalo. The four specimens designed and detailed as part of this program were cantilever CFSSP-Walls with a height-to-width aspect ratio of 2 and were fixed to a reinforced concrete base. Two different kinds of wall cross-sections were considered (as described in Section 4.2). In the following sections of this chapter, the details of the experimental program are presented in terms of the cross sections of the tested specimens (Section 4.2), data on the material properties used in construction of the tested specimens (Section 4.3), test set-up, foundation, and boundary conditions of the tested CFSSP-Walls (Section 4.4), typical assembly and lateral restraints of the tested specimens (Section 4.5), and instrumentation used to measure strains and deformations throughout testing of the specimen (Section 4.6). The loading protocol used through the experimental program is also presented. A detailed design of the tested specimens and the test rig is presented in Appendix B.

4.2 Cross Sections of the Tested CFSSP-Walls Specimens

The specimens tested in the experimental program are divided into two groups of two specimens.

In the first group, called Group NB, the CFSSP-Walls have no boundary elements and their cross section is composed of double web skin plates having thickness, t , of 5/16" and width, w , of 40", connected through circular tie bars spaced equally in both horizontal and vertical direction at a spacing, S , that varies from one specimen to the other. The flanges of the panel consist of half HSS sections, which were used (instead of flat cap plates) in order to avoid premature failure of the cross section's corner welds due to concentration of stresses that has been observed in prior research for rectangular sections (AISC-341 (2010; Samer El-Bahey and Michel Bruneau (2011)). Both specimens of Group NB have the same outer dimensions, plate thicknesses, aspect (height-to-width) ratio and the same specified material properties, such that they have the same plastic moment (although values could vary depending on the actual material properties of each specimen). The tested specimens were named specimen CFSSP-NB1 and CFSSP-NB2; they have a total width, W , of 4 feet and 0.625 inches (40" skin plates plus two half-HSS 8.625×0.325 of 8.625" diameter) and total thickness, b , of 8-5/8 inches. The height of both specimens in Group NB is 10 ft above the top of the footing, and their width is 4ft, resulting in an aspect ratio (height to total cross section depth), H/W , of 2.56. The detailed dimensions of Group NB specimens are shown in Figure 4-1.

For specimens in Group NB, the tie bars were welded to the web skin plate using plug welding: tie bars having a total length equal to $(b-t)$ were positioned to span the distance between the steel web plates center lines, and the remaining half thickness of the plate on each side was filled with welding material to create the plug weld. For specimen CFSSP-NB1, the spacing of the tie bars, S , in both horizontal and vertical direction is equal to 8 inches, giving a flat width-to-thickness ratio, S/t , of 25.6. The spacing of the tie bars in specimen CFSSP-NB2 in both horizontal and vertical directions is 12 inches, for a corresponding ratio, S/t , of 38.4. The tie bars were designed to remain elastic throughout the tests, and consequently have a diameter of 1 inch.

The HSS sections were cut using a water jet to avoid the need for annealing of the HSS after cutting. The half HSS section was welded to the steel web using full penetration welds; the procedure for specimen assembly is illustrated later in this chapter.

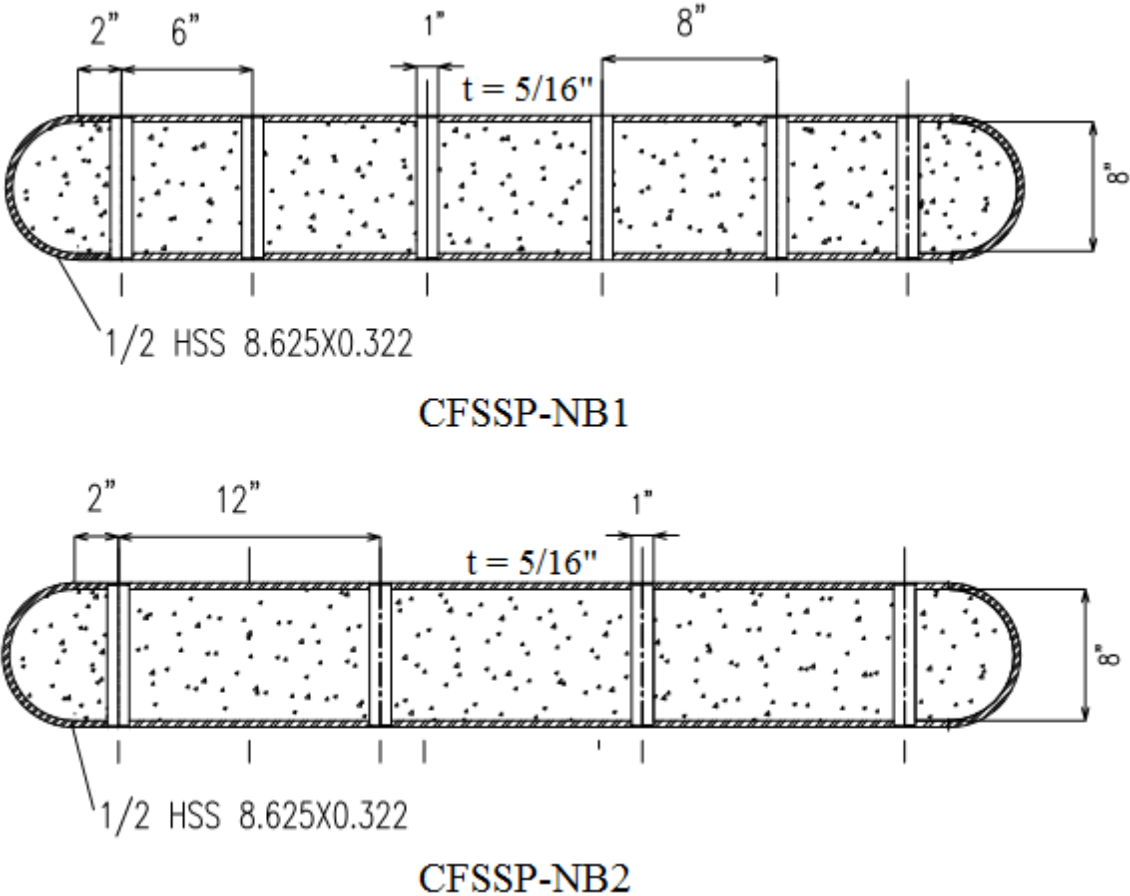


Figure 4-1 Cross Sections of Group NB Specimens

The second group of tested specimens, called Group B, are CFSSP-Walls having boundary elements (i.e., columns) consisting of concrete filled round HSS section. The walls' cross section consists of those HSS

columns and of double web skin plates having a width, w , of 30", a thickness, t , of 5/16", and connected through tie bars spaced equally in both horizontal and vertical direction at a spacing, S , that varies from one specimen to the other. The two specimens in Group B have the same outer dimensions, plate thicknesses, tie bar diameter, and aspect ratio, H/W , (height to total cross section depth) of 2.76. Specimen CFSSP-B1's tie bars were connected to the web plate through plug welding per the same technique used for the specimens of Group NB; tie bars are spaced at 8" center-to-center, leading to b/t ratio of 25.6 for the plate. However, for specimen CFSSP-B2, tie bars were assembled differently. Bars having a total length of $(b+2t)$ where used, where b is the total width of the wall. As such, when installed, the tie bar protruded a distance of 5/16 inches beyond the steel web plate on each side, and were fillet welded to the web steel plates. Tie bars for specimen CFSSP-B2 are spaced at 12" center-to-center, resulting in a S/t ratio of 38.4 for the plate. Figure 4-2 shows the detailed dimension of Group B specimens.

The boundary elements used in Group B specimens are round HSS 8.625x0.322 welded to the steel webs using full penetration welding. The web panels of CFSSP-Walls in Group B were filled with the same concrete as the HSS 8.625x0.322.

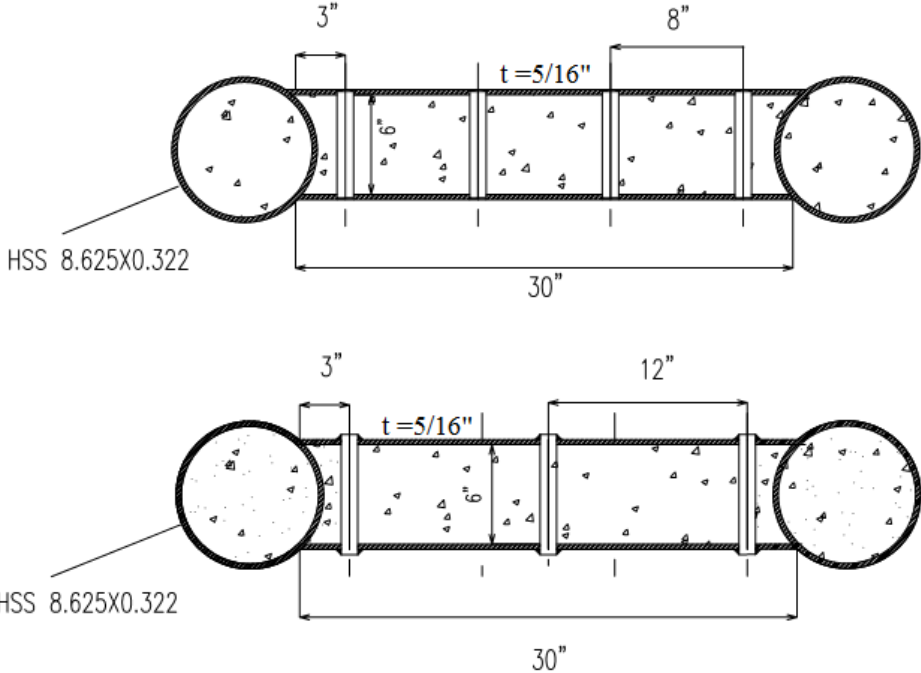


Figure 4-2 Cross Sections of Group B Specimens

Note that the design of the experimental program specimens started with the Group NB specimens, and that all the specimens' outer dimensions, height, and material properties were chosen such that the force needed to generate the plastic moment of the section could be applied using the available facilities at UB SEESL. Also, dimensions of the Group B specimens were chosen such that specimens in both groups B and NB would have approximately the same plastic moment capacity.

4.3 Materials

4.3.1 Concrete

The concrete used for filling the steel panels of the CFSSP-Walls specimens was ordered from a ready-mix plant in Western New York. The concrete used for the four specimens was self-consolidating concrete (SCC), with a prescribed strength of 4 ksi. The SCC had a slump of 3". This kind of concrete was used because of its high workability, which was desirable in this case so that the CFFSP-Wall specimens could be filled with concrete without the need to use a concrete vibrator (which would have been difficult to use given the height of the wall). For specimen CFSSP-B2, steel fibers were added to the SCC as an attempt to better distribute tension cracking of the concrete and possibly improve its ductility. The 2" length steel fibers used, shown in Figure 4-3, are known as NOVOCON XR produced by PROPEX concrete systems.

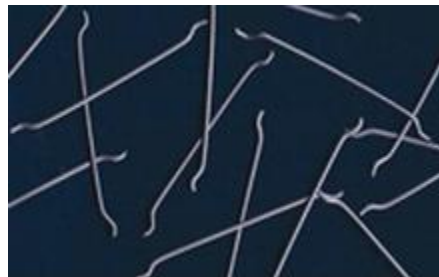


Figure 4-3 NOVOCON Steel Fibers used in Specimen CFSSP-B2, <http://www.novocon.co.nz>

The construction and assembly sequence for the tested specimens is described in details in Section 4.5. However, note that concrete for each tested CFSSP-Wall specimen and its reinforced concrete foundation was poured on the same day. More specifically, the foundation concrete and the concrete for each CFSSP-Wall specimen was poured from same batch. From each pour, three standard cylinders were prepared, having a diameter of 6" and height of 12". Each specimen and its respective cylinders were tested on the same day and after at least 14 days of curing. Table 4-1 shows a summary of the concrete strength, f'_c for each of the tested specimens

Table 4-1 Strength of Concrete in the Tested Specimens

Specimen	Cylinder 1 Strength (psi)	Cylinder 2 Strength (psi)	Cylinder 3 Strength (psi)	Average Strength (psi)	Curing Days
CFSSP-NB1	6780	7140	6900	6940	14
CFSSP-NB2	6580	6972	6820	6791	16
CFSSP-B1	7280	6450	7510	7080	13
CFSSP-B2	5440	4590	4310	4780	14

4.3.2 Steel

Specimens were designed assuming a yield strength of 50 ksi for both the HSS and plates with a factor of safety of 1.5 to account for variability and strain hardening of the supplied steel (see Appendix B for detailed design of the tested specimens) . However, it was recognized that HSS are known to have a significant variability in their yield strength attributed to the process of manufacturing (Atlas Tube, <http://www.atlastube.com>), generally exceeding 50ksi, often up to values of 65 ksi. As the steel for this project was being donated by the American Institute of Steel Construction, it was possible to work with the HSS suppliers, Atlas Tube, and to obtain HSS having mill-test certificate results close to 50ksi. The supplied HSS showed mill-test certificates, for steel ASTM A500-10A Grade B&C of 60.99 ksi and tensile strength of 71.87 ksi, which provided some assurances of actual yield strengths remaining close to the specified values.

For each of the tested specimens, the steel grade for the web flat plates were different from that for the HSS 8.625×0.322 used as boundary element or wall end-caps for the CFSSP-Walls. For the HSS 8.625×0.322, ASTM A252 Gr 3 steel was used (with a specified yield strength of 50 ksi), and ASTM A572 Gr.50 steel was used for the plates of the CFSSP-Walls webs.

For each specimen, 2 coupons were taken from the HSS part of the specimen and 2 coupons were taken from the web plates. All coupons were tested under monotonic tension. Results for one representative HSS coupon is shown in Figure 4.4 (all coupons tested exhibited a similar stress-strain curve and maximum elongation). Strains were monitored using a MTS extensometer with a 2" gage length, while the forces were monitored using an internally mounted load cell in a Tinius Olsen testing machine at the University at Buffalo. The resulting average yield strength of the HSS sections used in the experimental program, F_y , was 43.75 ksi and the average ultimate strength, F_u , was 62.125 ksi. Standard deviation for the 8 coupons tested was 1.71 and 2.01 ksi for the yield and ultimate strengths, respectively.

Maximum and minimum strengths measured were 46 and 42 ksi for the yield strengths, and 65 and 62 ksi for the ultimate strengths, resulting in an average ratio of F_u/F_y is 1.41. The tested coupons showed relatively good ductility and reached on average a strain of 21% before fracture. Note that that this steel didn't exhibit a distinct yield plateau and that yield strength was determined based on the 0.2% offset method.

Table 4-2 HSS Tested Coupons

Specimen	HSS, Average Coupon Results		Averaged Coupon Max. Strain	F_u/F_y
	F_y	F_u		
CFSSP-NB1	44	61	0.21	1.38
CFSSP-NB2	42	62	0.22	1.47
CFSSP-B1	46	65	0.19	1.41
CFSSP-B2	44	61	0.23	1.39

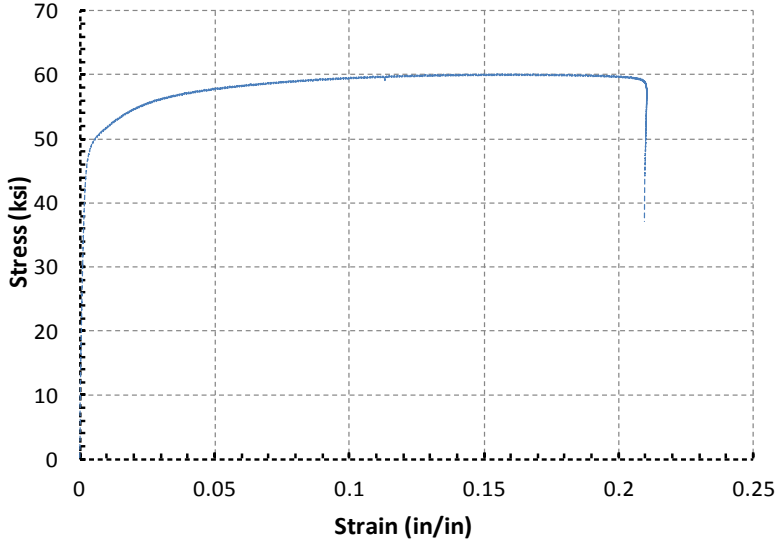


Figure 4-4 Tension Coupon Result for HSS from Flange/Boundary Element of CFSSP-Wall

Two coupons were also taken from each specimen web plates and tested as described previously. The web material was found to have an average yield strength, F_y , of 62.5 ksi and an average ultimate strength, F_u , of 73.75 ksi. Standard deviation for the 8 coupons tested was 1.3 and 2.4 ksi for the yield and ultimate strengths, respectively. Maximum and minimum strengths measured were 64 and 61 ksi for the yield strengths, and 77 and 71.50 ksi for the ultimate strengths, resulting in an average ratio of $F_u/F_y = 1.18$. The tested coupons showed relatively good ductility and reached on average a strain of 23% before fracture. Figure 4-5 shows a representative tension coupon result for CFSSP-Wall web material. Results for all specimen are summarized in Table 4-4.

Table 4-3 Web Plate Tested Coupons

Specimen	Web Plate, Average Coupon Results		Averaged Coupon Max. Strain	F_u/F_y
	F_y	F_u		
CFSSP-NB1	63	72.5	0.21	1.15
CFSSP-NB2	61	74	0.23	1.21
CFSSP-B1	62	71.50	0.24	1.15
CFSSP-B2	64	77	0.21	1.20

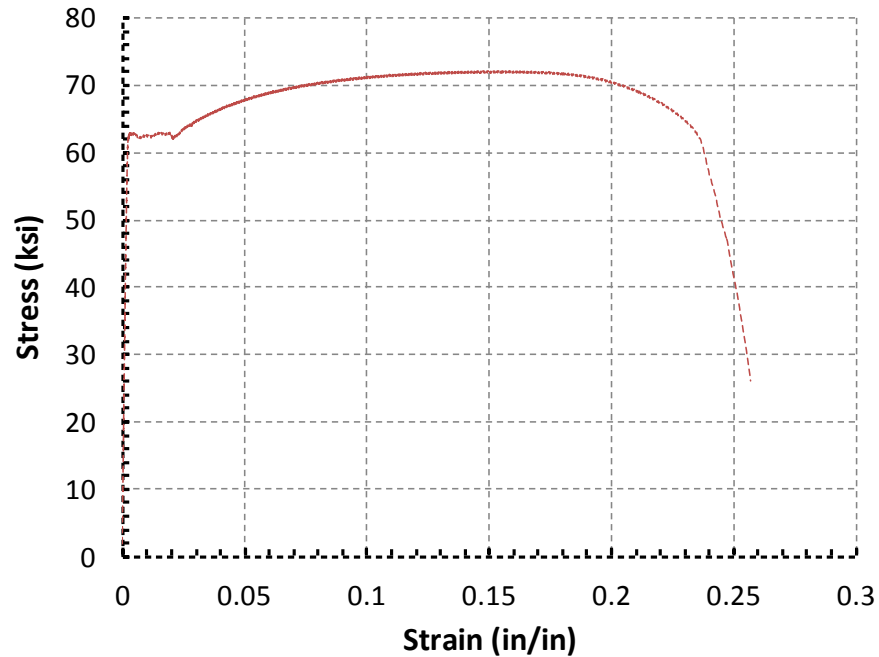


Figure 4-5 Tension Coupon Result for Plate from CFSSP-Wall Web

Table 4-4 Geometric and material properties of the Tested Specimens

Specimen	HSS, F_y (ksi)	Web, F_y (ksi)	Concrete, f'_c (ksi)	S	S/t	D/t	Aspect Ratio	Tie Bars Welding
CFSSP-NB1	42	63	6.94	8	25.6	26.77	2.56	Plug
CFSSP-NB2	43	61	6.79	8	25.6	26.77	2.56	Plug
CFSSP-B1	44	62	7.08	12	38.4	26.77	2.76	Plug
CFSSP-B2	46	64	4.78	12	38.4	26.77	2.76	Fillet

4.4 Test Setup Components

4.4.1 General

All of the tested specimens were loaded to bend about their strong axis and develop their plastic moment, denoted here M_p . The design values of M_p for all specimens in Groups NB and B was based on

specified material properties, namely strength of concrete, f'_c , of 4 ksi and yield strength, F_y , of 50 ksi for all steel in the sandwich panel, including both web plates and half or full HSS sections. To design the different components of the test setup, the plastic moment, M_p , calculated using these material properties was multiplied by 1.5. In other words, the possibility of developing $1.5M_p$ at the fixed base of the tested specimen was used as the basis for designing all test setup components. The 1.5 factor was intended to account for actual material strengths being possibly higher than the specified values considered during design and for strain hardening developing at large strains (some of the materials used in the specimens, as shown in Section 4.3, indeed had higher strengths than the specified values, but actual values were not known at the time of test-setup design).

The plastic moment of the specimens in Group NB, namely CFSSP-NB1 and CFSSP-NB2, is 2268 kip-ft; For Group B, namely CFSSP-B1 and CFSSP-B2, it is 2173 kip-ft. The larger of these two values multiplied by 1.5 gives 3402 kip-ft; for a specimen height of 10 ft, that results in an applied shearing force of 340 kips, requiring the use of one of SEELS's actuator of 400 kips capacity.

The test setup required design of a head plate at the top of the wall to transfer the actuator force to the tested specimen, a reinforced concrete foundation at its base designed to resist a moment of 3402 Kip-ft, pre-tensioned threaded bars (Dywidags) to tie the reinforced concrete foundation to the lab strong floor, structural components transferring the design load from the tested CFSSP-Wall to the reinforced concrete foundation, and finally a side restraint system to prevent the tested wall from lateral motions during testing. Figure 4.6 shows a typical test set-up elevation. In the following sections, some aspects of different components of the test setup are highlighted, while the detailed design of the test setup is presented in Appendix B.

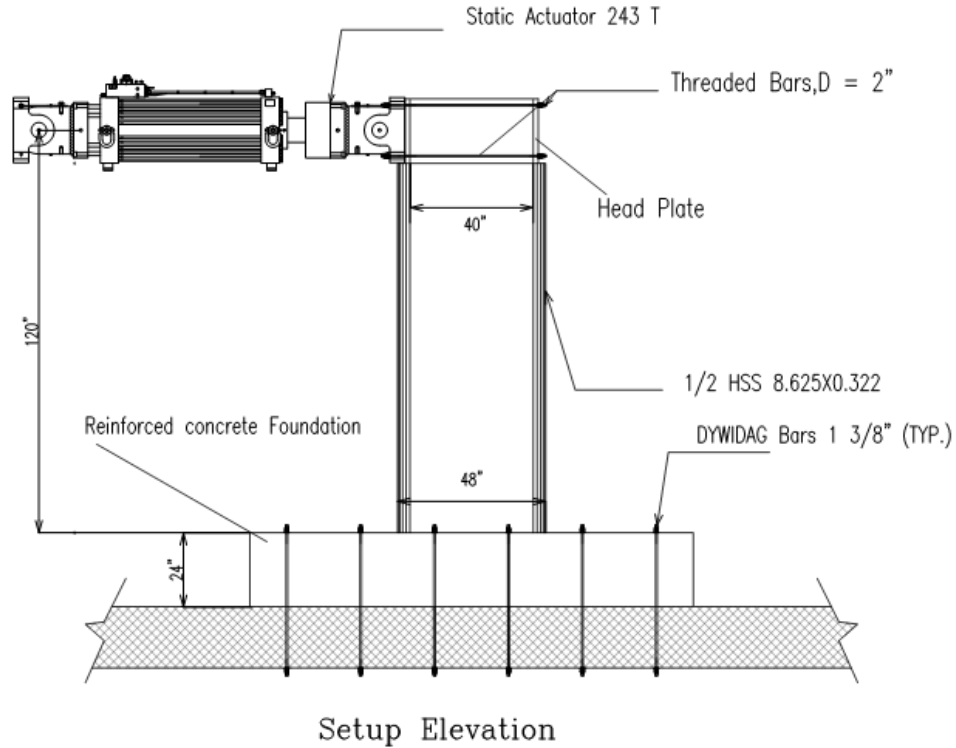


Figure 4-6 Elevation of Specimen CFSSP-NB1 Setup

4.4.2 Actuator Type

The shearing force acting on the specimen is on the order of 340 kips. The actuator selected to apply this load is an MTS 243.90T linear hydraulic actuator configured to be limited to a 446 kips capacity (to match rating of pivot head). The position of the actuator on the strong wall and calculations to verify the strong wall integrity in resisting the testing loads are presented in Appendix B of this document.

4.4.3 Head Plate and Threaded Bars

Subjecting the specimens to quasi-static cyclic loading required that the actuator alternatively pushed and pulled on the specimen. Accordingly, head plates transferring the load from the actuator to the specimens were designed for those loads, and sized to accommodate the dimensions of the MTS 243 T linear static actuator head. The thickness of the head plate was calculated such that it could elastically resist a maximum pulling/pushing load of 340 kips, distributed at the four holes of the head plate (i.e. point load of 85 kips at each hole). Details of the head plate are shown in Figure 4-7.

To transfer loads to the head plate while pulling the actuator, four pre-tensioned threaded bars were used to transfer the load from the actuator to the head plate. The force per threaded bar was 85 Kips and the

threaded bars were sized to remain elastic throughout the test. Due to geometric constraints, namely the size of the holes in the actuator head, 2 inch diameter threaded bar were chosen. Their ultimate strength in tension is 121 Kips and they were pre-tensioned to 90 kips.

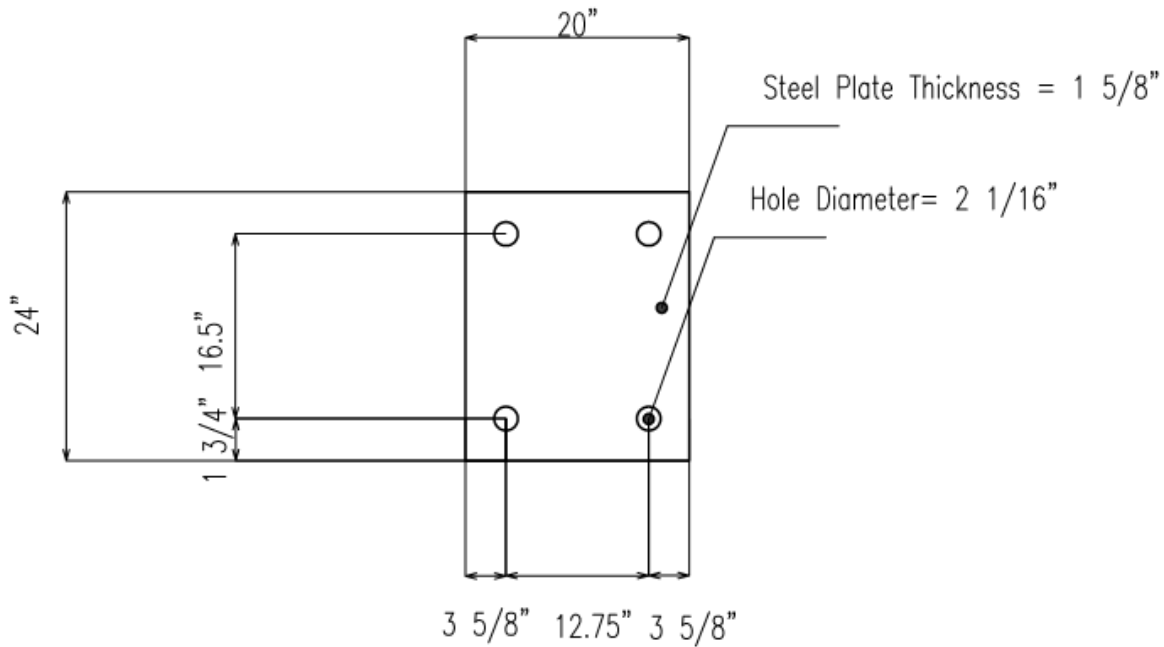


Figure 4-7 Head Plate Dimensions

4.4.4 Foundation and Strong Floor Connection

All of the tested specimens were cantilever type walls fixed to a reinforced concrete base, itself connected to the strong floor of the SEESL lab using pre-tensioned DYWIDAG bars. The size of the foundation and the pre-tension force in the DYWIDAG bars were selected such as to prevent uplift of the reinforced concrete foundation (i.e., designing to prevent tension stress between the foundation and strong floor), in order to achieve a full base fixity condition. The detailed design of the reinforced concrete footing is presented in Appendix B.

The thickness of the concrete foundation was chosen to be 24" to accommodate the length of the available DYWIDAG bars at UB SEESL, and the grid of holes at 2 feet spacing in the SEESL strong floor constrained where DYWIDAG bars could be used to connect the foundation to the strong floor. The foundation and DYWIDAG bars assembly were designed to sustain the $1.5M_p = 3402$ kip-ft moment mentioned earlier, together with the corresponding shearing force of 340 kips, shown in Figure 4.9.

The 1-3/8inch diameter DYWIDAG bars were distributed over three rows and pre-tensioned to a force, F_D , of 119 kips, which correspond to 63% of their prescribed yield load. The number of DYWIDAG bars, N , and foundation length, b , (parallel to depth of specimen) and width, a (normal to depth of specimen), were selected to prevent foundation uplift. This was achieved when calculations showed no resulting tension stresses between the specimen footing and the strong floor when using the following equation:

$$\frac{1.5M_p}{ab^3}(6b) \leq \frac{NF_D}{ab} \tag{4.1}$$

According to equation 4.1 the number of DYWIDAG bars needed was calculated such that compression stress on the strong floor due to pre-tension force of the DYWIDAGs, given by the right hand side of equation (4.1), was larger or equal to the theoretical tension stress on the floor induced due to $1.5M_p$ at the footing/strong floor interface (calculated using the left hand side of the equation, recognizing that the interface couldn't develop tension). Figure 4-8 shows the resulting size of the foundation footprint, the moment acting normal to the strong axis of the CFSSP-Wall, and the DYWIDAG bars locations.

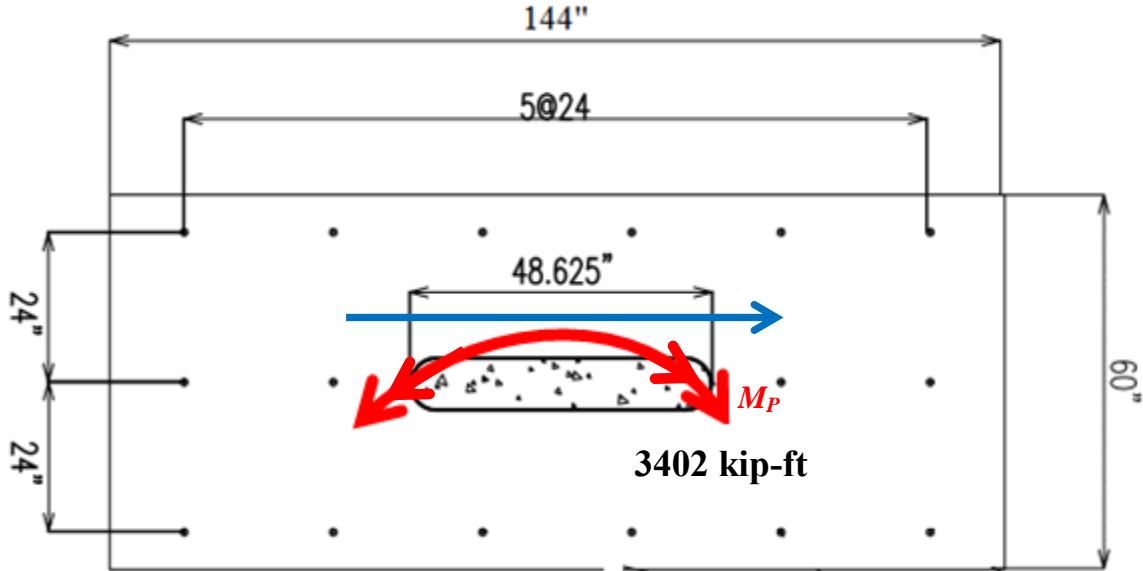


Figure 4-8 Footing Footprint and DYWIDAG Location

Reinforcement of the foundation was calculated considering the flexural and shear strengths needed to resist the pressures under the footing due to the applied flexural moment, for both longitudinal and

transversal direction reinforcement (as shown in Appendix B). Sliding of the foundation was prevented by checking that the maximum lateral load that could be applied to the specimen (i.e. maximum actuator force), V_A , could not exceed the friction forces between the foundation and strong floor:

$$V_A \leq \mu N F_D \quad (4.2)$$

where, μ is the friction coefficient between the reinforced concrete foundation and the strong floor, taken equal to 0.3

4.4.5 Load Transfer to Reinforced Concrete Foundation

Transferring the shear forces and moments to the foundation in a way that achieves the assumed condition of base fixity was the design goal. For the tested specimens in both groups NB and B, the cross section elements consisted of round HSS and double flat web plates, and each of these components were expected to develop their yield strength. Consequently, structural details were needed to transfer these yielding forces to the reinforced concrete foundation. The design strategy was to transfer both the shearing force and the corresponding moment to the footing of the tested specimen while keeping the footing elastic.

A common approach to transfer wall base moments to footings is to provide horizontally oriented structural elements able to develop a resisting couple in the footing (a.k.a. a shear head). This strategy is effective when the magnitude of the horizontal forces can be minimized by increasing the length of the forces lever arm, which requires the use of a deep footing. Here, because the footing depth was limited to 2 ft (due to the length of available DYWIDAGs, as mentioned earlier), an effective shear head could not be implemented. Instead, the design approach followed consisted of developing mechanisms to transfer the tension forces corresponding to the fully yielded steel parts of the walls.

The force to be transferred from the web of the CFSSP-Wall was conservatively taken as that resulting from axial yielding of the web when developing a moment equal to $1.5Mp$, and simplistically taken as :

$$1.5F_y h t_w \quad (4.3)$$

where,

h, t_w are the web height and thickness respectively.

The force given by equation (4.3), is to be transferred to the footing using re-bars passing through the part of the wall embedded in the footing, normal to the CFSSP-Wall steel web, assuming that these re-bars acted as shear connectors. This was done instead of using shear studs because of the concern that a group of shear studs used for this purpose could have pulled out as a unit and the lack of knowledge on proper detailing to prevent this failure mode for the current application, given the relatively shallow footing being used. Note that the re-bars were also relied upon to transfer the shear forces acting at the base of the CFSSP-Wall (simultaneously to the flexural moment), as described below.

Transfer of the yield forces from the specimen steel web was achieved by using three rows of reinforcing bars in the part of the CFSSP-Wall embedded in the foundation. These bars passed through the entire CFSSP-Wall web and extended to the edge of the foundation. The number of bars required to transfer the web forces was conservatively calculated using equation I3-3 in AISC 360-5 for the strength of a stud, (recognizing that the bars could provide more strength if fully yielding in shear):

$$Q_n = 0.5A_{sc}\sqrt{f'_c E_c} \quad (4.4)$$

Accordingly, the number of bars required to transfer the yield force in CFSSP-Wall web having a length h , thickness t_w , and yield strength F_y , is given by equation 4.5:

$$N_b = \frac{1.5F_y h}{0.85Q_n} t_w \quad (4.5)$$

The calculated number of re-bars needed was distributed over three rows. To ensure transfer of forces in the three rows to the concrete without pulling out of the top row from the cover concrete (i.e, making the three re-bar rows equally effective and acting simultaneously), stirrups were used to tie the three rows together. Note that to differentiate the re-bars (transferring shear) from the conventional reinforcement in the footing, these are called “connector re-bars” from here on.

Note that in flexure, only part of the web is in tension, but the above approach develops an adequate strength per unit length along the wall width to resist wall flexure, irrespectively of which part of the wall in tension. Furthermore, per this approach, the re-bars located in the part of the wall in compression are then available to transfer the shear forces from the walls to the footing.

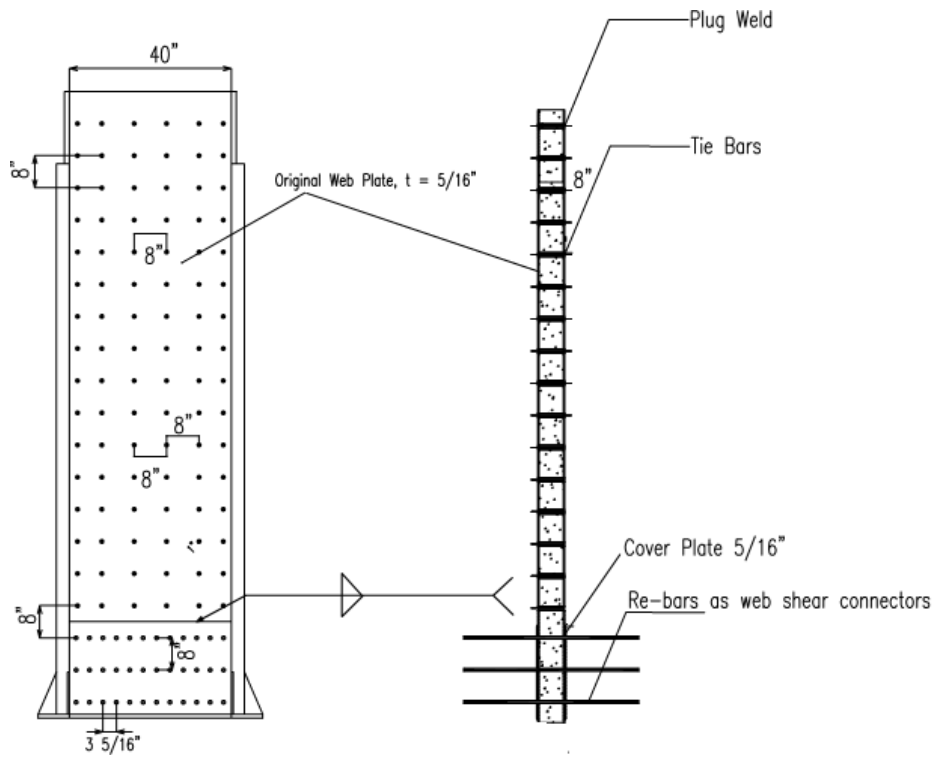
Also note that the footing transverse flexural reinforcement (i.e., spanning in the short direction of the footing) was interrupted at the location of the CFSSP-Walls. The connector re-bars therefore also served as transversal flexural reinforcement spanning through the CFSSP-Wall; for that reason, the upper and lower rows of the Connector Re-Bars were also checked to be able to resist the shear force (for which they were designed, as mentioned earlier) acting together with tension force resulting the bending moment acting on the footing on the short direction (foundation moment in the short direction divided by the distance between top and bottom rows of re-bars connectors generates tension force in the top/bottom rows). Appendix B shows the calculation of stresses in the connector re-bars that led to the selection of 1 inch diameter re-bars for all re-bar connectors.

For Group NB specimens, the resulting number of re-bar connectors per row needed to transfer the web force was 12 (for a total of 36 over 3 rows), and for Group B, that number was 9 (27 over 3 rows). To compensate for the reduced area of the steel web due to drilled holes in that region, a 5/16" thick cover plate was welded to the original web plate of the CFSSP-Wall. That plate thickness was sized such that:

$$A_{net} F_u \leq A_g F_y \quad (4.6)$$

Figure 4-9 to Figure 4-12 shows the web connector re-bars for specimens CFSSP-B1, CFSSP-B2, CFSSP-NB1 and CFSSP-NB2, respectively. The complete foundation reinforcement for a typical specimen is shown in Figure 4-15. The details of this footing and load transfers design are presented in Appendix B.

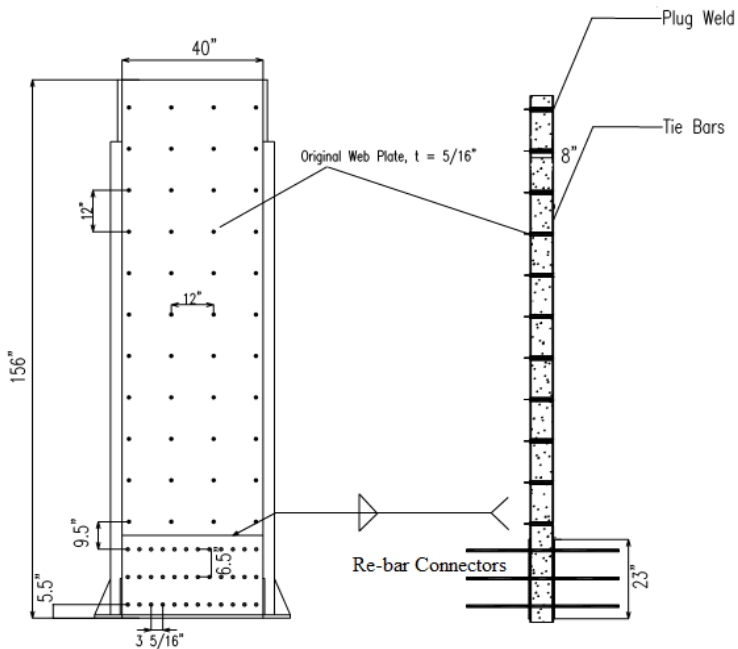
The forces generated due to yielding of the HSS part of the cross section required another form of connectors to transfer the tension forces at the toe of the CFSSP-Walls to the footing, because re-bars could not be easily “threaded” through the HSS. In this perspective, to anchor the circular segments of the CFSSP-Walls cross-section, an annular ring was used following the concept proposed by Roeder et al. (2004). More specifically, when the half tube forming the flange of the CFSSP-NB yields in tension, the strategy adopted here consisted of transferring this tension yield force to the foundation through the annular ring welded at the base of the half circular section. Roeder et al. commented that some of that force might be transferred through shear friction along the face of the steel, but the design approach adopted here was to neglect this possible contribution. The thickness of the annular ring required was calculated to be 1"; stiffeners were used to minimize the annular ring thickness. The annular ring used is shown in Figure 4-13 and Figure 4-14 Group NB and B specimens respectively. Design calculations for the annular rings are presented in Appendix B.



CFSSP-NB1 Elev.

CFSSP-NB1 Section

Figure 4-9 CFSSP-NB1 and Web Re-bar Connectors



CFSSP-NB2 Elevation

CFSSP-NB1 Section

Figure 4-10 CFSSP-NB2 and Web Re-bar Connectors

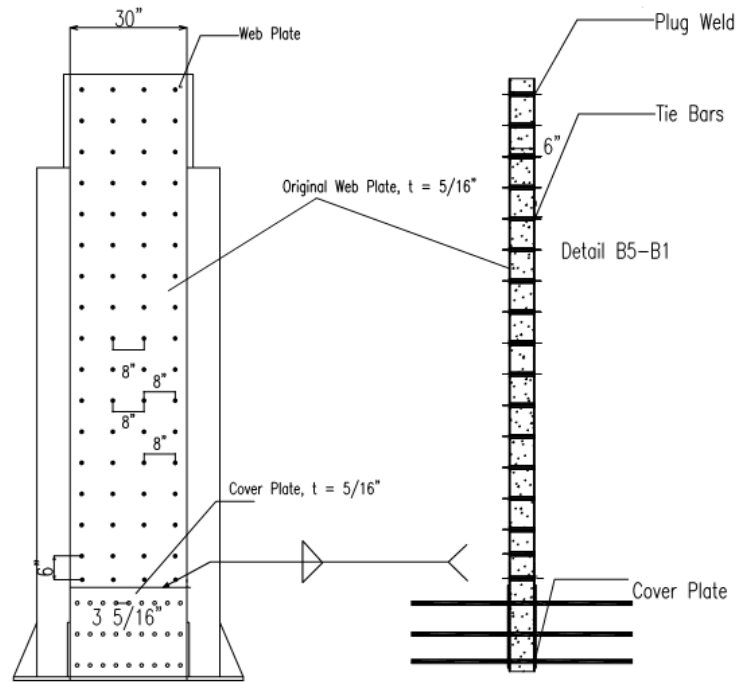


Figure 4-11 CFSSP-B1 and Web Re-bar Connectors

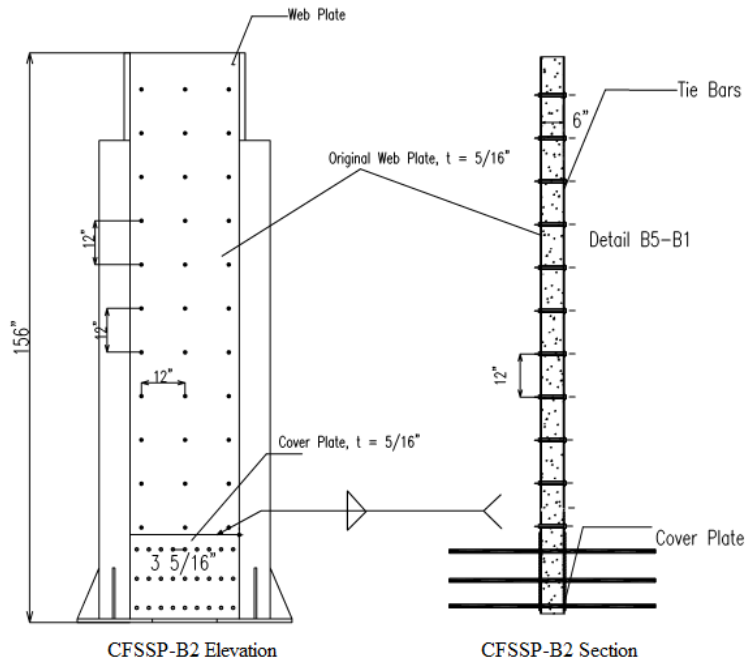


Figure 4-12 CFSSP-B2 and Web Re-bar Connectors

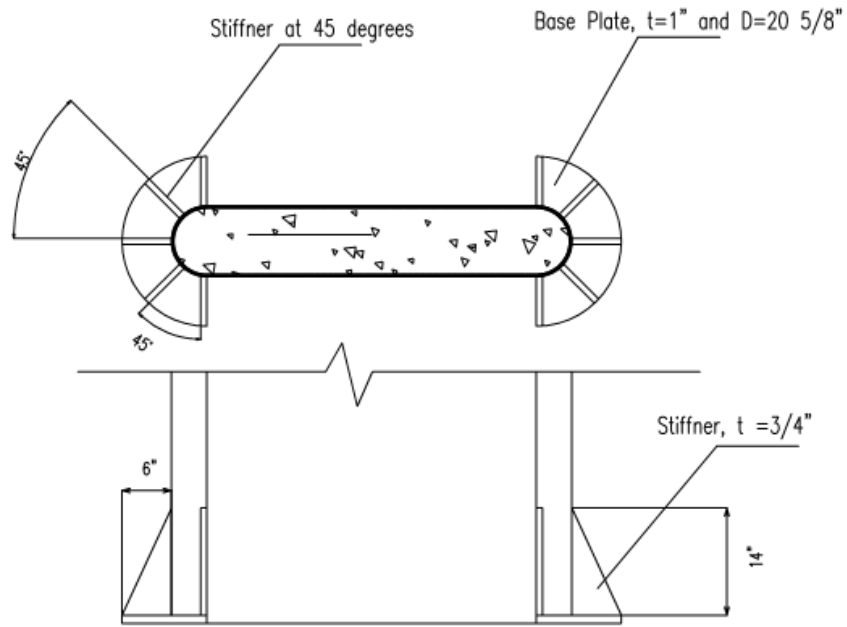


Figure 4-13 Stiffened Annular ring for Group NB Specimens

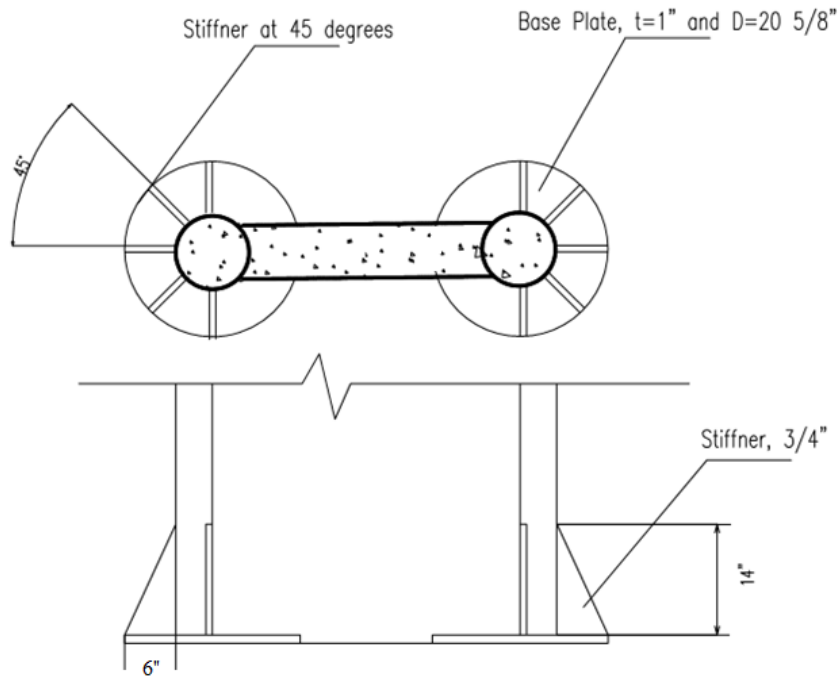


Figure 4-14 Stiffened Annular Ring used for Group B Specimens

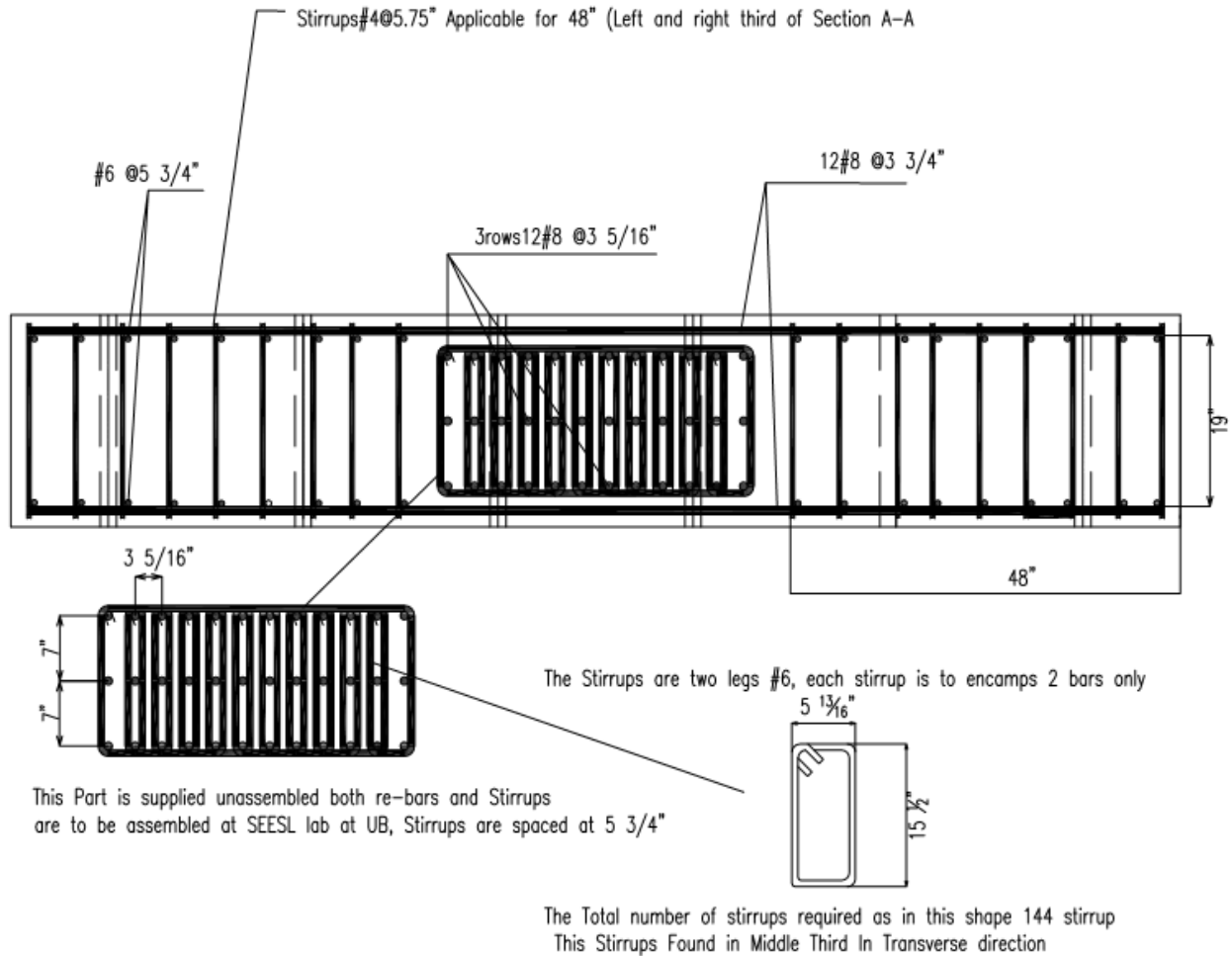


Figure 4-15 Re-bars Used to Transfer the Web Forces and Foundation Reinforcement

4.4.6 Side Restraint System

All of the tested specimens were loaded in a direction normal to their strong axis, in the plane of the wall, up to their maximum flexural capacity. In order to prevent lateral movement of the tested specimen (normal to the loading direction), either due to inelastic lateral torsional buckling of the wall, misalignment of the actuators, or other causes, a lateral restraint system was built and used as part of this test set-up. This system was designed to provide the stiffness and strength needed to prevent lateral motion of the tested walls.

The designed lateral support system consisted of truss towers connected to the laboratory's strong floor using threaded rods. One tower was used on each side of the tested specimen, to which bracing arms extended. Each tower was approximately square in plan, and 24 inches wide. The truss members are either single angles 4×4×5/16" or two angles back-to-back 4×4×5/16" (depending on location) and gusset plate thickness is 5/16". Figure 4-16 shows the lateral restraint system.

Each truss was designed for the lateral force given by equation A-6-7 of the AISC LRFD thirteenth edition

$$P_{br} = 0.02M_r C_d / h_o \quad (4.7)$$

and a required stiffness given by equation (A-6-8) of the same document

$$\beta_{br} = \frac{1}{\phi} \left(\frac{10M_r C_d}{L_b h_o} \right) \quad (4.8)$$

where

M_r is taken, here, as the plastic moment capacity of the relevant wall cross section multiplied by 1.5

L_b is the unbraced length of the tested CFSSP-Wall, in.

h_o is the distance between flanges centroids, in.

C_d is a coefficient taken equal to 1 for bending in single curvature

Note that strength and stiffness of the anchor bolts tying the truss towers to the floor were also taken into account in these calculations.

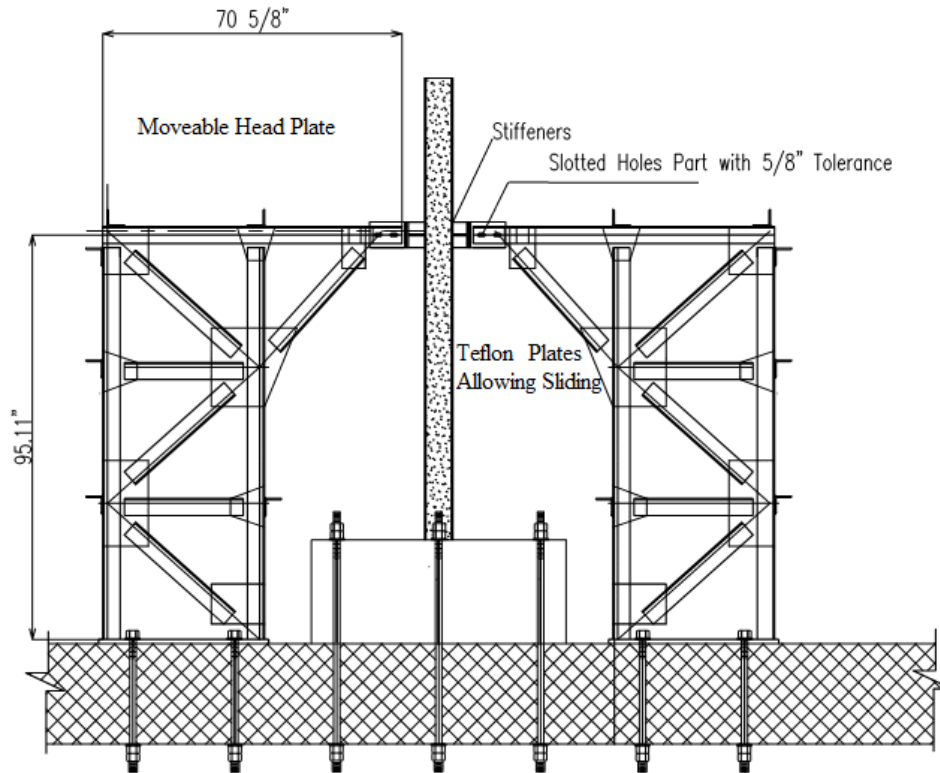


Figure 4-16 Side Restraint System

Using truss towers instead of single plane trusses facilitated handling and installation of the lateral restraint system and provided out-of-plane stability against lateral twisting to each of the two trusses in each direction constituting the truss tower. Incidentally, this lateral restraint system was also conveniently used to shore the CFSSP-Walls during pouring of their filling concrete.

Each lateral restraint system was also provided with a movable head-plate with a ± 1 " tolerance to allow adjusting the bracing point distance for different CFSSP-Wall specimens. A T-shaped stiffener was welded to the web of the CFSSP-Walls to provide a straight clean contact surface for the side restraints head plates. Teflon plates 1/8" thick were glued to the head plate to provide unrestrained longitudinal motion of the tested specimens. Figure 4-17 shows parts of this lateral restraint system during the process of placing the towers in position.

The moving head plate was designed to sustain the loads given by equation 4.5. The lateral restraints system was checked to be adequate for several loading scenarios, including some that involved lateral system twisting.

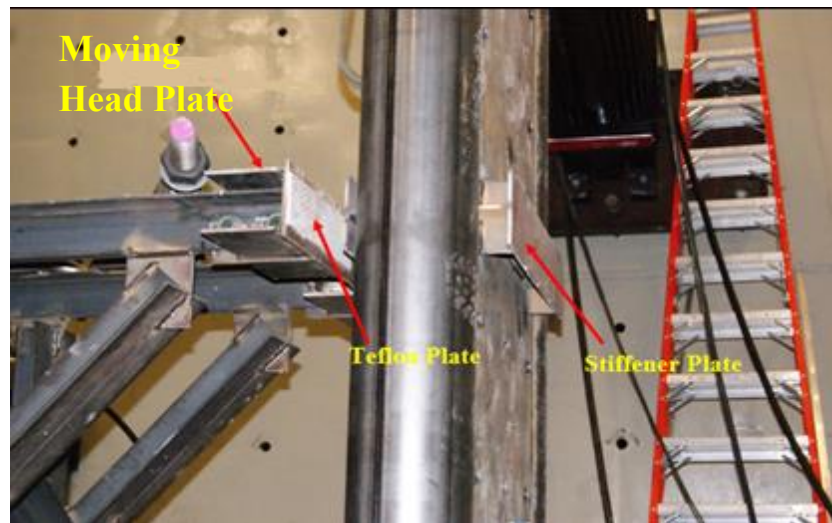


Figure 4-17 Parts of Lateral Restraint System

4.5 Specimen Assembly

This section describes specimen fabrication and issues related to test setup assembly in the testing laboratory.

All steel panels were built by a certified steel fabricator in the Buffalo area. For the Group NB specimens, the half HSS 8.622×0.322 used at their end was cut from a full HSS using water jet cutting to avoid over heating of the HSS which could lead to distortions or changing of material properties of the HSS. Figure 4-18 shows a typical water jet partial cut in a HSS section.

The skin plates were then assembled. Temporary internal spacers and bolts were used while the tie bars were welded in position. The half HSS (for Group NB specimens) or full HSS (for Group B specimens) were then welded to the web plates using full penetration groove welding. Note that no back-up bars were necessary for this weld. Figure 4-19 shows the welding between a CFSSP-Wall web and a half HSS section. Figure 4-20 shows the assembly of CFSSP-NB1 specimen. Figure 4-21 shows the lower part of the CFSSP-B2 specimen, with the holes for the re-bar connector (described in Section 4.4.4), cover plate, and stiffened annular ring.

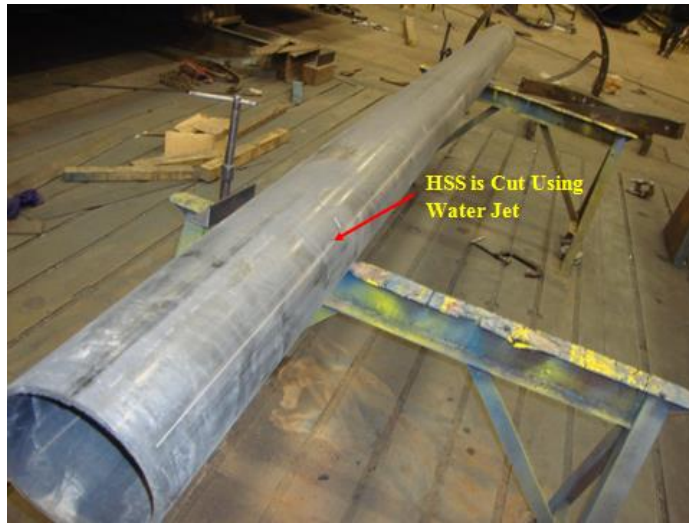


Figure 4-18 Water Jet Cutting of HSS



Figure 4-19 Welding between Half HSS and Steel Web Plate

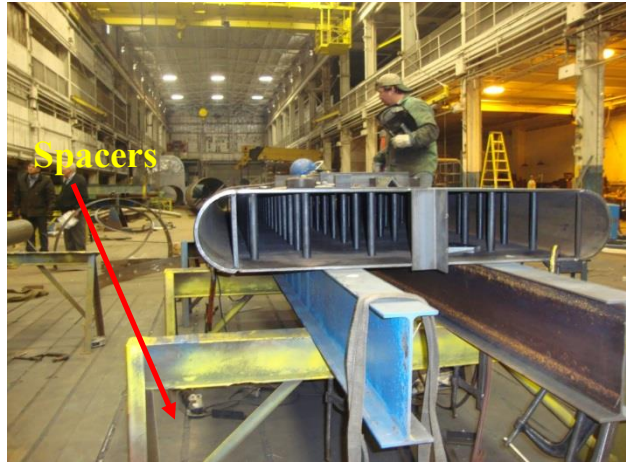


Figure 4-20 Assembly of CFFSP-NB1 Specimen

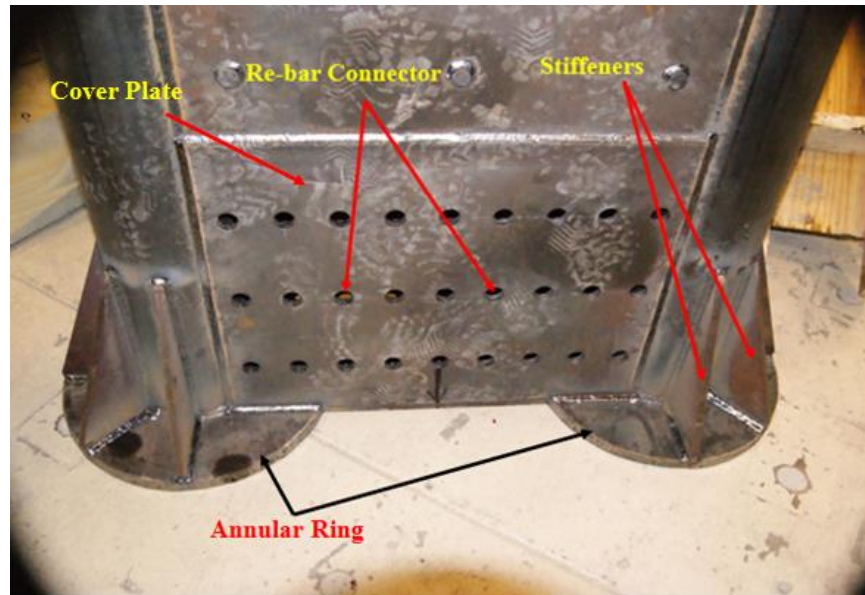


Figure 4-21 Base of Specimen CFSSP-B1

Steel specimens were shipped from the fabricator to the laboratory, where the footing and wall concrete infill were to be cast. For the foundation construction, a plywood base for the foundation formwork was assembled and supplied with wooden plugs at the location of the DYWIDAG bar holes. The foundation re-bars cage was placed over the formwork base, and steel sleeves were placed in location. Figure 4-22 shows the welding of the steel pipes (sleeves) to the steel cage (to keep them in place during concrete pouring).

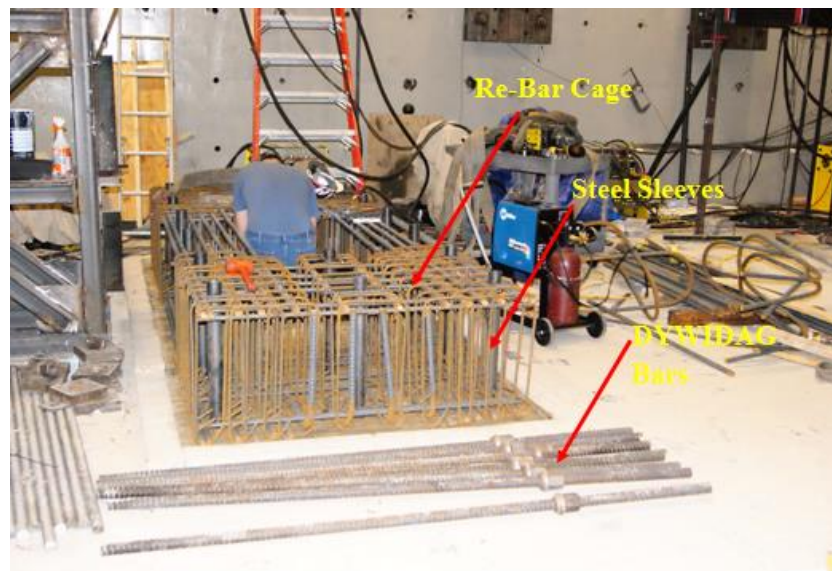


Figure 4-22 Welding Pipe Sleeves for the Steel Cage

The CFSSP-Wall was placed in its final position with respect to the foundation and plumbed; Figure 4-23 and Figure 4-24 shows the placing of CFSSP-Wall in position. After wall plumbing, the re-bar connectors were passed through the holes in the lower part of the CFSSP-Wall, and the stirrups for those bars were installed. All remaining reinforcement bars were then added in position, and all steel sleeves were plumbed and welded to the foundation steel reinforcement cage. Figure 4-25 shows the re-bar connectors and their stirrups. Some lifting hooks were then placed in the cage (to allow moving the footing after the test). Figure 4-26 shows the final arrangement of the foundation re-bars. Sides of the formwork were then assembled and one of the lateral bracing towers was placed in position and used to shore (and keep plumb) the CFSSP-Wall specimens during pouring of concrete, as shown in Figure 4-27.

The concrete filling a CFSSP-Wall specimen and its foundation was always poured from the same concrete batch. The sequence of concrete pouring was to pour the foundation concrete first, followed by filling the CFSSP-Wall. Figure 4-28 shows CFSSP-NB1 specimen just after concrete pouring. Concrete was left to cure for at least 14 days. The sides of the formwork were removed after no less than 7 days. To remove the formwork bottom sheet, the specimen and its foundation was lifted up and then the specimen was slightly moved to be placed at its prescribed location on the strong floor. DYWIDAG bars were then passed through the sleeves and the specimen was pre-tensioned to the laboratory floor approximately 9 days after casting of the concrete. The second lateral restraint tower was placed in position, their head plates were locked into position, and the lateral restraint system was tied to the strong floor using threaded bars. Figure 4-29 shows the erected lateral restraint system and a CFSSP-Wall specimen. The actuator was the connected to the specimen and instrumentation of the specimen took place.



Figure 4-23 Setting CFSSP-Wall in Position



Figure 4-24 Stiffened Annular Ring and CFSSP-Wall Positioning

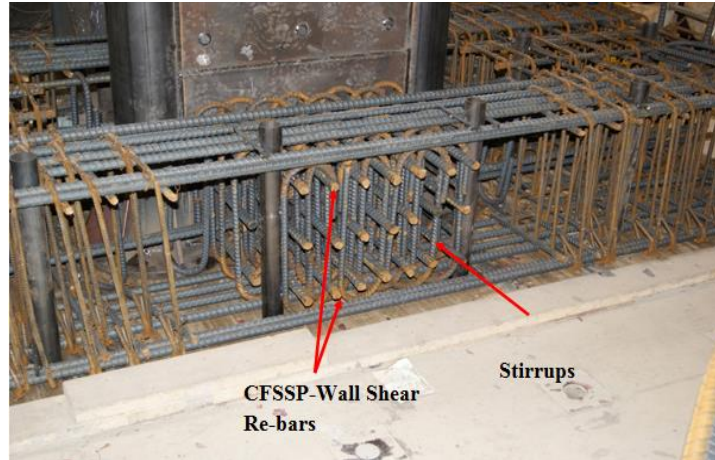


Figure 4-25 Web Re-bars and Stirrups



Figure 4-26 Final Assembly for the Foundation Re-bars



Figure 4-27 Shoring of Specimen Preparing for Concrete Pouring



Figure 4-28 Specimen CFSSP-NB1 After Concrete Pouring



Figure 4-29 Tested CFSSP-Wall Specimen after Erection of Lateral Restraint System

4.6 Instrumentation

Three parameters of interest were measured in this testing program:

First parameter, strains in the CFSSP-Wall steel plate to monitor the propagation of yielding along the width (and height to some degree to help define the length of the plastic hinge region). Second parameter was the rotations of the wall near the base in order to help establish the moment curvature relationship along the height of the wall in that region.

Third parameter, the wall displacement in the loading direction, at different points along the CFSSP-Wall height, to help establish force displacement relationship and monitor the wall deflected shape at the different stage of loading. In the following sections, the layout for the different types of instruments used to measure these values are described.

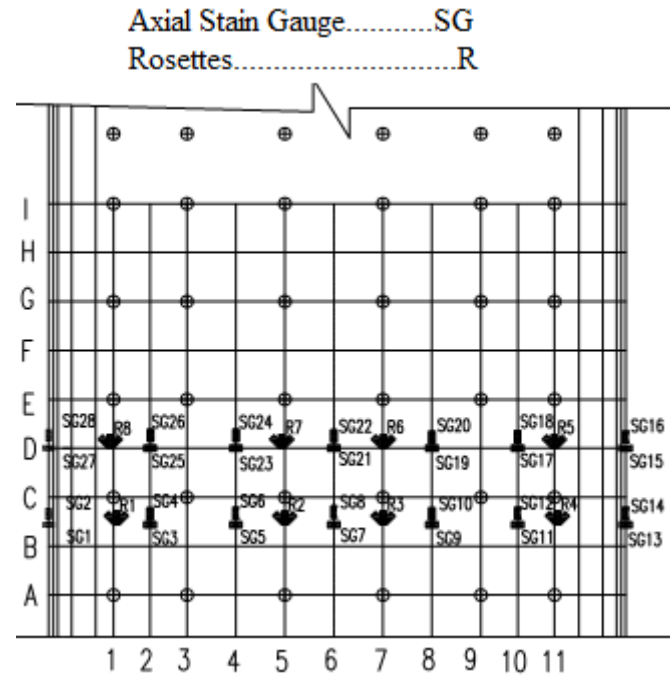
4.6.1 Strain Gauges

All specimens were instrumented with axial strain gauges (model CAE-06-125UW-120). In addition, specimens CFSSP-NB1, CFSSP-NB2, and CFSSP-B2 were supplied with rosettes (model CAE-06-125UR). Both types of gauges were manufactured by Micro Measurements (a division of Vishay Precision Group). Vertical and horizontal axial strains were measured at different locations, generally between the first and the second row of tie bars (counting from the base of the CFSSP-Wall at the top of the footing), and between the second and third row of tie bars. Figure 4-30 to Figure 4-33 show the strain gauges distribution for specimens CFSSP-NB1, CFSSP-NB1, CFSSP-B1, and CFSSP-B2, respectively.

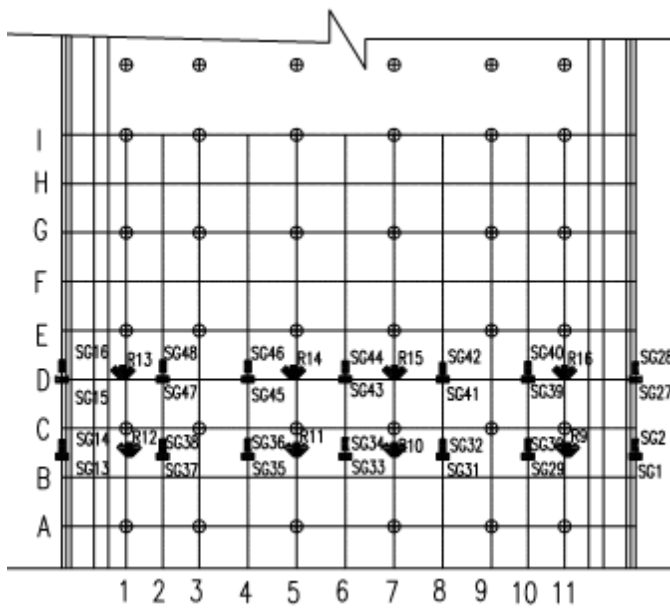
4.6.2 Displacement Potentiometers

A dozen of displacement potentiometers (linear potentiometers) were used for each of the tested specimens, namely 6 linear potentiometers installed sequentially on each of the HSS at the East and West ends of the tested specimens. Linear potentiometers were arranged vertically in a staggered pattern starting from the base (top of footing) up to 2 feet on the specimen, as shown in Figure 4-34 for specimen CFSSP-NB1.

The use of linear potentiometers in the aforementioned arrangement provided the ability (by using the displacements readings of linear potentiometers at the same height at opposed ends of the CFSSP-Wall specimen) to calculate rotation values, and consequently establish moment curvature relationships along the specimen height over the first two feet where most of the yielding was expected to occur. Aluminum angles were hot glued every 5" to the East and West HSS of the tested CFSSP-Wall specimens, to serve as supports for the linear potentiometers. The disposition in a staggered pattern (as shown in Figure 4.39 for the linear potentiometers arrangement at the CFSSP-NB1 East side) was necessary to avoid obstructions while locating instruments sequentially along the height. Linear potentiometers were mounted to the specimen using base magnets and the moving rod of each linear pot was attached to an aluminum angle using a magnet. Figure 4-37 show schematic diagrams for a typical linear potentiometers arrangement (for the CFSSP-Wall specimen West and East sides in this particular case).

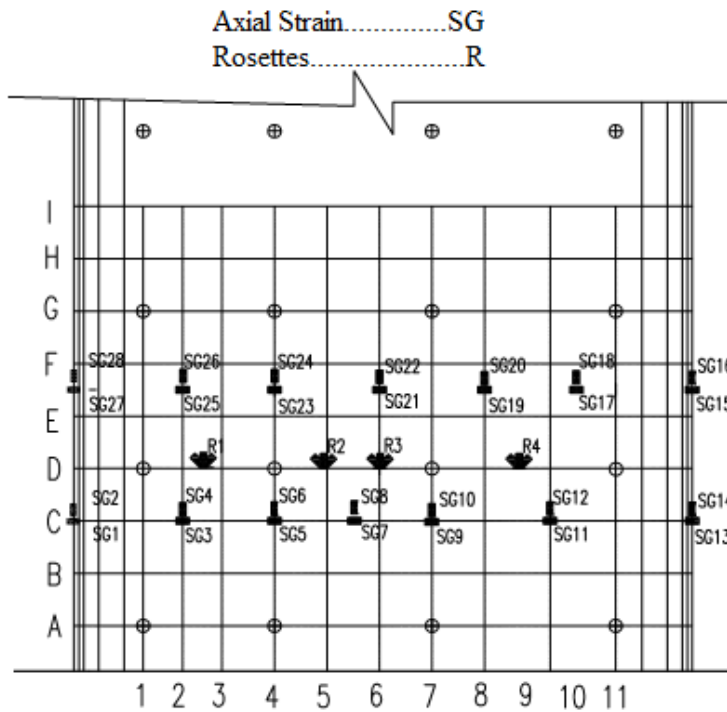


a) South North View

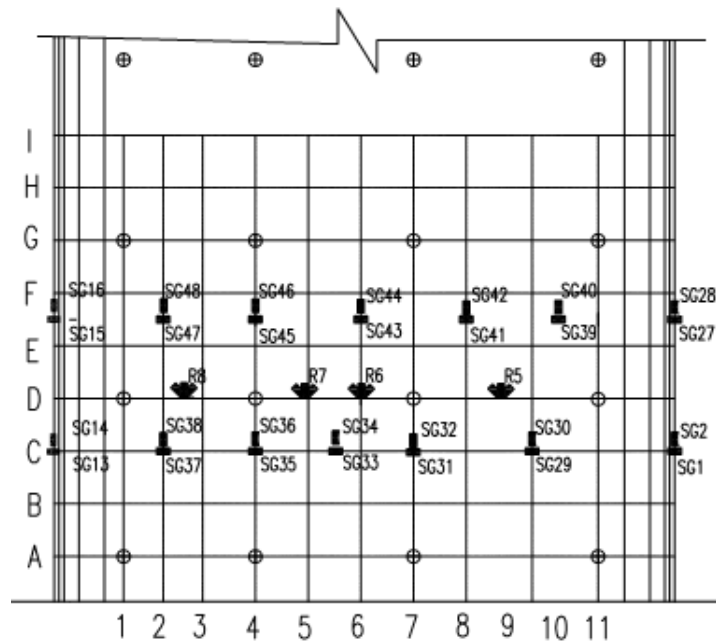


b) North South View

Figure 4-30 North South View of Strain Gauges Arrangement of Specimen CFSSP-NB1

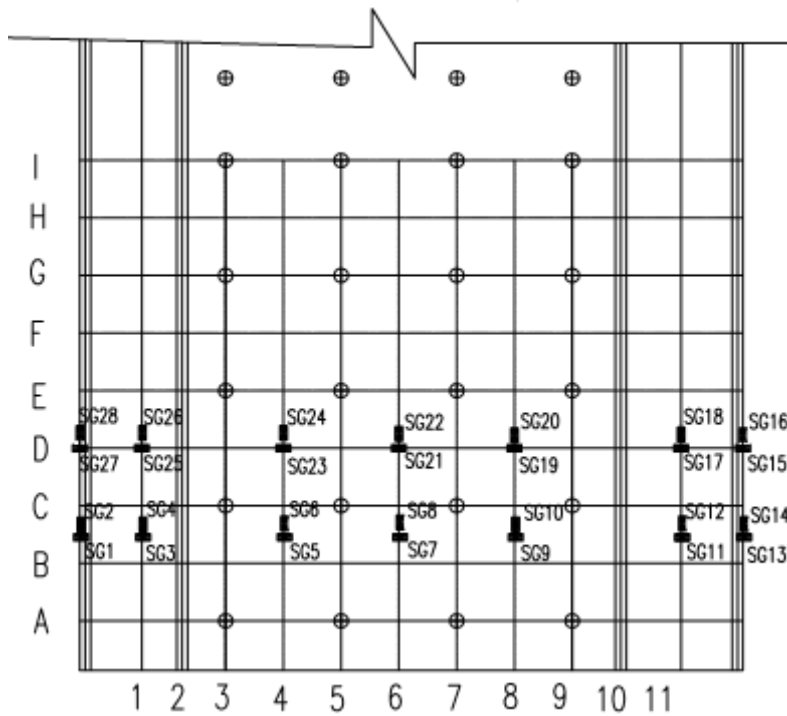


a) South North View

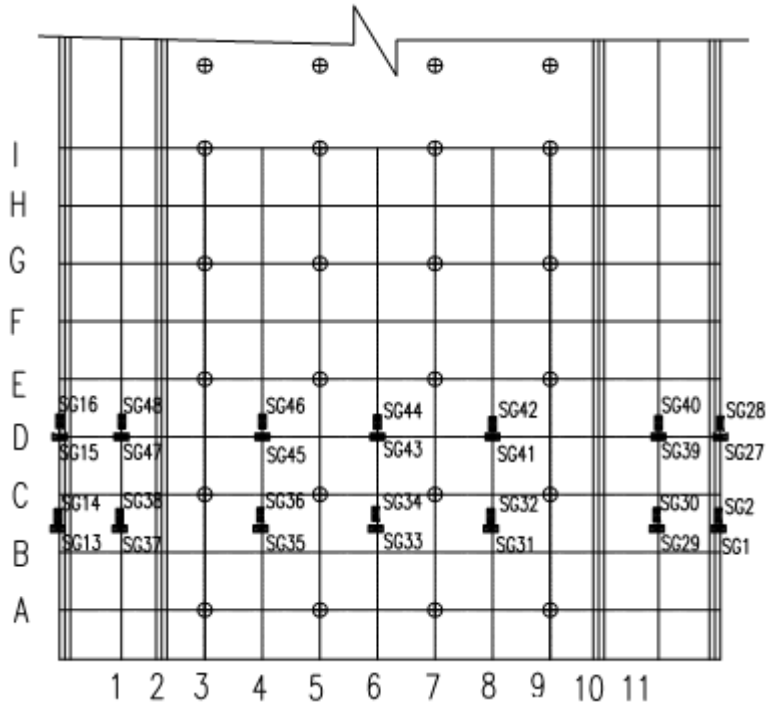


b) North South View

Figure 4-31 North South View of Strain Gauges Arrangement of Specimen CFSSP-NB2

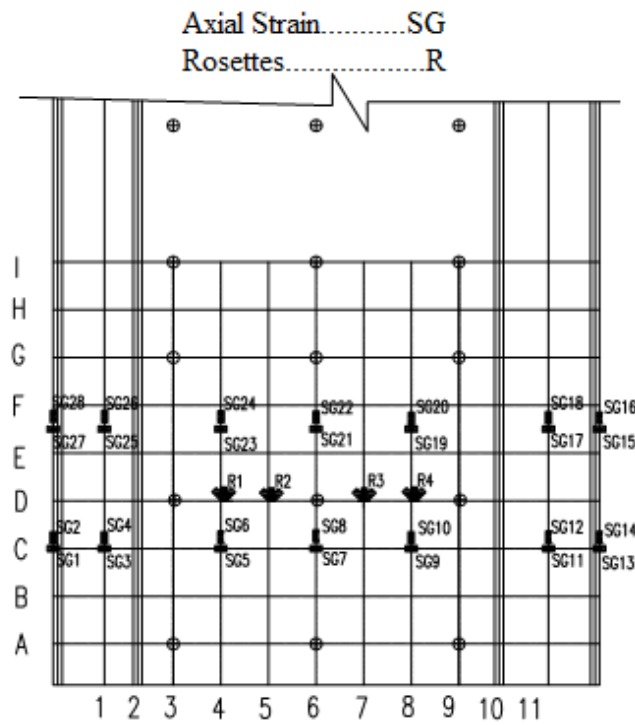


a) South North View

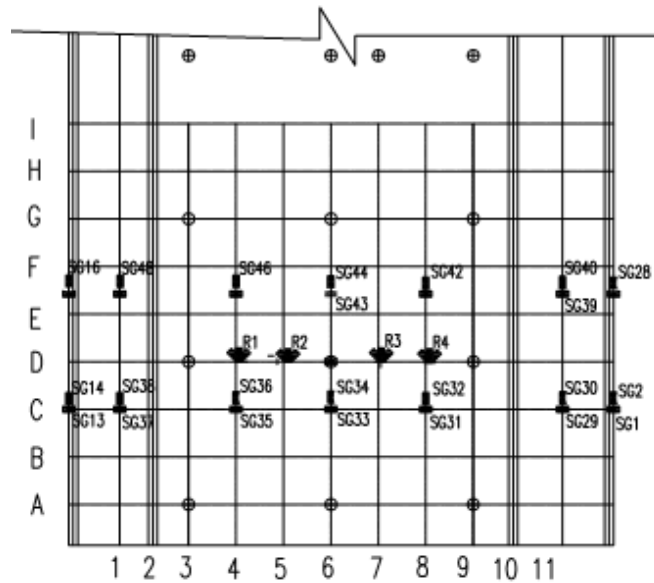


b) North South View

Figure 4-32 North South View of Strain Gauges Arrangement of Specimen CFSSP-B1



a) South North View



b) North South View

Figure 4-33 North South View of Strain Gauges Arrangement of Specimen CFSSP-B2



Figure 4-34 Liner Potentiometers Arrangement

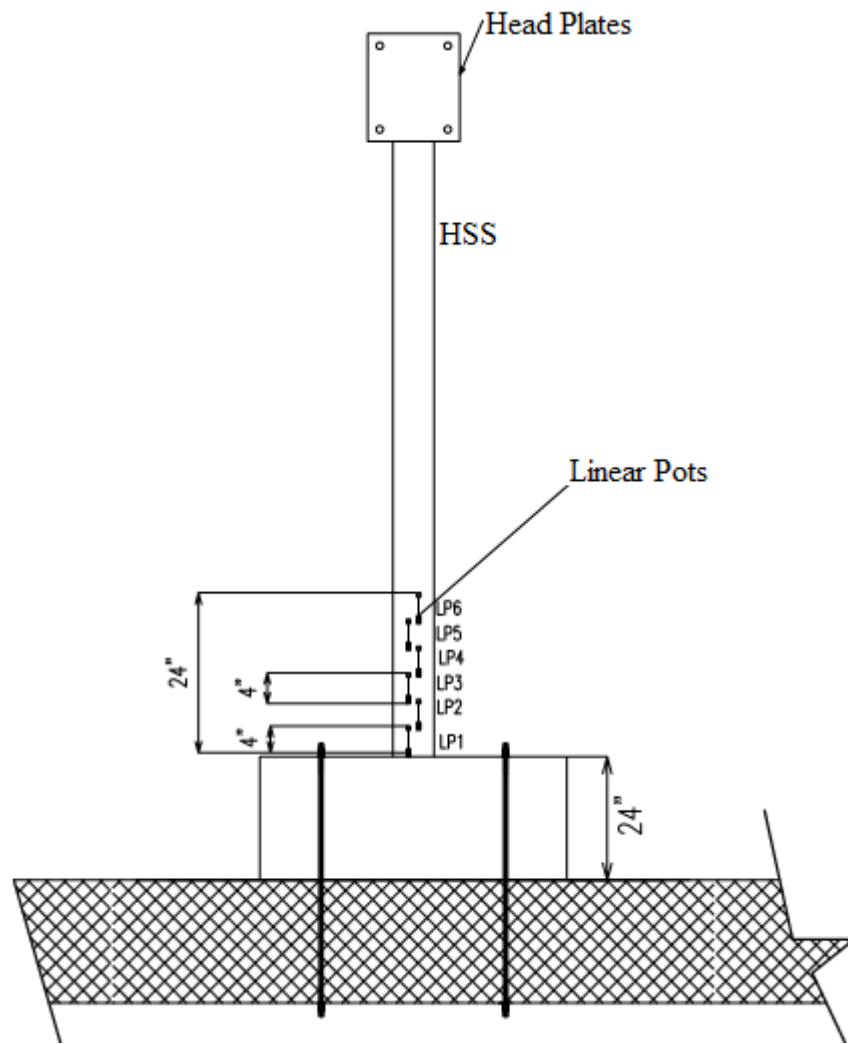


Figure 4-35 Schematic Diagram for a Typical West Side View of Tested CFSSP-Wall Specimen

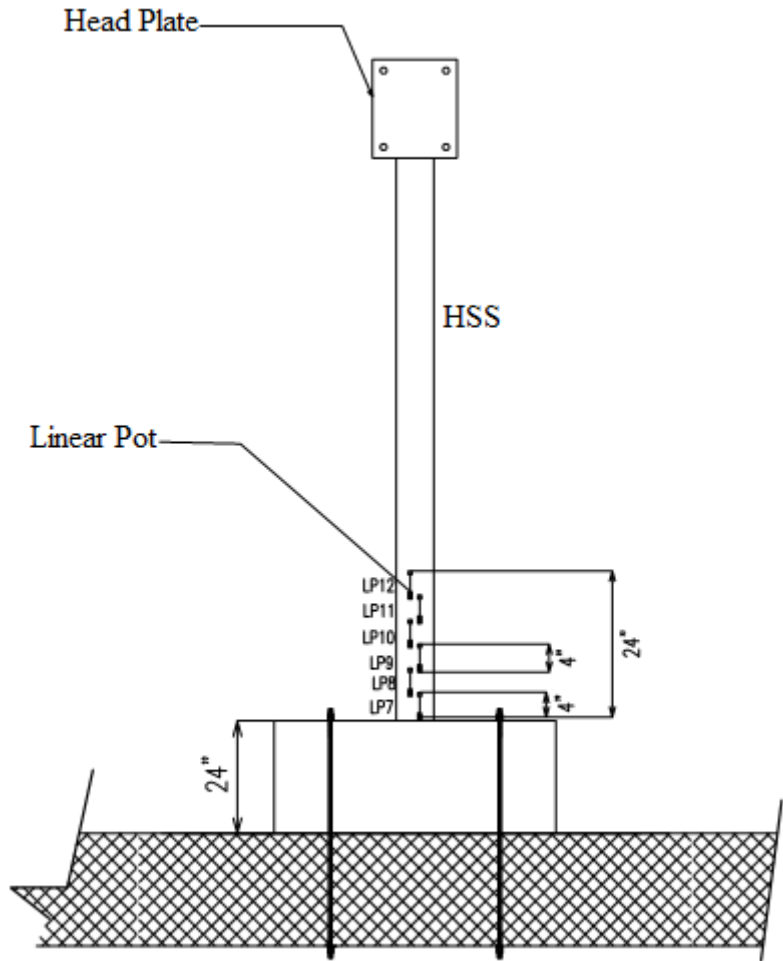


Figure 4-36 Schematic Diagram for a Typical West Side View of Tested CFSSP-Wall Specimen

Nine string displacement potentiometers (string-potentiometers) were used. Two string potentiometers were used as “backup” for the linear potentiometers used in measuring wall rotation and were installed to span a vertical distance of 30” from the top of the foundation (i.e. providing average curvature over a wall height of 30”), one at each end of the CFSSP-Wall specimen.

Five string potentiometers were mounted horizontally to read displacements in the loading direction at different locations along the CFSSP-Wall specimen height. These readings allowed for calculations used to determine the deflected shape of the tested specimen and establish force-displacement relationships. Two horizontal string potentiometers were also mounted at the loading head plate in the direction perpendicular to the loading direction, in order to monitor possible lateral displacements of the tested wall specimens.

Figure 4-37 shows some of the different string potentiometers used. Figure 4-38 shows the position of string potentiometers used to measure longitudinal displacement of the specimen.

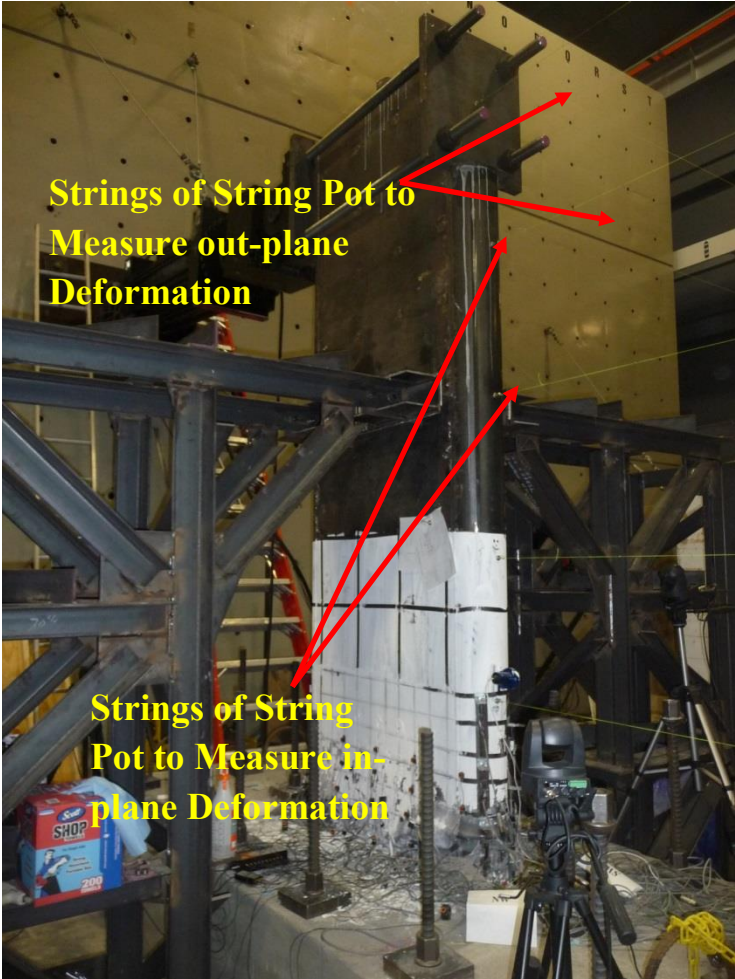


Figure 4-37 String Potentiometers Arrangement East Side

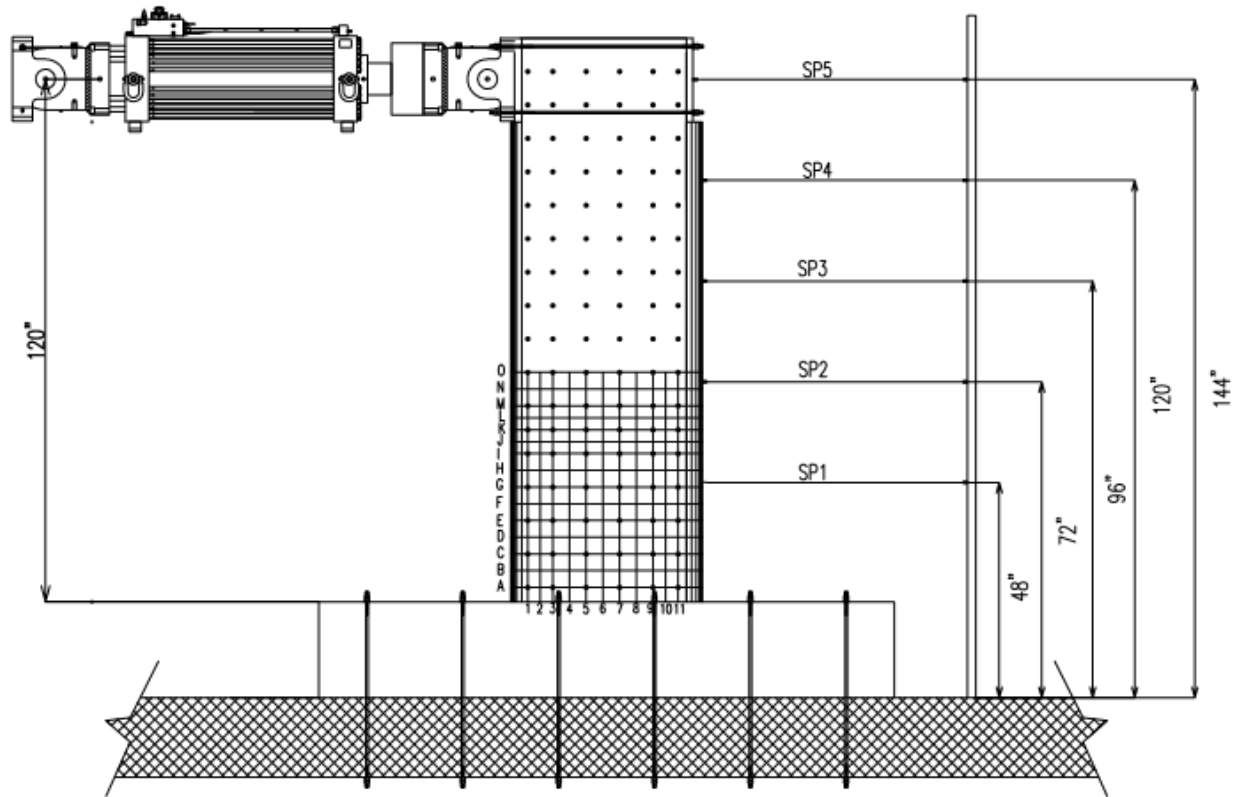


Figure 4-38 Typical Layout of String Potentiometers

4.6.3 Krypton Dynamic Measurement System

The Krypton Dynamic measurement system is composed of three sensitive infrared cameras mounted on a movable frame, numerous light emitting diodes (LEDs), and an independent data acquisition system. The LED's are 1" diameter and can be attached to the specimens or the test setup at any location visible to the camera, via hot glue, magnets, etc. The three cameras triangulate the location, velocity, and acceleration of the LEDs relative to a user defined coordinate system. Accuracy of the Krypton measurements is of the order 0.002" to 0.004" depending on the distance from camera to LEDs. Placement of the LEDs is dependent on the viewable window for the Krypton camera, which increases as the distance between the camera and the LEDs increases.

The Krypton camera was used only for specimens CFSSP-NB2, CFSSP-B1 and CFSSP-B2. The main objective for its use was to acquire extra data point to verify specimen rotation and evaluate possible relative motions between the tested CFSSP-Wall and the foundation. A total of 20 LEDs were used for each tested specimens distributed over five vertical columns and four horizontal rows. For the CFSSP-B1 and CFSSP-B2 specimens, the rows were spaced at 4". Horizontal spacing between the LEDs was

4 inches on the web plate, and 4 inches between the LEDs on the column and their adjacent one located on the web plate. In this case, LEDs on columns were located at the middle of the HSS (defined based on a side view of the wall). For specimen CFSSP-NB2 the same layout pattern was used, with the same vertical spacing between rows. Horizontal spacing between the LEDs was 4 inches on the plate, and 4 inches between the LEDs on the column and their adjacent one located on the web plate. In this case, LEDs on columns were located at the intersection between the half HSS and the steel web Figure 4-39 shows a typical distribution of the Krypton camera LEDs, in this case for specimen CFSSP-B2.

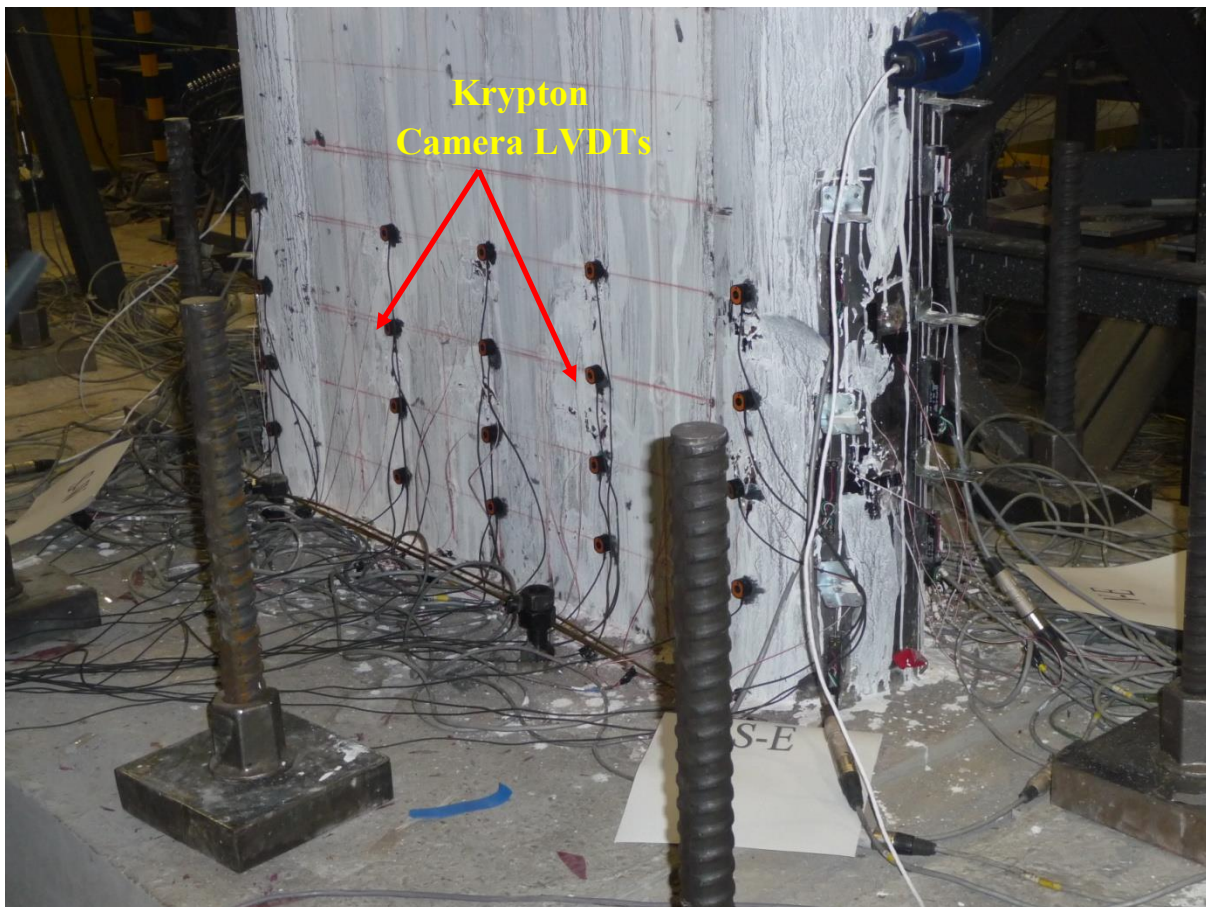


Figure 4-39 Krypton Camera LEDs Distribution for Specimen CFSSP-B2

4.6.4 Video Recording

All of the tests were video recorded digitally. Each test was documented using six high definitions cameras, recording a global view of the specimen, as well as local views that monitored the two ends of the specimens, each viewed from two different angles (to provide North-East, North-West, South-East and South-West views of the tested specimens), plus a close-up view of the lower 3 feet of the tested CFSSP-Wall specimens, in order to visually capture local buckling of steel skin of the wall and record the development and progression of fracture patterns. All videos were accelerated to help visualize and understand the behavior of the CFSSP-Walls, and monitor initiation and propagation of the fractures that developed at the CFSSP-Wall base. Videos are available at <http://seesl.buffalo.edu>.

CHAPTER 5

EXPERIMENTAL RESULTS AND OBSERVATIONS

5.1 General

This chapter describes the testing of specimens in Groups NB and B, including description of the loading protocol, and the observations made regarding the behavior of each of the specimens during testing in terms of maximum loads, specimen status at different deformations, and condition of the specimen at the end of the test.

In Section 5.2, the loading protocol used through the test is presented. Section 5.3 presents the test observations for the four tested specimens, including load levels (base shear) at different drifts, local buckling of the skin plates, and fracture of the skin plate.

5.2 Loading Protocol

Loading of all specimens was intended to proceed following quasi-static displacement control cycles carried in accordance with the ATC 24 loading protocol. This document specifies that the specimens should be subjected to a prescribed displacement history, with three displacement cycles at each displacement step, up to a displacement equal to three times the yield displacement, and two cycles at each displacement magnitude after that. The yield displacement is defined here as the displacement at which the extreme steel fibers of the CFSSP-wall skin plate starts to yield. The ATC 24 protocol specifies that reaching the yield displacement should be done in three steps as follows: three cycles at 1/3 of the yield displacement, three cycles at 2/3 of the yield displacement, and three cycles at the yield displacement, which is denoted by δ_y . Beyond that, every step should be multiples of the yield displacement ($2\delta_y$, $3\delta_y$, etc.) This protocol was adjusted during the tests, according to the observed behaviors (namely yielding of the skin plates). As one such adjustment, the displacement cycles at $1.5\delta_y$ does not exist in the original ATC 24 protocol but was added during testing to better capture the drift at which M_p was reached.

To implement the aforementioned loading protocol, it was necessary to estimate the yield displacement value measured at the load application point (i.e., 10 feet above the tested specimens' base, which is the height at which the actuator force is acting on the tested cantilever CFSSP-Walls). Preliminary finite element models were established using ABAQUS and analyzed using pushover analysis prior to testing of the CFSSP-Wall specimens in order to estimate their yield displacement value. Although the actual steel

material properties were available for those analyses (see coupon testing results in Chapter 4), specified strengths were used for the properties of the CFSSP-Wall filled-in concrete given that the actual concrete strength would not be known until the day of testing.

Table 5-1 shows the ATC 24 protocol used for testing Group NB specimens. Specimens of Group B followed the nearly identical protocol presented in Table 5-2. It should be noted that the estimated forces for a given displacements in that Table were more than those recorded during the test, which indicates that the finite element model used was stiffer than the actual tested specimen CFSSP-NB1. As described in Chapter 6 in more details, two factors had contributed to make the finite element wall stiffer than the actual one: (1) The finite element predictions were performed using the elastic modulus for regular normal weight concrete given by clause 8.5.1 in ACI 318-08 , whereas the actual value of elastic modulus for the self-compacting concrete used in the CFSSP-Wall specimens was approximately 50% of that value; (2) The finite element predictions neglected the contribution of the foundation to the specimen's flexibility

Table 5-1 Loading Protocol for Group NB Specimens

Order [1]	Total Number of Cycles [2]	Displacement factor of Δy [3]	Estimated Displacement (in) [4]	Drift% [5]	Estimated Force (kips) [6]
1	3	$\Delta y/3$	0.24	0.2	114
2	3	$2\Delta y/3$	0.4824	0.402	205
3	3	Δy	0.72	0.6	249
4	3	$1.5\Delta y$	1.08	0.9	253
4	3	$2\Delta y$	1.44	1.2	267
5	3	$3\Delta y$	2.16	1.8	242
6	2	$4\Delta y$	2.88	2.4	226
7	2	$5\Delta y$	3.6	3	222
8	2	$6\Delta y$	4.32	3.6	206
9	2	$7\Delta y$	5.04	4.2	182
10	2	$8\Delta y$	5.76	4.8	159

Table 5-2 Loading Protocol for Group B Specimens

Cycle Order	Total Number of Cycles	Displacement factor of Δy	Displacement (in)	Drift%	force (kips)
[1]	[2]	[3]	[4]	[5]	[6]
1	3	$\Delta y/3$	0.27	0.23	101
2	3	$2\Delta y/3$	0.53	0.44	182.46
3	3	Δy	0.8	0.67	230
4	3	$2\Delta y$	1.6	1.33	273.764
5	3	$3\Delta y$	2.4	2.00	280.326
6	2	$4\Delta y$	3.2	2.67	281.201
7	2	$5\Delta y$	4	3.33	269.101
8	2	$6\Delta y$	4.8	4.00	271.225
9	2	$7\Delta y$	5.6	4.67	271.787
10	2	$8\Delta y$	6.4	5.33	159.145

The specimens were cycled using the above protocols until substantial fracture of the steel plates and the HSS of the CFSSP-Wall specimens, although the degree of fracture that developed in each case before stopping the tests varied from specimen to specimen, as will be shown in the following sections.

5.3 Test Observations

5.3.1 General

In this section, observations made during the testing of Group NB and Group B specimens are described and illustrated. This includes reporting of peak loads and corresponding drifts in each cycles, maximum flexural strength developed, and progressive strength degradation, with strength values often expressed as percentage of the theoretical plastic moment capacity M_p , calculated based on the material properties identified through coupon and cylinder tests per Chapter 4. Also included are descriptions of buckling of the skin plates in terms of when and where it initiated and how it propagated. Observations are also made on the integrity of the instrumentation (such as strain gauges, and linear potentiometers) throughout the tests. Also reported are the drifts at which the tested specimen skin plates have yielded based on strain

gauges readings during testing. The plots for force-displacement relationships, moment-curvature relationship, and data evaluation altogether with ductility performance evaluation are presented in section 5.4 of this document.

5.3.2 Specimen CFSSP-NB1

The first step of the loading protocol, at a displacement of $\delta_y/3$, equivalent to 0.2% drift, allowed to verify that all instrumentation was working properly. At that stage, none of the components of the CFSSP-NB1 skin plate had suffered any buckling or yielding. Figure 5-1 shows the North West view of the CFSSP-NB1 specimen at $\delta_y/3$ displacement. Behavior was identical at the displacement of $2\delta_y/3$, equivalent to 0.40% drift, as shown in Figure 5-2. At this drift, the recorded strain in the part of HSS section farthest from the cross-section neutral axis was $1398 \mu\text{strain}$, which represents 89% of the average yield strain of $1566 \mu\text{strain}$ for the HSS part of the steel skin plate (based on material coupon properties of the round HSS as per Chapter 4 of this report).



Figure 5-1 North West View for Specimen CFSSP-NB1 at 0.2% Drift.



Figure 5-2 North West View for Specimen CFSSP-NB1 at 0.4% Drift

At the estimated displacement of δ_y , 0.6% drift, strain gages reading of 2248 $\mu strain$ indicated that the half round HSS part of the CFSSP-NB1 have exceeded its yield strain of 1566 $\mu strain$. However, the steel web plates of the CFSSP-NB1 specimen were still in the elastic range, as strain gauge readings there were less than the 2080 $\mu strain$ corresponding to their average yield strain (per coupon test results in chapter 4). There was no observation of local buckling in the steel web plate of the CFSSP-NB1, or of weld cracks. Figure 5-3 shows the North West view of the CFSSP-NB1 specimen at 0.6% drift which corresponds to the yield displacement, δ_y .

In an attempt to capture the drift value at which the entire CFSSP-NB1 steel section yielded, and consequently defining when the CFSSP-Wall section reached its plastic moment capacity, M_p , an extra step was added to the original ATC 24 loading protocol, with three cycles at a displacement of $1.5\delta_y$, equivalent to 0.9% drift. At that point, strain gages indicated that 30% of the entire steel part of the CFSSP-NB1 specimen cross-section had yielded, with values of strain gauge readings exceeding the yield strain values, ϵ_y of both the web plates (2080 $\mu strain$) and HSS (1566 $\mu strain$). Minor flaking of the white wash paint occurred on the HSS part of the cross-section, with no visual evidence of local buckling. Some minor hairline cracks in the paint at the intersection of the CFSSP-NB1 specimen and the reinforced concrete foundation were observed, indicating elongation of the steel. Figure 5-4 shows the North West view of the CFSSP-NB1 specimen at 0.9% drift.

At a lateral displacement equivalent to a drift of 1.2%, strain gauges readings indicated that 52%, of the steel part of specimen CFSSP-NB1 cross-section had yielded. at this point the moment acting on the wall cross section was 32,058 kip-in which represents 100% of the M_p .

Some paint flaking occurred on the steel plate web of the specimen, as well as at the intersection of the specimen and its reinforced concrete foundation. There was no visible local buckling observed. Figure 5-5 shows the North West view of the CFSSP-NB1 specimen at 1.2% Drift

At a displacement equivalent to 1.8% drift, during the first cycle of loading, a peak lateral load of 305 kips was reached, inducing a moment of 36,480 kip-in at the wall base, which is equivalent to 114% of M_p , and local buckling of the steel web plate of specimen CFSSP-NB1 specimen was visually observed for the first time. Buckling started at the North West side of the tested specimen, between the first and the second row of tie bars from the base. Figure 5-6 shows the local buckling of the web at 1.8 % drift. Figure 5-7 shows the South West view of the CFSSP-NB1 wall at 1.8% drift. Flaking of the white wash paint occurred on the perimeter of some of the first and second row tie bars from the base, as shown in Figure 5-8 on the third displacement cycle at 1.8 % drift, the previously observed local buckling wave was better defined, starting just above the first row of tie bars and ending before the bottom of the second row tie bars. In the horizontal direction, the buckling wave developed on approximately 10" of the web horizontal distance. The apex of the local buckling wave was approximately vertically located mid-distance between the first and second row of tie bars from the face of foundation.

At a displacement equivalent to 2.4% drift, a maximum lateral load of 302.7 kips was reached, exerting a base moment of 36324 kip-in corresponding to 113.6% M_p , and the half HSS part of the CFSSP-NB1 specimen developed local buckling, as shown in Figure 5-9, in a location between the first and the second row of tie bars from the reinforced concrete base (i.e., the local buckling of the HSS was an extension of the one that occurred in the web plate). Figure 5-10 shows that cracks were developed in the plug welds of the first row of tie bars; those cracks developed along the circumference of the tie bars, for projected horizontal lengths that ranged from between full diameter of the tie in the tie bars closer to the wall ends, and half diameter cracks for the tie bars further from the ends, as shown respectively in Figure 5-10 and Figure 5-11. Note that, at this drift level, the distortions from local buckling started to affect alignment of some of the linear potentiometers. In particular, the linear potentiometers LP1 and LP7 were displaced by the local buckling of the HSS part of the cross-section, while LP10 slipped from its original position. Readings from the string potentiometer SP6 and SP7 showed high curvature values as the magnet at the end of the string potentiometer was mounted on the buckled zone of the HSS.

At a displacement equivalent to 3% lateral drift, the maximum load attained was 295 kips, for a base moment of 35,400 kip-in which corresponded to 111% M_p , indicating that the wall section was still able to sustain its plastic moment capacity. Fracture developed on the full perimeter of some tie bars, as shown in Figure 5-12. That fracture also started to propagate horizontally from the circumference of the first tie bar in the first row towards both the half HSS and web plate on the South East part of the wall; the crack propagated about 3/4 of an inch, as shown in Figure 5-13. In the first row of tie bars, at the tie bar located in the South West corner of the wall (first tie bar), this fracture propagated from the tie bar circumference both left and right of the tie bar, as shown in Figure 5-14.

At a displacement equivalent to 3.6% drift, the maximum load reached was 208.4 kips which exerted a base moment of 25,008 kip-in on the wall, representing 78.2% of M_p . A first crack developed in the HSS part of the cross-section, initiating at the middle of the buckled wave in the half HSS section on the East side of the wall, as shown in Figure 5-15. After the third cycle at this displacement drift, at the other end of the wall, fractures also propagated from the tie bars on the first row of tie bars, through the centerline of the first row of tie bars, as shown in Figure 5-16. There were no deformations or fractures observed in the tie bars themselves.

The test was stopped after the second cycle at a displacement equivalent to 3.6% drift; maximum load reached was 109 kips which exerted a base moment of 13,080 kip-in on the wall, representing 40.5% of M_p . During this step, the wall fractured along a significant percentage of its base, in a plane passing through the center line of the first row of tie bars, over a distance of about 18 inch on the East side of the wall, as shown in Figure 5-17. As for the West side of the wall, the fracture in the HSS section remained located in the middle of the buckled wave, while a second fracture in the web extended through the centerline of the first row of tie bars for approximately 10", as shown in Figure 5-18. Note that both cracks did not connect. The middle third of the specimen was not fractured and the test was stopped at that point, for safety reasons.

After the wall was cut-off from its base, as part of the specimen demolition process, removal of the wall revealed that the concrete in the vicinity of the locally buckled skin plate was crushed. Figure 5-19 shows the cut section of the CSSP-NB1 wall at a section passing through the first row of tie bars.



Figure 5-3 North West View for Specimen CFSSP-NB1 at 0.6% Drift



Figure 5-4 North West View for Specimen CFSSP-NB1 at 0.9% Drift



Figure 5-5 North West View for Specimen CFSSP-NB1 at 1.2% Drift



Figure 5-6 North West View for Specimen CFSSP-NB1 at 1.8% Drift



Figure 5-7 South West View for Specimen CFSSP-NB1 at 1.8% Drift



Figure 5-8 Buckling Wave Between First and Second Row of Tie Bars at 1.8%



Figure 5-9 Local Buckling of the HSS Part at 2.4% Drift



Figure 5-10 Specimen CFSSP-NB1 Tie Bars Plug Welding Cracks at 2.4% Drift



Figure 5-11 Specimen CFSSP-NB1 Tie Bars Plug Welding Cracks Near Mid Cross-section at 2.4% Drift



Figure 5-12 Plug Welding Fracture on the Full Diameter of the Tie Bar at 3% Drift

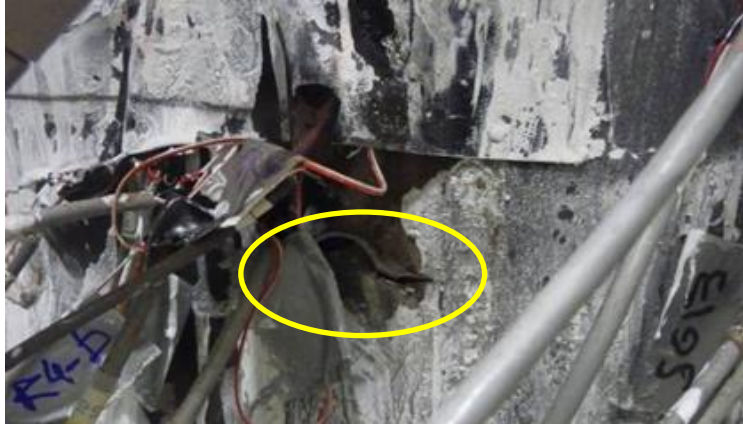


Figure 5-13 Propagation of Cracks from Tie Bar Circumference on East Side to CFSSP-NB1 Skin Plates at 3% Drift



Figure 5-14 Propagation of Cracks on the West Side Tie Bar Circumference to CFSSP-NB1 Skin Plates at 3% Drift



Figure 5-15 First Crack in the HSS Part of the CFSSP-NB1 at West side at 3.6% Drift



Figure 5-16 Fracture of the CFSSP-NB1 Specimen West Side at 3.6% Drift



Figure 5-17 Fracture of the CFSSP-NB1 Specimen East Side at 3.6% Drift



Figure 5-18 Propagation of Fracture of the CFSSP-NB1 for Specimen East Side at 3.6% Drift



Figure 5-19 The Cut Cross-section Part of Specimen CFSSP-NB1 attached to Foundation

5.3.3 Specimen CFSSP-NB2

For specimen CFSSP-NB2, the same loading protocol described earlier was followed. The first step of the loading protocol started with $\delta_y/3$ displacement cycles, which is equivalent to 0.2% drift, followed by displacement cycles at $2\delta_y/3$, equivalent to 0.4% drift. At that latter drift, the strain gauge at the point located at the apex of the HSS (i.e., at point farthest from wall's center of gravity) of the CFSSP-NB2 specimen read $1327 \mu\text{strain}$; all welds were intact and there was no evidence of local buckling or premature failure. Figure 5-20 shows the North West view for specimen CFSSP-NB2 at 0.4% drift displacement. During the load cycles at peak displacement of δ_y , equivalent to 0.6% drift, first yielding

of the HSS was reached at 0.475% drift; at the peak displacement of the cycles, the same strain gauges read $2137 \mu\text{strain}$. Figure 5-21 shows the North West view of the CFSSP-NB1 specimen at 0.6% displacement. At a lateral displacement of $1.5\delta_y$, equivalent to 0.9% drift, the two HSS parts of CFSSP-NB2 yielded in tension and compression, with strain values of $+3843 \mu\text{strain}$ and $-2125 \mu\text{strain}$, respectively. About 10.5" of the section depth had yielded at that stage, and the CFSSP-NB2 specimen reached 87% of its plastic moment capacity of 27,840 kip-in, for a corresponding actuator force of 232 kips. Some flaking of the white wash paint was observed, especially on the HSS.

At a displacement equivalent to 1.2% drift, the maximum lateral force was 270.2 kips, exerting a base moment of 32,424 kip-in on the wall, which corresponds to M_p . Cracks appeared in the plug welds of some of the tie bars in the first row above the footing; horizontal projection of the crack-lengths ranged between half diameter to full diameter of the tie bar. The onset of local buckling (hardly visible) in the steel web also started at this drift level, although the amplitude of this buckling was too small to capture in photos. Figure 5-23 shows flaking of paint on the HSS part of the section,

At a displacement equivalent to 1.8%, the peak load of 305 kips was attained, exerting a base moment of 36,600 kip-in, which corresponds to 114% M_p . More visually significant local buckling of the steel web plate was observed on the North West side of the tested specimen, between the first and the second row of tie bars from the footing. Figure 5-24 and Figure 5-25 shows the local buckling of the web at 1.8% drift. Local buckling of the web propagated to the edges of the HSS. Also, half diameter fracture of the plug weld of the first row of tie bars was noticed as shown in Figure 5-26. The length of the buckling wave extended from the top of the first row of tie bars from footing and ended almost at two thirds of the vertical distance to the second row of tie bars.

At a displacement equivalent to 2.4% drift, the maximum load during those cycles reached 302.9 kips, exerting a base moment of 36,348 kip-in on the wall, which is equivalent to 1.13 M_p . The half HSS part of the CFSSP-NB2 specimen developed local buckling as an extension of the web plate local buckling, as shown in Figure 5-27. The weld between the steel web and the half HSS section was intact at this stage of loading. There were fractures in some of the plug welds along the first row of tie bars; these typically were located in the upper half of the tie bars, and started to propagate in the web plates, as shown in Figure 5-28. It should be noted that, at this drift, the linear potentiometers LP1 and LP7 were displaced from their position due to local buckling of the half HSS.

At 3% drift, the lateral load attained was 278.92 kips exerting a moment of 33,470.4 kip-in, which corresponds to 104% of M_p and 8.66% drop from the peak value obtained at 1.8% drift. The amplitude

of local buckling became more significant, as shown in Figure 5-29. Fracture started to propagate, from the circumference of the first tie bar in the first row of tie bars, to the steel web and the half HSS; the crack propagated about 1 inch, as shown in Figure 5-30. By the second cycle of this displacement step, the crack propagated in the HSS, as shown in Figure 5-31. The plug weld of the exterior tie bars fractured along the tie bar perimeter, as shown in Figure 5-32.

At a displacement equivalent to 3.6% drift, the lateral load attained was 190.3 kips, exerting a base moment of 22836 kip-in, which corresponds to 71% of M_p . The crack that developed in the HSS propagated below the local buckling wave of the HSS, as shown in Figure 5-33. In the final cycles at this drift, some crushed concrete escaped through the cracks of the CFSSP-NB1 skin, as shown in Figure 5-34

At the lateral displacement that is equivalent to 4.3% lateral drift, the specimen was able to sustain 104 kips, exerting a base moment of 12,480 kip-in, which corresponds to 38.7% of the plastic moment, M_p . This was followed by subsequent displacement cycles, in steps of 0.5% drift, up to 7.2% drift, to record progressive strength degradation as the cracks propagated until they cumulatively reached one third of the total cross-section depth. At 7.2% drift, the CFSSP-NB2 specimen was only able to sustain approximately 30% of its plastic moment capacity and the test was stopped. Figure 5-35 shows the base of specimen CFSSP-NB2 at 4.3% drift.



Figure 5-20 North West View for Specimen CFSSP-NB2 at 0.4% Drift



Figure 5-21 North west View for Specimen CFSSP-NB2 at 0.6% Drift

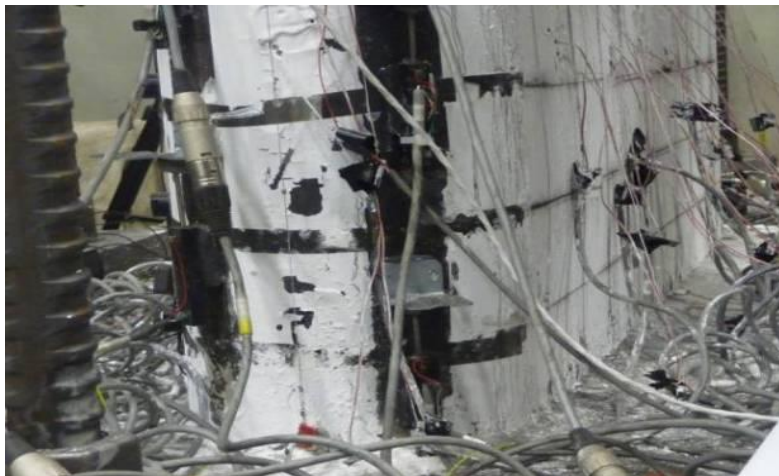


Figure 5-22 South West View for Specimen CFSSP-NB2 at 1.2% Drift

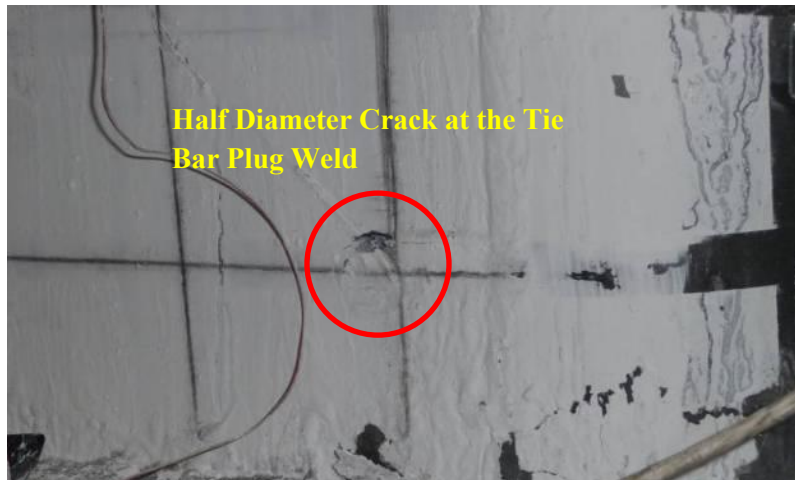


Figure 5-23 Flaking of Paint on Tie Bar Perimeter of Specimen CFSSP-NB2 at 1.2% Drift

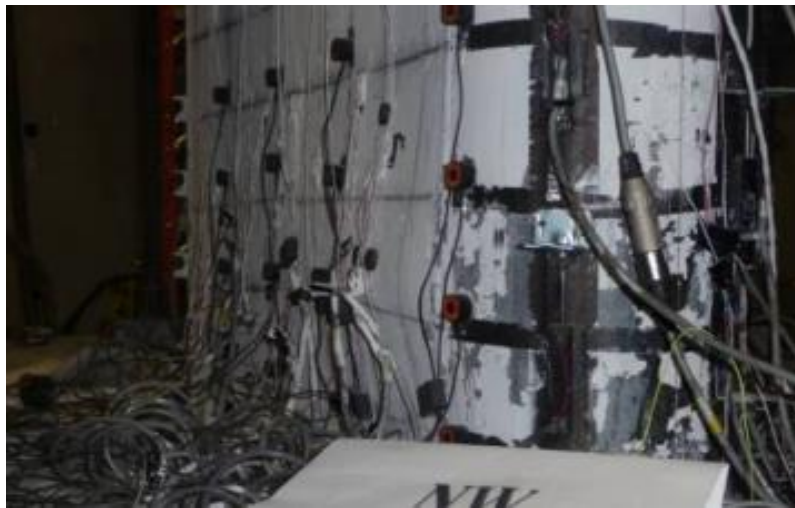


Figure 5-24 First Wave of Local Buckling Specimen, North West Side, CFSSP-NB2 at 1.8% Drift

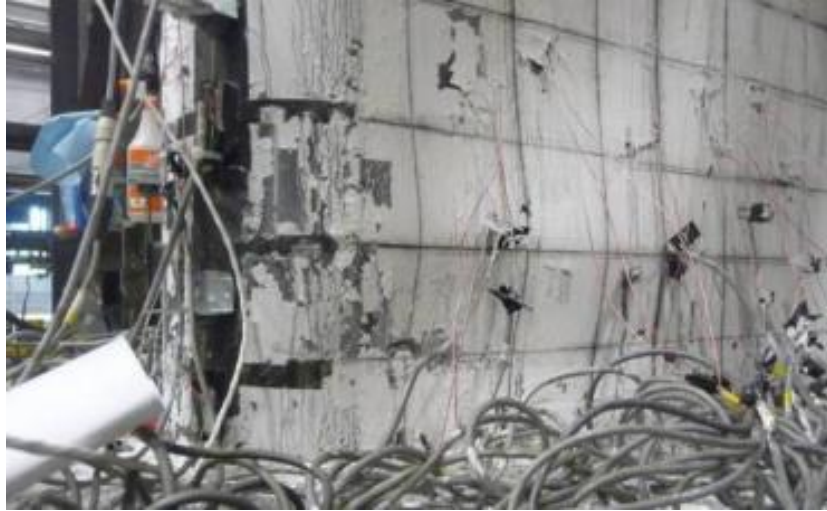


Figure 5-25 First Wave of Local Buckling Specimen, South East Side, CFSSP-NB2 at 1.8% Drift

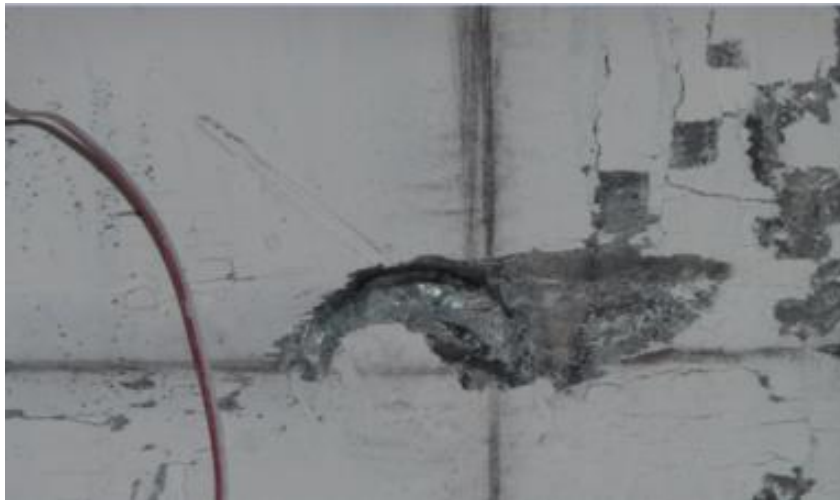


Figure 5-26 Fracture of Plug Weld at Half Diameter of Tie Bar of CFSSP-NB2 at 1.8% Drift

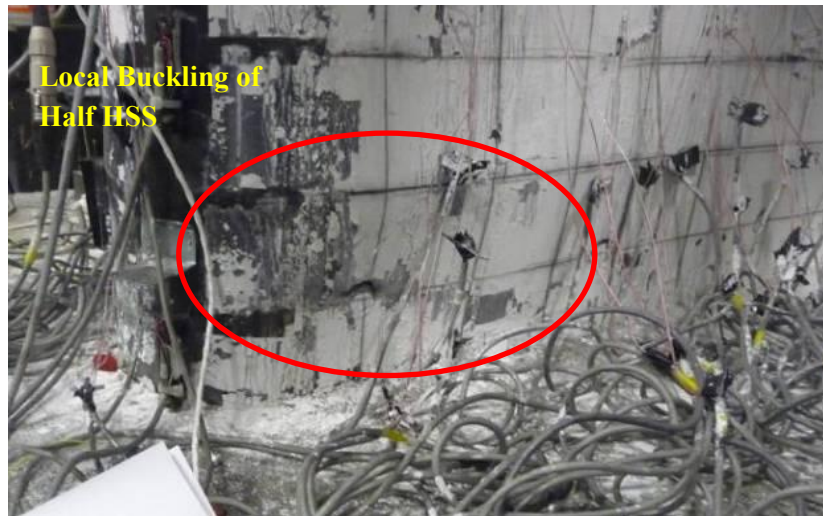


Figure 5-27 Local Buckling of the HSS Part in Specimen CFSSP-NB2 at 2.4% Drift

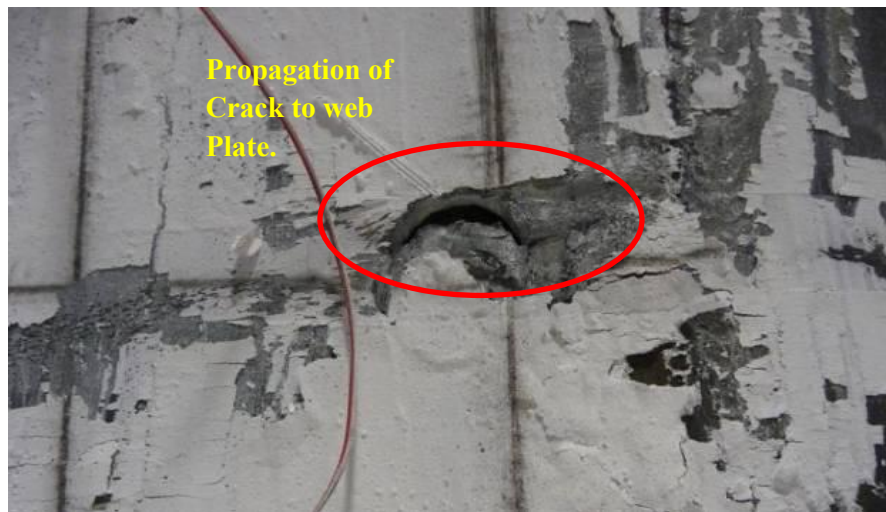


Figure 5-28 Propagation of Cracks in the Steel Web Specimen CFSSP-NB2 at 2.4% Drift



Figure 5-29 Propagation of Local Buckling in Specimen CFSSP-NB2 at 3% Drift



Figure 5-30 Fracture Propagation from Tie Bars Circumference in CFSSP-NB2 at 3.0% Drift



Figure 5-31 Fracture Propagated in the HSS part of Specimen CFSSP-NB2 at 3.0% Drift



Figure 5-32 Failure of Plug Weld for Inner Tie Bars of Specimen CFSSP-NB2 at 3.0% Drift



Figure 5-33 Propagation of Cracks in Specimen CFSSP-NB2 at 3.6% Drift



Figure 5-34 Crushed Concrete Debris Spalling from Cracked Skin of CFSSP-NB2 at 3.6% Drift



Figure 5-35 Fracture of Specimen CFSSP-NB2 at 4.2% Drift

5.3.4 Specimen CFSSP-B1

The cyclic displacement protocol used for specimens of Group B was slightly different from the one used for specimens NB, due to a 12% difference in the estimated yield displacement, δ_y . The test started by applying a lateral displacement value of $\delta_y/3$, equivalent to a drift of 0.23%. The specimen remained elastic. At a drift value of 0.44%, the outermost fiber on the round HSS of the CFSSP-B1 strain gauge reading were $1510 \mu\text{strain}$, which represents 96% of the yield strain for the HSS part of the cross section.

At the estimated displacement of δ_y , equal to 0.67% drift, part of the round HSS boundary elements of the wall cross-section yielded as the strain gauges readings were $-1782 \mu\text{strain}$ and $+2325 \mu\text{strain}$ on the outermost fiber of the HSS in both the compression and tension sides of the wall, respectively, while the steel web plate of the CFSSP-B1 specimen remained elastic; at this point, 17.78% of the total depth of the steel part of the cross-section had yielded. The specimen was subjected to a moment of 21360 kip-in, which corresponds to 78% of M_p . Flaking of the whitewash paint started to appear, especially on the HSS part of the wall cross-section, with no visual evidence of local buckling.

At a lateral drift of 1%, a moment of 27360 kip-in was exerted on the tested specimen, which corresponds to M_p . At that point, interpolation of strain reading data indicated that about 31% of the total cross-

section depth yielded. Figure 5-36 and Figure 5-37 shows specimen CFSSP-B1 at drift values of 1% and 1.33% respectively.

At a displacement equivalent to 1.33% drift, the specimen reached a moment of 30907kip-in, which corresponds to 113% of M_p , with all strain gages reading a strain larger or equal to the yield strain values. Figure 5-38 shows specimen CFSSP-B1 at 1.33% Drift.

At a displacement equivalent to 2% drift, the specimens attained a moment of 33669.6kip-in that corresponds to 123% of M_p . At 2% drift, first observation was made of cracks initiating along the plug welds in the first row of tie bars, as shown in

Figure 5-39 and Figure 5-40. The web plate of the CFSSP-B1 specimen started to locally buckle, as shown in Figure 5-41, with a buckling wave spanning the distance between the first and second horizontal rows of bars, and the apex of the buckled wave at mid-distance of these two rows. The HSS part of the cross-section exhibited the onset of local buckling (i.e., small buckling wave that cannot be captured through photos). At the end of this displacement step, fracture of the plug welds between the tie bars and steel web plate occurred, as shown in Figure 5-42.

At a displacement equivalent to 2.67% drift, the specimen attained a lateral moment of 33,360 kip-in which corresponds to 122% M_p . The HSS parts of the CFSSP-B1 specimen cross-section showed local buckling at their base. Note that local buckling of the steel web plates and the HSS section were not linked (i.e., they occurred at different elevations), and that the local buckling of the HSS part of the wall developed over the entire visible HSS perimeter. Figure 5-43 shows the local buckling of the HSS part of specimen CFSSP-B1. At the end of these displacement cycles, a crack was observed on the top of the reinforced concrete foundation; the crack propagated in a direction normal to the HSS part of the cross-section and extended for approximately 10" towards the foundation's edge, as shown in Figure 5-44.

At this drift, the linear potentiometers LP1 and LP7 displaced with the buckling wave, and data recorded by the string potentiometers SP6 and SP7 was negatively affected given that the magnets to which the string potentiometers were connected were located directly on top of the buckled zone of the HSS.

At a displacement equivalent to 3.33% drift, the specimen attained a moment of 33,186 kip-in, which corresponds 121% of M_p . Fracture of the all tie bars plug welds further developed, up to an horizontal projection length of full or half diameter of the tie bars. Some of the cracks propagated from the circumference of the tie bars into the web plate, as shown in Figure 5-45.

Figure 5-46. The longest cracks extended to 1-3/4" inch in the steel web, as shown in Figure 5-47. Some crushed concrete spilled from the open cracks in the CFSSP-B1 skin.

The specimen was finally subjected to cycles at a lateral drift of 4%, and the specimen attained a lateral moment of 31440 kip-in, which corresponds to 115% of M_p , during the first cycle of displacement at that drift. After that, the specimen's strength started to degrade rapidly and the test was stopped at 5% drift, where the strength of the wall was about 50% of the peak and the wall was fractured at the level of the first row of tie bars for almost about 20". The specimen was cut along the fractured zone, as shown in Figure 5-49. The concrete in the vicinity of the buckled steel plates was found to be crushed, as shown in Figure 5-50.



Figure 50-36 South West View of the Specimen CFSSP-B1 at 0.67% Drift



Figure 5-37 South East View of Specimen CFSSP-B1 at 1% Drift



Figure 5-38 South West View Specimen CFSSP-B1 at 1.33% Drift



Figure 5-39 Full Diameter Cracks in the Tie Bars Plug Welding of Specimen CFSSP-B1 at 2% Drift

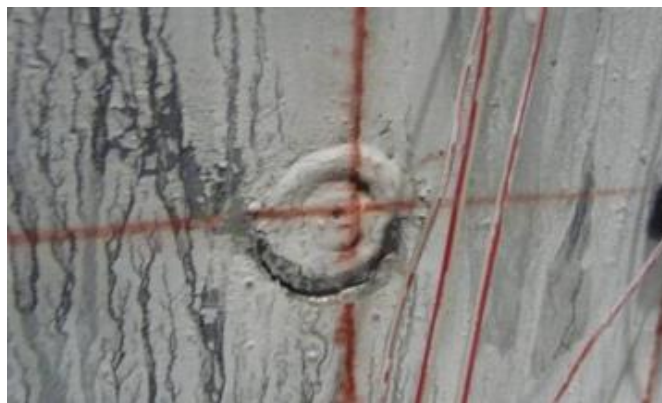


Figure 5-40 Half Diameter Crack of Inner Tie Bar Plug Welding of Specimen CFSSP-B1 at 2% Drift



Figure 5-41 Local Buckling of Web Plate for Specimen CFSSP-B1 at 2% Drift



Figure 5-42 Half Diameter Fracture of Tie Bars Plug Welding of CFSSP-B1 at 2% Drift



Figure 5-43 Local Buckling of the HSS in Specimen CFSSP-B1 at 2.67% Drift

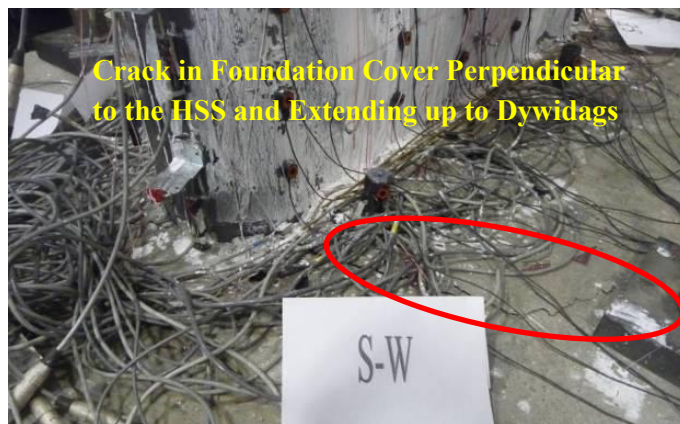


Figure 5-44 Crack in Foundation Top Cover of Specimen CFSSP-B1 at 2.67% Drift



Figure 5-45 Fracture of Plug Welding of an Inner Tie Bar of Specimen CFSSP-B1 at 3.33% Drift



Figure 5-46 Fracture Propagation at Specimen CFSSP-B1 at 3.33% Drift



Figure 5-47 Fracture Propagation Pattern in Specimen CFSSP-B1 at 4% Drift



Figure 5-48 Fracture of the HSS Portion of Specimen CFSSP-B1 at 4% Drift



Figure 5-49 Cut Base of Specimen CFSSP-B1 After Testing



Figure 5-50 Condition of Concrete in the Buckled Zone of Specimen CFSSP-B1

5.3.5 Specimen CFSSP-B2

At a lateral drift value of 0.23%, specimen CFSSP-B2 behaved elastically. During the second displacement step, at a value of $0.53 \delta_y$ (accidentally overshooting by 6% the $0.5 \delta_y$ target), which is equivalent to a lateral drift of 0.37%, the axial strain in the half HSS reached $1134 \mu\text{strain}$, which is 73% of the average yield strain of the round HSS part of specimen CFSSP-B1.

In the subsequent load step cycles, instead of applying displacements up to the estimated displacement of δ_y , displacements were only applied up to $0.84 \delta_y$, which is equivalent to 0.56% drift. The applied

moment reached a value of 21,700 kip-in, which corresponds to 83% of M_p . The HSS strains recorded at the top and bottom ends of Specimen CFSSP-B2's cross-section were +1717 $\mu strain$ on the tension side and -1259 $\mu strain$ on the compression side, and thus the round HSS part of the wall was still in the elastic range. Similarly, the steel web exhibited strain values within the elastic range (lower than 2080 $\mu strain$). Figure 5-51 shows specimen CFSSP-B2 at 0.56% drift.

At the loading step of $1.5 \delta_y$, equivalent to 1% lateral drift, at which a lateral load of 217 kips that exerted a moment of 26040 kip-in, which represents M_p , strain gage data suggested that about 30% of the total depth of specimen CFSSP-B2 cross-section had yielded. Flaking of whitewash paint started to appear, especially on the HSSs, with no visual evidence of local buckling. Figure 5.58 shows specimen CFSSP-B2 at drift value of 1%.

At a displacement equivalent to 1.33% drift, at which a lateral load of 249.8 kips that exerted a moment of 29976 kip-in, which corresponds to 116% of M_p , there was significant flaking of the whitewash on the round HSS part of the CFSSP-B2 cross-section. Figure 5-53 shows specimen CFSSP-B2 at 1.33% drift. Note that there were no whitewash flaking at the tie bar web plate intersection.

At a displacement equivalent to 2% drift, no cracks were observed in the fillet welds of the tie bars (or anywhere else in the specimen for that matter), but the onset of web local buckling occurred, as shown in Figure 5-54. At this stage, the specimen exhibited a strength of 33,960 kip-in, which corresponds to 131% M_p .

At a displacement equivalent to 2.67% drift, during the first displacement cycle, the specimen reached its peak flexural strength of 34299.6 kip-in, corresponding to 132% M_p . The steel web showed local buckling, where the local buckling wave started at the first row of tie bars and extended up to two thirds of the vertical spacing of tie bars, as shown in Figure 5-55. The HSS started to show local buckling at their base in a pattern similar to the buckling described earlier for specimen CFSSP-B1, as shown in Figure 5-56. Note that local buckling of the steel web plates and the HSS section occurred at different heights and were not linked, as shown in Figure 5-57. The welds between the tie bars and the CFSSP-B2 web were intact at that drift level. At the end of these cycles, a crack was observed at the top of the reinforced concrete foundation, propagating in a direction normal to the round HSS (at both the East and West ends of the wall) and extending for approximately 11". At this drift, the attachment points of linear potentiometers LP1 and LP7 and string potentiometers SP6 and SP7 were affected by local buckling of the skin plate.

At a displacement equivalent to 3.33% drift, the specimen sustained a lateral load 266 kip, which corresponds to 117% M_p . Amplitude of the local buckling of the steel web and the HSS increased and cracks started to develop at the tie bars fillet welds, as shown in Figure 5-58 and Figure 5-59, respectively. Fracture of the tie bars fillet welding developed on the full or half diameter of the tie bars.

At a lateral drift value of 4%, the cracks started to propagate from the tie bar circumference to the web plate of the specimen, as shown in Figure 5-60 and Figure 5-61. At the end the cycles, the wall was fractured along its base, as shown in Figure 5-62. Nevertheless, at this stage the specimen still resisted 108% M_p . Review of the videos recorded during the experiments showed that for Specimen CFSSP-B2, fracture started independently on the HSS at a different location, and propagated to join with the fractures that had initiated at the tie bars. This suggests that the wall would have failed pretty much at the same drifts even if fracture has not developed slightly earlier at the ties.

The specimen CFSSP-B2 was then pushed to a lateral drift of 4.67%, to observe the reduction in flexural strength as a function of crack propagation. The resulting fracture at the wall base is shown in Figure 5-63 and Figure 5-64.

After the end of the test, the specimen was cut to connect the already fractured zone, as shown in Figure 5-65. The concrete in the vicinity of the buckled steel plates was found to be crushed. The steel fibers added to the concrete mix to potentially enhance the ductility of the system (as described in Chapter 4), were observed to have pulled out of the concrete at the crack location, as shown in Figure 5-67, suggesting that the steel fibers slipped from the concrete and possibly did not provide much benefits (recall that using steel fiber reinforced concrete in the composite wall was done somewhat arbitrarily, with intent that the fibers could help distribute cracking along the height of the specimen; pull-out of the steel fibers from the concrete suggest an insufficient anchorage length). Unfortunately, the specimen was discarded before it could be opened up, so whether or not the fibers allowed a better distribution of cracking along the wall height could not be verified (although it is a minor point given that, in this particular case, the use of fibers didn't have a noticeable impact of the ultimate failure mode).



Figure 5-51 South West View Specimen CFSSP-B2 at 0.56% Drift



Figure 5-52 South West View Specimen CFSSP-B2 at 1% Drift



Figure 5-53 South West View Specimen CFSSP-B2 at 1.33% Drift



Figure 5-54 Onset of Local Buckling for Specimen CFSSP-B2 at 2% Drift



Figure 5-55 Local Buckling of Specimen CFSSP-B2 at 2.67% Drift



Figure 5-56 HSS Local Buckling in Specimen CFSSP-B2 at 2.67% Drift



Figure 5-57 Local Buckling of HSS in Specimen CFSSP-B2 at 2.67% Drift



Figure 5-58 South West View Specimen CFSSP-B2 at 3.33% Drift



Figure 5-59 Cracks in the Tie Bar Fillet Welds of CFSSP-B2 at 3.33% Drift



Figure 5-60 Intact Welding for Intermediate Tie Bar of Specimen CFSSP-B2 at 4% Drift



Figure 5-61 Propagation of Cracks at Outer Tie Bars in Specimen CFSSP-B2 at 4% Drift



Figure 5-62 Spalling of Crushed Concrete in Specimen CFSSP-B2 at 4% Drift



Figure 5-63 Fracture of the HSS Part of CFSSP-B2 at 4.67% Drift



Figure 5-64 Propagation of Crack from Web to HSS of Specimen CFSSP-B2 at 4.67% Drift



Figure 5-65 Base Fracture of Specimen CFSSP-B2 at 4.67% Drift



Figure 5-66 Cut Base of Specimen CFSSP-B2 After Testing



Figure 5-67 The Intact Steel Fiber Used in the Filled-in Concrete Mix

CHAPTER 6

TEST DATA ANALYSIS

6.1 Introduction

This chapter presents analysis of the experimental program data in terms of strain distributions across the steel skin plate of the tested specimens, force displacement relationships, moment curvature relationships, displacement ductility ratio, μ_d and curvature ductility ratio, μ_ϕ .

Section 6.2 provides analysis of the data generated from testing for each of the four specimens, providing in each case plots of strain distribution across the tested wall section, force displacement relationships, moment curvature relationships, and of shear strain distribution. The following parameters were calculated based on the aforementioned plots: Displacement ductility ratio, curvature ductility ratio, shape factor of the tested wall cross-section, and contribution of the steel skin plates to the shear resistance in the elastic range. Section 6.3 presents a summary of the experimental program outcomes.

6.2 Data Analysis

6.2.1 General

In this section, the data extracted from the 4 tested specimens' instrumentation is analyzed and used to identify: yielding of the steel skin of the CFSSP-Wall specimens and its propagation along the specimens height through axial strain gauges data; shear strength contribution of the steel web through Rosettes gauges data; deflected shape of the tested specimen; force displacement relationship, and; moment curvature relationships. The analyzed data are also used to calculate the displacement ductility factor μ_d , curvature ductility factor, μ_ϕ , and estimated length of the plastic hinge.

6.2.1 Strain Distribution for Specimen CFSSP-NB1

The first established relationship for specimen CFSSP-NB1 is the axial strain distribution across the specimen cross-section, for two sections at 10" and 16" above the top of the foundation. Location of the axial strain gauges and their distribution is illustrated in chapter 4 of this document. Figure 6-1 and Figure 6-2 shows the strain distribution across specimen CFSSP-NB1's steel skin at 10" and 16" above the foundation, respectively. The recorded strain values across the specimen cross-section is used to confirm percentage of cross section yielding, from which it can be inferred whether the plastic moment has been achieved; these values are also used to define the position of elastic and plastic neutral axis for comparison with the finite element analysis results (in Chapter 6) and the simple plastic analysis predicting the capacity of the CFSSP-Walls.

The average yield strain for the HSS 8.625×0.3225 and the web steel plate used in CFSSP-Wall specimens, using material properties obtained from coupon tests (as described in Chapter 4 of this document) is respectively given by,

$$\varepsilon_{y,HSS} = \frac{f_{y,HSS}}{E_{HSS}} = \frac{43}{27466} = 1566 \mu strain \quad (6.1)$$

$$\varepsilon_{y,web} = \frac{f_{y,web}}{E_{web}} = \frac{62}{29806} = 2080 \mu strain \quad (6.2)$$

According to the yield strain values in equations 6.1 and 6.2, the axial strain values for steel part of the cross-section of the CFSSP-NB1 at 10" and 16" above the foundation level started to yield at 0.9% drift (by interpolation of the curves shown). The fact that all strain gauges, except the one closest to the neutral axis, exceeded the yield strain at a drift of approximately 1.2% (again, interpolating from the curves shown) confirms the experimental observation that the plastic moment capacity was approximately reached at that drift during the tests. Note that strains are only presented for drift value of up to 1.8% because local buckling started to occur at a drift of 1.8%; accordingly, strain gauge results beyond this drift level started to be affected by the local buckling deformations (i.e, the bending of the steel plate in the buckled zone region affected the readings of the strain gauges. Furthermore, some gauges started to fail at large strains; for example, the strain gauge at the right edge of the wall (gauge SG10) malfunctioned at 1.8% drift, as its reading dropped from 9421 $\mu strain$ to 3973 $\mu strain$ (which is why this data point is not included in Figure 6-1).

Results show that the position of the elastic neutral axis is located at 19.5" from the outmost compressed edge, while the plastic neutral axis is located at 17" from that point; both axes are at about one third of the total depth of the CFSSP-NB1 wall cross-section. This compares reasonably well with the results obtained from XTRACT in Chapter 4, which indicated locations of elastic and plastic neutral axis of 18.7 and 15.0, respectively, corresponding to differences of 4.1% and 11.8%, respectively, between the theoretical and experimentally obtained values.

The axial vertical strain distribution across the section located at 16" from the top of the foundation is shown in Figure 5.75. For at least three of the strain gauges near the neutral axis of the steel web plate at 1.8% drift, strain values remained below the yield strain value, which indicates that this section did not attain its plastic moment.

The data presented were used to estimate the length of the plastic hinge, where according the monitored strain distribution, a value of 0.6% lateral drift could be considered where the first yield occurs (yield of

extreme steel fibers), at this drift a moment of 22,440 kip-in is reached if M_p is taken to be 32,058 kip-in. and considering linear interpolation over the cantilever length of the plastic hinge is calculated to 36 inches, which represents 0.75 W (total depth of the cross section) and 0.3 h (length of the cantilever wall).

6.2.2 Displacement Ductility Assessment for Specimen CFSSP-NB1

The relation between the force applied by the actuator at the top of the specimen and the displacement of the specimen at that location, were generated using displacement measurements from the string potentiometer SP5 reading the in-plane displacements at the top of the wall. The plot of the force-displacement hysteretic relationship for specimen CFSSP-NB1 is shown in Figure 6-3.

By definition, the displacement ductility factor, μ_D , is the ratio between maximum attained displacement and the yield displacement. For Specimen CFSSP-NB1, as shown in Figure 6-4, it is given by:

$$\mu_D = \frac{\Delta_{\max}}{\Delta_y} = \frac{4.10}{0.80} = 5.13 \quad (6.3)$$

where;

Δ_{\max} , is the maximum displacement, defined as the post peak displacement where strength has degraded down to 80% of the peak strength (80% of 304 kips = 243 kips), which is here equal to 4.1" (3.4% drift)

Δ_y , is the yield displacement calculated from the idealized elastic-perfectly plastic envelope curve, which is equal to 0.8"(0.67% drift) for this specimen.

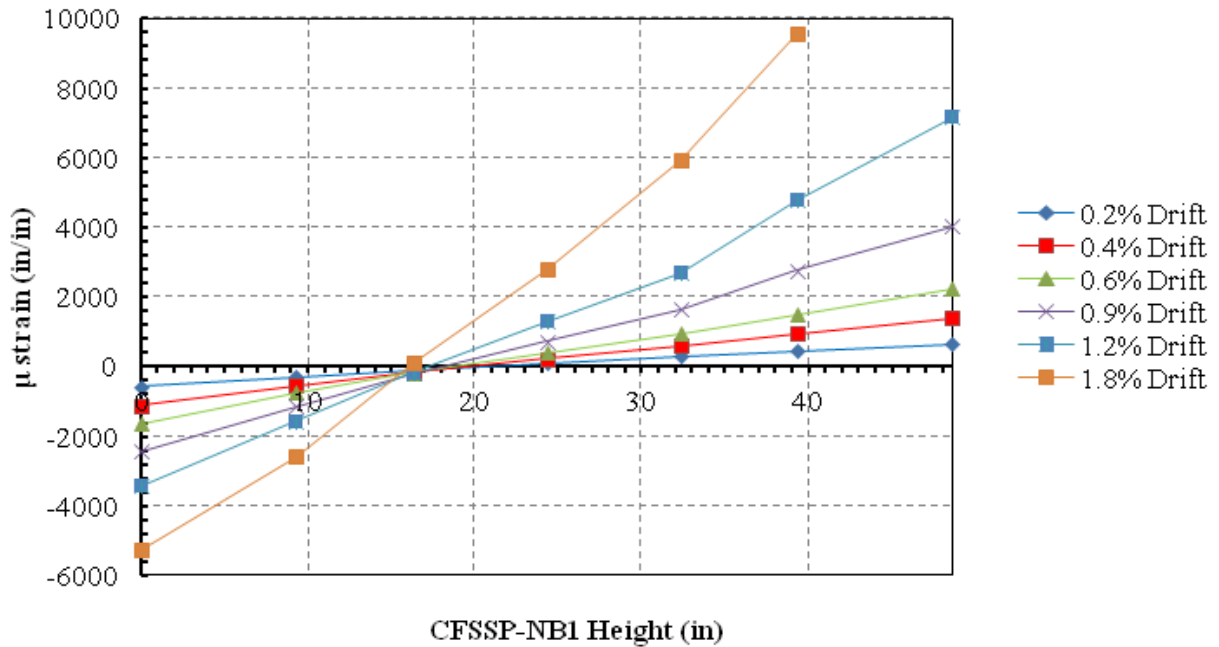


Figure 6-1 Vertical Axial Strain Distribution across CFSSP-NB1 Steel Skin at 10 inch from Base

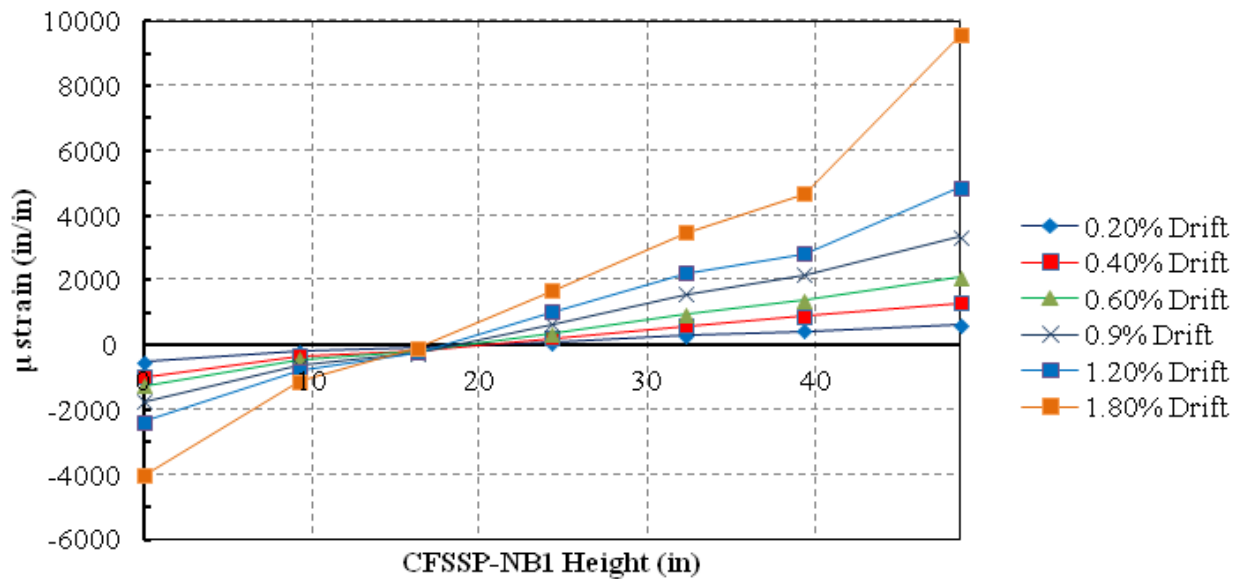


Figure 6-2 Vertical Axial Strain Distribution Across CFSSP-NB1 Steel Skin at 16 inch from Base

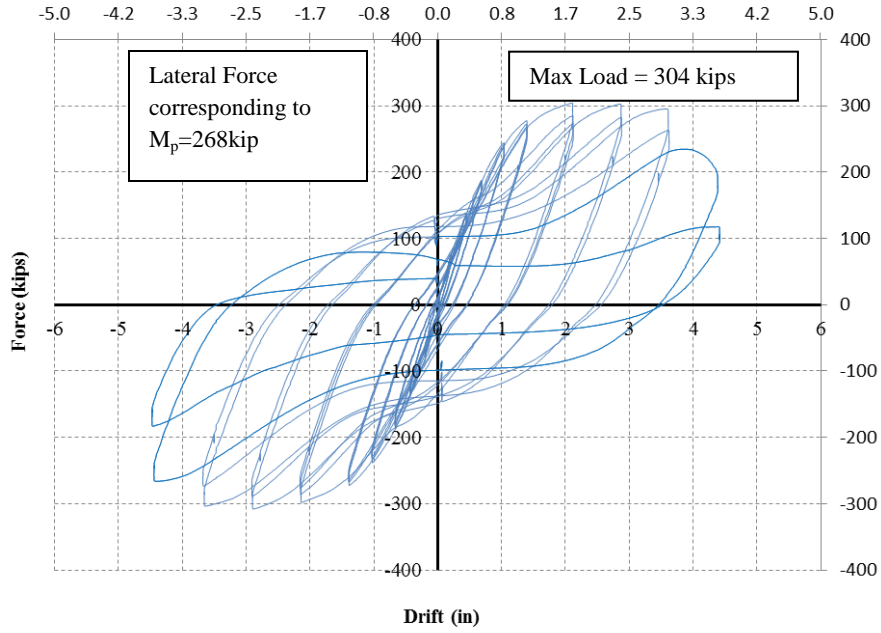


Figure 6-3 Force vs Displacement Relationship for Specimen CFSSP-NB1

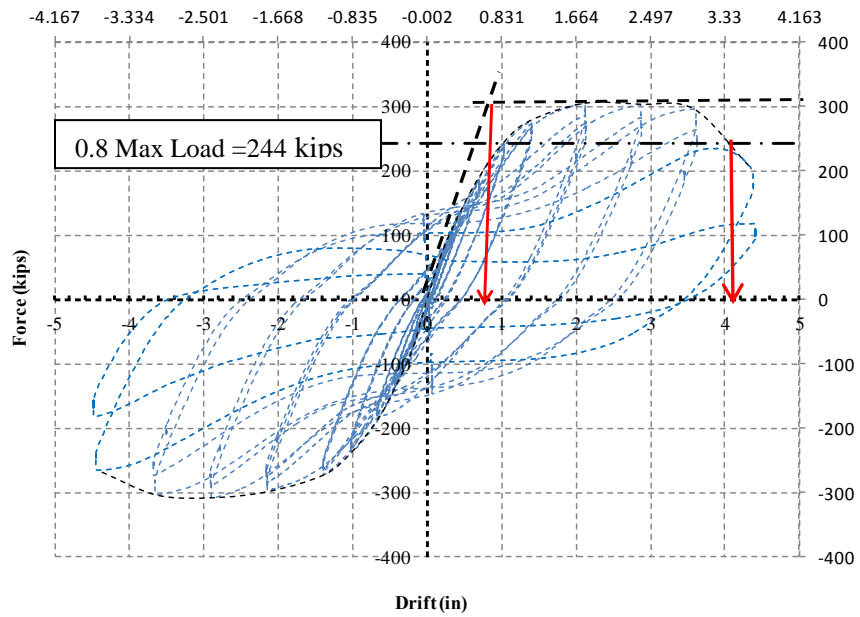


Figure 6-4 Force Displacement Envelope and Ductility Evaluation for CFSSP-NB1

6.2.4 Curvature Ductility for Specimen CFSSP-NB1

Moment-curvature relationships at various heights of the wall were calculated using the results from the linear potentiometers LP1 to LP12. The values from the corresponding linear potentiometers (as shown in the instrumentation layout in Chapter 4 of this document) In addition, the string potentiometers SP6 and SP7 were also used to calculate average curvatures over the -height spanned by these linear potentiometers, and compared to the results extracted from the linear potentiometers. Calculation of the moment curvature relationship is performed as follows, using linear potentiometers LP1 and LP7 as an example:

The difference between the corresponding linear potentiometers displacement is used to calculate the rotation, θ

$$\theta_1 = \frac{\Delta_{LP1} - \Delta_{LP7}}{h_{CFSSP-NB1}} \quad (6.4)$$

where $h_{CFSSP-NB1}$ is the total depth of the CFSSP-NB1 specimen cross-section.

Δ_{LP1} is the extension or contraction of the linear potentiometer, LP1, arm in inches

Δ_{LP2} is the extension or contraction of the linear potentiometer, LP2, arm in inches

The curvature, ϕ , is then given by:

$$\phi = \frac{\theta}{l} \quad (6.5)$$

where l is the length across which the linear potentiometer or string potentiometer reads the change in distance, Δ , which is typically 4" for the linear potentiometers used, and 30" for the string potentiometers.

The moment, M_1 is calculated at the mid height of the effective length of the pair of linear potentiometers to calculate curvature at a certain location, and is given (for example) by:

$$M_1 = P_{Actuator} \cdot L_1 \quad (6.6)$$

where $P_{Actuator}$ is the actuator force and L_1 is equal to 118" for LP1 and LP7. The same procedure is followed for all other corresponding linear potentiometer pairs, as well as for calculation of the moment-

curvature obtained from the string potentiometers SP6 and SP7. Table 6-1 summarizes the resulting moment-curvature parameters used in calculations for the different linear potentiometers and string potentiometers. In column (1) of Table 6-1, the formulas for rotation angle for each set of corresponding linear potentiometers/string potentiometers is presented; column (2) presents the curvature values, and finally column (3) presents the vertical length (moment arm) measured from the top of the specimen (line of actuator loading) to the level of the corresponding displacement transducers.

The moment-curvature relationships for specimen CFSSP-NB1, constructed for locations at 2", 6", 10", 14", 18" and 22" above the top of the foundation and extracted from the linear potentiometers data at those heights, are shown in Figure 6-5 to Figure 6-10, respectively. Figure 6-11 shows the moment-curvature relationship constructed from string potentiometers SP6 and SP7. Note that, as mentioned earlier, some linear potentiometers were displaced from their original positions at relatively high drift values due to local buckling of the steel skin of the specimen or slipping of the mounting magnets. Likewise, for the string potentiometers, the magnet at the end of the string was also displaced due to local buckling of the half HSS. Slipping of linear potentiometers leads to somewhat exaggerated, erroneous and inaccurate data; the data is nonetheless presented, as the trends can be of interest, but in all the figures presenting moment curvature relationships, the part of the curves calculated from the data collected after slipping of the potentiometers is presented in grey shaded box, to indicate that these portions of the moment curvature curves are less reliable and should be neglected when reaching conclusions regarding the curvatures developed by the specimen CFSSP-NB1. Likewise, for the string potentiometers results in Figure 6-11, the shaded rectangular zone encompasses the cycles that took place after local buckling of the specimen's skin plate, implying that those recorded rotations maybe be less reliable due to the distortions created by local buckling (although, since the error is averaged over a greater distance, the magnitude of the errors should be less).

The curvature ductility, μ_ϕ , was calculated based on the moment curvature relationship obtained from the string potentiometers as they provide the most complete set of data through the test different loading cycles. Two different curvature ductility values can be defined. For example, for the current specimen, curvature ductility based on first yield can be defined as:

$$\mu_\phi = \frac{\phi_{\max}}{\phi_y} = \frac{77.4}{5.68} = 16.63 \quad (6.7)$$

Where, ϕ_{\max} is the maximum curvature considered at the degraded strength equal to 80% of the maximum strength, while ϕ_y is the curvature corresponding to yielding of the steel skin extreme fiber (calculation

presented later in this section). Another approach to calculate μ_ϕ , is to use the bi-linearized cycles envelope, where, ϕ_y , is obtained from the bi-linear backbone curve shown in Figure 6-11 accordingly:

$$\mu_\phi = \frac{\phi_{\max}}{\phi_y} = \frac{77.4}{10} = 7.74 \quad (6.8)$$

The aforementioned expression is the most commonly used for representing curvature ductility, and is used for ductility evaluation through the following chapters.

The reason for calculating curvature ductility using data from the string potentiometers SP6 and SP7 is that they were more reliable to capture data through the test after local buckling of the specimen's skin plate, which is necessary to obtain the maximum curvature used in curvature ductility calculations. In that sense, the string potentiometers readings account for the large rotations that develop during local buckling, which are equivalent inelastic “curvature” that must be accounted for. The benefit of using data from the linear potentiometers is that it allows capturing the variation of curvature along the height of the specimen. Furthermore, curvature obtained from readings of these linear potentiometers can be averaged over the length of specimen instrumented, and the resulting average curvature values extracted from the linear potentiometers over that length can be compared to the value obtained from the string potentiometers. The comparison between the different curvature values is shown Figure 6-12 where the curvatures calculated using linear potentiometers is compared to that calculated using string potentiometers, comparing the curvature distribution along the length of the specimen at drift values of 0.6% and 1.8%, which are the values at which M_y and M_p are achieved respectively.

From Figure 6-12 it appears that there was a problem in the readings from linear potentiometers LP2, LP8, LP3, and LP9 as they are showing results less than expected. However, the average values of curvatures determined through linear potentiometers is equal to that determined using the string potentiometers. The curvature values obtained from the string potentiometers were used to calculate the curvature ductility of the specimen.

Table 6-1 Parameters Used in Moment Curvature Calculation

Rotation, θ (Rad) [1]	Curvature, ϕ (Rad/in) [2]	Moment Arm, L (in) [3]
$\theta_1 = \frac{\Delta_{LP1} - \Delta_{LP7}}{h_{CFSSP-NB1}}$	$\frac{\theta_1}{4}$	118
$\theta_2 = \frac{\Delta_{LP2} - \Delta_{LP8}}{h_{CFSSP-NB1}}$	$\frac{\theta_2}{4}$	114
$\theta_3 = \frac{\Delta_{LP3} - \Delta_{LP9}}{h_{CFSSP-NB1}}$	$\frac{\theta_3}{4}$	110
$\theta_4 = \frac{\Delta_{LP4} - \Delta_{LP10}}{h_{CFSSP-NB1}}$	$\frac{\theta_4}{4}$	106
$\theta_5 = \frac{\Delta_{LP5} - \Delta_{LP11}}{h_{CFSSP-NB1}}$	$\frac{\theta_5}{4}$	102
$\theta_6 = \frac{\Delta_{LP6} - \Delta_{LP12}}{h_{CFSSP-NB1}}$	$\frac{\theta_6}{4}$	98
$\theta_7 = \frac{\Delta_{SP6} - \Delta_{SP7}}{h_{CFSSP-NB1}}$	$\frac{\theta_7}{30}$	105

where,

$\Delta_{SP6}, \Delta_{SP7}$ are the extension or expansion of the string potentiometers SP1 and SP2 in (inches)

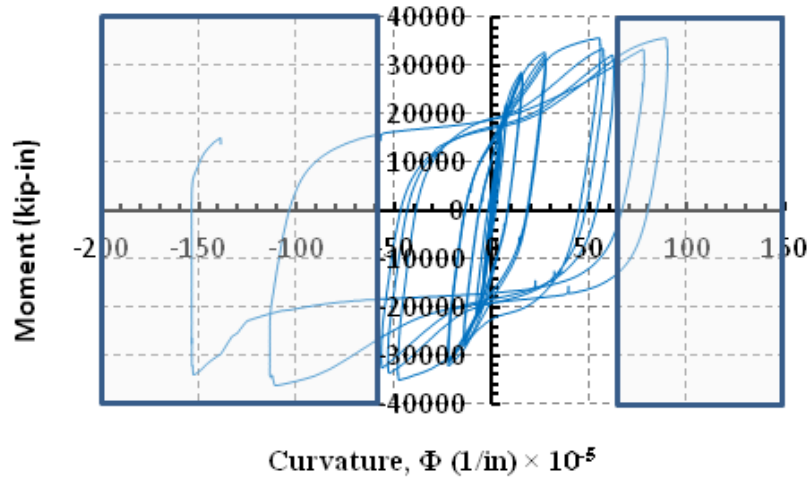


Figure 6-5 Moment vs Curvature for Specimen CFSSP-NB1 at 2 inch from Base

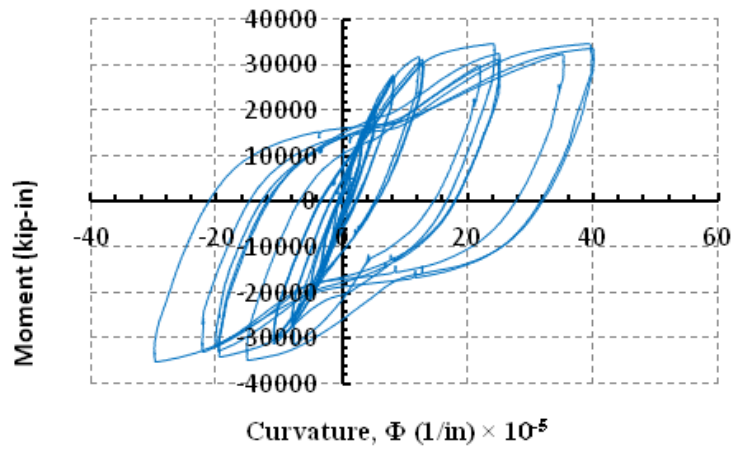


Figure 6-6 Moment vs Curvature for Specimen CFSSP-NB1 at 6 inch from Base

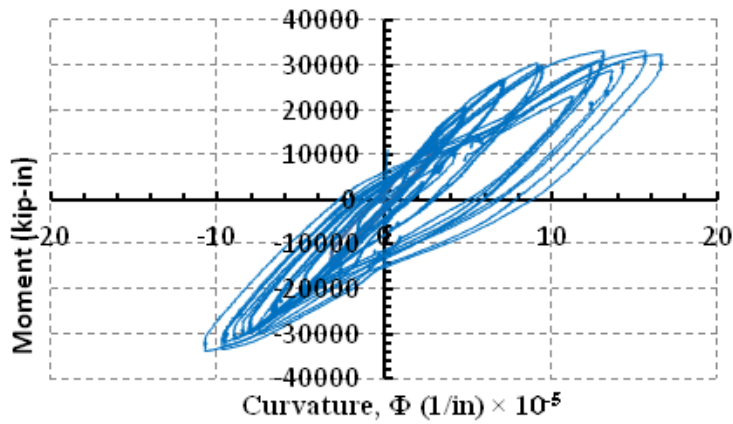


Figure 6-7 Moment vs Curvature for Specimen CFSSP-NB1 at 10 inch from Base

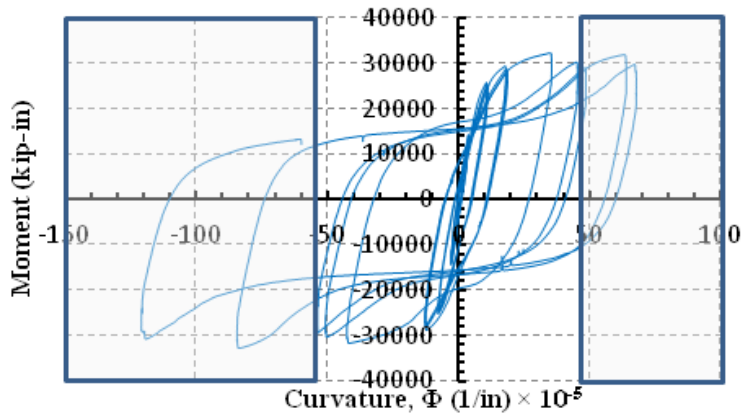


Figure 6-8 Moment vs Curvature for Specimen CFSSP-NB1 at 14 inch from Base

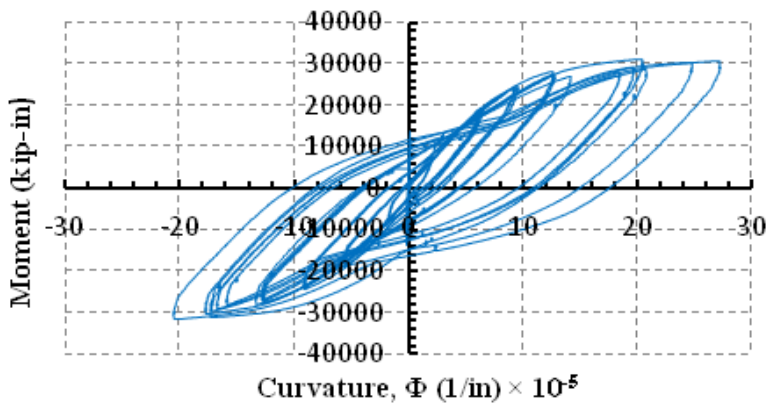


Figure 6-9 Moment vs Curvature for Specimen CFSSP-NB1 at 18 inch from Base

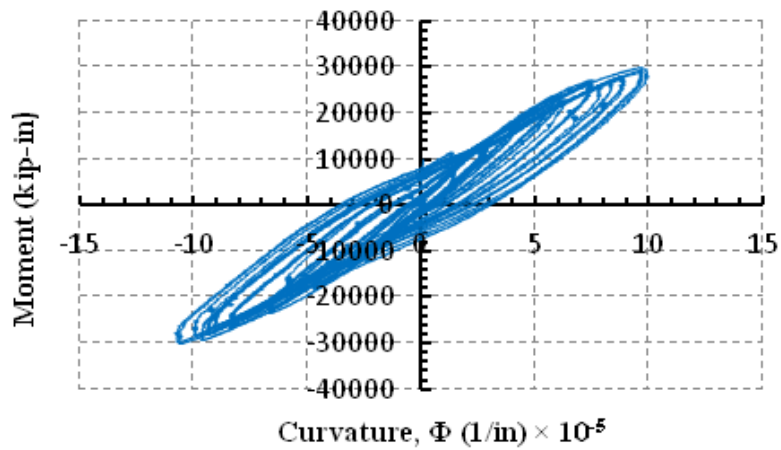


Figure 6-10 Moment vs Curvature for Specimen CFSSP-NB1 at 22 inch from Base

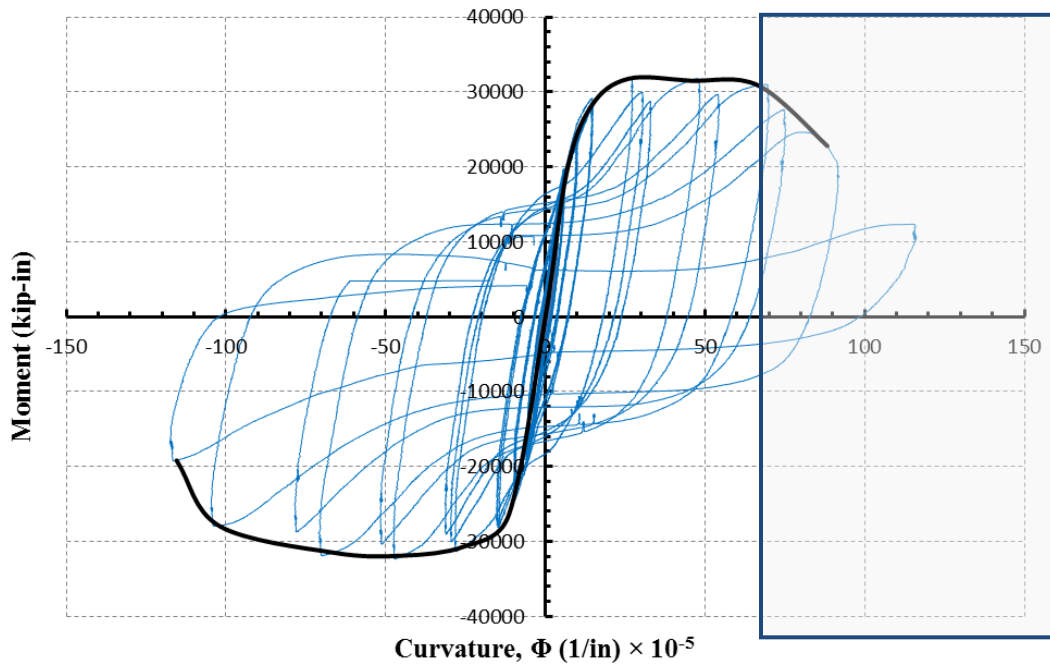


Figure 6-11 Moment vs Curvature for Specimen CFSSP-NB1 at 15 inch from Base

The curvature distribution along the instrumented height of specimen CFSSP-NB1 is shown in Figure 6-12, for a lateral drift of 1.8% (i.e. the point at which local buckling occurs and M_p was reached), which is considered to be the limit for which relatively reliable data could be obtained from all the linear potentiometers. This curvature distribution diagram along the length of the cantilever wall is useful to compare the average of the curvature values extracted from linear potentiometers with the value of curvature obtained from the string potentiometers.

As shown in Figure 6-12, the values of curvatures from the linear potentiometers decrease, from a maximum value at the base to the minimum recorded value at 24" from the foundation. Probably due to some malfunctioning in linear potentiometers LP2, LP8, LP3, and LP9, reading at those levels were less than expected values. However, this figure illustrates that the average of curvature obtained from the linear potentiometers over the instrumented height is approximately equal to the value obtained from string potentiometers, which provides confidence in the curvature ductility reported above. Also, it illustrates that the curvature ductility values reported above are conservative, as they represent an average curvature ductility measured over a vertical distance that approximately equals to 62% of the wall's all

over cross section depth, W , and that walls can actually develop higher curvature ductility locally if referring to curvature over smaller wall length.

The yield curvature, ϕ_y , corresponds to the curvature when yielding of the outermost fiber of the HSS part of the specimen, and the plastic curvature, ϕ_p , correspond to the curvature developed when the plastic moment capacity of the specimen is reached.. However, estimates of those values, when obtained experimentally, will vary depending on the method used to calculate them, and more specifically, the length over which measured values are averaged. Here, the values of ϕ_y and ϕ_p were calculated using the aforementioned instrumentation (linear potentiometers and string potentiometers). The 6 curvature values

calculated using linear potentiometers were averaged, $\frac{\sum_{i=1}^{i=6} \phi_{y/P}}{6}$ The values of yield curvature were

calculated at 0.6% drift where the value of M_y is attained and at 1.8% drift where M_p is attained. It should be mentioned here that since 0.6% drift is when yield occurs so any curvature measured at this point is named ϕ_y even it is not necessary reflect yield curvature (yield is not achieved at all measuring instruments at the same time and the same applies for ϕ_p . Another factor is that the vertical distances between linear potentiometers is relatively small that averaging could be a viable solution.

The curvature values calculated from linear potentiometers average are compared to those calculated using string potentiometer, the values were calculated using equations 5.5, 5.6, and equations in Table 6-1. The calculated values can be summarized as follows:

- The average yield curvature from the linear potentiometers, $\phi_y = 5.81 \times 10^{-5}$ 1/in
- The yield curvature from string potentiometers, $\phi_y = 5.86 \times 10^{-5}$ 1/in
- The average plastic curvature from the linear potentiometers, $\phi_p = 27.1 \times 10^{-5}$ 1/in
- The plastic curvature from string potentiometers, $\phi_p = 30.93 \times 10^{-5}$ 1/in

These results show that values obtained from the various instruments are in agreement, and validate the reported values of curvature calculated using string potentiometers.

For comparison, values of the yield and plastic curvatures calculated using strain values on the extreme fiber of the specimen and the position of neutral axis calculated using the axial strain distributions shown earlier are presented.

Yield curvature is calculated as follows:

$$\phi_y = \frac{\varepsilon_{y,HSS}}{h-c} = \frac{1566 \times 10^{-6}}{29.125} = 5.37 \times 10^{-5} \text{ 1/in} \quad (6.9)$$

where,

$h-c$, is the distance from the elastic neutral axis to the outermost yielding tension fiber of the CFSSP-NB1 section.

Plastic curvature is calculated as follows:

$$\phi_p = \frac{\varepsilon_{HSS,plastic}}{h-c'} = \frac{5274 \times 10^{-6}}{17} = 3.10 \times 10^{-4} \text{ 1/in} \quad (6.10)$$

where

$h-c'$, is the distance from the plastic neutral axis to the outermost yielding tension fiber of the CFSSP-NB1 section.

$\varepsilon_{HSS,plastic}$ is the strain at the HSS of the CFSSP-NB1 cross section at a drift value of 1.80%, which has been defined earlier at the point at which plastic moment capacity was attained.

The curvature values calculated using the different approaches using experimental results are summarized in Table 6-2, and it shows that the maximum difference between methods used at 0.6% drift is 8.2% and at 1.8% drift is 12.5% which give relatively good agreement between the different methods used to calculate curvature based on experimental results.

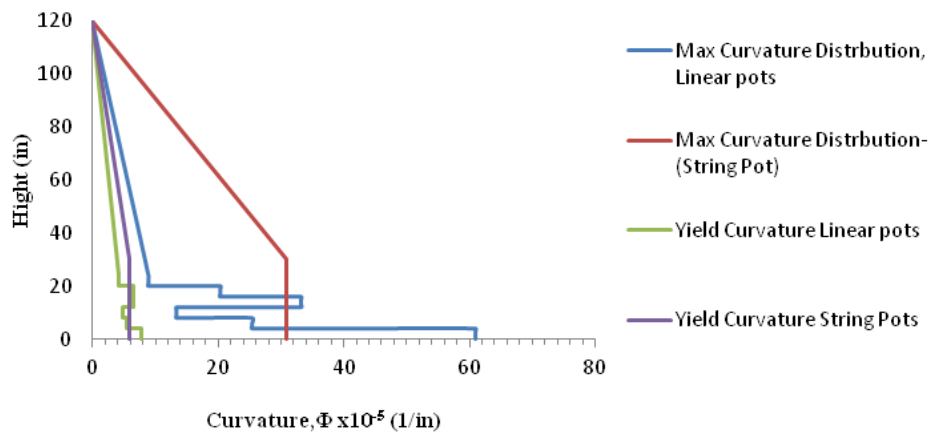


Figure 6-12 Curvature Distribution along CFSSP-NB1 at 0.6% and 1.8% Drift

Table 6-2 Curvature Values of Specimen CFSSP-NB1

Curvature Value, Φ	Averaged Linear Potentiometers	String Potentiometers	Axial Strain Distribution	Drift Value%
Yield Curvature, ϕ_y	5.81×10^{-5}	5.86×10^{-5}	5.37×10^{-5}	0.6%
Plastic Curvature, ϕ_p	27.1×10^{-5}	30.93×10^{-5}	31.0×10^{-5}	1.8%

6.2.5 Shape Factor for Specimen CFSSP-NB1

The information on yield and plastic moments were used to determine the cross-section's shape factor, K .

The factor K as calculated using XTRACT software is given by:

$$K = \left(\frac{M_P}{M_y} \right)_{EXTRACT} = \frac{26.36 \times 10^3}{17.173 \times 10^3} = 1.53 \quad (6.11)$$

The shape factor calculated using experimental results considering the value of M_y calculated at 0.6% drift and the value of M_P at 1.2% drift, the shape factor is given by:

$$K = \left(\frac{M_P}{M_y} \right)_{Experimental} = \frac{32424}{22553} = 1.43 \quad (6.12)$$

For comparison, note that the shape factor for the steel skin plate of the CFSSP-NB1 wall without the filled-in concrete can be given by:

$$K = \left(\frac{M_P}{M_y} \right)_{steel_skin} = \frac{23112}{16052} = 1.43 \quad (6.13)$$

The value for the shape factor is affected by the relatively large depth of the cross-section which leads to large strains at the outermost fibers and consequentially lower M_y and higher M_P value.

6.2.6 Shear Analysis for Specimen CFSSP-NB1

In order to evaluate the contribution of the steel skin web plates to the shear strength of the CFSSP-NB1 specimen, strain data from the 45° rectangular rosettes, shown in Figure 6-13, is used to calculate the shear strain, γ_{xy} . Using Mohr circle formulation in the elastic range, the shear stress, τ_{xy} , and consequentially the shearing force in the steel skin webs, can be calculated as follows:.

Considering the strain in the direction of each gage composing the Rosette

$$\varepsilon_a = \frac{\varepsilon_x + \varepsilon_y}{2} + \frac{\varepsilon_x - \varepsilon_y}{2} \cos 2(45^\circ) + \varepsilon_{xy} \sin 2(45^\circ) \quad (6.14)$$

$$\varepsilon_b = \frac{\varepsilon_x + \varepsilon_y}{2} + \frac{\varepsilon_x - \varepsilon_y}{2} \cos 2(90^\circ) + \varepsilon_{xy} \sin 2(90^\circ) \quad (6.15)$$

$$\varepsilon_c = \frac{\varepsilon_x + \varepsilon_y}{2} + \frac{\varepsilon_x - \varepsilon_y}{2} \cos 2(135^\circ) + \varepsilon_{xy} \sin 2(135^\circ) \quad (6.16)$$

By solving equation 5.12, 5.13 and 5.14, the shear strain, ε_{xy} is given by

$$\varepsilon_{xy} = \frac{\varepsilon_a - \varepsilon_c}{2} \quad (6.17)$$

and the engineering shear strain, γ_{xy}

$$\gamma_{xy} = \varepsilon_a - \varepsilon_c \quad (6.18)$$

The shear stress in the steel web is given by :

$$\tau_{xy} = G \cdot \gamma_{xy} \quad (6.19)$$

The shearing force acting on the steel web plate of the CFSSP-NB1 is given by:

$$V_{Steel} = \tau_{xy} \cdot (2l_w \cdot t_w) \quad (6.20)$$

where

G, steel shear modulus

l_w , length of the steel web

t_w , thickness of the steel web

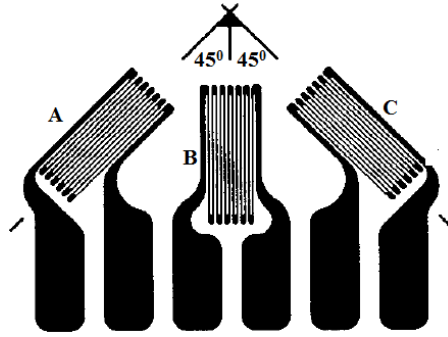


Figure 6-13 Typical 45° Rectangular Rosette gage, <http://www.ecourses.ou.edu/cgi-bin>

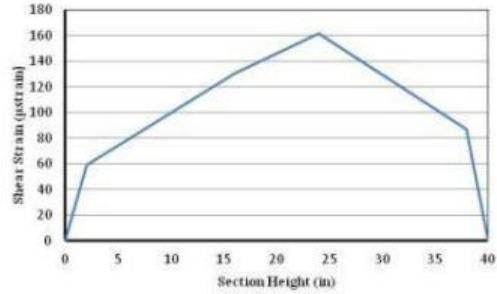
The contribution of the steel web to the shear strength of the CFSSP-NB1 is given by V_{steel} / V_b where V_b is the base shear (or equivalently, the lateral load applied to the specimen). Table 6-3 shows the contribution of the steel web to total specimen CFSSP-NB1 shear strength based on engineering shear strain distribution at different lateral drift values, shown in Figure 6-14, and computed using equations 5.17 and 5.18. The data from the rosettes can be used only as far as the vertical gauge B strain does not exceed the yield strain, as the entire calculation is based on Mohr's circle formulation in the elastic range. From the analysis, it was found that, in the elastic range, the steel web of specimen CFSSP-NB1 resisted about 50% of the shear strength of the entire section.

The above sequence of data presentation and organization used for specimen CFSSP-NB1 is also used for specimens CFSSP-NB2, CFSSP-B1 and CFSSP-B2 presented in the following sections.

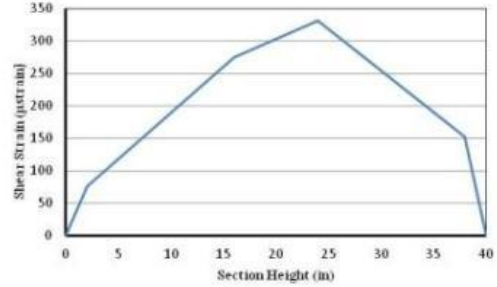
Table 6-3 Contribution of the Steel Web to the CFSSP-NB1 Shear Strength

Drift %	Average Shear Strain, $\mu strain$	Average Shear Stress, ksi	Web Shear Force, kip	Shear Force, kip	Shear Strength Steel Web Contribution, %
(1)	(2)	(3)	(4)	(5)	(6)
0.2	109.51	1.22	30.53	71.94	42.4
0.4	208.65	2.32	58.18	135.77	42.9
0.6	306.0	3.4	85.3	181.7	47.0

0.2% Drift



0.4% Drift



0.6% Drift

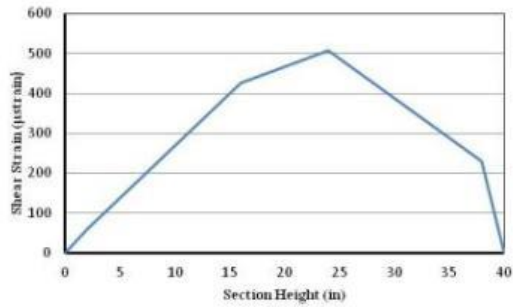


Figure 6-14 Shear Strain Distribution Across the Steel Web of Specimen CFSSP-NB1

6.2.7 Strain Distribution for Specimen CFSSP-NB2

For specimen CFSSP-NB2, the axial strain distribution across the specimen section at 12" and 22" from the foundation face is shown in Figure 6-15 and Figure 6-16 respectively. Specimen CFSSP-NB2 was able to attain its plastic moment capacity at 12" from the foundation between the lateral drifts of 1.2% and 1.8%. Strain gauge SG14 failed after reaching a strain of 7980 $\mu strain$ at 1.8% drift. The position of the elastic neutral axis and the plastic neutral axis are at 20" and 17.5", respectively, from the outer most fiber on the compression flange. Strains on the section at 22" above the top of the footing indicate that the middle portion of the web did not yield.

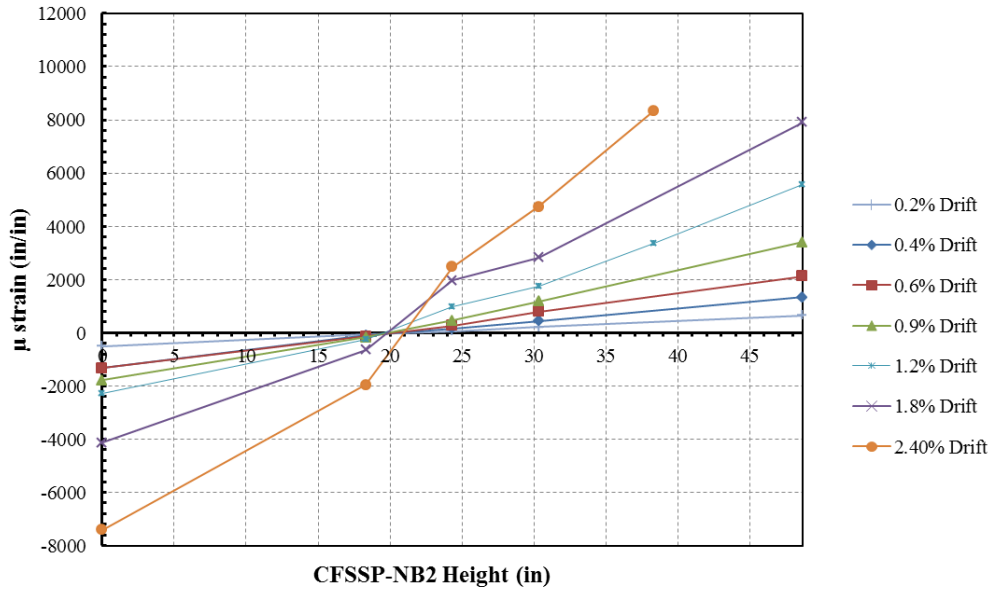


Figure 6-15 Vertical Axial Strain Distribution Across CFSSP-NB2 Steel Skin at 12 inch from Base

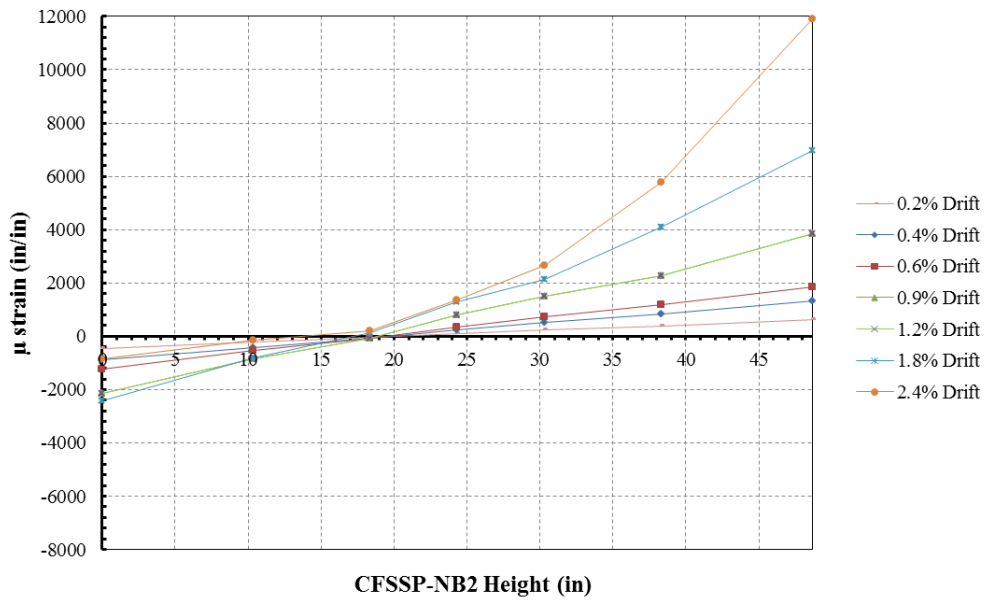


Figure 6-16 Vertical Axial Strain Distribution Across CFSSP-NB2 Steel Skin at 22 inch from Base

6.2.8 Displacement Ductility of Specimen CFSSP-NB2

The hysteretic force-displacement relationship is shown in Figure 6-17. The displacement ductility factor is obtained from the force displacement cycles envelope, using an idealized bi-linear relationship to establish the yield displacement to calculate this displacement ductility factor μ_D , such that, here:

$$\mu_D = \frac{\Delta_{\max}}{\Delta_y} = \frac{3.67}{1} = 3.67 \quad (6.21)$$

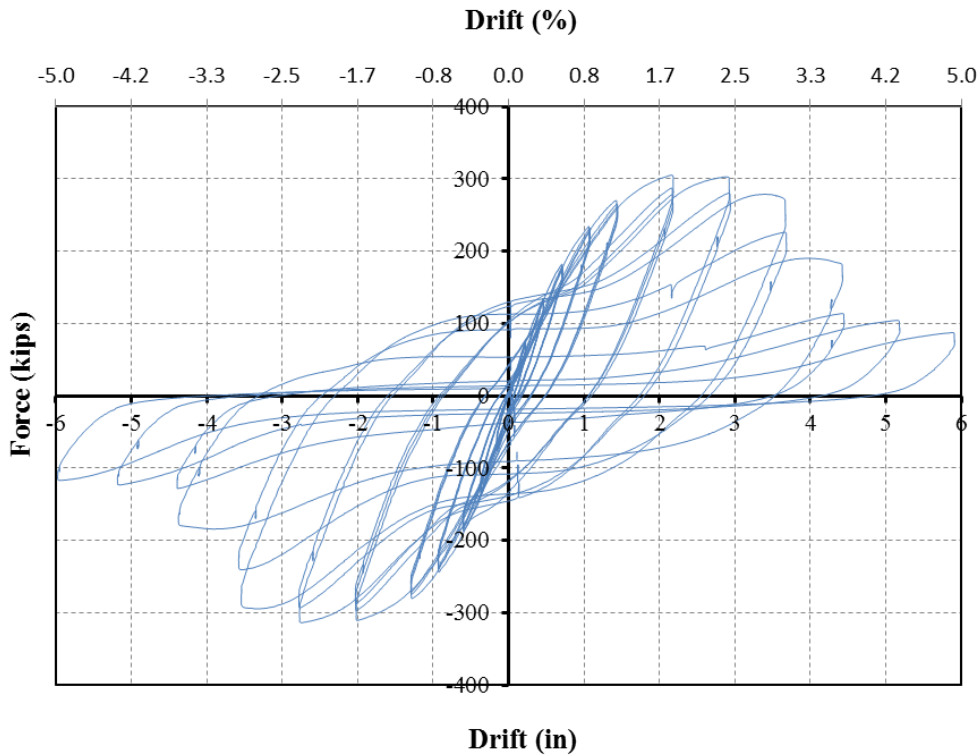


Figure 6-17 Actuator Force vs Lateral Displacement, Specimen CFSSP-NB2

6.2.9 Curvature Ductility of Specimen CFSSP-NB2

Curvatures were determined as described earlier for specimen CFSSP-NB2; the moment curvature relationships extracted from the linear potentiometers are presented in Figures 5.91 to 5.96. Figure 5.97 presents the curvature extracted from the string potentiometers. The curvature ductility based at first yield is given by:

$$\mu_{\phi} = \frac{\phi_{\max}}{\phi_y} = \frac{72}{3.87} = 18.6 \quad (6.22)$$

The curvature ductility based bi-linear moment-curvature is given by:

$$\mu_{\phi} = \frac{\phi_{\max}}{\phi_y} = \frac{72}{11} = 6.54 \quad (6.23)$$

Figure 5.98 shows the values of curvatures extracted from the linear potentiometers and string potentiometers. Due to some malfunctioning in the linear potentiometers LP2, LP8, LP3 and LP9, their reading were less than the expected values, however the average of curvature for the values extracted from linear potentiometers is consistent with values extracted from string potentiometers, as shown by the following results:

- The average yield curvature for the linear potentiometers, $\phi_y = 3.61 \times 10^{-5}$ 1/in
- The yield curvature from string potentiometers, $\phi_y = 3.87 \times 10^{-5}$ 1/in
- The average plastic curvature for the linear potentiometers, $\phi_p = 17.44 \times 10^{-5}$ 1/in
- The plastic curvature from string potentiometers, $\phi_p = 21.19 \times 10^{-5}$ 1/in

Using the values of the yield and plastic curvatures calculated using strain values from gages on the extreme fiber of the specimen, and the position of neutral axis determined using axial strain gages values (distributed across the tested specimen cross section) as shown in Chapter 4, the yield curvatures and plastic curvature can be calculated as follows:

Yield Curvature is given by

$$\phi_y = \frac{\epsilon_{y,HSS}}{h-c} = \frac{1566 \times 10^{-6}}{28} = 5.59 \times 10^{-5} \text{ 1/in} \quad (6.24)$$

where,

$h-c$, the distance from the elastic neutral axis to the outermost yielding tension fiber of the CFSSP-NB1 section.

Plastic curvature is given by

$$\phi_p = \frac{\epsilon_{HSS,plastic}}{h-c'} = \frac{8201 \times 10^{-6}}{30.5} = 2.69 \times 10^{-4} \text{ 1/in} \quad (6.25)$$

where

$h - c'$, the distance from the plastic neutral axis to the outermost yielding tension fiber of the CFSSP-NB1 section.

$\epsilon_{HSS, plastic}$ is the strain at the HSS corresponding to CFSSP-NB1 attaining its plastic moment capacity, M_p defined earlier in this Chapter.

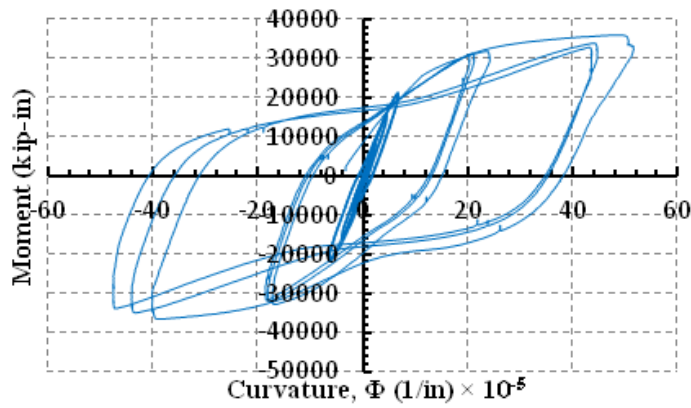


Figure 6-18 Moment vs Curvature using Linear Potentiometers at 2 inch from Base , CFSSP-NB2

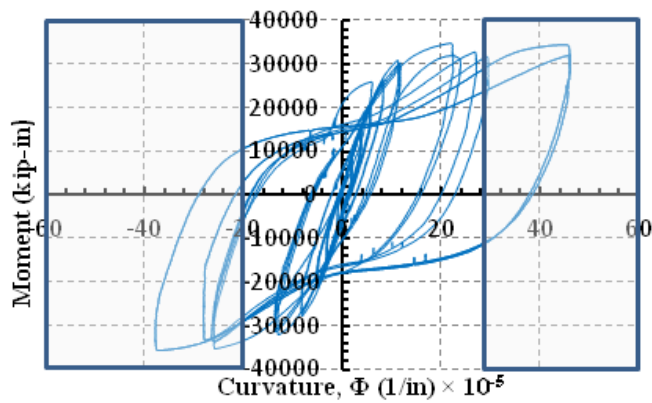


Figure 6-19 Moment vs Curvature using Linear Potentiometers at 6 inch from Base, CFSSP-NB2

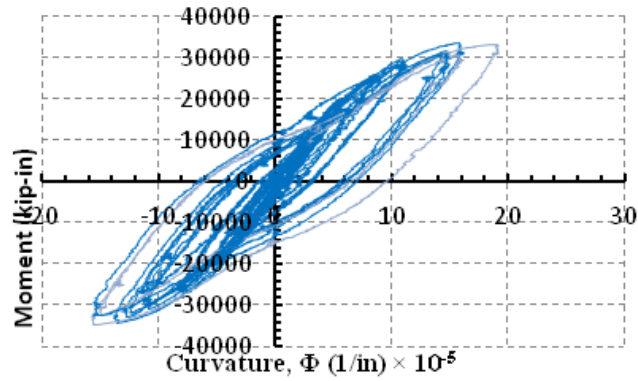


Figure 6-20 Moment Vs Curvature using Linear Potentiometer at 10 inch from Base, CFSSP-NB2

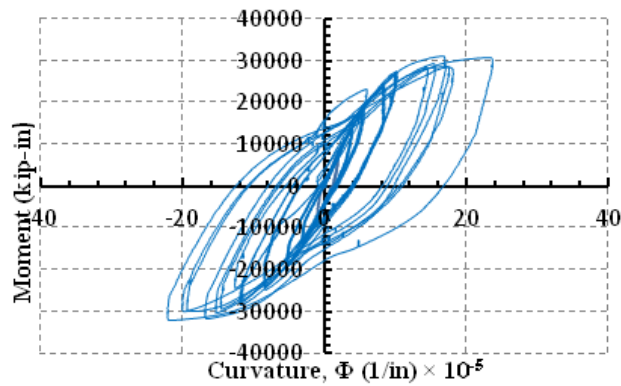


Figure 6-21 Moment vs Curvature using Linear Potentiometer at 18 inch from Base, CFSSP-NB2

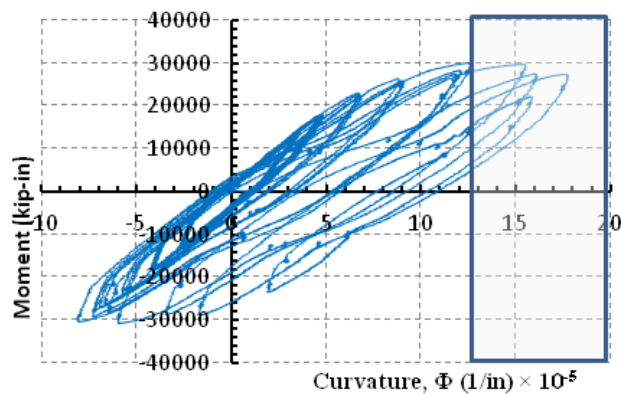


Figure 6-22 Moment vs Curvature using Linear Potentiometer at 22 inch from Base, CFSSP-NB2

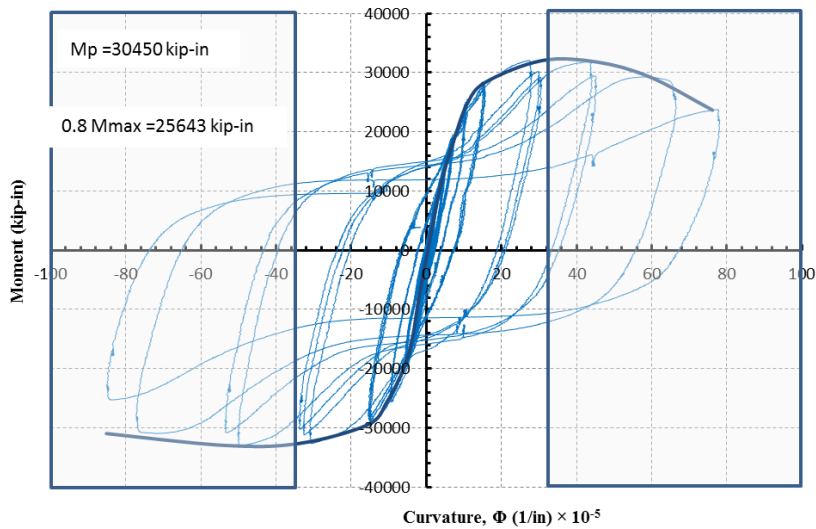


Figure 6-23 Moment vs Curvature using String Potentiometers at 15 inch from Base, CFSSP-NB2

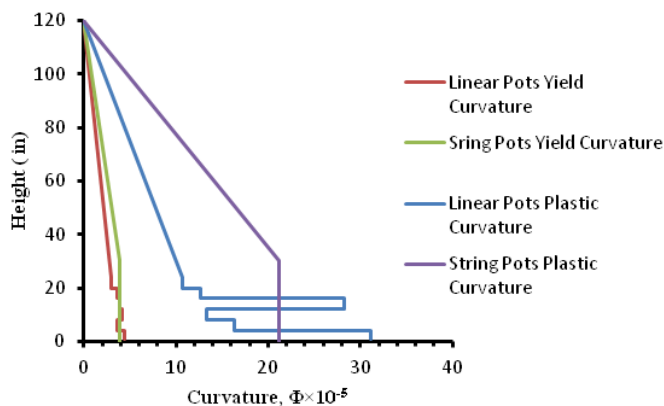


Figure 6-24 Curvature Distribution along the Length of Specimen CFSSP-NB2

6.2.10 Strain Distribution for Specimen CFSSP-B1

For specimen CFSSP-B1, the axial strain distribution across the specimen section at 10" and 16" from the top of foundation is shown in Figure 6-25 and Figure 6-26 respectively. Specimen CFSSP-B1 was able to attain its plastic moment capacity at 10" from foundation between lateral drifts of 1.0% and 1.33%. Strain gauge readings were recorded up to lateral drift of 2%; the outer most strain gauge on the HSS had strain of 9500 μ strain at 2% drift. The position of the elastic neutral axis and the plastic neutral axis are at 19.5" and 17" respectively from the outer most fiber on the compression flange. As for the section at 16"

from the top of the footing, 13" of the web did not exhibit yielding. From these strain distributions, it was estimated that the length of the plastic hinge could exceed 0.35h.

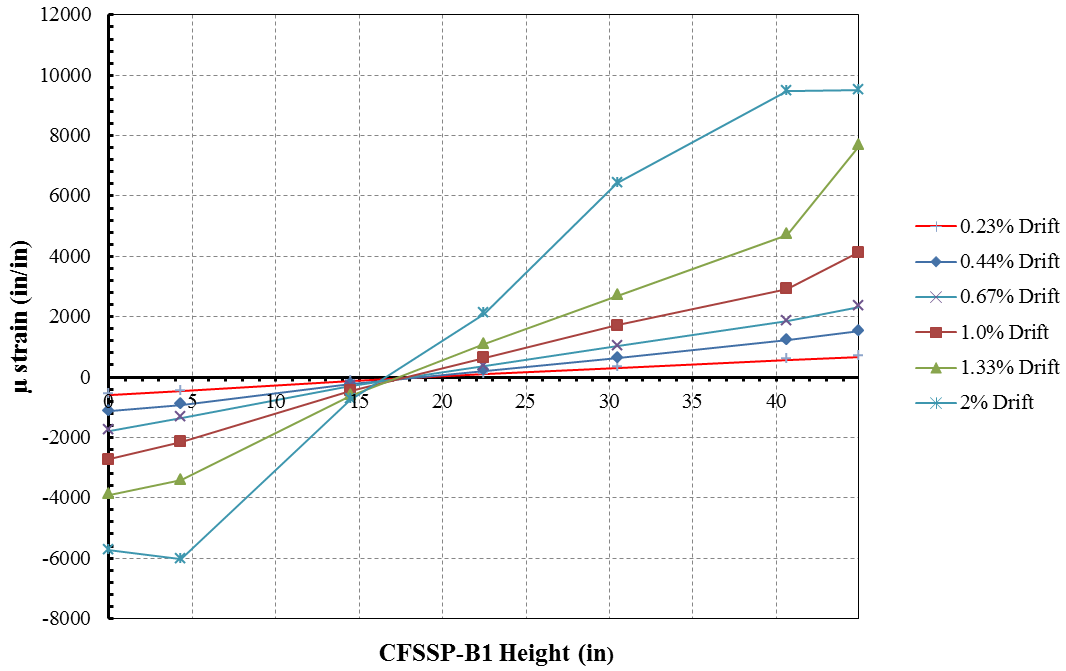


Figure 6-25 Vertical Axial Strain Distribution Across CFSSP-B1 Steel Skin at 10 inch from Base

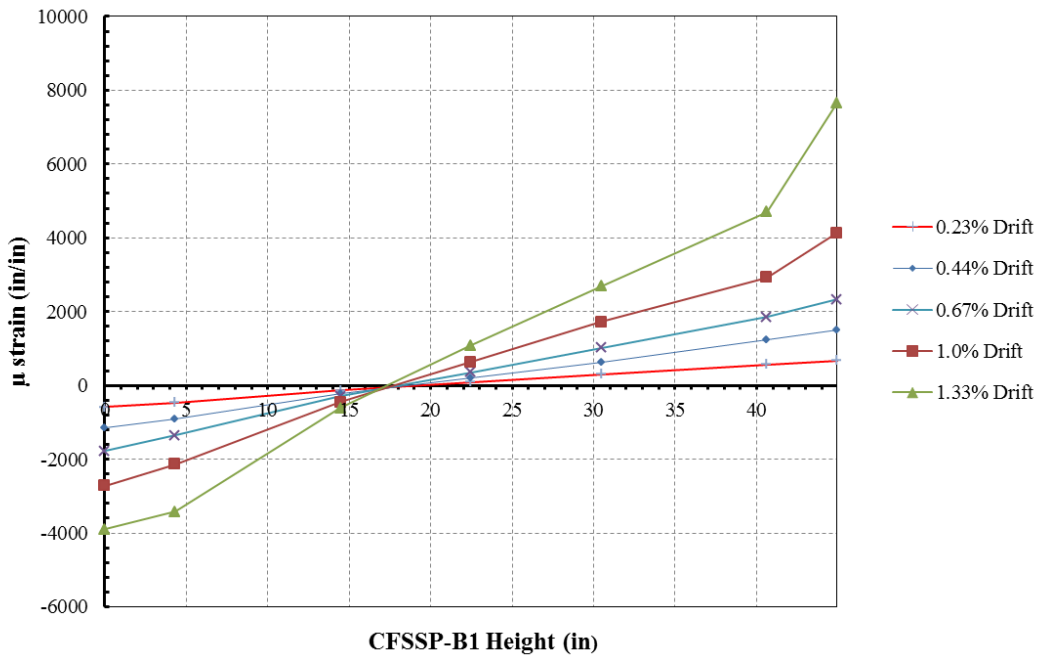


Figure 6-26 Vertical Axial Strain Distribution Across CFSSP-B1 Steel Skin at 16 inch from Base

6.2.11 Displacement Ductility for Specimen CFSSP-B1

The experimentally obtained force-displacement relationship for specimen CFSSP-NB2 is shown in Figure 6-27. The displacement ductility factor is obtained from the force displacement cycles envelope, used to calculate the linearized displacement ductility factor μ_D such that:

$$\mu_D = \frac{\Delta_{\max}}{\Delta_y} = \frac{4.80}{1.2} = 4.0 \quad (6.26)$$

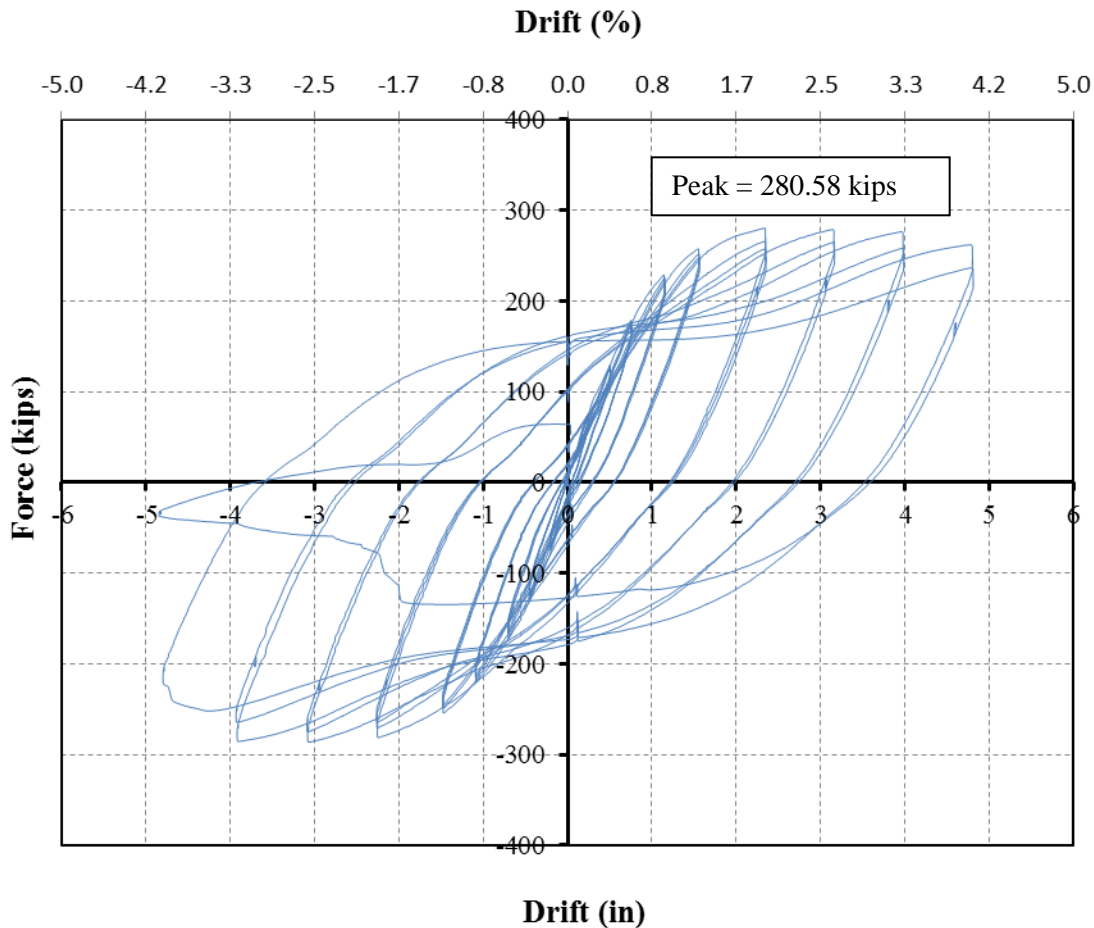


Figure 6-27 Actuator Force vs Lateral Drift for Specimen CFSSP-B1

For loading cycles up to 4% lateral drift, specimen, CFSSP-B1 managed to sustain a lateral load higher than that corresponding to the plastic moment capacity of the specimen cross-section. The degrading strength of the specimen was rather very sudden in the second cycle at 4% drift.

6.2.12 Curvature Ductility for Specimen CFSSP-B1

Curvatures were determined following the procedure mentioned earlier for specimen CFSSP-B1. The moment curvature relationships extracted from the linear potentiometers are presented in Figures 5.102 to 5.107. Figure 5.108 presents the curvature extracted from the string potentiometers. The curvature ductility based on the first yield is given by:

$$\mu_{\phi} = \frac{\phi_{\max}}{\phi_y} = \frac{92}{3.12} = 29.28 \quad (6.27)$$

The curvature ductility based on a bi-linear moment-curvature is given by:

$$\mu_{\phi} = \frac{\phi_{\max}}{\phi_y} = \frac{92}{8} = 11.5 \quad (6.28)$$

Figure 5.109 shows the values of curvatures extracted from the linear potentiometers and string potentiometers. There appeared to be some malfunctioning in linear potentiometers LP2, LP8, LP3 and LP9, as their readings were less than the expected values; however, the average curvature for the values extracted from the linear potentiometers is close to the values extracted from the string potentiometers such that:

- The average yield curvature for the linear potentiometers, $\phi_y = 5.21 \times 10^{-5}$ 1/in
- The yield curvature from string potentiometers, $\phi_y = 3.12 \times 10^{-5}$ 1/in
- The average plastic curvature for the linear potentiometers, $\phi_p = 14.49 \times 10^{-5}$ 1/in
- The plastic curvature from string potentiometers, $\phi_p = 11.58 \times 10^{-5}$ 1/in

The values of the yield and plastic curvatures calculated using strain values on the extreme fiber of the specimen and the position of neutral axis calculated using axial strain distribution were shown earlier.

Yield curvature is calculated as follows:

$$\phi_y = \frac{\varepsilon_{y,HSS}}{h - c} = \frac{1566 \times 10^{-6}}{25.5} = 6.14 \times 10^{-5} \text{ 1/in} \quad (6.29)$$

Plastic curvature is calculated as follows:

$$\phi_p = \frac{\varepsilon_{HSS,plastic}}{h - c'} = \frac{5325 \times 10^{-6}}{28} = 19 \times 10^{-5} \text{ 1/in} \quad (6.30)$$

6.2.13 Shape Factor for Specimen CFSSP-B1

The shape factor for the CFSSP-B1 wall can be given by:

$$K = \left(\frac{M_P}{M_y} \right)_{Experimental} = \frac{27360}{21360} = 1.28 \quad (6.31)$$

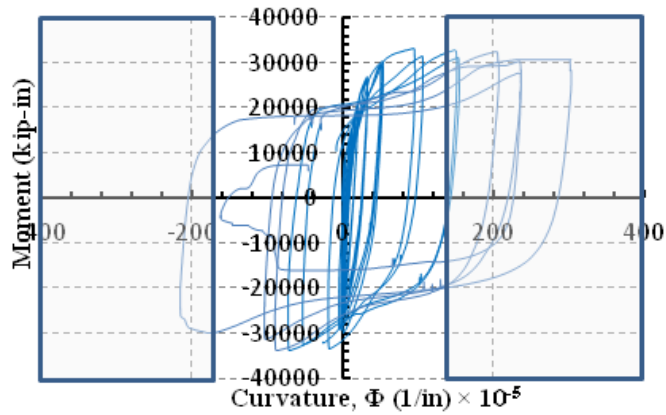


Figure 6-28 Moment Vs Curvature using Linear Potentiometer at 2 inch from Base, CFSSP-B1

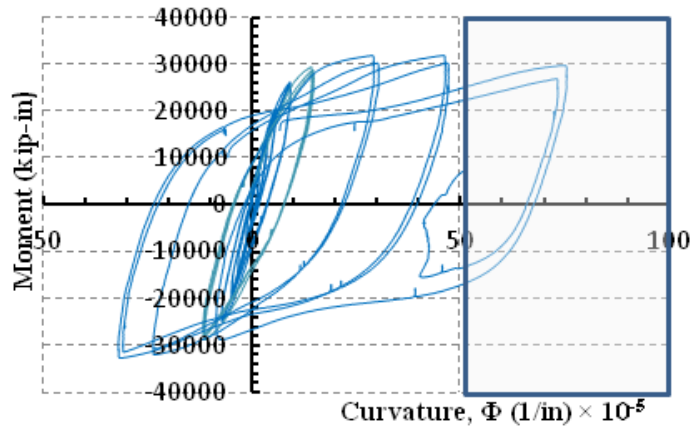


Figure 6-29 Moment Vs Curvature using Linear Potentiometer at 6 inch from Base, CFSSP-B1

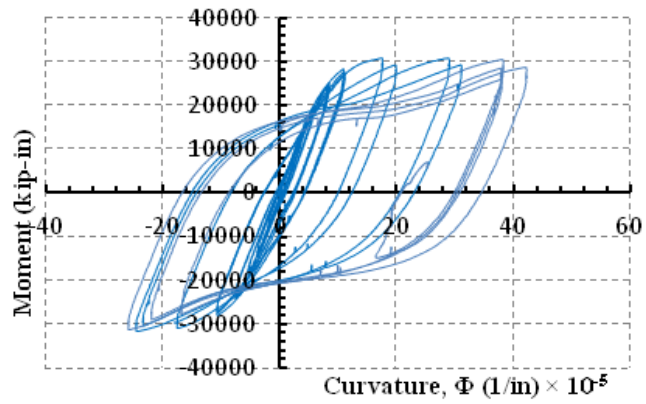


Figure 6-30 Moment Vs Curvature Linear Potentiometer at 10 inch from Base, CFSSP-B1

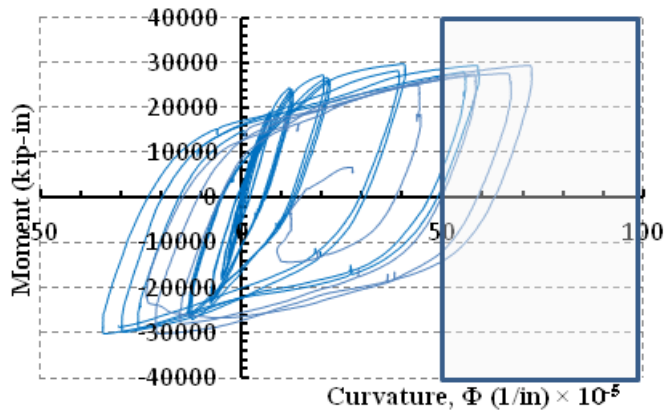


Figure 6-31 Moment vs Curvature using Linear Potentiometer at 2 inch from Base, CFSSP-B1

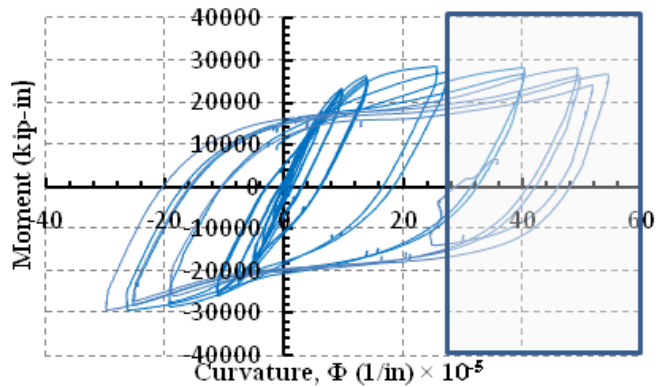


Figure 6-32 Moment vs Curvature using Linear Potentiometer at 6 inch from Base, CFSSP-B1

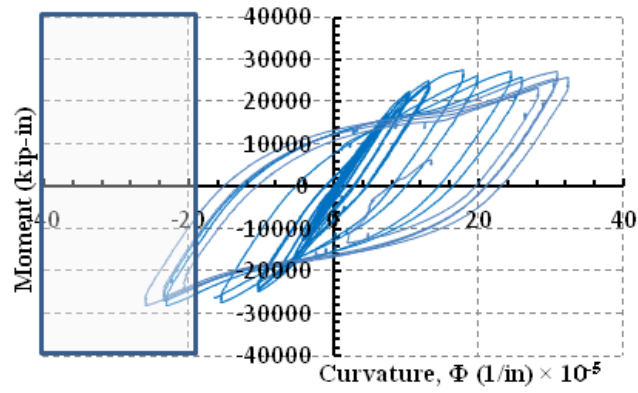


Figure 6-33 Moment vs Curvature using Linear Potentiometer at 10 inch from Base, CFSSP-B1

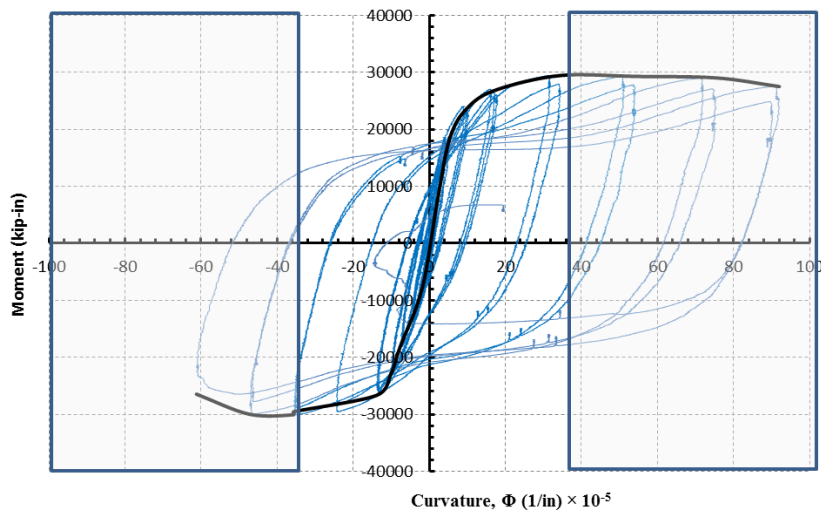


Figure 6-34 Moment vs Curvature using Linear Potentiometer at 15 inch from Base, CFSSP-B1

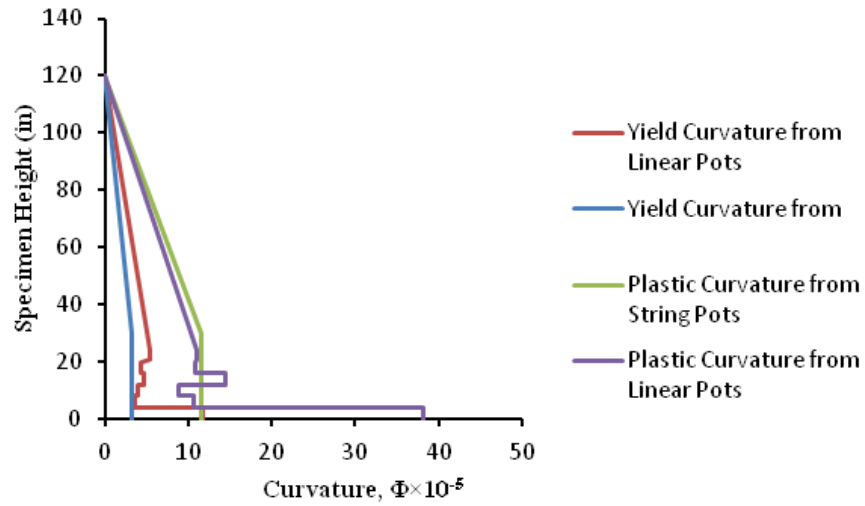


Figure 6-35 Curvature Distribution along the Length of Specimen CFSSP-B1

6.2.14 Strain Distribution for Specimen CFSSP-B2

For specimen CFSSP-B2, the axial strain distribution across the specimen section at 12" and 22" from the top of the foundation is shown in Figure 6-36 and Figure 6-37, respectively. Specimen CFSSP-B2 was able to attain its plastic moment capacity at 12" from the foundation between lateral drifts of 1.0% and 1.33%. Strain gauge readings were recorded up to a lateral drift of 2%; the outer most strain gauge on the HSS had strain of 8673 $\mu strain$ at 2% drift. The elastic neutral axis and the plastic neutral axis are at 19" and 17.5" respectively from the outer most fiber on the compression flange. As for the section at 22" from the footing face almost 20" of the web did not exhibit yielding.

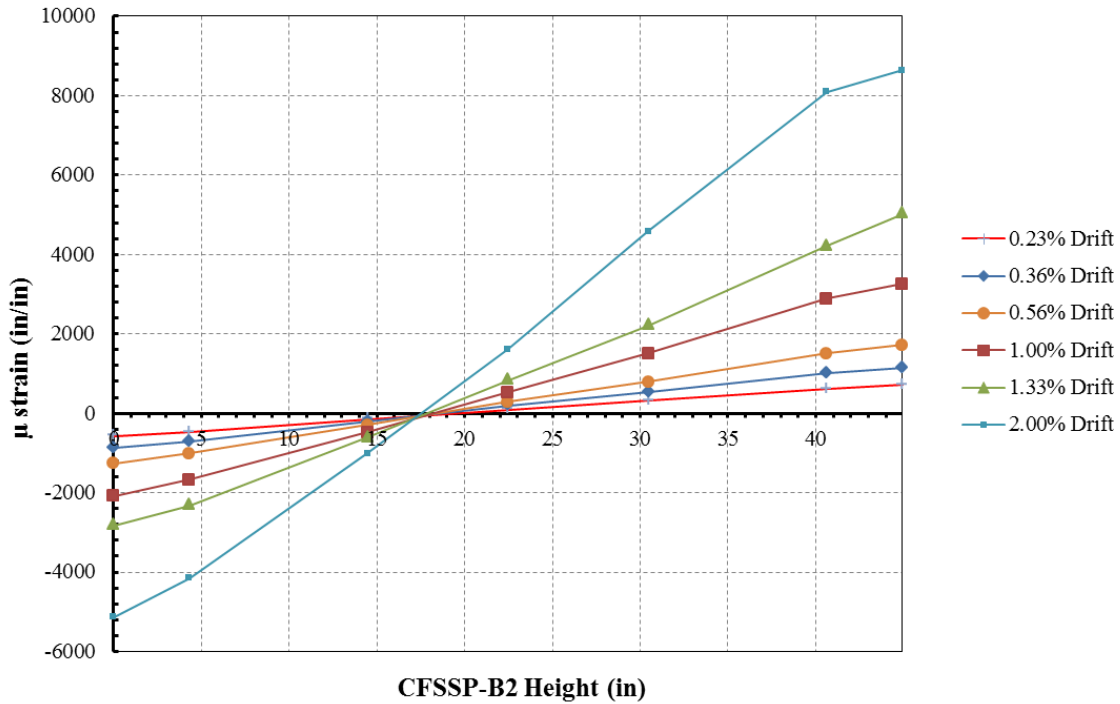


Figure 6-36 Vertical Axial Strain Distribution across CFSSP-B2 Steel Skin at 12 inch from Base

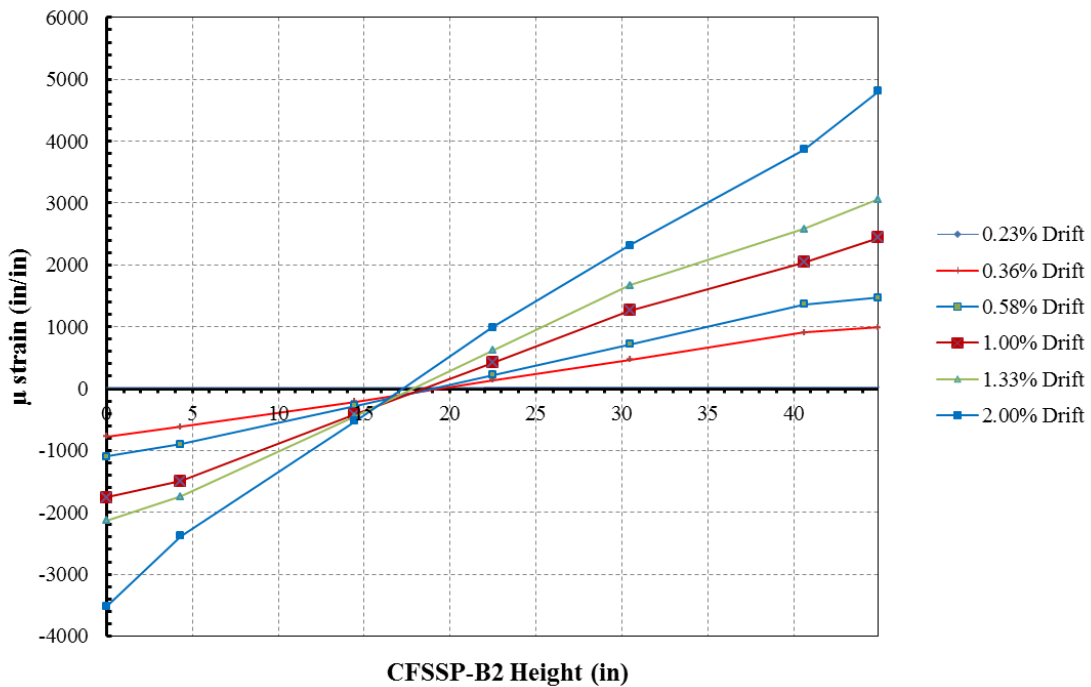


Figure 6-37 Vertical Axial Strain Distribution Across CFSS-B2 Steel Skin at 22 inch from Base

6.2.15 Displacement Ductility for Specimen CFSSP-B2

The experimentally obtained force-displacement relationship for specimen CFSSP-NB2 is shown in Figure 5.112. The displacement ductility factor is obtained from the force displacement cycles envelope, used to calculate the linearized displacement ductility factor μ_D such that:

$$\mu_D = \frac{\Delta_{\max}}{\Delta_y} = \frac{5.7}{0.90} = 7.125 \quad (6.32)$$

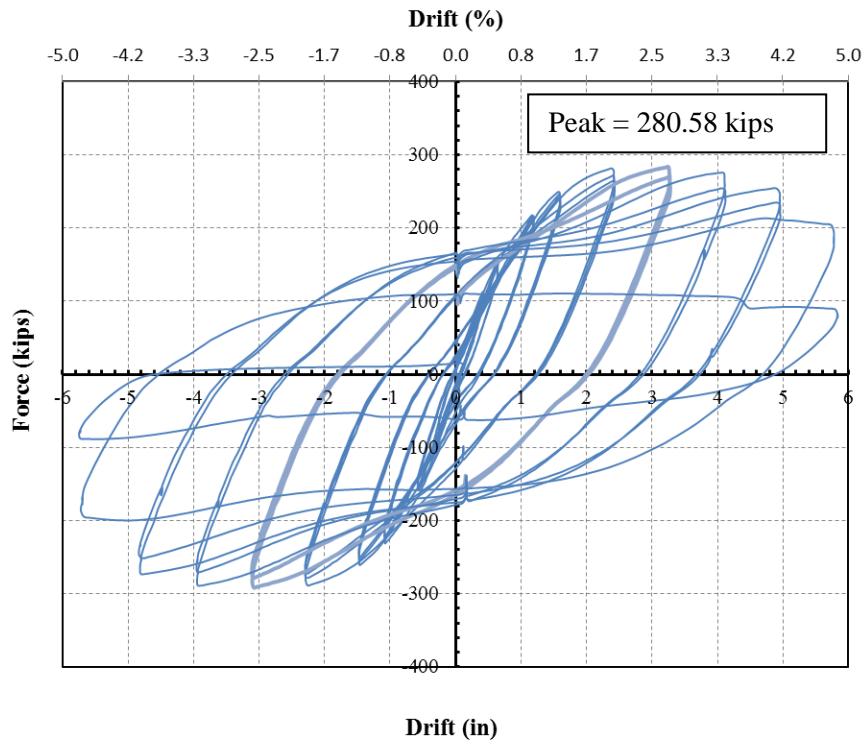


Figure 6-38 Actuator Force Vs Lateral Drift for Specimen CFSSP-B2

For loading cycles up to 4% lateral drift, specimen CFSSP-B1 managed to sustain a lateral load higher than that corresponding to plastic moment capacity of the specimen cross-section. The strength degradation in the specimen was rather sudden in the second cycle of 4% drift loading step.

6.2.16 Curvature Ductility for Specimen CFSSP-B2

Curvatures were determined as mentioned earlier for specimen CFSSP-B1. The moment curvature relationships extracted from the linear potentiometers are presented in Figure 6-39 to Figure 6-44. The moment curvature relationships extracted from the string potentiometers is presented in Figure 6-45. The curvature ductility based on the first yield is given by:

$$\mu_{\phi} = \frac{\phi_{\max}}{\phi_y} = \frac{66.61}{7.17} = 9.29 \quad (6.33)$$

The curvature ductility based bi-linear moment-curvature is given by:

$$\mu_{\phi} = \frac{\phi_{\max}}{\phi_y} = \frac{66.61}{12} = 5.55 \quad (6.34)$$

There were some malfunctioning in the linear potentiometers LP2, LP8, LP3 and LP4 as their reading included too much noise; for that reason, the average of curvature obtained from the values extracted from linear potentiometers deviates from the values extracted from string potentiometers by almost 35%. Results obtained are:

- The average yield curvature for the linear potentiometers, $\phi_y = 3.49 \times 10^{-5}$ 1/in
- The yield curvature from string potentiometers, $\phi_y = 7.46 \times 10^{-5}$ 1/in
- The average plastic curvature for the linear potentiometers, $\phi_p = 9.46 \times 10^{-5}$ 1/in
- The plastic curvature from string potentiometers, $\phi_p = 14.92 \times 10^{-5}$ 1/in

The values of the yield and plastic curvatures calculated using strain values on the extreme fiber of the specimen and the position of neutral axis calculated using axial strain distribution were shown earlier.

Yield curvature is calculated as follows:

$$\phi_y = \frac{\varepsilon_{y,HSS}}{h-c} = \frac{1566 \times 10^{-6}}{26} = 60.23 \times 10^{-5} \text{ 1/in} \quad (6.35)$$

Plastic curvature is calculated as follows:

$$\phi_p = \frac{\varepsilon_{HSS,plastic}}{h-c'} = \frac{4017 \times 10^{-6}}{27.5} = 14.6 \times 10^{-5} \text{ 1/in} \quad (6.36)$$

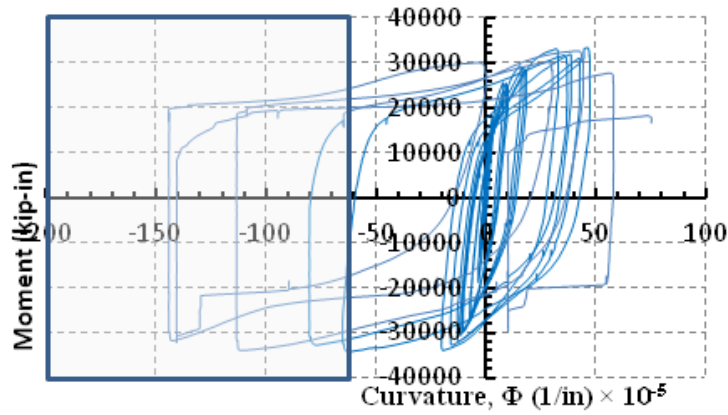


Figure 6-39 Moment Vs Curvature using Linear Potentiometer at 2 inch from Base, CFSSP-B2

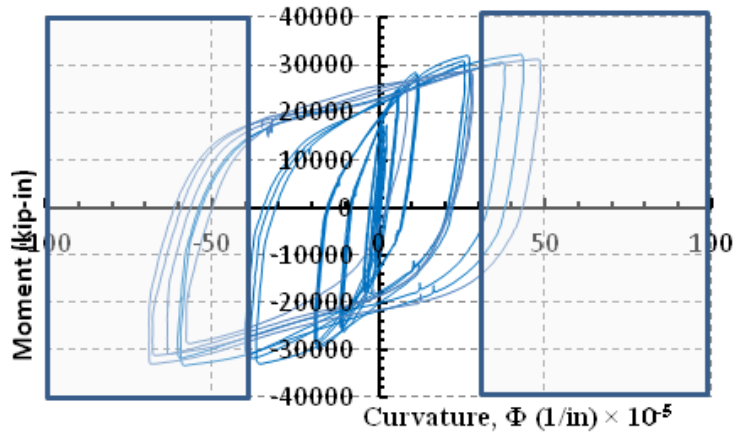


Figure 6-40 Moment vs Curvature using Linear Potentiometer at 6 inch from Base, CFSSP-B2

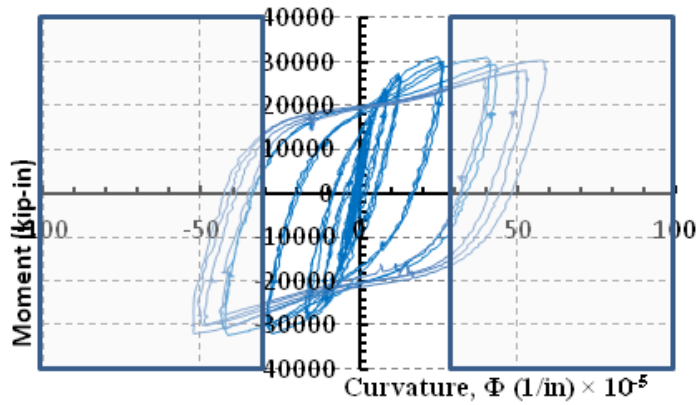


Figure 6-41 Moment vs Curvature using Linear Potentiometer at 10 from Base, CFSSP-B2

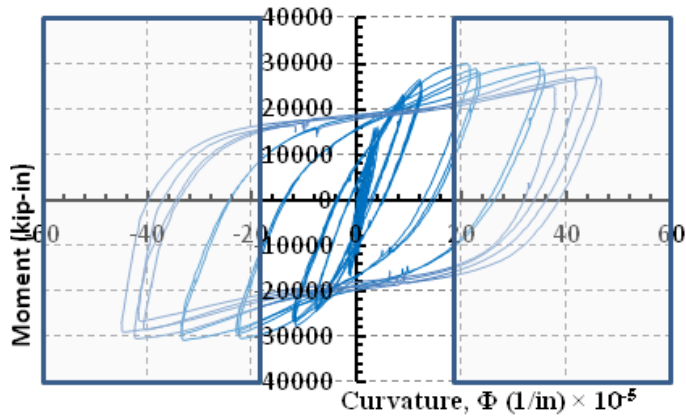


Figure 6-42 Moment vs Curvature using Linear Potentiometer at 14 inch from Base, CFSSP-B2

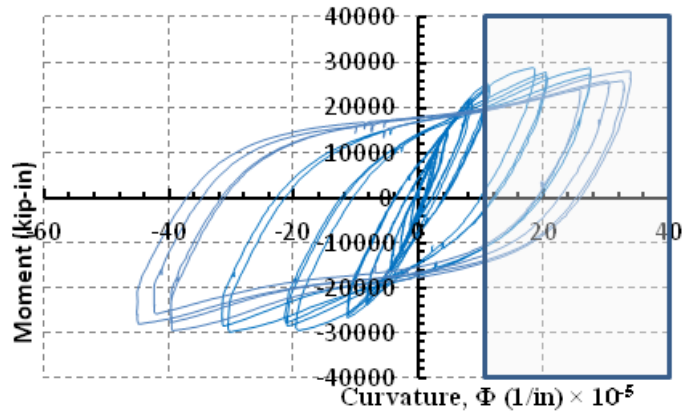


Figure 6-43 Moment vs Curvature using Linear Potentiometer at 18 inch from Base, CFSSP-B2

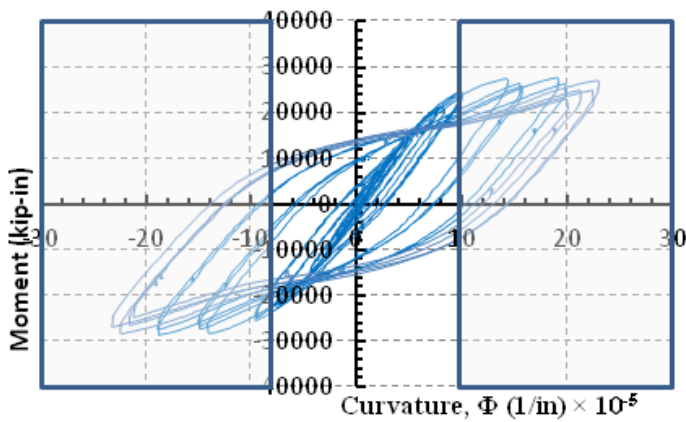


Figure 6-44 Moment vs Curvature using Linear Potentiometer at 22 inch from Base, CFSSP-B2

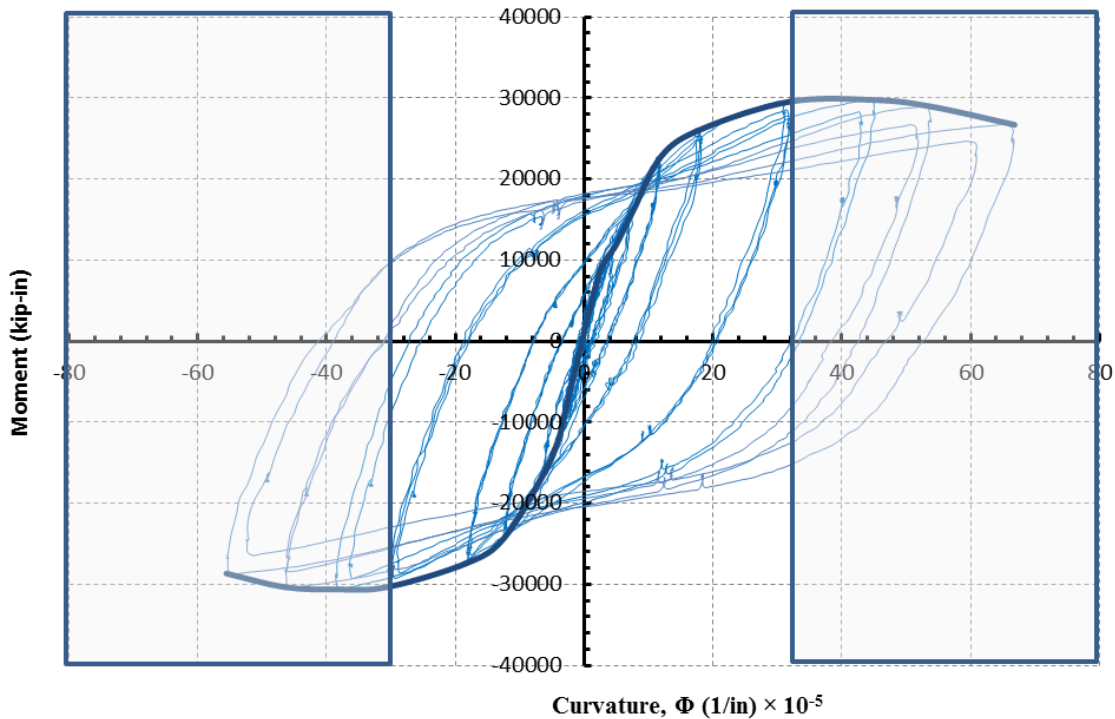


Figure 6-45 Moment vs Curvature using String Potentiometer at 15 inch from Base, CFSSP-B2

6.3 Summary of Test Results

As a general observation, all of the tested specimens were to sustain a lateral load higher than that corresponding to development of the plastic moment at the base of the wall, and all specimens developed a similar ultimate behavior, with local buckling developing during ductile response while sustaining a lateral load corresponding to M_p . Fracture in all specimens developed upon repeated cycles of local buckling of the steel web plate and of the HSS, and accelerated by fracture of the welding between the tie bars and skin plate. Test results are summarized in Table 6-4. Review of the videos recorded during the experiments showed that for Specimen CFSSP-B2, fracture started independently on the HSS at a different location, and that the wall would have failed at the same drifts even if fracture has not developed slightly earlier at the ties and that indicates that using different welding details between the tie bar and the skin plate is not the factor controlling the behavior of the tested walls.

Table 6-4 Summary of the Test Results

Specimen (1)	CFSSP-NB1 (2)	CFSSP-NB2 (3)	CFSSP-B1 (4)	CFSSP-B2 (5)
Peak Load, kips	305	304	281	283
$\frac{M_{\max}}{M_p}$	1.13	1.13	1.19	1.2
Max displ., Δ_{\max} (in)	4.10	3.67	4.8	5.0
Yield displ., Δ_y (in)	0.8	1	1.2	0.9
Displacement ductility, μ_D	5.13	3.67	4.0	5.50
Curvature ductility, μ_ϕ	7.74	6.54	11.5	5.55
Drift at local buckling	1.8	1.8	2	2

Chapter 7

ANALYSIS OF THE CFSSP-WALLS

7.1 Introduction

In this chapter, numerical analysis of the tested CFSSP-Walls is presented together with a limited study on the parameters affecting the design of the CFSSP-Walls. The chapter starts with fiber analysis using the XTRACT software in section 7.2, which is used to calculate the cross-section capacity for the tested CFSSP-Walls, calculate curvature ductility, estimate the length of the formed plastic hinge, and calculate the effective stiffness of the CFSSP-Walls with different configurations.

Then, in section 7.3, finite element analysis is used to construct mathematical models to simulate the structural behavior of CFSSP-Walls under in-plane static cyclic loading. These models are intended to provide calibrated information on the hysteretic behavior of CFSSP-Walls that could be extrapolated to investigate the seismic behavior of such walls. The modeling process started by building finite element models for the tested specimens presented in chapters 4 and 5 of this document in order to establish credible benchmarked models capturing as much as possible the different aspects of the CFSSP-Walls structural behavior. This section starts by explaining the model used, then the type of finite elements used to model the different structural components of the CFSSP-Walls. Section 7.3.3 presents the materials models used for the different structural components of the CFSSP-Walls, section 7.3.4 presents the methods used to model the interaction between the wall's different components, and section 7.3.5 presents the criteria used for acceptance the analysis results.

. In section 7.3.6, the simulation for specimens of Group CFSSP-NB is presented considering a fixed base models and models of the foundation, and section 7.3.8 presents the simulation of specimen of Group CFSSP-B considering fixed base models. These models where used to investigate the ductility of the walls, calculate their displacement ductility coefficient, and determine the length of their plastic hinge.

Section 7.3.9 presents a parametric study in which different aspects, not addressed in the experimental program of CFSSP-Walls design, are considered. The parameters considered are different D/t ratio for the CFSSP-Walls, different spacing of the tie bars, and larger thickness of concrete; more specifically, values of the parameters considered are D/t ratio equals to $0.076 E/F_y$, and S/t ratio of 50.

Section 7.4 presents a summary of the findings in chapter 6 together with a comparison between the results obtained in the experimental program, fiber analysis, plastic analysis, and the finite element analysis.

7.2 Analysis Using XTRACT

7.2.1 General

The XTRACT software was used to investigate the performance of the tested CFSSP-Walls, with emphasis on the values for ultimate moment, M_u , yield moment M_y , curvature values, and the effective value for elastic stiffness EI_{eff} , considering the difference in the steel strengths of the HSS part of the cross-section and the steel web. For the tested specimen CFSSP-NB, to be able to use XTRACT, the steel skin was replaced by reinforcement bars at the perimeter of the cross section. Where possible, the steel of the skin plate (HSS part or steel web) was considered to act as the cover for the cross-section. Note that the skin plate HSS had an average value F_y of 43 ksi and F_u of 73.67 ksi, while the web skin plate have F_y of 61.4 ksi and F_u of 82.47 ksi (section 4.3.2). An average bilinear steel material model was used for the skin plate and the HSS having F_y of 62 ksi. The concrete material model used was that for confined concrete shown in Figure 7-1.

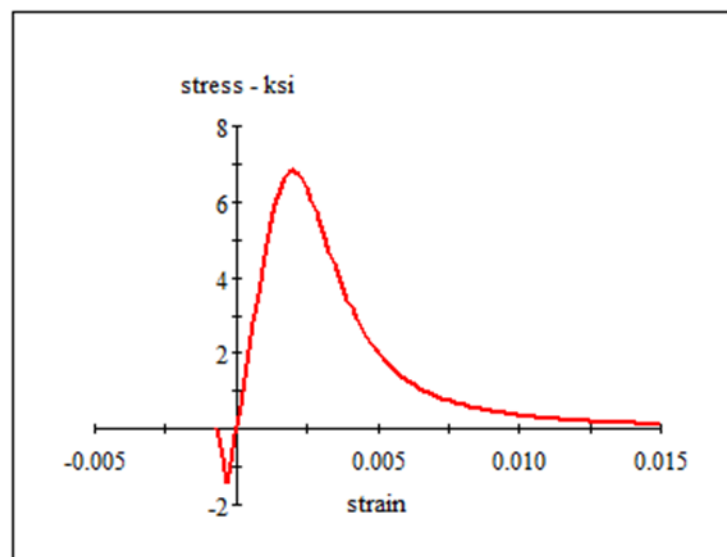


Figure 7-1 Confined Concrete Model Used in XTRACT Analysis

7.2.2 Specimen CFSSP-NB

Summary for the XTRACT analysis results is presented in Table 7-1. The analysis report can be found in Appendix C (which presents the analysis reports for all XTRACT models used in this project). The cross section showing the specimen CFSSP-NB used in XTRACT is shown in Figure 7-2. It was already shown in Chapter 3 that the XTRACT results, given the above assumed material properties, matched relatively well the value of the plastic moment. It was also shown in Chapter 5 that specimen CFSSP-NB developed a maximum flexural strength 14% greater than the theoretical value of M_p . It is therefore not

surprising that the strength provided by XTRACT also underestimated the CFSSP-NB cross-section capacity by 15%

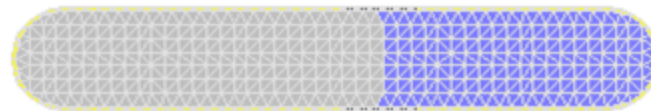
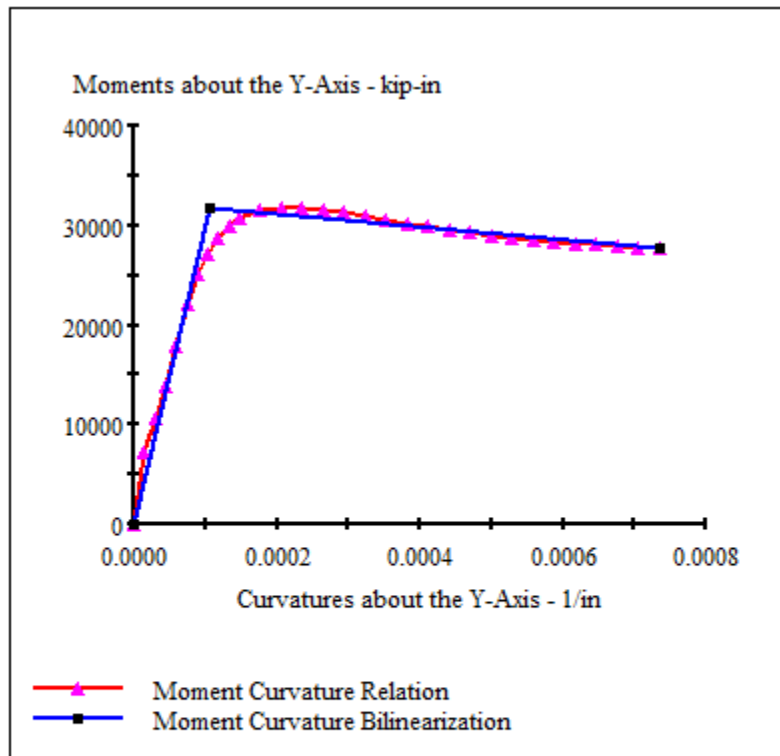


Figure 7-2 Moment Curvature Relation for Specimen CFSSP-NB in Xtract Analysis

The summary of the Xtract analysis is presented in Table 7-1, where the maximum capacity M_u is presented together with M_y , which is the moment corresponding to first yield of the steel fibers. The curvature ductility is presented as well, which is the ratio between curvature at maximum moment and curvatures that corresponds to curvature at first yield of the steel fibers. The value of M_p agrees with the ultimate moment predicted by using Xtract.

Table 7-1 Summary of Xtract Analysis for Specimen CFSSP-NB

Specimen	Xtract Moments (kip-in)		Xtract Curvature, and Curvature Ductility (1/in)		Test Results to
	M_u (1)	M_y (2)	Φ_y (3)	μ_ϕ (4)	M_{test}/M_{XTRACT} (5)
CFSSP-NB1	31760	22020	74.12E-6	6.871	1.15
CFSSP-NB2	31760	22020	74.12E-6	6.871	1.148

7.2.3 Specimen CFSSP-B

Summary for the XTRACT analysis results for specimen CFSSP-B1 is presented in Table 7-2, the analysis report can be found in Appendix C. The analysis predicted the M_p of the specimen with a 2.9% difference, Figure 7-3 presents moment curvature relationship for specimen CFSSP-B.

Table 7-2 XTRACT Analysis Results for Specimen CFSSP-B

Specimen	XTRACT Moments (kip-in)		XTRACT Curvature, and Curvature Ductility (1/in)		Test Results to
	M_u (1)	M_y (2)	Φ_y (3)	μ_ϕ (4)	M_{test}/M_{XTRACT} (5)
CFSSP-B1	29050	19520	80.67E-6	3.243	1.16
CFSSP-B2	29050	19520	80.67E-6	3.243	1.17

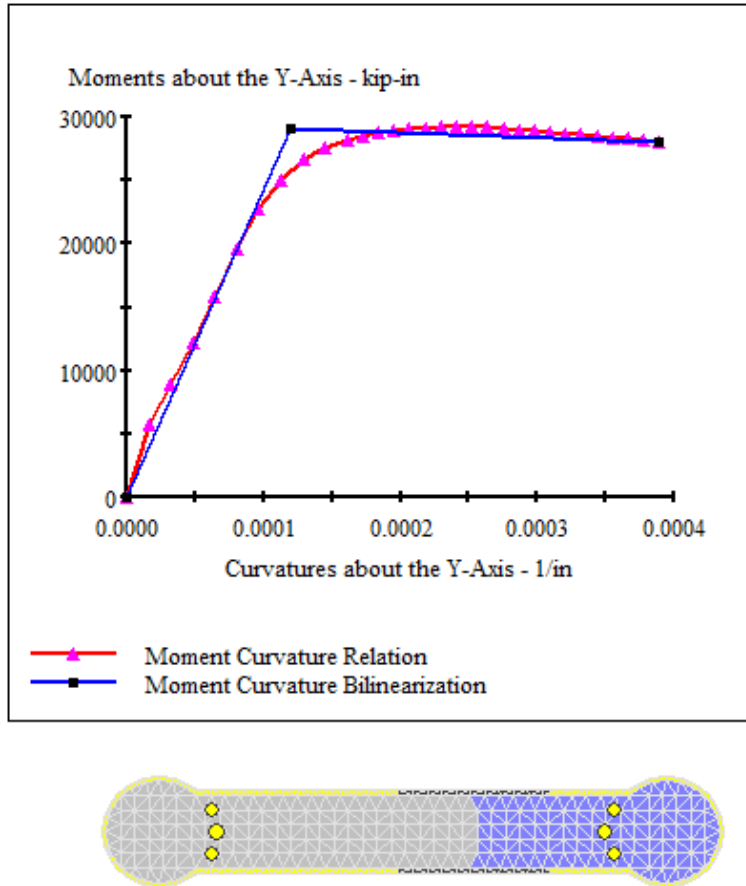


Figure 7-3 Moment Curvature Relationship for Specimen CFSSP-B in XTRACT

Noted that, in the above comparison, the XTRACT steel material used is effectively an elasto-perfectly plastic material with linear hardening,

7.3 Finite Element Analysis

7.3.1 General

The finite element models were constructed using the ABAQUS 6.10 EF2 software, as described in chapter 3 of this document. The benchmark models used structural material selected to represent the material properties obtained from tensile coupon testing of steel, and axial compressive concrete cylinder tests. Models used were meant to capture the behavior of the tested specimens in terms of elastic stiffness, plastic moment capacity M_p , ductility, and cyclic behavior. Building a model able to replicate the behavior of the tested specimen also provides opportunities to numerically investigate the behavior of walls having different geometry and material properties. The construction of adequate models involves choosing the type of elements that are most appropriate to model the different components of the CFSSP-

Walls, the selection of suitable material model parameters, the modeling of the interaction between the different structural components of the CFSSP-Walls, and finally selection of the most appropriate finite elements analysis method (analysis scheme) that could accommodate the high non-linearity (geometrical and material) of CFSSP-Walls subjected to large cyclic inelastic displacements.

7.3.2 Type of Finite Elements Used

The elements used for the different components of the finite elements models in this chapter are the same as those used in Chapter 3 of this document, where for the modeling of the steel skin plates and the concrete core, 8 nodes brick C3D8R element were used, while the tie bars were modeled using beam element B31.

7.3.3 Modeled Material Properties

7.3.3.1 Concrete Material Model

The concrete material model used in finite element simulation of the tested CFSSP-Wall specimen is the Concrete Damage Plasticity Model (CDP). The data used for this model was based on the average value of the concrete cylinders test results (presented in Chapter 4), and also based on Liang et al (2009) proposed concrete material model to be used for concrete in rectangular CFT. The proposed concrete model used assumes that the concrete material model has a ductile plateau (i.e., is able to sustain strength while undergoing large strains) in compression. The tensile strength of concrete was taken equal to $0.6\sqrt{f'_c}$ with ultimate tensile strain equals to 10 times the strain at cracking. All other parameters needed to establish the CDP model in Abaqus were described in Section 3.6.4, of this document.

For example, for the concrete model for specimen CFSSP-NB1, the average cylinder strength (reported in chapter 4), f'_c , was taken as equal to 6.83 ksi and, accordingly, the tension strength was taken as equal to 1.57 ksi. The concrete in the tension was considered to lose strength linearly for strains beyond the peak tension strength, as it was shown through preliminary analyses that the shape of the strength degradation curve on the tension side (be it linear or parabolic) does not affect the outcome of the analysis; this is attributed to the fact that tension strength is small compared to the compression strength and the fact that the contribution of the concrete strength to the total capacity of the cross section is on the order of 15%.

The concrete mix used in construction of the tested specimen had fly-ash in order to improve concrete workability and facilitate its casting in the relatively narrow steel sandwich panel. In the existing literature (e.g., Yoshitake et al 2012), a great variability is reported for the value of elastic modulus of such concrete, with values ranging between 50% to 80% of the E_c value specified by the ACI 318 (2008) for conventional concrete. For the tested specimen, three cylinders (of the concrete in specimen CFSSP-B2)

were tested while recording their force displacement relationship in an attempt to experimentally obtain the elastic modulus of the concrete used for the specimens (section 4.3.1), however the test rate for these cylinders was relatively fast, relatively few number of cylinders were used, and the results were deemed not representative of the actual elastic modulus value. Therefore, the value of E_c was taken equal to $0.8E_c$ of the value calculated by ACI 318 (2008). As a result, for that specimen, the value of E_c was taken equal to 3769 ksi. A poisson's ratio of 0.2 was also used in the analyses, it should be noted here that the values of elastic modulus was taken between $0.5E_c$ and $0.8 E_c$ in various analyses (not included in this report), before settling on the final value, based on results trying to match the initial elastic stiffness.

The concrete strength backbone curve used to simulate specimen CFSSP-NB1 is shown in Figure 7-4. The values of stresses and the inelastic strains used to construct the backbone curve for the concrete, together with the damage factors used for cyclic analysis, are summarized in Table 7-3. All other parameters needed for the CDP model were taken to be the same as what was reported in Chapter 3, section 3.6.

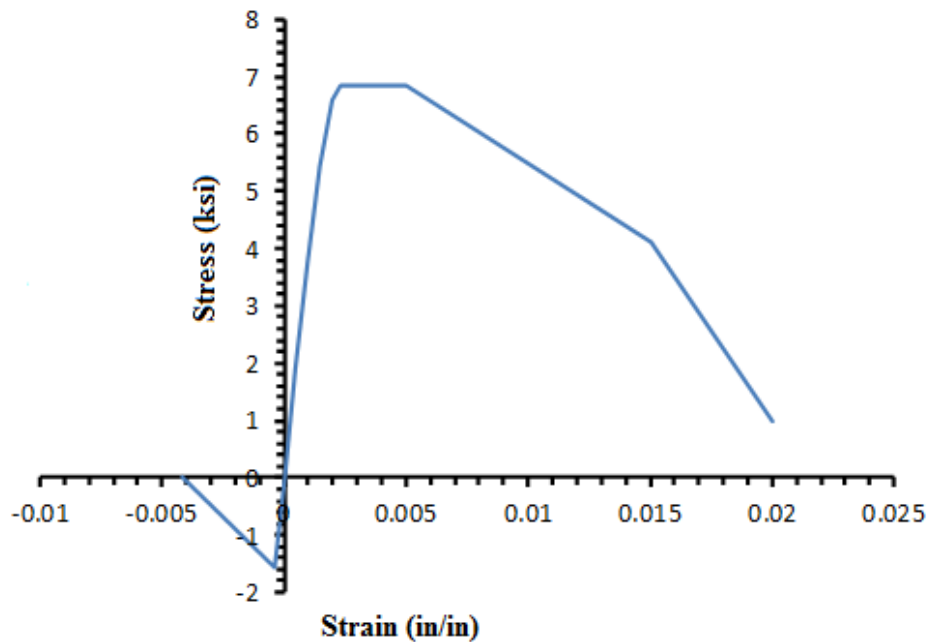


Figure 7-4 Concrete Backbone Curve Constructed for CFSSP-NB1Abaqus Model

Table 7-3 Stress-Strain Values used for Concrete Backbone Curve, Abaqus Model for CFSSP-NB1.

Strain	Stress	inelastic strain	Damage
-0.00416	0	0.00374	1
-0.00042	-1.568	0	0
0	0	0	0
0.0005	1.883759	0	0
0.001	3.742269	0	0
0.0015	5.426821	0.0005	0
0.002	6.57356	0.001	0
0.00235	6.83	0.00135	0
0.0025	6.83	0.0015	0
0.003	6.83	0.002	0
0.0035	6.83	0.0025	0
0.004	6.83	0.003	0
0.0045	6.83	0.0035	0
0.005	6.83	0.004	0
0.015	4.1	0.014	0.399471535
0.02	1	0.019	0.853529643

7.3.3.2 Steel Material Model

The tie bars were considered to be elastic and made of steel having $F_y = 50$ ksi and an elastic modulus E of 29000 ksi. However, for the modeling of the steel material used for the steel web and the HSS, the actual backbone curve obtained from test coupons was used to describe the material model that involves material damage evaluation, as shown below.

The backbone curve obtained from uniaxial tension coupon testing is the main source of data used to build the steel material models used to simulate the steel skin plates of the CFSSP-Walls. The coupon test results values for both the round HSS and the steel web were used to build their representative models in Abaqus finite element analysis.

However, true stress and true strain are used to establish the material backbone curve used to describe the material in Abaqus. Accordingly, the average engineering stress-strain values obtained from the uniaxial test (coupon test) were converted to true stress and logarithmic (true) plastic strain through the following equations: $\sigma_{true} = \sigma_{nom} (1 + \epsilon_{nom})$

$$\epsilon_{ln}^{pl} = \ln(1 + \epsilon_{nom}) - \frac{\sigma_{true}}{E}$$

The resulting average true stress-strain value for the HSS part of the tested CFSSP-Wall is shown in Figure 7-5, while that for the steel web of the tested CFSSP-Walls is shown in Figure 7-6.

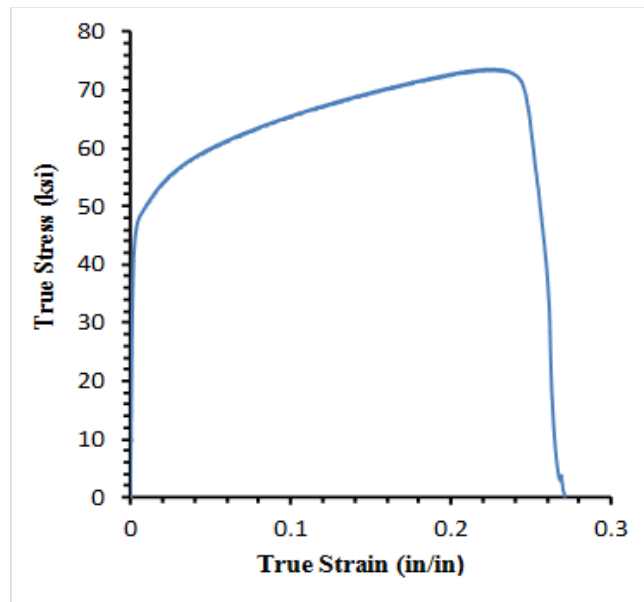


Figure 7-5 Average True Stress-True Strain for HSS

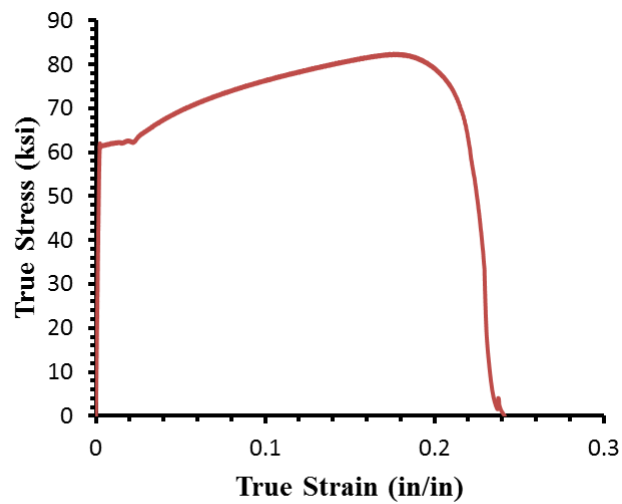


Figure 7-6 Average True Stress-Strain for the Steel Web

Abaqus identifies the steel ductile material response in three parts as identified in Figure 7-7, where part “a-b” is the elastic part of the curve defined by the elastic modulus and poisson’s ratio. The second part, segment “b-c”, represents the strain hardening part of the steel, where here a combined Kinematic/isotropic strain hardening rule was used. The third part of the curve, part “c-d”, models the damaged or degraded behavior of the material.

Note that the degraded part of the curve is identified by what Abaqus calls a “Ductile criterion”, expressed by a group of parameters that identify the onset of damage in the ductile material, and model strength degradation. These parameters are:

- ϵ_D^{pl} , the plastic strain at the onset of damage, effectively equal to the plastic strain at F_u
- $\eta = -p/q$, a tri-axiality ratio described to be the “ratio between axial pressure stress, P , and Von Misses stresses, q ”, which, in uniaxial tension test, at the fracture location of the coupon, is the ratio between axial stresses and Von Misses stresses. This value technically depends on the type of the coupon tested (i.e., flat plates, bars, etc) and the type of material tested.
- Strain rate of the tested coupons (in/in/sec), which refers to the strain rate at which the uniaxial coupon tests were performed. A summary of the damage initiation parameters used in the analyses presented in this chapter is provided in Table 7-4.

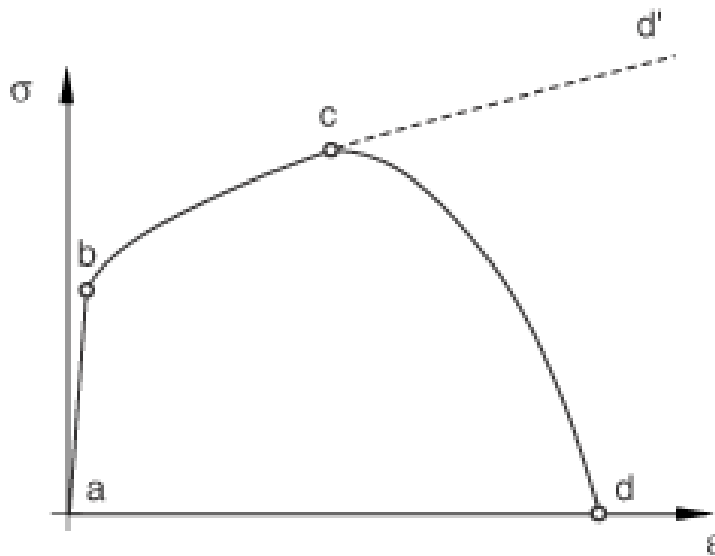


Figure 7-7 Typical uniaxial Stress-Strain Response of a metal Specimen, Abaqus User's Manual

Table 7-4 Damage Initiation Parameters

Damage Parameters	Reference/source of data	Steel Web Plate	Round HSS Part
$-p/q$	Ywan et al (2007)	0.8	0.8
Strain Rate	1/16 inch /min, data from SEESL	0.00052	0.00052
ε_D^{pl}	Extracted from average coupons data, used for each test	Varies	Varies

For cyclic loading, the “damage evolution” criterion is a parameter that allows to model the stiffness degradation that happens in the material during cyclic excursions beyond the ultimate strain.

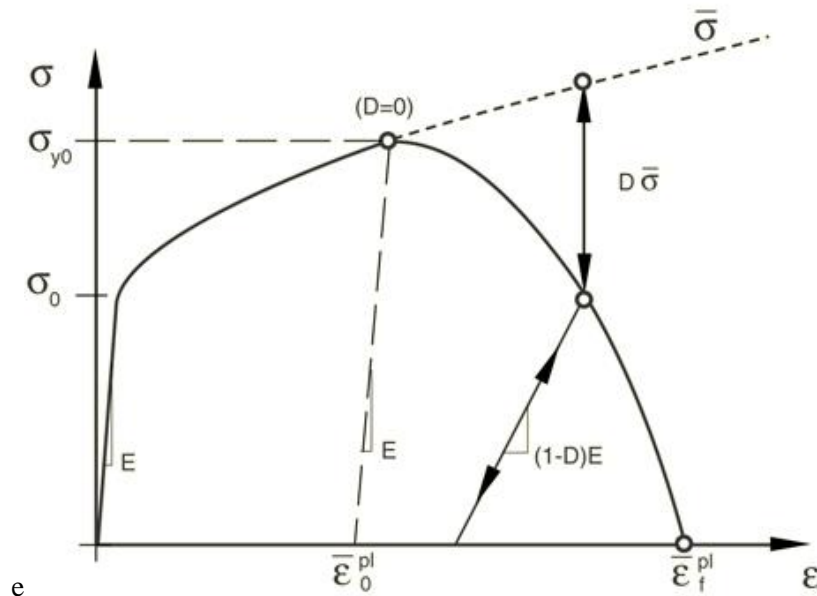


Figure 7-8 Calculation of the Damage Factor, Abaqus user's Manual

The selected parameters for this damage factor, D , for the steel material used were calculated based on the following

$$\bar{\sigma} = D\bar{\sigma} + \sigma$$

$$D = 1 - (\sigma/\bar{\sigma})$$

where,

- $\bar{\sigma}$ is the undamaged stress path (fictitious path assuming material would not degrade after reaching ultimate value), assumed here to be a linear value having value of maximum attained stress, This part is considered as if the plastic part of the curve would extend beyond ultimate strength value with no degrading.
- σ Stress at arbitrary point on the degrading part of the backbone curve, at which displacement reversal starts.

Finally after calculating the damage factor, the relationship between the damage factor and the plastic displacement is established and implemented in the damage evolution part of the material model. The plastic displacement in this case is the plastic strain multiplied by the smaller dimension of the element used to simulate the steel material under consideration. An example for the damage factor and plastic displacement is shown in Figure 7-9.

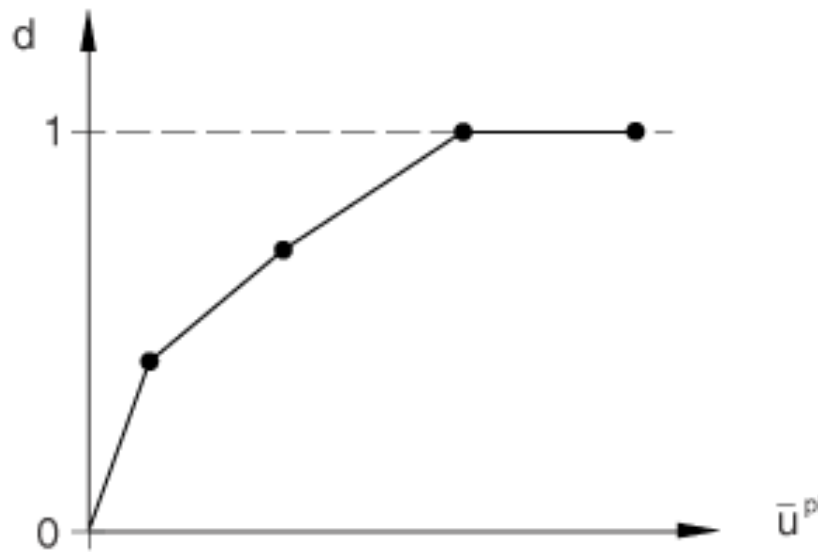


Figure 7-9 Damage factor vs Plastic Displacement (Abaqus User's Manual)

Incorporating the above damage model was done for all the Abaqus analyses used to simulate the tests results presented in chapter 5 for the CFSSP-Walls.

7.3.4 Interaction between Different Components of the Model

As described in Section 3.6.2, the interaction between the concrete core and steel skin plates was modeled by tangential friction with $\mu = 0.3$, and hard contact between steel skin and concrete in the normal direction, which allowed the skin plate to separate from the core. The tie bars were modeled as embedded (tied to) the concrete core elements, as described in Section 3.6 of Chapter 3.

7.3.5 Criteria for Analysis Acceptance and Parameters

The effectiveness of the model established in this section was evaluated based on the key information that needed to be captured by the models for the purpose of this study, namely peak load, ductility (ability of the model to sustain cyclic excursions while sustaining a large percentage of its load carrying capacity, M_p), and local buckling initiation and development. An effort was made to match the experimental results, only on that basis.

7.3.6 Specimen CFSSP-NB1 Simulation

A finite element model of specimen CFSSP-NB1 was built using Abaqus 6.10 EF2, and was subjected to same displacement history protocol as the tested specimen. Figure 7-10 shows the model, which a cantilever wall with fixed base, following the various modeling details and procedures outlined in Chapter 3.

The finite element model of specimens CFSSP-NB1 was subjected to the same displacements applied during the experiment. The first visual evidence of local buckling (out-of-plane deformation wave) was detected to occur at 1.5% drift, but it became having a significant buckling wave magnitude at a drift of 1.8%. These are almost the same drift at which local buckling was observed in the test for specimen CFSSP-NB1. Figure 7-11 shows the local buckling of the steel case at 1.8% drift. Note that the buckling wave developed between the first and the second rows of tie bars, and that local buckling occurred only in the steel web at this drift level. The HSS part of the cross section did not show any local buckling.

At drift value of 2.4%, local buckling developed in the HSS part of the cross section (Figure 7-12). Again, as observed in the experiment, the local buckling wave was continuous between the steel web and the HSS part of the cross section.

The force displacement relation resulting from the Abaqus Model, together with that of the tested specimen CFSSP-NB1, is shown in Figure 7-13. The Finite element model was able to capture the tested specimen ultimate capacity (maximum load of the analytical results is 302.56 kips which is 99.2% of the

experimental one) and was able to reasonably replicate the CFSSP-NB wall ductility. However, the model failed to perfectly represent the tested specimen based on the following observations:

- First, the finite element model (except for the first two loading cycles) developed higher strength than that obtained experimentally at given displacements. The model maximum forces in each cycle were about 20% higher than the corresponding experimental value and that up to a drift value of 0.4%. For drift values between 0.4% and 1.5% and for an additional 0.9% drift beyond that point of maximum moment, the numerically obtained strength of the model is almost agreeing with that of the tested specimens. In a general sense, such discrepancies are sometimes attributed to variability in the elastic modulus, or the speed of loading. However, this last item is not applicable here, as it was ensured in all explicit analyses done here that the kinetic energy produced in the analysis was almost zero; therefore, no inertial forces were produced during the analyses and results are believed to be representative of static analysis results.
- Second, after local buckling of the steel web, the strength obtained from the finite element model degraded faster than that in the tested specimen. More specifically, the strength in the model dropped by almost 15% over the drift from 1.75% to 2.25%, while the tested specimen developed almost the same strength over the same drifts. This difference is attributed to the limits of the mathematical model where strain values were specified to define the failure of the materials; these values are theoretical values which might not have been exceeded in the test.
- The state of stress triaxiality in the tested specimens is modeled through theoretical models where there is a relatively significant variability in the parameters that define failure criteria, specially in the case of concrete model.

In order to investigate the effect of elastic stiffness on the wall response, and to make sure that the effect of foundation flexibility were accounted for when determining the effective wall stiffness, a second model for the tested specimen was built, this time including the foundation and strong floor. The Dywidags pretension was replaced by compression forces acting on the foundation at the locations of the Dywidag bars. The foundation was modeled as an open groove (rectangular donut shaped), into which the wall was inserted and tied using tie constraint where the embedded wall was physically tied to the foundation by rebars. The foundation was modeled as elastic concrete, while the strong floor was considered as a rigid body. However, it was found that the gain of modeling full foundation instead of fixed base condition was limited compared to the variability attributed with the elastic modulus. Given the high computational cost of the full model, and because it was observed that for a given loading speed and the same elastic modulus, the fixed base model was able to capture the key features of the force displacement relationship (including the elastic portion of the curve, which indicates that the limited flexibility observed during the

test, specially at the initial cycles of loading, was not mainly attributed to foundation flexibility), all subsequent analyses use the fixed-base model. Another factor that helped to eliminate sources of flexibility of the test set-up (particularly, that of the strong wall in the lab on which the actuators reacted), was to feed the model with the measured displacement from the string potentiometer (instrument SP5, at the load application level). Thus, this displacement history was applied to the fixed base models considered as the basis for simulating all of the tested specimens.

The value of E_c was altered many times, between 0.5 and 0.8 of the value given by the ACI equation for regular concrete, in attempts to best match the experimental results. For the final analysis, E_c was taken equal to 0.8 of the value proposed by the ACI equation for regular concrete. The resulting force displacement relationship at 0.2% drift is shown in Figure 7-13 for a fixed base model, which shows a reasonable agreement in the analytical and experimental elastic stiffness values at low drift levels.

The resulting deflected shape for both the full model and the Tested specimen at 0.6% is shown in Figure 7-16. This figure represents the height of the tested specimen on the vertical axis, and in-plane displacement readings at five points where the string potentiometers SP1, SP2, SP3, SP4, and SP5 are attached and that is compared to displacements at the corresponding nodes on the Abaqus model. The Figure shows that the deflected shape of the specimen reasonably agrees with that of the tested specimen.

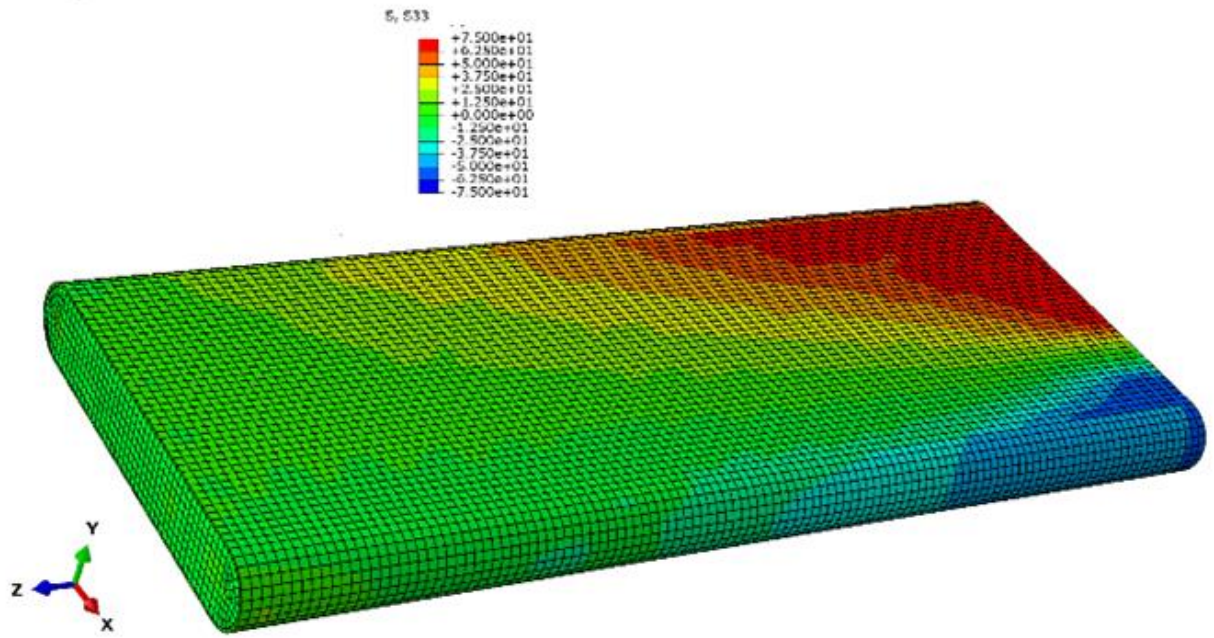


Figure 7-10 Analysis of Specimen CFSSP-NB1 using Abaqus, Stress distribution shown at 0.6% Drift

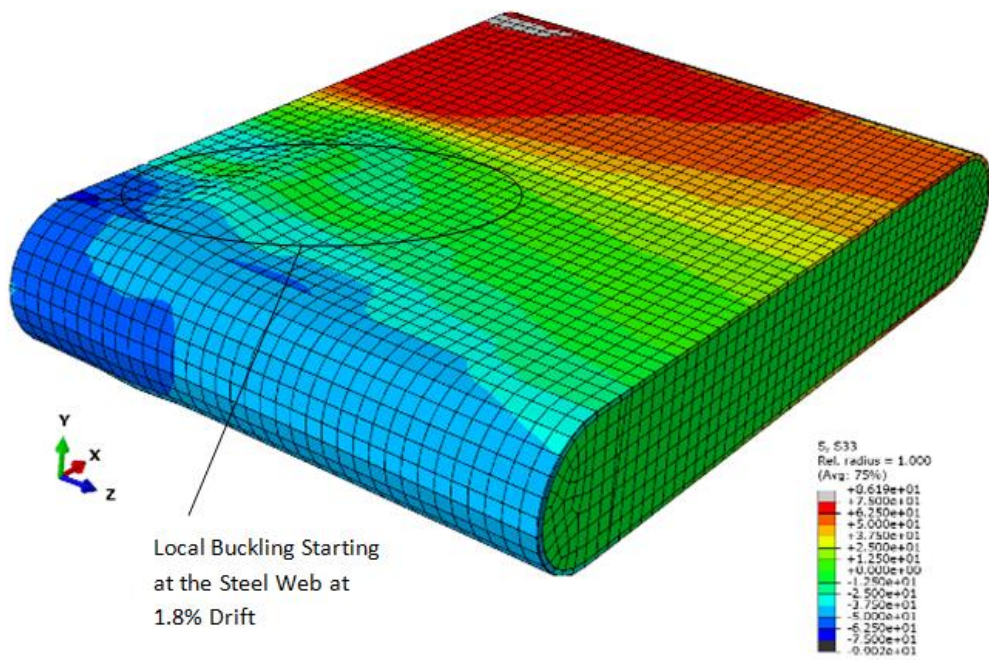
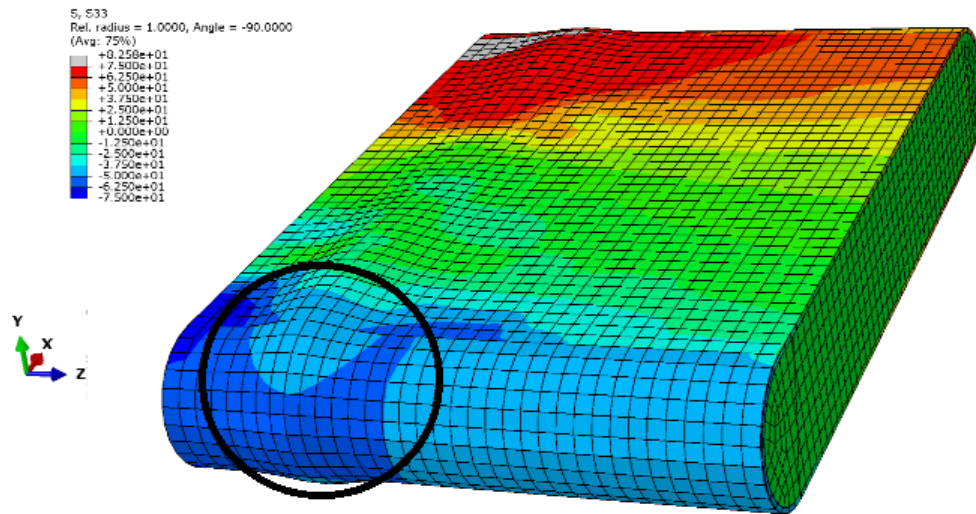


Figure 7-11 Local Buckling of the Web Plate at 1.8% Drift



Local Buckling of the HSS at
 2.4% Drift

Figure 7-12 Buckling of the HSS Part of CFSSP-NB1 at 2.4% Drift

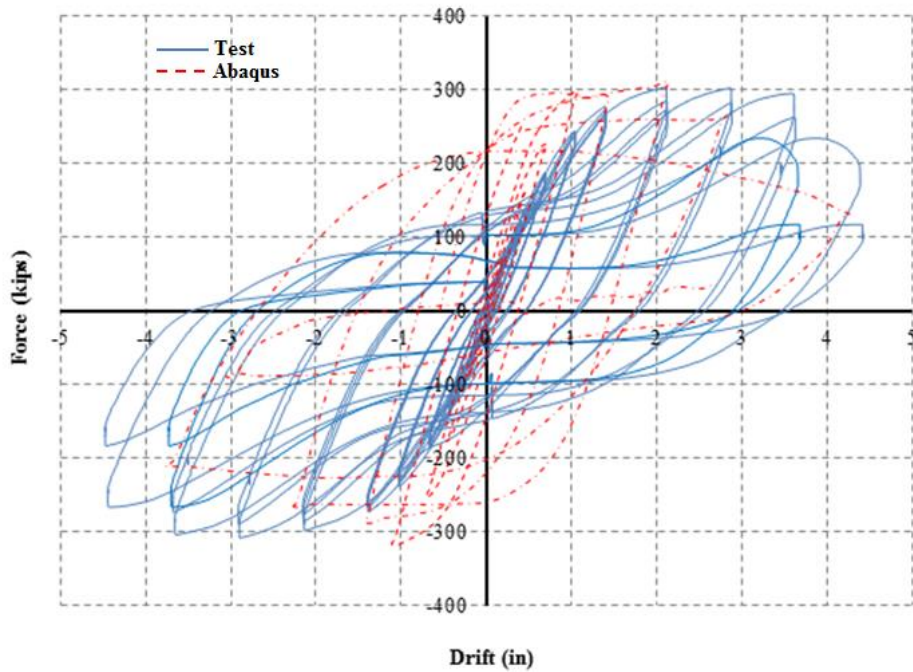


Figure 7-13 Force Displacement Relationship for Specimen CFSSP-NB1, Abaqus vs Test Values

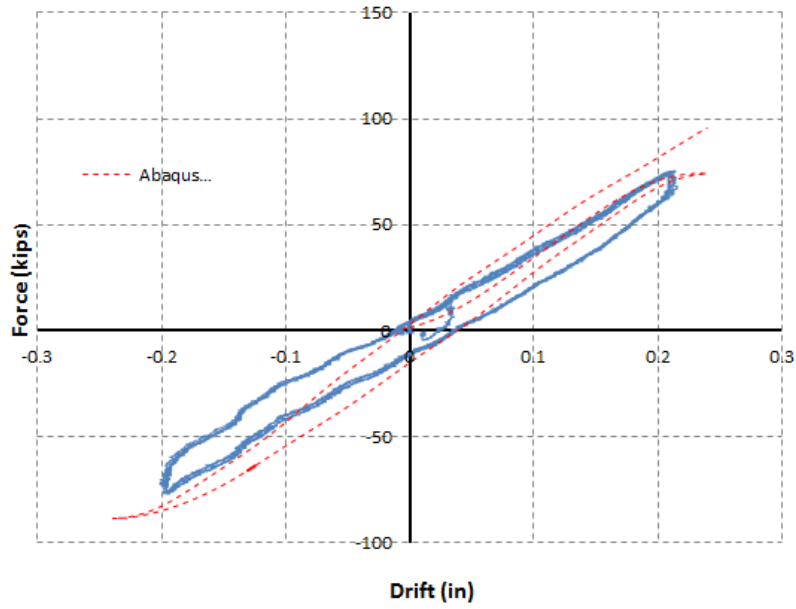


Figure 7-14 Elastic Stiffness of the Modeled CFSSP-NB1, Fixed Base Model

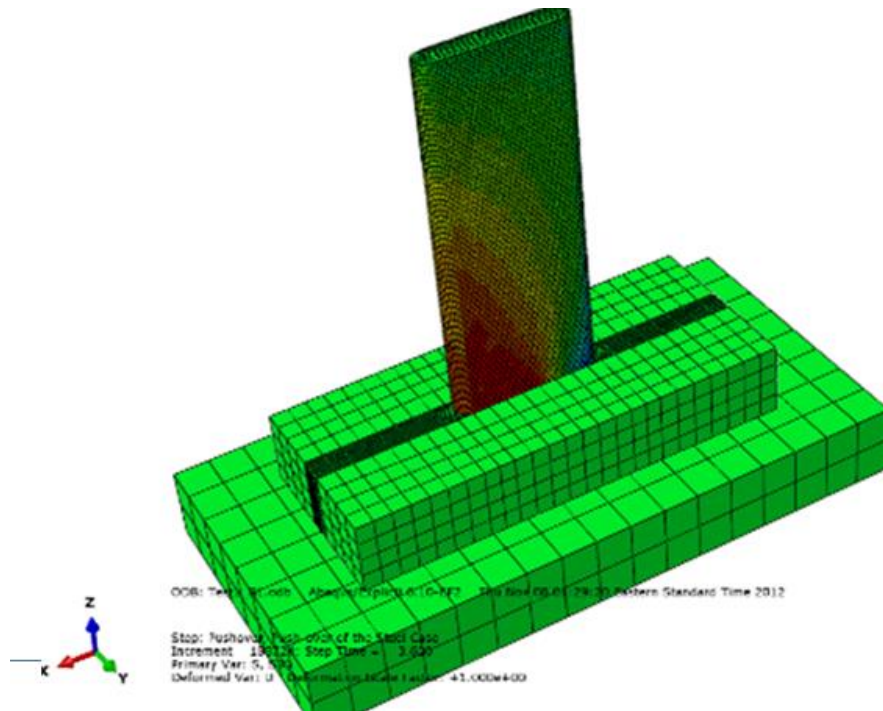


Figure 7-15 Full Model of Tested Specimen CFSSP-NB1

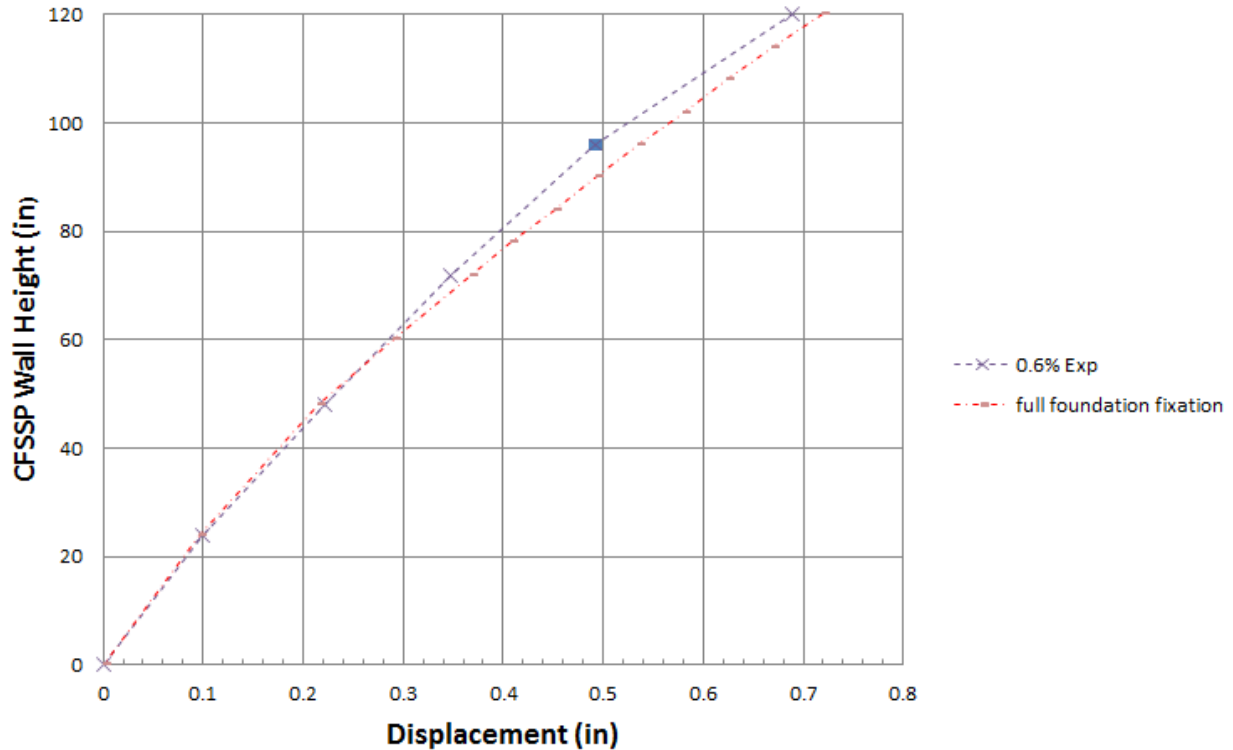


Figure 7-16 Deflected Shape for the Tested Specimen, Full Model

7.3.7 Specimen CFSSP-NB2 Simulation

Figure 7-17 shows the force displacement relationship for the Abaqus fixed base model of Specimen CFSSP-NB2 compared to the test results. The maximum load reached by the model was 284 kips, which is 94% of the load attained by the tested specimen. The modeled specimen is shown in Figure 7-18. The first local buckling starts to appear at 1.2% drift, as shown in Figure 7-19. Buckling of the round HSS part of the cross section followed, at 1.8% drift, as shown in Figure 7-20. At 2% drift, the load carrying capacity of the model degrades by about 30%, which is equivalent to 193 kips and 63% of the maximum load capacity. Note that, at the same drift, the tested specimen strength only degraded to 279 kips, which represents 92.3% of the maximum capacity. At 2.8% drift, the model degrades rapidly to reach almost 50% of its maximum value. Beyond that drift, there were significant degradation on the compression side of the specimen and high deformation in the buckled region. When the analysis was completed, the force sustained by the model was only 28 kips. Buckling of the skin plate at 2.8% drift is shown in Figure 7-21.

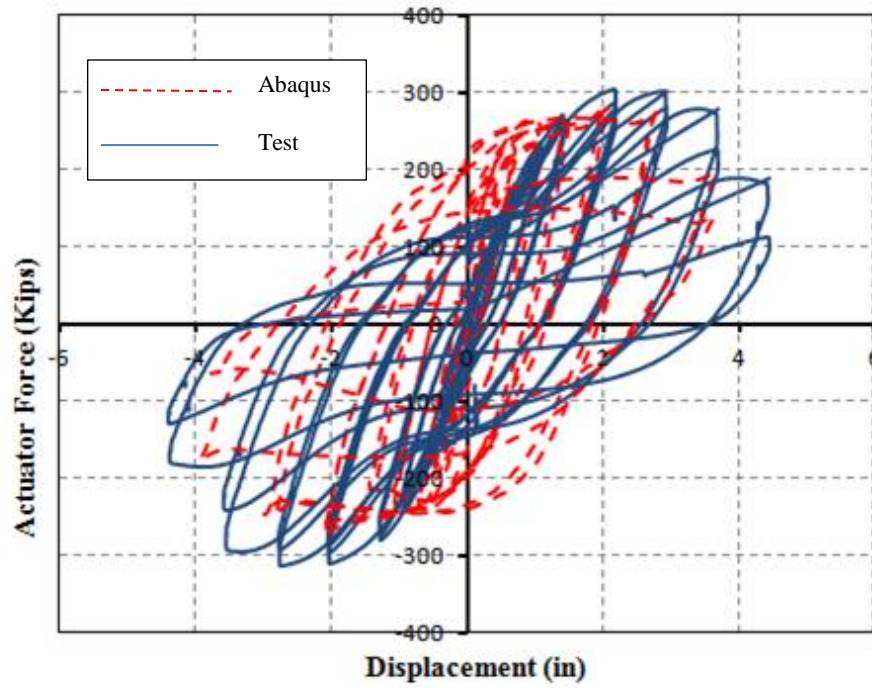


Figure 7-17 Comparison Test results to Analysis Results for Specimen CFSSP-NB2

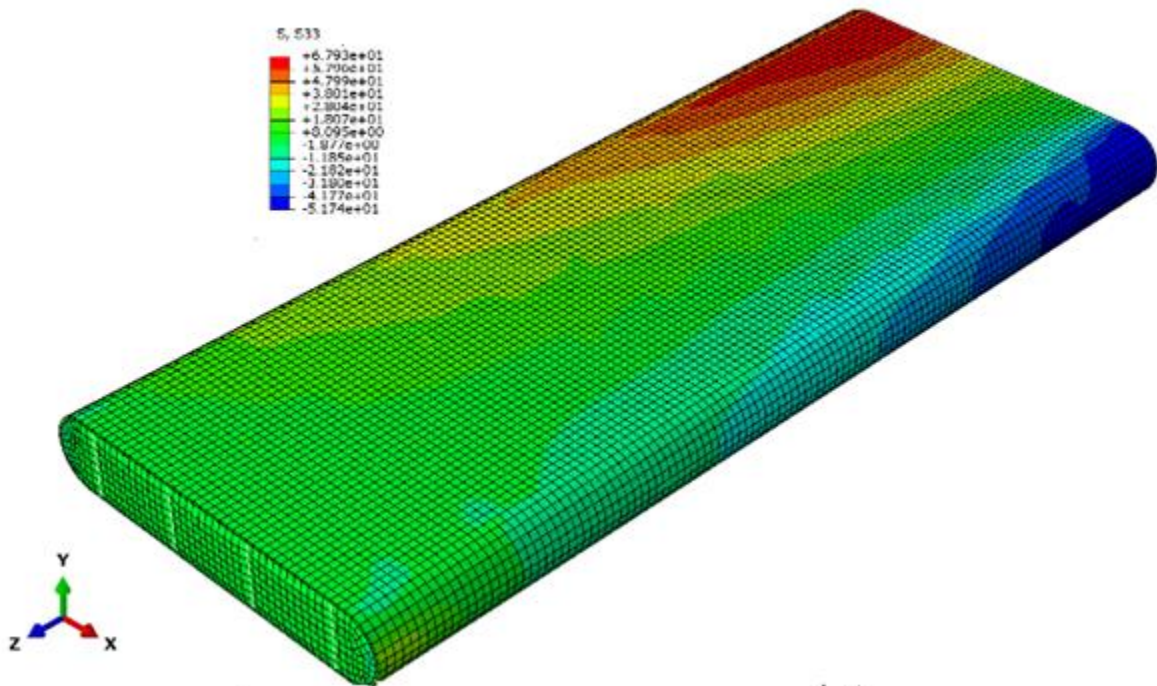


Figure 7-18 Fixed Base Abaqus Model for Specimen CFSSP-NB2, 0.6% Drift

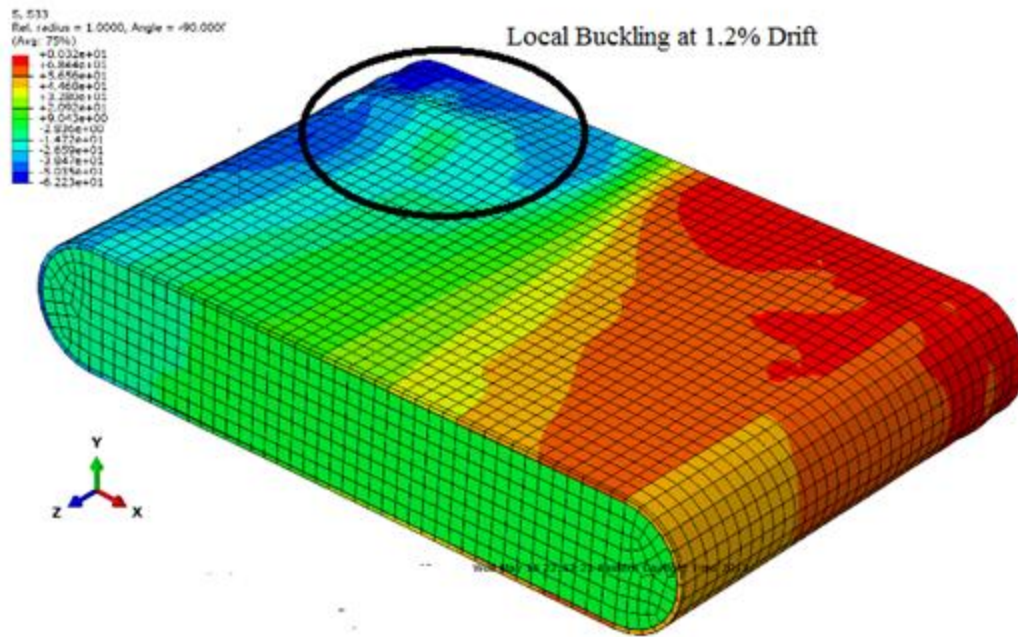


Figure 7-19 Local Buckling of the Web Plate at 1.2% Drift, CFSSP-NB2 Abaqus Model.

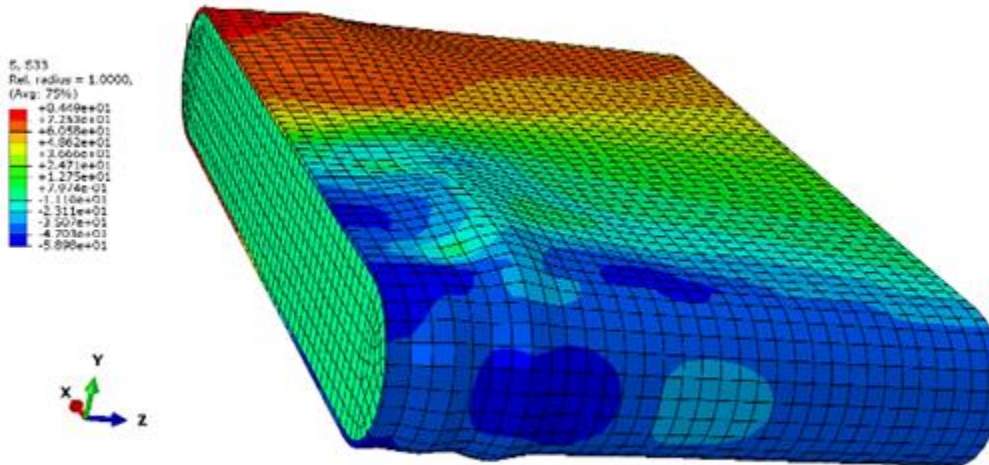


Figure 7-20 Buckling of the HSS part for the CFSSP-NB2 Model

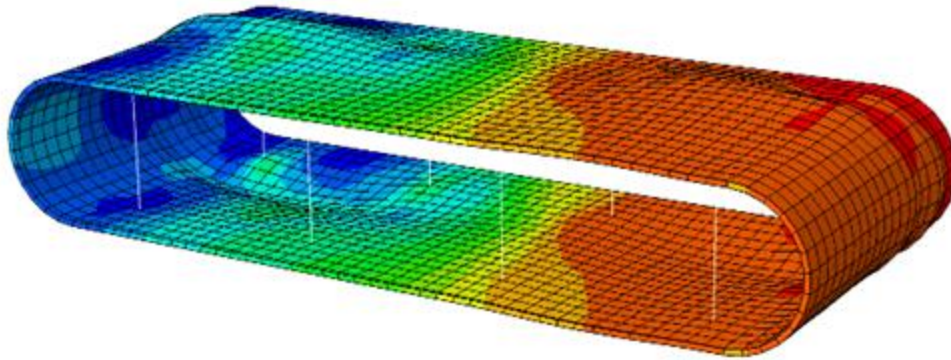


Figure 7-21 Local Buckling of the Skin Plate for Specimen CFSSP-NB2 at 2.8% Drift

7.3.8 Specimen CFSSP-B Simulation

Figure 7-22 shows the force displacement relationship for the Abaqus fixed base model of Specimen CFSSP-B1 compared to the test results. The maximum load reached by the model was 288 kips, which is 104% of the load attained by the tested specimen. The modeled specimen is shown in Figure 7-23 and skin plate and tie bars are shown in Figure 7-24. The first local buckling starts to appear at 1.67% drift, as shown in Figure 7-25, followed by buckling of the round HSS part of the cross section at 2.0% drift as shown in Figure 7-26. At 2% drift, the load carrying capacity of the model degrades by about 21.3% which is equivalent to 226.65 kips, which represents 76% of the maximum load capacity. At the same drift, the tested specimen degrades to 276 kips, which represents 96% of the maximum capacity. At 2.8% drift, the model degraded rapidly to reach almost 50% of the maximum strength value. Beyond that, there was significant degradation on the compression side of the specimen and high deformation in the buckled region, where the last sustained force by the model was 41 kips. It should be noticed that, as in the tested specimen, the web skin plate and the round HSS buckled at different locations.

As for Specimen CFSSP-B2 reached a maximum load of 274 kips which represents 96.8% of the maximum load reached in the test, however the concrete in the test had steel fibers in it which was not accounted for in the model (specially that it didn't show any significant impact during the testing). Local buckling of the web plate occurred at drift level of 1.67% at 2% the maximum load degraded by 27.2% with a value of 199.472 kips. Figure 7-27 shows the force displacement relationship for specimen CFSSP-B2. It should be noted here that despite the strength of concrete in specimen CFSSP-B2 was less than that for specimen CFSSP-B1 by 33%, yet specimen CFSSP-B2 performed slightly better.

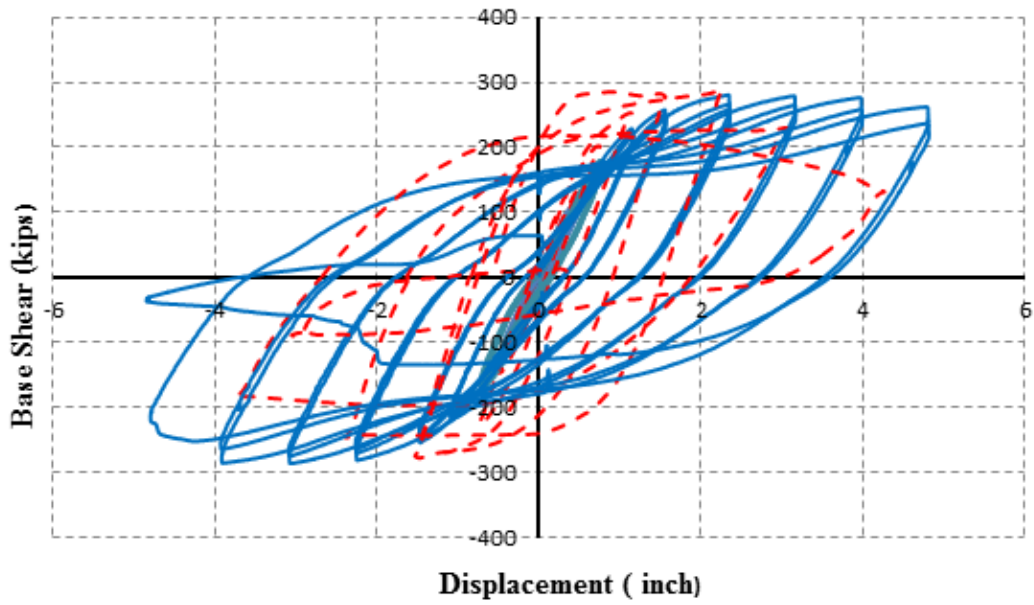


Figure 7-22 Force Displacement Relationship for Specimen CFSSP-B1

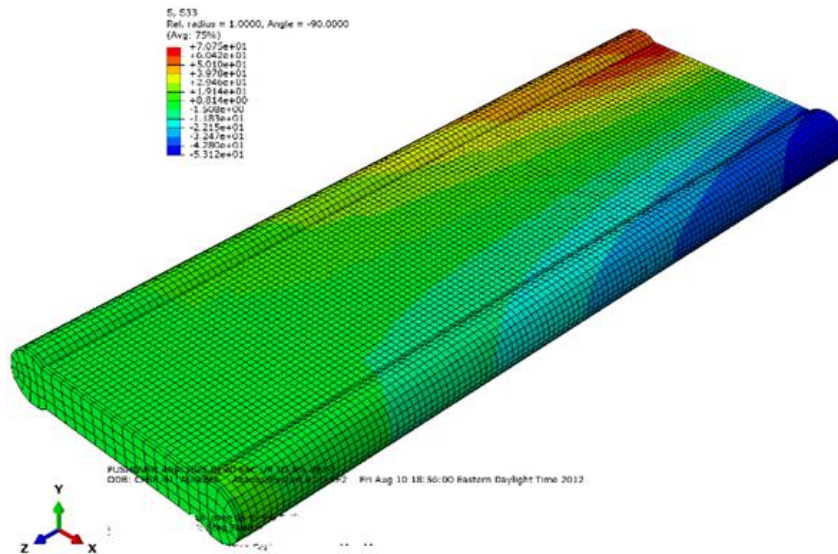


Figure 7-23 Model for Specimen CFSSP-B1

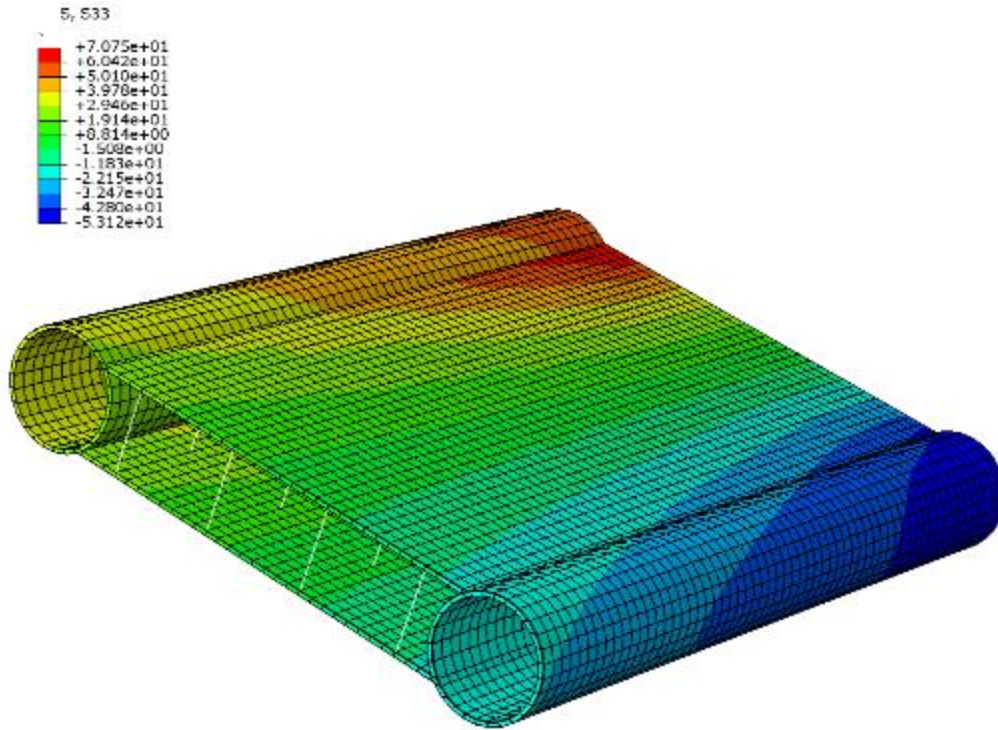


Figure 7-24 Skin Plate and Tie Bars for Specimen CFSSP-B1

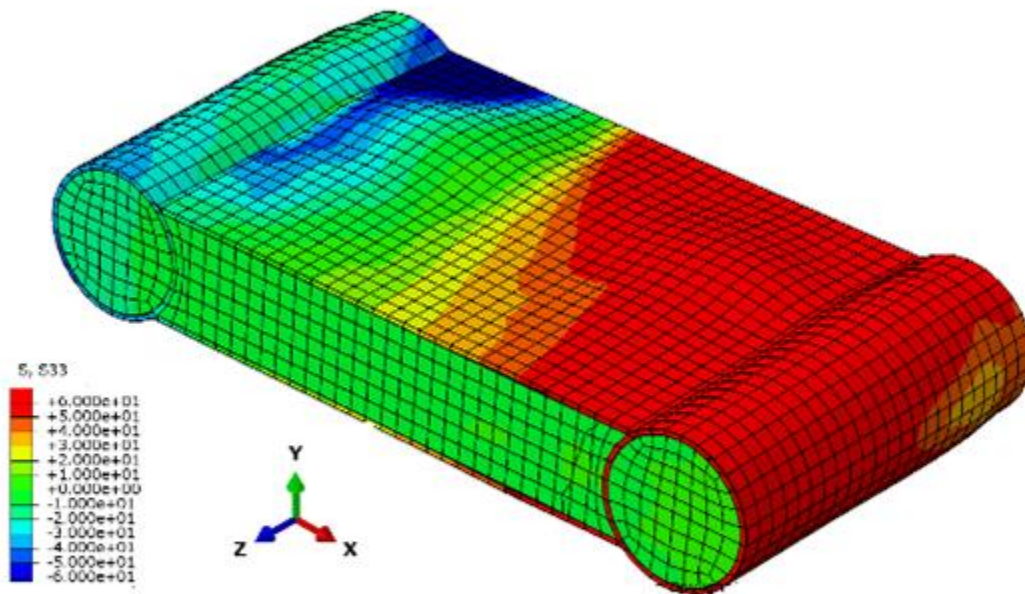
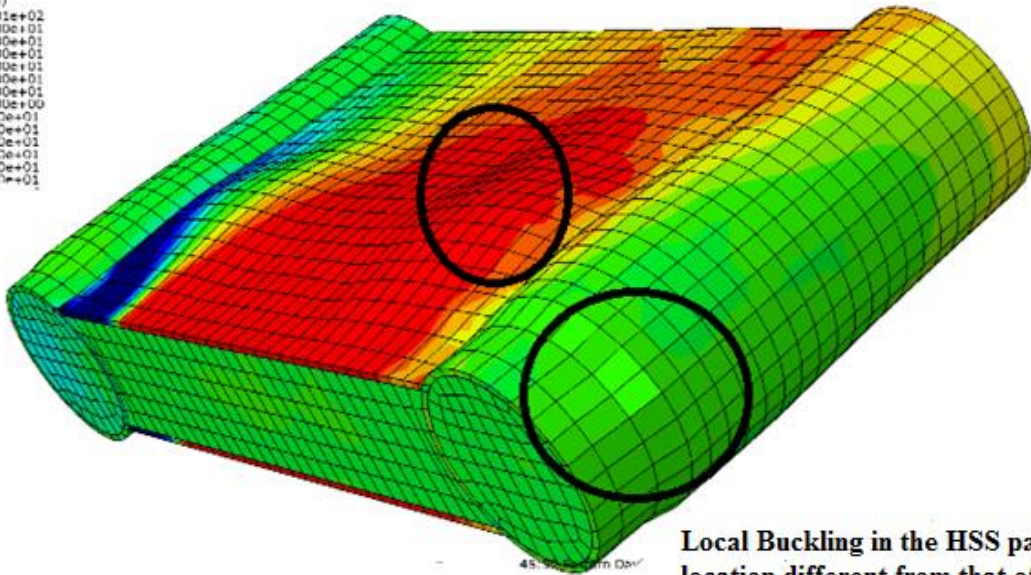
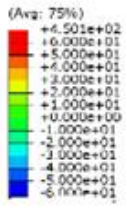


Figure 7-25 Buckled Web at 1.67% Drift, Abaqus Model CFSSP-B1

5, 533



Local Buckling in the HSS part is at a location different from that of the Web

Figure 7-26 Buckling of the Round HSS of Specimen CFSSP-B1

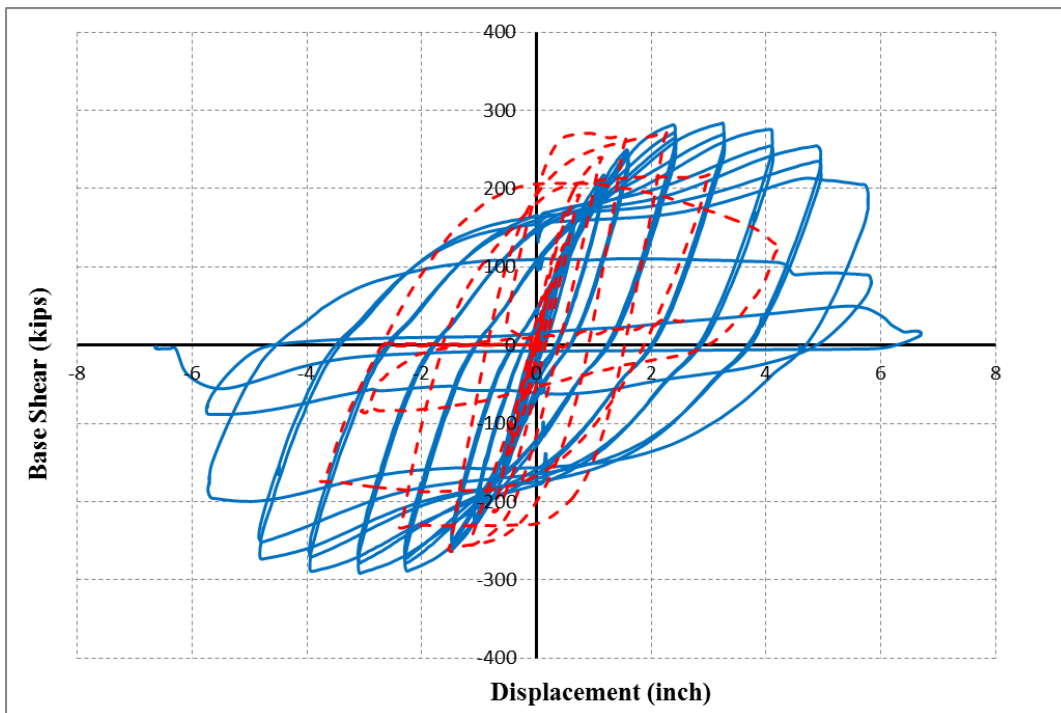


Figure 7-27 Force Displacement Relationship for Specimen CFSSP-B2

7.3.9 Parametric Study on the CFSSP-Walls

7.3.9.1 General

Finite element analysis was used to investigate the possible behavior of the proposed CFSSP-Walls configurations for values of some design parameters beyond those addressed in the experimental program.

The parametric study was limited and only covered the following aspects:

1. The D/t ratio, which is the ratio between the diameter of the HSS part of the cross-section and its thickness, must be chosen such that the composite cross-section can attain its plastic moment capacity, M_p (calculated as shown in previous chapters), prior to local buckling of the skin plate. The experimental program limited the D/t ratio values to $0.044 E/F_y$ for all of the tested specimen. Here, using finite element analysis, the behavior of CFSSP-wall with HSS having a D/t ratio of $0.076 E/F_y$ is investigated. That later ratio is the one recommended for seismically highly compact concrete filled round HSS as per AISC-341 (2010). This analysis is referred to as SPSSP-NB-M1.
2. The S/t ratio, which is the ratio between the tie bars spacing and thickness of the skin plate. Provided that tie bars have adequate stiffness, the S/t ratio is the main factor controlling the local buckling of the skin plate. The S/t ratio must be chosen such that the specimen can attain its plastic moment capacity, M_p , prior to local buckling of the skin plate. Here, an arbitrary S/t ratio of 50 was investigated, which is greater than the values of 25.6 and 38.4 investigated in the experimental program. This analysis is referred to as SPSSP-NB-M2.
3. The last design aspect is the ratio between the thickness of the concrete web and the length of the steel web. In the experimental program, it was taken equal to 0.2b. Here, a value of 0.35b was investigated as part of the parametric study. This analysis is referred to as SPSSP-NB-M3.

For all the analysis performed in the parametric study, the material models, selection of the finite elements used, and components interaction models, followed those presented in Section 3.6. As such, steel was taken as a bi-linear material having value $F_y = 50ksi$ (to generalize results, instead of taking the values obtained from the coupons for the experiment) and, concrete was selected to have $f'_c = 4ksi$. Note that when studying the effect of a certain parameter, all other parameters were kept equal to those used in the experimental program, as shown in the following subsections where the model used in each parametric study is presented together with the analysis results for each study. All examples were based on the CFSSP-NB walls. It is believed behavior observed for this CFSSP-NB will remain valid for CFSSP-B. The design parameter values considered in each model are summarized in Table 7-5 (where, again, it is shown that for a given model, only one parameter is changed while all other parameters are kept the same values as for the tested specimens). The displacement loading protocol for the models was

taken as per Table 7-6. It should be noted that for all models built for the parametric study axi-symmetry were used (symmetry around the weak axis) in order to cut down analysis time.

Table 7-5 Geometric Properties for Models Used in the Parametric Study.

Model (1)	D/t (2)	S/t (3)	tc (4)	b (6)	tc/b (6)	Aspect Ratio (5)	Web thickness (7)	HSS Diameter (8)	HSS thickness (9)	Design parameter investigated (10)
CFSSP-NB-M1	44.8	25.6	14	70	0.2	2.57	0.3125	14	0.3125	D/t
CFSSP-NB-M2	25.52	51.20	8	40	0.2	2.46	0.3125	8	0.3125	S/t
CFSSP-NB-M3	25.52	25.6	14	40	0.35	2.67	0.3125	14	0.5625	tc

Table 7-6 Loading Protocol for the Different Models

No of Cycles	2	2	2	2	2	2	2
Drift%	0.50	1.0	1.50	2.0	2.50	3.0	3.50

7.3.9.2 CFSSP-Walls with $D/t = 0.076 E/F_y$ (CFSSP-NB-M1)

The stress contours of the CFSSP-NB-M1 wall in the longitudinal direction on at a drift of 1.5% is shown in Figure 7-28. The height of the wall is 216 inches and total depth is 84 inches, depth of the web b is 70 inches, thickness for the web plate and thickness of the round HSS part of the cross section is 5/16 inch, the thickness of concrete/diameter of the round HSS is 14 inch, and finally the spacing of the tie bars is 8 inches in both the vertical and horizontal directions. The plastic moment capacity for the model was 89,675.

The resulting force displacement relationship for the CFSSP-NB-M1 wall is shown in Figure 7-29. The maximum base shear value is 533 kips which is equivalent to 1.28Mp. At a drift value of 0.8%, the web of the CFSSP-NB-M1 model showed local buckling by the second cycle at drift 1.5%, the HSS part of the specimen started to buckle. After 2% drift, there was a drop in the wall strength up to 0.9 Mp, after which it started to degrade gradually, the wall was able to sustain up 0.9 of its plastic moment capacity at 2.5%

drift indicating that the option of using $D/t = 0.076 E/F_y$ need to be investigate analytically and experimentally.

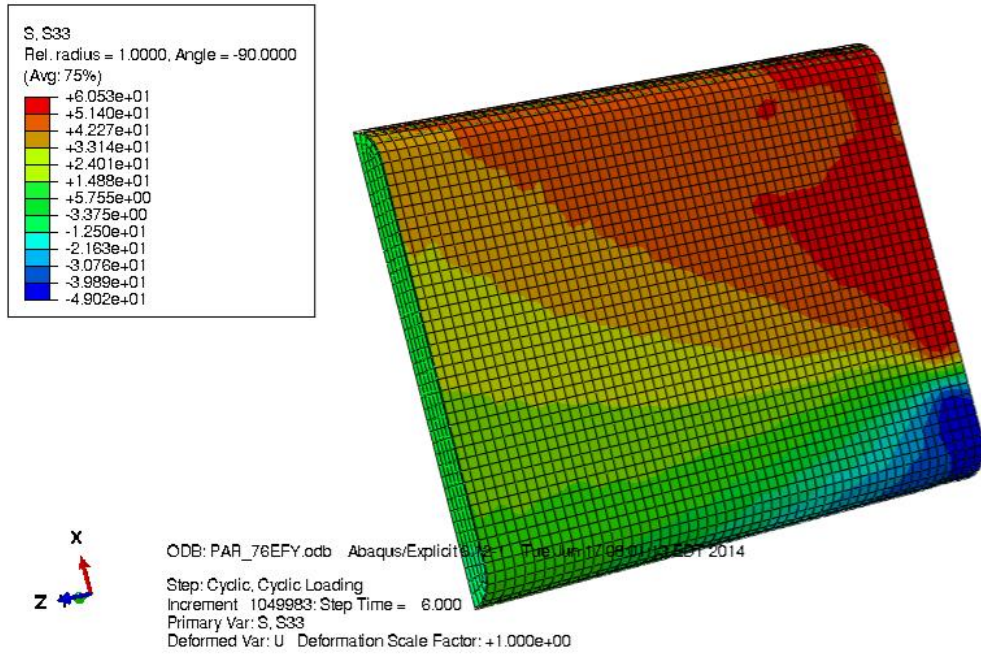


Figure 7-28 Model for CFSSP-NB-M1

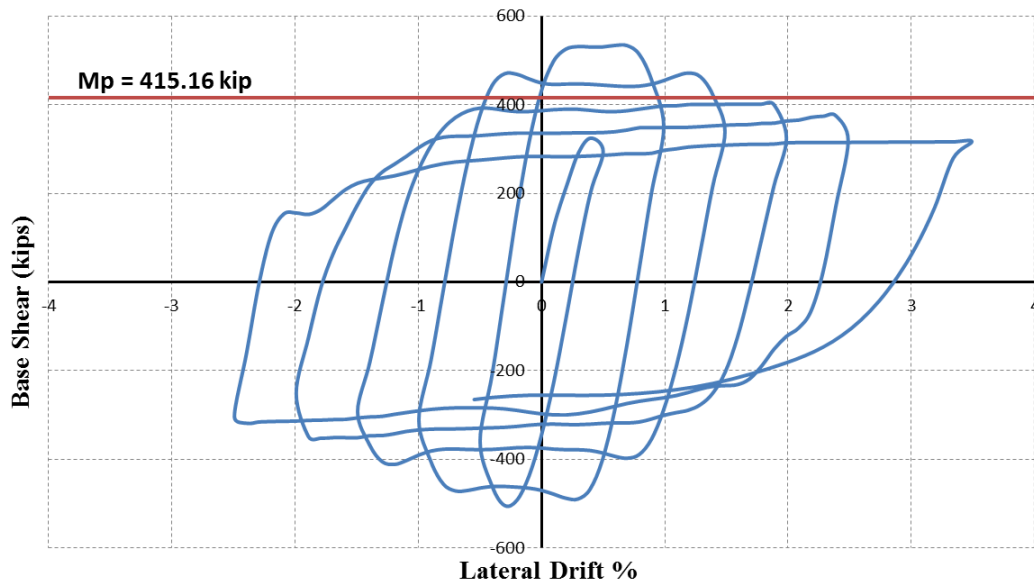


Figure 7-29 Base Shear vs Lateral Drift for CFSSP-NB-M1 Wall

7.3.9.3 CFSSP-Walls with $S/t = 50$ (CFSSP-NB-M2)

For the specimen CFSSP-NB or CFSSP-B, both cases of S/t ratio of 25.6 and 38.40 were tested. Here, an CFSSP-NB having an S/t ratio of 51.2, in the longitudinal direction, was modeled using finite elements to investigate how the higher S/t ratios would affect the ability of CFSSP-Walls to develop their M_p values and the required ductility performance. The model here is the same as that used for specimen CFSSP-NB, except that spacing of tie bars was changed to 16 inch, for a thickness of the skin plate of 0.3125 (5/16) of an inch. Most significantly, the model did not develop the cross-section plastic moment. The maximum moment that the model reached was 23,337.37 kip-in, which is equivalent to 0.78 M_p , the web plate buckled at 0.9% drift, and the model deteriorated rapidly after local buckling of the skin plate. Figure 7-30 shows the stress contours of the CFSSP-NB-M2 wall at 0.5% drift.

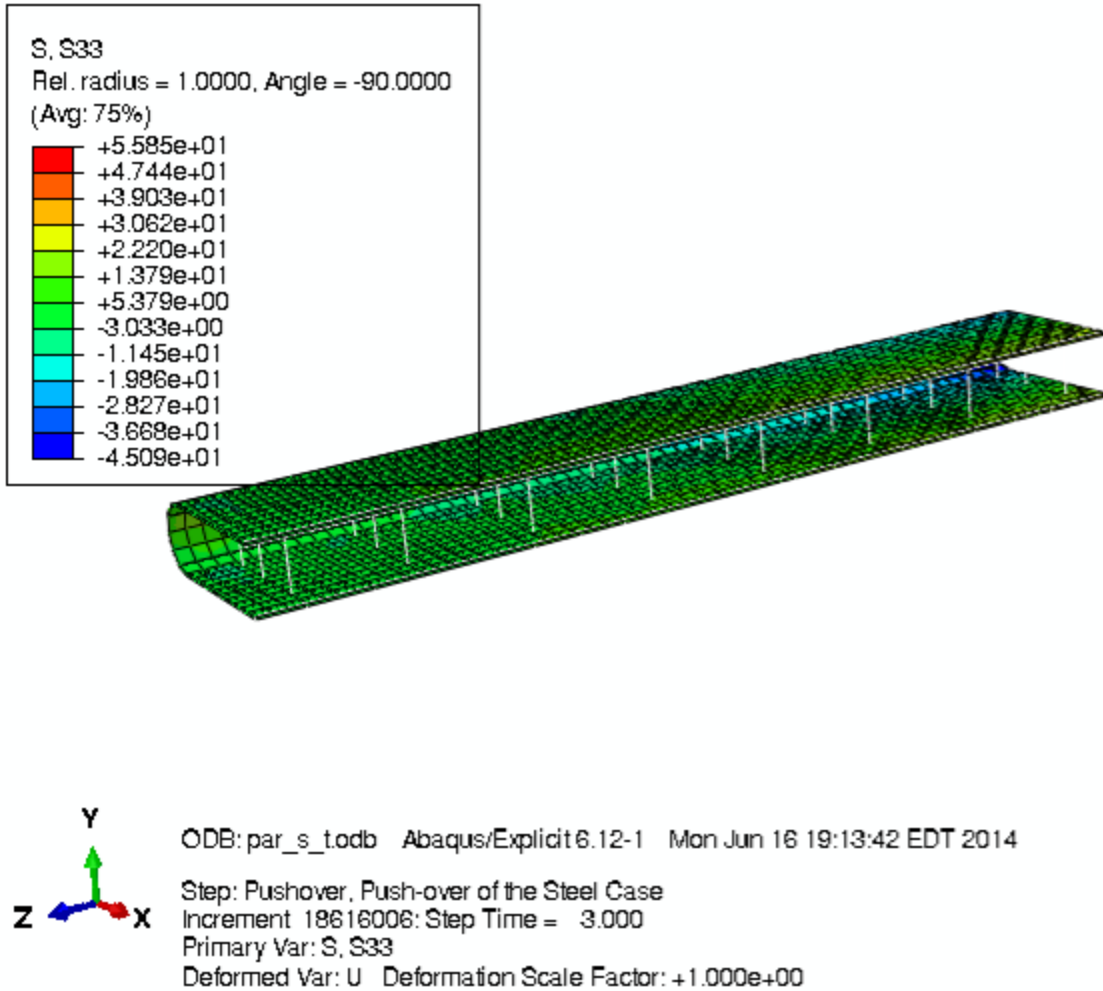


Figure 7-30 Model CFSSP-NB-M2 Stress Contours

7.3.9.4 Thickness of Wall = $0.35 b$

In tested specimens, the thickness of concrete was taken equal to $0.2b$, with a percentage of steel area, A_s , to the total area of the cross-section, A_p , (which is the summation of A_s and the concrete area, A_c), equals to 8.15% . Here, a model was developed for a CFSSP-NB wall having a thickness of concrete equal to $0.35 b$, where the depth of the web is 40 inches, thickness of the steel skin is $5/16$ of an inch, concrete thickness is 14 inches, and diameter and thickness of the HSS part of the cross-section is respectively 14 inches and $9/16$ inch. The spacing of the tie bars was taken equal to 8 inches in both the horizontal and vertical directions of the wall. The ratio of A_s/A_t is equal to 6.51% .

The resulting force displacement relationship is shown in Figure 7-32. A maximum capacity of 55,310.2kip-in was reached, which represents 1.19 Mp. The wall skin plate buckled at 1.5% drift, as shown in Figure 7-31 . The load carrying capacity was maintained up to 3% drift.

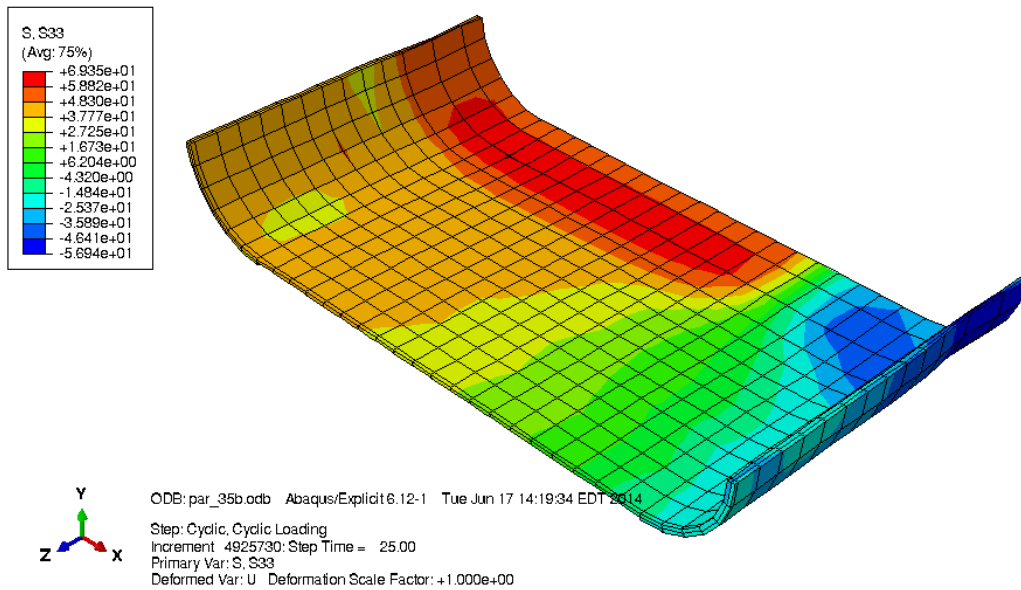


Figure 7-31 Longitudinal Stresses in CFSSP-NB-M3 Wall Skin Plate

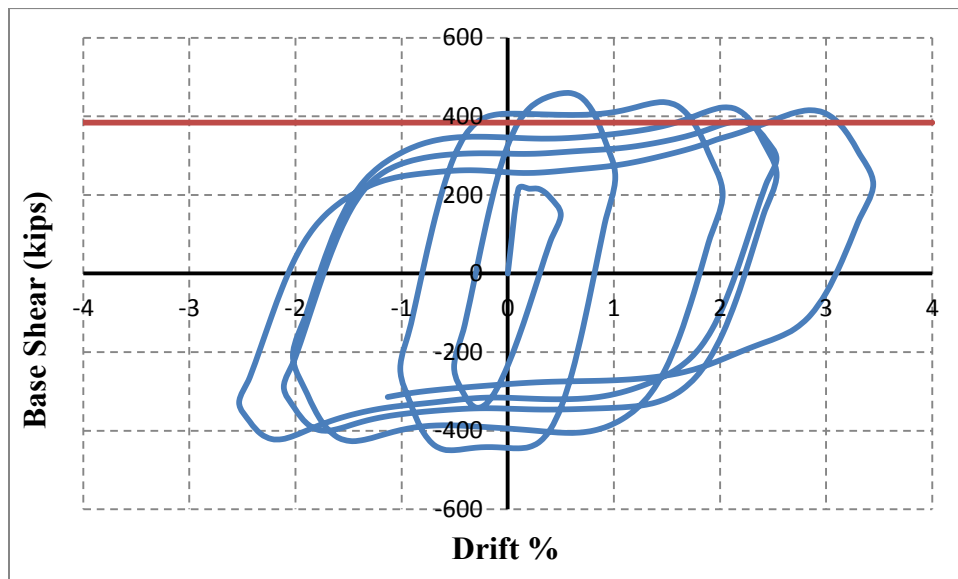


Figure 7-32 Force Displacement relationship for CFSSP-NB-M3

7.4 Summary

Finite element analyses were able to replicate three key aspects of the experimentally obtained results, namely, their ability to reach their theoretical composite plastic moment capacity, M_p , their initial elastic stiffness, and their ductility. Summary of the models simulating the tested specimen is shown in Table 7-7.

The finite element models simulating the tested specimens were not successful in capturing the degrading stiffness within the different displacement cycles. This was particularly true in the early stage of loading, when little degradation in stiffness was observed for the numerical models compared to the tested specimen. However, in the plastic range, strength degrading that developed in the numerical model was representative of that observed in the tested specimen, but not exact. This is attributed to shortcomings in the material models used for concrete, and limitations in the concrete damage plasticity parameters describing material damage. It was observed that results were sensitive to variability in the value of the elastic modulus of concrete E_c (although comparisons of results for various values of E_c were not presented here). For the specific type of concrete used in the experiment, self-consolidating concrete (SCC), best results were obtained when a value equal to 80% of that used for regular concrete was used.

The load carrying capacity of the finite element model degrades after local buckling occurs by 15% to 20% over drifts ranging approximately from 1.5% to 2%, while the tested specimen managed to hold its capacity over the same drifts. This is attributed to the damage criteria prescribed in the material models, where it is predetermined that at certain strains the material starts to degrade. The tested specimens eventually similarly degraded, but this occurred at drifts approximately 0.5% higher than predicted by the numerical models.

The value of S/t used in the numerical analyses was observed to have a small effect on the ability to predict the maximum strength of walls. Comparing with the test results, the analysis for S/t of 25.6 matched the maximum strength within approximately 1%, whereas the case with S/t of 38.4 only matched it within approximately 4%.

Results from a limited parametric study showed that it may be possible to obtain good results, ductile response, and development of full plastic moment, M_p , with D/t ratio equals to $0.076 E/F_y$ for the HSS part of the wall cross-section, and when wall have a concrete thickness of $0.35b$. However, the wall having S/t of 52 was unable to attain M_p and suffered rapid strength degradation after reaching $0.7M_p$.

Table 7-7 Finite Element Analysis Data Compared to Experimental Data

Specimen	Plastic Moment Capacity, $M_p(kip-in)$			Ductility Coefficient, μ	
	Test (1)	F.E (2)	Test/F.E (3)	Test (4)	F.E (5)
CFSSP-NB1	305	306	0.99	5.13	3.11
CFSSP-NB2	302	284	1.06	3.67	3.60
CFSSP-B1	281	288	0.96	4.0	4.40
CFSSP-B2	283	274	1.03	5.50	3.25

Chapter 8

CFSSP-WALLS DESIGN PROCEDURE

8.1 Introduction

Based on findings from the available literature review, experimental work, and analytical work presented in the previous chapters of this report, a method for the design of CFSSP-Walls with dominant flexural behavior was developed. The design principles revolve around the goal that the CFSSP-Wall section should be able to develop its full plastic moment capacity and maintain it while going through relatively large inelastic displacements. Accordingly, local buckling of the CFSSP-Wall skin plates should occur only post yielding, which dictates constraints on the diameter-to-thickness ratio, D/t , for the circular parts of the wall cross-section's skin plate and constraints on spacing of tie bars-to-web plate thickness ratio, w/t . The tie bars are spaced to minimize local buckling and to transfer shear between the skin plate and the concrete core.

In the following sections of this chapter, requirements for different parameters relevant to the seismic design of the proposed CFSSP-Walls cross-section are presented, in a format compatible with ASCE-7 (2010) and AISC-341 (2010) specifications. Section 8.2 reviews some seismic design parameters already used by those specifications in with regards to their applicability for CFSSP-Wall, in terms seismic design levels (i.e., strength, and ductility requirements for a given seismic demand. Then, expressions developed to calculate the plastic moment capacity of the proposed CFSSP-Wall cross section are presented (Section 8.3), followed by a description on how elastic buckling theory was used to specify vertical and horizontal spacing of the tie bars (Section 8.4), and how plastic deformation of the skin plate can be used to calculate their diameter (Section 8.5). Brief comments on calculation of effective flexural stiffness (Section 8.6) and plastic deformation limits (Section 8.7) are included. All of those parameters are used to establish a seismic design procedure for CFSSP-Walls, proposed for possible implementation in AISC-341 (Section 8.8). Finally an example showing the details of the design procedure for the proposed type of walls is presented (Section 8.9).

8.2 Seismic Design Recommendations for CFSSP-Wall Design

8.2.1 Introduction

Although the proposed CFSSP-Walls are not explicitly covered by current seismic design codes, there are some aspects of existing design codes that can be referenced in the design of CFSSP-Wall systems. ASCE-7 (2010) addresses system ductility performance, and AISC-341 (2010) has recommendations for the minimum thickness and maximum diameter-to-thickness ratio for the steel components and concrete-filled members that could be applicable to CFSSP-Walls. For example, the diameter-to-thickness limit ensures that the steel skin plates would not develop local buckling prior to the cross-section attaining its full plastic moment capacity (yielding of the steel components of the cross-section). In this section, parts of these existing codes and specifications addressing seismic design aspects that could be applicable to CFSSP-Walls are considered.

8.2.2 ASCE Seismic Design Recommendations for CFSSP-Walls

The type of CFSSP-Walls considered here provides is currently included in the general category of structural composite plate shear walls covered in section H6 of AISC-341 (2010), which states:

"Composite plate shear walls (C-PSW) shall be designed in conformance with this section. Composite plate shear walls consist of steel plates with reinforced concrete encasement on one or both sides of the plate, or steel plates on both sides of reinforced concrete infill, and structural steel or composite boundary members".

However, close scrutiny of the design and detailing provisions outlined in clause (H6) reveals that they are more specifically applicable to the design of steel plate shear walls encased in concrete, of the type tested by Zhao and Astanteh (2004). , their experimental and analytical work showed that this kind of walls could achieve up to 4.2% inter-story drift which indicates that this type of walls have relatively high ductility and that is revealed in the recommendations of the design codes for this type of walls (discussed later in this chapter).

As a consequence of the implied inclusion of CFSSP-Walls in AISC 341-10 Clause H6, this structural system would share the same seismic design factors specified for “building frame systems with steel and concrete composite plate shear walls” as per ASCE-7 (2010).

Table 8-1 presents seismic design parameters for CFSSP-Walls. Despite the fact that the type of CFSSP-Walls considered here provides ductility through flexural yielding (rather than shear yielding for the type of steel and concrete composite plate shear walls currently addressed by the provisions of AISC-341-10 clause H6), it is fortunate that the limited work done in Chapter 5 suggests that these design factors would be appropriate for CFSSP-Walls.

Table 8-1 Seismic Design Factors used for CFSSP-Wall Design as per ASCE 7

Building Frame System	Response Modification Factor, R	Over Strength Factor, Ω_o	Deflection Amplification Factor, C_d
(1)	(2)	(3)	(4)
Concrete Filled Sandwich Panel Wall	6.5	2.5	5.50

However more research is desirable to be able to validate these response modification factors for a broad range of composite concrete steel plate shear walls having different configurations, as changes in configuration of the wall could modify its ductile performance mechanism (e.g. developing shear yielding, or global walls instability for slender walls, instead of flexural yielding), which can have a profound effect on the displacement ductility capacity of the wall system (and consequently the above values of the seismic design factors).

8.2.3 AISC Seismic Design Recommendations

Although AISC-341 (2010) does not have specific recommendations for design of the proposed CFSSP-Walls, it provides limiting values for the diameter-to-thickness, D/t , ratio of compression elements for moderately ductile and highly ductile members, as specified in Table D1.1, including limits that could be applicable for the round HSS part of the proposed cross sections.

For composite, concrete-filled, round HSS, the limit value for highly ductile members, λ_{hd} , and moderately ductile limit, λ_{md} , respectively is given by:

$$\lambda_{hd} = 0.076(E/F_y) \quad (8.1)$$

$$\lambda_{md} = 0.15(E/F_y) \quad (8.2)$$

And twice that value for moderately ductile members.

For round HSS tubes (not filled with concrete), the D/t limit for highly ductile members λ_{hd} , and moderately ductile members, λ_{md} , respectively, are given by:

$$\lambda_{hd} = 0.038(E/F_y) \quad (8.3)$$

$$\lambda_{md} = 0.044(E/F_y) \quad (8.4)$$

These limits, however, were developed to achieve flexural ductile behavior of composite columns, rather than to ensure ductile cyclic compression/tension behavior of the wall's boundary elements. For the experimental program conducted in this project (Chapters 4 and 5), the limit specified by Equation 8.4 was used and shown to be effective to achieve the intended seismic performance, as mentioned earlier. Finite element analyses presented in Chapter 6 investigated the performance of CFSSP-Walls with round HSS having D/t ratio at the limit provided by Equation 8.1, and results indicated that these walls can provide the required plastic moment capacity and ductility, these limits were augmented in the proposed CFSSP-Wall design procedure presented later in this chapter. The experimental and analytical work presented in chapters 4 through 6 in this document the ratio of D/t that is equal to $0.044(E/F_y)$ seems to guarantee ductile performance for the CFSSP-Walls under consideration, however the limited finite element analysis presented in chapter 6 of this document shows that using D/t ratio equals to $0.076(E/F_y)$ for the HSS part of the CFSSP-Wall cross-section can provide the required ductile performance for the CFSSP-Walls.

8.3 Plastic Moment Capacity of the CFSSP-Wall

As described in Chapters 3, 4, and Appendix B, the plastic moment capacity of the proposed CFSSP-Wall cross section is calculated considering the following assumptions:

1. The stress distribution on the steel part of the cross section (i.e., the HSS and steel webs), is uniform and has a value of F_y
2. The stress distribution on concrete in compression is taken as uniform and having a value of f'_c
3. The factors accounting for actual shape of the stress distribution in concrete (typically equal to 0.85) are neglected here, and a uniform distribution of compression stresses is considered instead. Note

that, as shown in previous chapters, this provides good estimates of the cross-section strength (the reduction in strength that the 0.85 factors would provide is compensated by increases in the concrete core strength due to partial confinement).

The resulting expressions for the plastic moment capacity of CFSSP-Wall cross sections have been derived using basic principles and the above assumptions. For the CFSSP-NB cross-section, the stress distribution used to calculate M_p is shown in Figure 8-1.

Forces in the compressed part of the CFSSP-NB cross section are given by:

$$C_1 = 0.5A_{HSS}F_{y,HSS} \quad (8.5)$$

$$C_2 = \left(\pi d_{in}^2/8\right)f_c' \quad (8.6)$$

$$C_3 = 2t_s C \cdot F_{y(web)} \quad (8.7)$$

$$C_4 = t_c c \cdot f_c' \quad (8.8)$$

where,

c , is the length of the compressed part of the web part of the wall.

Forces in the tension part of the CFSSP-NB section are given by:

$$T_1 = 0.5A_{HSS}F_{y,HSS} \quad (8.9)$$

$$T_2 = 2(b-c)t_s F_{y,web} \quad (8.10)$$

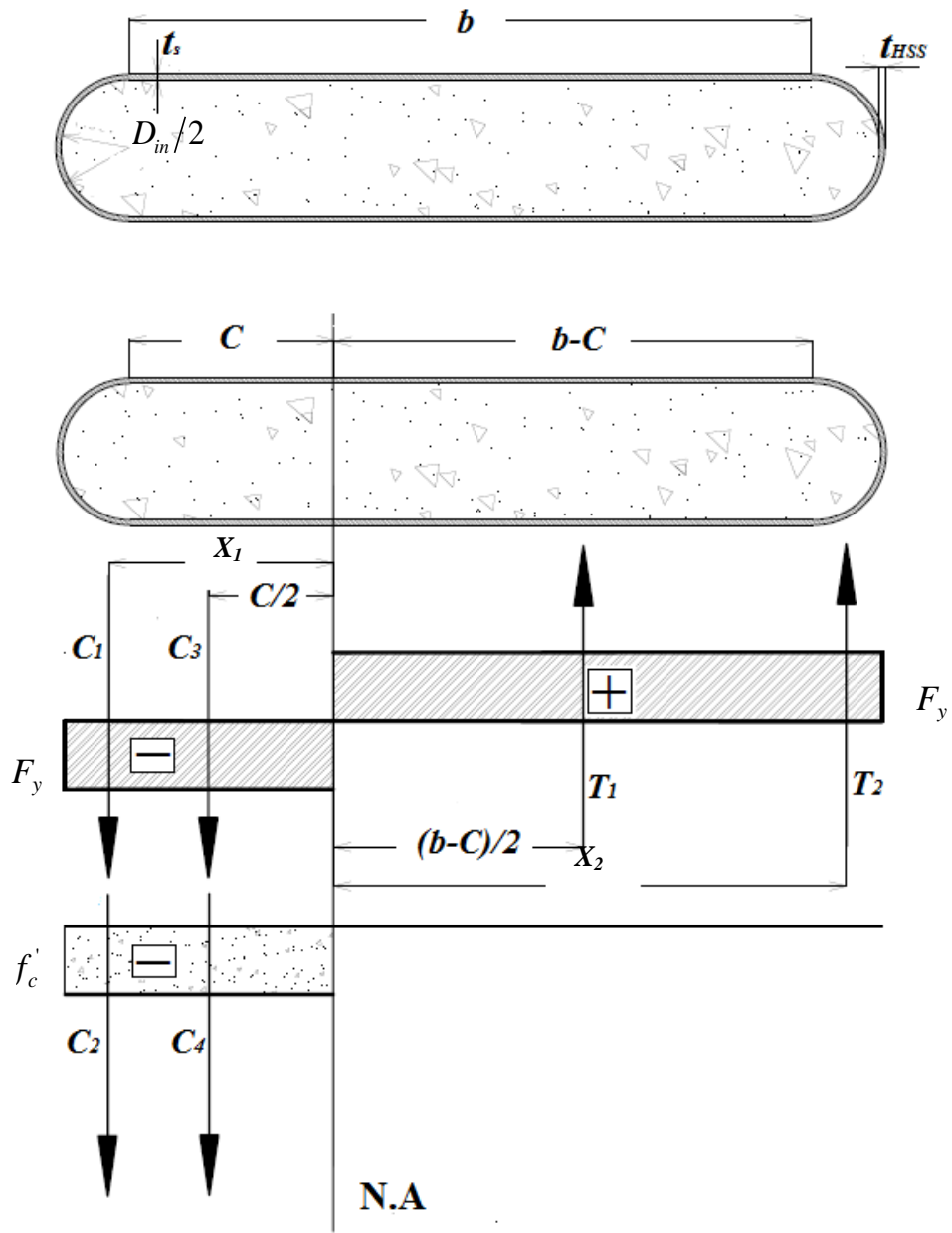


Figure 8-1 Schematic Diagram for Stress Distribution on CFSSP-NB cross-section

By applying equilibrium between tension and compression forces, an expression for the length of the web under compression, c can be calculated

$$C_1 + C_2 + C_3 + C_4 = T_1 + T_2 \quad (8.11)$$

$$c = \frac{2bt_s F_{y,web} - 0.125(\pi d_{in}^2) f_c'}{4t_s F_{y,web} + t_c f_c'} \quad (8.12)$$

The plastic moment capacity, M_p , of the section can be given by:

$$M_p = 0.5 A_{HSS} F_{y,HSS} \left(\frac{2d_{HSS}}{\pi} + b \right) + [b^2 + 2c^2 - 2cb] t_s F_{y,web} + \left(\frac{2d_{in}^3 + 3\pi d_{in}^2 c}{24} + \frac{c^2 t_c}{2} \right) f_c' \quad (8.13)$$

For the CFSSP-B cross-section, the stress distribution is shown in Figure 8-2. Forces in the part of the cross-section under compression are given by:

$$C_1 = A_{HSS} F_y \quad (8.14)$$

$$C_2 = 2t_s C \cdot F_{y,web} \quad (8.15)$$

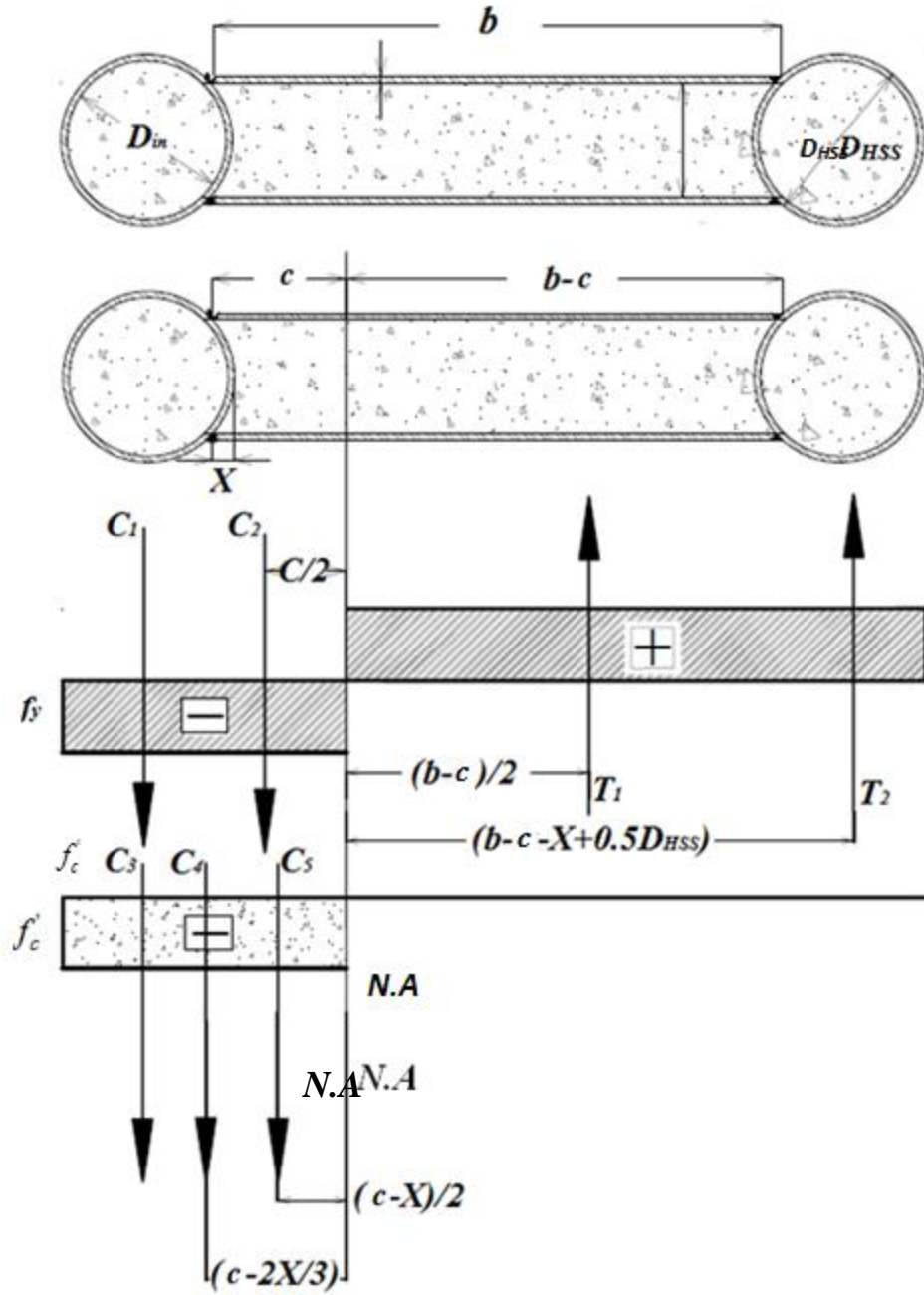


Figure 8-2 Schematic Diagram for Stress Distribution on CFSP-B Cross-section

$$C_3 = \frac{\pi d_{in}^2}{4} \cdot f_c' \quad (8.16)$$

$$C_4 = \frac{Xt_c}{3} \cdot f_c' \quad (8.17)$$

$$C_5 = (c - X)t_c \cdot f_c' \quad (8.18)$$

where,

$$X = 0.5 \left[d_{in} - \sqrt{d_{in}^2 - t_c^2} \right]$$

The forces in the part of the cross-section under tension are given by:

$$T_1 = 2(b - c)t_s \cdot F_{y,web} \quad (8.19)$$

$$T_2 = A_{HSS} F_{y,HSS} \quad (8.20)$$

By applying equilibrium between tension and compression forces, an expression for the length of the web under compression stresses, c , can be calculated

$$C_1 + C_2 + C_3 + C_4 + C_5 = T_1 + T_2 \quad (8.21)$$

$$c = \frac{2bt_s F_{y,web} + (0.67Xt_c - 0.25\pi d_{in}^2) f_c'}{4t_s F_{y,web} + t_c f_c'} \quad (8.22)$$

The plastic moment capacity, M_p , of the section can be given by:

$$M_p = A_{HSS} F_{y,HSS} [b - 2X + d_{HSS}] + [b^2 + 2c^2 - 2bc] t_s F_{y,web} + [0.25\pi d_{in}^2 (0.5d_{HSS} + c - X) + 0.33Xt_c (c - 0.67X) + 0.5t_c (c - X)^2] f_c' \quad (8.23)$$

Strengths obtained from those closed-form expressions to estimate the plastic moment capacity are compared with the maximum strengths developed by the tested specimens, in Table 8-2. The expressions derived based on the aforementioned assumptions are shown to conservatively estimate the plastic moment capacity, M_p , for the proposed cross-section configurations.

On average, for the two tested CFSSP- NB walls without boundary elements, the expression in 8.13 gives a value of M_p equal to 87% of the peak value obtained experimentally, while for the CFSSP-B walls with boundary elements, the expression in 8.23 gives a value of M_p that equal to 81% of the peak value.

This difference is attributed to strain hardening of the steel and confinement of the concrete. Note that the relatively larger difference obtained for CFSSP-B is possibly due to a more effective confinement of the concrete inside the round HSS (leading to higher peak concrete strength).

Table 8-2 Plastic Moment Capacity Expressions Compared to Tests Peak Values

Tested Specimen (1)	Test Results, M_{\max} (kip-in) (2)	Proposed Expressions, M_p (kip-in) (3)	M_p/M_{\max} (4)
CFSSP-NB1	36600	31969	0.87
CFSSP-NB2	36480	31969	0.88
CFSSP-B1	33720	27437	0.81
CFSSP-B2	33960	27437	0.81

8.4 Local Buckling of the CFSSP-Wall

8.4.1 Theoretical Plate Buckling Equation

The vertical and horizontal spacing of the tie bars, w_1 and w_2 , respectively, are calculated such that the skin plates would not experience local buckling before yielding. Beyond yielding, local buckling of the skin plates will unavoidably develop during cycling inelastic response; these are restrained due to presence of concrete such that buckling waves will only occur by deforming away from the concrete.

The elastic critical local buckling stress of a steel plate under uniform compression, neglecting the effect of initial plate imperfections, is given by:

$$\sigma_{cr} = \frac{k\pi^2 E}{12(1-\nu^2)(S/t)^2} \quad (8.24)$$

where,

k , is the buckling factor of the plate dependent on its end conditions taken equal to 4 in case of simple supported ends.

Wright (1995) used energy methods to derive closed-form expressions for the limits of the width-to-thickness ratio, S/t , under different loading conditions and that for sections filled with or encased in concrete, The plate buckling waves will be unidirectional waves due the presence of concrete on one side

of the plate. Wright equated the energy associated with the plate deformation into an assumed buckled shape to that associated with load application on the plate.

The case under consideration is the case where a compression flange in concrete filled section is subjected to uniform compression and have simply supported edges, and by considering yield stress as the critical stress in the energy expression, Wright showed that the b/t ratio should be less or equal 37 to assure ductile behavior, yielding prior to buckling of the plates. For the CFSSP-Walls tested in this research the maximum S/t ratio used were 38.40.

Assuming that plates having a simply supported edges is a conservative assumption, as the end condition of the plates are determined through the horizontal spacing of the tie bars and their stiffness.

8.4.2 Elastic Buckling of Skin Plate

In the CFSSP-Walls considered here, the skin plate is composed of a circular or half circular section welded to steel web plates.

Each web skin plate is considered as a column laterally-restrained at the tie-bars. Boundary conditions were considered to be fixed end (due to continuity of the plate and symmetry) at the location of the tie bars. The resulting “column” has a length of w_1 , a rectangular cross section of width, w_2 , and thickness, t , and a corresponding column buckling factor, K , of 0.5 (for the theoretical fix-fixed case, as also presented in AISC (2010)). Per the Euler column buckling equation, the critical buckling stress, σ_{cr} , for the column is given by:

$$\sigma_{cr} = \frac{\pi^2 E}{\left(\frac{L_e}{r}\right)^2} \quad (8.25)$$

By making the critical stress equal to the yield stress:

$$\sigma_{cr} = \sigma_y = \frac{\pi^2 E}{\left(\frac{Kw_1}{r}\right)^2} \quad (8.26)$$

and

$$r = \sqrt{\frac{w_2 t^3}{12w_2 t}} = \sqrt{\frac{t^2}{12}} = \frac{t}{2\sqrt{3}} = 0.289t$$

where,

r is the radius of gyration of column cross section $w_2 \times t$,

L_e is the effective buckling length = $K \cdot L$

L is the length of column, which is equal to the vertical spacing of tie bars, w_1

Accordingly, substituting the expression for r into equation 8.23, and re-arranging the equation, the w/t ratio that ensures yielding of the web plate prior to its local buckling is given by the expression:

$$\frac{w_1}{t} = 1.815 \sqrt{\frac{E}{F_y}} \quad (8.27)$$

For steel with, $E = 29000$ ksi and $F_y = 50$ ksi, the resulting $w/t = 43.7$

8.5 Design of the Tie Bars

The diameter of the tie bars should be selected such that they can provide adequate stiffness to control local buckling of the web plates, resist the shearing force transferred between the reinforced concrete core and the steel skin plate, and have adequate strength to resist the tensile force that develops during formation of the plastic mechanism created during inelastic buckling of the web skin plate.

The first of these requirements is not quantified here, as it is believed to not be a controlling parameter for most applications. Also, given the large number of ties typically used in such walls, the second requirement is not expected to govern design either. The tie bars could be conservatively sized by equally dividing the shearing force between the steel skin plate and the concrete core, as per chapter 5 of this document the steel web plates sustain approximately 50% of the shear acting on the panel.

The resulting shearing force per tie bar:

$$V_{bar} = \frac{V}{2n} \quad (8.28)$$

where,

V , is the total shearing force at each floor level

n , is the number of tie bars between two floor

Tensile force in the tie is calculated from the yielding of the web skin plate during buckling after the CFSSP-Wall has attained its plastic moment capacity. When the web plates buckle, plastic hinging of the skin plates forms as shown in Figure 8-3. Due to formation of this plastic mechanism, plastic moment capacity of the plates are reached at the plastic hinges locations. The shear forces that develop at the end of each buckled segment, obtained from equilibrium of the free-body-diagrams shown in Figure 8-3, induce tension forces on the tie bars.

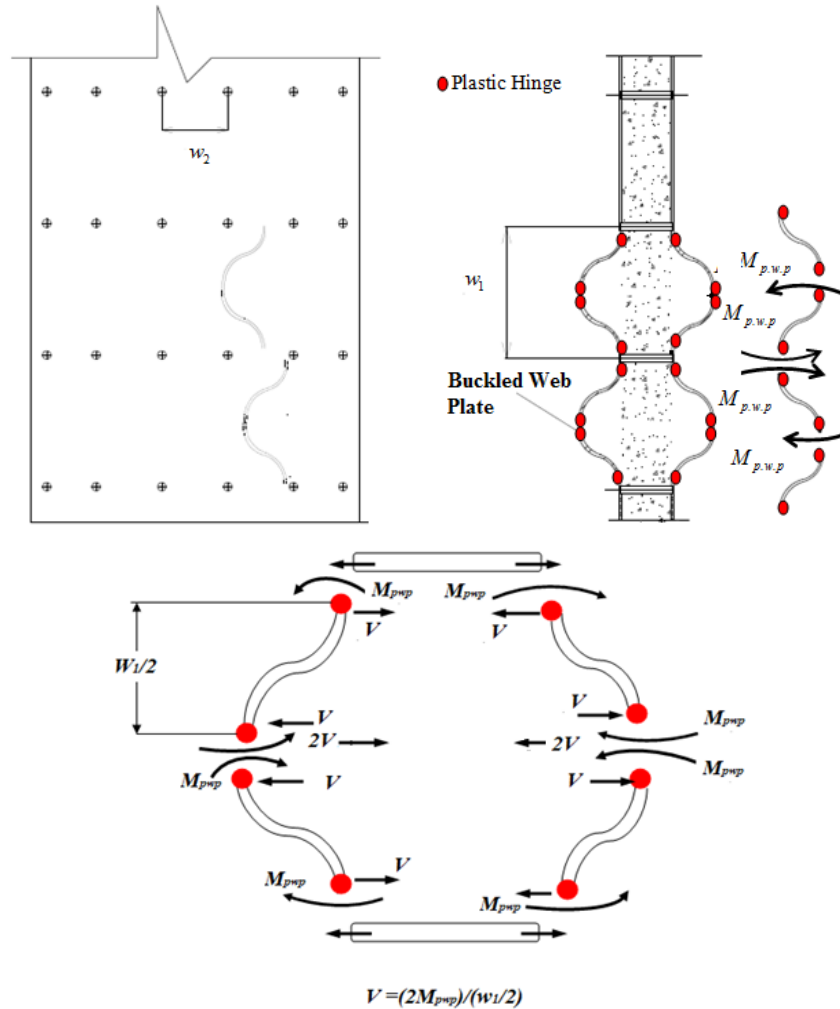


Figure 8-3 Buckling of the Skin Plates and Formation of Plastic Hinges

In this free-body diagram, the buckled zone mechanism is idealized as a fixed end beam having a span of w_1 , width w_2 , and thickness, t , with plastic hinges formed at the fixed ends and mid span of the beam.

The corresponding plastic moment capacity of the cross section is given by:

$$M_{p,w,p} = \frac{w_2 t^2}{4} \cdot F_y \quad (8.29)$$

The tensile forces acting on the tie bars due to formation of those plastic hinges in the buckled skin plate can be calculated from beam reactions on left and right of the tie bar. The reaction, V_{plate} from the buckled skin web plate can be calculated from the expression:

$$V_{plate} = \frac{2M_p}{(w_1/2)} = \frac{4M_p}{w_1} \quad (8.30)$$

The resulting tension force acting on the tie bar due to formation of the plastic hinging mechanism in the buckled web plate, is set as equal to the strength of the tie bar. This gives:

$$T_{tie.bar} = 2V_{plate} = 2 \times 4t^2 \left(\frac{w_2}{4w_1} \right) F_{y,plate} = 2t^2 \left(\frac{w_2}{w_1} \right) F_y = \frac{\pi d_{tie.bar}^2}{4} \cdot F_{y,tie.bar} \quad (8.31)$$

Re-arranging this equation, the following required tie bar diameter is obtained:

$$d_{min} = 1.59t_s \sqrt{\left(\frac{w_2}{w_1} \right) \left(\frac{F_{y,plate}}{F_{y,tie-bars}} \right)} \quad (8.32)$$

where

$F_{y,plate}$, $F_{y,tie-bars}$, yield stress for web plate and the tie bars respectively

Welds used to connect the tie bar to the skin plate should also be able to develop the force calculated by Equation 0.27.

8.6 Equivalent Elastic Stiffness

The effective flexural elastic stiffness for the CFSSP-Wall is to be calculated using Equations I2-14 and I2-15 in AISC-341 (2010), given by:

$$(EI)_{eff} = E_s I_s + C_3 E_c I_c \quad (8.33)$$

where,

I_s, I_c are the gross moment of inertia for the steel and concrete parts of the CFSSP-Wall cross-section, respectively.

C_3 is a reduction factor accounting for the cracking of concrete, and given by:

$$C_3 = 0.6 + 2 \left(\frac{A_s}{A_s + A_c} \right) \leq 0.90 \quad (8.34)$$

The effective stiffness is calculated as the summation of the full stiffness of the steel section and a portion of the concrete stiffness to account for cracking of the concrete. In order to calculate the C_1 factor based on the experimental program, the peak displacement, δ , and the corresponding load, P , at the first loading cycle were used to calculate the $(EI)_{eff}$ value considering the tested CFSSP-Walls as cantilever beams of length, L , with lateral load acting at their end, such that:

$$\delta = \frac{PL^3}{3(EI)_{eff}} \quad (8.35)$$

Since there were very little information about the actual elastic modulus for the concrete used in the testing specimens, and because of the variability involved with concrete having fly-ash the experimental data cannot be used to calculate the factor C_3 , yet the factor C_3 was calculated based on the finite element analysis for rectangular section used Chapter 3, push over analysis for the tested specimens, and finally using the $(EI)_{eff}$ from Xtract to calculate C_3 , the details of these calculation is placed in Appendix D. The estimated value of C_3 factor is summarized in Table 8-3.

Table 8-3 Calculated C_3 Factor Based on Test Results

<i>CFSSP-Wall</i>	$(EI)_{eff}$	C_3 , AISC-341	C_3 , Test
(1)	(2)	(5)	(6)
CFSSP-NB1	295,473,917	0.763	0.38
Rectangular CFSSP-Wall	1,102,486,803	0.80	0.33

8.7 Proposed Deformation Limit for the CFSSP-Walls

A limit to the in-plane lateral deformation of the CFSSP-Walls is determined based on the test results, by defining the maximum displacement permitted in design as corresponding to that at which the experimentally obtained CFSSP-Wall load bearing capacity degraded from the maximum value to eighty

percent of its peak capacity. As it is expected that this lateral displacement limit will change depending on wall geometry, the deformation limit is determined by first defining a limit strain value, then translated into a curvature limit.

The maximum curvature, ϕ_{\max} , is given by:

$$\phi_{\max} = \frac{\varepsilon_{c,\max}}{X_1} = \frac{\varepsilon_{t,\max}}{X_2} \quad (8.36)$$

where,

$\varepsilon_{c,\max}, \varepsilon_{t,\max}$ are maximum compression and tensile strain

X_1, X_2 are the distances from the plastic neutral axis and outermost compression or tension fibers

The relationship between maximum lateral displacement and curvature for a cantilever wall is given by:

$$\Delta_{\max} = \Delta_p + (\phi_{\max} - \phi_p) L_p \left(L - \frac{L_p}{2} \right) \quad (8.37)$$

where,

Δ_{\max}, Δ_p are maximum and plastic displacement

ϕ_p is the plastic curvature

L is the total length of the cantilever wall

L_p length of the plastic hinge which is equal to the total depth of the wall cross section, W , as described in Chapter 6 of this document

By considering that the value for $\phi_{\max} \gg \phi_p$ accordingly the Equation 8.37 can be reduced to the following form:

$$\Delta_{\max} = (\phi_{\max}) L_p \left(L - \frac{L_p}{2} \right) \quad (8.38)$$

The value of ϕ_{\max} can be taken as the maximum value reached in the experimental program, which were equal to 75×10^{-5} (1/in) and 79×10^{-5} (1/in) for the CFSSP-NB and CFSSP-B, respectively. An average value of 77×10^{-5} (1/in) can be considered for both CFSSP-Walls.

Accordingly the maximum displacement at the top of the CFSSP-Wall, wall, Δ_{\max} , should not exceed the value given by Equation 8.38. As part of the design process, this value would be the one calculated elastically for non-reduced seismic loads (i.e., before applying the R-factor).

8.8 Proposed Design Procedure for CFFSP-Walls

Designing a CFSSP-Wall is an iterative process that starts by selecting preliminary dimensions for the cross-section based solely on the calculated strength demand on the system (beyond architectural constraints, of course). After cross-section dimensions are selected, the actual plastic moment capacity of the section can be calculated, and spacing of tie bars is calculated such as to prevent local buckling in the skin plate prior to its yielding to ensure adequate transfer of the shearing force between the skin plate and the concrete core, and to elastically resist forces from plate buckling. Then, the wall deformation limit is checked by comparing the calculated curvature at the design drift to the curvature limit obtained from the testing program. The following outlines the steps of that process in slightly more details, and illustrates the sensitivity of some results to variations in the value of some parameters.

8.8.1 Preliminary Dimensions of the CFSSP-Wall Cross-section

CFSSP-Wall preliminary dimensions are calculated considering the strength demand on the wall, and some general assumptions (for both kinds of proposed CFSSP-Walls) that can be summarized as follows:

1. The axial force acting on the wall is neglected and CFSSP-Wall is subjected to flexural demand only. Interaction for combined axial load and flexure is to be checked in subsequent iterations.
2. Assume that both the HSS and the steel web parts of the skin plate have the same F_y . Although the equations in Section 8.3 allow for different materials for the HSS and plates, this can be more expedient in preliminary design.
3. Assume a concrete strength, f'_c . Note that, as far as flexural strength is concerned, selection of concrete strength, f'_c , is of limited significance, as results presented below will illustrate. Per available data strength of concrete should be taken between 4 and 7 ksi.
4. Assume a ratio between web thickness of the CFSSP-Wall and total web depth, b , that could range between $0.1b$ to $0.2b$.
5. Assume a thickness of the HSS (i.e., circular ends of the CFSSP-Wall) the same thickness as that of the web skin plate.

6. Assume that approximately 0.8 to 0.85 of the flexural demand is resisted by the steel part of the CFSSP-Wall cross-section

On the basis of the above assumptions, an expression to calculate the web depth of the CFSSP-Wall is derived for $0.8M_D$.

7. For CFSSP-NB wall web depth can be calculated according to the following:

i. $D/t_s = 0.044(E/F_y)$ (8.39)

- ii. The plastic section modulus for the steel skin of CFSSP-NB is given by:

$$Z_p = 22.73Xb^3 \left[X^2 + \frac{\pi}{2}X + 0.5 \right] \frac{F_y}{E} \quad (8.40)$$

- iii. The web depth, b , considering that 80% of the demand is resisted by the steel part of the CFSSP-Wall cross-section, can be estimated by:

$$b = 0.26 \sqrt[3]{\frac{M_D}{X \left(X^2 + \frac{\pi}{2}X + 0.5 \right)} \left[\frac{E}{F_y^2} \right]} \quad (8.41)$$

where,

M_D , Seismic demand calculated

X , ratio of half HSS diameter to the total web depth (taken between 0.1 to 0.2).

8. For CFSSP-B wall web can be calculated according to the following:

i. $D/t_s = 0.044(E/F_y)$ (8.42)

- ii. The plastic section modulus for the steel skin of CFSSP-NB is given by:

$$Z_p = 34.1Xb^3 \left[1.68\pi X^2 + 1.5\pi X + 0.5 \right] \frac{F_y}{E} \quad (8.43)$$

- iii. The web depth, b , can be estimated by:

$$b = 0.29 \sqrt[3]{\frac{M_D}{X (1.68\pi X^2 + 1.5\pi X + 0.5)} \left[\frac{E}{F_y^2} \right]} \quad (8.44)$$

where,

M_D , and X are as defined in item 7.

It should be noted here that D/t ratio chosen in the above steps reflects the limit that guarantee ductile performance per experimental and analytical work presented in earlier chapter of this document, however as mentioned earlier limited analytical work have shown that a value for $D/t_s = 0.076(E/F_y)$ can be used. The equations 8.41 and 8.44 are represented in Figure 8-4 to Figure 8-9 where this charts give the

value of web depth b , knowing the flexural demand, geometric configuration of the wall and finally the thickness of the concrete with regards to the web depth.

9. The preliminary dimensions obtained per the above steps and adjusted as necessary, the actual value of M_p is calculated using equations 8.12 and 8.13, and compared to the demand.
10. If $M_{p,calculated} < M_{Demand}$ changing the cross section dimensions or increasing steel strength is effective, while increasing the concrete strength will not significantly increase strength, as shown in Figure 8-4 to Figure 8-9 below. If $M_{p,calculated} \geq M_{Demand}$ the assumed cross-section dimensions is adequate (and could be optimized if over-strength is significant). Note that flexure-axial interaction can be taken into account at this stage, as appropriate.
11. Spacing of the tie bars is then calculated such that the CFSSP-Wall cross-section can attain its plastic moment capacity prior to local buckling of the skin plates.
12. In-plane displacement at the wall free end is calculated using the un-reduced seismic loads (i.e., for R factor of 1.0) considering the equivalent elastic stiffness using the equation provided in Section 8.6, and compared against the displacement limit given by equation 8.33. Note that this is in addition to the inter-story drift requirements of ASCE-7 (2010). If the lateral displacement limit are not satisfied, it is proposed to increase the depth of the wall cross-section to increase the section stiffness and increase the length of the plastic hinge.

To facilitate the preliminary design of the CFSSP-Walls, curves were constructed to help select preliminary dimensions of CFSSP-Walls based on the flexural demand on the wall system. The curves shown in Figure 8-4 to Figure 8-6 are used to design CFSSP-NB walls. The curves shown in Figure 8-7 to Figure 8-9 are used as design aids for the CFSSP-B walls. These figures were developed using the following assumptions:

- a. The strength of concrete, f'_c , is taken equal to 4, 5, 6, and 7 ksi.
- b. The yield stress, F_y , for the HSS and steel web is taken equal to 50 ksi.
- c. Total thickness of the wall is considered to be equal to $X_1 b$, where X_1 is taken equal to 0.10, 0.15, and 0.2.
- d. The thickness of the round half HSS of the CFSSP-NB cross section is the same as the steel web.
- e. The thickness of the skin plate is normalized by considering the following:
 - I. For CFSSP-NB walls, the diameter of the HSS, D , is taken equal to $X_1 b$, and the thickness of the skin plate is calculated using equation 8.1, such that, $t = 22.73D(F_y/E)$

- II. For CFSSP-B walls, the diameter of the HSS, D , is taken equal to $1.5X_1b$, and the thickness of the skin plate is calculated using equation 8.1, such that, $t = 19.725(F_y/E)$

For a given flexural demand on the wall, the charts can be used to select a depth of the wall's web and consequently the rest of the wall dimensions. After selection the cross-section dimensions, the actual plastic moment capacity of the wall is calculated, followed by selection of tie bars spacing, verification of in-plane displacement at the top of the wall and inter-story drift for the CFSSP--Walls.

Although the curves in Figures 8-4 to 8-9 were intended as design aid, they are useful to show that the changing concrete strength, f'_c , has an insignificant effect on M_p .

The relation between the wall capacity and the web depth, b , at concrete strength $f'_c = 4$ ksi, for different ratios of diameter of the HSS part to the total web depth is shown in Figure 8-10 for CFSSP-NB walls and shown in Figure 8-11 for CFSSP-B Walls.

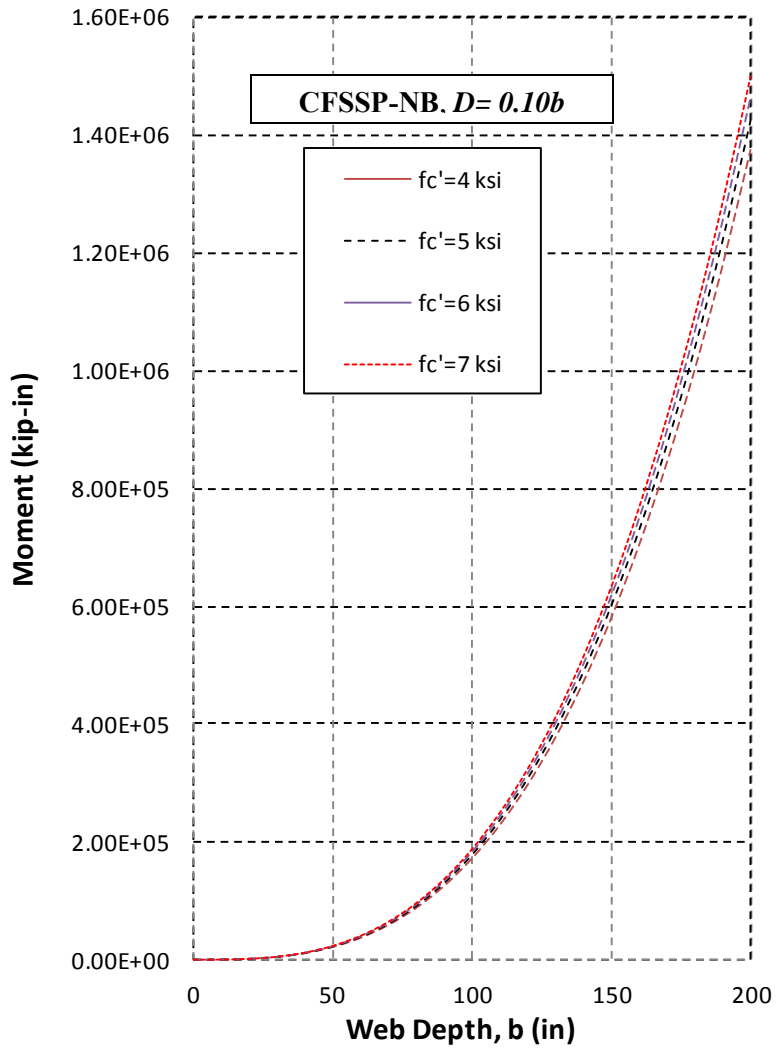


Figure 8-4 Design Curves for CFSSP-NB, $D = 0.10b$

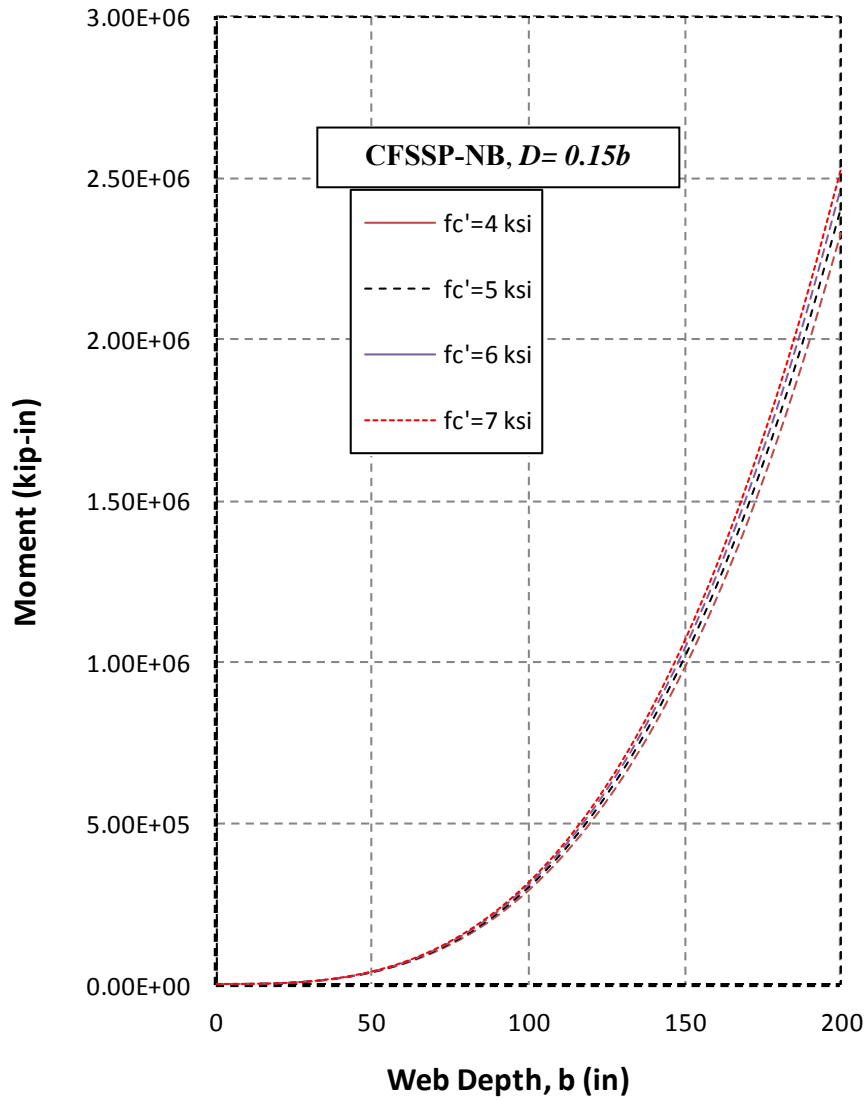


Figure 8-5 Design Curves for CFSSP-NB, $D=0.15b$

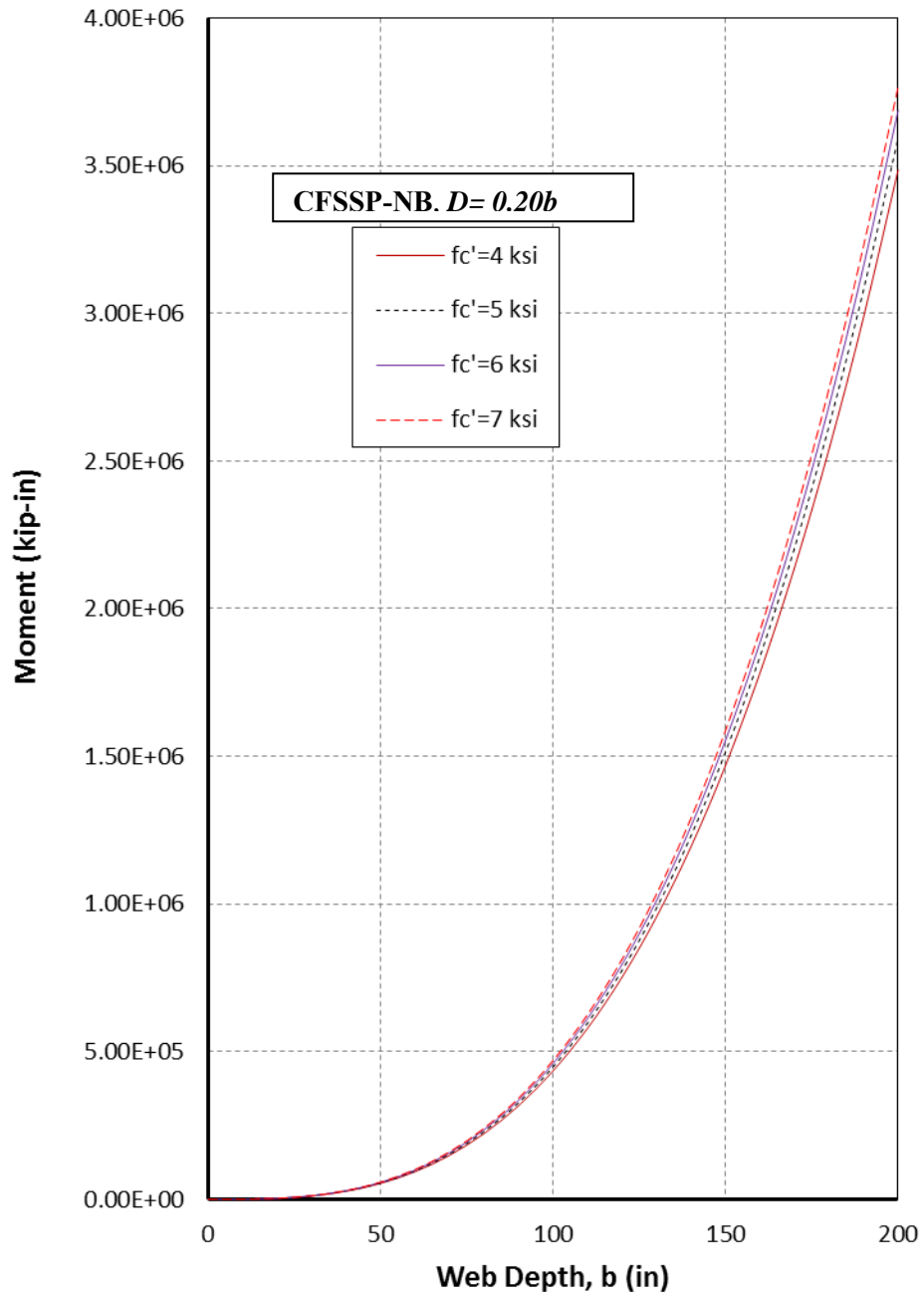


Figure 8-6 Design Curves for CFSSP-NB, $D = 0.20b$

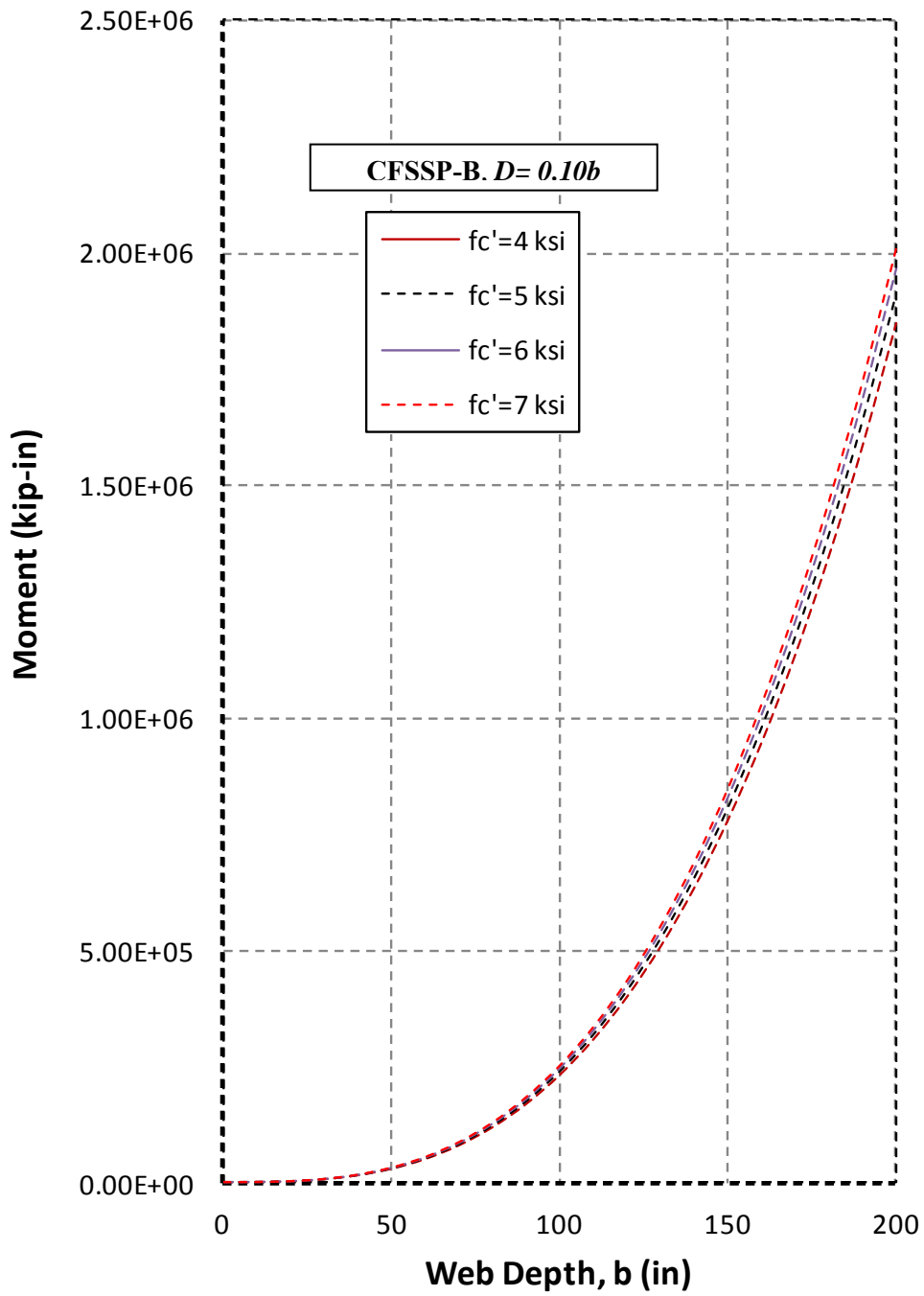


Figure 8-7 Design Curves for CFSSP-B, $D = 0.10b$

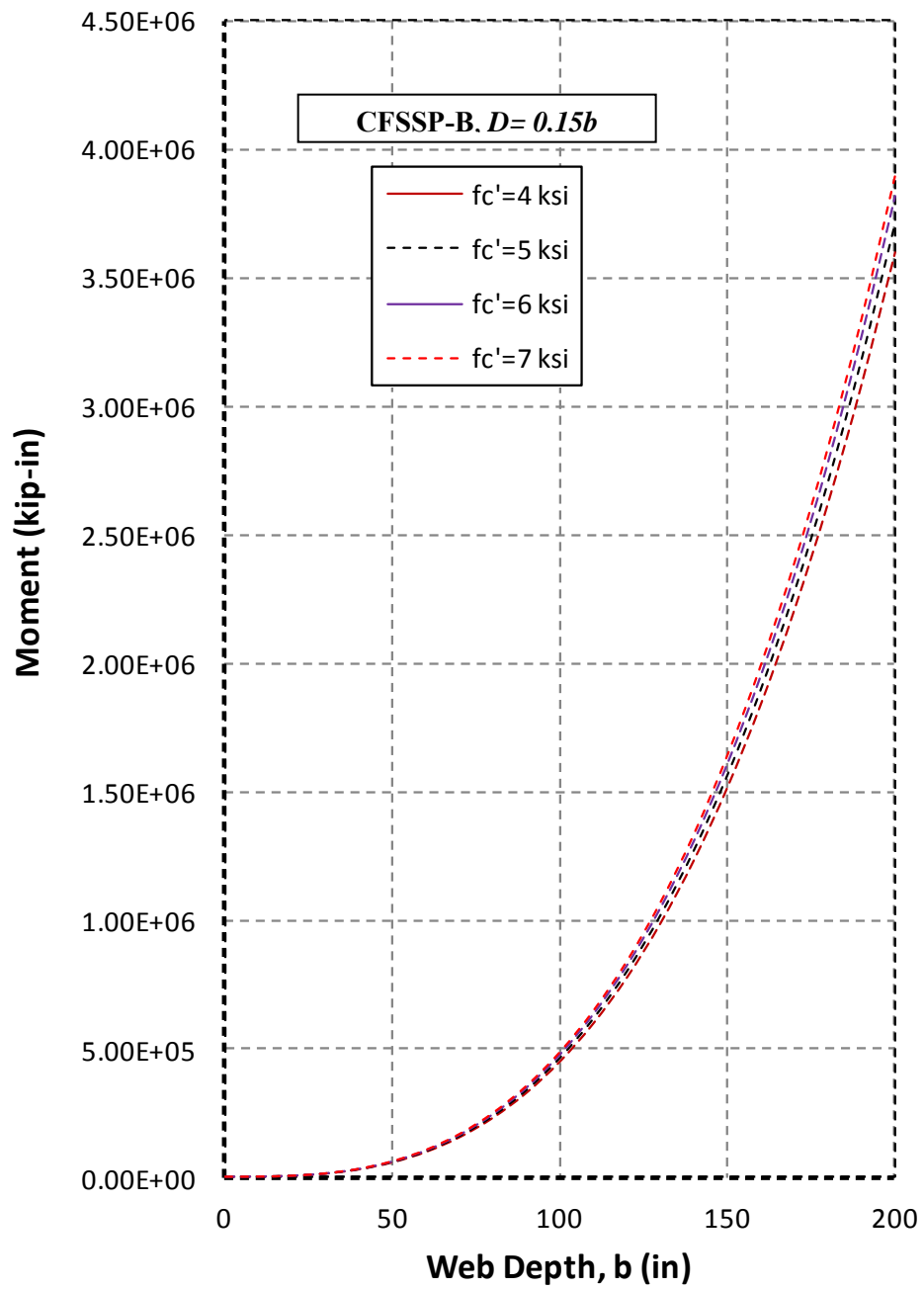


Figure 8-8 Design Curves for CFSSP-B, $D = 0.15b$

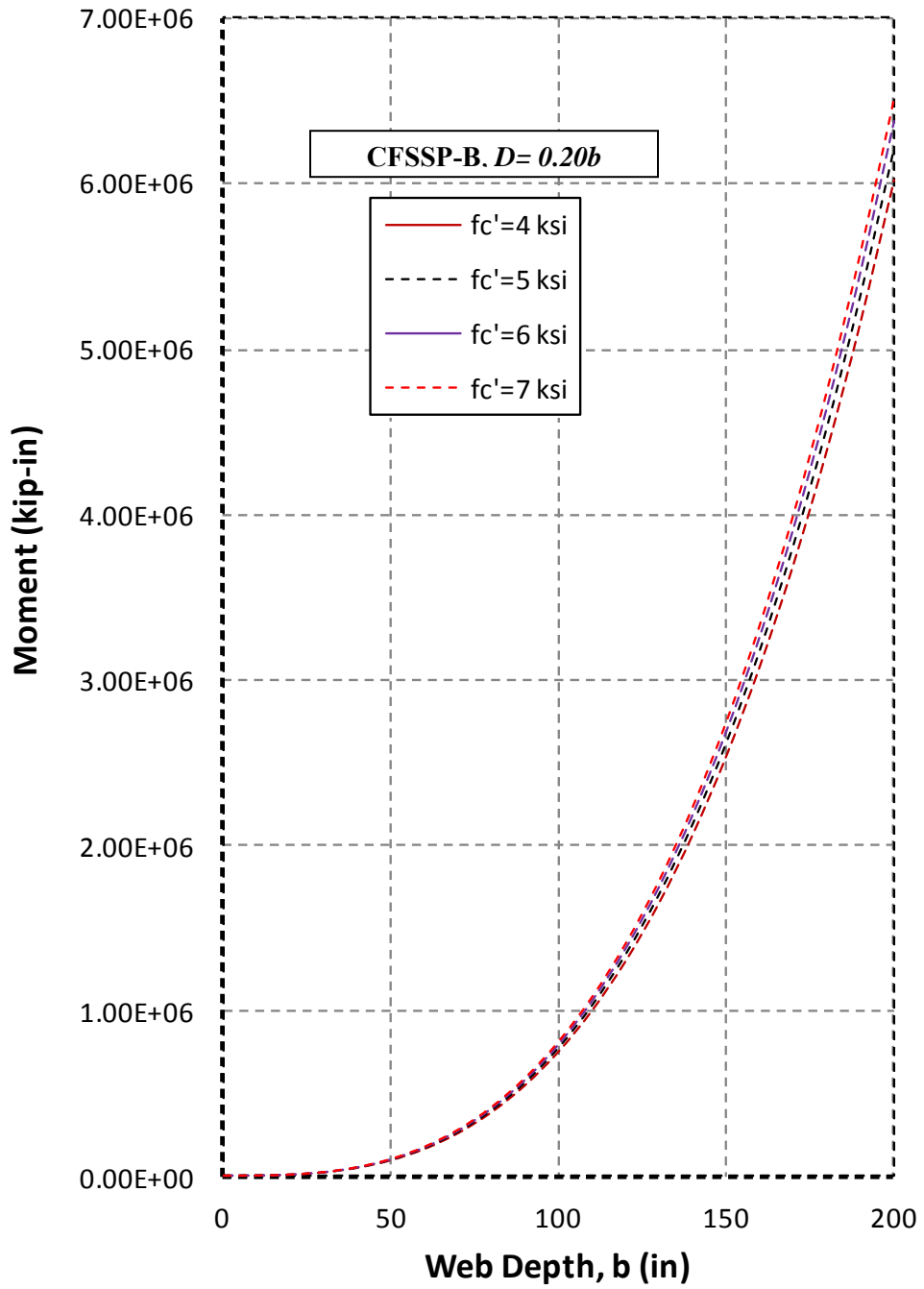


Figure 8-9 Design Curves for CFSSP-B, $D = 0.20b$

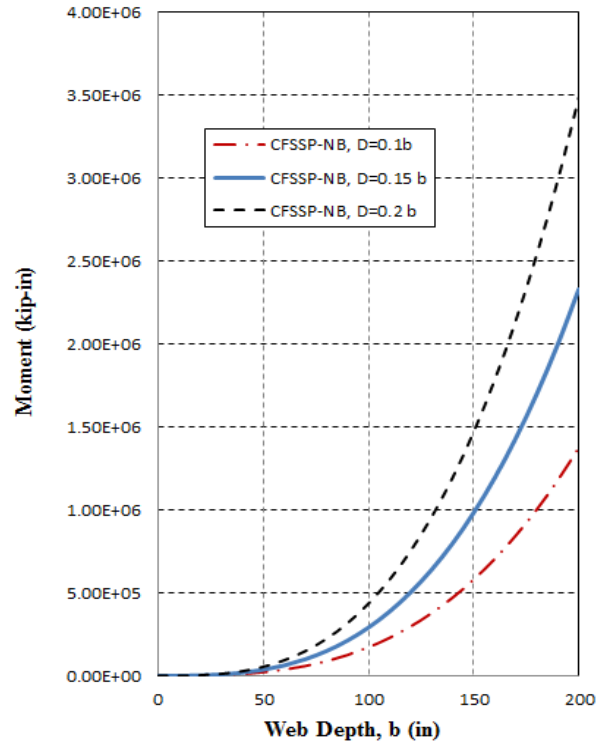


Figure 8-10 CFSSP-NB Wall Capacity for $f'_c=4$ ksi, and Different D Values

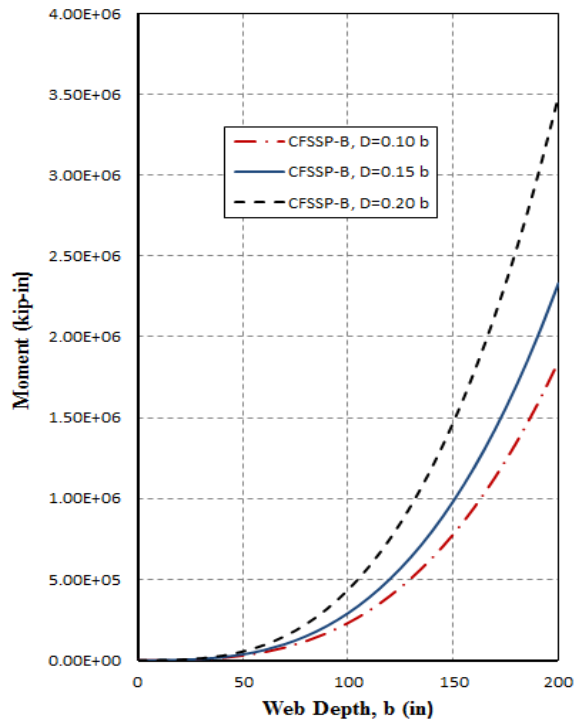


Figure 8-11 CFSSP-B Wall Capacity at $f'_c=4$ ksi, and Different D Values

8.9 Design Example

This section presents the design of a building having CFSSP-Walls with and without boundary elements, as the lateral load resisting system. The design example is based on "Design Example II: High Seismic Design" presented in Chapter 5 of the Steel Plate Shear Wall Design Guide (2006). The example was adjusted to be in compliance with the updated editions AISC-341 (2010) and ASCE-7 (2010), where relevant discrepancies with the new codes were adjusted to comply with the current versions of codes.

8.9.1 Building Description and Proposed Lateral Load Resisting System

The building is a 9 stories office building with a total height of 122', with a typical floor height of 13' and first floor height of 18', located in downtown San Francisco, on the corner of Montgomery and Market Streets. The typical floor plan is shown in Figure 9-1. Eight CFSSP-Walls are distributed on the perimeter of the buildings. The CFSSP-Walls have the same size and stiffness in order to eliminate irregularities that lead to torsion effects and to facilitate analysis using the equivalent static method.

8.9.2 Construction Materials used for the CFSSP-Walls

The skin plate material for the CFSSP-Walls is A572 Grade 50 (with $F_y = 50ksi$ and $F_u = 65ksi$) and concrete specified strength, $f'_c = 7ksi$.

8.9.3 Seismic Loads

The total weight of the building, W is 20,700 kips. The latitude and longitude values for the site (37.789° and -122.402° , respectively) were used to obtain the seismic ground motion values from USGS website. For the prescribed location, the Peak Ground Acceleration (PGA) is 0.7062g, the spectral accelerations at a period of 0.2 second, S_s , and at a period of 1.0 second, S_1 are:

$$S_s = 1.7035g \quad (8.45)$$

$$S_1 = 0.8501g \quad (8.46)$$

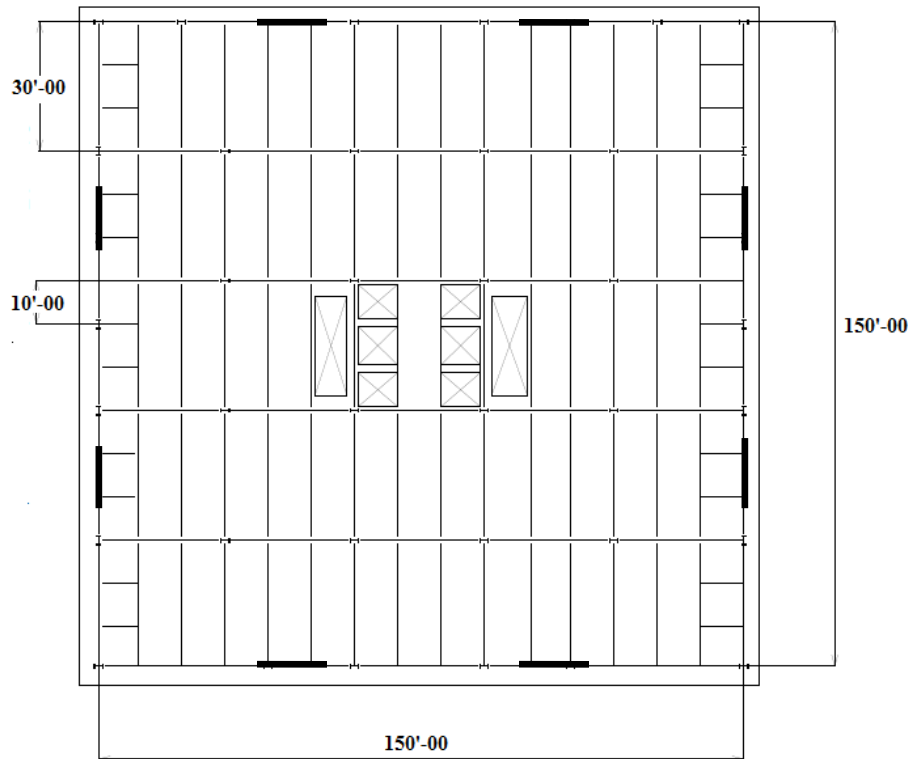


Figure 8-12 Schematic Plan of the Building and Location of CFSSP-Walls

Spectral values are modified based on site class in accordance to ASCE 7 Tables 11.4-1 and 11.4-2, by the modification factors:

$$F_a = 1, F_v = 1.5 \quad (8.47)$$

Spectral response acceleration parameters for short period, S_{MS} , and 1-second period, S_1 , calculated from ASCE 7 equations 11.4-1 and 11.4-2, are:

$$S_{MS} = F_a S_s = 1.70g \quad (8.48)$$

$$S_{M1} = F_v S_1 = 1.28g \quad (8.49)$$

Design earthquake spectral response acceleration parameters at short period, S_{DS} , and 1-second period, S_{D1} , determined from ASCE 7 equations 11.4-3 and 11.4-4, are:

$$S_{DS} = \frac{2}{3} S_{MS} = 1.13g \quad (8.50)$$

$$S_{D1} = \frac{2}{3} S_{M1} = 0.853g \quad (8.51)$$

Accordingly, the seismic design category is D, according to ASCE 7 Tables 11.6-1 and 11.6-2. The building has no structural irregularities and its height is less than 160 ft; consequently, according to ASCE 7 Table 12.6-1, the equivalent lateral force analysis method can be used.

The approximate building period is calculated using ASCE 7 equation 12.8-7:

$$T_a = C_t h_n^x = 0.02(122)^{0.75} = 0.734 \text{ sec} \quad (8.52)$$

$$\text{The period value, } T_s = \frac{S_{D1}}{S_{DS}} = \frac{0.853}{1.13} = 0.755 \text{ sec}$$

The associated seismic response coefficient, C_s , is determined in accordance to ASCE 7 equation 12.8-2, and the response modification factor from ASCE 7 Table 12.2-1 for steel and concrete composite plate shear wall, R , is equal to 6.5. The seismic importance factor from ASCE 7 Table 1.5-2, I_e , is taken equal to 1. Therefore:

$$C_s = \frac{S_{DS}}{R/I_e} = \frac{1.13g}{6.5/1} = 0.174g \quad (8.53)$$

The design base shear given by ASCE 7 equation 12.8-1 is:

$$V = C_s W = 0.174 \times 20,700 = 3601.8 \text{ kips} \quad (8.54)$$

The lateral seismic force, F_x , induced at any level is calculated from ASCE 7 equations 12.8-11 and 12.8-12:

$$F_x = C_{vx} V \quad (8.55)$$

$$C_{vx} = \frac{w_x h_x^k}{\sum_{i=1}^n w_i h_i^k} \quad (8.56)$$

The exponent k is calculated through interpolation between values of 0.5 seconds and 2.5 seconds, giving a value of 1.117, and the corresponding calculated load at each story is presented in Table 8-4.

Table 8-4 Vertical Distribution Factors and Floor Forces

Floor Level	Vertical Load Distribution Factor, C_{vx}	Floor Force, F_x (kips)
Roof	0.225	809
8th	0.174	625
7th	0.152	546
6th	0.129	464
5th	0.107	384
4th	0.0847	305
3rd	0.0635	228
2nd	0.0429	154
1st	0.0238	86

The accidental torsion was neglected on calculating the forces acting on the CFSSP-Wall, the forces acting on the CFSSP-Wall are presented in Table 8-5.

Table 8-5 Forces and Shear on CFSSP-Wall

Floor Level	Load per Floor (kips)	Shearing Force (kips)	Height from Ground (ft)
Roof	213	213	122
8th	164	377	109
7th	144	521	96
6th	122	643	83
5th	101	744	70
4th	80	824	57
3rd	60	884	44
2nd	41	925	31
1st	22	947	18

8.9.4 Design of the CFSSP-Walls

As the step of interest of this example, CFSSP-Walls are designed to resist the flexural demands calculated in the previous sections. However, for the more general case, in addition to resisting seismically induced shear forces and moments, CFSSP-Walls will also be subjected to axial force due to gravity loads acting on the wall's effective tributary area as well as due to the self-weight. A number of load combinations may have to be considered as part of design. Here, for expediency, only the following load case is considered:

$$0.9D+1.0E \quad (8.57)$$

For expediency, to obtain the axial force acting on the wall, the floor load is approximately calculated by dividing the total weight of the building (20,700 kips) by the number of floors (9) and then by the square foot area of one floor (150 ft²), which gives: $\frac{20700}{9 \times 150^2} = 0.102 \text{ kip/ft}^2$

The resulting axial Load per CFSSP-Wall = Floor Load \times Tributary Area \times Number of Floors = $0.1 \times 15 \times 20 \times 9 = 270 \text{ kip}$

The corresponding moment due to seismic load acting on the cantilever CFSSP-Wall to consider for this load combination is = $213 \times 122 + 164 \times 109 + 144 \times 96 + 122 \times 83 + 101 \times 70 + 80 \times 57 + 60 \times 44 + 41 \times 31 + 22 \times 18 = 83,749 \text{ kip-ft} = 1,004,988 \text{ kip-in}$

Note that, as mentioned in the procedure outline in Section 8.8, axial loads are not considered during preliminary design of the walls, but considered in later design iterations, as will be seen in the following section.

8.9.5 Design Procedure of CFSSP-Wall

Following the design procedure illustrated in 8.8 of this report, numerical calculations to design the proposed CFSSP-Wall systems are illustrated below, for cases with and without boundary elements.

Starting with the CFSSP-Wall without boundary elements, design proceeds as follows (per the steps in 8.8.1:

1. The type of CFSSP-Wall considered here is CFSSP-NB, with material properties as given in section 8.9.2, concrete strength 7 ksi and steel yield strength of 50 ksi
2. Using previously presented set of design charts to select preliminary dimensions of the CFSSP-NB wall. Here, by assuming the thickness of the wall to be 10% of its web depth, the chart shown in Figure

8-13 (for CFSSP-NB having $d = 0.10b$) can be used. For the given moment demand of 83,749 kip-ft (vertical axis), using the curve for $f'_c = 7$ ksi, an approximate value of steel web depth of 180 inches is obtained (horizontal axis), as shown in Figure 8-13

3. For a web height of approximately 180 inches, a corresponding 18" diameter round HSS is selected. Note that the inner diameter of the HSS is equal to the inner thickness of the wall.

4. The thickness of the steel skin plates is taken equal to that of the half HSS, which (for a steel elastic modulus, E of 29000 ksi and the yield stress of #) is given by:

$$D/t = 0.044(E/F_y) = 0.044(29,000/50) = 25.52$$

, which give, for D=18", a minimum thickness, $t = 0.71in$

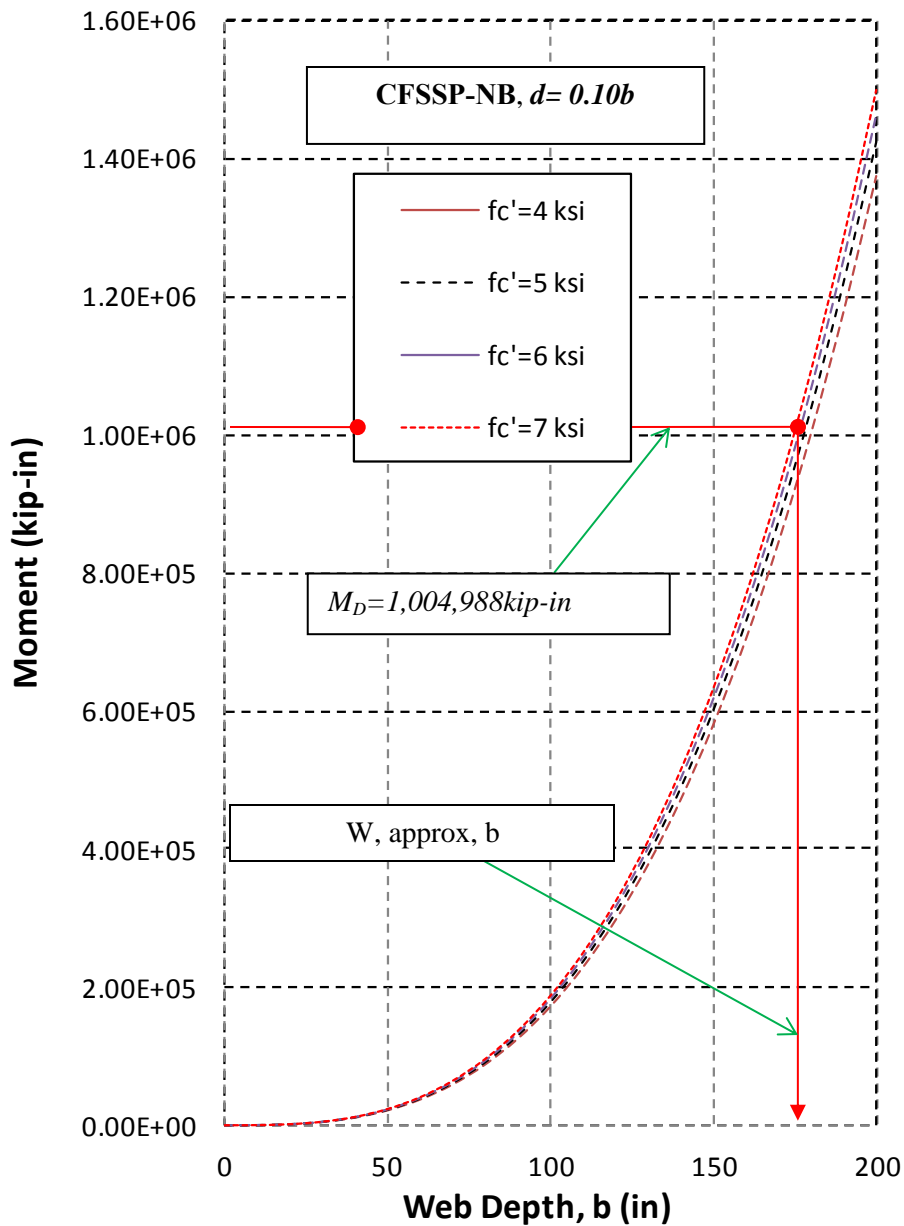


Figure 8-13 Preliminary Design of CFSSP-NB Walls using Aid of Curves

Note that a round HSS having this diameter and thickness is not listed in the AISC Construction Manual, and likely would have to be custom made from a rolled steel plate with the required thickness. Likewise, selection of the web thickness would be rounded up to the nearest available thickness. However, calculations from here proceed with the exact thickness value calculated above.

5. The plastic moment capacity of the cross-section can be calculated using equation 8.13 for:

$$t_s=0.71 \text{ inch.}, b=180 \text{ inch.}, t_c=18 \text{ inch.}, A_{HSS/pipe}=2\pi r t_s=40.15 \text{ in}^2$$

Then: $M_p = 1,082,053 \text{ kip-in} > M_u = 1,004,988 \text{ kip-in}$ (Ok)

6. The spacing of the tie bar can be calculated, assuming single buckling curvature mode in the vertical direction (direction of the flexural compression forces) considering the equation:

$$S_x = \sqrt{\frac{\pi^2}{3(1-\nu^2)} \left(\frac{E}{\sigma_{cr}} \right)} t = 32.51" , \text{ the spacing of tie bars is taken equal to } 32"$$

That will lead to 6 bars per horizontal row ($180''/32'' = 5.63$, rounded up to 6).

It is assumed that the vertical spacing is taken equal to the horizontal spacing of the tie bars

Therefore, for an inter-story height of 156'', the number of tie bars per vertical rows =

$$\frac{156}{32} = 4.875 \approx 5 \text{ Rows} .$$

Summing the tie bars over horizontal and vertical rows, the total number of tie bars between two floors is $6 \times 5 = 30$ tie bars

7. The minimum diameter of the tie bars, considering equal vertical and horizontal spacing of the tie bars and the same yield stress for the steel of skin plates and the tie bars, can be calculated according to:

$$d_{\min} = 1.59 t_s \sqrt{\left(\frac{w_2}{w_1} \right) \left(\frac{F_{y,plate}}{F_{y,tie-bars}} \right)} = 1.59 \times 0.71 = 1.12" = 1 \frac{1}{8}"$$

8. Assuming a tie-bar connection detail similar to that used in Wall CFSSP-B2 (Chapter 4), design of the fillet weld between the tie bars and the web skin plate can be accomplished as follows:

I. Consider thickness of weld to be $\frac{1}{4}"$

$$\text{II. } A_w = \pi d_{tb} t_w = \pi \times \left(1 \frac{1}{8}" \right) \times \frac{1}{4}" = 0.88 \text{ in}^2$$

III. The tension capacity of the tie bar = $A_{tie_bar} \times F_y = 49.7 \text{ kips}$

$$\text{IV. } \phi R_w = 2 \times 0.75 \times 0.6 \times 70 \times 0.88 = 55.44 \text{ kips} > 49.7 \text{ kip}$$

9. Check for shear strength of the tie bars:

The shearing force per one tie bar is given by:

$$V_n = (\text{Maximum Floor Load} / 2 \times \text{No. of Tie bars between floors}) = (213 / 2 \times 30) = 3.05 \text{ kips} < A_s F_u = 61.62 \text{ kip}$$

10. Check for strength of the wall combining both axial load and moment as per loading case given by equation 8.57, according to the following:

I. The axial capacity of the CFSSP-NB cross section is given by equation I2-13 in AISC-360 (2010)

$$P_o = A_s F_y + C_2 A_c f_c' = 295.7 \times 50 + 0.85 \times 3494.5 \times 7 = 35577.275 \text{ kips}$$

II. For the flexural buckling limit state based on column slenderness, considering the buckling to occur in the direction of the Y-axis of the wall

$$(EI_{eff})_y = E_s I_{ys} + 0.45 E_c I_{yc} = 29000 \times 24005 + 0.45 \times 4768 \times 92633 = 894,898,364$$

$$P_e = \pi^2 (EI_{eff}) / (KL)^2 = \pi^2 (89.5 \times 10^7) / (1 \times (18 \times 12)^2) = 189328 \text{ kips}$$

$$P_e \geq 0.44 P_o$$

$$P_n = P_o \left[0.658 \left(\frac{P_o}{P_e} \right) \right] = 32886.3 \text{ kips}$$

$$P_c = \phi_c P_n = 0.75 \times 32886.3 = 24664.725 \text{ kips}$$

$$P_r = 0.9 \times 270 = 243 \text{ kip}, \frac{P_r}{P_c} = 0.0098 < 0.20,$$

The interaction equation as per in AISC-360(2010), using equation (H1-1B)

$$\text{III. } \frac{P_r}{2P_c} + \frac{M_{rx}}{M_{cx}} = \frac{243}{2 \times 24665} + \frac{1004988}{1082053} = 0.933 \leq 1.0$$

11. The check for deflection can be calculated considering the CFSSP-Wall as a cantilever beam having flexural stiffness given by:

$$EI_{eff} = E_s I_s + c_3 E_c I_c = 5.42 \text{E}10 \text{ kip.in}^2$$

where,

$$E_c = 57000 \sqrt{f_c'} = 4,768 \text{ ksi}$$

$$c_3 = 0.45., I_s = 1,058,212 \text{ in}^4., I_c = 10,989,315 \text{ in}^4$$

$$\Delta_{\text{max/top_wall}} = 17.62''$$

To convert the displacement into equivalent elastic displacement the values should be multiplied by the factor R of 6.5, leading to:

$$\Delta_{\text{max,elastic_equ}} = 17.62 \times 6.5 = 114.53''$$

This value is checked against the limit provided by Equation #, for a plastic hinge length, L_p , taken equal to total depth of the CFSSP-NB wall of 198". This results in:

$$\Delta_{\max,elastic_equ} < \phi_{\max} \times L_p \left(L - \frac{L_p}{2} \right) = 77 \times 10^{-5} \times 198 \times \left(1464 - \frac{198}{2} \right) = 208.1''$$

Accordingly the wall deflection remains within the permissible limit.

Re-solving the Example but for CFSSP-B walls will go as follows:

1. In this case CFSSP-B is chosen together with material properties given in section 8.9.2
2. Using the set of design charts presented to set preliminary dimensioning of the CFSSP-NB wall by assuming that thickness of the wall to be 10% of its web depth, and diameter of the HSS will be 1.5 times the web thickness. Using the chart shown in Figure 8-7. Construct a horizontal line from the moment demand till it hit the curve for $f'_c = 7$ ksi and draw a vertical line from the intersection point to read approximated value for the steel web height as shown in Figure 8-14
3. The web height is approx. 160 inch, accordingly the diameter of the round HSS is 24"
4. The Thickness of the steel skin plates, considering that the steel elastic modulus, E equals to 29000 ksi web and half HSS is given by:

$D/t = 0.076(E/F_y)$, such that, $t = 0.54in$. Approximated to 9/16", The diameter of the HSS is taken equal to 24"

5. The plastic moment capacity of the cross-section can be calculated using 8.22, where:
 $t_s = 9/16$ inch., $b = 160$ inch., $t_c = 16$ inch., $d_{in} = 24''$, $A_{HSS/pipe} = 2\pi r t_s = 42.411 in^2$
The $M_p = 1,044,242$ kip-in $>$ $1,004,988$ kip-in (Ok)
6. The spacing of the tie bar can be calculated, assuming single buckling curvature mode in the vertical direction (direction of the flexural compression forces) considering the equation:

$$S_x = \sqrt{\frac{\pi^2}{3(1-\nu^2)} \left(\frac{E}{\sigma_{cr}} \right) t} = 25.75'' \approx 25''$$

, the spacing of tie bars is taken equal to 25",

Accordingly 7 bars per row can be used.

It is assumed that the vertical spacing is taken equal to the horizontal spacing of the tie bars, which leads to number of tie bars between two floors, can be calculated as follows:

The number of tie bars rows = $\frac{156}{25} = 6.24 \approx 6$ Rows , edge distance will need to be adjusted. The

total number of tie bars between two floors = $6 \times 7 = 42$ tie bars

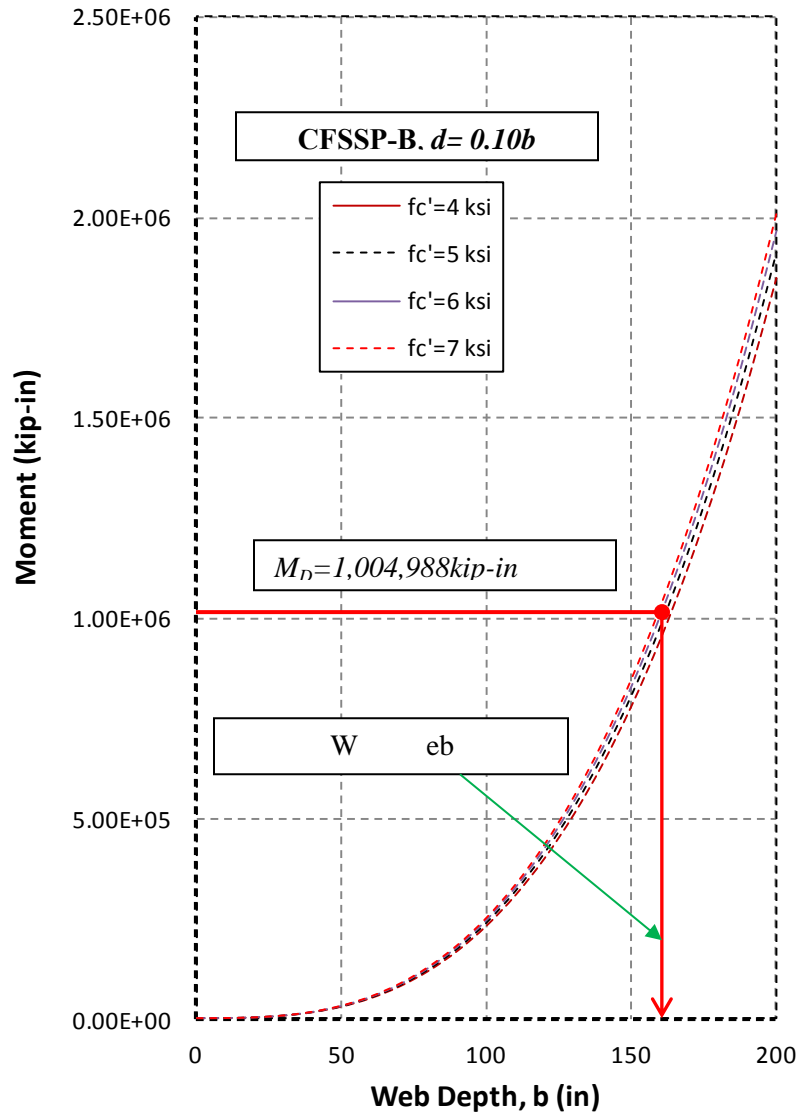


Figure 8-14 Preliminary Design of CFSSP-B Walls using Aid of Curves

7. The minimum diameter of the tie bars, considering equal vertical and horizontal spacing of the tie bars and the same yield stress for the steel of skin plates and the tie bars, can be calculated according to:

$$d_{\min} = 1.59t_s \sqrt{\left(\frac{w_2}{w_1}\right) \left(\frac{F_{y,plate}}{F_{y,tie-bars}}\right)} = 1.59 \times 0.5625 = \frac{7}{8}$$

8. Design of the fillet weld between the tie bars and the web skin plate:

I. Consider thickness of weld to be $\frac{1}{4}$ "

$$\text{II. } A_w = \pi d_{tb} t_w = \pi \times \left(\frac{7}{8}\right) \times \frac{1}{4} = 0.69 \text{ in}^2$$

III. The Tension capacity of the tie bar = $A_{tie_bar} \times F_y = 30.06 \text{ kips}$

$$\text{IV. } \phi R_w = 2 \times 0.75 \times 0.6 \times 70 \times 0.69 = 43.47 \text{ kips} > 30.06 \text{ kip}$$

8. Check for shear strength of the tie bars:

The shearing force per one tie bar is given by:

$$V_n = (\text{Maximum Floor Load} / 2 \times \text{No. of Tie bars between floors}) = (213 / 2 \times 42) = 2.53 \text{ kips} < A_s F_u = 61.62 \text{ kip}$$

9. Check for strength of the wall combining both axial load and moment as per loading case given by equation 8.57 according to the following:

I. The axial capacity of the CFSSP-NB cross section is given by equation I2-13 in AISC-360 (2010)

$$P_o = A_s F_y + C_2 A_c f_c' = 264.82 \times 50 + 0.85 \times 3432.7 \times 7 = 33666 \text{ kips}$$

II. For the flexural buckling limit state based on column slenderness, considering the buckling to occur in the direction of the Y-axis of the wall

$$(EI_{eff})_y = E_s I_{ys} + 0.45 E_c I_{yc} = 29000 \times 18456 + 0.74 \times 4768 \times 89871 = 852,317,647$$

$$P_e = \pi^2 (EI_{eff}) / (KL)^2 = \pi^2 (85.2 E \times 10^7) / (1 \times (18 \times 12)^2) = 180232 \text{ kips}$$

$$P_e \geq 0.44 P_o$$

$$P_n = P_o \left[0.658^{\left(\frac{P_o}{P_e}\right)} \right] = 31134 \text{ kips}$$

$$P_c = \phi_c P_n = 0.75 \times 32886.3 = 24664.725 \text{ kips}$$

$$P_r = 0.9 \times 270 = 243 \text{ kip}, \frac{P_r}{P_c} = 0.0098 < 0.20,$$

The interaction equation as per in AISC-360(2010), using equation (H1-1B)

$$\frac{P_r}{2P_c} + \frac{M_{rx}}{M_{cx}} = \frac{243}{2 \times 24665} + \frac{1004988}{1044242} = 0.97 \leq 1.0$$

9. The check for deflection can be calculated considering the CFSSP-Wall as a cantilever beam having flexural stiffness given by:

$$EI_{eff} = E_s I_s + c_3 E_c I_c = 6.83E10 \text{ kip.in}^2$$

where,

$$E_c = 57000 \sqrt{f'_c} = 4,768 \text{ ksi}$$

$$c_3 = 0.74., I_s = 1,061,160 \text{ in}^4., I_c = 10,645,729 \text{ in}^4$$

$$\Delta_{\text{max/top_wall}} = 13.98''$$

To convert the displacement into equivalent elastic displacement the values in should be multiplied by the factor R leading to:

The plastic hinge length, L_p , is taken equal to total depth of the CFSSP-NB wall, 198".

$$\Delta_{\text{max,elastic_equ}} = 13.98 \times 6.5 = 90.87''$$

$$\Delta_{\text{max,elastic_equ}} < \phi_{\text{max}} \times L_p \left(L - \frac{L_p}{2} \right) = 77 \times 10^{-5} \times 201.89 \times (1464 - 201.89) = 196.2''$$

Chapter 9

SUMMARY, CONCLUSIONS, AND RECOMMENDATIONS FOR FUTURE WORK

9.1 Summary

Research was conducted on concrete filled steel sandwich panel walls (CFSSP-Walls) in order to investigate the ductility and seismic performance of this structural system under in-plane flexure. The research focused onto walls which have an aspect ratio (height to cross section depth), h/W , over 2, such that the ductile behavior of the wall is induced by developing the plastic moment capacity of the cross section, M_p . Accordingly, an experimental program was executed at the SEESL lab at University at Buffalo, followed by analytical investigation that involved plastic analysis, fiber analysis, and finite element analysis. The experimental and analytical results were used to develop seismic design recommendations for the CFSSP-Wall.

Previous studies on composite shear walls focused on walls developing the ductile behavior through shear yielding, with relatively little available work on walls developing flexural yielding, as reflected in existing design recommendations in AISC 341-10.

In the experimental program, 4 CFSSP-Walls specimens were tested under quasi-static cyclic loading (following the ATC-24 protocols). These walls were divided into two groups, namely: Group NB and B. Group NB consisted of walls with no boundary elements, where the specimens end flanges consisted of half round HSS in order to avoid stress concentration at the corner welds. The specimens of group NB had an aspect ratio h/W of 2.54. The two tested walls were different in their S/t ratio (expressing steel plate slenderness, as a function of the spacing of ties, S , divided by the thickness of the plates), which was taken as equal to 25.6 in specimen CFSSP-NB1 and 38.4 in specimen CFSSP-NB2. In both specimens of Group NB, the tie bars interconnecting the two steel web plates were seamless 1 inch diameter bars plug welded to the web steel plate.

The two Group B specimens had full round HSS at their ends, serving as boundary elements. The tested walls of Group B had h/W of 2.67, and again the two tested walls were different in their S/t ratio, which was taken as equal to 25.6 in specimen CFSSP-B1 and 38.4 in specimen CFSSP-B2. Other differences from group B include the fact that specimen CFSSP-B2 tie bars were fillet welded to the web skin plates (instead of plug welded), and that fiber concrete was used in that specimen in an attempt to reduce the tension cracks in the concrete at ultimate behavior.

The tested specimens of both groups performed well. The four tested specimens were able to attain/exceed the expected plastic moment capacity and were able to sustain their load capacity up to a drift exceeding 3%, which emphasized the ductile behavior of these CFSSP-Walls. Strength degradation of the tested specimens started with local buckling of the web skin plate between the first two rows of tie bars, after attaining their M_p values. Then, cracks in the steel web started to develop at the tie bar web skin plate connection, followed by local buckling in the round HSS part of the specimen. Fracture eventually propagated from the location of the tie bars to the rest of the tested specimens. Local buckling in the CFSSP-NB walls developed at similar height from the base in the steel web and the round HSS, while for the CFSSP-B walls, local buckling developed in the web between the rows of the tie bars and at the base of the HSS. The test results were used to evaluate the ductility of the CFSSP-Walls, and calculation of their displacement and curvature ductility.

The finite element method using ABAQUS 6.10EF2 explicit solver was then used to establish models simulating the behavior of the tested walls, and the calibrated models were further used to carry a limited parametric study investigating design parameters that were not covered in the experimental program. This included cases with S/t ratio of 50, D/t equal to 0.076 (E/F_y), h/W of 5.9, and finally the use of thicker concrete (taken equal to 0.35b instead of 0.2b, where b is the length of the steel web of the CFSSP-Wall).

Finally, the experimental and analytical results were used to develop design recommendations for CFSSP-B and CFSSP-NB walls, including expressions to limit the S/t and D/t ratios, and an expression to calculate the required diameter of the tie bars (based on the plastic deformation of the steel skin plate during local buckling). Simple plastic theory was used to derive expressions to calculate the plastic moment capacity of CFSSP-NB and CFSSP-B walls. Graphical design aids were developed to facilitate preliminary cross-section design of CFSSP-NB and CFSSP-B walls.

9.2 Conclusions

From the experimental and analytical work conducted in this research program, the following conclusions are obtained:

1. CFSSP-Walls detailed in accordance to the procedures presented in this report can exhibit satisfactory ductile performance through flexural yielding.
2. The use of round HSS at the end of the CFSSP-Walls cross-section is effective to avoid the premature failure of the wall due to stress concentration at the right angle corners of composite members of rectangular cross-section and observed by other researchers.
3. The tie bars linking the two sides of the steel sandwich panel plays an important role in the behavior of the CFSSP-Wall and have to be adequately spaced in both the horizontal and vertical directions to

prevent elastic plate buckling, to make it possible for the CFSSP-Wall to attain its M_p value, and sustain this capacity through cyclic excursions with limited strength degradation up to 3% lateral drift. The tie bar sizes are designed to sustain the tension force resulting from plastic deformation of the buckled web skin plate.

4. The D/t ratio of the HSS part of the proposed CFSSP-Wall configuration need not be more than $0.044 E/F_y$ for the wall to perform adequately, however, the performed limited finite element analysis showed that if the HSS part of the cross-section has a D/t equals to $0.076E/F_y$ it could still perform in a ductile manner.
5. Calculating the plastic moment capacity of the proposed wall can be done assuming that the steel skin plates have reached F_y in both tension and compression on their respective sides of the wall's neutral axis (considering bending around the strong axis of the wall) and considering that the concrete over the entire compressed part of the wall has reached f'_c . Note that this simplification neglects factors typically used in concrete design to account for the rectangular stress block and for the fact that concrete is assumed to attain only 0.85 of its strength. Experimental results have shown the simplified approach proposed here to be conservative.
6. Fiber analysis techniques can be used to estimate the capacity of the CFSSP-Walls, even when considering different concrete models. When using bi-linear material models for both steel and concrete, results will match those calculated in item 5 above.
7. Finite Element modeling can be used effectively to obtain the capacity, ductility, and modes of local buckling of CFSSP-Walls. However, results can be sensitive to the types of material models used in the simulation, and it is recommended to use the material models presented in this report.
8. CFSSP-Walls can be designed using the same seismic performance factors, R , specified in ASCE-7 (2010) for special composite shear walls.
9. Seismic design of CFSSP-Walls can be facilitated by the procedures developed to calculate preliminary cross-section dimensions.

9.3 Recommendations for Future Work

Beyond the current study, many factors still need to be researched to develop a better understanding of the behavior of CFSSP-Walls in seismic applications. This section highlights some of this needed research.

- First, different configurations of CFSSP-Walls should be investigated, including walls with rectangular cross-sections or with square HSS boundary elements. Different configurations studied could also include coupled wall systems.

- Walls with h/W ratio that is less than 2 should be studied. Particularly, for some low aspect ratios, yielding will include contributions from both shear and flexural yielding.
- Effect of the rigidity of the tie bars and its effect on the local buckling of the skin plates need to be investigated. The primary role of tie bars is to provide supports for the steel panel. There may be instances when the forces for which the tie bars are designed could give tie bar sizes that can provide adequate strength but that might not be able to provide sufficient stiffness to adequately restrain the ends of the buckled part of the steel web panel. A formulation for the required stiffness of tie bars need to be established.
- The possibility of using different vertical and horizontal spacing of tie bars could be investigated, if instances exist where this could lead to more economical designs (taking into account possible changes in the buckling mode in such conditions).
- Other methods for tie bar skin plate connection should be investigated, including threaded tie bars with nut welded to skin plate, or ordinary long bolts with head and nuts.
- Applications with higher strength concrete (above 8ksi), as well as use of Engineered Cementitious Composite (also called bendable concrete) that can provide improved tension behavior, needs to be investigated.
- Methods to design the seismic collectors that would have to be used with CFSSP-Walls need to be investigated, with special attention to the connection between the collector and the wall to achieve effective load transfer in this case.
- The design of horizontal and vertical field splices for CFSSP-Walls need to be investigated, to develop details that can achieve appropriate load transfer.
- The connection between the wall and the foundation need to be further studied, and details should be developed to economically transfer to the foundation the large moments generated at the wall foundation interface.
- In terms of analysis, more rigorous concrete models need to be used, particularly for cross-sections where the concrete portion of the wall has a significant effect on the total wall capacity. In this case, using a concrete model that can appropriately account for material damage under cyclic displacement excursions is of paramount importance.
- Due to eccentric load, the CFSSP-Walls could be subjected to in-plane and out-of-plane loading. Out-of-plane loading with relatively small magnitudes will induce additional compression stress into one of the skin plates, which could change the pattern of local buckling of the skin plate and could even trigger local buckling at lower drifts compared to walls subjected to in-plane loading. It is recommended to study the effect of simultaneous bi-axial loading on the behavior of CFSSP-Walls.

CHAPTER 10

REFERENCES

- AISC-341 (2010). "*Seismic Provisions for Structural Steel Buildings.*" American Institute of Steel Construction, Chicago, Illinois.
- Amit H. Varma, K. C. S., Kai Zhang, Keith Coogler, Sanjeev R. Malushte (2011b). "Out-of-Plan SHEAR Behavior of SC Composite Structures." Transactions of the 21st SMiRT Conference, New Delhi, India.
- Arabzadeh, A., Soltani, M., and Ayazi, A. (2011). "Experimental investigation of composite shear walls under shear loadings." *Thin-Walled Structures*, 49(7), 842-854.
- ASCE-7 (2010). "*Minimum Design Loads for Buildings and other Structures.*" American Society of Civil Engineers, Reston, VA, 2011
- Astaneh-Asl, A. (2002). "*Seismic Behavior and Design of Composite Steel Plate Shear Walls*", Structural Steel Educational Council, Moraga, California.
- Astaneh-Asl, A., and Zhao, Q. (2001). "Cyclic tests of steel shear walls." *Report Number UCB/CE-Steel-01/01, Department of Civil and Environmental Engineering, University of California, Berkeley, August.*
- BS8110 (1985). "Structural Use of Concrete." British Standard, London
- Bowerman, H., Gough, M., and King, C. (1999). "Bi-Steel Design and Construction Guide." British Steel Ltd, Scunthorpe, London.
- Dan, D., Fabian, A., and Stoian, V. (2011). "Theoretical and experimental study on composite steel–concrete shear walls with vertical steel encased profiles." *Journal of Constructional Steel Research*, 67(5), 800-813.
- Driver, R., Abbas, H., and Sause, R. (2002). "Local buckling of grouted and ungrouted internally stiffened double-plate HPS webs." *Journal of Constructional Steel Research*, 58(5), 881-906.
- El-Bahey, S., and Bruneau, M. (2011). "Bridge piers with structural fuses and bi-steel columns. I: Experimental testing." *Journal of Bridge Engineering*, 17(1), 25-35.

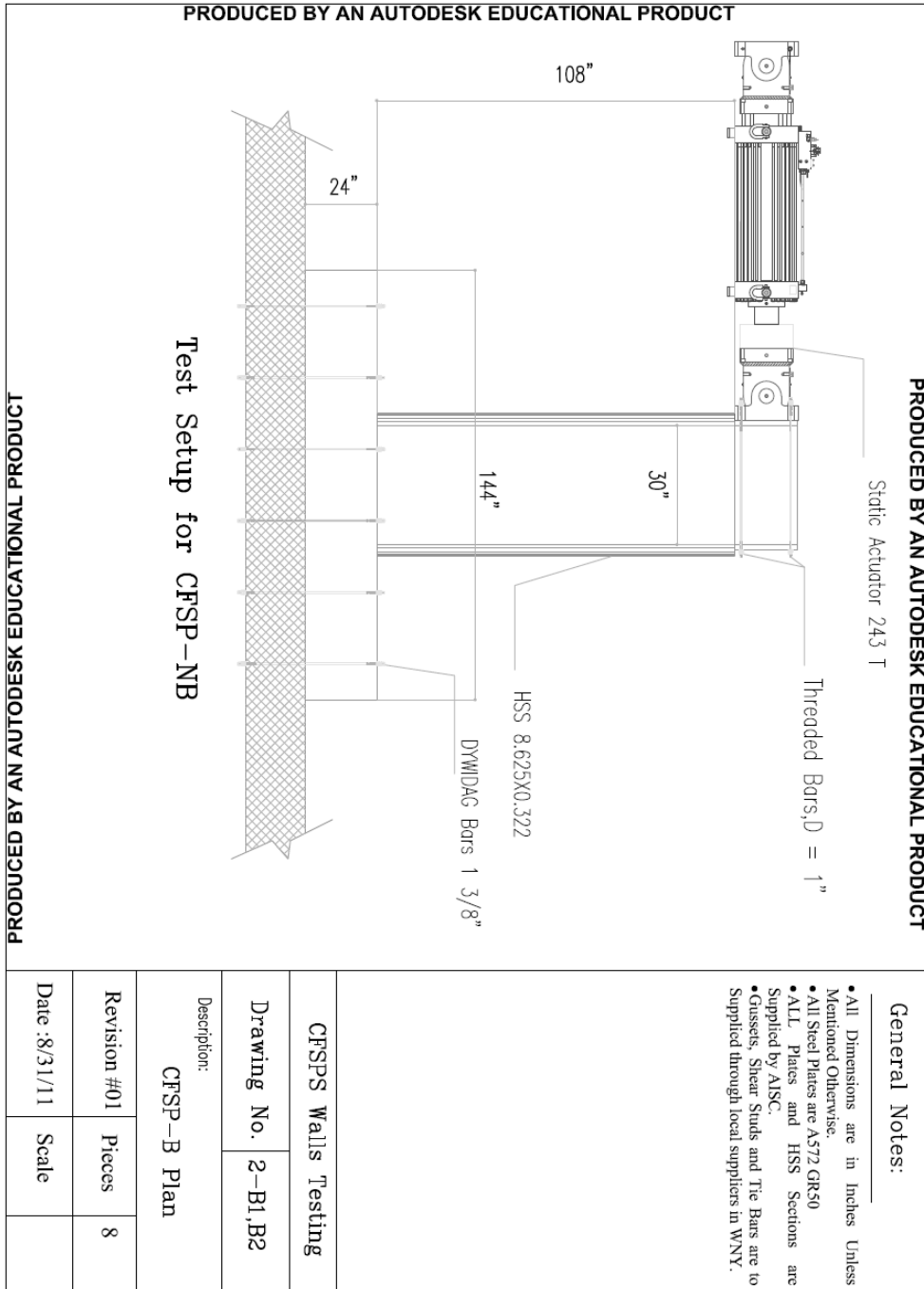
- Eom, T.-S., Park, H.-G., Lee, C.-H., Kim, J.-H., and Chang, I.-H. (2009). "Behavior of double skin composite wall subjected to in-plane cyclic loading." *Journal of Structural Engineering*, 135(10), 1239-1249.
- Foundoukos, N., and Chapman, J. (2008). "Finite element analysis of steel–concrete–steel sandwich beams." *Journal of Constructional Steel Research*, 64(9), 947-961.
- Hossain, K. A., and Wright, H. D. (1998). "Performance of profiled concrete shear panels." *Journal of Structural Engineering*, 124(4), 368-381.
- Hossain, K. M. A., and Wright, H. D. (2004). "Design Aspects of Double Skin Profiled Composite Framed Shearwalls in Construction and Service Stages." *ACI Structural Journal*, 101(1).
- Liao, F.-Y., Han, L.-H., and Tao, Z. (2012). "Performance of reinforced concrete shear walls with steel reinforced concrete boundary columns." *Engineering structures*, 44(0), 186-209.
- Ozaki, M., Akita, S., Osuga, H., Nakayama, T., and Adachi, N. (2004). "Study on steel plate reinforced concrete panels subjected to cyclic in-plane shear." *Nuclear engineering and design*, 228(1), 225-244.
- Rahai, A., and Hatami, F. (2009). "Evaluation of composite shear wall behavior under cyclic loadings." *Journal of Constructional Steel Research*, 65(7), 1528-1537.
- Sener, K. C., Malushte, S. R., Booth, P. N., and Varma, A. H. (2012). "Analysis Recommendations for Steel-Composite (SC) Walls of Safety-Related Nuclear Facilities." *Structures Congress 2012*, 1871-1880.
- Varma, A. H., Malushte, S. R., Sener, K., and Lai, Z. (2011). "Steel-Plate Composite (SC) Walls for Safety Related Nuclear Facilities: Design For In-Plane and Out-of-Plane Demands." Transactions of the 21st SMiRT Conference, New Delhi, India.
- Wright, H. (1998). "Axial and Bending Behavior of Composite Walls." *Journal of Structural Engineering*, 124(7), 758-764.
- Zhao, Q., and Astanteh-Asl, A. (2004). "Cyclic behavior of traditional and innovative composite shear walls." *Journal of Structural Engineering*, 130(2), 271-284.
- Zhao, Q., and Astanteh-Asl, A. (2007). "Seismic behavior of composite shear wall systems and application of smart structures technology." *Steel Structures*, 7, 69-75.
- Qian, J., Z. Jiang, et al. (2012). "Behavior of steel tube-reinforced concrete composite walls subjected to high axial force and cyclic loading." *Engineering structures* 36(0): 173-184.

Sabelli, R., and Bruneau, M. (2007). "Steel Design Guide 20: Steel Plate Shear Walls." American Institute of Steel Construction, Chicago, Illinois.

Wright, H. (1995). "Local stability of filled and encased steel sections." *Journal of Structural Engineering*, 121(10), 1382-1388.

APPENDIX A

EXCERPT OF TEST SETUP CONSTRUCTION DRAWING



General Notes:

- All Dimensions are in Inches Unless Mentioned Otherwise.
- All Steel Plates are A572 GR50
- ALL Plates and HSS Sections are Supplied by AISI.
- Gussers, Shear Studs and Tie Bars are to Supplied through local suppliers in WNY.

CFSPS Walls Testing

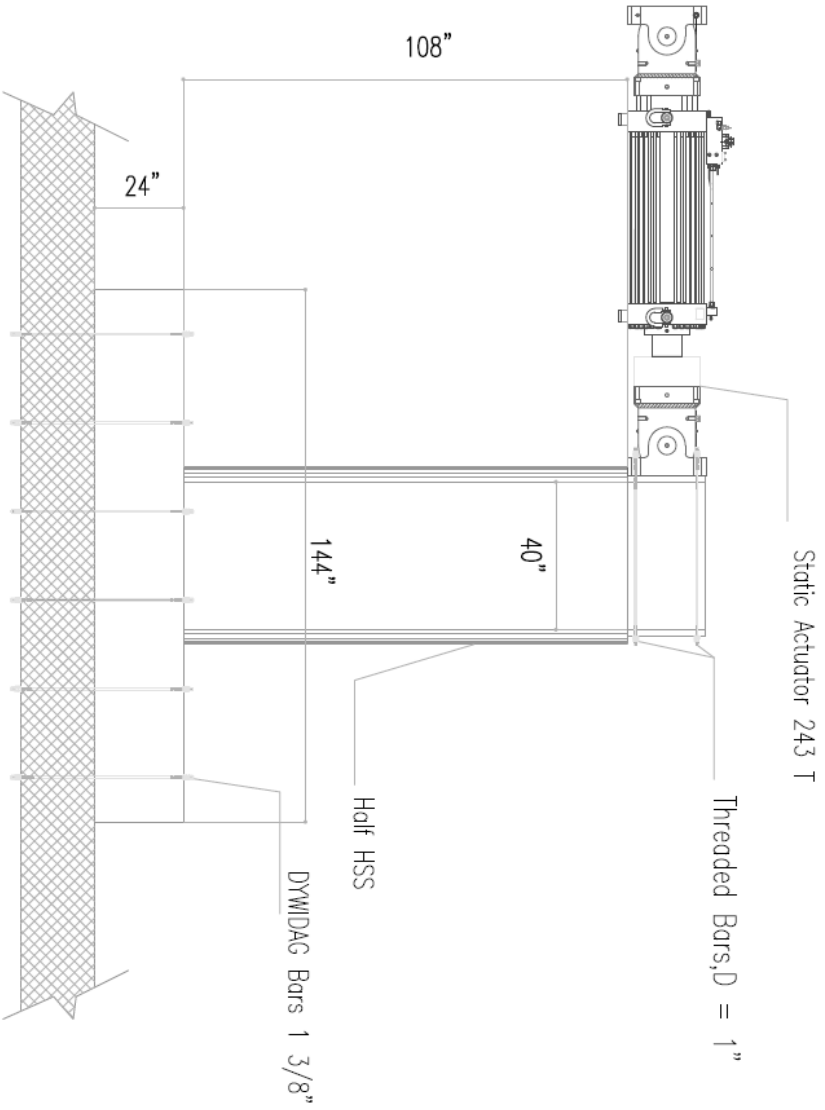
Drawing No. 2-B1,B2

Description:

CFSP-B Plan

Revision #01	Pieces	8
--------------	--------	---

Date :8/31/11	Scale	
---------------	-------	--



PRODUCED BY AN AUTODESK EDUCATIONAL PRODUCT

General Notes:

- All Dimensions are in Inches Unless Mentioned Otherwise.
- All Steel Plates are A572 GR50
- ALL Plates and HSS Sections are Supplied by AISC.
- Gussets, Shear Studs and Tie Bars are to Supplied through local suppliers in WNY.

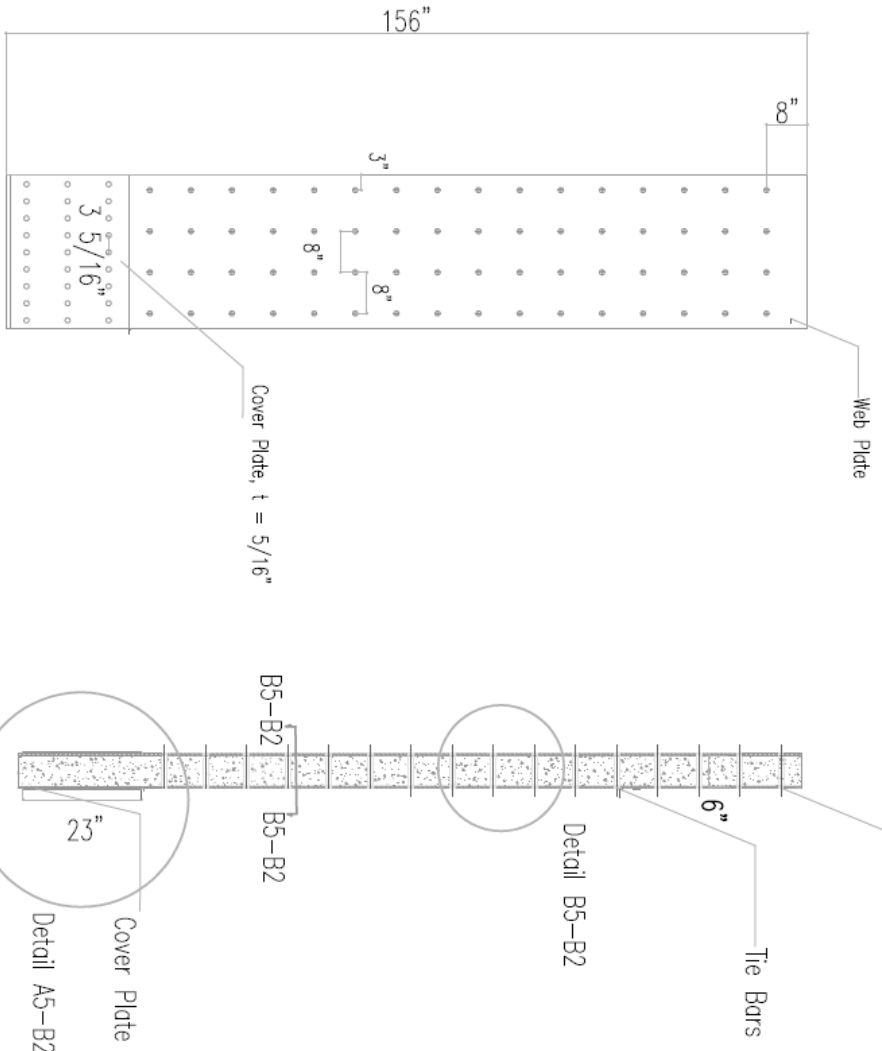
CFSPS Walls Testing

Drawing No. 2-NB1,NB2

Description:
CFSP-NB Plan

Revision #01	Pieces	8
Date :8/31/11	Scale	

PRODUCED BY AN AUTODESK EDUCATIONAL PRODUCT



Web Assembly Elevation

Web Assembly Elevation

General Notes:

- All Dimensions are in Inches Unless Mentioned Otherwise.
- All Steel Plates are A572 GR50
- ALL Plates and HSS Sections are Supplied by AISC.
- Gussets, Shear Studs and Tie Bars are to Supplied through local suppliers in WNY.

CFRSPS Walls Testing

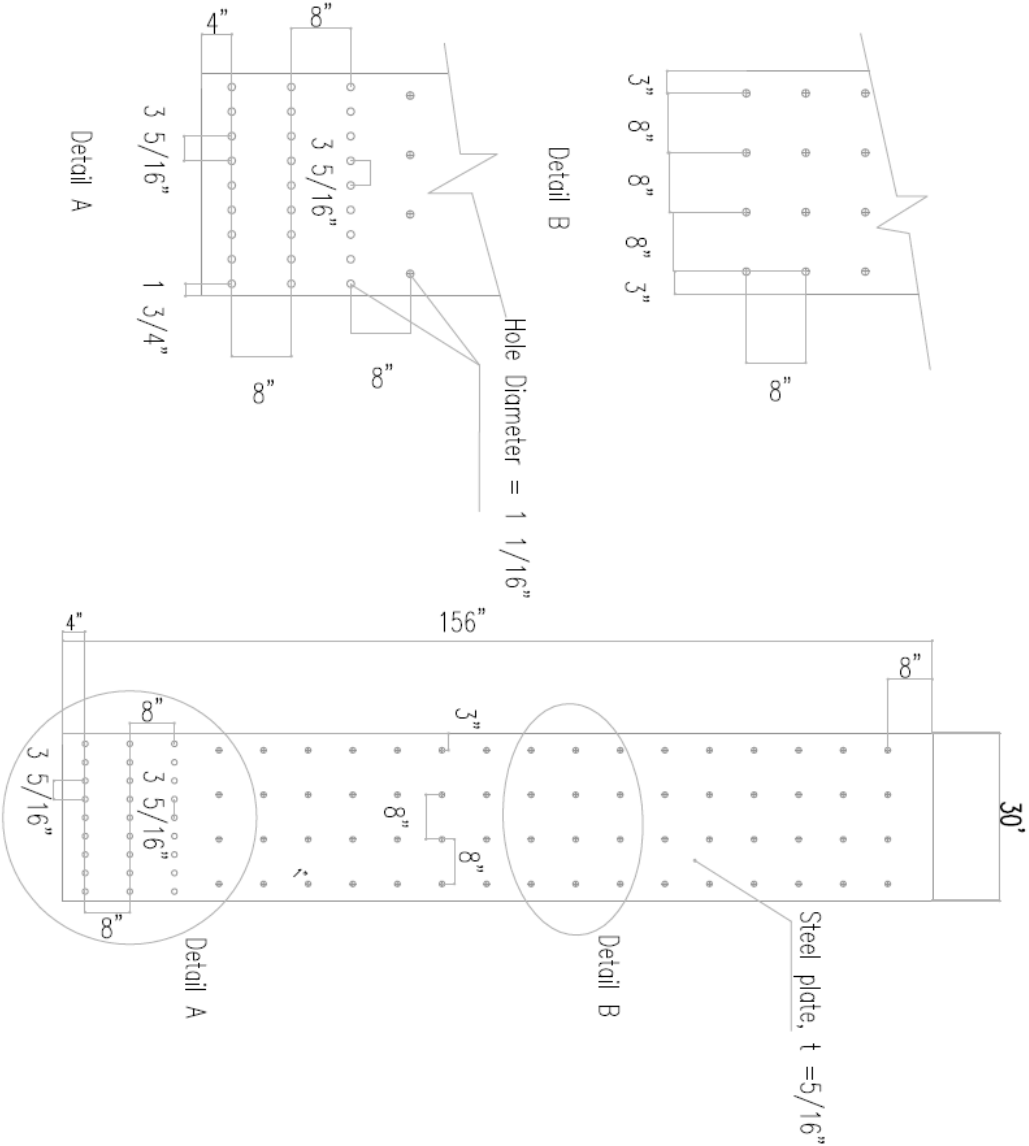
Drawing No. 5-B2

Description:
Web Assembly

Revision #01	Pieces	2
Date :8/31/11	Scale	

PRODUCED BY AN AUTODESK EDUCATIONAL PRODUCT

PRODUCED BY AN AUTODESK EDUCATIONAL PRODUCT



PRODUCED BY AN AUTODESK EDUCATIONAL PRODUCT

General Notes:

- All Dimensions are in Inches Unless Mentioned Otherwise.
- All Steel Plates are A572 GR50
- ALL Plates and HSS Sections are Supplied by AISC.
- Gussets, Shear Studs and Tie Bars are to be Supplied through local suppliers in WNY.

CFSPS Walls Testing

Drawing No. 6-B1

Description:
Cover Plates

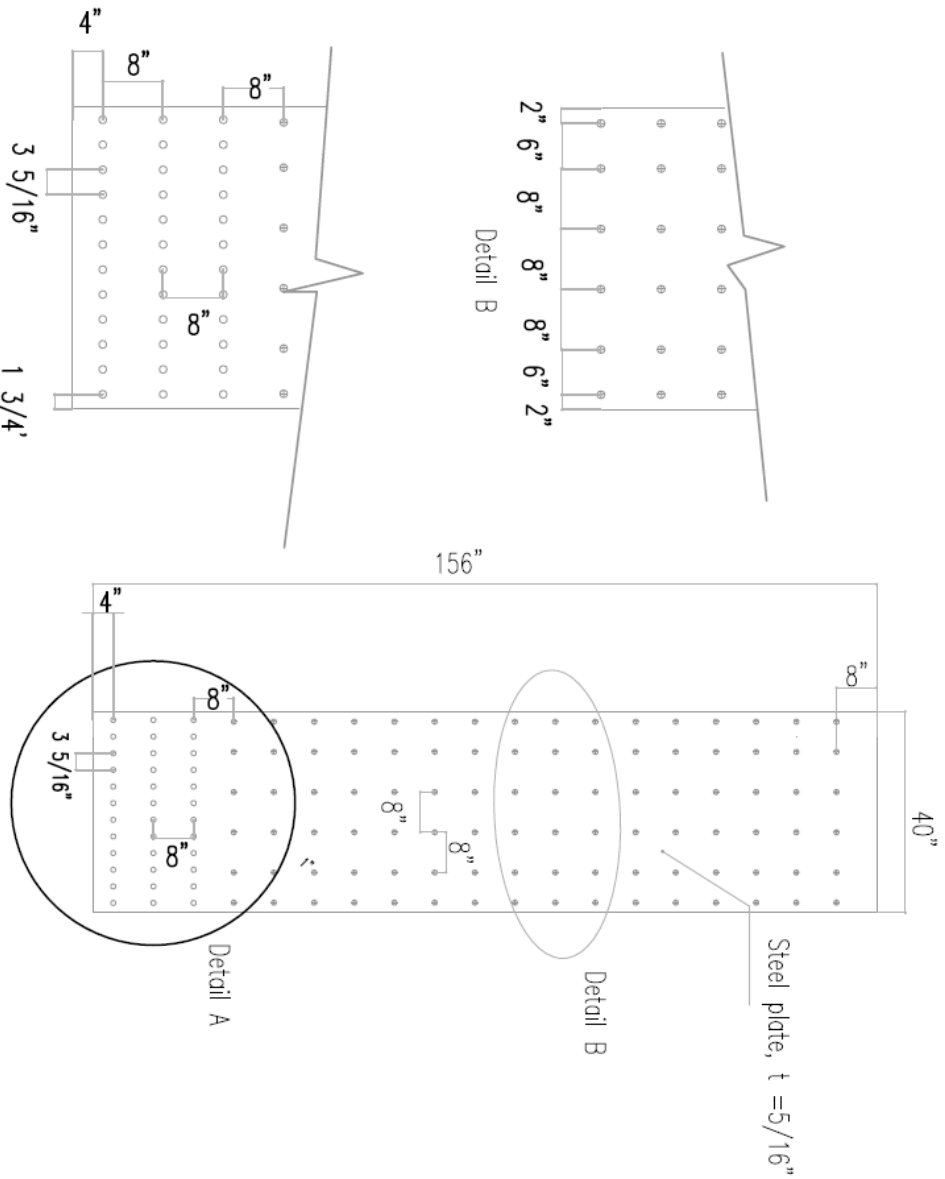
Revision #01	Pieces	2
--------------	--------	---

Date :8/31/11	Scale	
---------------	-------	--

Web Plate Elevation

PRODUCED BY AN AUTODESK EDUCATIONAL PRODUCT

PRODUCED BY AN AUTODESK EDUCATIONAL PRODUCT



Web Plate Elevation

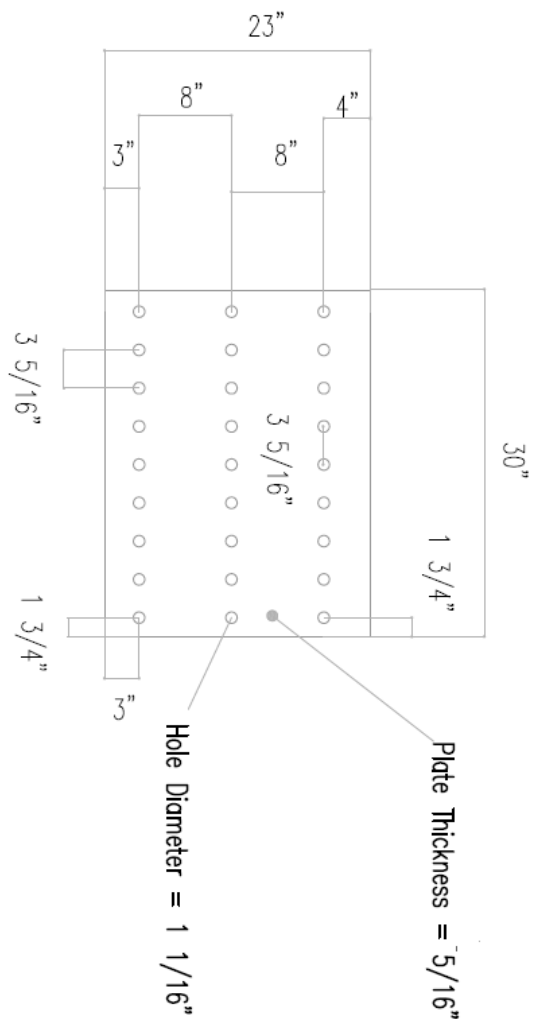
PRODUCED BY AN AUTODESK EDUCATIONAL PRODUCT

General Notes:

- All Dimensions are in Inches Unless Mentioned Otherwise.
- All Steel Plates are A572 GR50
- ALL Plates and HSS Sections are Supplied by AISC.
- Gussets, Shear Studs and Tie Bars are to Supplied through local suppliers in WNY.

CFSPS Walls Testing		
Drawing No.	6-NB2	
Description: Cover Plates		
Revision #01	Pieces	2
Date :8/31/11	Scale	

PRODUCED BY AN AUTODESK EDUCATIONAL PRODUCT



Cover Plate Dimensions

PRODUCED BY AN AUTODESK EDUCATIONAL PRODUCT

General Notes:

- All Dimensions are in Inches Unless Mentioned Otherwise.
- All Steel Plates are A572 GR50
- ALL Plates and HSS Sections are Supplied by AISC.
- Gussets, Shear Studs and Tie Bars are to Supplied through local suppliers in WNY.

CFSPS Walls Testing

Drawing No. 7-B1

Description:
Cover Plates

Revision #01	Pieces	2
Date :8/31/11	Scale	

APPENDIX B

SPECIMEN DESIGN

B.1 Introduction

The specimen of the flexural concrete filled steel plate sandwich wall (CFSP Sandwich wall) under consideration is a hollow built up steel section filled with concrete. For flexure about the strong axis of the wall, the built up section is composed of a double skin steel plate acting as a web and half or full an HSS sections acting as flange. The CFSP sandwich wall specimens with just half an HSS acting as a flange is referred to as CFSP-NB_n, the NB stands for that there is no boundary elements in such walls and then refers to the specimen number i.e CFSP-NB1 is a CFSP Sandwich wall specimen that have half an HSS as a flange and it is number one in the test series. Using the same nomenclature the CFSP Sandwich walls having a full HSS section, boundary element, at their ends are named CFSP-B_n i.e CFSP-B1 is a CFSP Sandwich wall specimen that have a full HSS as a boundary element and it is number one in the test series.

The circular HSS welded to the web plates were used to avoid premature failure of the welds at sharp corners, as described in the literature review Chapter 2. In the following sections design of both the specimen and the test setup are presented.

B.2 Plastic Moment Capacity of the CFSP-NB Sandwich Wall Specimen

For the specimen under consideration, the plastic moment capacity was calculated using basic principles of plastic analysis (implemented in an Excel Spreadsheet) and verified through using both the EXTRACT software and the finite element analysis program ABAQUS. Only results obtained using EXTRACT are presented in this appendix the predicted plastic moment capacity of the tested specimens using finite element analysis is presented in Table 3-4 in chapter 4 of this document.

The parametric dimensions of the proposed specimens are shown in Figure B-1. The section of the specimen is typically formed of two steel plates, representing the web of the wall, having length L and thickness t . Tie bars are placed between the two steel plates and plug welded to each of them. Tie bars are spaced at a distance S . The half HSS section is welded to the web skin plates through using complete joint penetration single bevel groove weld. The calculations used to predict the plastic moment capacity of the tested walls are shown in the following sections.

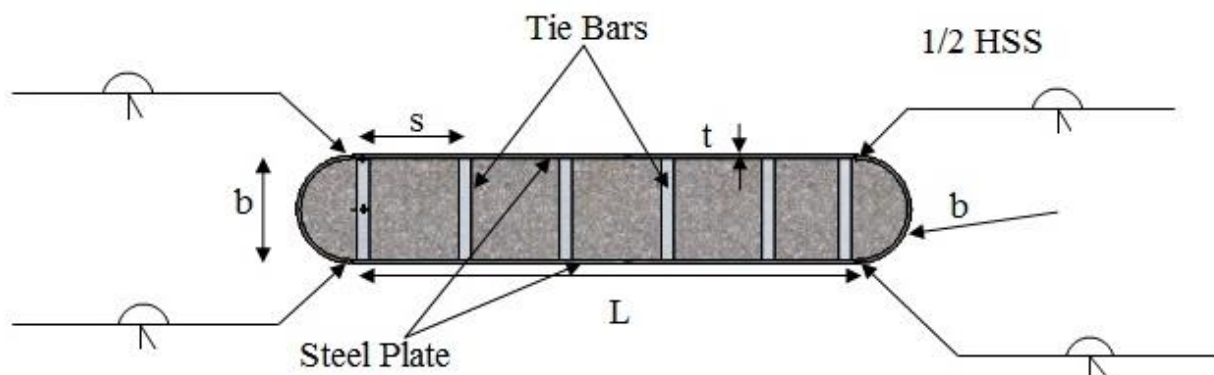


Figure B-1 Specimen CFSSP-NB

B.3 Moment Capacity of CFSSP-NB Sandwich Walls Using Plastic Analysis

At the location of the plastic hinge, the corresponding stress distribution on the cross section of the CFSSP Sandwich wall is shown in Figure B-2. C1 to C4 are the compression forces and T1 and T2 are the tension forces resulting from stresses acting on specific parts of the HSS section respectively (as described below), and H1 to H6 are their corresponding lever-arms.

An EXCEL spreadsheet implementing the equations below has been used to calculate the plastic moment capacity of various contemplated designs. The steps for calculation of the plastic moment are outlined below. In this analysis, the steel section is assumed have reached the plastic limit, and nominal values of material strengths are used assuming bi-linear material properties. Therefore, the stresses in the steel section are taken as F_y in either tension and compression, and the concrete in compression is assumed to reach an ultimate strength f'_c . Concrete in tension is assumed to be cracked and not contributing to the plastic moment capacity of the section.

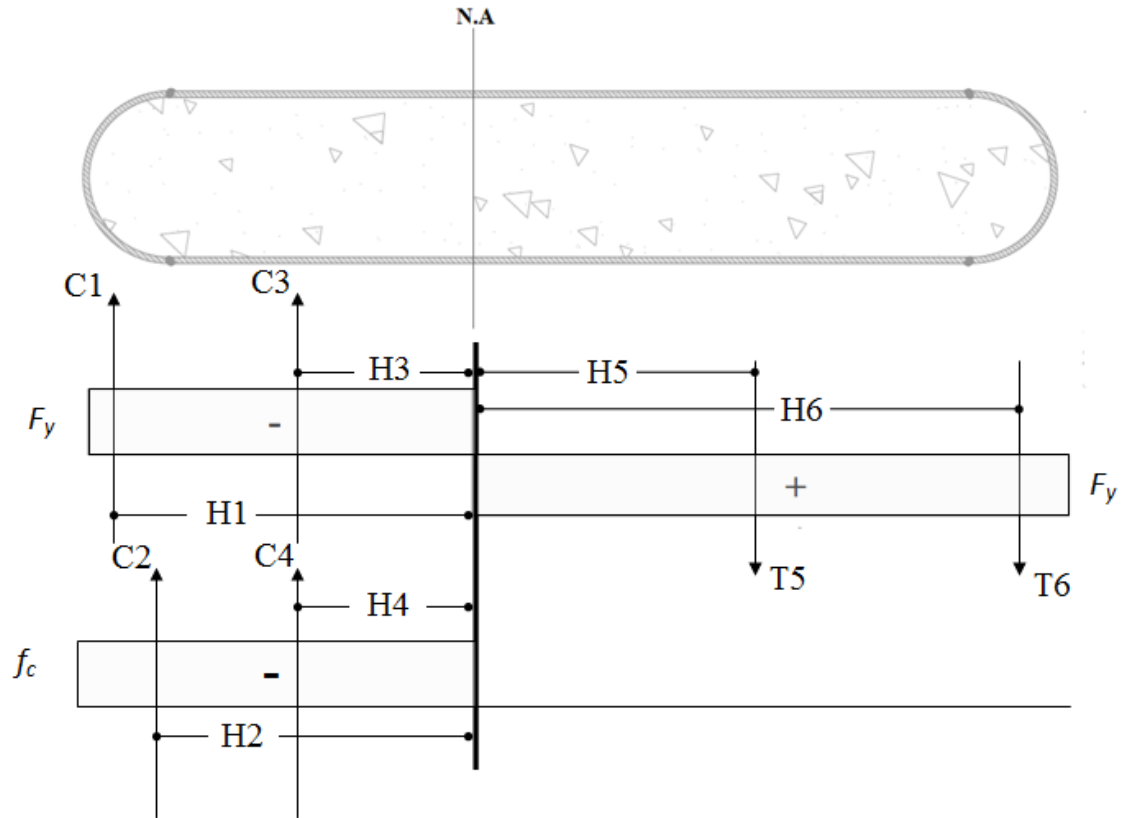


Figure B-2 Free Body Diagram for Specimen CFSSP-NB

Accordingly the forces acting on the section can be summarized as follows:

C1 and T6 are the compression and tension forces respectively developed in the half HSS sections at the end of the wall cross-section.

$$C1 \text{ and } T6 = F_y \times A_{HSS/2}$$

where,

$$A_{HSS/2} = \text{Cross section area of the half HSS}$$

The arm of the force C1 is H₁ and is given by

$$H_1 = (2r_1/\pi) + y$$

where

$r_1 = 0.5(D-t)$, is the radius from the center of the HSS to its mid-thickness.

and

Similarly, H_6 is given by

$$H_6 = (2r_1/\pi) + (L-y)$$

C_2 is the compressive force in the concrete enclosed by the HSS section.

$$C_2 = \pi \times (D-2t)^2 \times f'_c$$

Its lever arm H_2 is given by

$$H_2 = 4(D-2t) / (3\pi + y)$$

C_3 is the force in the steel web under compression, equal to $2yt_s F_y$

where, y is the length of the web under compression.

Its lever arm, H_3 , is given by

$$H_3 = \frac{y}{2}$$

C_4 is the force in the concrete web under compression, given by $y(b-2t_s) f'_c$

The corresponding lever arm, H_4 is given by

$$H_4 = \frac{y}{2} \quad T_5 \text{ is the force in the steel web under tension, and equal to } (L-y)t_s f_y$$

The corresponding value of H_5 is $\frac{(L-y)}{2}$

The neutral axis position is calculated by setting the equilibrium between tension forces (in the steel) and compression forces (in both concrete and steel), or equivalently setting the compression forces equal to the tension forces. As such, the value of y can be calculated by solving the following equation after substitution of the above expression into it:

$$C_1 + C_2 + C_3 + C_4 = T_5 + T_6$$

The plastic moment is calculated with respect to the plastic neutral axis of the CFSSP wall section.

$$M_p = C1.H_1 + C2.H_2 + (C3 + C4).H_3 + T5.H_5 + T6.H_6$$

The dimensions of the proposed CFSSP wall specimens are shown in Table B-1. Specimens CFSSP-NB1 and CFSSP-NB2 respectively have the same outer dimensions and the same material properties the only difference is the spacing of the tie bars. Spacing of the tie bars is very crucial in minimizing local buckling of the web steel plate and it is one of the main parameters under investigation in this research.

Table B-1 Dimensions of the Proposed CFSSP-NB

Specimen	Web Plate Length, L (in)	Web Thickness, in	HSS	S	f_y (ksi)	f'_c (ksi)
CFSSP-NB1	40	5/16	8.625×0.322	8	50	4
CFSSP-NB2	40	5/16	8.625×0.322	12	50	4

The plastic moment capacity of the proposed specimens is calculated as follows:

$$A_{HSS/2} = 7.85 \times 0.5 = 3.925 \text{ in}^2$$

$$C1 = T6 = 3.925 \times 50 = 196.25 \text{ kips}$$

$$H_1 = (2 \times 4.161 / \pi) + y = 2.648 + y$$

$$H_6 = (2r_1 / \pi) + (40 - y)$$

$$C2 = 0.5 \times (\pi \cdot r^2) \times 4 = 0.5 \times (\pi \times 4^2) \times 4 = 25.13 \times 4 = 100.52 \text{ KIPS}$$

$$H_2 = 4 \times 4 / (3\pi) + y = 1.697 + y$$

$$C3 = 2 \times 0.315y \times 50 = 31.5y,$$

$$H_3 = y/2$$

$$C4 = 8 \times 4 \times y = 32y$$

$$H_4 = y/2$$

$$T5 = 2 \times 0.315 \times (40 - Y) \times 50 = 1260 - 31.5y$$

$$H_5 = (40 - y) / 2$$

By equilibrium the value of y can be calculated as follows:

$$C1 + C2 + C3 + C4 = T5 + T6$$

$$100.52 + 31.5y + 32y = 1260 - 31.5y$$

$$95y = 1159.48$$

$$y = 12.205 \text{ in}''$$


The corresponding plastic moment for the specimen is:

$$M_p = C1.H_1 + C2.H_2 + (C3 + C4).H_3 + C5.H_4 + C6.H_5$$

$$M_p = 196.25 \times (2.648 + 12.205) + 100.52 \times (1.697 + 12.205) + 31.5 \times 12.205 \times (0.5 \times 12.205) + 32 \times 12.205 \times (0.5 \times 12.205) + 875.5425 \times (40 - 12.205) \times 0.5 + 196.25 \times 30.443 = 27223 \text{ kip-in}$$

These analysis steps were implemented in a spreadsheet to calculate the plastic moment capacity of CFSSP Sandwich walls, with no boundary elements having different dimensions. Table B-2 shows the corresponding spreadsheet results for Specimen CFSSP-NB1. The final outer dimensions of specimens CFSSP-NB1 and CFSSP-NB2 are shown in Figure B-3.

Table B-2 Capacity of the CFSSP-NB Wall

<i>Values used to calculate Plastic Moment Capacity for Composite Shear Walls (CSW)*</i>			
<i>Section Properties</i>			
Web Plate thickness , t	0.315	HSS Cross Section Area, in ²	7.85
Diamter of HSS, D	8.625	Thickness of HSS	0.322
Web Plate length, L	40	Total wall width, b (in)	8.62
Inner wall Thickness, b-2t	8	Inner Radius of HSS, 0.5× (D-t)	4
Concrete Strength, f'_c (Ksi)	4	f_y (Ksi)	50
Steel Area, A_s .(in ²)	33.05	 HSS 8.625X0.322	0.322
Outer Radius of HSS, (D-t)	4.31	y (in)	12.20
Total Steel Area %	8.20	Neutral Axis from Top (in)	16.52
<i>Section Forces (Kips)</i>			
C1=C6	196.25	C2	100.48
C3	384.46	C4	390.56
C5	875.54	Mp (Kip.in)	27223

*All units are in Kip-inch

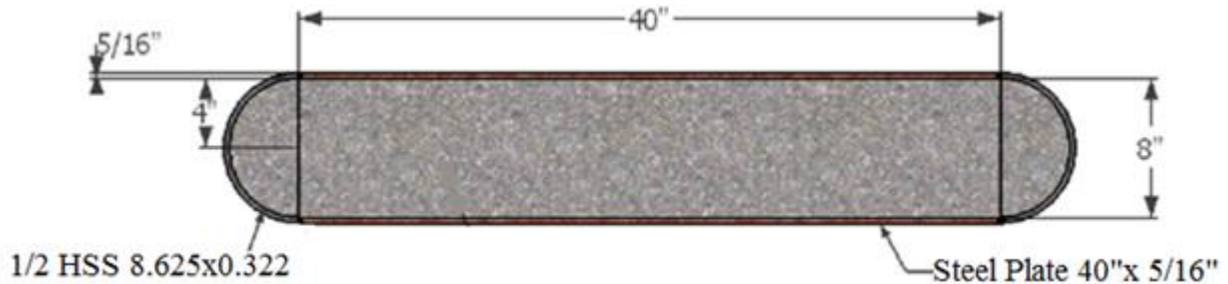


Figure B-3 Outer Dimensions for Specimen of Group CFSSP-NB

B.4 Moment Capacity of CFSSP-NB Sandwich Walls Using Fiber Analysis

To verify the above analysis results, the XTRACT software was used. The material models used for both of the concrete core and the steel case were elastic perfectly plastic models with no strain hardening. The mesh used was half by half inch. The results from the XTRACT analysis report are shown in Figure B-3.

In the XTRACT analysis the concrete elements under tension have the red color, crushed concrete elements have the light grey color and un-crushed concrete under compression have the blue color.

The plastic moment obtained by XTRACT is $M_p = 26360$ Kip-in. Given that the plastic moment calculated using plastic section properties in Section B2.1 is 27107 Kip-in, this corresponds to a difference of 2.83%. This small discrepancy is attributed to size of the mesh, the approximation used at the round parts of the section and the fact that there is some bilinear hardening slope in the moment curvature relationship despite the analysis used bi-linear elastic perfectly plastic steel material model.

Section Details:

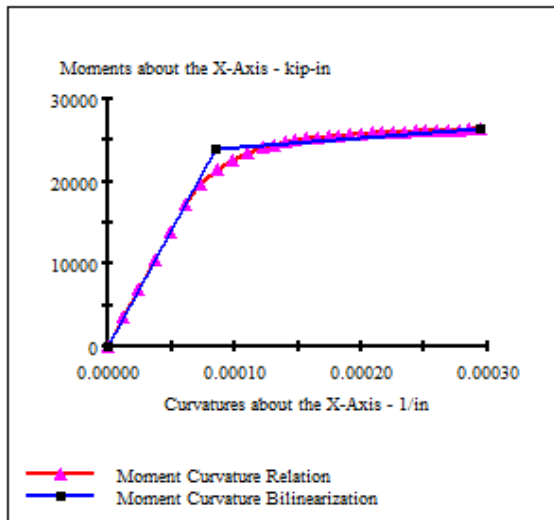
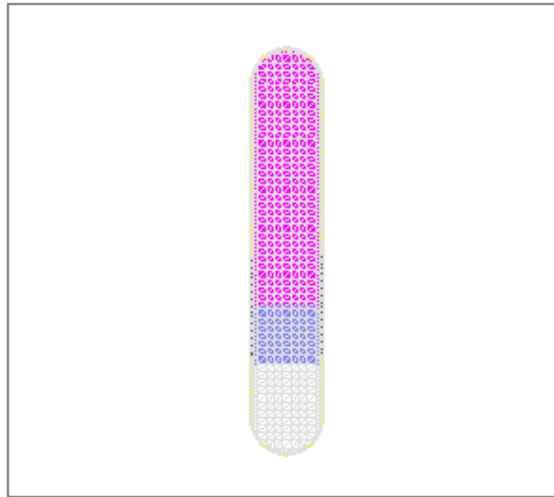
X Centroid: 4.000 in
Y Centroid: 20.00 in
Section Area: 368.8 in²

Loading Details:

Constant Load - Mxx: -2.000 kip-in
Incrementing Loads: Mxx Only
Number of Points: 30
Analysis Strategy: Displacement Control

Analysis Results:

Failing Material: Unconfined1
Failure Strain: 5.000E-3 Compression
Curvature at Initial Load: 6.971E-9 1/in
Curvature at First Yield: 61.35E-6 1/in
Ultimate Curvature: .2943E-3 1/in
Moment at First Yield: 17.17E+3 kip-in
Ultimate Moment: 26.36E+3 kip-in
Centroid Strain at Yield: .2616E-3 Ten
Centroid Strain at Ultimate: 1.895E-3 Ten
N.A. at First Yield: 4.264 in
N.A. at Ultimate: 6.440 in
Energy per Length: 6.269 kips
Effective Yield Curvature: 85.37E-6 1/in
Effective Yield Moment: 23.89E+3 kip-in
Over Strength Factor: 1.104
EI Effective: 2.80E+8 kip-in²
Yield EI Effective: 1.18E+7 kip-in²
Bilinear Hardening Slope: 4.234 %
Curvature Ductility: 3.447



Comments:

User Comments

B.5 Plastic Moment Capacity of the CFSSP-B Walls

CFSSP sandwich walls having boundary elements consisting of complete HSS columns were considered. This cross-section is an extension of the previous one, modified by replacing the half HSS at its ends by a full HSS section instead. In this case CFSSP sandwich walls are considered to be having boundary elements, the diameter of the HSS is selected to be larger than the width of the wall's web. In the following calculations, the dimensions of the CFSSP sandwich wall with boundary elements were chosen such that the plastic moment capacities of the wall specimens with and without boundary elements were almost the same.

The proposed section of the CFSSP sandwich wall with boundary elements is shown in Figure B-4 for a generic cross-section. The total length of the web is L and thickness of each web steel plates is t . The total width of the wall is b and spacing of the tie bars is S . Note that the steel web plates are to be welded to the HSS using full penetration groove welds. The different parameters were used to illustrate how the plastic moment capacity is calculated. The procedure to calculate the plastic moment capacity of the proposed section is presented below.

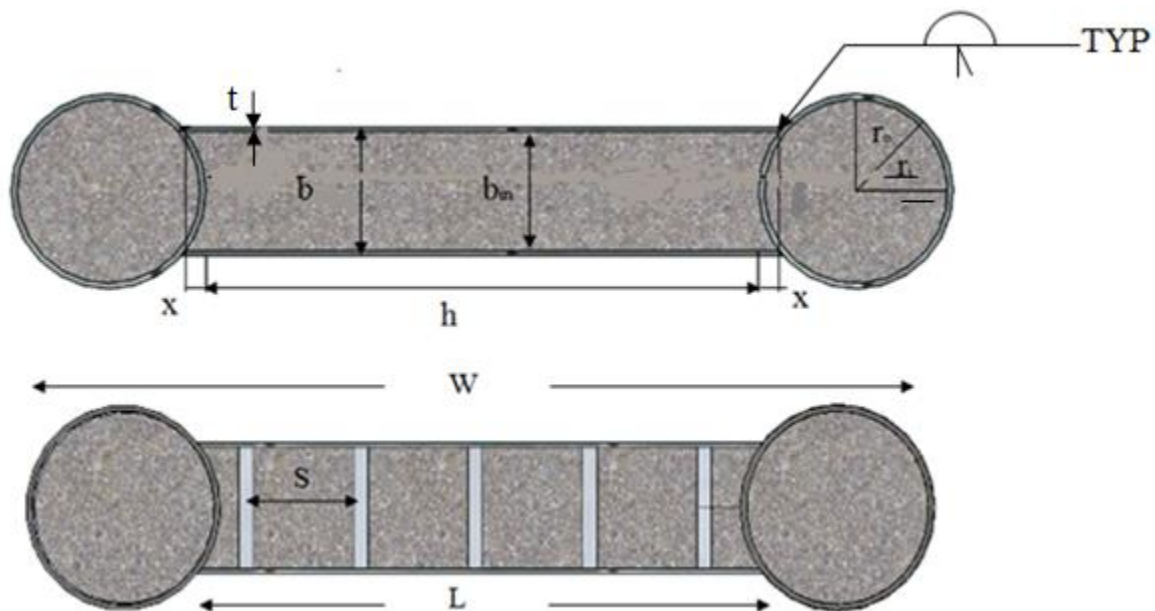


Figure B-4 Cross-section of the CFSSP-B Specimens

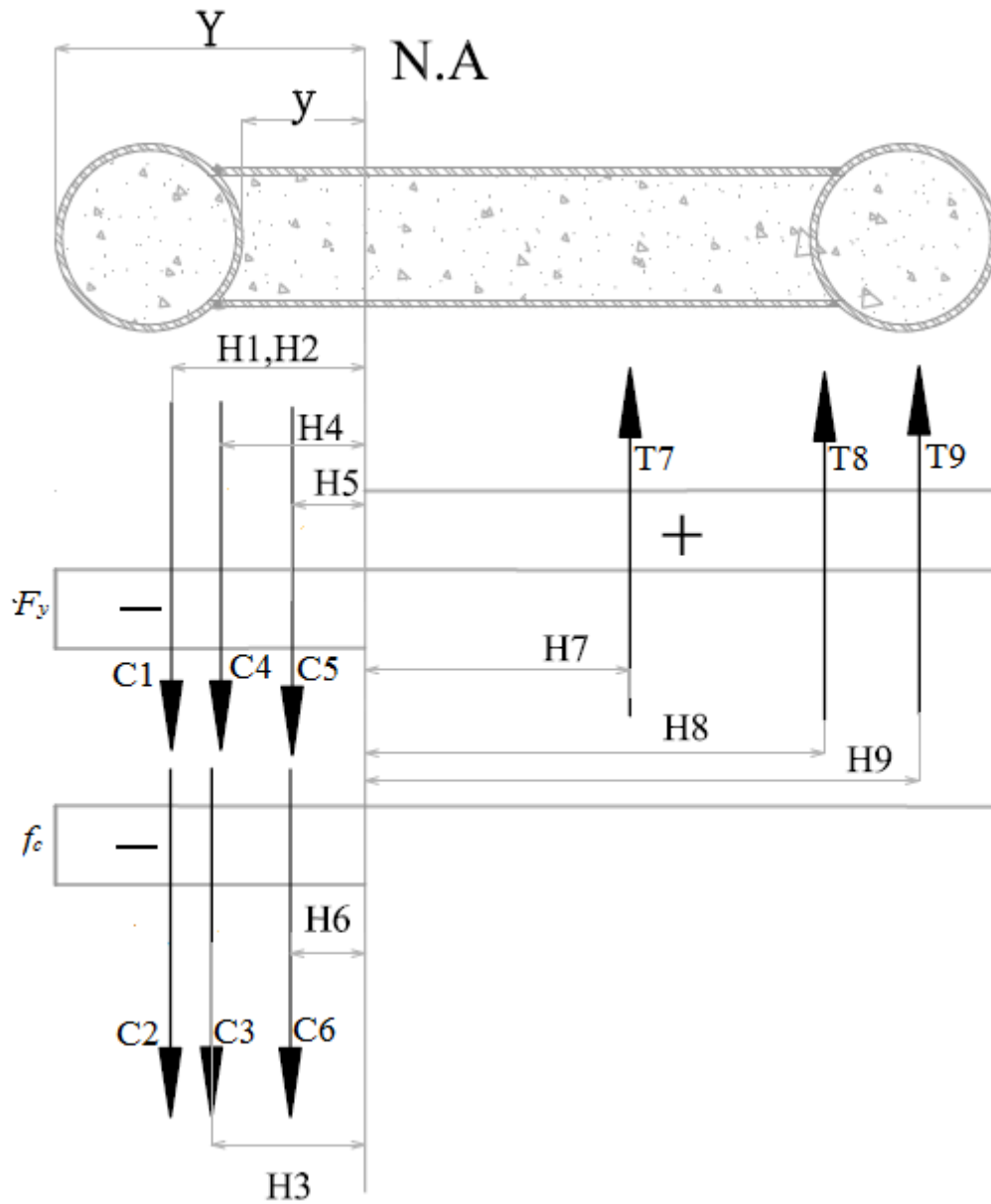


Figure B-5 Free Body Diagram for Specimen CFSSP-B

Similar to the case CFSSP-NB, the steel section is assumed have reached its nominal yield strength, F_y in both tension and compression above and below the neutral axis. Concrete under tension is cracked and does not contribute to the plastic moment capacity of the section while the concrete under compression is assumed to reach an ultimate strength equals to f_c' .

Figure B-5 shows the internal forces generated in the section and their respective lever arms. The forces generated in the section and the moment arms are summarized as follows:

C1 and T9 are the compressive and the tension force in the HSS section respectively, defined as,

$$C1 = C9 = A_{HSS} \times F_y$$

C2 is the compressive force in the concrete enclosed by the HSS section.

The corresponding lever arms are

$$H_1 = H_2 = r_o + y$$

$$H_9 = r_o + (h - 2x - y)$$

C3 and T8 are the forces in the steel web over the distance X in compression and tension respectively, given by.

$$C3 = C8 = 2tsXf_y$$

The lever arm H_3 is given by

$$H_3 = X/2 + y$$

And H_8 is given by

$$H_8 = X/2 + (h - 2x - y)$$

C4 is the compression force in concrete for the area of the parabolic segment over distance X, given by

$$C4 = \frac{Xb}{6} \times f'_c$$

with a corresponding lever arm H_4 given by

$$H_4 = 0.3X + y$$

where X is the height of the parabola and 0.3X is the position of the parabola c-g measured from the base according to the geometric relationships.

C5 is the force in the concrete web under compression, equal to

$$C5 = 2 \times t \times Y \times f_y$$

The lever arm H_5 is given by

$$H_5 = Y/2$$

C6 is the force in the steel web under compression

$$C6 = b_{in} \times y \times f'_c$$

The corresponding value of H_6 is given by

$$H_6 = Y/2$$

C7 is the force in Steel web under tension, equal to

$$C7 = (h - 2x - y) \times t_s \times f_y$$

H_7 is given by

$$H7 = (h - 2x - y) \times 0.5$$

As a result of axial force equilibrium, the value of y can be calculated as follows:

$$C1 + C2 + C3 + C4 + C5 + C6 = T7 + T8 + T9$$

$$y = [2ht_s f_y - C2 - C4] / [4t_s f_y - bf_c]$$

The plastic moment is then calculated with respect to the neutral axis of the wall section.

$$M_p = C1.H1 + C2.H2 + C3.H3 + C4.H4 + C5.H5 + C6.H6 + T7.H7 + T8.H8 + T9.H9$$


The cross section dimensions for the CFSSP sandwich walls with boundary elements specimens are shown in Table B-4. The only difference between the two proposed specimens is the spacing of the tie bars and consequently the b/t ratio for the steel skin plate of the wall. Table B-4 Proposed Dimensions of CFSSP Wall Specimens with Boundary Elements, CFSSP-B.

Table B-3 Specimens of Group NB

Specimen	Web Plate Length, L (in)	Web Thickness, (in)	HSS	S	F_y (ksi)	f'_c (ksi)
CFSSP-NB1	40	5/16	8.625×0.322	8	50	4
CFSSP-NB2	40	5/16	8.625×0.322	12	50	4

A spreadsheet was developed to calculate the plastic moment capacity of a CFSSP sandwich wall with boundary elements having arbitrary cross section geometry. Table B-5 shows the spreadsheet results for the dimensions of Specimen CFSSP-B1. As mentioned earlier, dimensions of that specimen were chosen such that its plastic moment capacity is of the same order of magnitude as that of the CFSSP sandwich wall specimen without boundary elements.

Table B-4 Specimen CFSSP-B M_p

<i>Values used to calculate Plastic Moment Capacity for CFSP walls with Boundary Elements</i>			
<i>Section Dimensions</i>			
<i>Web</i>		<i>HSS Section</i> 	
Web Plate thickness, t	0.315	<i>HSS SELECTED</i>	<i>Diameter</i> / <i>Thickness</i>
			8.625 / 0.322
Web Plate length, L	30	HSS Cross Section Area, in ²	7.85
Inner wall, b (in)	6	Outer Radius of HSS, r_o , (in)	4.47
Total Web Thickness, (steel - Concrete) in.	6.63	Inner Radius of HSS, r_i , (in)	4.15
Concrete Strength, F_c (Ksi)	4	F_y (Ksi)	50
Overlab, X, in	1.16	$r_o - X$	3.32
Segment Area	4.75	Parbola Spanderl Area	2.18
Area of Concrete enclosed in HSS	54.15	Area of Steel Part X	0.73
<i>Section Forces (Kips)</i>			
C1=C9	392.50	C2	216.58
C3=C8	36.38	C4	8.70
C5	234.24	C6	178.47
C7	637.9927617		
<i>The Force Arm</i>			
H1=H2	11.91	H3	8.01
H4	7.78	H5	3.72
H6	3.72	H7	10.13
H8	20.83	H9	24.73
y (in)	7.44	M_p (Kip.in)	26072

B.6 Design of the Test Rig Components

To design all elements of the test setup, the plastic moment value was multiplied by a factor of 1.5 to account for expected values of yield strength higher than nominal values and for the development of strain hardening in the steel elements in the CFSSP sandwich walls during testing.

Accordingly, in all following calculations, the following magnified value of M_p is used:

$$M_p = 1.5 \times 27107 = 40660.5 \text{ kip-in} = 3388 \text{ Kip-ft.}$$

For the selected specimen geometry, in which a force is laterally applied at a proposed height of 10 ft, the corresponding horizontal load (and horizontal shear force in the specimen) is equal to 338.8 Kips.

design procedure that lead to its selected dimensions. In all of the following sections the forces considered in the design includes the 1.5 safety factor on the plastic moment mentioned above.

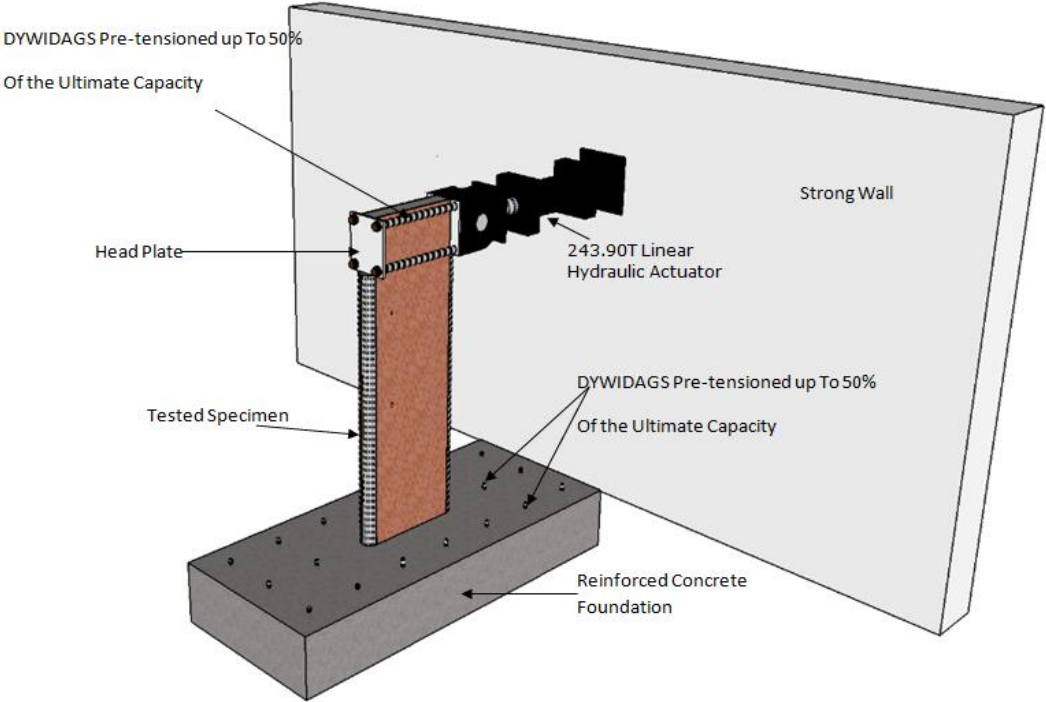


Figure B-6 Different Components of Test Setup

B.6.1 Actuator Type

The shearing force acting on the specimen is in the order of 340 kips. The actuator to be used is the MTS 243.90T linear hydraulic actuator of 243.9T capacity, which is equivalent to 536.54 kips capacity. The position of the actuator on the strong wall and check for the strong wall integrity under the testing loads is illustrated in later sections of this Appendix.

B.6.2 Head Plate Design

The size of the hydraulic actuator head governs the dimensions of the head plate used to apply compression forces at the far end of the wall when the actuator is pulling. The plate dimensions are 18"x21" inches. To calculate the thickness of the end plate a force of $(340/4) = 85$ kips is considered to act at each bolt location. The failure mechanism shown in Figure B-7 is considered.

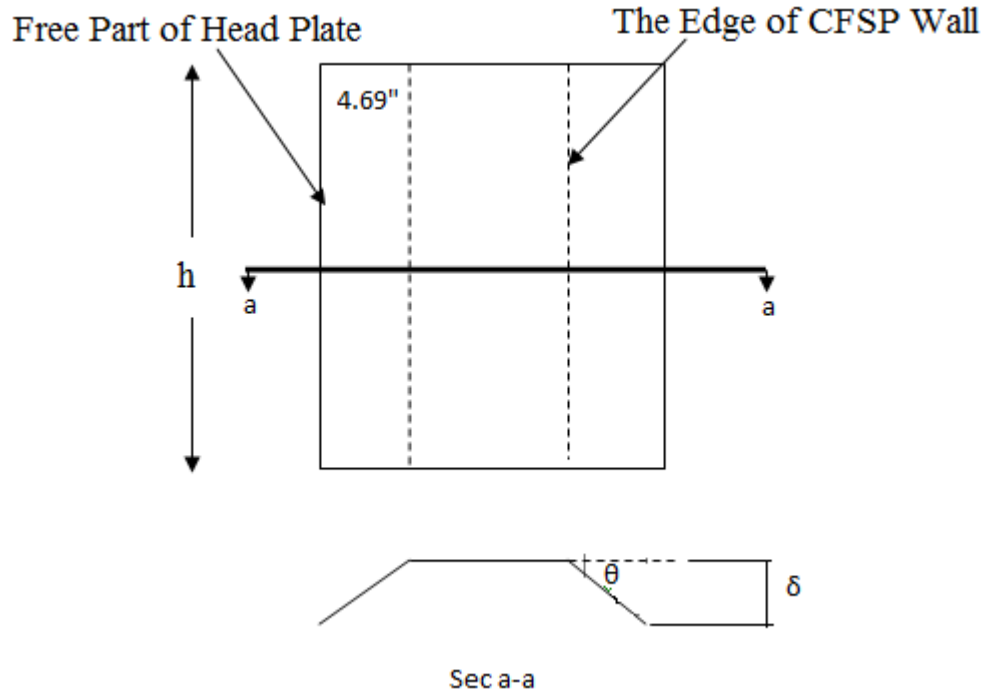


Figure B-7 Failure Mechanism of the Head Plate

Using yield line theory and the energy approach, the head plate thickness can be calculated as follows:

$$\theta = \frac{\delta}{4.69}$$

$P = 180 \text{ Kip}$, $h = 21 \text{ inch}$

$$P \cdot \frac{\delta}{2} = M_p \cdot h \cdot \theta = 50 \left(\frac{t^2}{6} \right) \cdot h \cdot \theta$$

$t = 1.55 \text{ inch} = 1 \frac{5}{8}''$

If stiffeners are to be used to support the free edge of the head plate such as to create three supporting points as shown in Figure B-8, this will force the failure mechanism shown in the same figure and consequently the thickness of the head plate can be reduced.

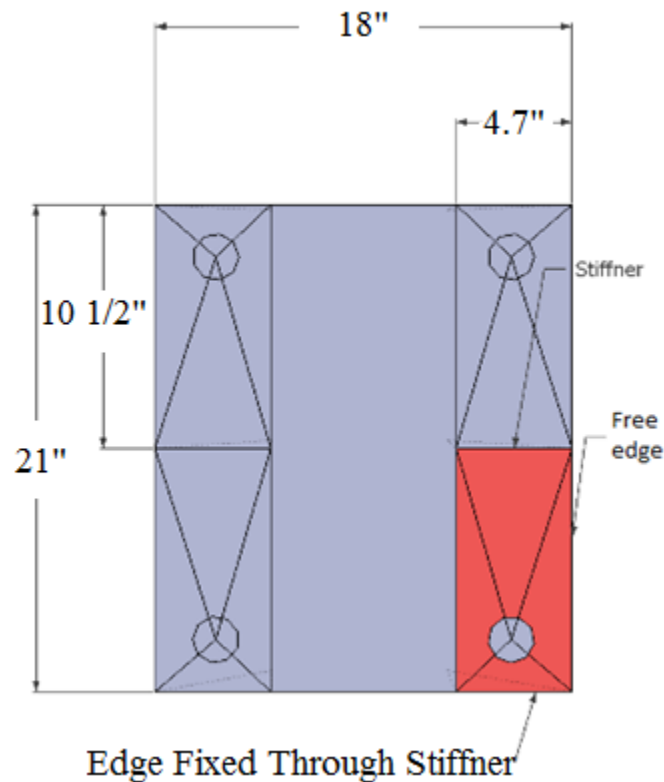


Figure B-8 Failure of Head Plate In Case of Stiffeners

Again, using the energy approach, for the assumed yield line pattern shown in Figure B-8, thickness of the end plate can be calculated as follows:

$$4.7 \times 2 \times M_p \times \theta_1 + 10.5 \times 3 \times M_p \times \theta_2 + 4.7 \times 2 \times M_p \times \theta_3 = P \cdot \delta$$

The relation between the various angles, θ_i 's, and the deflection under the load point, δ , are:

$$\theta_1 = \delta/2.25$$

$$\theta_2 = \delta/2.625$$

$$\theta_3 = \delta/8.25$$

Using $M_p = 50 \cdot (t^2/4)$ for a unit width of plate, the required thickness can be calculated. However, since the intent is to keep the plate elastic, the value of $M_y (=M_p/1.5)$ is substituted in the above equations, and the calculated needed thickness of the steel plate is equal to, $t = 0.77$ inch.

The corresponding actual plate thickness is selected to be equal to $\frac{7}{8}$ inch.

Option one is to be selected due to ease of construction and because it is not significantly more expensive when factoring labor costs. This was established as follows:

1) Alternative 1

- Weight of the head plate = 173.83 Ibs.
- Considering 2 dollars per pound, cost of the plate = \$347.66

2) Alternative 2

- Total weight including the stiffeners = 152.82 Ibs.
- The cost of the head plate in this case is \$305, by adding a cost of one hour of labor required to weld stiffeners and estimating that to be \$60 per hour. The total cost of alternative two is \$365. Since the first alternative is easier in construction and gives a cleaner solution it was the chosen alternative.
- The final dimensions of the head plate is 20"×24" with hole diameters is 2 1/16".

B.6.3 Threaded Bars at the Head Plate

Four threaded bars are to be used to transfer the load from the actuator to the head plate. The force per threaded bar is 85 Kips. The threaded bars are meant to remain elastic throughout the test. For some geometric constraints, namely the size of the holes in the actuator head, the diameter of the used threaded bars should not be less than 2 inches. Accordingly, 2 inch diameter threaded bar are chosen. Their ultimate strength in Tension is 121 Kips and pre-tensioned to 90 kips.

B.7 Load Transfer to the Foundation

A reinforced concrete foundation was used for the tested specimens. The following section focuses on the load transfer from CFSSP wall specimens to the reinforced concrete foundation.

There are some constraints that dictate the proposed foundation dimensions. In particular, the foundation depth is limited to two feet because of the limited length of the DYWIDAGS bars available in the laboratory and used to connect the footing to the strong floor (purchasing longer bars was not a more cost-effective solution).

The wall to footing connection has to be able to transfer the wall's full plastic moment (magnified by a safety factor of 1.5, as mentioned previously).

Since the wall cross section has reached its plastic capacity, the concrete is assumed to have reached f'_c and the steel F_y , Figure B-10 shows the stress distribution on the wall section, the forces resulting from this stress distribution is to be transferred to the foundation. The forces in the concrete is transferred to foundation through bearing while the force in the steel case is transferred as shearing forces acting on the interface surface between the steel case and the reinforced concrete foundation. Here, the effect of strain hardening and higher than expected yield stresses values are considered by multiplying the yield stresses by a factor of 1.5.

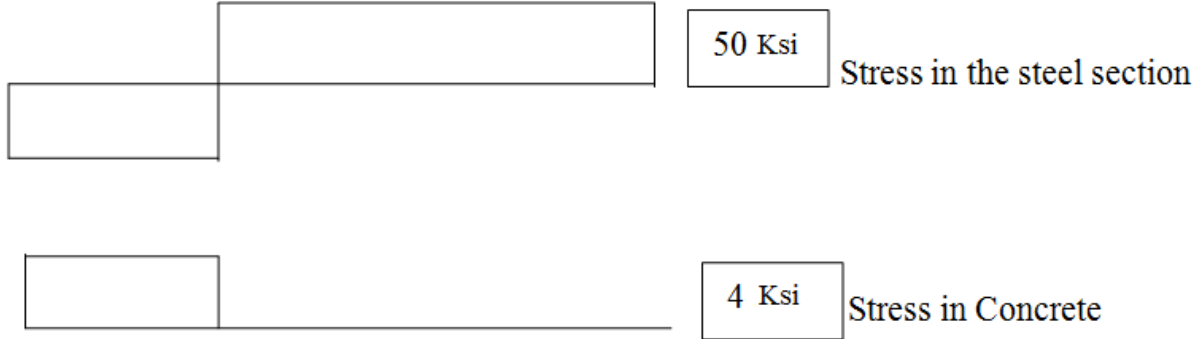


Figure B-10 Stress Distribution at Wall-Foundation Interface

The corresponding tension force to be transferred through unit length of one web plate of the CFSSP sandwich wall specimens:

$$F_T = F_y t_s = 15.75 \text{ kip/in}$$

where,

$$t_s = 0.315''$$

Given the aforementioned desired safety factor of 1.5, a value of 1.5 F_T is considered in the following calculations.

B.8 Load Transfer at the Web Using Reinforcement Bars

In this option reinforcing bars are passed through holes in the part of the wall that is embedded in the foundation. These bars are subjected to shearing forces generated at the interface between steel and concrete. Considering re-bars transferring shearing forces to be # 8 re-bars, having a diameter of one inch.

$$D_{\text{rebar}} = 1''$$

The shear strength of the re-bars are calculated using the AISC equation for calculating the nominal shear capacity of stud shear connectors (i.e. AISC 360-5 Eq. I3-3)

$$Q_n = 0.5A_{sc} \sqrt{f'_c E_c} = 0.5 \times \frac{\pi(1)^2 \sqrt{4 \times 3605}}{4} = 50.33 < A_{sc} F_u = 65A_{sc} = 65 \times 0.78 = 51 \text{ kip}$$

If two horizontal layers of re-bars are used to resist the pull from one of the wall's web steel plate, and using a safety factor of 1.5, the number of connectors needed to resist the tension force applied over the entire length of the plate in tension when M_p is reached (i.e. length $h-y$ as shown in Figure B-2) is calculated as follows

$$\text{Number of Bars, } N_b = \frac{1.5F_T (h-y)}{0.85Q_n} = 15.34 \text{ bars}$$

For both specimens of CFSSP sandwich walls with no boundary elements, CFSSP-NB1 and CFSSP-NB2, this number of bars is distributed over the length ($h-y$) of a tension stresses zone equal to 27.795".

$$\text{The number of bars per horizontal layer, } N_{bl} = \frac{N_b}{2} = 7.67 \approx 8 \text{ bars/ layer over the tension part}$$

$$\text{The corresponding spacing of bars is } S = \frac{h-y}{N_{bl}} = 3.47''$$

For the specimen's web of height the total number of bars per layer, N_{TL} is given by:

$$N_{TL} = h/S = 11.52 = 12 \text{ bar/layer}$$

The actual spacing of bars $h/12 = 3.33''$, or equivalently 3-5/16" when rounded to the nearest 16th of an inch.

On the compression side of the web and disregarding the effect of local buckling the stress in the steel will reach F_y and consequently the distribution of the bars on the compression side is the same as that on the tension side of the web, given the condition of cyclic loading. The distribution of the bars in part of the wall embedded in the foundation is shown in Figure B-11 for the specimen CFSSP-NB1.

For the case of specimens CFSSP-B1 and CFSSP-B2 the load transfer will follow the same concept presented for CFSSP-NB1 and CFSSP-NB2. The web width in this case is only 30" and calculations are done using the same bar diameter and using again two horizontal layers of re-bars to transfer the load. The resulting number of re-bars per layer is 9#8 spaced at 3 5/16".

To ensure that the force is going to be distributed evenly between the top and bottom rows of re-bars, it is essential to provide stirrups in order to make sure that both upper and lower rows are engaged in the load transfer. As a critical condition top bars should be checked for pulling out from the footing.

The following calculations assume that the stirrups used for this are #6 bars

The nominal strength of #6 bar in tension is $\phi A_b f_y = 0.85 A_b f_y = 0.85(0.44)(50) = 18.77$ Kip

The number of re-bars needed = $2 \times 51 / 18.77 = 5.43 = 6$ vertical re-bars

Figure B-9 show the free body diagram of equilibrium between the shearing forces transmitted through the re-bars that are transferred as a tension force in the stirrups.

The stirrups are spaced at $3 \frac{1}{2}$ " in the short direction of the foundation normal to the re-bars used to transfer loads from the wall to foundation Figure B-12 shows the arrangement of the reinforcement bar used to transfer loads into the foundation.

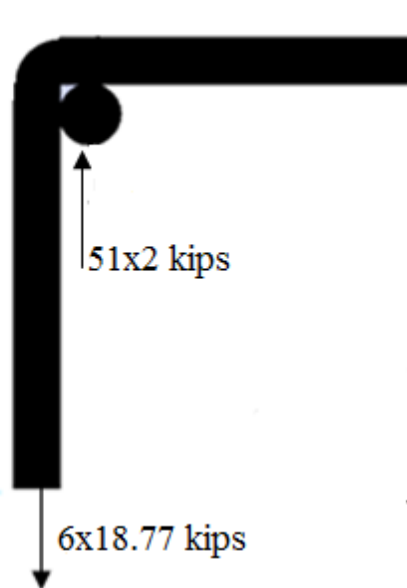


Figure B-9 Stirrups used to Transfer Load to shear Connectors Group

The second step is that to check that the top re-bars will not pull out from the concrete foundation. Accordingly it is assumed that the top bar will pull out from foundation through a failure surface formed at 45° as shown in Figure B-13. The stress formed at the failure surface is calculated and compared to the permissible stress considering that the re-bar attain its maximum capacity.

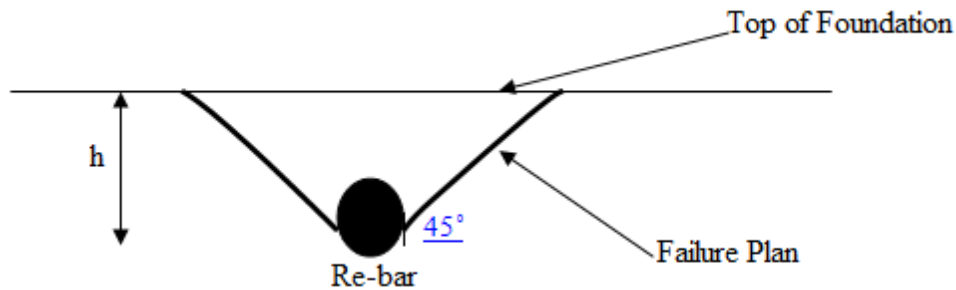


Figure B-10 Formed Cone for Top Bar Pulling

since h is equal to 5" and the length of the rebar embedded s equal to 23.7"

$$Q_n = \sigma_c \sin 45(5 / \sin 45)(23.7) = 51$$

$$\sigma_c = 0.43 \text{ksi} < f'_c / 2$$

Finally, to be able to develop yielding of the wall's steel plate, the tensile strength at the net section along the plane of the holes must be greater than the gross section yield strength.

The corresponding calculations at the net section of the wall at the location of the re-bar connectors are:

The spacing of the re-bars is 3 5/16".

The tributary area of the re-bar = $S \cdot t_s = 1.04 \text{ in}^2$

The net area, $A_{\text{net}} = S \cdot t_s - (D + 1/8) \cdot t = 0.685 \text{ in}^2$ (this accounts for the usual 1/16" tolerance for drilled holes, and an additional 1/8" to account for the fact that the outside diameter of a #8 deformed bar is greater than its nominal diameter).

The gross section yield force of $(1.04)(50)(1.5) = 78$

Nominal strength of the net area = $\phi_t \cdot (F_u) \cdot A_{\text{net}} = 30.825 < A_g \cdot f_y = 52 \text{ Kips}$ (need reinforcement)

The web plate needs reinforcement. This is accomplished by welding on each web additional cover plate having a thickness of 5/16" to meet the conditions and requirements of the AISC 314-10 were addressed on reinforcing the wall web. The nominal strength of the steel plates used as reinforcement are the same as that of the original steel web plate. Considering the kind of steel used to be ASTM 1043/1043M Gr 50(345), which in case of steel plates have R_y and R_t have a value of 1.2 and 1.1 respectively according to table A3.1 in AISC 341-10, then:

$$A_{net} R_t F_u > A_g R_y F_y$$

$$A_{net} = 2 \times 0.685 \text{ in}^2 = 1.37 \text{ in}^2$$

$$A_g = 1.04 \text{ in}^2$$

$1.37 \times 1.1 \times 65 > 1.04 \times 1.2 \times 50$, Accordingly yielding of gross section will occur instead of fracture of the net section.

Another way to check feasibility of the section reinforcement is to assume that the resulting thickness of the first 2 feet of the wall is doubled such that the thickness of the steel plate embedded in the foundation is 10/16". Accordingly the check for wall net section will be as follows:

- The spacing of the re-bars is 3 5/16".
- The tributary area of the re-bar = $S.t_s = 2.08 \text{ in}^2$
- The net area, $A_{net} = S.t_s - (D+1/8).t = 1.37 \text{ in}^2$
- The force at the bar = 50.33 Kips
- The nominal strength of the net area = $\phi_t.(1.2.F_y). A_{net} = 58$,> the force at the bolt = 50.33 Kip > $A_g f_y = 52$ Kips

B.9 Load Transfer at the Flanges using Annular Rings

Each flange of the wall is composed of either a full HSS tube a half circular tube. When the half tube forming the flange of the CFSSP-NB yields in tension it the strategy adopted here to is suppose to transfer this tension force to the foundation is through the annular ring welded to the base of the half circular section, (Roeder et al 2003)..The maximum tension force in the tube is T_s . This force is transferred to the footing through shear friction along the embedded length (neglected here as it cannot be reliably quantified) and anchorage at the annular ring welded to the half HSS section. As a first step in load transfer of the flange forces to the foundation, the embedment length of the CFSSP sandwich walls in the concrete foundation must be large enough to assure that the stresses induced in concrete along an assumed failure surface should not exceed the permissible limit. The conical failure surface proposed by (Roeder et al 2004) for concrete filled steel tubes was considered and extrapolated for the case of CFSSP sandwich walls under study. Figure B- 13 shows the proposed failure surface which is at 45 degrees starting from the edge of the annular ring. Figure B-14 shows the plan view of the failure surface and the location of the infinitesimal wedge subjected to forces at failure surface. According to Figure B-15 shows the wedge under study that used to calculate the stress at the concrete proposed failure surface.

$$T_s = \sigma_c \cdot \cos\beta \cdot A_{conc}$$

$$T_s = d\gamma \frac{D}{2} t f_y$$

$$A_{conc} = \int_0^{l_e} \left(\frac{D}{2} + b_f + \rho \cot\beta \right) \frac{d\gamma}{\sin\beta} d\rho = \left(\frac{D}{2} l_e + b_f l_e + l_e^2 \cot\beta \right) \frac{d\gamma}{\sin\beta}$$

where:

b_f is the width of the ring embedded in the foundation

D is the diameter of the HSS circular tube.

β is the angle of the failure plan

$d\gamma$ is the infinitesimal angle for the wedge under study

ρ is the vertical height of the failure surface measured for the base line of foundation

l_e is the length of the part of the wall embedded in foundation

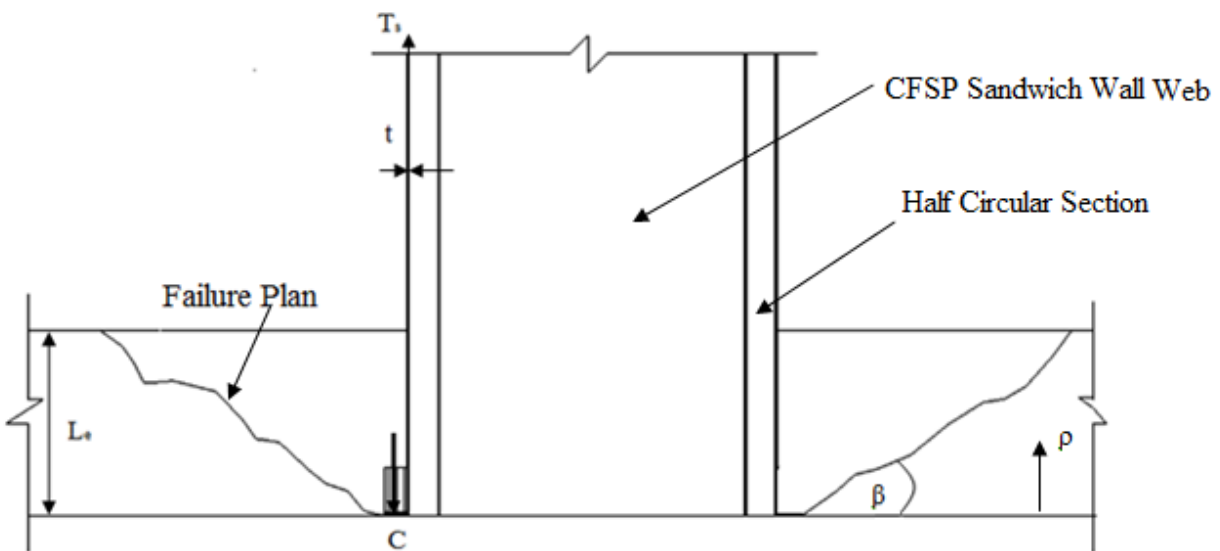


Figure B-11 Proposed Concrete Fracture Surface in Foundation

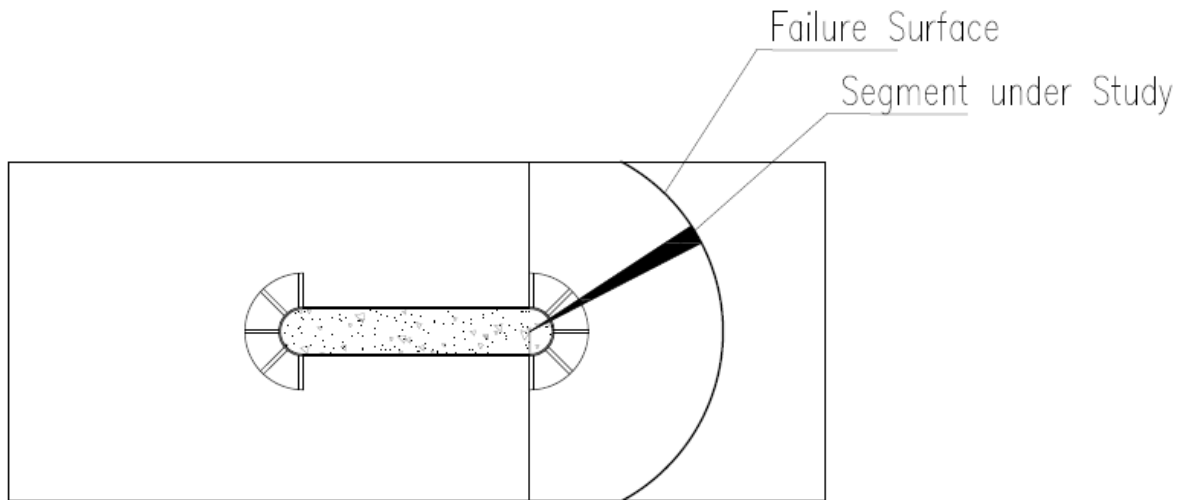


Figure B-12 Plan of the Failure Surface

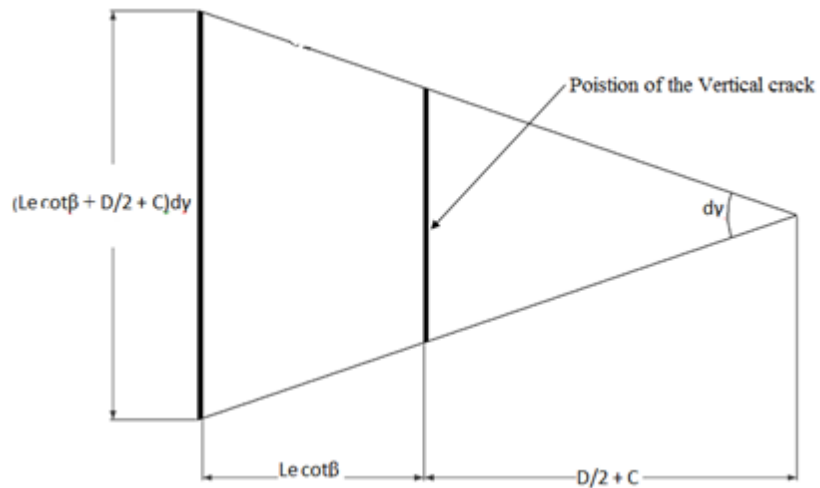


Figure B-13 Failure Wedge in the Annular Ring, Roeder et al 2003

For an angle $\beta = 45^\circ$, the expression for the stress in concrete will take the form

$$\sigma_c = \frac{\frac{D}{2} t f_y}{\left(\frac{D}{2} + b_f\right) l_e + \frac{l_e^2}{2}}$$

Considering the following

$D = 8.625 \text{ in}$, $t = 0.322 \text{ in}$, $f_y = 50 \text{ Ksi}$, $b_f = 2 \text{ in}$, $l_e = 24 \text{ in}$

$$\sigma_c = 0.157 \text{ Ksi} < 4 \text{ Ksi}$$

The stresses in the foundation concrete are less than the permissible value. The embedment depth is therefore sufficient to transfer the load.

\therefore Concrete at the proposed failure surface is not crushed consequently the distance of the wall embedded in the foundation is sufficient to develop the required load transfer.

As a next stage the width of the annular ring embedded in concrete foundation, b_f , should be chosen such that the thickness of the annular ring is economic and constructible.

The annular ring thickness is calculated such that the force in the half circular section is transmitted to the foundation considering that the concrete strength applied to the ring, $f'_c = 4 \text{ ksi}$

The Force acting on a half cylinder is therefore equal to $= 1.5tF_y = 1.5 \times 0.322 \times 50 = 24.15 \text{ kip} / \text{in}$

where A is the area of unit length of the perimeter multiplied by the HSS thickness

The tensile force is transferred as a shearing force acting on the annular ring, the free body diagram is shown in Figure B-14

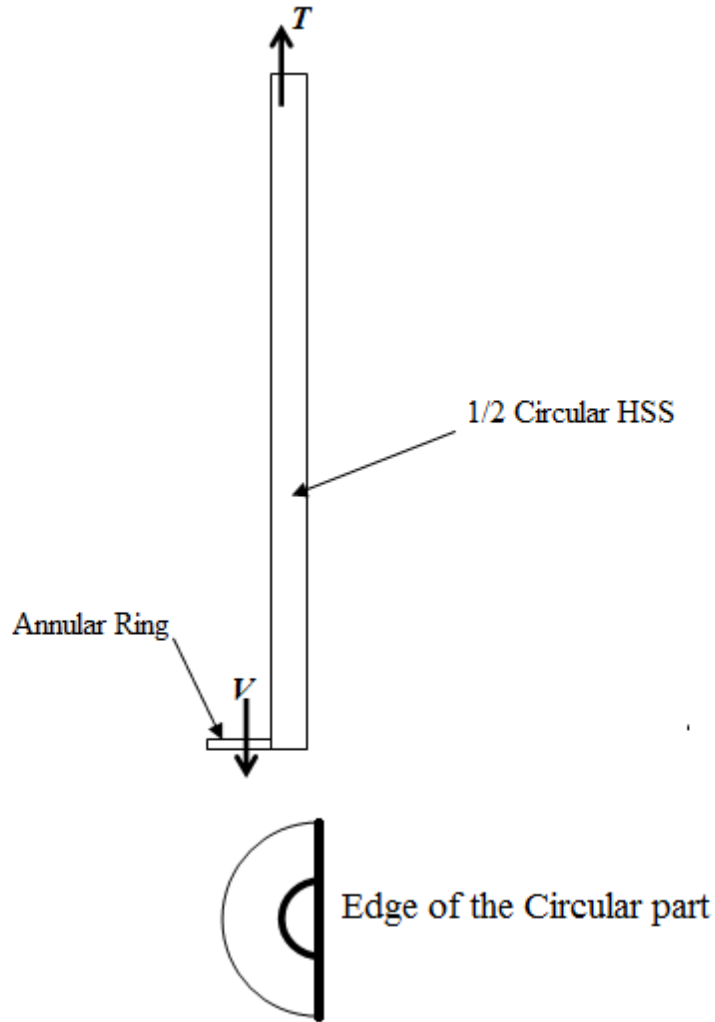


Figure B-14 Free Body Diagram Showing Force Transferred to Annular Ring

The unit shear strength of the annular ring = $0.6F_y t = 30t$

Therefore

$30t = 24.15$, and $t_{\min} = 0.805'' \approx 7/8''$

In order to find the width and the thickness of the annular ring, the yielding force acting on the half cylinder section is equated to the concrete pressure force acting on the annular ring, this is illustrated through the free body diagram shown in Figure B-15.

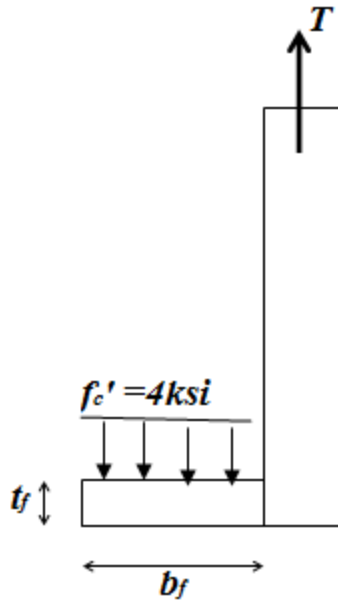


Figure B-15 Free Body Diagram for the Loads on the Annular Ring

The width of the annular ring b_f can be conservatively calculated assuming a rectangular strip cantilevering from the HSS tube such that

$$f_c' b_f = T$$

$$4 \times b_f = 24.15 \text{ Kips}$$

$$b_f = 6''$$

$$M = \frac{f_c' b_f^2}{2} = \frac{b h^2}{6} F_y$$

$$\frac{4 \times 6^2}{2} = \frac{1 \times t_f^2}{6} \times 50$$

$$t_f = 2.93 \text{ inch}$$

This calculated thickness is excessively large and it can be reduced by using a stiffened annular ring instead.. Plan of stiffened annular ring is shown in Figure B-16. The marked region between the stiffeners is the critical part for the study. Two yielding mechanisms were considered in studying the annular ring plate between the stiffeners. Figure B-18 shows the proposed failure mechanisms, assuming rectangular plates to simplify calculations. The value c is taken as the largest width of the plate wedge for conservatism.

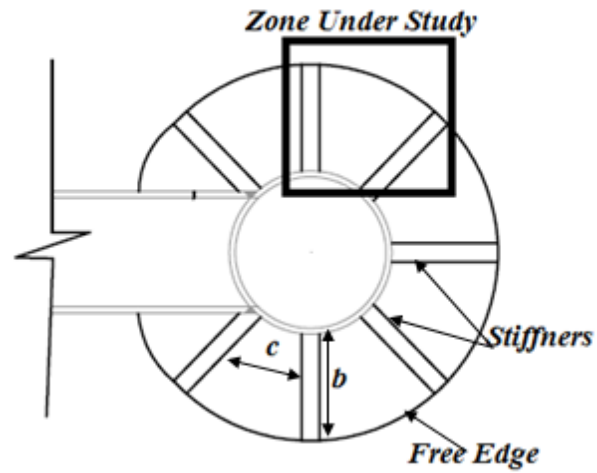


Figure B-16 Stiffened Annular Ring

In the Zone under study the stiffened edges are considered fixed ends together with edge toward the circular section.

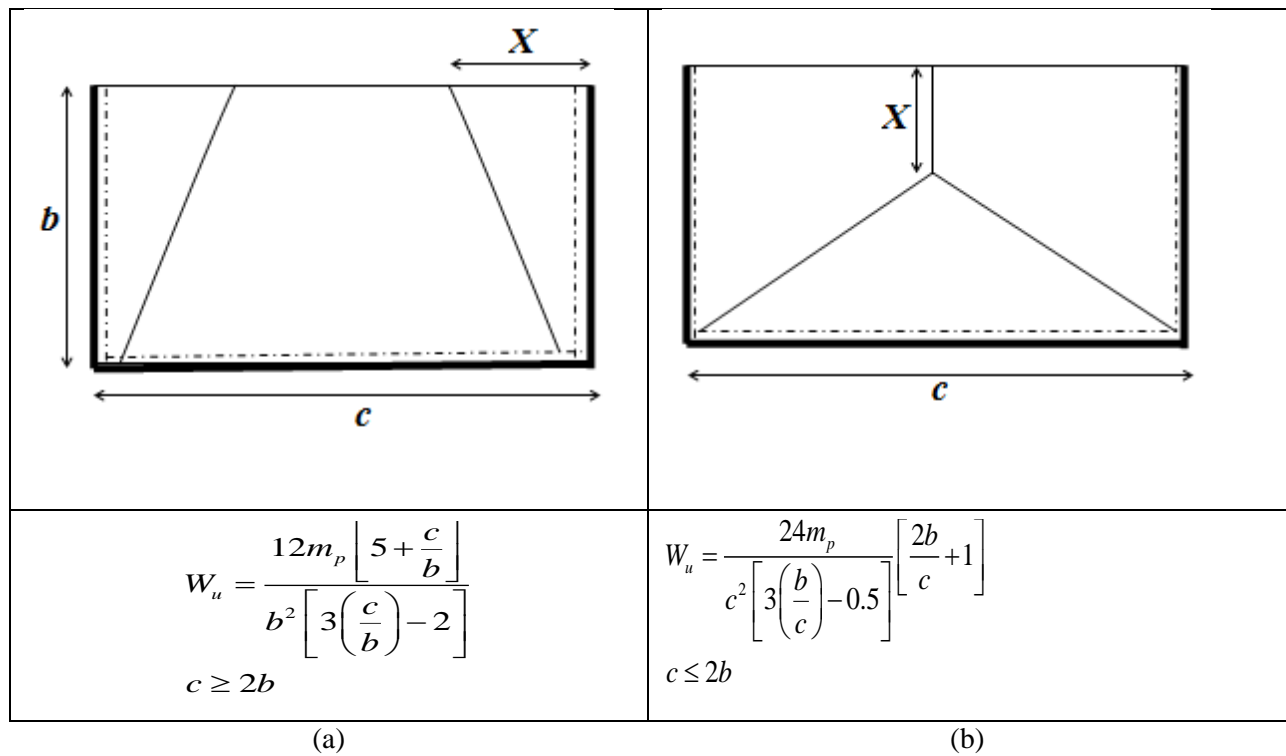


Figure B-17 Proposed Failure Mechanisms of Annular Ring Plate

For the proposed failure mechanisms the load W_u is equal to 4 ksi (strength of concrete used in foundation).

The radius of the annular ring , $R = r_{HSS8.625 \times 0.322} + 6" = 10.322"$

According to the geometry chosen a vertical stiffener is used at 45° and the distances b and c can have the following values:

$b = 6", c = \frac{2\pi R}{8} = 8.11"$ accordingly mechanism (b) is chosen

$b/c = 0.74$

$$4ksi = \frac{24}{8.11^2 [3 \times 0.74 - 0.5]} [2 \times 0.74 + 1] t^2 \left(\frac{50}{4} \right)$$

$t = 0.78"$

If the annular ring plate thickness is taken equal to 1 inch that will give a safety factor = $(1^2/0.78^2) = 1.64$

The annular ring will have a 6" width and thickness of 1

The stiffeners used to reinforce the annular ring are subjected to shearing force that can be calculated considering that the spacing between the stiffeners is 8.1", measured on the outer perimeter of the annular ring, the width of the annular ring is 6". The tributary area acting on a single stiffener is 8.1×6 .

The shear force acting on the stiffener is equal to $= 6 \times 8.11 \times 4 = 194.64 kips$

Figure B-18 shows the annular ring stiffener and the forces acting on its sides. Where the force of 196.64 kips act on side A of the stiffener as tension force, while the same force will be acting as a shear force on side B of the stiffener.

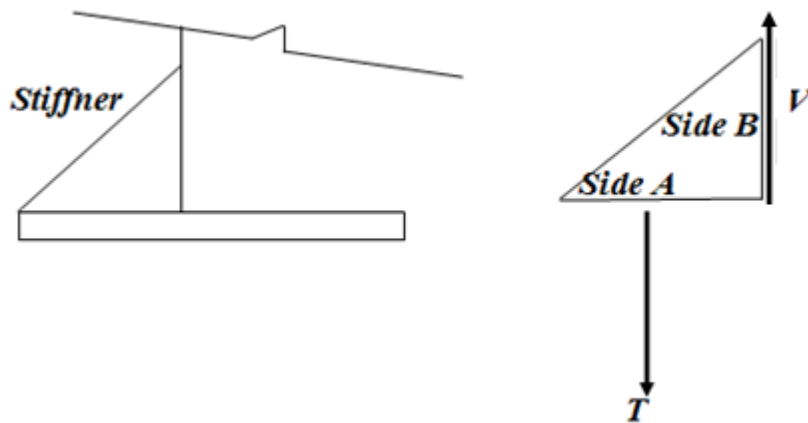


Figure B-18 Forces Acting on Stiffeners of Annular Ring

Side A of the stiffener is subjected to tensile force and the stress on this side is

$$6 \times t \times 50 = 194.64 \text{ kip}$$

$$t = 0.64" \approx 5/8"$$

For side B of the stiffener it is subjected to shear force,

$$\tau_y = 0.6F_y = \frac{194.6}{t \times h} = \frac{194.6}{5/8" \times h}$$

$$h = 10.37" \approx 10.5"$$

Stiffener final dimension is shown in Figure B-19

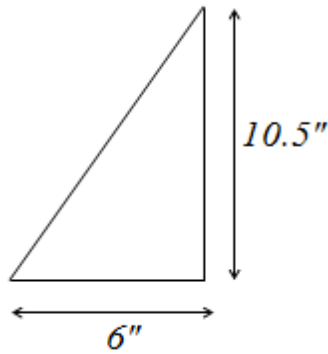


Figure B-19 Dimensions of the Annular Ring Stiffeners

The force is transferred from the circular HSS to the stiffener through fillet welds that can be calculated considering fillet weld of thickness 5/16" and E70 electrode. .

The strength of the weld is equal to $= \phi F_w S_w L_w = 0.75 \times 0.6 \times 70 \times (5/16) \times 0.707 \times 10.5 = 73 \text{ kips}$

For two lines of fillet weld the total welding resistance = 146 kip

The height of the stiffener is increased to 14" to obtain the needed weld strength of $\frac{146 \times 14}{10.5} = 194.67 \text{ kip}$,

The welding between stiffeners and the base plate is designed such that it could transfer the load of 194.6 kips.

The thickness of the welding can be calculated such that :

$$S_w = \frac{194.6}{\phi F_w L_w} = \frac{194.6}{0.75 \times 0.6 \times 70 \times 0.707 \times 6} = 1.45''$$

that will lead to thickness of welding is 3/4" on each side of the stiffener and consequentially the thickness of the stiffener should be 3/4". The final arrangement of the of the annular ring and the stiffeners is shown in Figure B-20.

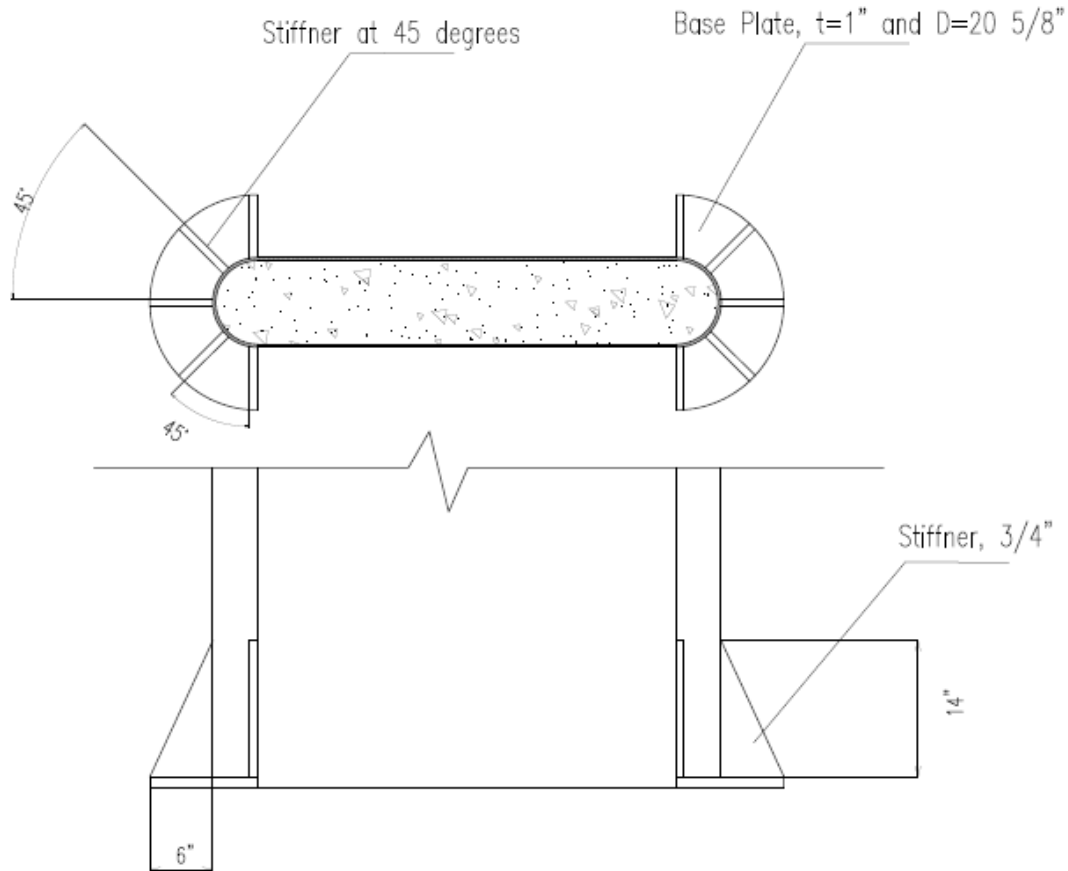


Figure B-20 Annular Ring and the Stiffeners

B.10 Foundation Design

The foundation design is first subjected to the constraint that its thickness should not exceed two feet, as the DYWIDAG bars available in the laboratory and used to tie the foundation to the strong floor have a limited length.

The length and width of foundation are chosen such that there is no uplift of the foundation away from the strong floor during testing of the composite wall. The tension force, uplifting force, developed due to 1.5 times the plastic moment capacity of concrete filled sandwich panel wall, $1.5 M_P$, is resisted by prestressed DYWIDAGS tied to the lab floor. The proposed dimensions of the foundation are $5' \times 12'$ with 16 DYWIDAGS having $1 \frac{3}{8}$ " diameter.

Using a simple rectangular cross-section analogy for the footprint of the footing, the inertia of the foundation is:

$$I_x = \frac{b.h^3}{12} = \frac{5 \times 12^3}{12} = 720 \text{ ft}^3$$

and the corresponding linearly varying stresses under the foundation resulting from the wall's factored plastic moment can be calculated. Using this model, the maximum flexural stress at the edge of the foundation would be:

$$F_M = 1.5 \frac{M_p}{I_x} \cdot y = \frac{1.5 \times 2268.5}{720} \times 6 = 28.35 = 0.196 \text{ kip/in}^2 < \phi f'_c \text{ (note that the laboratory's strong}$$

floor compressive strength is 4 ksi)

The DYWIDAGS used to connect the specimen to the laboratory strong floor are to be pre-tensioned to 50% of their ultimate strength. For a diameter of 1 3/8" the pretension up to 50% of the ultimate strength, T_{DYW}, is equal to 118 Kips per DYWIDAG information presented in Figure B-21.

DYWIDAG-SYSTEMS INTERNATIONAL



DYWIDAG THREADBAR® - TECHNICAL DATA [IMPERIAL UNITS]

May 16, 2011

Steel Grade f _y / f _u ksi	Nominal Bar Diameter		Steel Area A _s in ²	Yield Load P _y = f _y A _s kips	Ult. Load P _u = f _u A _s kips	Nominal Wt. lbs/ft	Max. Bar Ø Across Ribs in	Mill length ft	Direction of Thread L or R
	in	in							
130/160 ksi Hot-Rolled THREADBAR® Form-Ties, Post-Tensioning, Ground Anchors	5/8	5/8"	0.27	35.7	43.6	0.99	0.693	19.3	R
	3/4	3/4"	0.49	63.4	77.5	1.74	0.900	39	R
120/150 ksi ASTM A722 except 3" Ø Hot-Rolled THREADBAR® PT Ground Anchors Post-Tensioning *Cold-Rolled THREADBAR®	1	1"	0.85	102.0	127.5	3.01	1.201	60	R
	1 1/4	1 1/4"	1.25	150.0	187.5	4.39	1.457	60	R
	1 3/8	1 3/8"	1.58	189.6	237.0	5.56	1.630	60	R
	*1 3/4	1 3/4"	2.58	320.0	400.0	9.22	2.009	45	R
	*2 1/2	2 1/2"	5.16	619.2	774.0	18.20	2.790	45	R
75/100 ksi CSA G30.18 ASTM A615 except #20, #24, #28 Hot-Rolled THREADBAR® Tie Rods Hanging Rods Micropiles (GEWI® Piles) Anchor Bolts Concrete Reinforcing Seismic Anchors Rock Bolts Ground Anchors Soil Nailing Precast Connections	3/4	#6	0.44	33.0	44.0	1.50	0.862	48	L
	7/8	#7	0.60	45.0	60.0	2.04	0.996	60	L
	1	#8	0.79	59.3	79.0	2.67	1.122	60	L
	1 1/8	#9	1.00	75.0	100.0	3.40	1.268	60	L
	1 1/4	#10	1.27	95.3	127.0	4.30	1.433	60	L
	1 3/8	#11	1.56	117.0	156.0	5.31	1.614	60	L
	1 3/4	#14	2.25	168.8	225.0	7.65	1.862	60	R
	2 1/4	#18	4.00	300.0	400.0	13.60	2.504	60	R
	** 2 1/2	#20	4.91	393.0	520.0	16.70	2.717	60	L

Figure B-21 Technical Data for DYWIDAG Bars, Dywidag System International

The corresponding uniform compressive stress on the strong floor due to pre-tensioning of the DYWIDAGS is given by $F_D = (\text{Number of Dywidags}/A_f) \cdot T_{DYW}$

where :

A_f = foot print area of the foundation.

To apply stress on floor such that no uplift occurs (which is equivalent to ensuring that no resulting tension stresses exist when superposing the stress diagrams), the compression stress imposed by the pre-tensioned DYWIDAG bars must be larger than the tension stresses caused by the moments. This is achieved using 18 Dywidag bars, such that:

$$F_D = \frac{16 \times 118}{5 \times 12} = 0.219 \text{ksi} > F_M$$

In order check for the uplift of the foundation a 3D model for the wall and foundation was built in STAAD Pro software. In the model both the wall and the foundation were represented as a shells. The model presented take into account the contact between the foundation and the strong floor through considering a link element under the entire foundation. In the 3D model shown in Figure B-20 the link element with compression only feature was used. A hinged support was used at the edge of foundation to assure stability. The deformation showed uplift at the tension side of the foundation. The compressed side of the foundation showed below floor level deformation. In both cases a relatively small deformation values in the order of 0.01 inch were recorded and shown in Figure B-21. The deformation of the foundation under the floor level is attributed to the fact that the link elements simulating the strong floor is modeled as a columns having a cross section area equal to that of the tributary area for the link element. and this assumption gives less stiffness than that of a continuous strong floor. However as aforementioned the deformation is relatively small and in the order of 0.01 inch. If the stiffness of the link elements at the compression side of the foundation becomes too high that will be the same as cancelling the link element and using a hinged support at directly attached to the slab. Link elements showed compression force only no tension. The Dywidags bars were modeled as a pre-tensioned element having a pre tension force of 118 kips.

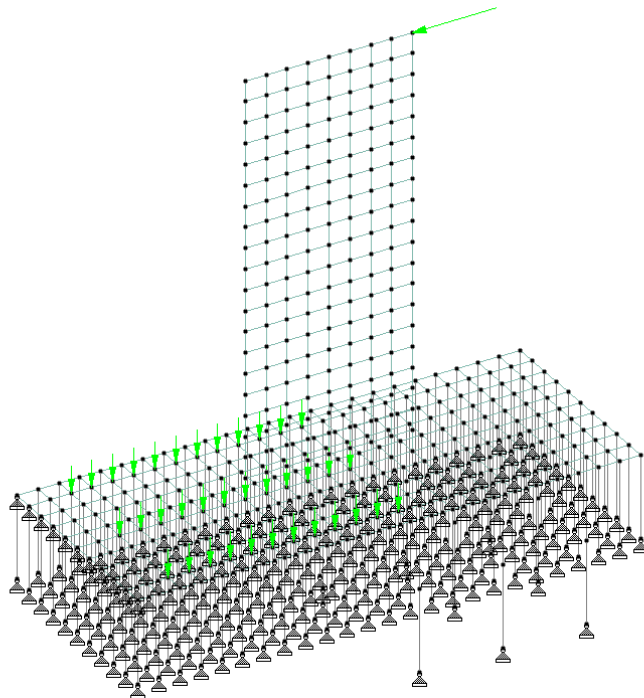


Figure B-22 3-D STAAD Pro Model

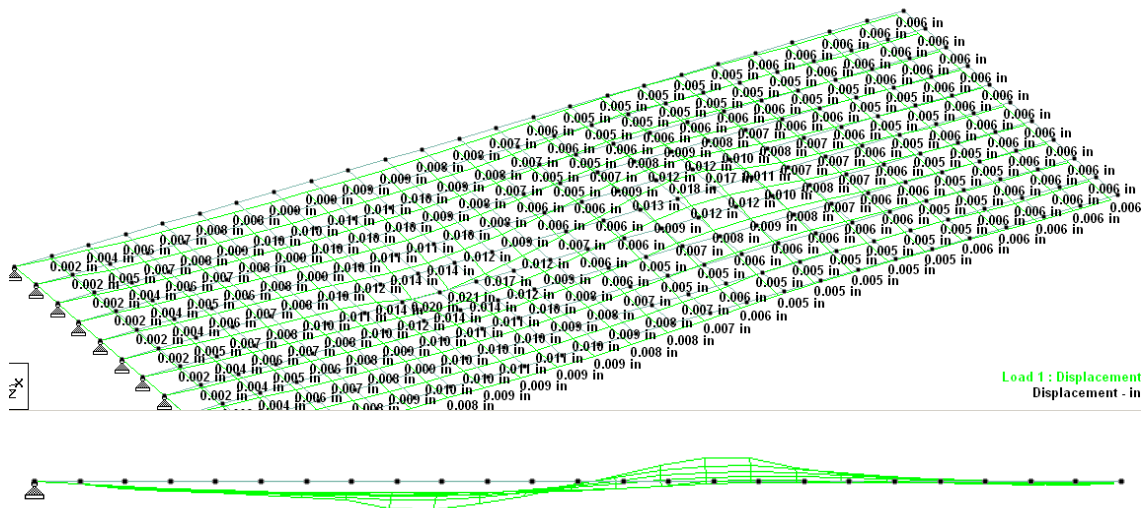


Figure B-23 Foundation Deformation

The net stress distribution under the foundation obtained from simplified analysis is the summation of the stresses F_M and F_D . However, the stress distribution used to calculate the internal moment and shear to design the foundation is the result of only the wall moment capacity F_M . This is because the Dywidag bars only apply a pre-compression between the specimen and the strong floor. That clamping force is uniform and produce no flexural strains in the specimen (by analogy, just like pre-tensioned bolts clamping two flush flat plates together in bolted connections). The stress distribution under the foundation is given in the Figure-B-24.

The shear and flexural forces acting on the critical section in the longitudinal direction can be calculated considering the stress diagram adjacent to the critical section multiplied by its tributary area, and by its lever arm for the flexure case. The location of the critical sections in both short and long directions is shown in Figure B-25.

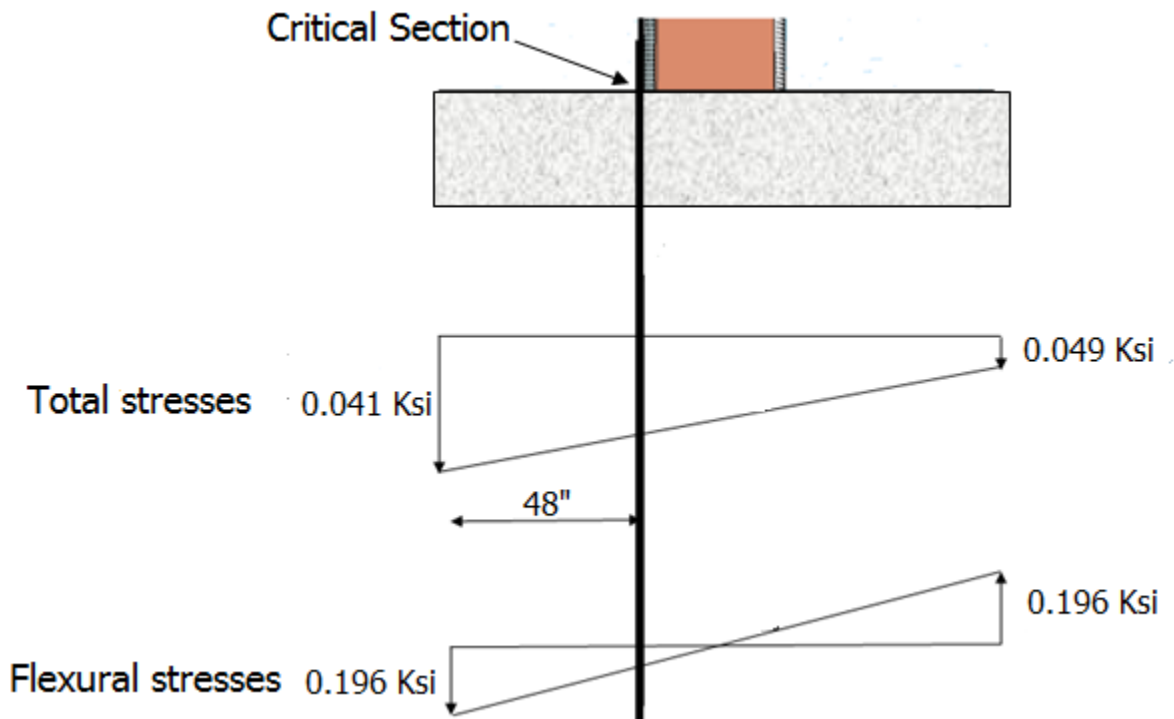


Figure B-24 Stress Distribution Under Foundation

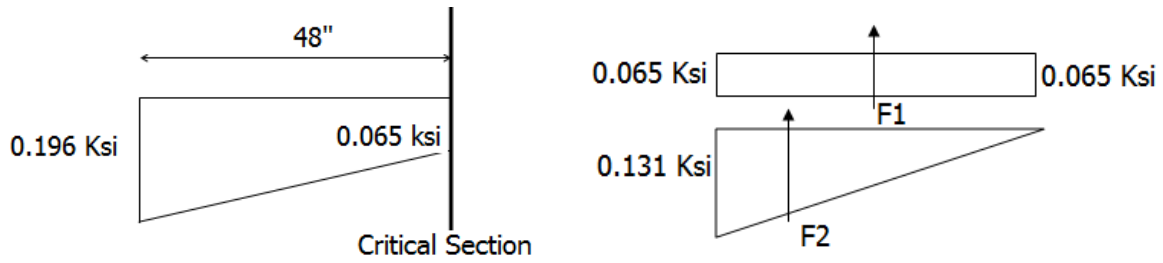


Figure B-25 Forces Acting on the Foundation Critical Section

The resultant forces for the stress diagram shown in Figure B-26, in terms of the average compression stress , σ , are:

$$F1 = \sigma \cdot b \cdot w_c = 0.065 \times 48 \times 60 = 187.2 \text{ kip}$$

$$F2 = 188.64 \text{ kip}$$

where:

b = Width of foundation

w_c = The length of the foundation subjected to compressive stress measured from the edge of the foundation up to the critical section.

The moment at the critical section can be calculated as follows:

$$M_1 = F1. (0.5 w_c) + F2. (0.67 w_c) = 10559 \text{ kip-in (long direction)}$$

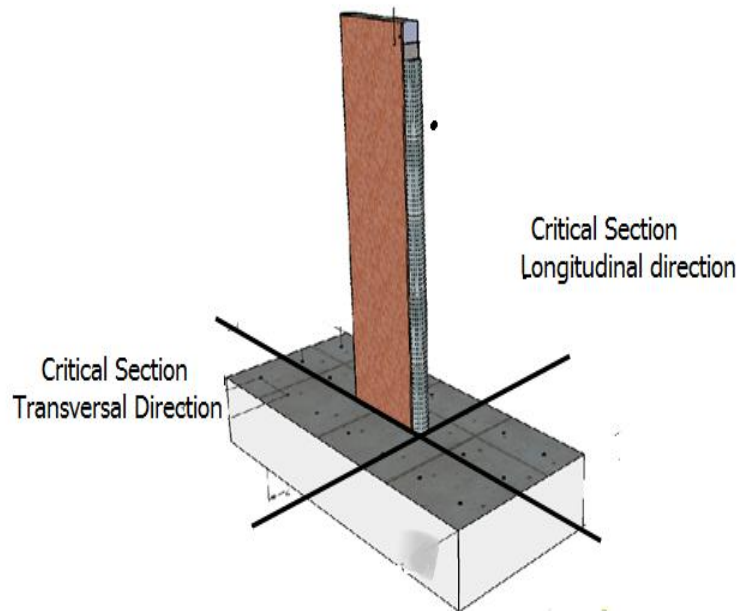


Figure B-26 Foundation Critical Section

Reinforcement of the foundation is calculated as follows:

Flexural reinforcement in long direction (to resist M_1 shown above)

$$A_s = \frac{M_u}{\phi f_y (jd)} = \frac{10599}{0.9 \times 50 \times 0.95 \times 20} = 12.4 \text{ in}^2$$

$$A_{s \text{ min}} = \frac{200bd}{f_y} = 4.8 \text{ in}^2$$

Taking into account symmetry considerations and practical spacing requirements, a total of 16#8 bar are used in each of the top and bottom layers of the foundations, with a spacing of 3.5" between re-bars.

Flexural reinforcement in short direction to resist M_2

$$M_{\text{short}} = (0.196 + 0.065) \times 0.5 \times 0.1305 \times 48 \times 25.68 \times 0.5 \times 25.68 = 2066 \text{ Kip.in}$$

$$A_s = \frac{2066}{0.9 \times 50 \times 0.95 \times 20} = 2.41 \text{ in}^2$$

In this direction the required reinforcement is less than that of the minimum ACI requirement given by

$$A_{s_{\min}} = 200. bd / f_y = 11.52 \text{ in}^2$$

Therefore, 27 bars # 6 (total area of 11.92 in² are used in the short direction

Shear strength

$$T V_u = 375.84 \text{ Kip}$$

he shear stress and forces at the critical section, considering forces developed in the long direction, is

$$q = \frac{375.84}{60 \times 20} = 0.313 \text{ ksi}$$

Shear strength of the corresponding cross section is

$$V_c = 2\sqrt{f'_c} b_w d = 151.78 \text{ kip}$$

Using the strength reduction factor for shear, $\phi_s = 0.75$

$V_u / \phi = 501.12 \text{ Kips} > V_c / 2 = 75.98 \text{ Kip}$, therefore stirrups are required.

The needed stirrups are designed considering the following:

The effective width of foundation = 56"

The number of stirrups branches = 12

The stirrups used are # 4 having 12 branches

The effective depth of the section is 20"

$$F_{yt} = 40 \text{ ksi}$$

$$A_v = 12 \times 0.196 = 2.352 \text{ in}^2$$

The spacing of the stirrups is given by ACI section 11.4.5.1

$$S = \frac{A_v f_{yt} d}{\frac{V_u}{\phi} - V_c} = 5.4" \approx 5"$$

Recognizing that minimum reinforcement controlled the design of flexural reinforcement in the transverse direction and in order to be able to minimize the number of the drilled holes in the part of the wall specimen embedded in concrete, an alternative for the reinforcement arrangement is proposed here. In this alternative the upper and lower main reinforcement in the short direction are used to resist flexure as well as to transfer the shear forces from the wall to the foundation. In order to reduce the shearing force acting on the re-bars an extra row of re-bars is used at mid-depth of the foundation. Accordingly, the reinforcement bars in the short direction will all be 1" diameter re-bars.

Revising the above calculations, the shearing force acting on a single re-bars = $102 / 3 = 34$ Kips

The average stress under the foundation = 0.131 Ksi

Moment acting in the short direction = 1048 Kip-in

The tension force acting on the flexural re-bars = $(1048/18)/12 = 4.85$ Kips

The tensile stress and the shear stress in the bar are given by

$Q =$ the shearing force per bar = 34 Kips

$S_x = 0.78 \times 0.5 \times 0.212 = 0.083$

$I_x = 0.196$ Ksi

$$\sigma = \frac{T}{A_b} = \frac{4.85}{0.78} = 6.21 \text{ Ksi}$$

$$\tau = \frac{QS_x}{tI_x} = 14.31 \text{ Ksi}$$

$$\sigma = \frac{\sigma_x}{2} + \sqrt{\left(\frac{\sigma_x}{2}\right)^2 + \tau_{xy}^2}$$

$$\tau = \frac{QS_x}{tI_x} = 14.31 \text{ Ksi}$$

$$\sigma = \frac{\sigma_x}{2} + \sqrt{\left(\frac{\sigma_x}{2}\right)^2 + \tau_{xy}^2} = 17.74 \text{ Ksi}$$

The arrangements for the reinforcements bars and the stirrups used to transfer the load from the web of the concrete filled sandwich panel wall to the foundation is shown in Figure B-27. The final arrangement of the reinforcement bars is shown in Figure B-28.

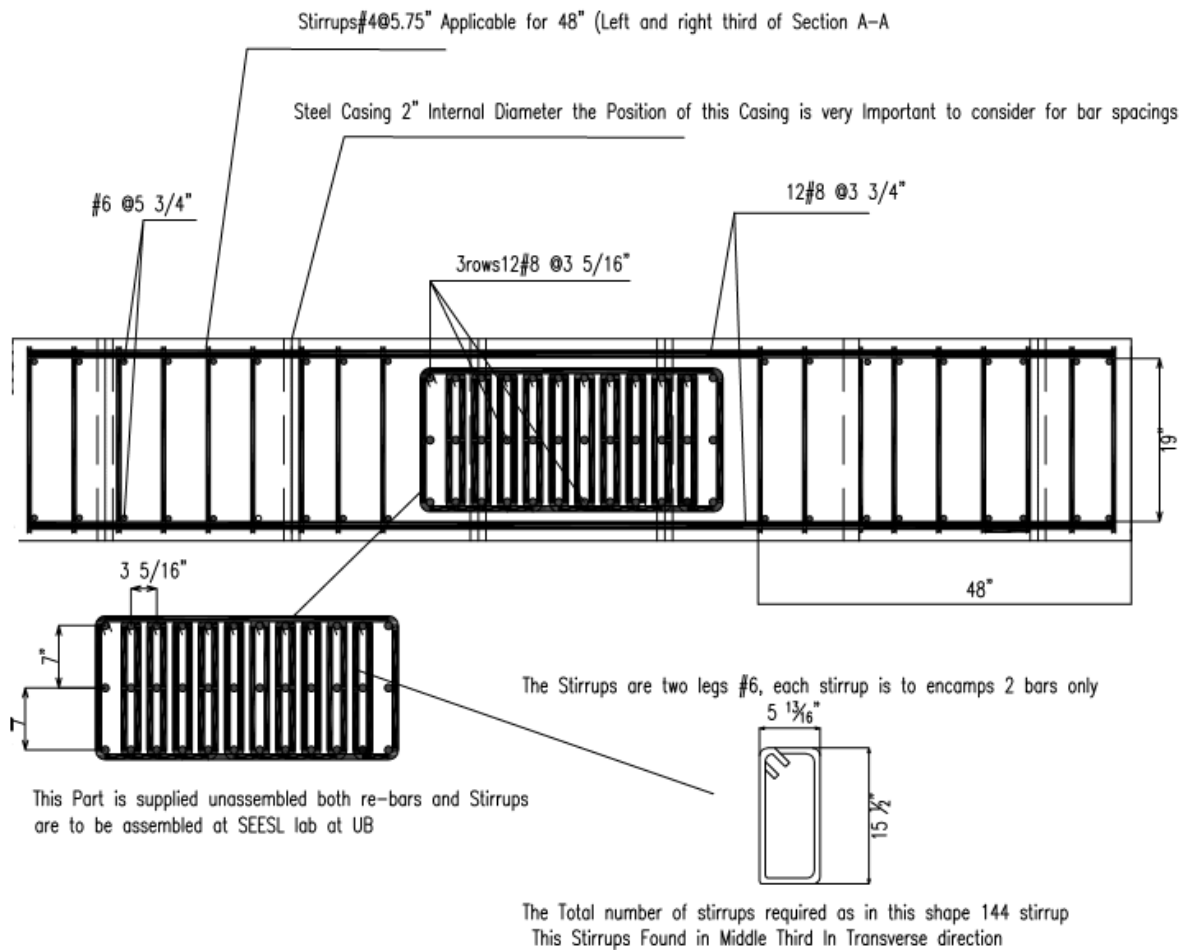


Figure B-27 Reinforced Bars and Stirrups Transferring Load from Wall Web

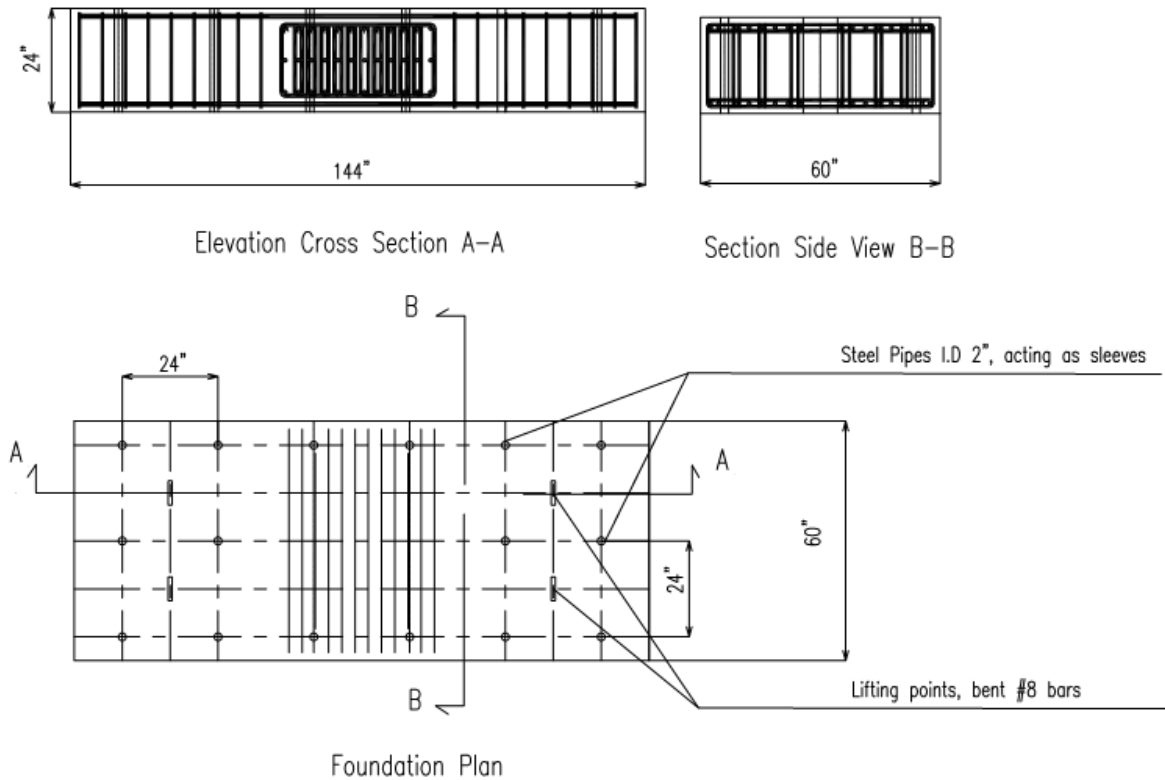


Figure B-28 Foundation Reinforced Arrangement

B.11 Check for Foundation Sliding

The shear force at the base of the foundation is transferred to the strong floor through friction resistance achieved by pre-stressing of the foundation to the strong floor of the laboratory. DYWIDAGS pre-tensioned to 50% of their yielding force give a total compression force acting on the foundation, $C = N_D \cdot (0.5 P_y) = 18(118.33) = 2129.94$ Kips. Considering a friction coefficient μ between concrete surfaces equal to 0.25, the sliding resistance = $\mu \cdot C = 0.25 \times 2129 = 532.25 > 340$ Kips (i.e. the lateral horizontal force applied to develop $1.5 M_p$ of the wall). Therefore sliding resistance is satisfactory.

B.12 Design of Lifting Points

The tested specimen is composed of concrete filled sandwich panel and the reinforced concrete foundation. The total weight of the specimen is 12 ton and in order to facilitate the mobilization of the specimen before and after testing anchorage points should be designed to sustain the weight of the specimens. There is four anchorage points which is essentially a bent # 8 bar embedded in the reinforced concrete foundation. Figure B-18 shows the anchored bent bars used as lifting points. The bar should

sustain the tension force applied on each lifting points, 4 ton, and should be embedded in the foundation through a sufficient distance.

The Tensile capacity of the #8 bar is given by:

$$\phi A_b f_y = 0.75 \times 0.785 \times 50 = 29.43 \text{ kips}$$

According to the ACI code section 12.2.3 the development length required for a # 8bar can be given by the following equation:

$$l_d = \frac{f_y \psi_t \psi_e}{20 \lambda \sqrt{f_c}} d_b = \frac{50,000 \times 1 \times 1}{20 \times 1 \times \sqrt{4000}} \times 1 = 39.52''$$

B.13 Design of the Lateral Support System

To avoid lateral buckling of the CFSSP sandwich wall section and prevent global out of plan movement of the wall, a bracing system is used. Figure B-29 shows the schematic diagram for the proposed lateral support system. The dotted lines represent the presence of a truss normal to the view under study.

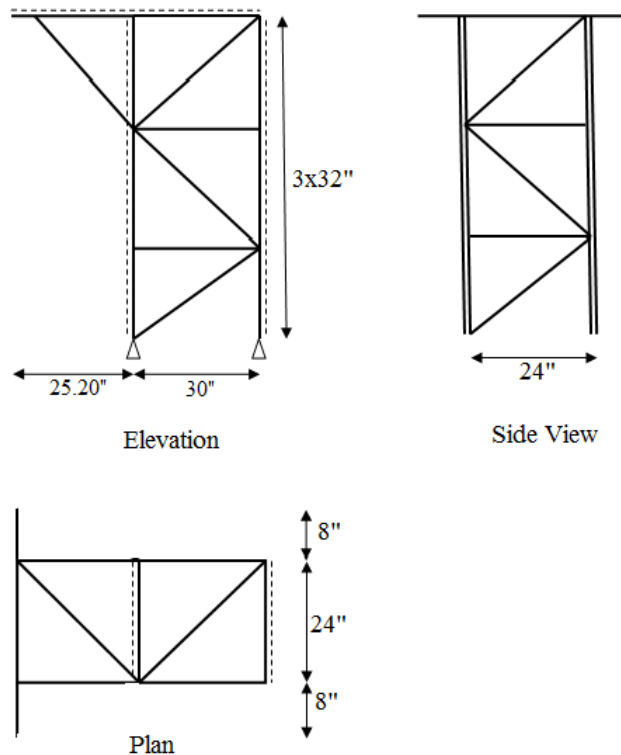


Figure B-29 Schematic Diagram for Lateral Bracing System

The force required to provide nodal displacement at the tip of the wall is given by the equation (A-6-7) in AISC LRFD Thirteenth edition.

$$P_{br} = 0.02M_r C_d / h_o = 24.48 \text{Kips}$$

The minimum required stiffness for the lateral bracing system is given by equation (A-6-8) AISC LRFD thirteenth edition

$$\beta_{br} = \frac{1}{\phi} \left(\frac{10M_r C_d}{L_b h_o} \right) = 136.05 \text{Kip / in}$$

Where:

$$\phi = 0.75$$

$$h_o = 35.28 \text{in}$$

$$C_d = 1.0$$

$$L_b = 120''$$

$$M_r = 43200 \text{Kip.in}$$

The forces acting on the bracing system can be illustrated in Figure B-30 showing the truss used as a lateral support for the wall during testing and the estimated force acting on it.

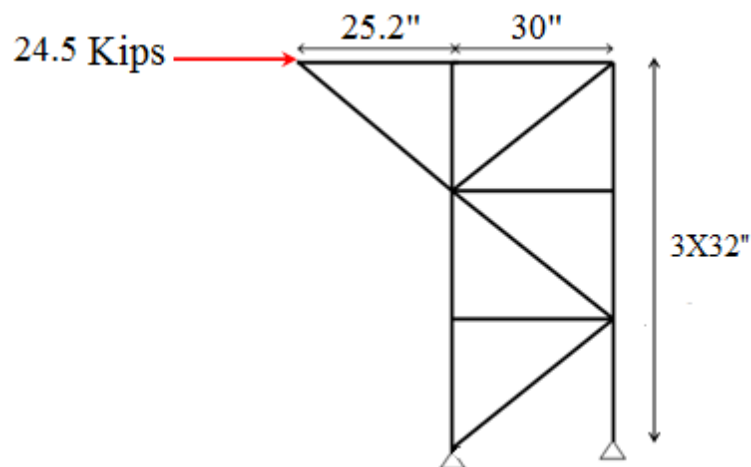


Figure B-30 Loading of Lateral Bracing System

All truss members were selected to be double angles back to back with a gusset plate thickness of 3/8" for the vertical chord members and one angle for diagonal and horizontal members. A summary of the forces and buckling lengths is shown in Table B-6. Members were designed depending on the AISC thirteen's edition design tables for one angle and two equal angles under compression. For the double angle section Table 4-8 of AISC thirteen was used as or the one angle section Table 4-11 was used. The results for the 3D structural analysis, forces and displacements, using STAAD Pro V8 is shown in Figure B-31.

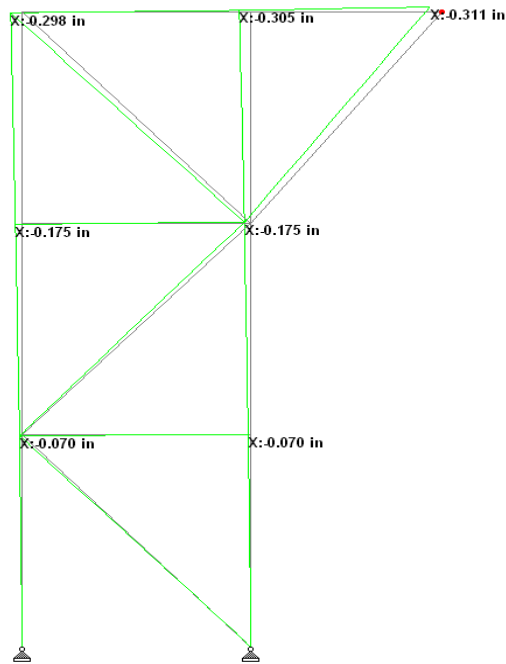


Figure B-31 Bracing System Displacements in Horizontal Direction

Table B-5 Member Forces

Member Max Forces	Force (Kips)	In-plan Buckling (in)	Out of plan Buckling (in)	Proposed Section
Chord Members	78.4	32	32	2Ls 3 ×3×5/16
Verticals	Zero	30	30	L 3×3×5/16
Diagonals	35.81	43.86	43.86	L 3×3×5/16

The stiffness of the truss can be calculated through dividing the force by horizontal displacement

$$k = \frac{F}{\delta} = \frac{24.5}{0.311} = 78.77 \text{ kip / in}$$

Since there will be always two trusses acting at the same time the total stiffness will be 157.54 kip/in which is more than the stiffness demand.

All of the lateral support system members were welded. The grade of steel used for the bracing system is assumed to be A36 having a yield stress of 36 ksi. The electrode classification number, F_{EXX} , is taken equal to 70 ksi.

As an example the length of welding in the diagonal member is be calculated as follows:

The maximum force acting on a diagonal member is equal to 41 kips as per Table B-6

The thickness of the welding S_w , is assumed= 5/16", and length of weld, L_w is unknown

$$41 = \phi R_n = 0.75(0.6F_{EXX})(\cos 45^\circ) S_w L_w$$

$$L_w = 5.92 \text{ in}$$

Distributed on the two sides of the weld

$$L_{w1} = 5.89(2/3) = 3.92 \text{ in}$$

$$L_{w2} = 5.89(1/3) = 1.96 \text{ in}$$



The lateral load will be transmitted to the lateral support system Through member M1 as illustrated in Figure B-21. Member M1 is composed of steel plates having thickness of $3/8''$ the proposed cross section is shown in FigureB-22. The Straining actions acting on member M1and its proposed cross sectional properties is summarized in Table B-6.

Table B-6 Member M1 Straining Actions and Properties

Moment, kip.in	Shear Force, kips	Moment of inertia, in⁴	Web Area, in²
196	24.5	28.76	4.5

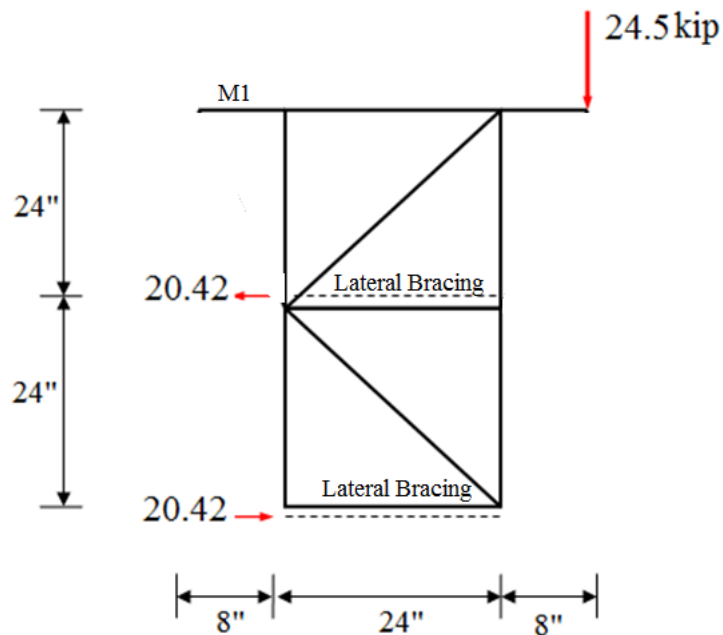


Figure B-32 Out of Plan Force acting on the Bracing System

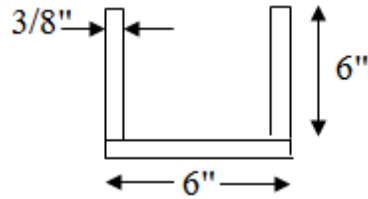


Figure B-33 Cross Section of Member M1

The stresses in the section is given by:

$$f = \frac{M}{I_x} y = \frac{196}{28.76} \times 4.0625 = 27.68 \text{ksi}$$

Considering the case in which one side only is subjected to the force. The members of the lateral bracing systems are designed to resist the reactions shown in Figure B-34. This members are bolted to the main structures through A490 bolts having 5/8" diameter.

For the lateral bracing, shown in Figure B-35, the maximum force in the diagonal members can be designed considering the forces and the buckling lengths shown below.

$$F_D = \frac{20.42}{\text{COS}53.13} = 34 \text{kip}$$

Buckling length of the diagonal member =40"

The selected section is L 3×3×5/16 and that according to the design Table

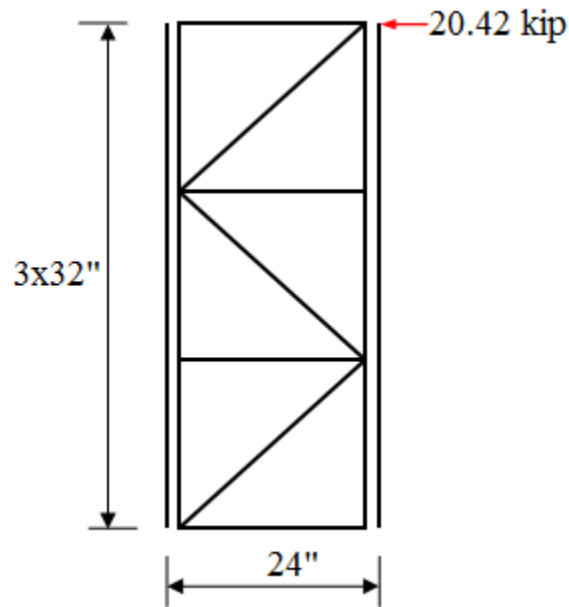


Figure B-34 Schematic Side View of Lateral Bracing

Members of the lateral bracing are connected using bolts grade A490 having $\frac{3}{4}$ " diameter. Two bolts are needed for each diagonal member. In order to assure the freedom of motion of the wall in the direction of the applied Load the point of contact between the lateral support system and the wall is provided with Teflon plate having $\frac{3}{8}$ " thickness. In order to accommodate for the difference in the thickness between the tested wall groups a T- shaped stiffener welded to the wall web is provided at the intersection of the lateral support system and the wall. Figure B-36 Shows the Elevation of the truss used as a lateral support system and illustrates the different components of the proposed lateral support system. Figure B-37 shows the plan for the lateral support system and how it is connected to the tested specimens of group NB-CFSSP.

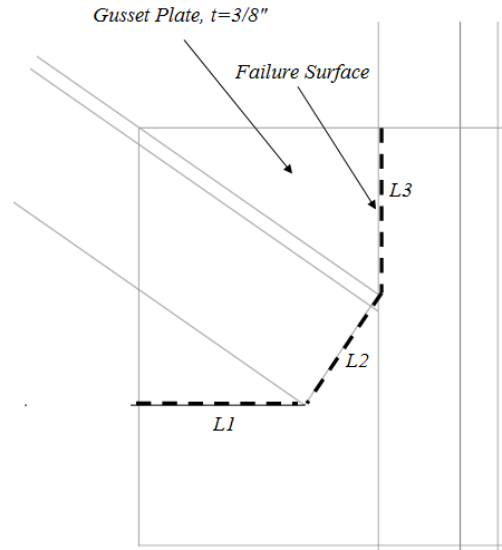


Figure B-35 Failure Mechanism for Gusset Plate

For the gusset plate of the diagonal member with the maximum force of 35.82 kips the failure surface is shown by the dotted line in Figure B-22 the length of failure lines L1, L2 and L3 is 3.71", 3" and 3.77". The thickness of the gusset plate is 3/8.

The fractured area = $(3.71 + 3 + 3.77) \times 3/8" = 3.93 in^2$

The nominal resistance of the Gusset plate in tension = $\phi R_n = 0.75 \times 3.93 \times 50 = 147.375 kips > 35.82$

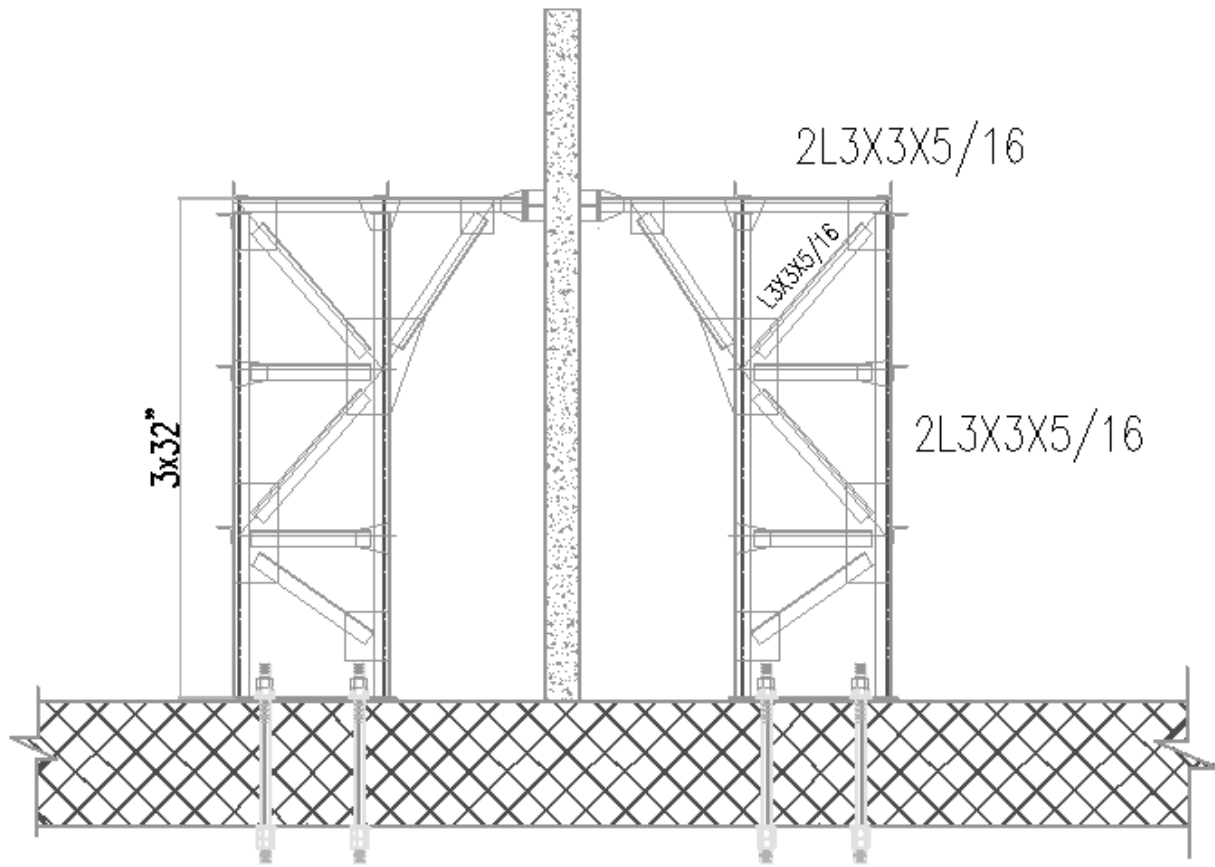


Figure B-36 Elevation of the Bracing System

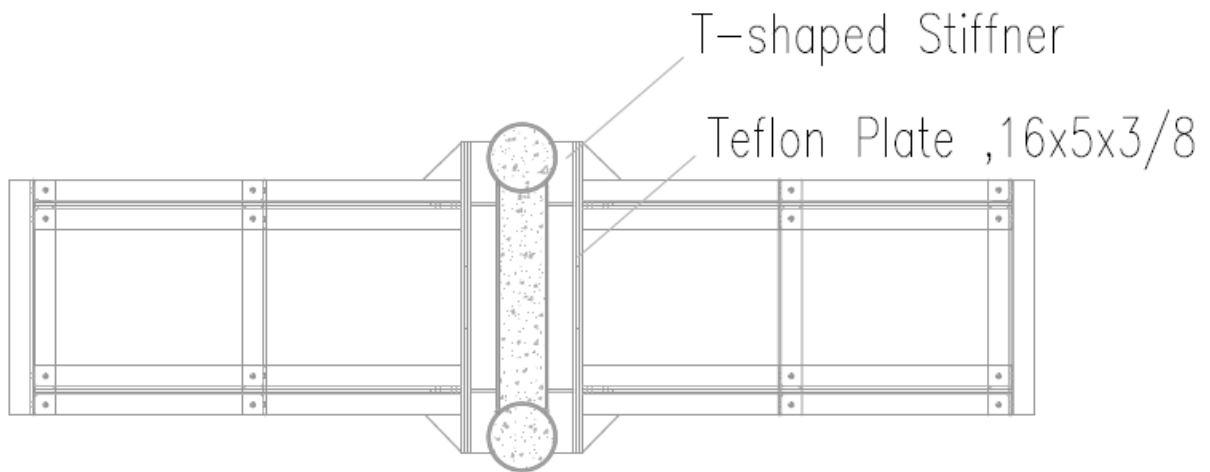


Figure B-37 Plan of Lateral Support System in Case of Group B Specimen

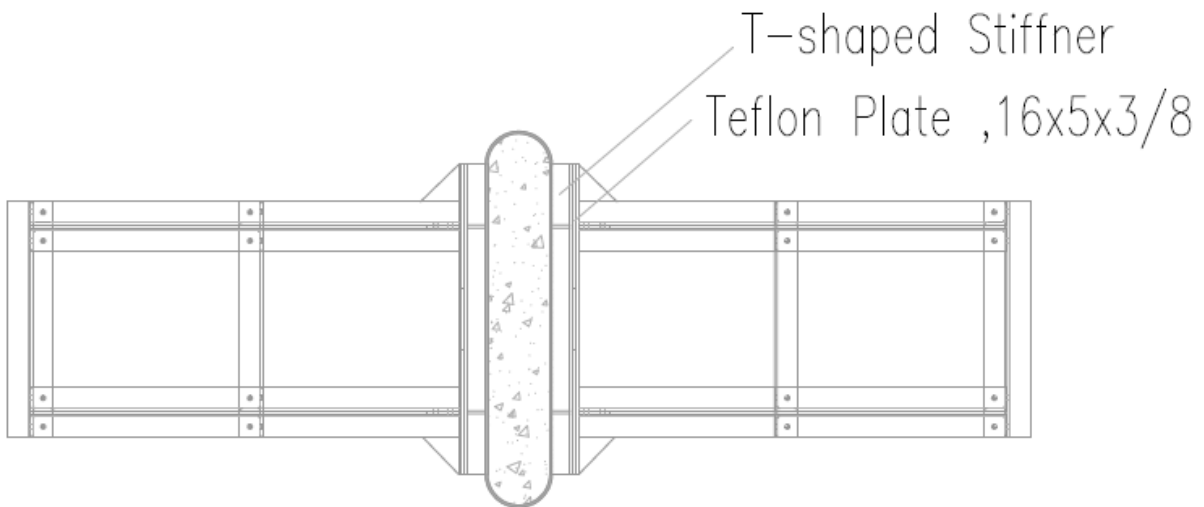


Figure B-38 Plan of Lateral Support System in Case of Group NB Specimen

As for the Anchorage of the trusses to the lab floor a pretension threaded is to be used the diameter of the threaded bar is calculated such that the pretension force can provide enough friction forces which are greater than the lateral load acting on the lateral support system. The diameter of the threaded bar can be calculated as follows:

the friction between the base plate and the concrete floor, $\mu = 0.2$ and considering that pretension force is equal to 60% of the threaded bar ultimate strength.

$$\mu N = 24.5, \therefore N = 122.5 \text{ kips}$$

Accordingly the diameter of the threaded bar used is 1 3/8" having a minimum ultimate strength of 237 kips.

B.14 Stability of the Specimen During Construction

During specimen construction and concrete casting the stability of the steel sandwich panel should be checked. Any permanent deformation in the steel sandwich panel should be calculated and accounted for as initial imperfection in the steel plates of the sandwich panel. For the stability checks the procedures and formulations proposed by Corus Bi-steel design guide second edition (2003).

APPENDIX C

EXCERPTS FROM XTRACT ANALYSIS

XTRACT Analysis Report -

Section Name: Section1
 Loading Name: M_C
 Analysis Type: Moment Curvature

UB
 8/17/2014
 Section analysis
 CFSSP-B
 Page __ of __

Section Details:

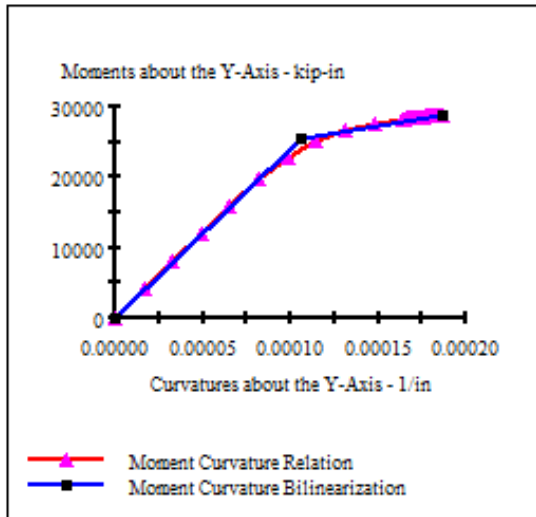
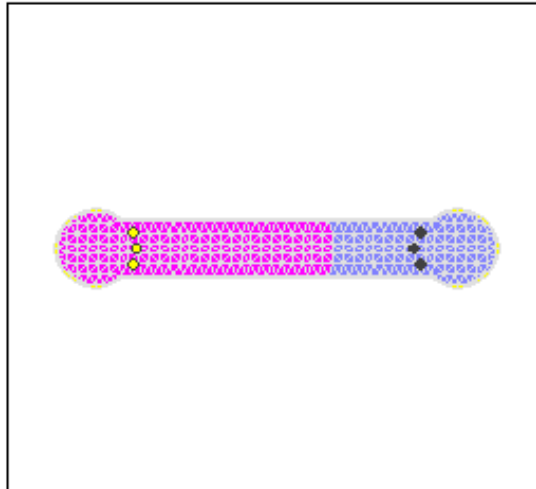
X Centroid: -2.436E-3 in
 Y Centroid: -.1222E-15 in
 Section Area: 268.4 in²

Loading Details:

Constant Load - Myy: -10.00 kip-in
 Increasing Loads: Myy Only
 Number of Points: 30
 Analysis Strategy: Displacement Control

Analysis Results:

Failing Material: BiLinear1
 Failure Strain: 5.000E-3 Tension
 Curvature at Initial Load: 28.29E-9 1/in
 Curvature at First Yield: 82.00E-6 1/in
 Ultimate Curvature: .1866E-3 1/in
 Moment at First Yield: 19.77E+3 kip-in
 Ultimate Moment: 28.85E+3 kip-in
 Centroid Strain at Yield: .3190E-3 Ten
 Centroid Strain at Ultimate: .9888E-3 Ten
 N.A. at First Yield: 3.891 in
 N.A. at Ultimate: 5.299 in
 Energy per Length: 3.546 kips
 Effective Yield Curvature: .1059E-3 1/in
 Effective Yield Moment: 25.54E+3 kip-in
 Over Strength Factor: 1.130
 Plastic Rotation Capacity: 2.662E-3 rad
 EI Effective: 2.41E+8 kip-in²
 Yield EI Effective: 4.10E+7 kip-in²
 Bilinear Hardening Slope: 17.03 %
 Curvature Ductility: 1.761



Comments:

User Comments

XTRACT Analysis Report -

Section Name: Section1
 Loading Name: P-M
 Analysis Type: PM Interaction

UB
 8/17/2014
 Section analysis
 CFSSP-B
 Page __ of __

Section Details:

X Centroid: -2.436E-3 in
 Y Centroid: -.1222E-15 in
 Section Area: 268.4 in²

Loading Details:

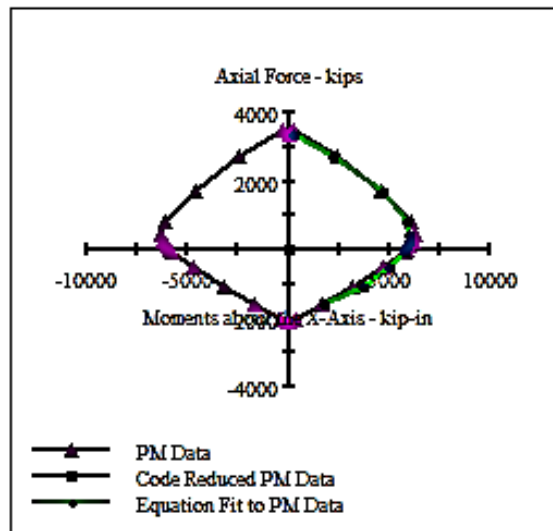
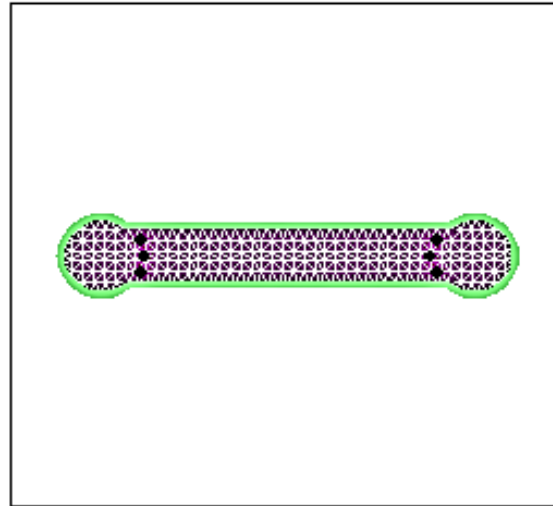
Angle of Loading: 0 deg
 Number of Points: 40
 Min. Core Concrete Strain: 3.000E-3 Comp
 Max. Core Concrete Strain: 1.0000 Ten
 Min. BiLinear1 Strain: 10.00E-3 Comp
 Max. BiLinear1 Strain: 10.00E-3 Ten

Analysis Results:

Max. Compression Load: 3498 kips
 Max. Tension Load: -2123 kips
 Maximum Moment: 6318 kip-in
 P at Max. Moment: 449.5 kips
 Minimum Moment: -6318 kip-in
 P at Min. Moment: 449.5 kips
 Moment (Max) at P=0: -8433 kip-in
 Max. Code Comp. Load: 0 kips
 Max. Code Ten. Load: 0 kips
 Maximum Code Moment: 0 kip-in
 P at Max. Code Moment: 0 kips
 Minimum Code Moment: 0 kip-in
 P at Min. Code Moment: 0 kips
 PM Interaction Equation: Units in kip-in

Comments:

User Comments



$$M(P) = 5307 + 2797*(P/P_u) - 1.120E-3*(P/P_u)^2 + 2852*(P/P_u)^3$$

Section Details:

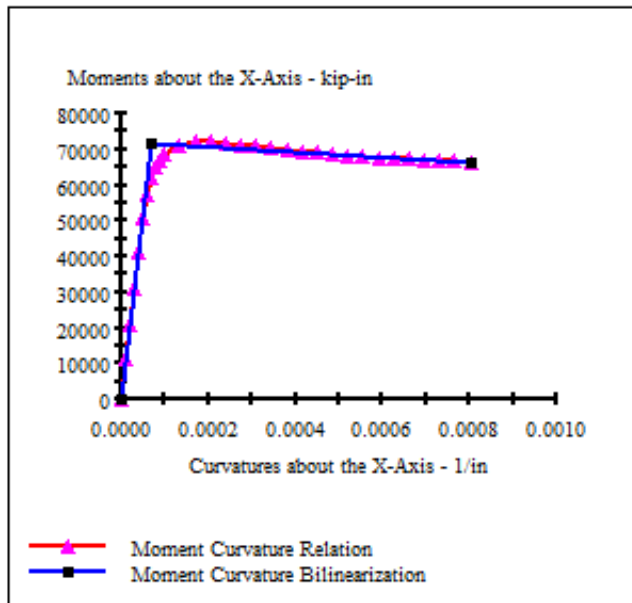
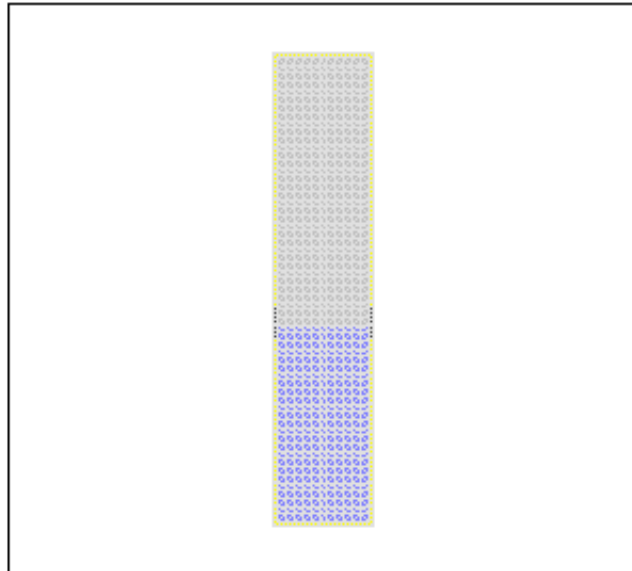
X Centroid: .4130E-14 in
Y Centroid: -.2870E-15 in
Section Area: 720.0 in²

Loading Details:

Constant Load - Mxx: -100.0 kip-in
Incrementing Loads: Mxx Only
Number of Points: 30
Analysis Strategy: Displacement Control

Analysis Results:

Failing Material: Confined1
Failure Strain: 20.00E-3 Compression
Curvature at Initial Load: 67.44E-9 1/in
Curvature at First Yield: 49.42E-6 1/in
Ultimate Curvature: .8021E-3 1/in
Moment at First Yield: 50.71E+3 kip-in
Ultimate Moment: 66.41E+3 kip-in
Centroid Strain at Yield: .2498E-3 Ten
Centroid Strain at Ultimate: 3.396E-3 Ten
N.A. at First Yield: 5.054 in
N.A. at Ultimate: 4.234 in
Energy per Length: 52.99 kips
Effective Yield Curvature: 69.65E-6 1/in
Effective Yield Moment: 71.46E+3 kip-in
Over Strength Factor: .9294
EI Effective: 1.03E+9 kip-in²
Yield EI Effective: -6.886E+6 kip-in²
Bilinear Harding Slope: -.6715 %
Curvature Ductility: 11.52



Comments:

User Comments

XTRACT Analysis Report -

Section Name: Section1
Loading Name: MC1
Analysis Type: Moment Curvature

UB
8/17/2014
Section analysis
CFSSP-NB
Page __ of __

Section Details:

X Centroid: -1.511E-3 in
Y Centroid: 33.72E-6 in
Section Area: 369.6 in²

Loading Details:

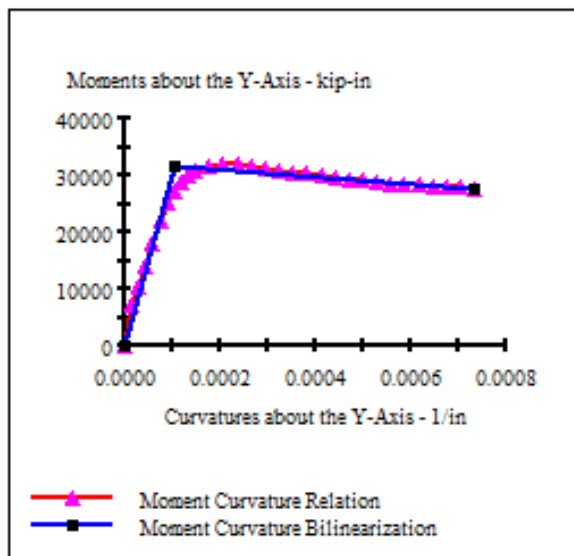
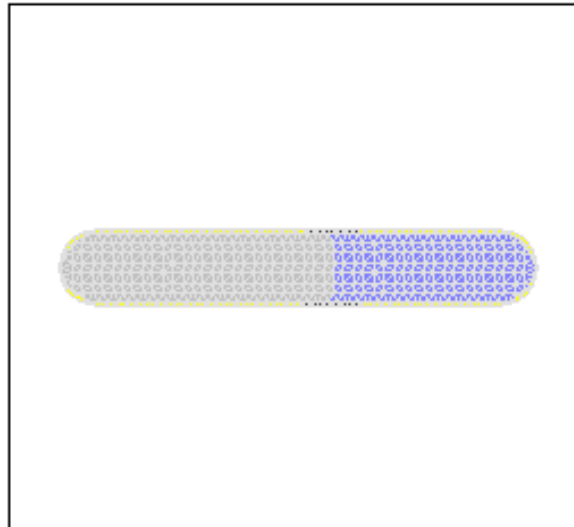
Constant Load - Myy: -10.00 kip-in
Incrementing Loads: Myy Only
Number of Points: 30
Analysis Strategy: Displacement Control

Analysis Results:

Failing Material: Bilinear1
Failure Strain: 20.00E-3 Tension
Curvature at Initial Load: 20.65E-9 1/in
Curvature at First Yield: 74.12E-6 1/in
Ultimate Curvature: .7345E-3 1/in
Moment at First Yield: 22.02E+3 kip-in
Ultimate Moment: 27.71E+3 kip-in
Centroid Strain at Yield: .3702E-3 Ten
Centroid Strain at Ultimate: 2.487E-3 Ten
N.A. at First Yield: 4.994 in
N.A. at Ultimate: 3.386 in
Energy per Length: 20.36 kips
Effective Yield Curvature: .1069E-3 1/in
Effective Yield Moment: 31.76E+3 kip-in
Over Strength Factor: .8725
Plastic Rotation Capacity: 30.13E-3 rad
EI Effective: 2.97E+8 kip-in²
Yield EI Effective: -6.454E+6 kip-in²
Bilinear Hardening Slope: -2.173 %
Curvature Ductility: 6.871

Comments:

User Comments



MCEER Technical Reports

MCEER publishes technical reports on a variety of subjects written by authors funded through MCEER. These reports are available from both MCEER Publications and the National Technical Information Service (NTIS). Requests for reports should be directed to MCEER Publications, MCEER, University at Buffalo, State University of New York, 133A Ketter Hall, Buffalo, New York 14260. Reports can also be requested through NTIS, P.O. Box 1425, Springfield, Virginia 22151. NTIS accession numbers are shown in parenthesis, if available.

- NCEER-87-0001 "First-Year Program in Research, Education and Technology Transfer," 3/5/87, (PB88-134275, A04, MF-A01).
- NCEER-87-0002 "Experimental Evaluation of Instantaneous Optimal Algorithms for Structural Control," by R.C. Lin, T.T. Soong and A.M. Reinhorn, 4/20/87, (PB88-134341, A04, MF-A01).
- NCEER-87-0003 "Experimentation Using the Earthquake Simulation Facilities at University at Buffalo," by A.M. Reinhorn and R.L. Ketter, not available.
- NCEER-87-0004 "The System Characteristics and Performance of a Shaking Table," by J.S. Hwang, K.C. Chang and G.C. Lee, 6/1/87, (PB88-134259, A03, MF-A01). This report is available only through NTIS (see address given above).
- NCEER-87-0005 "A Finite Element Formulation for Nonlinear Viscoplastic Material Using a Q Model," by O. Gyebe and G. Dasgupta, 11/2/87, (PB88-213764, A08, MF-A01).
- NCEER-87-0006 "Symbolic Manipulation Program (SMP) - Algebraic Codes for Two and Three Dimensional Finite Element Formulations," by X. Lee and G. Dasgupta, 11/9/87, (PB88-218522, A05, MF-A01).
- NCEER-87-0007 "Instantaneous Optimal Control Laws for Tall Buildings Under Seismic Excitations," by J.N. Yang, A. Akbarpour and P. Ghaemmaghami, 6/10/87, (PB88-134333, A06, MF-A01). This report is only available through NTIS (see address given above).
- NCEER-87-0008 "IDARC: Inelastic Damage Analysis of Reinforced Concrete Frame - Shear-Wall Structures," by Y.J. Park, A.M. Reinhorn and S.K. Kunnath, 7/20/87, (PB88-134325, A09, MF-A01). This report is only available through NTIS (see address given above).
- NCEER-87-0009 "Liquefaction Potential for New York State: A Preliminary Report on Sites in Manhattan and Buffalo," by M. Budhu, V. Vijayakumar, R.F. Giese and L. Baumgras, 8/31/87, (PB88-163704, A03, MF-A01). This report is available only through NTIS (see address given above).
- NCEER-87-0010 "Vertical and Torsional Vibration of Foundations in Inhomogeneous Media," by A.S. Veletsos and K.W. Dotson, 6/1/87, (PB88-134291, A03, MF-A01). This report is only available through NTIS (see address given above).
- NCEER-87-0011 "Seismic Probabilistic Risk Assessment and Seismic Margins Studies for Nuclear Power Plants," by Howard H.M. Hwang, 6/15/87, (PB88-134267, A03, MF-A01). This report is only available through NTIS (see address given above).
- NCEER-87-0012 "Parametric Studies of Frequency Response of Secondary Systems Under Ground-Acceleration Excitations," by Y. Yong and Y.K. Lin, 6/10/87, (PB88-134309, A03, MF-A01). This report is only available through NTIS (see address given above).
- NCEER-87-0013 "Frequency Response of Secondary Systems Under Seismic Excitation," by J.A. HoLung, J. Cai and Y.K. Lin, 7/31/87, (PB88-134317, A05, MF-A01). This report is only available through NTIS (see address given above).
- NCEER-87-0014 "Modelling Earthquake Ground Motions in Seismically Active Regions Using Parametric Time Series Methods," by G.W. Ellis and A.S. Cakmak, 8/25/87, (PB88-134283, A08, MF-A01). This report is only available through NTIS (see address given above).
- NCEER-87-0015 "Detection and Assessment of Seismic Structural Damage," by E. DiPasquale and A.S. Cakmak, 8/25/87, (PB88-163712, A05, MF-A01). This report is only available through NTIS (see address given above).

- NCEER-87-0016 "Pipeline Experiment at Parkfield, California," by J. Isenberg and E. Richardson, 9/15/87, (PB88-163720, A03, MF-A01). This report is available only through NTIS (see address given above).
- NCEER-87-0017 "Digital Simulation of Seismic Ground Motion," by M. Shinozuka, G. Deodatis and T. Harada, 8/31/87, (PB88-155197, A04, MF-A01). This report is available only through NTIS (see address given above).
- NCEER-87-0018 "Practical Considerations for Structural Control: System Uncertainty, System Time Delay and Truncation of Small Control Forces," J.N. Yang and A. Akbarpour, 8/10/87, (PB88-163738, A08, MF-A01). This report is only available through NTIS (see address given above).
- NCEER-87-0019 "Modal Analysis of Nonclassically Damped Structural Systems Using Canonical Transformation," by J.N. Yang, S. Sarkani and F.X. Long, 9/27/87, (PB88-187851, A04, MF-A01).
- NCEER-87-0020 "A Nonstationary Solution in Random Vibration Theory," by J.R. Red-Horse and P.D. Spanos, 11/3/87, (PB88-163746, A03, MF-A01).
- NCEER-87-0021 "Horizontal Impedances for Radially Inhomogeneous Viscoelastic Soil Layers," by A.S. Veletsos and K.W. Dotson, 10/15/87, (PB88-150859, A04, MF-A01).
- NCEER-87-0022 "Seismic Damage Assessment of Reinforced Concrete Members," by Y.S. Chung, C. Meyer and M. Shinozuka, 10/9/87, (PB88-150867, A05, MF-A01). This report is available only through NTIS (see address given above).
- NCEER-87-0023 "Active Structural Control in Civil Engineering," by T.T. Soong, 11/11/87, (PB88-187778, A03, MF-A01).
- NCEER-87-0024 "Vertical and Torsional Impedances for Radially Inhomogeneous Viscoelastic Soil Layers," by K.W. Dotson and A.S. Veletsos, 12/87, (PB88-187786, A03, MF-A01).
- NCEER-87-0025 "Proceedings from the Symposium on Seismic Hazards, Ground Motions, Soil-Liquefaction and Engineering Practice in Eastern North America," October 20-22, 1987, edited by K.H. Jacob, 12/87, (PB88-188115, A23, MF-A01). This report is available only through NTIS (see address given above).
- NCEER-87-0026 "Report on the Whittier-Narrows, California, Earthquake of October 1, 1987," by J. Pantelic and A. Reinhorn, 11/87, (PB88-187752, A03, MF-A01). This report is available only through NTIS (see address given above).
- NCEER-87-0027 "Design of a Modular Program for Transient Nonlinear Analysis of Large 3-D Building Structures," by S. Srivastav and J.F. Abel, 12/30/87, (PB88-187950, A05, MF-A01). This report is only available through NTIS (see address given above).
- NCEER-87-0028 "Second-Year Program in Research, Education and Technology Transfer," 3/8/88, (PB88-219480, A04, MF-A01).
- NCEER-88-0001 "Workshop on Seismic Computer Analysis and Design of Buildings With Interactive Graphics," by W. McGuire, J.F. Abel and C.H. Conley, 1/18/88, (PB88-187760, A03, MF-A01). This report is only available through NTIS (see address given above).
- NCEER-88-0002 "Optimal Control of Nonlinear Flexible Structures," by J.N. Yang, F.X. Long and D. Wong, 1/22/88, (PB88-213772, A06, MF-A01).
- NCEER-88-0003 "Substructuring Techniques in the Time Domain for Primary-Secondary Structural Systems," by G.D. Manolis and G. Juhn, 2/10/88, (PB88-213780, A04, MF-A01).
- NCEER-88-0004 "Iterative Seismic Analysis of Primary-Secondary Systems," by A. Singhal, L.D. Lutes and P.D. Spanos, 2/23/88, (PB88-213798, A04, MF-A01).
- NCEER-88-0005 "Stochastic Finite Element Expansion for Random Media," by P.D. Spanos and R. Ghanem, 3/14/88, (PB88-213806, A03, MF-A01).

- NCEER-88-0006 "Combining Structural Optimization and Structural Control," by F.Y. Cheng and C.P. Pantelides, 1/10/88, (PB88-213814, A05, MF-A01).
- NCEER-88-0007 "Seismic Performance Assessment of Code-Designed Structures," by H.H-M. Hwang, J-W. Jaw and H-J. Shau, 3/20/88, (PB88-219423, A04, MF-A01). This report is only available through NTIS (see address given above).
- NCEER-88-0008 "Reliability Analysis of Code-Designed Structures Under Natural Hazards," by H.H-M. Hwang, H. Ushiba and M. Shinozuka, 2/29/88, (PB88-229471, A07, MF-A01). This report is only available through NTIS (see address given above).
- NCEER-88-0009 "Seismic Fragility Analysis of Shear Wall Structures," by J-W Jaw and H.H-M. Hwang, 4/30/88, (PB89-102867, A04, MF-A01).
- NCEER-88-0010 "Base Isolation of a Multi-Story Building Under a Harmonic Ground Motion - A Comparison of Performances of Various Systems," by F-G Fan, G. Ahmadi and I.G. Tadjbakhsh, 5/18/88, (PB89-122238, A06, MF-A01). This report is only available through NTIS (see address given above).
- NCEER-88-0011 "Seismic Floor Response Spectra for a Combined System by Green's Functions," by F.M. Lavelle, L.A. Bergman and P.D. Spanos, 5/1/88, (PB89-102875, A03, MF-A01).
- NCEER-88-0012 "A New Solution Technique for Randomly Excited Hysteretic Structures," by G.Q. Cai and Y.K. Lin, 5/16/88, (PB89-102883, A03, MF-A01).
- NCEER-88-0013 "A Study of Radiation Damping and Soil-Structure Interaction Effects in the Centrifuge," by K. Weissman, supervised by J.H. Prevost, 5/24/88, (PB89-144703, A06, MF-A01).
- NCEER-88-0014 "Parameter Identification and Implementation of a Kinematic Plasticity Model for Frictional Soils," by J.H. Prevost and D.V. Griffiths, not available.
- NCEER-88-0015 "Two- and Three- Dimensional Dynamic Finite Element Analyses of the Long Valley Dam," by D.V. Griffiths and J.H. Prevost, 6/17/88, (PB89-144711, A04, MF-A01).
- NCEER-88-0016 "Damage Assessment of Reinforced Concrete Structures in Eastern United States," by A.M. Reinhorn, M.J. Seidel, S.K. Kunnath and Y.J. Park, 6/15/88, (PB89-122220, A04, MF-A01). This report is only available through NTIS (see address given above).
- NCEER-88-0017 "Dynamic Compliance of Vertically Loaded Strip Foundations in Multilayered Viscoelastic Soils," by S. Ahmad and A.S.M. Israil, 6/17/88, (PB89-102891, A04, MF-A01).
- NCEER-88-0018 "An Experimental Study of Seismic Structural Response With Added Viscoelastic Dampers," by R.C. Lin, Z. Liang, T.T. Soong and R.H. Zhang, 6/30/88, (PB89-122212, A05, MF-A01). This report is available only through NTIS (see address given above).
- NCEER-88-0019 "Experimental Investigation of Primary - Secondary System Interaction," by G.D. Manolis, G. Juhn and A.M. Reinhorn, 5/27/88, (PB89-122204, A04, MF-A01).
- NCEER-88-0020 "A Response Spectrum Approach For Analysis of Nonclassically Damped Structures," by J.N. Yang, S. Sarkani and F.X. Long, 4/22/88, (PB89-102909, A04, MF-A01).
- NCEER-88-0021 "Seismic Interaction of Structures and Soils: Stochastic Approach," by A.S. Veletsos and A.M. Prasad, 7/21/88, (PB89-122196, A04, MF-A01). This report is only available through NTIS (see address given above).
- NCEER-88-0022 "Identification of the Serviceability Limit State and Detection of Seismic Structural Damage," by E. DiPasquale and A.S. Cakmak, 6/15/88, (PB89-122188, A05, MF-A01). This report is available only through NTIS (see address given above).
- NCEER-88-0023 "Multi-Hazard Risk Analysis: Case of a Simple Offshore Structure," by B.K. Bhartia and E.H. Vanmarcke, 7/21/88, (PB89-145213, A05, MF-A01).

- NCEER-88-0024 "Automated Seismic Design of Reinforced Concrete Buildings," by Y.S. Chung, C. Meyer and M. Shinozuka, 7/5/88, (PB89-122170, A06, MF-A01). This report is available only through NTIS (see address given above).
- NCEER-88-0025 "Experimental Study of Active Control of MDOF Structures Under Seismic Excitations," by L.L. Chung, R.C. Lin, T.T. Soong and A.M. Reinhorn, 7/10/88, (PB89-122600, A04, MF-A01).
- NCEER-88-0026 "Earthquake Simulation Tests of a Low-Rise Metal Structure," by J.S. Hwang, K.C. Chang, G.C. Lee and R.L. Ketter, 8/1/88, (PB89-102917, A04, MF-A01).
- NCEER-88-0027 "Systems Study of Urban Response and Reconstruction Due to Catastrophic Earthquakes," by F. Kozin and H.K. Zhou, 9/22/88, (PB90-162348, A04, MF-A01).
- NCEER-88-0028 "Seismic Fragility Analysis of Plane Frame Structures," by H.H-M. Hwang and Y.K. Low, 7/31/88, (PB89-131445, A06, MF-A01).
- NCEER-88-0029 "Response Analysis of Stochastic Structures," by A. Kardara, C. Bucher and M. Shinozuka, 9/22/88, (PB89-174429, A04, MF-A01).
- NCEER-88-0030 "Nonnormal Accelerations Due to Yielding in a Primary Structure," by D.C.K. Chen and L.D. Lutes, 9/19/88, (PB89-131437, A04, MF-A01).
- NCEER-88-0031 "Design Approaches for Soil-Structure Interaction," by A.S. Veletsos, A.M. Prasad and Y. Tang, 12/30/88, (PB89-174437, A03, MF-A01). This report is available only through NTIS (see address given above).
- NCEER-88-0032 "A Re-evaluation of Design Spectra for Seismic Damage Control," by C.J. Turkstra and A.G. Tallin, 11/7/88, (PB89-145221, A05, MF-A01).
- NCEER-88-0033 "The Behavior and Design of Noncontact Lap Splices Subjected to Repeated Inelastic Tensile Loading," by V.E. Sagan, P. Gergely and R.N. White, 12/8/88, (PB89-163737, A08, MF-A01).
- NCEER-88-0034 "Seismic Response of Pile Foundations," by S.M. Mamoon, P.K. Banerjee and S. Ahmad, 11/1/88, (PB89-145239, A04, MF-A01).
- NCEER-88-0035 "Modeling of R/C Building Structures With Flexible Floor Diaphragms (IDARC2)," by A.M. Reinhorn, S.K. Kunnath and N. Panahshahi, 9/7/88, (PB89-207153, A07, MF-A01).
- NCEER-88-0036 "Solution of the Dam-Reservoir Interaction Problem Using a Combination of FEM, BEM with Particular Integrals, Modal Analysis, and Substructuring," by C-S. Tsai, G.C. Lee and R.L. Ketter, 12/31/88, (PB89-207146, A04, MF-A01).
- NCEER-88-0037 "Optimal Placement of Actuators for Structural Control," by F.Y. Cheng and C.P. Pantelides, 8/15/88, (PB89-162846, A05, MF-A01).
- NCEER-88-0038 "Teflon Bearings in Aseismic Base Isolation: Experimental Studies and Mathematical Modeling," by A. Mokha, M.C. Constantinou and A.M. Reinhorn, 12/5/88, (PB89-218457, A10, MF-A01). This report is available only through NTIS (see address given above).
- NCEER-88-0039 "Seismic Behavior of Flat Slab High-Rise Buildings in the New York City Area," by P. Weidlinger and M. Ettouney, 10/15/88, (PB90-145681, A04, MF-A01).
- NCEER-88-0040 "Evaluation of the Earthquake Resistance of Existing Buildings in New York City," by P. Weidlinger and M. Ettouney, 10/15/88, not available.
- NCEER-88-0041 "Small-Scale Modeling Techniques for Reinforced Concrete Structures Subjected to Seismic Loads," by W. Kim, A. El-Attar and R.N. White, 11/22/88, (PB89-189625, A05, MF-A01).
- NCEER-88-0042 "Modeling Strong Ground Motion from Multiple Event Earthquakes," by G.W. Ellis and A.S. Cakmak, 10/15/88, (PB89-174445, A03, MF-A01).

- NCEER-88-0043 "Nonstationary Models of Seismic Ground Acceleration," by M. Grigoriu, S.E. Ruiz and E. Rosenblueth, 7/15/88, (PB89-189617, A04, MF-A01).
- NCEER-88-0044 "SARCF User's Guide: Seismic Analysis of Reinforced Concrete Frames," by Y.S. Chung, C. Meyer and M. Shinozuka, 11/9/88, (PB89-174452, A08, MF-A01).
- NCEER-88-0045 "First Expert Panel Meeting on Disaster Research and Planning," edited by J. Pantelic and J. Stoyle, 9/15/88, (PB89-174460, A05, MF-A01).
- NCEER-88-0046 "Preliminary Studies of the Effect of Degrading Infill Walls on the Nonlinear Seismic Response of Steel Frames," by C.Z. Chrysostomou, P. Gergely and J.F. Abel, 12/19/88, (PB89-208383, A05, MF-A01).
- NCEER-88-0047 "Reinforced Concrete Frame Component Testing Facility - Design, Construction, Instrumentation and Operation," by S.P. Pessiki, C. Conley, T. Bond, P. Gergely and R.N. White, 12/16/88, (PB89-174478, A04, MF-A01).
- NCEER-89-0001 "Effects of Protective Cushion and Soil Compliancy on the Response of Equipment Within a Seismically Excited Building," by J.A. HoLung, 2/16/89, (PB89-207179, A04, MF-A01).
- NCEER-89-0002 "Statistical Evaluation of Response Modification Factors for Reinforced Concrete Structures," by H.H-M. Hwang and J-W. Jaw, 2/17/89, (PB89-207187, A05, MF-A01).
- NCEER-89-0003 "Hysteretic Columns Under Random Excitation," by G-Q. Cai and Y.K. Lin, 1/9/89, (PB89-196513, A03, MF-A01).
- NCEER-89-0004 "Experimental Study of 'Elephant Foot Bulge' Instability of Thin-Walled Metal Tanks," by Z-H. Jia and R.L. Ketter, 2/22/89, (PB89-207195, A03, MF-A01).
- NCEER-89-0005 "Experiment on Performance of Buried Pipelines Across San Andreas Fault," by J. Isenberg, E. Richardson and T.D. O'Rourke, 3/10/89, (PB89-218440, A04, MF-A01). This report is available only through NTIS (see address given above).
- NCEER-89-0006 "A Knowledge-Based Approach to Structural Design of Earthquake-Resistant Buildings," by M. Subramani, P. Gergely, C.H. Conley, J.F. Abel and A.H. Zaghaw, 1/15/89, (PB89-218465, A06, MF-A01).
- NCEER-89-0007 "Liquefaction Hazards and Their Effects on Buried Pipelines," by T.D. O'Rourke and P.A. Lane, 2/1/89, (PB89-218481, A09, MF-A01).
- NCEER-89-0008 "Fundamentals of System Identification in Structural Dynamics," by H. Imai, C-B. Yun, O. Maruyama and M. Shinozuka, 1/26/89, (PB89-207211, A04, MF-A01).
- NCEER-89-0009 "Effects of the 1985 Michoacan Earthquake on Water Systems and Other Buried Lifelines in Mexico," by A.G. Ayala and M.J. O'Rourke, 3/8/89, (PB89-207229, A06, MF-A01).
- NCEER-89-R010 "NCEER Bibliography of Earthquake Education Materials," by K.E.K. Ross, Second Revision, 9/1/89, (PB90-125352, A05, MF-A01). This report is replaced by NCEER-92-0018.
- NCEER-89-0011 "Inelastic Three-Dimensional Response Analysis of Reinforced Concrete Building Structures (IDARC-3D), Part I - Modeling," by S.K. Kunnath and A.M. Reinhorn, 4/17/89, (PB90-114612, A07, MF-A01). This report is available only through NTIS (see address given above).
- NCEER-89-0012 "Recommended Modifications to ATC-14," by C.D. Poland and J.O. Malley, 4/12/89, (PB90-108648, A15, MF-A01).
- NCEER-89-0013 "Repair and Strengthening of Beam-to-Column Connections Subjected to Earthquake Loading," by M. Corazao and A.J. Durrani, 2/28/89, (PB90-109885, A06, MF-A01).
- NCEER-89-0014 "Program EXKAL2 for Identification of Structural Dynamic Systems," by O. Maruyama, C-B. Yun, M. Hoshiya and M. Shinozuka, 5/19/89, (PB90-109877, A09, MF-A01).

- NCEER-89-0015 "Response of Frames With Bolted Semi-Rigid Connections, Part I - Experimental Study and Analytical Predictions," by P.J. DiCorso, A.M. Reinhorn, J.R. Dickerson, J.B. Radzimirski and W.L. Harper, 6/1/89, not available.
- NCEER-89-0016 "ARMA Monte Carlo Simulation in Probabilistic Structural Analysis," by P.D. Spanos and M.P. Mignolet, 7/10/89, (PB90-109893, A03, MF-A01).
- NCEER-89-P017 "Preliminary Proceedings from the Conference on Disaster Preparedness - The Place of Earthquake Education in Our Schools," Edited by K.E.K. Ross, 6/23/89, (PB90-108606, A03, MF-A01).
- NCEER-89-0017 "Proceedings from the Conference on Disaster Preparedness - The Place of Earthquake Education in Our Schools," Edited by K.E.K. Ross, 12/31/89, (PB90-207895, A012, MF-A02). This report is available only through NTIS (see address given above).
- NCEER-89-0018 "Multidimensional Models of Hysteretic Material Behavior for Vibration Analysis of Shape Memory Energy Absorbing Devices, by E.J. Graesser and F.A. Cozzarelli, 6/7/89, (PB90-164146, A04, MF-A01).
- NCEER-89-0019 "Nonlinear Dynamic Analysis of Three-Dimensional Base Isolated Structures (3D-BASIS)," by S. Nagarajaiah, A.M. Reinhorn and M.C. Constantinou, 8/3/89, (PB90-161936, A06, MF-A01). This report has been replaced by NCEER-93-0011.
- NCEER-89-0020 "Structural Control Considering Time-Rate of Control Forces and Control Rate Constraints," by F.Y. Cheng and C.P. Pantelides, 8/3/89, (PB90-120445, A04, MF-A01).
- NCEER-89-0021 "Subsurface Conditions of Memphis and Shelby County," by K.W. Ng, T-S. Chang and H-H.M. Hwang, 7/26/89, (PB90-120437, A03, MF-A01).
- NCEER-89-0022 "Seismic Wave Propagation Effects on Straight Jointed Buried Pipelines," by K. Elhadi and M.J. O'Rourke, 8/24/89, (PB90-162322, A10, MF-A02).
- NCEER-89-0023 "Workshop on Serviceability Analysis of Water Delivery Systems," edited by M. Grigoriu, 3/6/89, (PB90-127424, A03, MF-A01).
- NCEER-89-0024 "Shaking Table Study of a 1/5 Scale Steel Frame Composed of Tapered Members," by K.C. Chang, J.S. Hwang and G.C. Lee, 9/18/89, (PB90-160169, A04, MF-A01).
- NCEER-89-0025 "DYNA1D: A Computer Program for Nonlinear Seismic Site Response Analysis - Technical Documentation," by Jean H. Prevost, 9/14/89, (PB90-161944, A07, MF-A01). This report is available only through NTIS (see address given above).
- NCEER-89-0026 "1:4 Scale Model Studies of Active Tendon Systems and Active Mass Dampers for Aseismic Protection," by A.M. Reinhorn, T.T. Soong, R.C. Lin, Y.P. Yang, Y. Fukao, H. Abe and M. Nakai, 9/15/89, (PB90-173246, A10, MF-A02). This report is available only through NTIS (see address given above).
- NCEER-89-0027 "Scattering of Waves by Inclusions in a Nonhomogeneous Elastic Half Space Solved by Boundary Element Methods," by P.K. Hadley, A. Askar and A.S. Cakmak, 6/15/89, (PB90-145699, A07, MF-A01).
- NCEER-89-0028 "Statistical Evaluation of Deflection Amplification Factors for Reinforced Concrete Structures," by H.H.M. Hwang, J-W. Jaw and A.L. Ch'ng, 8/31/89, (PB90-164633, A05, MF-A01).
- NCEER-89-0029 "Bedrock Accelerations in Memphis Area Due to Large New Madrid Earthquakes," by H.H.M. Hwang, C.H.S. Chen and G. Yu, 11/7/89, (PB90-162330, A04, MF-A01).
- NCEER-89-0030 "Seismic Behavior and Response Sensitivity of Secondary Structural Systems," by Y.Q. Chen and T.T. Soong, 10/23/89, (PB90-164658, A08, MF-A01).
- NCEER-89-0031 "Random Vibration and Reliability Analysis of Primary-Secondary Structural Systems," by Y. Ibrahim, M. Grigoriu and T.T. Soong, 11/10/89, (PB90-161951, A04, MF-A01).

- NCEER-89-0032 "Proceedings from the Second U.S. - Japan Workshop on Liquefaction, Large Ground Deformation and Their Effects on Lifelines, September 26-29, 1989," Edited by T.D. O'Rourke and M. Hamada, 12/1/89, (PB90-209388, A22, MF-A03).
- NCEER-89-0033 "Deterministic Model for Seismic Damage Evaluation of Reinforced Concrete Structures," by J.M. Bracci, A.M. Reinhorn, J.B. Mander and S.K. Kunnath, 9/27/89, (PB91-108803, A06, MF-A01).
- NCEER-89-0034 "On the Relation Between Local and Global Damage Indices," by E. DiPasquale and A.S. Cakmak, 8/15/89, (PB90-173865, A05, MF-A01).
- NCEER-89-0035 "Cyclic Undrained Behavior of Nonplastic and Low Plasticity Silts," by A.J. Walker and H.E. Stewart, 7/26/89, (PB90-183518, A10, MF-A01).
- NCEER-89-0036 "Liquefaction Potential of Surficial Deposits in the City of Buffalo, New York," by M. Budhu, R. Giese and L. Baumgrass, 1/17/89, (PB90-208455, A04, MF-A01).
- NCEER-89-0037 "A Deterministic Assessment of Effects of Ground Motion Incoherence," by A.S. Veletsos and Y. Tang, 7/15/89, (PB90-164294, A03, MF-A01).
- NCEER-89-0038 "Workshop on Ground Motion Parameters for Seismic Hazard Mapping," July 17-18, 1989, edited by R.V. Whitman, 12/1/89, (PB90-173923, A04, MF-A01).
- NCEER-89-0039 "Seismic Effects on Elevated Transit Lines of the New York City Transit Authority," by C.J. Costantino, C.A. Miller and E. Heymsfield, 12/26/89, (PB90-207887, A06, MF-A01).
- NCEER-89-0040 "Centrifugal Modeling of Dynamic Soil-Structure Interaction," by K. Weissman, Supervised by J.H. Prevost, 5/10/89, (PB90-207879, A07, MF-A01).
- NCEER-89-0041 "Linearized Identification of Buildings With Cores for Seismic Vulnerability Assessment," by I-K. Ho and A.E. Aktan, 11/1/89, (PB90-251943, A07, MF-A01).
- NCEER-90-0001 "Geotechnical and Lifeline Aspects of the October 17, 1989 Loma Prieta Earthquake in San Francisco," by T.D. O'Rourke, H.E. Stewart, F.T. Blackburn and T.S. Dickerman, 1/90, (PB90-208596, A05, MF-A01).
- NCEER-90-0002 "Nonnormal Secondary Response Due to Yielding in a Primary Structure," by D.C.K. Chen and L.D. Lutes, 2/28/90, (PB90-251976, A07, MF-A01).
- NCEER-90-0003 "Earthquake Education Materials for Grades K-12," by K.E.K. Ross, 4/16/90, (PB91-251984, A05, MF-A05). This report has been replaced by NCEER-92-0018.
- NCEER-90-0004 "Catalog of Strong Motion Stations in Eastern North America," by R.W. Busby, 4/3/90, (PB90-251984, A05, MF-A01).
- NCEER-90-0005 "NCEER Strong-Motion Data Base: A User Manual for the GeoBase Release (Version 1.0 for the Sun3)," by P. Friberg and K. Jacob, 3/31/90 (PB90-258062, A04, MF-A01).
- NCEER-90-0006 "Seismic Hazard Along a Crude Oil Pipeline in the Event of an 1811-1812 Type New Madrid Earthquake," by H.H.M. Hwang and C-H.S. Chen, 4/16/90, (PB90-258054, A04, MF-A01).
- NCEER-90-0007 "Site-Specific Response Spectra for Memphis Sheahan Pumping Station," by H.H.M. Hwang and C.S. Lee, 5/15/90, (PB91-108811, A05, MF-A01).
- NCEER-90-0008 "Pilot Study on Seismic Vulnerability of Crude Oil Transmission Systems," by T. Ariman, R. Dobry, M. Grigoriu, F. Kozin, M. O'Rourke, T. O'Rourke and M. Shinozuka, 5/25/90, (PB91-108837, A06, MF-A01).
- NCEER-90-0009 "A Program to Generate Site Dependent Time Histories: EQGEN," by G.W. Ellis, M. Srinivasan and A.S. Cakmak, 1/30/90, (PB91-108829, A04, MF-A01).
- NCEER-90-0010 "Active Isolation for Seismic Protection of Operating Rooms," by M.E. Talbott, Supervised by M. Shinozuka, 6/8/9, (PB91-110205, A05, MF-A01).

- NCEER-90-0011 "Program LINEARID for Identification of Linear Structural Dynamic Systems," by C-B. Yun and M. Shinozuka, 6/25/90, (PB91-110312, A08, MF-A01).
- NCEER-90-0012 "Two-Dimensional Two-Phase Elasto-Plastic Seismic Response of Earth Dams," by A.N. Yiagos, Supervised by J.H. Prevost, 6/20/90, (PB91-110197, A13, MF-A02).
- NCEER-90-0013 "Secondary Systems in Base-Isolated Structures: Experimental Investigation, Stochastic Response and Stochastic Sensitivity," by G.D. Manolis, G. Juhn, M.C. Constantinou and A.M. Reinhorn, 7/1/90, (PB91-110320, A08, MF-A01).
- NCEER-90-0014 "Seismic Behavior of Lightly-Reinforced Concrete Column and Beam-Column Joint Details," by S.P. Pessiki, C.H. Conley, P. Gergely and R.N. White, 8/22/90, (PB91-108795, A11, MF-A02).
- NCEER-90-0015 "Two Hybrid Control Systems for Building Structures Under Strong Earthquakes," by J.N. Yang and A. Daniellians, 6/29/90, (PB91-125393, A04, MF-A01).
- NCEER-90-0016 "Instantaneous Optimal Control with Acceleration and Velocity Feedback," by J.N. Yang and Z. Li, 6/29/90, (PB91-125401, A03, MF-A01).
- NCEER-90-0017 "Reconnaissance Report on the Northern Iran Earthquake of June 21, 1990," by M. Mehrain, 10/4/90, (PB91-125377, A03, MF-A01).
- NCEER-90-0018 "Evaluation of Liquefaction Potential in Memphis and Shelby County," by T.S. Chang, P.S. Tang, C.S. Lee and H. Hwang, 8/10/90, (PB91-125427, A09, MF-A01).
- NCEER-90-0019 "Experimental and Analytical Study of a Combined Sliding Disc Bearing and Helical Steel Spring Isolation System," by M.C. Constantinou, A.S. Mokha and A.M. Reinhorn, 10/4/90, (PB91-125385, A06, MF-A01). This report is available only through NTIS (see address given above).
- NCEER-90-0020 "Experimental Study and Analytical Prediction of Earthquake Response of a Sliding Isolation System with a Spherical Surface," by A.S. Mokha, M.C. Constantinou and A.M. Reinhorn, 10/11/90, (PB91-125419, A05, MF-A01).
- NCEER-90-0021 "Dynamic Interaction Factors for Floating Pile Groups," by G. Gazetas, K. Fan, A. Kaynia and E. Kausel, 9/10/90, (PB91-170381, A05, MF-A01).
- NCEER-90-0022 "Evaluation of Seismic Damage Indices for Reinforced Concrete Structures," by S. Rodriguez-Gomez and A.S. Cakmak, 9/30/90, PB91-171322, A06, MF-A01).
- NCEER-90-0023 "Study of Site Response at a Selected Memphis Site," by H. Desai, S. Ahmad, E.S. Gazetas and M.R. Oh, 10/11/90, (PB91-196857, A03, MF-A01).
- NCEER-90-0024 "A User's Guide to Strongmo: Version 1.0 of NCEER's Strong-Motion Data Access Tool for PCs and Terminals," by P.A. Friberg and C.A.T. Susch, 11/15/90, (PB91-171272, A03, MF-A01).
- NCEER-90-0025 "A Three-Dimensional Analytical Study of Spatial Variability of Seismic Ground Motions," by L-L. Hong and A.H.-S. Ang, 10/30/90, (PB91-170399, A09, MF-A01).
- NCEER-90-0026 "MUMOID User's Guide - A Program for the Identification of Modal Parameters," by S. Rodriguez-Gomez and E. DiPasquale, 9/30/90, (PB91-171298, A04, MF-A01).
- NCEER-90-0027 "SARCF-II User's Guide - Seismic Analysis of Reinforced Concrete Frames," by S. Rodriguez-Gomez, Y.S. Chung and C. Meyer, 9/30/90, (PB91-171280, A05, MF-A01).
- NCEER-90-0028 "Viscous Dampers: Testing, Modeling and Application in Vibration and Seismic Isolation," by N. Makris and M.C. Constantinou, 12/20/90 (PB91-190561, A06, MF-A01).
- NCEER-90-0029 "Soil Effects on Earthquake Ground Motions in the Memphis Area," by H. Hwang, C.S. Lee, K.W. Ng and T.S. Chang, 8/2/90, (PB91-190751, A05, MF-A01).

- NCEER-91-0001 "Proceedings from the Third Japan-U.S. Workshop on Earthquake Resistant Design of Lifeline Facilities and Countermeasures for Soil Liquefaction, December 17-19, 1990," edited by T.D. O'Rourke and M. Hamada, 2/1/91, (PB91-179259, A99, MF-A04).
- NCEER-91-0002 "Physical Space Solutions of Non-Proportionally Damped Systems," by M. Tong, Z. Liang and G.C. Lee, 1/15/91, (PB91-179242, A04, MF-A01).
- NCEER-91-0003 "Seismic Response of Single Piles and Pile Groups," by K. Fan and G. Gazetas, 1/10/91, (PB92-174994, A04, MF-A01).
- NCEER-91-0004 "Damping of Structures: Part 1 - Theory of Complex Damping," by Z. Liang and G. Lee, 10/10/91, (PB92-197235, A12, MF-A03).
- NCEER-91-0005 "3D-BASIS - Nonlinear Dynamic Analysis of Three Dimensional Base Isolated Structures: Part II," by S. Nagarajaiah, A.M. Reinhorn and M.C. Constantinou, 2/28/91, (PB91-190553, A07, MF-A01). This report has been replaced by NCEER-93-0011.
- NCEER-91-0006 "A Multidimensional Hysteretic Model for Plasticity Deforming Metals in Energy Absorbing Devices," by E.J. Graesser and F.A. Cozzarelli, 4/9/91, (PB92-108364, A04, MF-A01).
- NCEER-91-0007 "A Framework for Customizable Knowledge-Based Expert Systems with an Application to a KBES for Evaluating the Seismic Resistance of Existing Buildings," by E.G. Ibarra-Anaya and S.J. Fennes, 4/9/91, (PB91-210930, A08, MF-A01).
- NCEER-91-0008 "Nonlinear Analysis of Steel Frames with Semi-Rigid Connections Using the Capacity Spectrum Method," by G.G. Deierlein, S-H. Hsieh, Y-J. Shen and J.F. Abel, 7/2/91, (PB92-113828, A05, MF-A01).
- NCEER-91-0009 "Earthquake Education Materials for Grades K-12," by K.E.K. Ross, 4/30/91, (PB91-212142, A06, MF-A01). This report has been replaced by NCEER-92-0018.
- NCEER-91-0010 "Phase Wave Velocities and Displacement Phase Differences in a Harmonically Oscillating Pile," by N. Makris and G. Gazetas, 7/8/91, (PB92-108356, A04, MF-A01).
- NCEER-91-0011 "Dynamic Characteristics of a Full-Size Five-Story Steel Structure and a 2/5 Scale Model," by K.C. Chang, G.C. Yao, G.C. Lee, D.S. Hao and Y.C. Yeh, 7/2/91, (PB93-116648, A06, MF-A02).
- NCEER-91-0012 "Seismic Response of a 2/5 Scale Steel Structure with Added Viscoelastic Dampers," by K.C. Chang, T.T. Soong, S-T. Oh and M.L. Lai, 5/17/91, (PB92-110816, A05, MF-A01).
- NCEER-91-0013 "Earthquake Response of Retaining Walls; Full-Scale Testing and Computational Modeling," by S. Alampalli and A-W.M. Elgamal, 6/20/91, not available.
- NCEER-91-0014 "3D-BASIS-M: Nonlinear Dynamic Analysis of Multiple Building Base Isolated Structures," by P.C. Tsopelas, S. Nagarajaiah, M.C. Constantinou and A.M. Reinhorn, 5/28/91, (PB92-113885, A09, MF-A02).
- NCEER-91-0015 "Evaluation of SEAOC Design Requirements for Sliding Isolated Structures," by D. Theodossiou and M.C. Constantinou, 6/10/91, (PB92-114602, A11, MF-A03).
- NCEER-91-0016 "Closed-Loop Modal Testing of a 27-Story Reinforced Concrete Flat Plate-Core Building," by H.R. Somaprasad, T. Toksoy, H. Yoshiyuki and A.E. Aktan, 7/15/91, (PB92-129980, A07, MF-A02).
- NCEER-91-0017 "Shake Table Test of a 1/6 Scale Two-Story Lightly Reinforced Concrete Building," by A.G. El-Attar, R.N. White and P. Gergely, 2/28/91, (PB92-222447, A06, MF-A02).
- NCEER-91-0018 "Shake Table Test of a 1/8 Scale Three-Story Lightly Reinforced Concrete Building," by A.G. El-Attar, R.N. White and P. Gergely, 2/28/91, (PB93-116630, A08, MF-A02).
- NCEER-91-0019 "Transfer Functions for Rigid Rectangular Foundations," by A.S. Veletsos, A.M. Prasad and W.H. Wu, 7/31/91, not available.

- NCEER-91-0020 "Hybrid Control of Seismic-Excited Nonlinear and Inelastic Structural Systems," by J.N. Yang, Z. Li and A. Daniellians, 8/1/91, (PB92-143171, A06, MF-A02).
- NCEER-91-0021 "The NCEER-91 Earthquake Catalog: Improved Intensity-Based Magnitudes and Recurrence Relations for U.S. Earthquakes East of New Madrid," by L. Seeber and J.G. Armbruster, 8/28/91, (PB92-176742, A06, MF-A02).
- NCEER-91-0022 "Proceedings from the Implementation of Earthquake Planning and Education in Schools: The Need for Change - The Roles of the Changemakers," by K.E.K. Ross and F. Winslow, 7/23/91, (PB92-129998, A12, MF-A03).
- NCEER-91-0023 "A Study of Reliability-Based Criteria for Seismic Design of Reinforced Concrete Frame Buildings," by H.H.M. Hwang and H-M. Hsu, 8/10/91, (PB92-140235, A09, MF-A02).
- NCEER-91-0024 "Experimental Verification of a Number of Structural System Identification Algorithms," by R.G. Ghanem, H. Gavin and M. Shinozuka, 9/18/91, (PB92-176577, A18, MF-A04).
- NCEER-91-0025 "Probabilistic Evaluation of Liquefaction Potential," by H.H.M. Hwang and C.S. Lee, 11/25/91, (PB92-143429, A05, MF-A01).
- NCEER-91-0026 "Instantaneous Optimal Control for Linear, Nonlinear and Hysteretic Structures - Stable Controllers," by J.N. Yang and Z. Li, 11/15/91, (PB92-163807, A04, MF-A01).
- NCEER-91-0027 "Experimental and Theoretical Study of a Sliding Isolation System for Bridges," by M.C. Constantinou, A. Kartoum, A.M. Reinhorn and P. Bradford, 11/15/91, (PB92-176973, A10, MF-A03).
- NCEER-92-0001 "Case Studies of Liquefaction and Lifeline Performance During Past Earthquakes, Volume 1: Japanese Case Studies," Edited by M. Hamada and T. O'Rourke, 2/17/92, (PB92-197243, A18, MF-A04).
- NCEER-92-0002 "Case Studies of Liquefaction and Lifeline Performance During Past Earthquakes, Volume 2: United States Case Studies," Edited by T. O'Rourke and M. Hamada, 2/17/92, (PB92-197250, A20, MF-A04).
- NCEER-92-0003 "Issues in Earthquake Education," Edited by K. Ross, 2/3/92, (PB92-222389, A07, MF-A02).
- NCEER-92-0004 "Proceedings from the First U.S. - Japan Workshop on Earthquake Protective Systems for Bridges," Edited by I.G. Buckle, 2/4/92, (PB94-142239, A99, MF-A06).
- NCEER-92-0005 "Seismic Ground Motion from a Haskell-Type Source in a Multiple-Layered Half-Space," A.P. Theoharis, G. Deodatis and M. Shinozuka, 1/2/92, not available.
- NCEER-92-0006 "Proceedings from the Site Effects Workshop," Edited by R. Whitman, 2/29/92, (PB92-197201, A04, MF-A01).
- NCEER-92-0007 "Engineering Evaluation of Permanent Ground Deformations Due to Seismically-Induced Liquefaction," by M.H. Baziar, R. Dobry and A-W.M. Elgamel, 3/24/92, (PB92-222421, A13, MF-A03).
- NCEER-92-0008 "A Procedure for the Seismic Evaluation of Buildings in the Central and Eastern United States," by C.D. Poland and J.O. Malley, 4/2/92, (PB92-222439, A20, MF-A04).
- NCEER-92-0009 "Experimental and Analytical Study of a Hybrid Isolation System Using Friction Controllable Sliding Bearings," by M.Q. Feng, S. Fujii and M. Shinozuka, 5/15/92, (PB93-150282, A06, MF-A02).
- NCEER-92-0010 "Seismic Resistance of Slab-Column Connections in Existing Non-Ductile Flat-Plate Buildings," by A.J. Durrani and Y. Du, 5/18/92, (PB93-116812, A06, MF-A02).
- NCEER-92-0011 "The Hysteretic and Dynamic Behavior of Brick Masonry Walls Upgraded by Ferrocement Coatings Under Cyclic Loading and Strong Simulated Ground Motion," by H. Lee and S.P. Prawel, 5/11/92, not available.
- NCEER-92-0012 "Study of Wire Rope Systems for Seismic Protection of Equipment in Buildings," by G.F. Demetriades, M.C. Constantinou and A.M. Reinhorn, 5/20/92, (PB93-116655, A08, MF-A02).

- NCEER-92-0013 "Shape Memory Structural Dampers: Material Properties, Design and Seismic Testing," by P.R. Witting and F.A. Cozzarelli, 5/26/92, (PB93-116663, A05, MF-A01).
- NCEER-92-0014 "Longitudinal Permanent Ground Deformation Effects on Buried Continuous Pipelines," by M.J. O'Rourke, and C. Nordberg, 6/15/92, (PB93-116671, A08, MF-A02).
- NCEER-92-0015 "A Simulation Method for Stationary Gaussian Random Functions Based on the Sampling Theorem," by M. Grigoriu and S. Balopoulou, 6/11/92, (PB93-127496, A05, MF-A01).
- NCEER-92-0016 "Gravity-Load-Designed Reinforced Concrete Buildings: Seismic Evaluation of Existing Construction and Detailing Strategies for Improved Seismic Resistance," by G.W. Hoffmann, S.K. Kunnath, A.M. Reinhorn and J.B. Mander, 7/15/92, (PB94-142007, A08, MF-A02).
- NCEER-92-0017 "Observations on Water System and Pipeline Performance in the Limón Area of Costa Rica Due to the April 22, 1991 Earthquake," by M. O'Rourke and D. Ballantyne, 6/30/92, (PB93-126811, A06, MF-A02).
- NCEER-92-0018 "Fourth Edition of Earthquake Education Materials for Grades K-12," Edited by K.E.K. Ross, 8/10/92, (PB93-114023, A07, MF-A02).
- NCEER-92-0019 "Proceedings from the Fourth Japan-U.S. Workshop on Earthquake Resistant Design of Lifeline Facilities and Countermeasures for Soil Liquefaction," Edited by M. Hamada and T.D. O'Rourke, 8/12/92, (PB93-163939, A99, MF-E11).
- NCEER-92-0020 "Active Bracing System: A Full Scale Implementation of Active Control," by A.M. Reinhorn, T.T. Soong, R.C. Lin, M.A. Riley, Y.P. Wang, S. Aizawa and M. Higashino, 8/14/92, (PB93-127512, A06, MF-A02).
- NCEER-92-0021 "Empirical Analysis of Horizontal Ground Displacement Generated by Liquefaction-Induced Lateral Spreads," by S.F. Bartlett and T.L. Youd, 8/17/92, (PB93-188241, A06, MF-A02).
- NCEER-92-0022 "IDARC Version 3.0: Inelastic Damage Analysis of Reinforced Concrete Structures," by S.K. Kunnath, A.M. Reinhorn and R.F. Lobo, 8/31/92, (PB93-227502, A07, MF-A02).
- NCEER-92-0023 "A Semi-Empirical Analysis of Strong-Motion Peaks in Terms of Seismic Source, Propagation Path and Local Site Conditions, by M. Kamiyama, M.J. O'Rourke and R. Flores-Berrones, 9/9/92, (PB93-150266, A08, MF-A02).
- NCEER-92-0024 "Seismic Behavior of Reinforced Concrete Frame Structures with Nonductile Details, Part I: Summary of Experimental Findings of Full Scale Beam-Column Joint Tests," by A. Beres, R.N. White and P. Gergely, 9/30/92, (PB93-227783, A05, MF-A01).
- NCEER-92-0025 "Experimental Results of Repaired and Retrofitted Beam-Column Joint Tests in Lightly Reinforced Concrete Frame Buildings," by A. Beres, S. El-Borgi, R.N. White and P. Gergely, 10/29/92, (PB93-227791, A05, MF-A01).
- NCEER-92-0026 "A Generalization of Optimal Control Theory: Linear and Nonlinear Structures," by J.N. Yang, Z. Li and S. Vongchavalitkul, 11/2/92, (PB93-188621, A05, MF-A01).
- NCEER-92-0027 "Seismic Resistance of Reinforced Concrete Frame Structures Designed Only for Gravity Loads: Part I - Design and Properties of a One-Third Scale Model Structure," by J.M. Bracci, A.M. Reinhorn and J.B. Mander, 12/1/92, (PB94-104502, A08, MF-A02).
- NCEER-92-0028 "Seismic Resistance of Reinforced Concrete Frame Structures Designed Only for Gravity Loads: Part II - Experimental Performance of Subassemblages," by L.E. Aycaardi, J.B. Mander and A.M. Reinhorn, 12/1/92, (PB94-104510, A08, MF-A02).
- NCEER-92-0029 "Seismic Resistance of Reinforced Concrete Frame Structures Designed Only for Gravity Loads: Part III - Experimental Performance and Analytical Study of a Structural Model," by J.M. Bracci, A.M. Reinhorn and J.B. Mander, 12/1/92, (PB93-227528, A09, MF-A01).

- NCEER-92-0030 "Evaluation of Seismic Retrofit of Reinforced Concrete Frame Structures: Part I - Experimental Performance of Retrofitted Subassemblages," by D. Choudhuri, J.B. Mander and A.M. Reinhorn, 12/8/92, (PB93-198307, A07, MF-A02).
- NCEER-92-0031 "Evaluation of Seismic Retrofit of Reinforced Concrete Frame Structures: Part II - Experimental Performance and Analytical Study of a Retrofitted Structural Model," by J.M. Bracci, A.M. Reinhorn and J.B. Mander, 12/8/92, (PB93-198315, A09, MF-A03).
- NCEER-92-0032 "Experimental and Analytical Investigation of Seismic Response of Structures with Supplemental Fluid Viscous Dampers," by M.C. Constantinou and M.D. Symans, 12/21/92, (PB93-191435, A10, MF-A03). This report is available only through NTIS (see address given above).
- NCEER-92-0033 "Reconnaissance Report on the Cairo, Egypt Earthquake of October 12, 1992," by M. Khater, 12/23/92, (PB93-188621, A03, MF-A01).
- NCEER-92-0034 "Low-Level Dynamic Characteristics of Four Tall Flat-Plate Buildings in New York City," by H. Gavin, S. Yuan, J. Grossman, E. Pekelis and K. Jacob, 12/28/92, (PB93-188217, A07, MF-A02).
- NCEER-93-0001 "An Experimental Study on the Seismic Performance of Brick-Infilled Steel Frames With and Without Retrofit," by J.B. Mander, B. Nair, K. Wojtkowski and J. Ma, 1/29/93, (PB93-227510, A07, MF-A02).
- NCEER-93-0002 "Social Accounting for Disaster Preparedness and Recovery Planning," by S. Cole, E. Pantoja and V. Razak, 2/22/93, (PB94-142114, A12, MF-A03).
- NCEER-93-0003 "Assessment of 1991 NEHRP Provisions for Nonstructural Components and Recommended Revisions," by T.T. Soong, G. Chen, Z. Wu, R-H. Zhang and M. Grigoriu, 3/1/93, (PB93-188639, A06, MF-A02).
- NCEER-93-0004 "Evaluation of Static and Response Spectrum Analysis Procedures of SEAOC/UBC for Seismic Isolated Structures," by C.W. Winters and M.C. Constantinou, 3/23/93, (PB93-198299, A10, MF-A03).
- NCEER-93-0005 "Earthquakes in the Northeast - Are We Ignoring the Hazard? A Workshop on Earthquake Science and Safety for Educators," edited by K.E.K. Ross, 4/2/93, (PB94-103066, A09, MF-A02).
- NCEER-93-0006 "Inelastic Response of Reinforced Concrete Structures with Viscoelastic Braces," by R.F. Lobo, J.M. Bracci, K.L. Shen, A.M. Reinhorn and T.T. Soong, 4/5/93, (PB93-227486, A05, MF-A02).
- NCEER-93-0007 "Seismic Testing of Installation Methods for Computers and Data Processing Equipment," by K. Kosar, T.T. Soong, K.L. Shen, J.A. HoLung and Y.K. Lin, 4/12/93, (PB93-198299, A07, MF-A02).
- NCEER-93-0008 "Retrofit of Reinforced Concrete Frames Using Added Dampers," by A. Reinhorn, M. Constantinou and C. Li, not available.
- NCEER-93-0009 "Seismic Behavior and Design Guidelines for Steel Frame Structures with Added Viscoelastic Dampers," by K.C. Chang, M.L. Lai, T.T. Soong, D.S. Hao and Y.C. Yeh, 5/1/93, (PB94-141959, A07, MF-A02).
- NCEER-93-0010 "Seismic Performance of Shear-Critical Reinforced Concrete Bridge Piers," by J.B. Mander, S.M. Waheed, M.T.A. Chaudhary and S.S. Chen, 5/12/93, (PB93-227494, A08, MF-A02).
- NCEER-93-0011 "3D-BASIS-TABS: Computer Program for Nonlinear Dynamic Analysis of Three Dimensional Base Isolated Structures," by S. Nagarajaiah, C. Li, A.M. Reinhorn and M.C. Constantinou, 8/2/93, (PB94-141819, A09, MF-A02).
- NCEER-93-0012 "Effects of Hydrocarbon Spills from an Oil Pipeline Break on Ground Water," by O.J. Helweg and H.H.M. Hwang, 8/3/93, (PB94-141942, A06, MF-A02).
- NCEER-93-0013 "Simplified Procedures for Seismic Design of Nonstructural Components and Assessment of Current Code Provisions," by M.P. Singh, L.E. Suarez, E.E. Matheu and G.O. Maldonado, 8/4/93, (PB94-141827, A09, MF-A02).
- NCEER-93-0014 "An Energy Approach to Seismic Analysis and Design of Secondary Systems," by G. Chen and T.T. Soong, 8/6/93, (PB94-142767, A11, MF-A03).

- NCEER-93-0015 "Proceedings from School Sites: Becoming Prepared for Earthquakes - Commemorating the Third Anniversary of the Loma Prieta Earthquake," Edited by F.E. Winslow and K.E.K. Ross, 8/16/93, (PB94-154275, A16, MF-A02).
- NCEER-93-0016 "Reconnaissance Report of Damage to Historic Monuments in Cairo, Egypt Following the October 12, 1992 Dahshur Earthquake," by D. Sykora, D. Look, G. Croci, E. Karaesmen and E. Karaesmen, 8/19/93, (PB94-142221, A08, MF-A02).
- NCEER-93-0017 "The Island of Guam Earthquake of August 8, 1993," by S.W. Swan and S.K. Harris, 9/30/93, (PB94-141843, A04, MF-A01).
- NCEER-93-0018 "Engineering Aspects of the October 12, 1992 Egyptian Earthquake," by A.W. Elgamal, M. Amer, K. Adalier and A. Abul-Fadl, 10/7/93, (PB94-141983, A05, MF-A01).
- NCEER-93-0019 "Development of an Earthquake Motion Simulator and its Application in Dynamic Centrifuge Testing," by I. Krstelj, Supervised by J.H. Prevost, 10/23/93, (PB94-181773, A-10, MF-A03).
- NCEER-93-0020 "NCEER-Taisei Corporation Research Program on Sliding Seismic Isolation Systems for Bridges: Experimental and Analytical Study of a Friction Pendulum System (FPS)," by M.C. Constantinou, P. Tsopelas, Y-S. Kim and S. Okamoto, 11/1/93, (PB94-142775, A08, MF-A02).
- NCEER-93-0021 "Finite Element Modeling of Elastomeric Seismic Isolation Bearings," by L.J. Billings, Supervised by R. Shepherd, 11/8/93, not available.
- NCEER-93-0022 "Seismic Vulnerability of Equipment in Critical Facilities: Life-Safety and Operational Consequences," by K. Porter, G.S. Johnson, M.M. Zadeh, C. Scawthorn and S. Eder, 11/24/93, (PB94-181765, A16, MF-A03).
- NCEER-93-0023 "Hokkaido Nansei-oki, Japan Earthquake of July 12, 1993, by P.I. Yanev and C.R. Scawthorn, 12/23/93, (PB94-181500, A07, MF-A01).
- NCEER-94-0001 "An Evaluation of Seismic Serviceability of Water Supply Networks with Application to the San Francisco Auxiliary Water Supply System," by I. Markov, Supervised by M. Grigoriu and T. O'Rourke, 1/21/94, (PB94-204013, A07, MF-A02).
- NCEER-94-0002 "NCEER-Taisei Corporation Research Program on Sliding Seismic Isolation Systems for Bridges: Experimental and Analytical Study of Systems Consisting of Sliding Bearings, Rubber Restoring Force Devices and Fluid Dampers," Volumes I and II, by P. Tsopelas, S. Okamoto, M.C. Constantinou, D. Ozaki and S. Fujii, 2/4/94, (PB94-181740, A09, MF-A02 and PB94-181757, A12, MF-A03).
- NCEER-94-0003 "A Markov Model for Local and Global Damage Indices in Seismic Analysis," by S. Rahman and M. Grigoriu, 2/18/94, (PB94-206000, A12, MF-A03).
- NCEER-94-0004 "Proceedings from the NCEER Workshop on Seismic Response of Masonry Infills," edited by D.P. Abrams, 3/1/94, (PB94-180783, A07, MF-A02).
- NCEER-94-0005 "The Northridge, California Earthquake of January 17, 1994: General Reconnaissance Report," edited by J.D. Goltz, 3/11/94, (PB94-193943, A10, MF-A03).
- NCEER-94-0006 "Seismic Energy Based Fatigue Damage Analysis of Bridge Columns: Part I - Evaluation of Seismic Capacity," by G.A. Chang and J.B. Mander, 3/14/94, (PB94-219185, A11, MF-A03).
- NCEER-94-0007 "Seismic Isolation of Multi-Story Frame Structures Using Spherical Sliding Isolation Systems," by T.M. Al-Hussaini, V.A. Zayas and M.C. Constantinou, 3/17/94, (PB94-193745, A09, MF-A02).
- NCEER-94-0008 "The Northridge, California Earthquake of January 17, 1994: Performance of Highway Bridges," edited by I.G. Buckle, 3/24/94, (PB94-193851, A06, MF-A02).
- NCEER-94-0009 "Proceedings of the Third U.S.-Japan Workshop on Earthquake Protective Systems for Bridges," edited by I.G. Buckle and I. Friedland, 3/31/94, (PB94-195815, A99, MF-A06).

- NCEER-94-0010 "3D-BASIS-ME: Computer Program for Nonlinear Dynamic Analysis of Seismically Isolated Single and Multiple Structures and Liquid Storage Tanks," by P.C. Tsopelas, M.C. Constantinou and A.M. Reinhorn, 4/12/94, (PB94-204922, A09, MF-A02).
- NCEER-94-0011 "The Northridge, California Earthquake of January 17, 1994: Performance of Gas Transmission Pipelines," by T.D. O'Rourke and M.C. Palmer, 5/16/94, (PB94-204989, A05, MF-A01).
- NCEER-94-0012 "Feasibility Study of Replacement Procedures and Earthquake Performance Related to Gas Transmission Pipelines," by T.D. O'Rourke and M.C. Palmer, 5/25/94, (PB94-206638, A09, MF-A02).
- NCEER-94-0013 "Seismic Energy Based Fatigue Damage Analysis of Bridge Columns: Part II - Evaluation of Seismic Demand," by G.A. Chang and J.B. Mander, 6/1/94, (PB95-18106, A08, MF-A02).
- NCEER-94-0014 "NCEER-Taisei Corporation Research Program on Sliding Seismic Isolation Systems for Bridges: Experimental and Analytical Study of a System Consisting of Sliding Bearings and Fluid Restoring Force/Damping Devices," by P. Tsopelas and M.C. Constantinou, 6/13/94, (PB94-219144, A10, MF-A03).
- NCEER-94-0015 "Generation of Hazard-Consistent Fragility Curves for Seismic Loss Estimation Studies," by H. Hwang and J-R. Huo, 6/14/94, (PB95-181996, A09, MF-A02).
- NCEER-94-0016 "Seismic Study of Building Frames with Added Energy-Absorbing Devices," by W.S. Pong, C.S. Tsai and G.C. Lee, 6/20/94, (PB94-219136, A10, A03).
- NCEER-94-0017 "Sliding Mode Control for Seismic-Excited Linear and Nonlinear Civil Engineering Structures," by J. Yang, J. Wu, A. Agrawal and Z. Li, 6/21/94, (PB95-138483, A06, MF-A02).
- NCEER-94-0018 "3D-BASIS-TABS Version 2.0: Computer Program for Nonlinear Dynamic Analysis of Three Dimensional Base Isolated Structures," by A.M. Reinhorn, S. Nagarajaiah, M.C. Constantinou, P. Tsopelas and R. Li, 6/22/94, (PB95-182176, A08, MF-A02).
- NCEER-94-0019 "Proceedings of the International Workshop on Civil Infrastructure Systems: Application of Intelligent Systems and Advanced Materials on Bridge Systems," Edited by G.C. Lee and K.C. Chang, 7/18/94, (PB95-252474, A20, MF-A04).
- NCEER-94-0020 "Study of Seismic Isolation Systems for Computer Floors," by V. Lambrou and M.C. Constantinou, 7/19/94, (PB95-138533, A10, MF-A03).
- NCEER-94-0021 "Proceedings of the U.S.-Italian Workshop on Guidelines for Seismic Evaluation and Rehabilitation of Unreinforced Masonry Buildings," Edited by D.P. Abrams and G.M. Calvi, 7/20/94, (PB95-138749, A13, MF-A03).
- NCEER-94-0022 "NCEER-Taisei Corporation Research Program on Sliding Seismic Isolation Systems for Bridges: Experimental and Analytical Study of a System Consisting of Lubricated PTFE Sliding Bearings and Mild Steel Dampers," by P. Tsopelas and M.C. Constantinou, 7/22/94, (PB95-182184, A08, MF-A02).
- NCEER-94-0023 "Development of Reliability-Based Design Criteria for Buildings Under Seismic Load," by Y.K. Wen, H. Hwang and M. Shinozuka, 8/1/94, (PB95-211934, A08, MF-A02).
- NCEER-94-0024 "Experimental Verification of Acceleration Feedback Control Strategies for an Active Tendon System," by S.J. Dyke, B.F. Spencer, Jr., P. Quast, M.K. Sain, D.C. Kaspari, Jr. and T.T. Soong, 8/29/94, (PB95-212320, A05, MF-A01).
- NCEER-94-0025 "Seismic Retrofitting Manual for Highway Bridges," Edited by I.G. Buckle and I.F. Friedland, published by the Federal Highway Administration (PB95-212676, A15, MF-A03).
- NCEER-94-0026 "Proceedings from the Fifth U.S.-Japan Workshop on Earthquake Resistant Design of Lifeline Facilities and Countermeasures Against Soil Liquefaction," Edited by T.D. O'Rourke and M. Hamada, 11/7/94, (PB95-220802, A99, MF-E08).

- NCEER-95-0001 “Experimental and Analytical Investigation of Seismic Retrofit of Structures with Supplemental Damping: Part I - Fluid Viscous Damping Devices,” by A.M. Reinhorn, C. Li and M.C. Constantinou, 1/3/95, (PB95-266599, A09, MF-A02).
- NCEER-95-0002 “Experimental and Analytical Study of Low-Cycle Fatigue Behavior of Semi-Rigid Top-And-Seat Angle Connections,” by G. Pekcan, J.B. Mander and S.S. Chen, 1/5/95, (PB95-220042, A07, MF-A02).
- NCEER-95-0003 “NCEER-ATC Joint Study on Fragility of Buildings,” by T. Anagnos, C. Rojahn and A.S. Kiremidjian, 1/20/95, (PB95-220026, A06, MF-A02).
- NCEER-95-0004 “Nonlinear Control Algorithms for Peak Response Reduction,” by Z. Wu, T.T. Soong, V. Gattulli and R.C. Lin, 2/16/95, (PB95-220349, A05, MF-A01).
- NCEER-95-0005 “Pipeline Replacement Feasibility Study: A Methodology for Minimizing Seismic and Corrosion Risks to Underground Natural Gas Pipelines,” by R.T. Eguchi, H.A. Seligson and D.G. Honegger, 3/2/95, (PB95-252326, A06, MF-A02).
- NCEER-95-0006 “Evaluation of Seismic Performance of an 11-Story Frame Building During the 1994 Northridge Earthquake,” by F. Naeim, R. DiSulio, K. Benuska, A. Reinhorn and C. Li, not available.
- NCEER-95-0007 “Prioritization of Bridges for Seismic Retrofitting,” by N. Basöz and A.S. Kiremidjian, 4/24/95, (PB95-252300, A08, MF-A02).
- NCEER-95-0008 “Method for Developing Motion Damage Relationships for Reinforced Concrete Frames,” by A. Singhal and A.S. Kiremidjian, 5/11/95, (PB95-266607, A06, MF-A02).
- NCEER-95-0009 “Experimental and Analytical Investigation of Seismic Retrofit of Structures with Supplemental Damping: Part II - Friction Devices,” by C. Li and A.M. Reinhorn, 7/6/95, (PB96-128087, A11, MF-A03).
- NCEER-95-0010 “Experimental Performance and Analytical Study of a Non-Ductile Reinforced Concrete Frame Structure Retrofitted with Elastomeric Spring Dampers,” by G. Pekcan, J.B. Mander and S.S. Chen, 7/14/95, (PB96-137161, A08, MF-A02).
- NCEER-95-0011 “Development and Experimental Study of Semi-Active Fluid Damping Devices for Seismic Protection of Structures,” by M.D. Symans and M.C. Constantinou, 8/3/95, (PB96-136940, A23, MF-A04).
- NCEER-95-0012 “Real-Time Structural Parameter Modification (RSPM): Development of Innervated Structures,” by Z. Liang, M. Tong and G.C. Lee, 4/11/95, (PB96-137153, A06, MF-A01).
- NCEER-95-0013 “Experimental and Analytical Investigation of Seismic Retrofit of Structures with Supplemental Damping: Part III - Viscous Damping Walls,” by A.M. Reinhorn and C. Li, 10/1/95, (PB96-176409, A11, MF-A03).
- NCEER-95-0014 “Seismic Fragility Analysis of Equipment and Structures in a Memphis Electric Substation,” by J-R. Huo and H.H.M. Hwang, 8/10/95, (PB96-128087, A09, MF-A02).
- NCEER-95-0015 “The Hanshin-Awaji Earthquake of January 17, 1995: Performance of Lifelines,” Edited by M. Shinozuka, 11/3/95, (PB96-176383, A15, MF-A03).
- NCEER-95-0016 “Highway Culvert Performance During Earthquakes,” by T.L. Youd and C.J. Beckman, available as NCEER-96-0015.
- NCEER-95-0017 “The Hanshin-Awaji Earthquake of January 17, 1995: Performance of Highway Bridges,” Edited by I.G. Buckle, 12/1/95, not available.
- NCEER-95-0018 “Modeling of Masonry Infill Panels for Structural Analysis,” by A.M. Reinhorn, A. Madan, R.E. Valles, Y. Reichmann and J.B. Mander, 12/8/95, (PB97-110886, MF-A01, A06).
- NCEER-95-0019 “Optimal Polynomial Control for Linear and Nonlinear Structures,” by A.K. Agrawal and J.N. Yang, 12/11/95, (PB96-168737, A07, MF-A02).

- NCEER-95-0020 "Retrofit of Non-Ductile Reinforced Concrete Frames Using Friction Dampers," by R.S. Rao, P. Gergely and R.N. White, 12/22/95, (PB97-133508, A10, MF-A02).
- NCEER-95-0021 "Parametric Results for Seismic Response of Pile-Supported Bridge Bents," by G. Mylonakis, A. Nikolaou and G. Gazetas, 12/22/95, (PB97-100242, A12, MF-A03).
- NCEER-95-0022 "Kinematic Bending Moments in Seismically Stressed Piles," by A. Nikolaou, G. Mylonakis and G. Gazetas, 12/23/95, (PB97-113914, MF-A03, A13).
- NCEER-96-0001 "Dynamic Response of Unreinforced Masonry Buildings with Flexible Diaphragms," by A.C. Costley and D.P. Abrams, 10/10/96, (PB97-133573, MF-A03, A15).
- NCEER-96-0002 "State of the Art Review: Foundations and Retaining Structures," by I. Po Lam, not available.
- NCEER-96-0003 "Ductility of Rectangular Reinforced Concrete Bridge Columns with Moderate Confinement," by N. Wehbe, M. Saiidi, D. Sanders and B. Douglas, 11/7/96, (PB97-133557, A06, MF-A02).
- NCEER-96-0004 "Proceedings of the Long-Span Bridge Seismic Research Workshop," edited by I.G. Buckle and I.M. Friedland, not available.
- NCEER-96-0005 "Establish Representative Pier Types for Comprehensive Study: Eastern United States," by J. Kulicki and Z. Prucz, 5/28/96, (PB98-119217, A07, MF-A02).
- NCEER-96-0006 "Establish Representative Pier Types for Comprehensive Study: Western United States," by R. Imbsen, R.A. Schamber and T.A. Osterkamp, 5/28/96, (PB98-118607, A07, MF-A02).
- NCEER-96-0007 "Nonlinear Control Techniques for Dynamical Systems with Uncertain Parameters," by R.G. Ghanem and M.I. Bujakov, 5/27/96, (PB97-100259, A17, MF-A03).
- NCEER-96-0008 "Seismic Evaluation of a 30-Year Old Non-Ductile Highway Bridge Pier and Its Retrofit," by J.B. Mander, B. Mahmoodzadegan, S. Bhadra and S.S. Chen, 5/31/96, (PB97-110902, MF-A03, A10).
- NCEER-96-0009 "Seismic Performance of a Model Reinforced Concrete Bridge Pier Before and After Retrofit," by J.B. Mander, J.H. Kim and C.A. Ligozio, 5/31/96, (PB97-110910, MF-A02, A10).
- NCEER-96-0010 "IDARC2D Version 4.0: A Computer Program for the Inelastic Damage Analysis of Buildings," by R.E. Valles, A.M. Reinhorn, S.K. Kunnath, C. Li and A. Madan, 6/3/96, (PB97-100234, A17, MF-A03).
- NCEER-96-0011 "Estimation of the Economic Impact of Multiple Lifeline Disruption: Memphis Light, Gas and Water Division Case Study," by S.E. Chang, H.A. Seligson and R.T. Eguchi, 8/16/96, (PB97-133490, A11, MF-A03).
- NCEER-96-0012 "Proceedings from the Sixth Japan-U.S. Workshop on Earthquake Resistant Design of Lifeline Facilities and Countermeasures Against Soil Liquefaction, Edited by M. Hamada and T. O'Rourke, 9/11/96, (PB97-133581, A99, MF-A06).
- NCEER-96-0013 "Chemical Hazards, Mitigation and Preparedness in Areas of High Seismic Risk: A Methodology for Estimating the Risk of Post-Earthquake Hazardous Materials Release," by H.A. Seligson, R.T. Eguchi, K.J. Tierney and K. Richmond, 11/7/96, (PB97-133565, MF-A02, A08).
- NCEER-96-0014 "Response of Steel Bridge Bearings to Reversed Cyclic Loading," by J.B. Mander, D-K. Kim, S.S. Chen and G.J. Premus, 11/13/96, (PB97-140735, A12, MF-A03).
- NCEER-96-0015 "Highway Culvert Performance During Past Earthquakes," by T.L. Youd and C.J. Beckman, 11/25/96, (PB97-133532, A06, MF-A01).
- NCEER-97-0001 "Evaluation, Prevention and Mitigation of Pounding Effects in Building Structures," by R.E. Valles and A.M. Reinhorn, 2/20/97, (PB97-159552, A14, MF-A03).
- NCEER-97-0002 "Seismic Design Criteria for Bridges and Other Highway Structures," by C. Rojahn, R. Mayes, D.G. Anderson, J. Clark, J.H. Hom, R.V. Nutt and M.J. O'Rourke, 4/30/97, (PB97-194658, A06, MF-A03).

- NCEER-97-0003 "Proceedings of the U.S.-Italian Workshop on Seismic Evaluation and Retrofit," Edited by D.P. Abrams and G.M. Calvi, 3/19/97, (PB97-194666, A13, MF-A03).
- NCEER-97-0004 "Investigation of Seismic Response of Buildings with Linear and Nonlinear Fluid Viscous Dampers," by A.A. Seleemah and M.C. Constantinou, 5/21/97, (PB98-109002, A15, MF-A03).
- NCEER-97-0005 "Proceedings of the Workshop on Earthquake Engineering Frontiers in Transportation Facilities," edited by G.C. Lee and I.M. Friedland, 8/29/97, (PB98-128911, A25, MR-A04).
- NCEER-97-0006 "Cumulative Seismic Damage of Reinforced Concrete Bridge Piers," by S.K. Kunnath, A. El-Bahy, A. Taylor and W. Stone, 9/2/97, (PB98-108814, A11, MF-A03).
- NCEER-97-0007 "Structural Details to Accommodate Seismic Movements of Highway Bridges and Retaining Walls," by R.A. Imbsen, R.A. Schamber, E. Thorkildsen, A. Kartoum, B.T. Martin, T.N. Rosser and J.M. Kulicki, 9/3/97, (PB98-108996, A09, MF-A02).
- NCEER-97-0008 "A Method for Earthquake Motion-Damage Relationships with Application to Reinforced Concrete Frames," by A. Singhal and A.S. Kiremidjian, 9/10/97, (PB98-108988, A13, MF-A03).
- NCEER-97-0009 "Seismic Analysis and Design of Bridge Abutments Considering Sliding and Rotation," by K. Fishman and R. Richards, Jr., 9/15/97, (PB98-108897, A06, MF-A02).
- NCEER-97-0010 "Proceedings of the FHWA/NCEER Workshop on the National Representation of Seismic Ground Motion for New and Existing Highway Facilities," edited by I.M. Friedland, M.S. Power and R.L. Mayes, 9/22/97, (PB98-128903, A21, MF-A04).
- NCEER-97-0011 "Seismic Analysis for Design or Retrofit of Gravity Bridge Abutments," by K.L. Fishman, R. Richards, Jr. and R.C. Divito, 10/2/97, (PB98-128937, A08, MF-A02).
- NCEER-97-0012 "Evaluation of Simplified Methods of Analysis for Yielding Structures," by P. Tsopelas, M.C. Constantinou, C.A. Kircher and A.S. Whittaker, 10/31/97, (PB98-128929, A10, MF-A03).
- NCEER-97-0013 "Seismic Design of Bridge Columns Based on Control and Repairability of Damage," by C-T. Cheng and J.B. Mander, 12/8/97, (PB98-144249, A11, MF-A03).
- NCEER-97-0014 "Seismic Resistance of Bridge Piers Based on Damage Avoidance Design," by J.B. Mander and C-T. Cheng, 12/10/97, (PB98-144223, A09, MF-A02).
- NCEER-97-0015 "Seismic Response of Nominally Symmetric Systems with Strength Uncertainty," by S. Balopoulou and M. Grigoriu, 12/23/97, (PB98-153422, A11, MF-A03).
- NCEER-97-0016 "Evaluation of Seismic Retrofit Methods for Reinforced Concrete Bridge Columns," by T.J. Wipf, F.W. Klaiber and F.M. Russo, 12/28/97, (PB98-144215, A12, MF-A03).
- NCEER-97-0017 "Seismic Fragility of Existing Conventional Reinforced Concrete Highway Bridges," by C.L. Mullen and A.S. Cakmak, 12/30/97, (PB98-153406, A08, MF-A02).
- NCEER-97-0018 "Loss Assessment of Memphis Buildings," edited by D.P. Abrams and M. Shinozuka, 12/31/97, (PB98-144231, A13, MF-A03).
- NCEER-97-0019 "Seismic Evaluation of Frames with Infill Walls Using Quasi-static Experiments," by K.M. Mosalam, R.N. White and P. Gergely, 12/31/97, (PB98-153455, A07, MF-A02).
- NCEER-97-0020 "Seismic Evaluation of Frames with Infill Walls Using Pseudo-dynamic Experiments," by K.M. Mosalam, R.N. White and P. Gergely, 12/31/97, (PB98-153430, A07, MF-A02).
- NCEER-97-0021 "Computational Strategies for Frames with Infill Walls: Discrete and Smeared Crack Analyses and Seismic Fragility," by K.M. Mosalam, R.N. White and P. Gergely, 12/31/97, (PB98-153414, A10, MF-A02).

- NCEER-97-0022 "Proceedings of the NCEER Workshop on Evaluation of Liquefaction Resistance of Soils," edited by T.L. Youd and I.M. Idriss, 12/31/97, (PB98-155617, A15, MF-A03).
- MCEER-98-0001 "Extraction of Nonlinear Hysteretic Properties of Seismically Isolated Bridges from Quick-Release Field Tests," by Q. Chen, B.M. Douglas, E.M. Maragakis and I.G. Buckle, 5/26/98, (PB99-118838, A06, MF-A01).
- MCEER-98-0002 "Methodologies for Evaluating the Importance of Highway Bridges," by A. Thomas, S. Eshenaur and J. Kulicki, 5/29/98, (PB99-118846, A10, MF-A02).
- MCEER-98-0003 "Capacity Design of Bridge Piers and the Analysis of Overstrength," by J.B. Mander, A. Dutta and P. Goel, 6/1/98, (PB99-118853, A09, MF-A02).
- MCEER-98-0004 "Evaluation of Bridge Damage Data from the Loma Prieta and Northridge, California Earthquakes," by N. Basoz and A. Kiremidjian, 6/2/98, (PB99-118861, A15, MF-A03).
- MCEER-98-0005 "Screening Guide for Rapid Assessment of Liquefaction Hazard at Highway Bridge Sites," by T. L. Youd, 6/16/98, (PB99-118879, A06, not available on microfiche).
- MCEER-98-0006 "Structural Steel and Steel/Concrete Interface Details for Bridges," by P. Ritchie, N. Kauh and J. Kulicki, 7/13/98, (PB99-118945, A06, MF-A01).
- MCEER-98-0007 "Capacity Design and Fatigue Analysis of Confined Concrete Columns," by A. Dutta and J.B. Mander, 7/14/98, (PB99-118960, A14, MF-A03).
- MCEER-98-0008 "Proceedings of the Workshop on Performance Criteria for Telecommunication Services Under Earthquake Conditions," edited by A.J. Schiff, 7/15/98, (PB99-118952, A08, MF-A02).
- MCEER-98-0009 "Fatigue Analysis of Unconfined Concrete Columns," by J.B. Mander, A. Dutta and J.H. Kim, 9/12/98, (PB99-123655, A10, MF-A02).
- MCEER-98-0010 "Centrifuge Modeling of Cyclic Lateral Response of Pile-Cap Systems and Seat-Type Abutments in Dry Sands," by A.D. Gadre and R. Dobry, 10/2/98, (PB99-123606, A13, MF-A03).
- MCEER-98-0011 "IDARC-BRIDGE: A Computational Platform for Seismic Damage Assessment of Bridge Structures," by A.M. Reinhorn, V. Simeonov, G. Mylonakis and Y. Reichman, 10/2/98, (PB99-162919, A15, MF-A03).
- MCEER-98-0012 "Experimental Investigation of the Dynamic Response of Two Bridges Before and After Retrofitting with Elastomeric Bearings," by D.A. Wendichansky, S.S. Chen and J.B. Mander, 10/2/98, (PB99-162927, A15, MF-A03).
- MCEER-98-0013 "Design Procedures for Hinge Restrainers and Hinge Sear Width for Multiple-Frame Bridges," by R. Des Roches and G.L. Fenves, 11/3/98, (PB99-140477, A13, MF-A03).
- MCEER-98-0014 "Response Modification Factors for Seismically Isolated Bridges," by M.C. Constantinou and J.K. Quarshie, 11/3/98, (PB99-140485, A14, MF-A03).
- MCEER-98-0015 "Proceedings of the U.S.-Italy Workshop on Seismic Protective Systems for Bridges," edited by I.M. Friedland and M.C. Constantinou, 11/3/98, (PB2000-101711, A22, MF-A04).
- MCEER-98-0016 "Appropriate Seismic Reliability for Critical Equipment Systems: Recommendations Based on Regional Analysis of Financial and Life Loss," by K. Porter, C. Scawthorn, C. Taylor and N. Blais, 11/10/98, (PB99-157265, A08, MF-A02).
- MCEER-98-0017 "Proceedings of the U.S. Japan Joint Seminar on Civil Infrastructure Systems Research," edited by M. Shinozuka and A. Rose, 11/12/98, (PB99-156713, A16, MF-A03).
- MCEER-98-0018 "Modeling of Pile Footings and Drilled Shafts for Seismic Design," by I. PoLam, M. Kapuskar and D. Chaudhuri, 12/21/98, (PB99-157257, A09, MF-A02).

- MCEER-99-0001 "Seismic Evaluation of a Masonry Infilled Reinforced Concrete Frame by Pseudodynamic Testing," by S.G. Buonopane and R.N. White, 2/16/99, (PB99-162851, A09, MF-A02).
- MCEER-99-0002 "Response History Analysis of Structures with Seismic Isolation and Energy Dissipation Systems: Verification Examples for Program SAP2000," by J. Scheller and M.C. Constantinou, 2/22/99, (PB99-162869, A08, MF-A02).
- MCEER-99-0003 "Experimental Study on the Seismic Design and Retrofit of Bridge Columns Including Axial Load Effects," by A. Dutta, T. Kokorina and J.B. Mander, 2/22/99, (PB99-162877, A09, MF-A02).
- MCEER-99-0004 "Experimental Study of Bridge Elastomeric and Other Isolation and Energy Dissipation Systems with Emphasis on Uplift Prevention and High Velocity Near-source Seismic Excitation," by A. Kasalanati and M. C. Constantinou, 2/26/99, (PB99-162885, A12, MF-A03).
- MCEER-99-0005 "Truss Modeling of Reinforced Concrete Shear-flexure Behavior," by J.H. Kim and J.B. Mander, 3/8/99, (PB99-163693, A12, MF-A03).
- MCEER-99-0006 "Experimental Investigation and Computational Modeling of Seismic Response of a 1:4 Scale Model Steel Structure with a Load Balancing Supplemental Damping System," by G. Pekcan, J.B. Mander and S.S. Chen, 4/2/99, (PB99-162893, A11, MF-A03).
- MCEER-99-0007 "Effect of Vertical Ground Motions on the Structural Response of Highway Bridges," by M.R. Button, C.J. Cronin and R.L. Mayes, 4/10/99, (PB2000-101411, A10, MF-A03).
- MCEER-99-0008 "Seismic Reliability Assessment of Critical Facilities: A Handbook, Supporting Documentation, and Model Code Provisions," by G.S. Johnson, R.E. Sheppard, M.D. Quilici, S.J. Eder and C.R. Scawthorn, 4/12/99, (PB2000-101701, A18, MF-A04).
- MCEER-99-0009 "Impact Assessment of Selected MCEER Highway Project Research on the Seismic Design of Highway Structures," by C. Rojahn, R. Mayes, D.G. Anderson, J.H. Clark, D'Appolonia Engineering, S. Gloyd and R.V. Nutt, 4/14/99, (PB99-162901, A10, MF-A02).
- MCEER-99-0010 "Site Factors and Site Categories in Seismic Codes," by R. Dobry, R. Ramos and M.S. Power, 7/19/99, (PB2000-101705, A08, MF-A02).
- MCEER-99-0011 "Restrainer Design Procedures for Multi-Span Simply-Supported Bridges," by M.J. Randall, M. Saiidi, E. Maragakis and T. Isakovic, 7/20/99, (PB2000-101702, A10, MF-A02).
- MCEER-99-0012 "Property Modification Factors for Seismic Isolation Bearings," by M.C. Constantinou, P. Tsopelas, A. Kasalanati and E. Wolff, 7/20/99, (PB2000-103387, A11, MF-A03).
- MCEER-99-0013 "Critical Seismic Issues for Existing Steel Bridges," by P. Ritchie, N. Kauh and J. Kulicki, 7/20/99, (PB2000-101697, A09, MF-A02).
- MCEER-99-0014 "Nonstructural Damage Database," by A. Kao, T.T. Soong and A. Vender, 7/24/99, (PB2000-101407, A06, MF-A01).
- MCEER-99-0015 "Guide to Remedial Measures for Liquefaction Mitigation at Existing Highway Bridge Sites," by H.G. Cooke and J. K. Mitchell, 7/26/99, (PB2000-101703, A11, MF-A03).
- MCEER-99-0016 "Proceedings of the MCEER Workshop on Ground Motion Methodologies for the Eastern United States," edited by N. Abrahamson and A. Becker, 8/11/99, (PB2000-103385, A07, MF-A02).
- MCEER-99-0017 "Quindío, Colombia Earthquake of January 25, 1999: Reconnaissance Report," by A.P. Asfura and P.J. Flores, 10/4/99, (PB2000-106893, A06, MF-A01).
- MCEER-99-0018 "Hysteretic Models for Cyclic Behavior of Deteriorating Inelastic Structures," by M.V. Sivaselvan and A.M. Reinhorn, 11/5/99, (PB2000-103386, A08, MF-A02).

- MCEER-99-0019 "Proceedings of the 7th U.S.- Japan Workshop on Earthquake Resistant Design of Lifeline Facilities and Countermeasures Against Soil Liquefaction," edited by T.D. O'Rourke, J.P. Bardet and M. Hamada, 11/19/99, (PB2000-103354, A99, MF-A06).
- MCEER-99-0020 "Development of Measurement Capability for Micro-Vibration Evaluations with Application to Chip Fabrication Facilities," by G.C. Lee, Z. Liang, J.W. Song, J.D. Shen and W.C. Liu, 12/1/99, (PB2000-105993, A08, MF-A02).
- MCEER-99-0021 "Design and Retrofit Methodology for Building Structures with Supplemental Energy Dissipating Systems," by G. Pekcan, J.B. Mander and S.S. Chen, 12/31/99, (PB2000-105994, A11, MF-A03).
- MCEER-00-0001 "The Marmara, Turkey Earthquake of August 17, 1999: Reconnaissance Report," edited by C. Scawthorn; with major contributions by M. Bruneau, R. Eguchi, T. Holzer, G. Johnson, J. Mander, J. Mitchell, W. Mitchell, A. Papageorgiou, C. Scaethorn, and G. Webb, 3/23/00, (PB2000-106200, A11, MF-A03).
- MCEER-00-0002 "Proceedings of the MCEER Workshop for Seismic Hazard Mitigation of Health Care Facilities," edited by G.C. Lee, M. Ettouney, M. Grigoriu, J. Hauer and J. Nigg, 3/29/00, (PB2000-106892, A08, MF-A02).
- MCEER-00-0003 "The Chi-Chi, Taiwan Earthquake of September 21, 1999: Reconnaissance Report," edited by G.C. Lee and C.H. Loh, with major contributions by G.C. Lee, M. Bruneau, I.G. Buckle, S.E. Chang, P.J. Flores, T.D. O'Rourke, M. Shinozuka, T.T. Soong, C-H. Loh, K-C. Chang, Z-J. Chen, J-S. Hwang, M-L. Lin, G-Y. Liu, K-C. Tsai, G.C. Yao and C-L. Yen, 4/30/00, (PB2001-100980, A10, MF-A02).
- MCEER-00-0004 "Seismic Retrofit of End-Sway Frames of Steel Deck-Truss Bridges with a Supplemental Tendon System: Experimental and Analytical Investigation," by G. Pekcan, J.B. Mander and S.S. Chen, 7/1/00, (PB2001-100982, A10, MF-A02).
- MCEER-00-0005 "Sliding Fragility of Unrestrained Equipment in Critical Facilities," by W.H. Chong and T.T. Soong, 7/5/00, (PB2001-100983, A08, MF-A02).
- MCEER-00-0006 "Seismic Response of Reinforced Concrete Bridge Pier Walls in the Weak Direction," by N. Abo-Shadi, M. Saiidi and D. Sanders, 7/17/00, (PB2001-100981, A17, MF-A03).
- MCEER-00-0007 "Low-Cycle Fatigue Behavior of Longitudinal Reinforcement in Reinforced Concrete Bridge Columns," by J. Brown and S.K. Kunnath, 7/23/00, (PB2001-104392, A08, MF-A02).
- MCEER-00-0008 "Soil Structure Interaction of Bridges for Seismic Analysis," I. PoLam and H. Law, 9/25/00, (PB2001-105397, A08, MF-A02).
- MCEER-00-0009 "Proceedings of the First MCEER Workshop on Mitigation of Earthquake Disaster by Advanced Technologies (MEDAT-1), edited by M. Shinozuka, D.J. Inman and T.D. O'Rourke, 11/10/00, (PB2001-105399, A14, MF-A03).
- MCEER-00-0010 "Development and Evaluation of Simplified Procedures for Analysis and Design of Buildings with Passive Energy Dissipation Systems, Revision 01," by O.M. Ramirez, M.C. Constantinou, C.A. Kircher, A.S. Whittaker, M.W. Johnson, J.D. Gomez and C. Chrysostomou, 11/16/01, (PB2001-105523, A23, MF-A04).
- MCEER-00-0011 "Dynamic Soil-Foundation-Structure Interaction Analyses of Large Caissons," by C-Y. Chang, C-M. Mok, Z-L. Wang, R. Settgast, F. Waggoner, M.A. Ketchum, H.M. Gonnermann and C-C. Chin, 12/30/00, (PB2001-104373, A07, MF-A02).
- MCEER-00-0012 "Experimental Evaluation of Seismic Performance of Bridge Restrainers," by A.G. Vlassis, E.M. Maragakis and M. Saiid Saiidi, 12/30/00, (PB2001-104354, A09, MF-A02).
- MCEER-00-0013 "Effect of Spatial Variation of Ground Motion on Highway Structures," by M. Shinozuka, V. Saxena and G. Deodatis, 12/31/00, (PB2001-108755, A13, MF-A03).
- MCEER-00-0014 "A Risk-Based Methodology for Assessing the Seismic Performance of Highway Systems," by S.D. Werner, C.E. Taylor, J.E. Moore, II, J.S. Walton and S. Cho, 12/31/00, (PB2001-108756, A14, MF-A03).

- MCEER-01-0001 "Experimental Investigation of P-Delta Effects to Collapse During Earthquakes," by D. Vian and M. Bruneau, 6/25/01, (PB2002-100534, A17, MF-A03).
- MCEER-01-0002 "Proceedings of the Second MCEER Workshop on Mitigation of Earthquake Disaster by Advanced Technologies (MEDAT-2)," edited by M. Bruneau and D.J. Inman, 7/23/01, (PB2002-100434, A16, MF-A03).
- MCEER-01-0003 "Sensitivity Analysis of Dynamic Systems Subjected to Seismic Loads," by C. Roth and M. Grigoriu, 9/18/01, (PB2003-100884, A12, MF-A03).
- MCEER-01-0004 "Overcoming Obstacles to Implementing Earthquake Hazard Mitigation Policies: Stage 1 Report," by D.J. Alesch and W.J. Petak, 12/17/01, (PB2002-107949, A07, MF-A02).
- MCEER-01-0005 "Updating Real-Time Earthquake Loss Estimates: Methods, Problems and Insights," by C.E. Taylor, S.E. Chang and R.T. Eguchi, 12/17/01, (PB2002-107948, A05, MF-A01).
- MCEER-01-0006 "Experimental Investigation and Retrofit of Steel Pile Foundations and Pile Bents Under Cyclic Lateral Loadings," by A. Shama, J. Mander, B. Blabac and S. Chen, 12/31/01, (PB2002-107950, A13, MF-A03).
- MCEER-02-0001 "Assessment of Performance of Bolu Viaduct in the 1999 Duzce Earthquake in Turkey" by P.C. Roussis, M.C. Constantinou, M. Erdik, E. Durukal and M. Dicleli, 5/8/02, (PB2003-100883, A08, MF-A02).
- MCEER-02-0002 "Seismic Behavior of Rail Counterweight Systems of Elevators in Buildings," by M.P. Singh, Rildova and L.E. Suarez, 5/27/02. (PB2003-100882, A11, MF-A03).
- MCEER-02-0003 "Development of Analysis and Design Procedures for Spread Footings," by G. Mylonakis, G. Gazetas, S. Nikolaou and A. Chauncey, 10/02/02, (PB2004-101636, A13, MF-A03, CD-A13).
- MCEER-02-0004 "Bare-Earth Algorithms for Use with SAR and LIDAR Digital Elevation Models," by C.K. Huyck, R.T. Eguchi and B. Houshmand, 10/16/02, (PB2004-101637, A07, CD-A07).
- MCEER-02-0005 "Review of Energy Dissipation of Compression Members in Concentrically Braced Frames," by K.Lee and M. Bruneau, 10/18/02, (PB2004-101638, A10, CD-A10).
- MCEER-03-0001 "Experimental Investigation of Light-Gauge Steel Plate Shear Walls for the Seismic Retrofit of Buildings" by J. Berman and M. Bruneau, 5/2/03, (PB2004-101622, A10, MF-A03, CD-A10).
- MCEER-03-0002 "Statistical Analysis of Fragility Curves," by M. Shinozuka, M.Q. Feng, H. Kim, T. Uzawa and T. Ueda, 6/16/03, (PB2004-101849, A09, CD-A09).
- MCEER-03-0003 "Proceedings of the Eighth U.S.-Japan Workshop on Earthquake Resistant Design of Lifeline Facilities and Countermeasures Against Liquefaction," edited by M. Hamada, J.P. Bardet and T.D. O'Rourke, 6/30/03, (PB2004-104386, A99, CD-A99).
- MCEER-03-0004 "Proceedings of the PRC-US Workshop on Seismic Analysis and Design of Special Bridges," edited by L.C. Fan and G.C. Lee, 7/15/03, (PB2004-104387, A14, CD-A14).
- MCEER-03-0005 "Urban Disaster Recovery: A Framework and Simulation Model," by S.B. Miles and S.E. Chang, 7/25/03, (PB2004-104388, A07, CD-A07).
- MCEER-03-0006 "Behavior of Underground Piping Joints Due to Static and Dynamic Loading," by R.D. Meis, M. Maragakis and R. Siddharthan, 11/17/03, (PB2005-102194, A13, MF-A03, CD-A00).
- MCEER-04-0001 "Experimental Study of Seismic Isolation Systems with Emphasis on Secondary System Response and Verification of Accuracy of Dynamic Response History Analysis Methods," by E. Wolff and M. Constantinou, 1/16/04 (PB2005-102195, A99, MF-E08, CD-A00).
- MCEER-04-0002 "Tension, Compression and Cyclic Testing of Engineered Cementitious Composite Materials," by K. Kesner and S.L. Billington, 3/1/04, (PB2005-102196, A08, CD-A08).

- MCEER-04-0003 "Cyclic Testing of Braces Laterally Restrained by Steel Studs to Enhance Performance During Earthquakes," by O.C. Celik, J.W. Berman and M. Bruneau, 3/16/04, (PB2005-102197, A13, MF-A03, CD-A00).
- MCEER-04-0004 "Methodologies for Post Earthquake Building Damage Detection Using SAR and Optical Remote Sensing: Application to the August 17, 1999 Marmara, Turkey Earthquake," by C.K. Huyck, B.J. Adams, S. Cho, R.T. Eguchi, B. Mansouri and B. Houshmand, 6/15/04, (PB2005-104888, A10, CD-A00).
- MCEER-04-0005 "Nonlinear Structural Analysis Towards Collapse Simulation: A Dynamical Systems Approach," by M.V. Sivaselvan and A.M. Reinhorn, 6/16/04, (PB2005-104889, A11, MF-A03, CD-A00).
- MCEER-04-0006 "Proceedings of the Second PRC-US Workshop on Seismic Analysis and Design of Special Bridges," edited by G.C. Lee and L.C. Fan, 6/25/04, (PB2005-104890, A16, CD-A00).
- MCEER-04-0007 "Seismic Vulnerability Evaluation of Axially Loaded Steel Built-up Laced Members," by K. Lee and M. Bruneau, 6/30/04, (PB2005-104891, A16, CD-A00).
- MCEER-04-0008 "Evaluation of Accuracy of Simplified Methods of Analysis and Design of Buildings with Damping Systems for Near-Fault and for Soft-Soil Seismic Motions," by E.A. Pavlou and M.C. Constantinou, 8/16/04, (PB2005-104892, A08, MF-A02, CD-A00).
- MCEER-04-0009 "Assessment of Geotechnical Issues in Acute Care Facilities in California," by M. Lew, T.D. O'Rourke, R. Dobry and M. Koch, 9/15/04, (PB2005-104893, A08, CD-A00).
- MCEER-04-0010 "Scissor-Jack-Damper Energy Dissipation System," by A.N. Sigaher-Boyle and M.C. Constantinou, 12/1/04 (PB2005-108221).
- MCEER-04-0011 "Seismic Retrofit of Bridge Steel Truss Piers Using a Controlled Rocking Approach," by M. Pollino and M. Bruneau, 12/20/04 (PB2006-105795).
- MCEER-05-0001 "Experimental and Analytical Studies of Structures Seismically Isolated with an Uplift-Restraint Isolation System," by P.C. Roussis and M.C. Constantinou, 1/10/05 (PB2005-108222).
- MCEER-05-0002 "A Versatile Experimentation Model for Study of Structures Near Collapse Applied to Seismic Evaluation of Irregular Structures," by D. Kusumastuti, A.M. Reinhorn and A. Rutenberg, 3/31/05 (PB2006-101523).
- MCEER-05-0003 "Proceedings of the Third PRC-US Workshop on Seismic Analysis and Design of Special Bridges," edited by L.C. Fan and G.C. Lee, 4/20/05, (PB2006-105796).
- MCEER-05-0004 "Approaches for the Seismic Retrofit of Braced Steel Bridge Piers and Proof-of-Concept Testing of an Eccentrically Braced Frame with Tubular Link," by J.W. Berman and M. Bruneau, 4/21/05 (PB2006-101524).
- MCEER-05-0005 "Simulation of Strong Ground Motions for Seismic Fragility Evaluation of Nonstructural Components in Hospitals," by A. Wanitkorkul and A. Filiatrault, 5/26/05 (PB2006-500027).
- MCEER-05-0006 "Seismic Safety in California Hospitals: Assessing an Attempt to Accelerate the Replacement or Seismic Retrofit of Older Hospital Facilities," by D.J. Alesch, L.A. Arendt and W.J. Petak, 6/6/05 (PB2006-105794).
- MCEER-05-0007 "Development of Seismic Strengthening and Retrofit Strategies for Critical Facilities Using Engineered Cementitious Composite Materials," by K. Kesner and S.L. Billington, 8/29/05 (PB2006-111701).
- MCEER-05-0008 "Experimental and Analytical Studies of Base Isolation Systems for Seismic Protection of Power Transformers," by N. Murota, M.Q. Feng and G-Y. Liu, 9/30/05 (PB2006-111702).
- MCEER-05-0009 "3D-BASIS-ME-MB: Computer Program for Nonlinear Dynamic Analysis of Seismically Isolated Structures," by P.C. Tsopelas, P.C. Roussis, M.C. Constantinou, R. Buchanan and A.M. Reinhorn, 10/3/05 (PB2006-111703).
- MCEER-05-0010 "Steel Plate Shear Walls for Seismic Design and Retrofit of Building Structures," by D. Vian and M. Bruneau, 12/15/05 (PB2006-111704).

- MCEER-05-0011 "The Performance-Based Design Paradigm," by M.J. Astrella and A. Whittaker, 12/15/05 (PB2006-111705).
- MCEER-06-0001 "Seismic Fragility of Suspended Ceiling Systems," H. Badillo-Almaraz, A.S. Whittaker, A.M. Reinhorn and G.P. Cimellaro, 2/4/06 (PB2006-111706).
- MCEER-06-0002 "Multi-Dimensional Fragility of Structures," by G.P. Cimellaro, A.M. Reinhorn and M. Bruneau, 3/1/06 (PB2007-106974, A09, MF-A02, CD A00).
- MCEER-06-0003 "Built-Up Shear Links as Energy Dissipators for Seismic Protection of Bridges," by P. Dusicka, A.M. Itani and I.G. Buckle, 3/15/06 (PB2006-111708).
- MCEER-06-0004 "Analytical Investigation of the Structural Fuse Concept," by R.E. Vargas and M. Bruneau, 3/16/06 (PB2006-111709).
- MCEER-06-0005 "Experimental Investigation of the Structural Fuse Concept," by R.E. Vargas and M. Bruneau, 3/17/06 (PB2006-111710).
- MCEER-06-0006 "Further Development of Tubular Eccentrically Braced Frame Links for the Seismic Retrofit of Braced Steel Truss Bridge Piers," by J.W. Berman and M. Bruneau, 3/27/06 (PB2007-105147).
- MCEER-06-0007 "REDARS Validation Report," by S. Cho, C.K. Huyck, S. Ghosh and R.T. Eguchi, 8/8/06 (PB2007-106983).
- MCEER-06-0008 "Review of Current NDE Technologies for Post-Earthquake Assessment of Retrofitted Bridge Columns," by J.W. Song, Z. Liang and G.C. Lee, 8/21/06 (PB2007-106984).
- MCEER-06-0009 "Liquefaction Remediation in Silty Soils Using Dynamic Compaction and Stone Columns," by S. Thevanayagam, G.R. Martin, R. Nashed, T. Shenthan, T. Kanagalingam and N. Ecemis, 8/28/06 (PB2007-106985).
- MCEER-06-0010 "Conceptual Design and Experimental Investigation of Polymer Matrix Composite Infill Panels for Seismic Retrofitting," by W. Jung, M. Chiewanichakorn and A.J. Aref, 9/21/06 (PB2007-106986).
- MCEER-06-0011 "A Study of the Coupled Horizontal-Vertical Behavior of Elastomeric and Lead-Rubber Seismic Isolation Bearings," by G.P. Warn and A.S. Whittaker, 9/22/06 (PB2007-108679).
- MCEER-06-0012 "Proceedings of the Fourth PRC-US Workshop on Seismic Analysis and Design of Special Bridges: Advancing Bridge Technologies in Research, Design, Construction and Preservation," Edited by L.C. Fan, G.C. Lee and L. Ziang, 10/12/06 (PB2007-109042).
- MCEER-06-0013 "Cyclic Response and Low Cycle Fatigue Characteristics of Plate Steels," by P. Dusicka, A.M. Itani and I.G. Buckle, 11/1/06 06 (PB2007-106987).
- MCEER-06-0014 "Proceedings of the Second US-Taiwan Bridge Engineering Workshop," edited by W.P. Yen, J. Shen, J-Y. Chen and M. Wang, 11/15/06 (PB2008-500041).
- MCEER-06-0015 "User Manual and Technical Documentation for the REDARSTM Import Wizard," by S. Cho, S. Ghosh, C.K. Huyck and S.D. Werner, 11/30/06 (PB2007-114766).
- MCEER-06-0016 "Hazard Mitigation Strategy and Monitoring Technologies for Urban and Infrastructure Public Buildings: Proceedings of the China-US Workshops," edited by X.Y. Zhou, A.L. Zhang, G.C. Lee and M. Tong, 12/12/06 (PB2008-500018).
- MCEER-07-0001 "Static and Kinetic Coefficients of Friction for Rigid Blocks," by C. Kafali, S. Fathali, M. Grigoriu and A.S. Whittaker, 3/20/07 (PB2007-114767).
- MCEER-07-0002 "Hazard Mitigation Investment Decision Making: Organizational Response to Legislative Mandate," by L.A. Arendt, D.J. Alesch and W.J. Petak, 4/9/07 (PB2007-114768).
- MCEER-07-0003 "Seismic Behavior of Bidirectional-Resistant Ductile End Diaphragms with Unbonded Braces in Straight or Skewed Steel Bridges," by O. Celik and M. Bruneau, 4/11/07 (PB2008-105141).

- MCEER-07-0004 "Modeling Pile Behavior in Large Pile Groups Under Lateral Loading," by A.M. Dodds and G.R. Martin, 4/16/07(PB2008-105142).
- MCEER-07-0005 "Experimental Investigation of Blast Performance of Seismically Resistant Concrete-Filled Steel Tube Bridge Piers," by S. Fujikura, M. Bruneau and D. Lopez-Garcia, 4/20/07 (PB2008-105143).
- MCEER-07-0006 "Seismic Analysis of Conventional and Isolated Liquefied Natural Gas Tanks Using Mechanical Analogs," by I.P. Christovasilis and A.S. Whittaker, 5/1/07, not available.
- MCEER-07-0007 "Experimental Seismic Performance Evaluation of Isolation/Restraint Systems for Mechanical Equipment – Part 1: Heavy Equipment Study," by S. Fathali and A. Filiatrault, 6/6/07 (PB2008-105144).
- MCEER-07-0008 "Seismic Vulnerability of Timber Bridges and Timber Substructures," by A.A. Sharma, J.B. Mander, I.M. Friedland and D.R. Allicock, 6/7/07 (PB2008-105145).
- MCEER-07-0009 "Experimental and Analytical Study of the XY-Friction Pendulum (XY-FP) Bearing for Bridge Applications," by C.C. Marin-Artieda, A.S. Whittaker and M.C. Constantinou, 6/7/07 (PB2008-105191).
- MCEER-07-0010 "Proceedings of the PRC-US Earthquake Engineering Forum for Young Researchers," Edited by G.C. Lee and X.Z. Qi, 6/8/07 (PB2008-500058).
- MCEER-07-0011 "Design Recommendations for Perforated Steel Plate Shear Walls," by R. Purba and M. Bruneau, 6/18/07, (PB2008-105192).
- MCEER-07-0012 "Performance of Seismic Isolation Hardware Under Service and Seismic Loading," by M.C. Constantinou, A.S. Whittaker, Y. Kalpakidis, D.M. Fenz and G.P. Warn, 8/27/07, (PB2008-105193).
- MCEER-07-0013 "Experimental Evaluation of the Seismic Performance of Hospital Piping Subassemblies," by E.R. Goodwin, E. Maragakis and A.M. Itani, 9/4/07, (PB2008-105194).
- MCEER-07-0014 "A Simulation Model of Urban Disaster Recovery and Resilience: Implementation for the 1994 Northridge Earthquake," by S. Miles and S.E. Chang, 9/7/07, (PB2008-106426).
- MCEER-07-0015 "Statistical and Mechanistic Fragility Analysis of Concrete Bridges," by M. Shinozuka, S. Banerjee and S-H. Kim, 9/10/07, (PB2008-106427).
- MCEER-07-0016 "Three-Dimensional Modeling of Inelastic Buckling in Frame Structures," by M. Schachter and AM. Reinhorn, 9/13/07, (PB2008-108125).
- MCEER-07-0017 "Modeling of Seismic Wave Scattering on Pile Groups and Caissons," by I. Po Lam, H. Law and C.T. Yang, 9/17/07 (PB2008-108150).
- MCEER-07-0018 "Bridge Foundations: Modeling Large Pile Groups and Caissons for Seismic Design," by I. Po Lam, H. Law and G.R. Martin (Coordinating Author), 12/1/07 (PB2008-111190).
- MCEER-07-0019 "Principles and Performance of Roller Seismic Isolation Bearings for Highway Bridges," by G.C. Lee, Y.C. Ou, Z. Liang, T.C. Niu and J. Song, 12/10/07 (PB2009-110466).
- MCEER-07-0020 "Centrifuge Modeling of Permeability and Pinning Reinforcement Effects on Pile Response to Lateral Spreading," by L.L. Gonzalez-Lagos, T. Abdoun and R. Dobry, 12/10/07 (PB2008-111191).
- MCEER-07-0021 "Damage to the Highway System from the Pisco, Perú Earthquake of August 15, 2007," by J.S. O'Connor, L. Mesa and M. Nykamp, 12/10/07, (PB2008-108126).
- MCEER-07-0022 "Experimental Seismic Performance Evaluation of Isolation/Restraint Systems for Mechanical Equipment – Part 2: Light Equipment Study," by S. Fathali and A. Filiatrault, 12/13/07 (PB2008-111192).
- MCEER-07-0023 "Fragility Considerations in Highway Bridge Design," by M. Shinozuka, S. Banerjee and S.H. Kim, 12/14/07 (PB2008-111193).

- MCEER-07-0024 "Performance Estimates for Seismically Isolated Bridges," by G.P. Warn and A.S. Whittaker, 12/30/07 (PB2008-112230).
- MCEER-08-0001 "Seismic Performance of Steel Girder Bridge Superstructures with Conventional Cross Frames," by L.P. Carden, A.M. Itani and I.G. Buckle, 1/7/08, (PB2008-112231).
- MCEER-08-0002 "Seismic Performance of Steel Girder Bridge Superstructures with Ductile End Cross Frames with Seismic Isolators," by L.P. Carden, A.M. Itani and I.G. Buckle, 1/7/08 (PB2008-112232).
- MCEER-08-0003 "Analytical and Experimental Investigation of a Controlled Rocking Approach for Seismic Protection of Bridge Steel Truss Piers," by M. Pollino and M. Bruneau, 1/21/08 (PB2008-112233).
- MCEER-08-0004 "Linking Lifeline Infrastructure Performance and Community Disaster Resilience: Models and Multi-Stakeholder Processes," by S.E. Chang, C. Pasion, K. Tatebe and R. Ahmad, 3/3/08 (PB2008-112234).
- MCEER-08-0005 "Modal Analysis of Generally Damped Linear Structures Subjected to Seismic Excitations," by J. Song, Y-L. Chu, Z. Liang and G.C. Lee, 3/4/08 (PB2009-102311).
- MCEER-08-0006 "System Performance Under Multi-Hazard Environments," by C. Kafali and M. Grigoriu, 3/4/08 (PB2008-112235).
- MCEER-08-0007 "Mechanical Behavior of Multi-Spherical Sliding Bearings," by D.M. Fenz and M.C. Constantinou, 3/6/08 (PB2008-112236).
- MCEER-08-0008 "Post-Earthquake Restoration of the Los Angeles Water Supply System," by T.H.P. Tabucchi and R.A. Davidson, 3/7/08 (PB2008-112237).
- MCEER-08-0009 "Fragility Analysis of Water Supply Systems," by A. Jacobson and M. Grigoriu, 3/10/08 (PB2009-105545).
- MCEER-08-0010 "Experimental Investigation of Full-Scale Two-Story Steel Plate Shear Walls with Reduced Beam Section Connections," by B. Qu, M. Bruneau, C-H. Lin and K-C. Tsai, 3/17/08 (PB2009-106368).
- MCEER-08-0011 "Seismic Evaluation and Rehabilitation of Critical Components of Electrical Power Systems," S. Ersoy, B. Feizi, A. Ashrafi and M. Ala Saadeghvaziri, 3/17/08 (PB2009-105546).
- MCEER-08-0012 "Seismic Behavior and Design of Boundary Frame Members of Steel Plate Shear Walls," by B. Qu and M. Bruneau, 4/26/08 . (PB2009-106744).
- MCEER-08-0013 "Development and Appraisal of a Numerical Cyclic Loading Protocol for Quantifying Building System Performance," by A. Filiatrault, A. Wanitkorkul and M. Constantinou, 4/27/08 (PB2009-107906).
- MCEER-08-0014 "Structural and Nonstructural Earthquake Design: The Challenge of Integrating Specialty Areas in Designing Complex, Critical Facilities," by W.J. Petak and D.J. Alesch, 4/30/08 (PB2009-107907).
- MCEER-08-0015 "Seismic Performance Evaluation of Water Systems," by Y. Wang and T.D. O'Rourke, 5/5/08 (PB2009-107908).
- MCEER-08-0016 "Seismic Response Modeling of Water Supply Systems," by P. Shi and T.D. O'Rourke, 5/5/08 (PB2009-107910).
- MCEER-08-0017 "Numerical and Experimental Studies of Self-Centering Post-Tensioned Steel Frames," by D. Wang and A. Filiatrault, 5/12/08 (PB2009-110479).
- MCEER-08-0018 "Development, Implementation and Verification of Dynamic Analysis Models for Multi-Spherical Sliding Bearings," by D.M. Fenz and M.C. Constantinou, 8/15/08 (PB2009-107911).
- MCEER-08-0019 "Performance Assessment of Conventional and Base Isolated Nuclear Power Plants for Earthquake Blast Loadings," by Y.N. Huang, A.S. Whittaker and N. Luco, 10/28/08 (PB2009-107912).

- MCEER-08-0020 “Remote Sensing for Resilient Multi-Hazard Disaster Response – Volume I: Introduction to Damage Assessment Methodologies,” by B.J. Adams and R.T. Eguchi, 11/17/08 (PB2010-102695).
- MCEER-08-0021 “Remote Sensing for Resilient Multi-Hazard Disaster Response – Volume II: Counting the Number of Collapsed Buildings Using an Object-Oriented Analysis: Case Study of the 2003 Bam Earthquake,” by L. Gusella, C.K. Huyck and B.J. Adams, 11/17/08 (PB2010-100925).
- MCEER-08-0022 “Remote Sensing for Resilient Multi-Hazard Disaster Response – Volume III: Multi-Sensor Image Fusion Techniques for Robust Neighborhood-Scale Urban Damage Assessment,” by B.J. Adams and A. McMillan, 11/17/08 (PB2010-100926).
- MCEER-08-0023 “Remote Sensing for Resilient Multi-Hazard Disaster Response – Volume IV: A Study of Multi-Temporal and Multi-Resolution SAR Imagery for Post-Katrina Flood Monitoring in New Orleans,” by A. McMillan, J.G. Morley, B.J. Adams and S. Chesworth, 11/17/08 (PB2010-100927).
- MCEER-08-0024 “Remote Sensing for Resilient Multi-Hazard Disaster Response – Volume V: Integration of Remote Sensing Imagery and VIEWS™ Field Data for Post-Hurricane Charley Building Damage Assessment,” by J.A. Womble, K. Mehta and B.J. Adams, 11/17/08 (PB2009-115532).
- MCEER-08-0025 “Building Inventory Compilation for Disaster Management: Application of Remote Sensing and Statistical Modeling,” by P. Sarabandi, A.S. Kiremidjian, R.T. Eguchi and B. J. Adams, 11/20/08 (PB2009-110484).
- MCEER-08-0026 “New Experimental Capabilities and Loading Protocols for Seismic Qualification and Fragility Assessment of Nonstructural Systems,” by R. Retamales, G. Mosqueda, A. Filiatrault and A. Reinhorn, 11/24/08 (PB2009-110485).
- MCEER-08-0027 “Effects of Heating and Load History on the Behavior of Lead-Rubber Bearings,” by I.V. Kalpakidis and M.C. Constantinou, 12/1/08 (PB2009-115533).
- MCEER-08-0028 “Experimental and Analytical Investigation of Blast Performance of Seismically Resistant Bridge Piers,” by S.Fujikura and M. Bruneau, 12/8/08 (PB2009-115534).
- MCEER-08-0029 “Evolutionary Methodology for Aseismic Decision Support,” by Y. Hu and G. Dargush, 12/15/08.
- MCEER-08-0030 “Development of a Steel Plate Shear Wall Bridge Pier System Conceived from a Multi-Hazard Perspective,” by D. Keller and M. Bruneau, 12/19/08 (PB2010-102696).
- MCEER-09-0001 “Modal Analysis of Arbitrarily Damped Three-Dimensional Linear Structures Subjected to Seismic Excitations,” by Y.L. Chu, J. Song and G.C. Lee, 1/31/09 (PB2010-100922).
- MCEER-09-0002 “Air-Blast Effects on Structural Shapes,” by G. Ballantyne, A.S. Whittaker, A.J. Aref and G.F. Dargush, 2/2/09 (PB2010-102697).
- MCEER-09-0003 “Water Supply Performance During Earthquakes and Extreme Events,” by A.L. Bonneau and T.D. O’Rourke, 2/16/09 (PB2010-100923).
- MCEER-09-0004 “Generalized Linear (Mixed) Models of Post-Earthquake Ignitions,” by R.A. Davidson, 7/20/09 (PB2010-102698).
- MCEER-09-0005 “Seismic Testing of a Full-Scale Two-Story Light-Frame Wood Building: NEESWood Benchmark Test,” by I.P. Christovasilis, A. Filiatrault and A. Wanitkorkul, 7/22/09 (PB2012-102401).
- MCEER-09-0006 “IDARC2D Version 7.0: A Program for the Inelastic Damage Analysis of Structures,” by A.M. Reinhorn, H. Roh, M. Sivaselvan, S.K. Kunnath, R.E. Valles, A. Madan, C. Li, R. Lobo and Y.J. Park, 7/28/09 (PB2010-103199).
- MCEER-09-0007 “Enhancements to Hospital Resiliency: Improving Emergency Planning for and Response to Hurricanes,” by D.B. Hess and L.A. Arendt, 7/30/09 (PB2010-100924).

- MCEER-09-0008 "Assessment of Base-Isolated Nuclear Structures for Design and Beyond-Design Basis Earthquake Shaking," by Y.N. Huang, A.S. Whittaker, R.P. Kennedy and R.L. Mayes, 8/20/09 (PB2010-102699).
- MCEER-09-0009 "Quantification of Disaster Resilience of Health Care Facilities," by G.P. Cimellaro, C. Fumo, A.M. Reinhorn and M. Bruneau, 9/14/09 (PB2010-105384).
- MCEER-09-0010 "Performance-Based Assessment and Design of Squat Reinforced Concrete Shear Walls," by C.K. Gulec and A.S. Whittaker, 9/15/09 (PB2010-102700).
- MCEER-09-0011 "Proceedings of the Fourth US-Taiwan Bridge Engineering Workshop," edited by W.P. Yen, J.J. Shen, T.M. Lee and R.B. Zheng, 10/27/09 (PB2010-500009).
- MCEER-09-0012 "Proceedings of the Special International Workshop on Seismic Connection Details for Segmental Bridge Construction," edited by W. Phillip Yen and George C. Lee, 12/21/09 (PB2012-102402).
- MCEER-10-0001 "Direct Displacement Procedure for Performance-Based Seismic Design of Multistory Woodframe Structures," by W. Pang and D. Rosowsky, 4/26/10 (PB2012-102403).
- MCEER-10-0002 "Simplified Direct Displacement Design of Six-Story NEESWood Capstone Building and Pre-Test Seismic Performance Assessment," by W. Pang, D. Rosowsky, J. van de Lindt and S. Pei, 5/28/10 (PB2012-102404).
- MCEER-10-0003 "Integration of Seismic Protection Systems in Performance-Based Seismic Design of Woodframed Structures," by J.K. Shinde and M.D. Symans, 6/18/10 (PB2012-102405).
- MCEER-10-0004 "Modeling and Seismic Evaluation of Nonstructural Components: Testing Frame for Experimental Evaluation of Suspended Ceiling Systems," by A.M. Reinhorn, K.P. Ryu and G. Maddaloni, 6/30/10 (PB2012-102406).
- MCEER-10-0005 "Analytical Development and Experimental Validation of a Structural-Fuse Bridge Pier Concept," by S. El-Bahey and M. Bruneau, 10/1/10 (PB2012-102407).
- MCEER-10-0006 "A Framework for Defining and Measuring Resilience at the Community Scale: The PEOPLES Resilience Framework," by C.S. Renschler, A.E. Frazier, L.A. Arendt, G.P. Cimellaro, A.M. Reinhorn and M. Bruneau, 10/8/10 (PB2012-102408).
- MCEER-10-0007 "Impact of Horizontal Boundary Elements Design on Seismic Behavior of Steel Plate Shear Walls," by R. Purba and M. Bruneau, 11/14/10 (PB2012-102409).
- MCEER-10-0008 "Seismic Testing of a Full-Scale Mid-Rise Building: The NEESWood Capstone Test," by S. Pei, J.W. van de Lindt, S.E. Pryor, H. Shimizu, H. Isoda and D.R. Rammer, 12/1/10 (PB2012-102410).
- MCEER-10-0009 "Modeling the Effects of Detonations of High Explosives to Inform Blast-Resistant Design," by P. Sherkar, A.S. Whittaker and A.J. Aref, 12/1/10 (PB2012-102411).
- MCEER-10-0010 "L'Aquila Earthquake of April 6, 2009 in Italy: Rebuilding a Resilient City to Withstand Multiple Hazards," by G.P. Cimellaro, I.P. Christovasilis, A.M. Reinhorn, A. De Stefano and T. Kirova, 12/29/10.
- MCEER-11-0001 "Numerical and Experimental Investigation of the Seismic Response of Light-Frame Wood Structures," by I.P. Christovasilis and A. Filiatrault, 8/8/11 (PB2012-102412).
- MCEER-11-0002 "Seismic Design and Analysis of a Precast Segmental Concrete Bridge Model," by M. Anagnostopoulou, A. Filiatrault and A. Aref, 9/15/11.
- MCEER-11-0003 "Proceedings of the Workshop on Improving Earthquake Response of Substation Equipment," Edited by A.M. Reinhorn, 9/19/11 (PB2012-102413).
- MCEER-11-0004 "LRFD-Based Analysis and Design Procedures for Bridge Bearings and Seismic Isolators," by M.C. Constantinou, I. Kalpakidis, A. Filiatrault and R.A. Ecker Lay, 9/26/11.

- MCEER-11-0005 “Experimental Seismic Evaluation, Model Parameterization, and Effects of Cold-Formed Steel-Framed Gypsum Partition Walls on the Seismic Performance of an Essential Facility,” by R. Davies, R. Retamales, G. Mosqueda and A. Filiatrault, 10/12/11.
- MCEER-11-0006 “Modeling and Seismic Performance Evaluation of High Voltage Transformers and Bushings,” by A.M. Reinhorn, K. Oikonomou, H. Roh, A. Schiff and L. Kempner, Jr., 10/3/11.
- MCEER-11-0007 “Extreme Load Combinations: A Survey of State Bridge Engineers,” by G.C. Lee, Z. Liang, J.J. Shen and J.S. O’Connor, 10/14/11.
- MCEER-12-0001 “Simplified Analysis Procedures in Support of Performance Based Seismic Design,” by Y.N. Huang and A.S. Whittaker.
- MCEER-12-0002 “Seismic Protection of Electrical Transformer Bushing Systems by Stiffening Techniques,” by M. Koliou, A. Filiatrault, A.M. Reinhorn and N. Oliveto, 6/1/12.
- MCEER-12-0003 “Post-Earthquake Bridge Inspection Guidelines,” by J.S. O’Connor and S. Alampalli, 6/8/12.
- MCEER-12-0004 “Integrated Design Methodology for Isolated Floor Systems in Single-Degree-of-Freedom Structural Fuse Systems,” by S. Cui, M. Bruneau and M.C. Constantinou, 6/13/12.
- MCEER-12-0005 “Characterizing the Rotational Components of Earthquake Ground Motion,” by D. Basu, A.S. Whittaker and M.C. Constantinou, 6/15/12.
- MCEER-12-0006 “Bayesian Fragility for Nonstructural Systems,” by C.H. Lee and M.D. Grigoriu, 9/12/12.
- MCEER-12-0007 “A Numerical Model for Capturing the In-Plane Seismic Response of Interior Metal Stud Partition Walls,” by R.L. Wood and T.C. Hutchinson, 9/12/12.
- MCEER-12-0008 “Assessment of Floor Accelerations in Yielding Buildings,” by J.D. Wieser, G. Pekcan, A.E. Zaghi, A.M. Itani and E. Maragakis, 10/5/12.
- MCEER-13-0001 “Experimental Seismic Study of Pressurized Fire Sprinkler Piping Systems,” by Y. Tian, A. Filiatrault and G. Mosqueda, 4/8/13.
- MCEER-13-0002 “Enhancing Resource Coordination for Multi-Modal Evacuation Planning,” by D.B. Hess, B.W. Conley and C.M. Farrell, 2/8/13.
- MCEER-13-0003 “Seismic Response of Base Isolated Buildings Considering Pounding to Moat Walls,” by A. Masroor and G. Mosqueda, 2/26/13.
- MCEER-13-0004 “Seismic Response Control of Structures Using a Novel Adaptive Passive Negative Stiffness Device,” by D.T.R. Pasala, A.A. Sarlis, S. Nagarajaiah, A.M. Reinhorn, M.C. Constantinou and D.P. Taylor, 6/10/13.
- MCEER-13-0005 “Negative Stiffness Device for Seismic Protection of Structures,” by A.A. Sarlis, D.T.R. Pasala, M.C. Constantinou, A.M. Reinhorn, S. Nagarajaiah and D.P. Taylor, 6/12/13.
- MCEER-13-0006 “Emilia Earthquake of May 20, 2012 in Northern Italy: Rebuilding a Resilient Community to Withstand Multiple Hazards,” by G.P. Cimellaro, M. Chiriatti, A.M. Reinhorn and L. Tirca, June 30, 2013.
- MCEER-13-0007 “Precast Concrete Segmental Components and Systems for Accelerated Bridge Construction in Seismic Regions,” by A.J. Aref, G.C. Lee, Y.C. Ou and P. Sideris, with contributions from K.C. Chang, S. Chen, A. Filiatrault and Y. Zhou, June 13, 2013.
- MCEER-13-0008 “A Study of U.S. Bridge Failures (1980-2012),” by G.C. Lee, S.B. Mohan, C. Huang and B.N. Fard, June 15, 2013.
- MCEER-13-0009 “Development of a Database Framework for Modeling Damaged Bridges,” by G.C. Lee, J.C. Qi and C. Huang, June 16, 2013.

- MCEER-13-0010 “Model of Triple Friction Pendulum Bearing for General Geometric and Frictional Parameters and for Uplift Conditions,” by A.A. Sarlis and M.C. Constantinou, July 1, 2013.
- MCEER-13-0011 “Shake Table Testing of Triple Friction Pendulum Isolators under Extreme Conditions,” by A.A. Sarlis, M.C. Constantinou and A.M. Reinhorn, July 2, 2013.
- MCEER-13-0012 “Theoretical Framework for the Development of MH-LRFD,” by G.C. Lee (coordinating author), H.A. Capers, Jr., C. Huang, J.M. Kulicki, Z. Liang, T. Murphy, J.J.D. Shen, M. Shinozuka and P.W.H. Yen, July 31, 2013.
- MCEER-13-0013 “Seismic Protection of Highway Bridges with Negative Stiffness Devices,” by N.K.A. Attary, M.D. Symans, S. Nagarajaiah, A.M. Reinhorn, M.C. Constantinou, A.A. Sarlis, D.T.R. Pasala, and D.P. Taylor, September 3, 2014.
- MCEER-14-0001 “Simplified Seismic Collapse Capacity-Based Evaluation and Design of Frame Buildings with and without Supplemental Damping Systems,” by M. Hamidia, A. Filiatrault, and A. Aref, May 19, 2014.
- MCEER-14-0002 “Comprehensive Analytical Seismic Fragility of Fire Sprinkler Piping Systems,” by Siavash Soroushian, Emmanuel “Manos” Maragakis, Arash E. Zaghi, Alicia Echevarria, Yuan Tian and Andre Filiatrault, August 26, 2014.
- MCEER-14-0003 “Hybrid Simulation of the Seismic Response of a Steel Moment Frame Building Structure through Collapse,” by M. Del Carpio Ramos, G. Mosqueda and D.G. Lignos, October 30, 2014.
- MCEER-14-0005 “Seismic Performance of Steel Plate Shear Walls Considering Various Design Approaches,” by R. Purba and M. Bruneau, October 31, 2014.
- MCEER-14-0006 “Air-Blast Effects on Civil Structures,” by Jinwon Shin, Andrew S. Whittaker, Amjad J. Aref and David Cormie, October 30, 2014.
- MCEER-14-0007 “Seismic Performance Evaluation of Precast Girders with Field-Cast Ultra High Performance Concrete (UHPC) Connections,” by G.C. Lee, C. Huang, J. Song, and J. S. O’Connor, July 31, 2014.
- MCEER-14-0008 “Post-Earthquake Fire Resistance of Ductile Concrete-Filled Double-Skin Tube Columns,” by Reza Imani, Gilberto Mosqueda and Michel Bruneau, December 1, 2014.
- MCEER-14-0009 “Cyclic Inelastic Behavior of Concrete Filled Sandwich Panel Walls Subjected to In-Plane Flexure,” by Y. Alzeni and M. Bruneau, December 19, 2014.



EARTHQUAKE ENGINEERING TO EXTREME EVENTS

University at Buffalo, The State University of New York

133A Ketter Hall ■ Buffalo, New York 14260-4300

Phone: (716) 645-3391 ■ Fax: (716) 645-3399

Email: mceer@buffalo.edu ■ Web: <http://mceer.buffalo.edu>



University at Buffalo *The State University of New York*

ISSN 1520-295X